Indira Gandhi Centre for Atomic Research

Annual Report 2023

Government of India
Department of Atomic Energy
Indira Gandhi Centre for Atomic Research
Kalpakkam - 603 102

IGC ANNUAL REPORT - 2023

IGCAR

2023

INDIRA GANDHI CENTRE FOR ATOMIC RESEARCH

ANNUAL REPORT

Government of India
Department of Atomic Energy
Indira Gandhi Centre for
Atomic Research
Kalpakkam 603 102

CONTENTS

Address for Correspondence

Shri J. Rajan
Chairman, Editorial Committee
Head, Scientific Information & Networking Division
Indira Gandhi Centre for Atomic Research
Kalpakkam - 603 102
Phone : +91-44-27480281
Email : rjn@igcar.gov.in

e-Copy available at: http://www.igcar.gov.in

Published by
Safety, Quality & Resource Management Group
Indira Gandhi Centre for Atomic Research, Kalpakkam - 603 102

Back to Main

Foreword

Dear Colleagues,

I am delighted to release the IGCAR Annual report of 2023. The report highlights accomplishments in R&D pertaining to fast reactor and associated fuel cycle technologies as well as in the frontier areas of basic and applied research.

Fast Breeder Test Reactor (FBTR) successfully completed 32 irradiation campaigns including three irradiation campaigns at 40 MWt since its first criticality in 1985. In 2023, 21.5 Million units of electricity was generated, which is equivalent to savings of 21,500 tones of CO_2 emission with a cumulative Effective Full Power Days (EFPD) of operation of 115 days. Testing of different composition of Pu/U/Zr metallic fuel is continuing, production of strontium isotope and revamping of many safety related systems has been completed. FBTR has been relicensed for operation up to June 28, 2028. The ^{233}U based Kalpakkam Mini Reactor (KAMINI) continued to operate up to 30 kWt for neutron radiography of irradiated fuel pins, activation analysis of samples from AMD-Hyderabad, ASI, National Forensic Sciences University, other institutions and testing of neutron detectors from M/s ECIL.

The Prototype Fast Breeder Reactor (PFBR) at BHAVINI is in an advanced stage of integrated commissioning and IGCAR continues to provide the required technical support. Many colleagues from various groups of IGCAR are working in synergy with BHAVINI team for the commissioning activities. Major activities like sodium performance testing of the integrated Failed Fuel Location Module (FFLM), the Independent Verification and Validation (IV&V) activities of 17 Real Time Computing (RTC) systems required for Main Vessel Sodium Filling, obtaining regulatory clearances, Support for completion of sodium filling in Main vessel, transfer arm modification works, and operation of primary sodium pumps have been successfully accomplished. Support has also been provided towards commissioning of shutdown systems, fuel handling systems, Primary and secondary sodium pumps, Eddy current flow meter, Annular Linear Induction pumps etc. in PFBR. Activities towards transfer of sodium to the upcoming Sodium Technology Complex (STC) are in full swing.

COmpact Reprocessing facility for Advanced fuels in Lead shielded cells (CORAL), facility has successfully completed its 65th campaign and is continuing to function normally well beyond its design intent. CORAL facility has been relicensed for operation by AERB for a further period of 5 years (up to 2028). Commissioning of Demonstration fast reactor Fuel Reprocessing Plant (DFRP), has reached an advanced stage after the successful completion of the cold run with natural uranium. Necessary responses to queries from AERB for hot commissioning are being addressed and the final approval is expected soon.

As part of metal fuel development activities, the metal fuel, U-Zr, about 200 slugs was produced through injection casting technique. Following electro-refining of uranium metal using pyro-process from a 10 kg facility, the heavy metal from cathode product was consolidated for its ingot production. The radioisotope, Y-90 was isolated from FR-HLLW by separating it out from Sr-90. The first batch of the product has been prepared for its qualification.

In our endeavour towards indigenous development of improved materials and processes, a new Ni-base super-alloy for use in boilers operating at high temperatures has been indigenously manufactured through a multi-organisation collaborative effort involving IGCAR, MIDHANI and NFC. PIE of high LHR operated Mark – I SA has been completed. A facility for studying the structural stability simultaneously at various pressures and temperatures by X-ray diffraction has been established at beam line of INDUS-2, RRCAT (Raja Ramanna Centre for Advanced Technology) through collaborative efforts of scientists from IGCAR & RRCAT units. Control system for 1.7 MV tandetron accelerator has been recently developed with in-house expertise and successfully tested.

Two technologies developed under “Atma Nirbhar Bharat” programmes of IGCAR have been successfully transferred to industry through the Incubation Centre. Two Indian patents have been granted. A collaborative incubation agreement is in place with an industry for completing development of IGCAR’s “Oil Level Measurement System” technology.

Continuing the commitment towards neighborhood community welfare, IGCAR facilitated a Memorandum of Agreement (MoA) between BARC (DAE) and Gram Panchayats of four neighbouring villages around Kalpakkam DAE Complex, Chengalpet District, Tamil Nadu; for setting-up of BARC developed desalination and membrane based RO water purification plant, ultra filtration-membrane based POU (Point-Of-Use) devices and water treatment plant which were installed at different places to benefit the local population.

As part of implementation of DAE Technologies of societal relevance, “Mobile Health – Wellness Program for the Rural Population” has been carried out in the rural areas in and around Chengalpet region, in collaboration with SRM Institute of Science and Technology and SRM Hospitals, Kattankulathur, Tamilnadu. DAE developed health care technologies like OncoDiagnoscope (RRCAT) for detecting oral cancer, Tubercular Scope (RRCAT) for detecting TB, Tele ECG (BARC) for monitoring activity of heart along with IR camera for breast cancer detection (IGCAR) in women are deployed in a mobile van. During May 2023, camps were conducted in the villages in and around Chengalpet, TN. More than 1400 villagers attended and benefited from this free medical camp. Free health camps are being planned by IGCAR in collaboration with SRM University, AP Amaravati & AIIMS – Mangalagiri for benefitting people from surrounding villages.

Towards production of Sr-89 radiopharmaceutical from yttria, production of five batches has been successfully completed and radiochemical quality control has been established. Further activities, including scaling up of the process, Bio-distribution studies etc. are in progress. More than 600 numbers of radiation protection instruments from Hospitals, Nuclear Medicine Centres, Industry, and Research organizations apart from DAE institutions, have been calibrated at the NABL Accredited, Regional Calibration Facility (RCF) which has been augmented with a highly radioactive Co-60 source of 20Ci.

The “Anu Awareness Yatra - 2023” with the theme of ‘ATOMS IN THE SERVICE OF THE NATION’ was organized by IGCAR, Kalpakkam in association with the National Council of Science Museum (NCSM), Ministry of Culture, Government of India, Vigyan Bharathi – Arivial Sangam, Tamil Nadu and Indian Association for Radiation Protection. This awareness program was organized in nodal institutions across 7 districts of Tamil Nadu & 3 districts of Kerala as part of ‘Azadi Ka Amrit Mahotsav’, to showcase the indigenous progress in Science and Technology, from July 24 to August 14, 2023. An exhibition displaying India’s nuclear power programme and societal applications of technologies developed by DAE was also organised with more than 15,000 foot falls.

Towards human resources development, twenty nine young trained scientists and engineers (OCES-2022, 17th Batch) have successfully completed their orientation programme at BARC Training School at IGCAR and have been placed in various units of DAE. About 200 students have pursued project work and about 1200 students and faculty have visited the Centre in the last year. STIPAC and BITS Practice School programmes continue as in the previous years.

Engineering Services has made significant and unique contribution by way of repair/modification of critical components of PFBR. Among various infrastructures that were completed by CEG & ESG to support the R&D activities, a notable achievement is the commissioning of Tertiary water treatment plant of capacity 400 cu. m per day.

Towards the way forward in 2024, apart from the other R&D and regular activities at the various groups of IGCAR and GSO, our focus would continue to be providing support for the integrated commissioning activities of PFBR towards higher temperature operation after Main Vessel Sodium Filling, Completion of IV&V activities of balance RTC systems required for Initial Fuel Loading and subsequent First Approach to Criticality. The hot commissioning of DFRP and operation of DFRP with spent fuel from fast reactor, continuing to operate FBTR at 40 MWt for 90 EFPD, irradiation of advanced FBR structural materials, study the feasibility of producing hydrogen from FBTR super heated steam in collaboration with BARC, commissioning of 1 m fuel pin fabrication facility towards casting U-Pu-Zr metal fuel along with electro-refining facility, producing radioisotope P-32 through irradiation of SrSO4 at FBTR and supply the first batch of radioisotope P-32 to BRIT; and dedication of Doppler Weather Radar Facility would be the milestones to complete in 2024.

I look forward to your support and co-operation in the coming year 2024!.

(B. Venkatraman)
Distinguished Scientist &
Director, IGCAR

Our Primary Mission

To conduct a broad based multidisciplinary programme of scientific research and advanced engineering development, directed towards the establishment of the technology of Sodium Cooled Fast Breeder Reactors (FBR) and associated fuel cycle facilities in the Country. The mission includes the development and applications of new and improved materials, techniques, equipment and systems for FBRs, pursue basic research to achieve breakthroughs in Fast Reactor technology.

Back to Main

Editor's Desk

Dear Reader,

I am pleased to present the Annual Report of IGCAR for 2023 as the Editorial Committee Chairman.

This year, the annual report has 164 technical articles. A significant portion of this report reflects the progress in mission-specific activities of IGCAR concerning FBTR, PFBR, R&D on Fast Breeder Reactors, and the Fuel Cycle. The rest of the chapters indicate the basic research essential for sustained growth in research and development, technology transfers and societal benefit programs. Other supporting development activities are part of the chapter on infrastructure, and resource management.

The articles have gone through multiple editing stages to ensure accuracy and readability. I convey my sincere thanks to the Editorial Committee for their dedicated efforts in successfully bringing out the Annual Report.

Chapter I on Fast Breeder Test Reactor has a few articles that focus on the design and development carried out to operate the reactor at a design power level of 40 MWt, ageing management of Class-II Power Supply System of FBTR and up-gradation of SG pressure control system for reactor operation at 40 MWt.

Chapter II on Prototype Fast Breeder Reactor highlights the commissioning status of PFBR. Articles on the sodium performance testing of the integrated Failed Fuel Location Module (FFLM), and manufacturing & inspection of components for PFBR main vessel pre-heating and sodium filling are given..

Chapter III on R&D for FBR has articles about the center's efforts to develop indigenous technology for future nuclear reactor programs. There are various articles on life-estimation of labyrinth Type V-Ring seal used in shut down mechanisms of PFBR, sodium testing of dismountable type Ultrasonic Transducer, and challenges in QA during leak testing of SS 316L pipe weld joints of sodium technology complex using MSLD.

Chapter IV on Fuel Cycle has articles that provide the latest development carried out towards the hot commissioning of DFRP which includes modification and execution of the process flowsheet and corresponding changes in the plant, a compilation of recent R&D activities towards the process, equipment, materials and analytical tools developed for bettering the technology of FBR spent fuel reprocessing. DFRP is all set for hot commissioning with the plant being dedicated to the nation by the honorable PM Shri Narendra Modi.

Chapter V on Basic Research contains articles covering electronics and instrumentation hardware development for indigenous control system of 1.7 MV accelerator, development of IR microscope to characterize the Te inclusion defects in CdZnTe-based gamma detectors, and positron annihilation spectroscopy study of irradiation-induced defects in Tungsten.

Chapter VI on Infrastructure and Resource Management is a chapter that highlights the efforts and augmentation of essential services, public awareness, and infrastructure management. Article on "Anu Awareness Yatra-2023" with the theme of 'Atoms in the service of the Nation'. Chapter VII has details on the publications, the events, awards, organization, and a summary of the activities of the various groups.

We welcome feedback from readers concerning the quality of the presentation and the technical content therein. We thank the Group Directors for their support and the enthusiastic authors for providing quality articles in the stipulated time. I take this opportunity to thank the editorial team and Dr. Vidya Sundararajnan, Associate Director, RESG in bringing out the Annual Report in expected quality.

The committee sincerely thank Dr. B. Venkatraman, Director, IGCAR, for his keen interest, continued guidance and support towards bringing out the publication in its present form.

Shri. J. Rajan,
Chairman, Editorial Committee &
Head, Scientific Information & Networking Division

Articles at a Glance

Back to Main

Back to Main

IV. Fuel Cycle

Back to Main

Back to Main

Back to Main

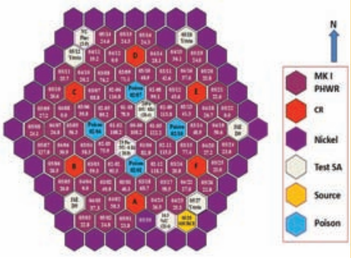

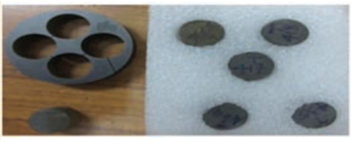

CHAPTER I

Fast Breeder Test Reactor

I.01 Operation of FBTR at Design Power Level of 40 MWt

FBTR, the flagship of the Indira Gandhi Centre for Atomic Research, is continuing its missions of testing metallic fuels, advanced structural materials, indigenously developed neutron detectors, production of radioisotope (Sr89) for societal applications etc. in the fast flux environment and acts as a training facility for future sodium cooled fast reactor operators.

FBTR operation history

FBTR driver fuel consists of indigenously developed Mark-I fuel assembly consisting of 70% PuC & 30% UC. Initially reactor was operated with a small carbide core rated for 10.5 MWt. After gaining confidence on the performance of fuel, reactor power was progressively increased from 10.5 MWt to 32 MWt by expanding the core by adding fresh SAs. After introducing 4 nos of poison subassemblies (B4C enriched with 50% B10) in 2nd ring for enhancing Shut Down Margin (SDM), reactor power could be raised to the designed power of 40 MWt with 68 nos of Mark-I fuel subassemblies in the 30th irradiation campaign in Mar '22. Since then, reactor has been operated at the target power of 40 MWt for its mission based campaigns.

Reactor operation in the 32nd campaign

After completing the 31st irradiation campaign at 40 MWt for about 100 EFPDs on 12 Jan'23, necessary core changes were made for the 32nd irradiation campaign. The core of the 32nd campaign had 69 MK I FSAs, four poison SAs in the second ring, four ISZ SAs with metal fuel pins i.e. two in first ring & the other two in fifth ring and three ISZ experimental SAs with Yttria pins in fifth ring for Strontium production.

The 32nd irradiation campaign at a target power of 40 MWt with 69 MARK-I FSA core was commenced on 10th May 2023. Low power physics experiments such as measurement of control rod worth, isothermal temperature coefficient of reactivity and calibration of Steam Generator Leak Detection System (SGLDS) were completed.

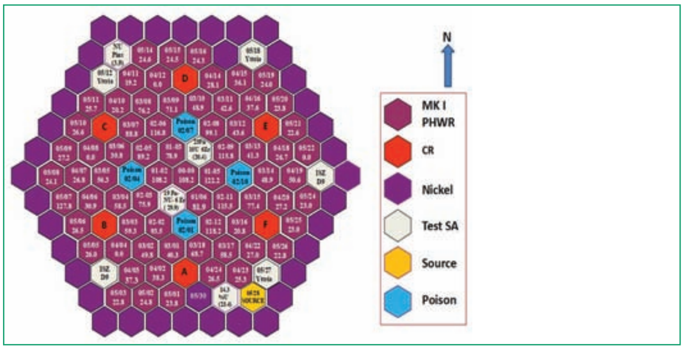

Fig. 1: View of 32nd campaign core configuration

Reactor power was gradually increased to 32 MWt & Turbine Generator was synchronized to the grid. The power coefficient of reactivity was measured while raising the power. After stabilizing the reactor parameters for 24 h, the thermal balance was calculated and neutronic channels were normalized. On 20th May 23, reactor power was raised to 40 MWt with TG output of 10.0 MWe. On 24th May 23, reactor underwent LOR on "East loop SG safe configuration" spuriously due to suspected loose contact in the safe configuration circuit. After rectification, reactor power was again raised to 40 MWt on 28th May 23. After cumulative operation of reactor for ~100 EFPDs at 40 MWt, 32nd irradiation campaign was completed on 8th Sep'23. Reactor was brought to fuel handling state to discharge 3 Yttria SAs from the core & SAs were sent to RML for further processing to extract Strontium-89.

Reactor physics and thermal parameters observed in the 32nd campaign at 40 MWt are as follows:-

Reactor Physics parameters	
Parameters	Value
Temperature Coefficient of reactivity	-3.58 pcm/^{O}C
Power Coefficient of reactivity	-5.84 pcm/MWt
Burn up Coefficient	0.62 pcm/MWd
Shut down margin at BOC (at 180°C)	5429.2 pcm
Total CR worth	9606.3 pcm

Thermal parameters	
32nd campaign	Parameters
Reactor Power/TG Power	40 MWt/10MWe
Beginning of the campaign	10.05.2023
End of the campaign dated	08.09.2023
Reactor inlet/outlet sodium temperature	381 / 480°C
Central SA outlet temperature	515°C
Primary sodium loop flow	650 m^3/h
Secondary sodium loop flow	340 m^3/h
SG inlet/ outlet temperature	191 / 461°C
Feed water flow	72 m^3/h
SG inlet/ outlet pressure	135 /120 kg/cm^2
Cumulative operating days of reactor in 2023	120 days
Electricity generated in this year	21.5 MU

I.02 Periodic Safety Review (PSR) of FBTR for Relicensing

Relicensing of FBTR

The existing license for regular operation of FBTR under Atomic Energy Act, 1962 was valid up to 30.06.2023. As per the AERB safety guidelines for renewal of Operating license (AERB Safety Guide No. AERB/ SG/ O-12), Periodic Safety Review (PSR) needs to be carried out once in 10 years of operation. PSR includes an assessment of plant design, operation against applicable current safety standards & operating practices with an objective of ensuring a high level of safety throughout the plant's operating lifetime.

PSR involves detailed review of plant design w.r.t current codes & guides, performance of safety systems & safety support systems, status of Systems, Structures & Components (SSCs) important to safety, effects of system modifications, ageing management, results of In-Service Inspection (ISI), Safety analysis, use of experience from other NPPs & research findings, qualified manpower and training, radiological protection practices, leadership & management for Safety, human factors, Emergency preparedness & pending regulatory issues etc. The focus areas are divided into 14 Safety Factors (SF) and their review observations and findings are addressed in individual Safety Factor (SF) reports, which are mentioned below:-

PSR Safety Factors as per AERB guide	Description
01	Plant Design
02	Actual condition of SSCs
03	Equipment Qualification
04	Ageing Management
05	Utilization
06	Deterministic Safety Analysis
07	Hazard Analysis
08	Operational Safety Performance
09	Use of experience from other NPPs & research findings
10	Leadership & Management for Safety
11	Procedures
12	Human Factors
13	Emergency Planning
14	Radiological Impact on Environment

Design compliance to present practices was studied. One of the major exercises required was the residual life assessment of the plant equipment as a part of ageing management for components and equipment, which cannot be replaced like block pile components, reactor vessel, grid plate etc. This was done by analysis to estimate the material damage due to neutron dose. Since FBTR was operated below creep range until 14th irradiation campaign, enough residual life is available for the components whose life is governed by creep fatigue damage and the life of FBTR is found to be essentially governed by the neutron dose on the grid plate. Towards assessing the strength and ductility changes of grid plate material subjected to low neutron doses and facilitating life extension of FBTR, accelerated irradiation experiment was conducted in FBTR. Tensile test specimens and disc specimens fabricated from archival FBTR grid plate stainless steel of grade 316 were irradiated in an experimental capsule to a neutron dose of 2.30 to 6.75 dpa at 380°C. Tensile testing of grid plate grade SS 316 samples indicated progressive increase in yield and ultimate tensile strength (UTS) and a corresponding reduction in elongation with increasing dpa. It is inferred that FBTR grid plate can be operated up to about 6.3 dpa based on the design limit of 10% ductility. Cumulative dpa seen by the guide plate of grid plate at the end of the 32nd irradiation campaign was ~3.00. At the target power of 40 MWt in the forthcoming campaigns, dpa/EFPY is estimated as 0.87.

To reduce the neutron flux on the grid plate, tungsten carbide (WC) is used as lower axial shielding material in place of steel for fresh MK I FSAs that are loaded in the reactor core thereby extending the life of grid plate further. When the whole core 70 FSAs are replaced with WC pins as lower axial shielding, the reduction in DPA to the grid plate is 40.5 %. DPA per year (Effective Full Power Year -EFPY) will come down from 0.87 (with SS pins in axial lower shield region) to 0.52 (with WC pins in lower axial shielding).

Detailed assessment was done for equipment qualification, qualification of the plant structures, systems and components for ensuring safe shutdown, decay heat removal and containment, to ensure capability of systems for mitigation of the consequences of events like extended station black out, loss of coolant accident etc. Qualification of instrumentation from sensor to the final element in the channel is ensured for monitoring of temperature, radiation and pressure as part of post accident management taking into account the harsh ambient condition and high radiation.

Equipment like obsolete switch gears, protective instrumentation and plant computers were replaced with state of the art systems.

Based on the detailed PSR, Global Assessment Report (GAR) and Integrated Implementation Plan (IIP) were prepared to collect all the gaps identified in safety factors, to convert into action items/jobs, to prioritize these jobs and to prepare action plans for these. The improvements described in the IIP will resolve the associated gaps to enhance safe and reliable operation of FBTR over the designated PSR period.

This Global Assessment shows that the overall risk associated with operation of FBTR over the designated PSR period is acceptably low. Continued operation of FBTR over the designated PSR period is acceptable based on the results of the Global Assessment. The improvements identified will be implemented through the Integrated Implementation Plan (IIP). Based on the detailed assessment and thorough multi-tier safety review, AERB granted the license to continue reactor operation up to 30th June 2028.

I.03 Life Extension of FBTR Grid Plate

FBTR is operating at design power of 40 MWt from 30th irradiation campaign onwards. The life of FBTR is limited by the residual life of grid plate assembly which supports all the 745 core sub-assemblies, ten cylindrical neutron shields and the diffuser assembly. The irradiation-induced loss of ductility governs the life of grid plate which is a non-replaceable component.

Towards assessing the strength and ductility changes of grid plate material, specimens were subjected to accelerated irradiation in reactor in two irradiation campaigns. PIE results indicated that limiting residual ductility of 10% uniform elongation would be attained at 6.3 dpa.

At present, steel rods are used as lower axial shield material in fuel subassemblies. Hence, in order to reduce neutron-induced damage, various alternate lower axial shield materials were studied considering factors such as reduction in fluence to the grid plate, density changes and loss of reactivity.

Comparison among FeB, WC, B4C and Mo with steel as a reference material was studied. The effectiveness of the shielding material to reduce the neutron damage to grid plate and the reactivity loss caused by their introduction in the FBTR core was evaluated by neutronic computation. While B4C could reduce the grid plate dpa by 60% and FeB by 18%, higher loss of reactivity due to B4C and FeB favored the choice of WC. Tungsten Carbide (WC) is as effective as B4C in reducing the fluence to the grid plate with lowest reactivity loss in comparison to other materials. WC could reduce the dpa by 40.5 % with minimal loss of reactivity. Core reactivity change is only (-) 6 pcm/ FSA which is quite small and hence no reactivity feedback coefficient will get affected.

Studies also indicated that WC does not react on sustained exposure to reactor grade sodium. To study the irradiation behavior of WC, an irradiation experiment was conducted during the 27th and 28th irradiation campaigns of FBTR in which pellets and discs of WC as well as Tungsten were irradiated to a peak fluence of 1.64×10^{22} n/cm^2.

Post irradiation examinations such as visual examination, neutron radiography, dimensional measurement, density measurement and clad micro structural analysis were carried out in RML. Based on very low swelling of WC and no evidence of chemical interaction between WC and SS 316L clad under the test irradiation conditions, WC was considered for replacing the stainless steel rods in the lower axial shield region of core sub-assemblies in place of existing SS shielding pins.

Fig. 1: WC pellets stack, SS 316L clad tube and end plugs

Fig. 2: Sintered WC disc of 40 mm dia &13.1 mm dia WC pellets

Design configuration of WC axial shielding pin is similar to thoria axial blanket pin. For maintaining same hydraulic characteristics as that of existing SS shielding pin, overall length of the pin, wire diameter and pitch of the bundle are maintained same as that of SS shielding pin.

WC pellets were fabricated through powder metallurgy route in MMG. Disc of 40 mm dia was sintered from plasma sintering machine. Further pellets of size 13.1 mm are cut from 40 mm dia disc by EDM wire cut in CWD.

WC axial shielding pin consists of a stack of pellets closed at both the ends by end plugs. Stack length of 231.7 mm & dia 13.1 mm of WC pellets is considered from radial swelling and maximum DPA reduction point of view.

It is planned to load FSAs with WC as lower axial shield progressively from 33rd irradiation campaign onwards. DPA per EFPY is expected to reduce to 0.52 from 0.87 when all 70 FSAs are loaded with WC pins as bottom axial shield.

In the current 33rd irradiation campaign, seven fresh Mark-1 FSAs having WC as lower shield have been loaded. When the whole core is replaced with FSAs having WC pins as lower axial shield, the reduction in DPA will be 40.5 % thereby increasing the life of Grid plate.

The deployment of WC in the lower axial shield region of fuel sub-assembly stands as a promising solution to reduce the neutron induced damage and enhance the overall life span of grid plate and thereby operating life time of FBTR. This proactive approach not only contributes to the ageing management; but also aligns with the commitment to continuous improvement and technological innovation in the realm of nuclear energy.

I.04 Ageing Management of Class-II Power Supply System of FBTR

To cater to the requirements of DC Control and Instrument Power supply of FBTR at various voltage levels, 3 nos 24 V DC, 2 nos 48 V DC, 2 nos 220 V DC battery banks are provided. In addition, 2 nos 220 V single phase, 50 Hz AC Uninterruptible Power Supply (UPS) system provides uninterrupted AC power to various important loads such as chartless recorders, alarm panels, CDPS, control supply for valves, control cards of Primary and Secondary sodium pumps etc. Each UPS system includes a 220 V DC, 645 Ah battery bank, rectifier/charger and inverter. Each battery bank consists 110 nos cells of 2 V rated “Exide” make flooded lead acid type cells. These cells are mounted on the seismically qualified stands.

The rectifier/charger of the UPS system draws input power from emergency buses (Class III), converts into DC which will be again inverted into 220 V 1 Phase 50 Hz AC supply for supplying to the load. Battery Bank is normally in floating mode with rectifier/ charger supplying charging current. Battery Bank supplies the load only during failure of emergency (Class III) power supply. Each battery bank is rated such that it can supply the entire load on the bus for a period of at least 30 minutes.

Though the battery bank is in floating mode, performance may get deteriorated due to ageing related issues over the years. To mitigate the effect of ageing and to avoid catastrophic failure of cells in battery bank, it is replaced after 10 years of service as per the recommendation of SORC.

As a part of ageing management, UPS battery banks (I & II) were replaced in December 2023 one by one. The battery bank under replacement was isolated and the loads were transferred to the other available UPS. Inter-cell connectors were disconnected and the electrolyte present in cells was drained, safely neutralized and disposed. Empty cells were unloaded from the battery stand and handed over to the vendor as a part of buyback scheme; complete cleaning of battery stand was carried out.

Fig. 1: Battery stand after removal of old cells

Fig. 2: Newly replaced UPS battery bank-I

Fig. 3: Newly replaced UPS battery bank II

Wherever required, base plywood plates were replaced. New cells of Exide make and of same capacity were installed and arranged in the stands as per existing layout. The intercell connectors were terminated and petroleum jelly was applied to the terminal posts. Electrolyte was filled. After a soaking period of 12 hours, initial charging was carried out. After initial charging, it was ensured that the new battery bank qualified for 2 consecutive C10 capacity tests followed by half an hour discharge test. Both the battery banks have qualified the site acceptance tests and they are put into service successfully.

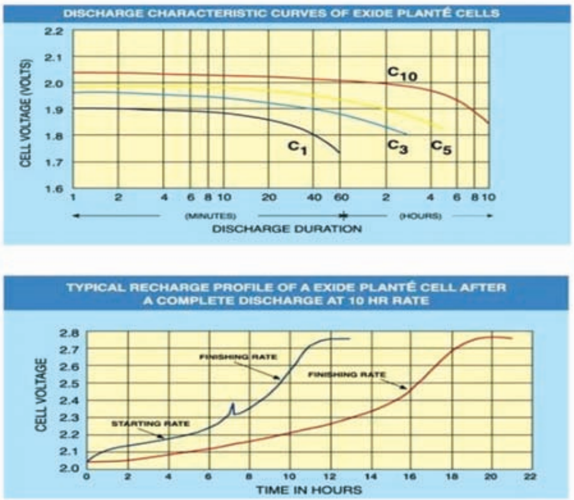

Fig. 4: Discharge and recharge profile of exide plante cells

I.05 Up-gradation of SG Pressure Control System for Reactor Operation at 40 MWt

FBTR heat transport system consists of two primary sodium loops, two secondary sodium loops and one common tertiary steam & water circuit. Steam & water system mainly consists of a once-through steam generator, which produces superheated steam at a pressure of 125 bar and temperature of 480° C, feed water system and condensate system.

Steam pressure at the inlet of steam turbine is maintained at 125 bar (g) and a minimum steam flow of 5 to 9 ton/h is maintained through bypass steam circuit to maintain auxiliary header pressure during normal operation of the plant. Spring loaded safety valves are provided at the common SG outlet steam header of each secondary loop as the ultimate safety against any SG over pressure. To limit the steam header pressure well below the trip setting on 'SG pressure high' during transient conditions such as turbine trip, an instrumented safety relief valve (VRst 818) is provided at the outlet of SG.

The existing VRst 818 is a diaphragm actuated globe type control valve connected to the SG common outlet main steam header at the inlet and the outlet is vented to atmosphere. The valve control logic gives command to open the valve at 129 kg/cm^2 (g) and resets the command when steam pressure reduces below 126 kg/cm^2 (g). It can also be opened and closed from control room console in case manual operation is demanded after satisfying certain conditions.

In the 29th irradiation campaign, it was observed that the steam pressure was crossing LOR thresholds immediately after turbine trip prior to take over of SG relief valve VRst 818. To overcome the issue of delayed opening (~5 sec) of the existing instrumented relief valve, a new relief valve with fast response characteristics has been installed in parallel to the existing SG relief control valve (VRst 818). For installing this valve, a new branch line has been provided in the 150 NB size main steam header. The outlet from the valve after the expander is 200 NB and is vented to atmosphere through the existing vent-line of the existing control valve.

The salient features of new control valve are

(i) It is on-off type valve with a response time of ~1 sec for opening / closing.

(ii) This valve is of 100 NB size & ANSI 1500 class and designed as per ASME B16.34 standards.

Fig.1: Valve installed on pipe line at outlet of SG

(iii) The control valve is provided with pneumatic volume booster and quick exhaust valve to achieve an operating time of 1 second for opening and closing.

(iv) SIL qualified pressure regulators, solenoid valves are used.

As part of quality assurance procedure for the control valve, the following tests were carried

(i) 100% Radiography examination of the valve body and all the welded joints

(ii) Post weld treatment of the welds

(iii) Hydrostatic test for the shell

(iv) Seat leakage test

(v) Functional & performance tests.

Necessary piping modifications were carried out to install the new valve VRst 818A in parallel to the existing valve. Valve body was welded to the new pipeline and actuator was installed. Necessary modifications were carried out in the control logic to operate both valves simultaneously. 'Open / Close' indications for new valve are provided in control room synoptic panel. Functional tests are in progress and its performance will be checked in the forthcoming 33rd irradiation campaign.

I.06

Orifice Diameter Optimization to Avoid Cavitation in FBTR Carrier Subassembly

FBTR Carrier subassembly (Fig. 1) is a special subassembly which holds an irradiation capsule carrying specimens for irradiation in FBTR reactor core, to study the irradiation properties of different materials. The original design of the FBTR carrier subassembly consists of 4 mm diameter orifice (flow restriction sleeve) at the foot of subassembly. Based on pressure drop analysis, the calculated nominal coolant flow rate through subassembly is 0.205 kg/s, for FBTR core pressure drop of 33 m of Na. Hydraulic tests of full scale model of this subassembly were conducted in Hall-II by HES/ETHD/FRTG. Experimental results showed good match with the flow rate estimation values, but cavitation test of the subassembly showed the presence of cavitation near to foot during 100% flow rate condition. It was also found that for orifice value of 15 mm (bare foot), in water hydraulic test conducted previously for Large Bore SA which had the same SA head design as that of carrier SA, cavitation was noticed near to the coolant exit region of SA. Hence, it was needed to check whether the subassembly can be free of cavitation, both in foot and SA head, for any other diameter value of orifice.

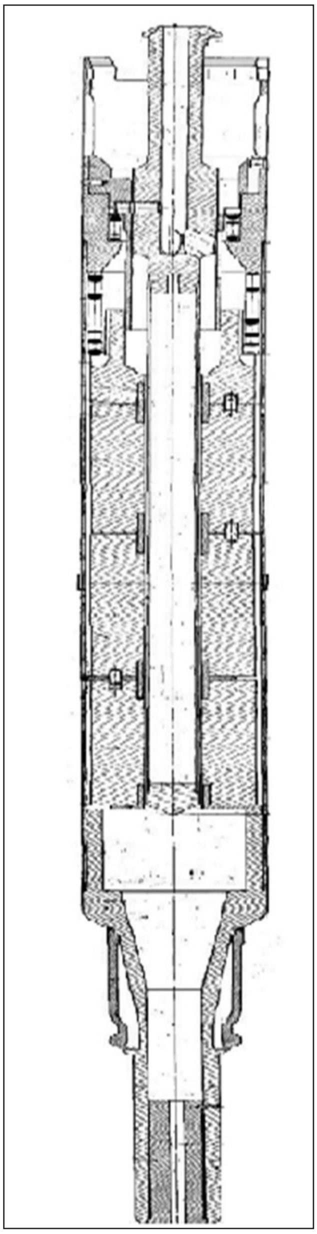

Fig. 1: FBTR Carrier SA

To analyse cavitation in subassembly, pressure drop and flow calculations were carried out for orifice diameter varying from 4 mm to 15 mm. For a fixed value of SA total pressure drop (equal to FBTR core pressure drop), flow rate through SA increases monotonously with increase in orifice diameter, due to decrease in orifice pressure drop. Cavitation Index(CI=(Upstream Pr - Vapour Pr)/∆P) values were calculated for orifice and SA head region for these different flow values.

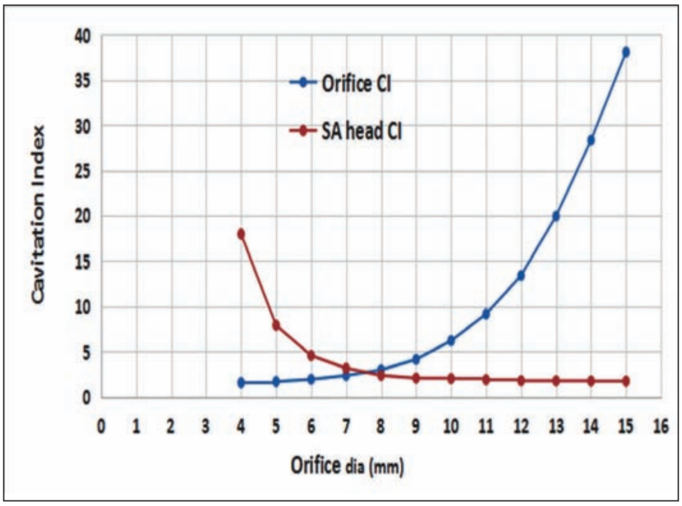

Fig. 2: Orifice CI and SA head CI vs Orifice diameters

It was obtained that the CI of orifice increases and CI of SA head decreases with increase in orifice diameter. The CI of 4mm orifice which had cavitation, near to orifice region, is 1.556. Also, orifice with 6 mm hole diameter was found to cavitate near to foot as per hydraulic test conducted earlier for LBSA (Orifice CI = 1.916). LBSA had same nominal flow rate as that of carrier SA with 6 mm orifice. Hence, to avoid cavitation in orifice region, orifice CI value needs to be kept reasonably high (above 1.916). But, for very high orifice CI values, the corresponding SA head CI will be very low due to increase in flow through SA. Also, water hydraulic test conducted previously for LBSA with the same SA head design as that of carrier SA and orifice value of 15 mm, had indicated cavitation near to the coolant exit region of SA (for SA head CI=1.723).

With these considerations, orifice diameter values in range of 8 mm to 11 mm were opted (Fig. 2), with higher CI values for both orifice region and SA head region. As a first step, 8 mm orifice diameter was chosen for Carrier SA, and when tested experimentally in Hall-II, it was found to be cavitation free. The flow rate estimated was 0.720 kg/s which matched well with experimental value within 5 % accuracy. Hence, 8 mm was opted as the final orifice dimension for FBTR carrier subassembly to avoid cavitation during 100% flow rate condition.

I.07 Performance Assessment of 105GWd/t Burn Up Carbide Fuel Sub-assembly Operated at 400W/cm

A Mk-I carbide fuel sub-assembly (FSA) of FBTR irradiated to 105 GWd/t burnup at uniform LHR of 400 W/cm right from the beginning of irradiation and inlet sodium temperature of 380˚C was taken for Post-Irradiation Examinations (PIE) in hot cells of Radio Metallurgy laboratory. The objective was to assess the life limiting factors and explore the feasibility of extending the burn-up. Non-destructive examinations revealed dimensional changes in the fuel and clad/wrapper of 105 GWd/t FSA, close to that of previous carbide FSA of 155 GWd/t operated at 320 W/cm and sodium inlet temperatures of (350˚C). The results of fission gas release (FGR), fuel-clad microstructure, void swelling and mechanical properties of SS316 clad and wrapper are briefly presented here.

FGR measurements were carried out on eight fuel pins by puncturing the plenum region and collecting the gases in a vial followed by its analysis using gas chromatography and mass spectrometer. The internal pressure in the fuel pins were in the range of 1.3-2 MPa and fission gas release was in the range of 10-17 %.The fuel pin exhibiting maximum increase in length and diameter as well as significant fuel stack length increase was chosen for destructive examinations. Cross sectional and longitudinal fuel clad sections molded in epoxy resin were metallographically prepared and examined under an optical microscope and in Scanning Electron Microscope (SEM). Clad segments after defueling were subjected to density measurements for swelling evaluation and tensile test in a universal testing machine. Swelling and tensile properties of SS316 wrapper were determined using disc and flat tensile specimens.

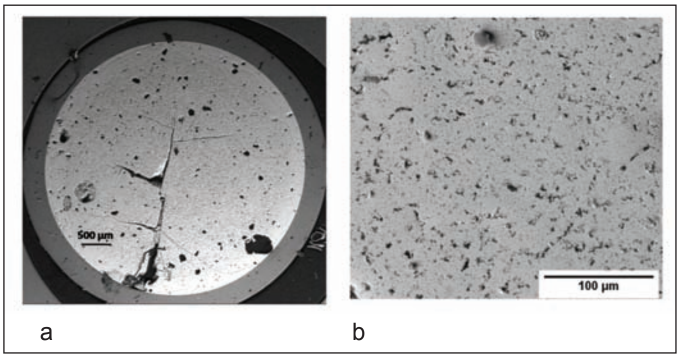

Fig. 1: SEM micrograph of (a) fuel pin cross section (b) Magnified view at the centre-showing presence of porosities

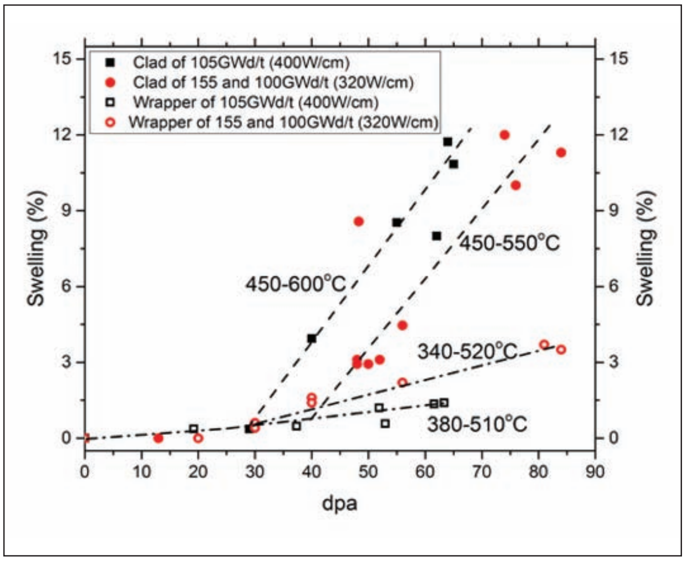

Fig. 2: Comparison of swelling curve of clad and wrapper operated at LHRs 400 & 320 W/cm

The SEM micrograph of fuel pin cross section at peak power location indicated closure of fuel-clad gap and a combination of radial and circumferential cracks (Fig. 1a). The estimated average fuel swelling is ~1.6 per atom % BU, whereas the swelling of fuel of similar burnup operated at lower LHR (320 W/cm) was 1.1% per atom % BU. However, porosities (Fig.1b) existed in the fuel to accommodate further swelling. There was no evidence of clad carburization. The 316 cladding of 105 GWd/t FSA attained 11 % swelling (Fig. 2) at 65 dpa, which is at a faster rate than the cladding exposed to 85 dpa at lower temperatures. The swelling trends of 316 wrappers were similar to previous FSAs of similar dpa. The stress-strain plots of irradiated 316 clad and wrapper specimens of 105 GWd/t indicated residual ductility of ~1% for cladding and ~2% for wrapper at 62 dpa. Both clad and wrapper retained sufficient strength.

The various burnup limiting factors include (i) fission gas pressure, (ii) fuel-clad gap closure and FCMI induced stress, (iii) clad strains due to swelling and clad ductility exhaustion, and (iv) dilation and residual ductility of wrapper. Of the above factors, clad swelling and ductility loss seem to be the dominant factor influencing the burnup extension beyond 105 GWd/t. The PIE results of 105 GWd/t FSA will serve to fine tune the thermo-mechanical model of the fuel assembly behaviour and to explore the possibility of burnup extension.

Back to Main

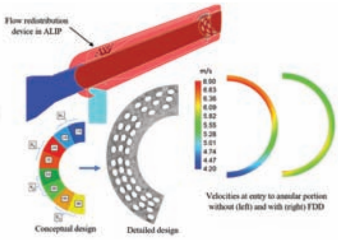

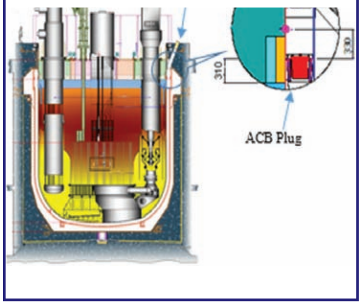

CHAPTER II

Prototype Fast Breeder Reactor

II.01 Commissioning Status of PFBR

Prototype Fast Breeder Reactor (PFBR) at Kalpakkam is a 500 MWe (1250 MWt) liquid sodium cooled, pool type fast reactor using mixed oxide of uranium and plutonium as fuel. The plant is located 500 m south of the existing Madras Atomic Power Station. After completion of manufacture, construction, & erection of all the structures, systems & components of PFBR, commissioning of the individual systems and the integrated commissioning is in progress. Figure 1 shows the overall view of PFBR.

The major works that have been completed during the year 2023 are as follows:

After installation of spare Intermediate Heat Exchanger (IHX) on reactor, an alternate Main Vessel preheating scheme was evolved to start the Main vessel preheating keeping only 3 out of 4 IHXs in place. Accordingly, a modified-spool with increased flow rate was fabricated and installed in position.

Subsequently, Main Vessel was purged with nitrogen and after achieving the required purity; Main Vessel was preheated to 150°C.

Further, testing of in-vessel fuel handling machine (Transfer Arm) and performance testing of Control Rod Safety Drive Mechanism (CSRDM) was completed prior to sodium filling.

The proposal for sodium filling into Main Vessel was submitted and upon thorough review by Regulatory body, clearance from Atomic Energy Regulatory Board (AERB) was obtained. Major milestone of sodium filling of 1150 t in Main Vessel was completed in record time with meticulous planning.

After filling of sodium, primary sodium temperature was raised to 200°C by operating both the secondary sodium pumps. Purification of Sodium in Main vessel at 200°C was completed and the plugging temperature of sodium in Main Vessel was brought down to less than 105°C (impurity level less than 1 ppm) in two weeks' time.

The indigenously designed and developed Primary Sodium Pumps meant for pumping the primary sodium through the reactor core for removing the heat has been commissioned and put into operation. With this, all the four primary and secondary sodium pumps were put into operation.

Prior to installation of Diverse Safety Rod Drive Mechanism (DSRDM) in its positions on pile, three nos. of Ferromagnetic particle collectors were installed in the DSRDM locations to collect the magnetic impurities in the sodium, if any. After confirming that no magnetic impurities are present in the sodium, the DSRDM's were installed and Performance testing of CSRDMs and DSRDMs in Sodium at 200°C was carried out.

As a part of in-core Fuel handling demonstrations, five full rotation of Small Rotatable Plug is completed and 5 nos. of SAs were handled as a part in-core fuel handling trials in sodium at 200ºC.

Commissioning of both Cell Transfer Machines and Spent Sub-assembly Transfer Machine are completed in air atmosphere. Preparatory works are in progress for Nitrogen filling in Fuel Transfer Cell. De-mineralized water filling in Spent Sub-assembly Storage Bay has been commenced.

Back charging of Generator Transformer was completed and Unit Auxiliary Transformer-1&2 was energised and both are in service.

Fig. 1: BHAVINI

II.02

Integrated Transient Thermo-mechanical Analysis Towards Identifying the Potential Cause of IHX leakage During Pre-Commissioning Operations

Prototype Fast Breeder Reactor (PFBR) consists of 4 Intermediate Heat Exchangers (IHXs) with equal capacity connected to two secondary loops (loop-1 and loop-2), each loop containing two IHXs. It is a vertical, counter current, shell and tube type, sodium to sodium heat exchanger. Primary sodium from the hot pool (at 547°C) enters the shell through the windows at the top of the tube bundle region and exits to the cold pool (at 397°C) through the windows at the bottom. The secondary sodium (at 355°C) enters the IHX through the downcomer pipe, flows downwards and then rises through the tubes gaining heat from the primary sodium (reaches 525°C).

During the pre-commissioning activities of the secondary sodium circuit, the IHX was filled with sodium on the tube side and the shell side was heated through nitrogen gas. The co-existence of high heat transfer behaviour sodium on one side and a relatively low heat transfer behaviour nitrogen on the other side of a thin shell develops significant temperature differences during the thermal transient conditions such as secondary sodium filling and draining cycles. A maximum ΔT of ~94°C (sodium is at 260°C and nitrogen is at 166°C) is experienced in loop-1 during sodium draining condition.

Detailed integrated transient thermal stress analysis of IHX assembly is carried out to estimate the impact of these cycles on critical junctions viz. tube-to-tube sheet and inner shell-tube sheet. The finite element model of the IHX assembly is shown in Fig.1. The critical junctions are modelled with solid elements to capture the maximum stress responsible for the damage.

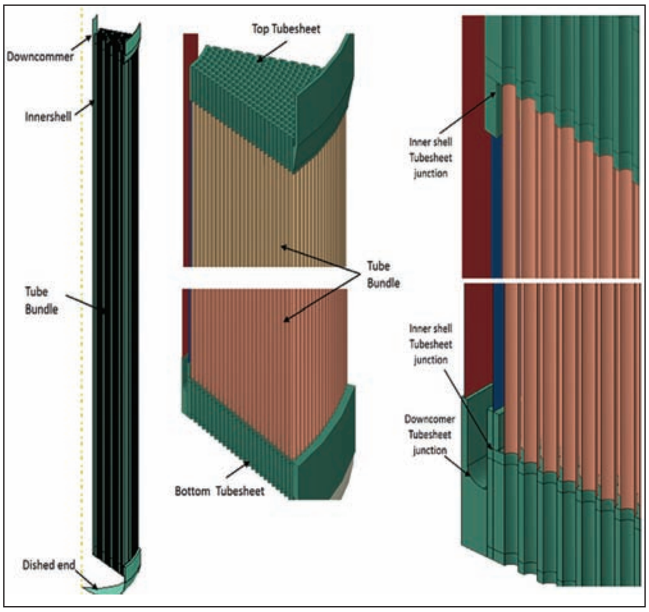

Fig. 1: Intermediate Heat Exchangers Finite Element Model

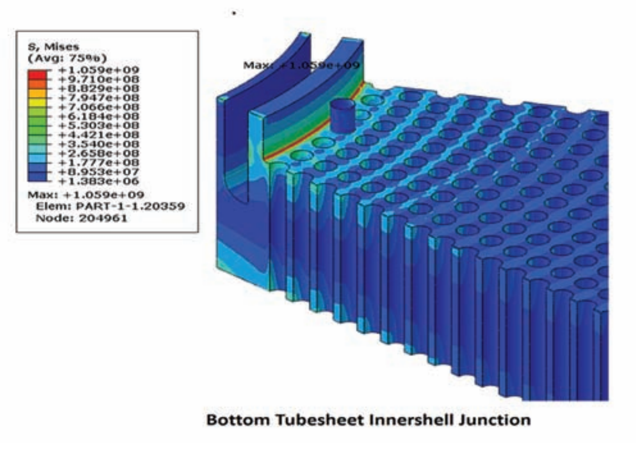

Fig. 2: Stress distribution in innershell-tubesheet junction for top and bottom tubesheet during the sodium drain cycle.

Transient temperature evolution is imposed on each row of the tube, tube sheet (axial & radial) gradient inner shell, downcomer and other locations. The temperature evolution suggests that the innermost row of the tube bundle is cooled relatively slower than the outer rows and results in the bending of the tube sheets. This behaviour causes relative straining between the different parts of IHX and developed stress.

The maximum stress observed during the pre-commissioning transients is at the bottom tube sheet to the inner shell junction of 1059 MPa, as shown in Fig.2. The other critical locations are the top tubesheet-inner shell junction of 660 MPa and the bottom tube-tubesheet junction belonging to the innermost row of 547 MPa. These results suggest that at least 85 times the occurrence of the sodium draining corresponds to a maximum ΔT of ~94°C shall be experienced in secondary sodium loop-1 during the pre-commissioning operation to initiate the crack at the bottom tube sheet to the inner shell junction. Other locations need more cycles, and these situations are ruled out from the operated history of PFBR. Hence, the potential cause of early leakage could be due to the other issues associated with manufacturing defects or corrosion.

II.03

Alternate Design of Subassembly Discriminator and Handling Head to Avoid Stuck-Up and Scoring of Subassembly of PFBR

During qualification tests of Transfer Arm (TA) under pre-heated condition of PFBR Reactor Assembly, few subassemblies (SA) were found stuck in grid plate (GP). During further investigations, scoring marks were observed on the SA hexcan. Root cause analysis (RCA) of the SA stuck up and hexcan scoring was carried out and following inferences were made.

1. Discriminator is a part of a SA foot for identification / avoiding wrong loading in the core. It has machined flat surfaces for coolant flow. The edge formed after machining operation was sharp, which interacted with GP sleeve guide where the gap was already less (~30-60 µm radial). These interactions with high contact pressures resulted in cold bonding between the components. Higher force was required to break the bond and extract the SA.

2. Handling head of a SA has self-orientation feature (SOF) so that the SA can properly align itself in the core passively. Combined effect of sharp edges of SOF of neighboring SAs & SA being handled with offset TA resulted in scoring on hexcan of a handled SA as well as neighboring SAs.

Based on the RCA, the sharp edges on SA foot discriminator guide and corners of SOF were smoothened to the extent possible. Also, the clearance at the guide region was increased by reducing diameter of discriminator guide. These modifications are suffice for limited instances of SA handling. Any increased number of handling events may increase extraction loads/scoring of hexcan. Hence, it is required to eliminate the stuck up & scoring marks possibilities all-together by design. Thus, alternate design of SA discriminator and handling head has been carried out.

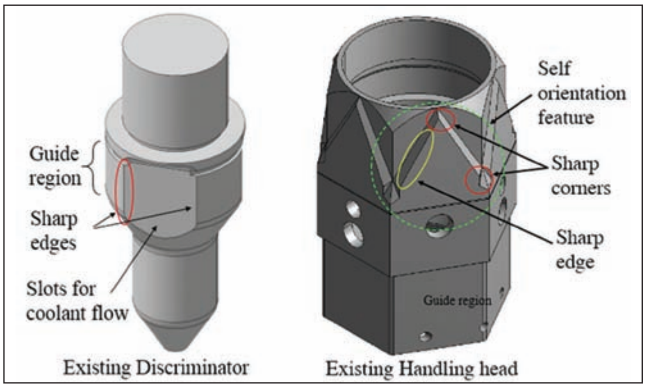

Fig. 1: Existing designs of Discriminator and handling head

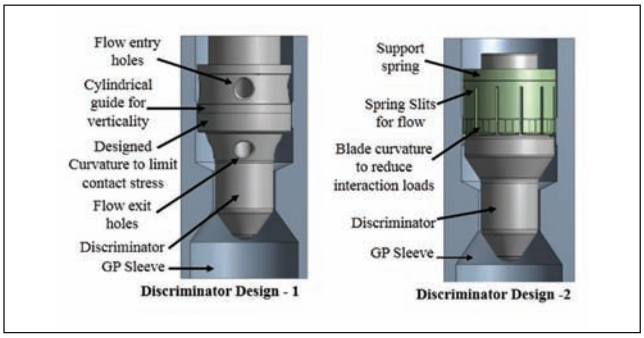

Fig. 2: Alternate designs of discriminator

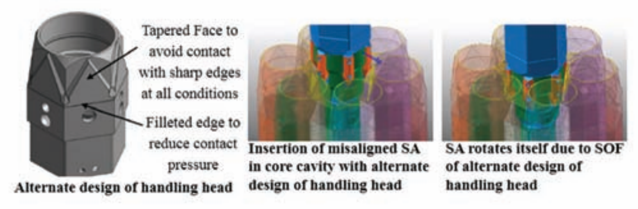

Fig. 3: Alternate Design of Handling head

Alternate Design of Discriminator

The alternate discriminator design was envisaged considering identification of wrong loading, limited contact stress upon interaction, no change in hydraulic performance for bottom leakage flow, etc. Two designs were arrived at viz.

i) Design 1: Discriminator with cylindrical guide (Fig 1) – no sharp edges and curvature at guide location will limit the contact stress within limit,

ii) Design 2: Discriminator with support spring (Fig 2) - continuous contact of the foot with sleeve, which minimizes FIV and provides more fault tolerance in case interaction debris is generated.

Selection and implementation of the most desirable Discriminator will be made after successful experimental demonstration of the design concepts which is under progress.

Alternate Design of handling head

The alternate design of handling head was carried out to avoid contact between hexcan of handled SA and SOF of adjacent SAs by giving taper to the head. The taper angle 2° was arrived at considering maximum possible tilt in SA during handling, bowing effect, etc. It is verified with MBD code that the tapering within the provided angle does not affect the self-orientation of a SA during insertion. The changes will be implemented after verifying the effectiveness through testing.

II.04 Seismic Analysis of PFBR Trailing Cable System Support Structure

In PFBR, cables are used to carry power, control and instrumentation signals from top shield and other equipment located in top shield to their associated control panels located outside top shield. Cable connections carrying vital signals related to reactor safety, which are required even during the rotation of the Large Rotating Plug (LRP) and Small Rotating Plug (SRP) are maintained through a special arrangement known as trailing cable system. Trailing cable system consists of three posts each mounted in SRP, LRP, and roof slab respectively along with overhanging arms through which cables are routed in a predetermined way from each post as shown in Fig-1. The cables originating from the LRP are first taken up the LRP post top and routed between LRP-SRP posts through two overhanging arms A & B. In SRP, the cables originating from SRP joins the cables from LRP and are taken up further along the SRP post to the top. From the SRP post top, the cables are routed through another set of overhanging arms 'C' and 'D' using cable guiding mechanism to the outside of roof slab.

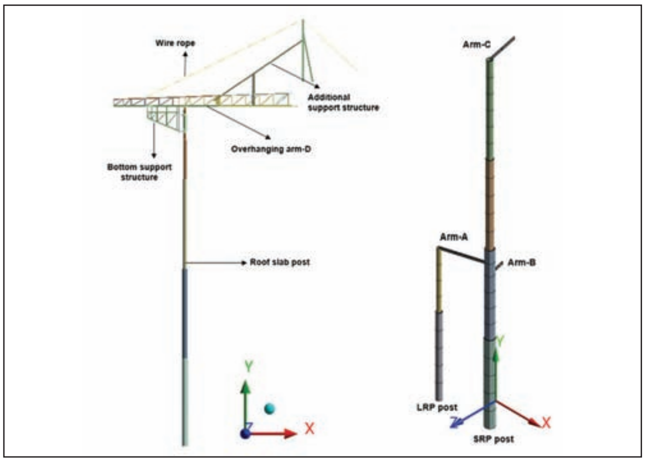

Fig. 2: FE models of trailing cable system support structure

Trailing cable system is classified as safety class III and categorized under seismic category-I, since even under Safe Shutdown Earthquake (SSE) these cable systems are required for the reactor scram. The system is designed as per the requirements laid out in AERB safety standard AERB/SS/CSE-2 and IS: 800-code of practice for general construction in steel. Based on site constraints during erection and to meet single failure proof criteria, design configuration of trailing cable system was modified. Modelling, Finite Element Analysis (FEA) and design check of the trailing cable system were performed as per AERB codal rules to ensure

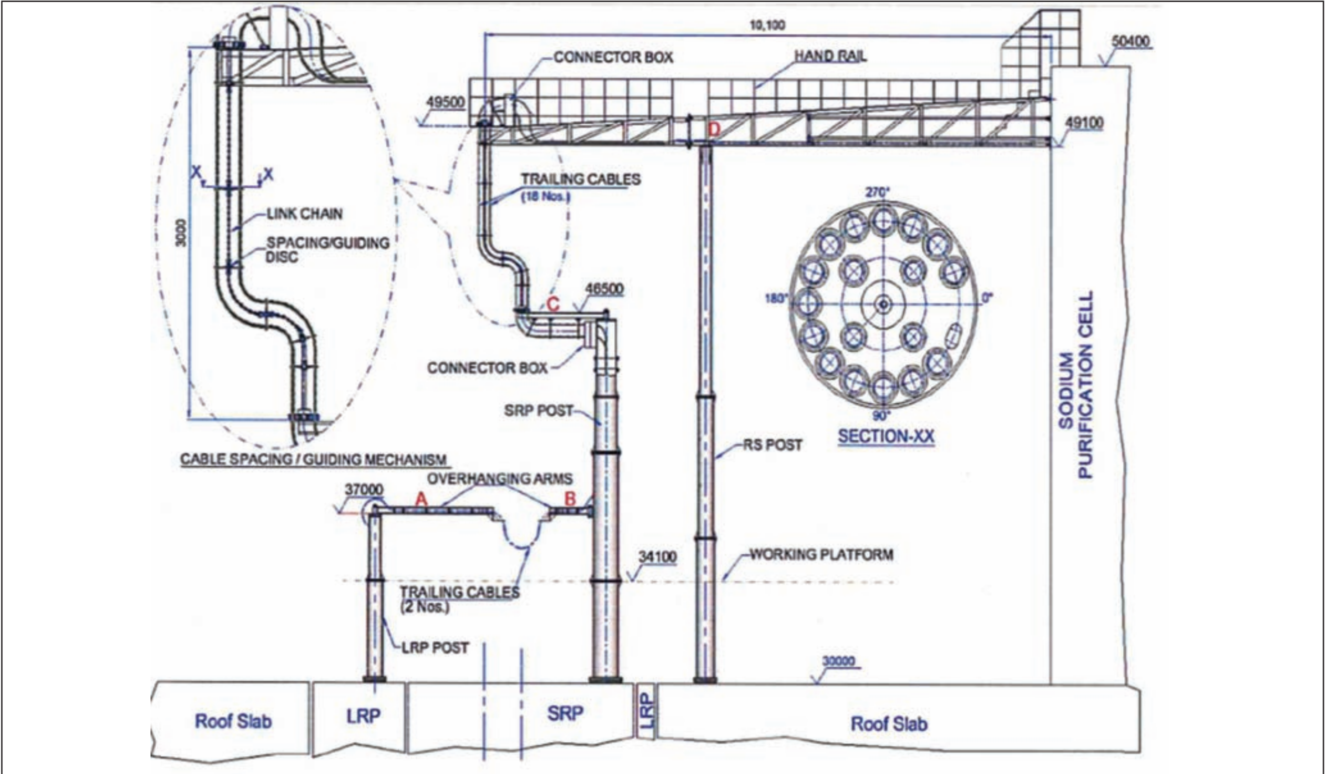

Fig. 1: Schematic of Trailing Cable system

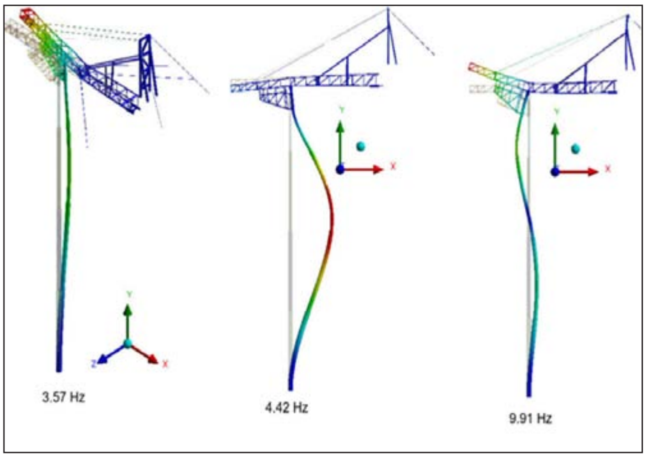

Fig. 3: Important mode of roof slab post FE model

the structural integrity for the as-built configuration for operating basis earthquake (OBE) and safe shutdown earthquake (SSE) conditions.

FEA of trailing cable system

Three independent models of the structural support members of trailing cable system (considering cables flexibility) were developed using beam, shell and truss elements as shown in Fig-2.

i. LRP post with overhanging arm-A

ii. SRP post with overhanging arm-B & C

iii. Roof slab post with overhanging arm-D

Initially, static analysis was carried out for all the FE models considering self-weight, distributed (cable) and lumped masses (connector discs, connector box etc). Static analysis was followed by modal analysis to determine the dynamic characteristics. Fundamental frequencies of Roof slab post, SRP post and LRP post are 3.57Hz, 1.5Hz and 5.5Hz respectively. Mode analysis results indicated that typical beam bending mode shapes of all the posts have higher effective masses. Some critical mode shapes of RS post FE model are given in Fig.3.

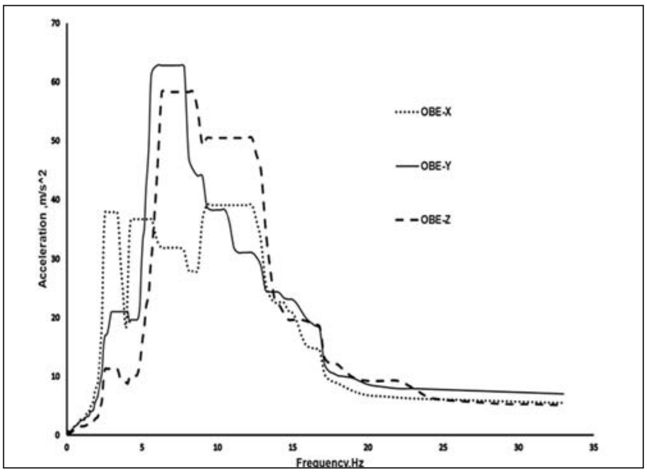

Fig. 4: Enveloped response spectrums corresponding to 2% damping for OBE

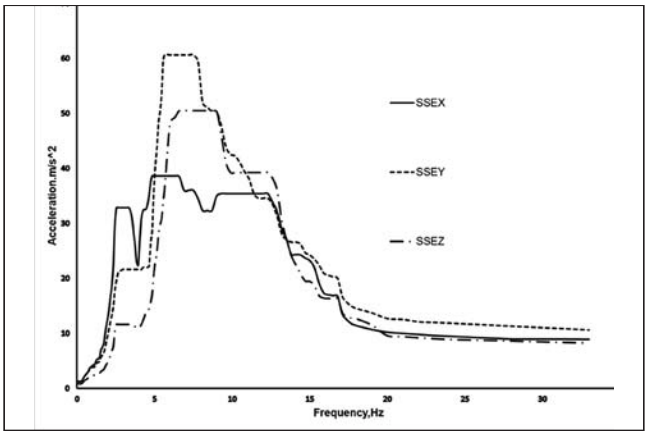

Fig. 5: Enveloped response spectrums corresponding to 4% damping for SSE

Subsequent to modal analysis, seismic analyses of all the posts with over hanging frame were carried out by response spectrum method for OBE and SSE loads. Spectrums corresponding to the elevations EL29.550 m, EL46.860 m, EL50 m in Reactor containment building corresponding to 2% damping for OBE (fig.4) and 4 % damping for SSE (fig.5) were enveloped and used for seismic analysis of Roof slab post model. For LRP and SRP post spectrums corresponding to the elevations EL29.550 Modal combination and directional combinations are done using SRSS combination method. Missing mass correction is considered to account for contributions of the modes above the cutoff frequency of 33 Hz

Design check and iterative analysis

Design check of the structural members of the trailing cable systems was carried out as per the AERB standard on steel design. Induced stresses due to static and seismic loads for all the posts (LRP, SRP and Roof slab post) and the overhanging arms (A to C) of trailing cable system were within the allowable limits. But induced stress in the overhanging arm-D connected to roof slab post was exceeding the allowable limit for seismic loads. Hence, iterative response spectrum analysis was carried out and the weak regions of the overhanging arm-D was strengthened to respect the allowable limits.

II.05

Prediction of Performance of SGDHR Circuit with Different Hot Pool Temperature and Damper Opening Angle

In PFBR, there are 4 independent Safety Grade Decay Heat Removal system (SGDHR) loops each having thermal capacity of 8 MW for hot pool temperature of 550° C [1]. Each loop of SGDHR system consists of a sodium-to-sodium heat exchanger (DHX), sodium to air heat exchanger (AHX), an expansion tank, connected piping, an insulated chimney with top hood and damper at AHX airside inlet and outlet as shown in Fig. 1. DHX transfers the heat from hot pool to the intermediate loop of the SGDHR system. The heat transferred to the intermediate loop is dumped to the atmospheric air through AHX which is located at a higher elevation. The piping from DHX outlet to expansion tank and further to AHX inlet is called as hot leg and the piping from AHX outlet to DHX inlet is called as cold leg. The density difference caused by the temperature difference between the hot and cold legs along with the elevation difference between the DHX and AHX induces buoyancy driven sodium flow in the intermediate loop. The 30 m tall chimney induces the cross flow of air through the finned sodium tubes of AHX. A damper system with two louvers located at both AHX inlet and outlet, minimises heat loss from the reactor during normal operation. During normal operation of the reactor, the damper will be in crack open condition to ensure a sodium flow in the favourable direction in intermediate loop and it will be full open when the SGDHR system is on demand.

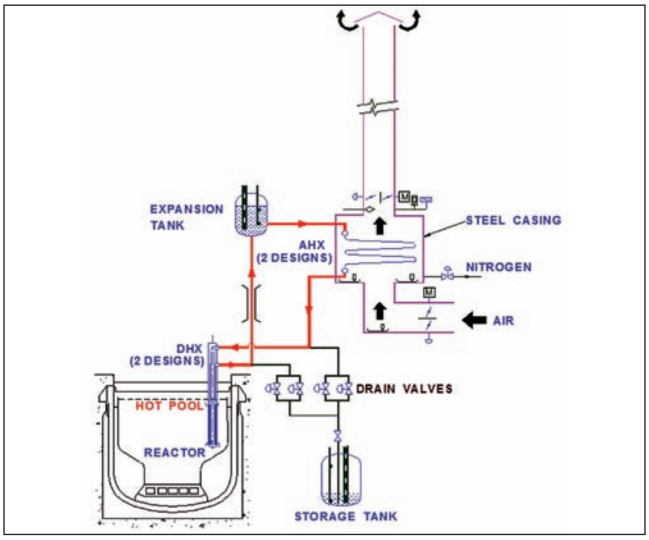

Fig. 1: Schematic arrangement of Safety Grade Decay Heat Removal system

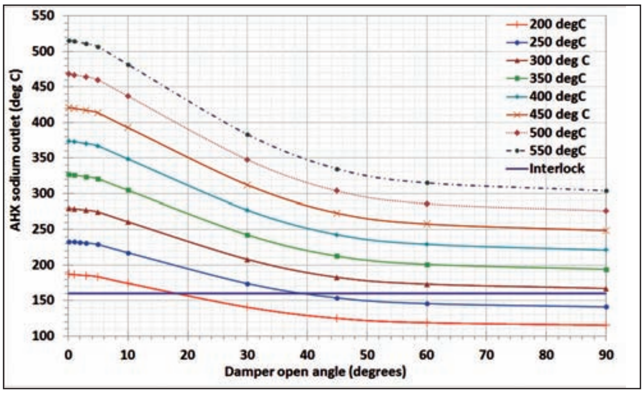

Fig. 2: AHX sodium outlet temperature with respect to damper opening angle

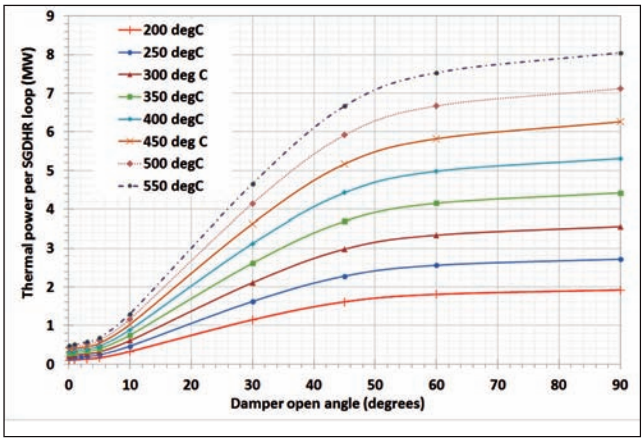

Fig. 3: Thermal power capacity per loop with respect to damper opening angle

The performance of SGDHR circuit like, thermal power capacity of the loop, flow through shell and tube side of both DHX & AHX, inlet and outlet temperatures of both sodium and air are predicted using in-house code "SGDHR" for different hot pool temperatures from 200 to 550° C and for damper opening angle from 0.1 to 90° . Predicted AHX sodium outlet temperature for various hot pool temperature and damper opening angle is given in Fig. 2. It is observed that the AHX sodium outlet temperature falls below 160° C, for damper opening angle above 16 ° and 36° for hot pool sodium temperature of 200 °C and 250 °C respectively, which is the interlock limit for damper closure to avoid sodium freezing at AHX outlet.

The overall thermal power capacities for each damper open case are also predicted for various sodium temperature and given in Fig. 3. It can be inferred that about 60° damper opening is able to remove about 93% of the rated thermal power of the loop. The obtained results will be beneficial for initial commissioning and for future operation of SGDHR loops in PFBR.

II.06

Design of a Flow Redistribution Device to Achieve Uniform Flow of Entry into the Annular Portion of ALIP for SSFDC

The entry to the annular passage of Annular Linear Induction Pump (ALIP) of secondary sodium fill and drain circuit (SSFDC), receives sodium from single radial nozzle that injects fluid into a transition region (inlet plenum) between the inner and outer ducts. This leads to a significant flow mal-distribution at the inlet of the annular portion. Such mal-distribution can lead to onset of magneto-hydrodynamic instability. In order to achieve a circumferential uniform velocity of entry into the annular portion of ALIP, a variable porosity porous plate has been conceived and devised with the help of CFD studies. Towards this, a three-dimensional 180° sector model of modified ALIP, currently installed at PFBR is developed. The model is meshed using about 2.9 million hexahedral elements. A variable porosity device with porosities distributed in five sectors was arrived at after an initial set of studies. In addition to reduction in velocity mal-distribution, additional pressure drop was minimised. Further, for ease of implementation, the device is kept at an angle of 45° with horizontal. This maximises area available and allows flexibility during manufacturing process. In the final configuration arrived at, the difference between maximum and minimum velocities reduces from 2.4 m/s to 0.3 m/s after installation of the device.The pressure drop increases by about 20 %.

The conceptual design is converted into a detailed design with the help of variable distributed circular holes in a plate of thickness 3 mm. This is the Flow Distribution Device (FDD). The hole size and number of holes are decided to match with the porosity requirement with limitation on minimal ligament length between holes and uniform spacing within each sector. The hole size is restricted to minimum of 10 mm for the FDD based on engineering judgement to minimise flow blockage in the sodium flow path during long term operation. The number of holes is decided for each sector based on the correlation of Ward-Smith and maintaining minimum ligament size required for forming. Based on the proposed configuration, an actual porous plate that can be manufactured and installed in an ALIP is devised and numerically analysed and validated. The mal-distribution in velocity at inlet to the annular portion is reduced significantly in line with earlier studies. Contours of velocity magnitudes with and without FDD are presented in Fig. 1. The device has been subjected to further testing at in-house water loops.

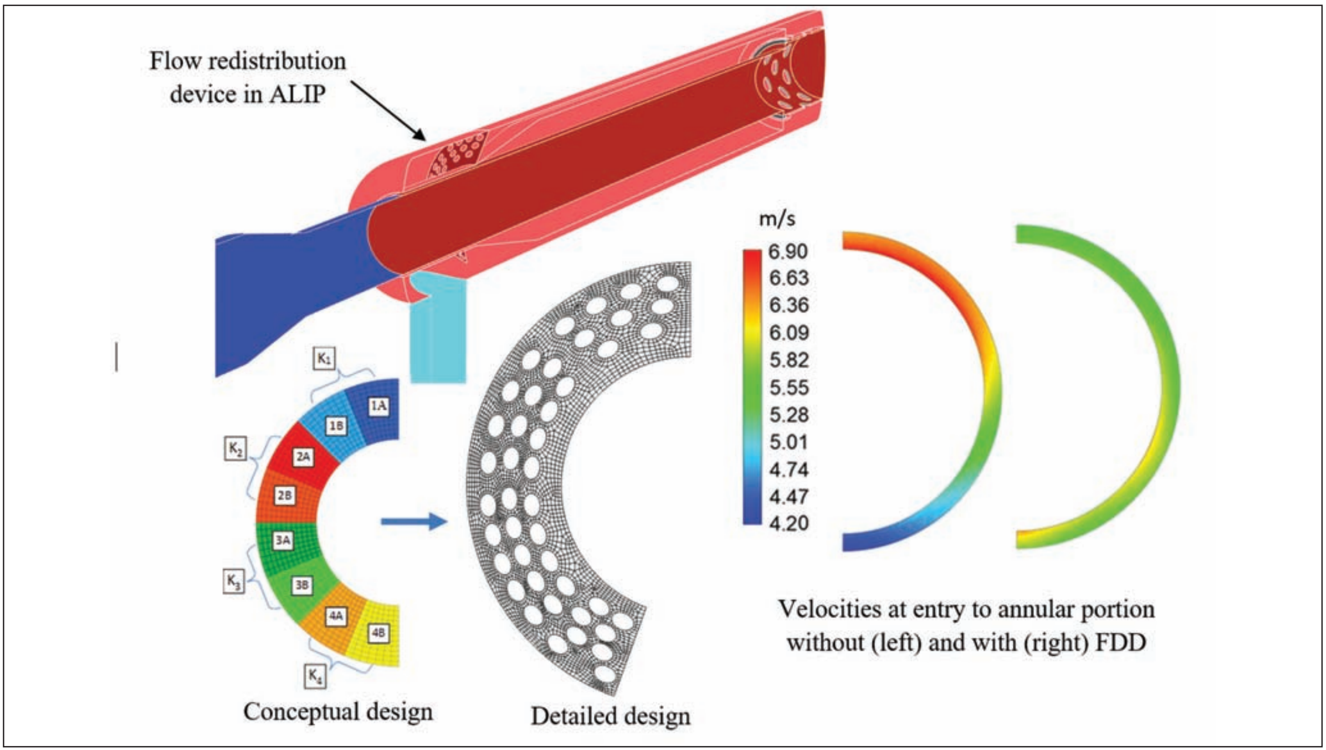

Fig. 1: Modelling approach followed for design of Flow Distribution Device

II.07 Design Improvements to Under Sodium Ultra Sonic Scanner and its implementation based on Commissioning Feedback

Under Sodium Ultra Sonic Scanner (USUSS) will be used in PFBR to scan the region below control plug to check for presence of any protrusion prior to start of rotation of rotatable plugs. The device has been developed, tested at IGCAR and being commissioned at PFBR site. During commissioning trails of USUSS at site, high torque was observed during rotary motion and issues were faced in the shear pin. Based on theoretical study & manual torque investigations, it was understood that increase in torque is due to issues in the Harmonic drive gearbox in the Upper part of USUSS. Decision was taken to replace the same.

Planetary gearbox was selected to replace the imported Harmonic drive gearbox, considering the gear reduction ratio, compact size requirement, conventional type, ease of availability, experience in usage and preference for Indian make. Many arrangements were studied to incorporate the planetary gear box in the existing USUSS design. Based on the study, connecting the gearbox directly with motor was chosen. In this option, the number of parts & number of modifications required is less and it meets the design and functional requirements. Shear pin, which act as a protection against higher torque is also replaced with torque limiter, which provides reliable protection. The modifications required to incorporate the torque limiter was also carried out. Considering the difficulty in assembly & disassembly of hollow shaft encoder in upper part, a solid shaft encoder was chosen as an alternate and a provision to incorporate the same in the existing USUSS was carried out. Upper part assembly with modifications is shown in Fig. 1.

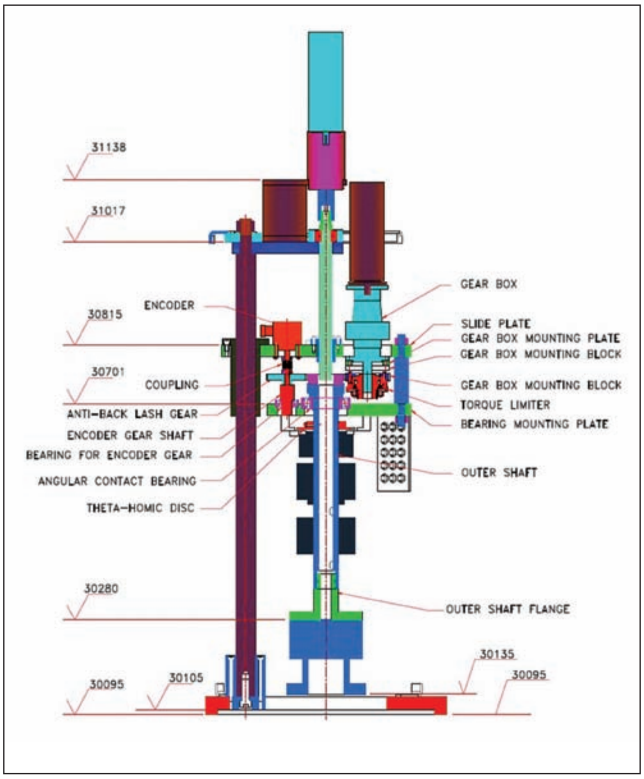

Fig. 1: Upper Part of Under Sodium Ultra Sonic Scanner with modifications

Currently the movable parts of lower part of USUSS are supported on the upper part and there is no independent support for lower part as well as no provision to separately measure the torque in the lower part. Hence, design changes were made to support the lower part using thrust bearing to measure the torque in it.

Considering the issues faced during routing of MI cables in the radiation shielding block, modifications were carried out in radiation shielding block by cutting it into two halves for easy routing of MI cables. Two dynamic O – ring seals are provided in series at the top of the spinner tube to arrest the argon leak. These seals rub against spinner tube during rotary and translatory motion. Design modification and procedure are made to replace these dynamic O – rings, in case seals are damaged.

The above mentioned recommendations are implemented in USUSS of PFBR at the site through disassembly of existing USUSS, procurement of items, fabrication of few parts of Upper Part & Lower part and assembly of Upper Part with Lower Part. All the modification works were carried out in house.

The measured torque in the coupled USUSS after completing modification works & assembly was within the limit. The trial runs for checking the functionality were successfully completed and the scanner is ready for deployment inside the reactor for commissioning activities in hot sodium.

II.08

Design & Development of Bore Dimension Measurement System for the Precise Remote Measurement of ISI Port in PFBR Using Laser Range Sensor

The In-service Inspection (ISI) port of PFBR provide access to the ISI vehicle to be deployed into the reactor and the overall inner dimensions of the ISI port only govern the maximum permissible dimension of the ISI vehicle. Hence, a comprehensive system to measure the inner dimensions (both shape and size) of the ISI port is designed and developed with the bore dimension measurement system (BDMS). The BDMS uses a laser-based range sensor to measure the inner dimensions of the ISI port. The mechanical design of BDMS consists of a compact z-stage involving axial motion of 2 metre stroke length with nut and screw mechanism and a complete 360° rotation θ-stage gear mechanism for cross-section dimension profile mapping using the laser sensor with 1° angular interval.

The mechanical system of BDMS is integrated with PLC and the Human Machine Interface (HMI) for the control of motors, laser sensor and data acquisition system to carry out the internal dimension measurement of the ISI port. Two axes motion control system consists of two numbers of BLDC servo drives, integrated HMI with PLC connected through CANopen communication protocol. Data acquisition of the non-contact laser sensor is carried out by analog input module and program is developed for storing sensor data. Home and end limit switches were implemented in the drive level. It is programmed for in-situ calibration, auto sequencing of z-stage & θ-stage, homing and data acquisition storage in memory card for post-processing. Fig. 1 shows the HMI operations screen of BDMS device. The integrated BDMS system is qualified with extensive trial tests at RHS building and subsequently deployed in the reactor. Fig. 2 shows the photograph of BDMS installed in one of the ISI port of PFBR. Fig. 3 shows precise scanning of the rectangular cross-section profile using the laser range measurement sensor of BDMS. The internal dimensions of the ISI port of PFBR were successfully measured using the BDMS device. The acquired data were post-processed to generate the internal profile of the ISI port. Fig.4 shows the 3D reconstructed inner surface profile of the ISI port generated from the post-processing of the acquired data.

Range 279.655 4900

1 1 00:00:00.000

720 720 00:00:00.000

File Name Te[illegible]03042950-1-720

Z Count _Pitch 57344 Theta POS 15

Theta + 452100 Z POS 0

Theta - -452100

Fig. 1: HMI operations screen of bore dimension measurement system device

Fig. 2: Photograph showing bore dimension measurement system installed in 152° ISI port of PFBR

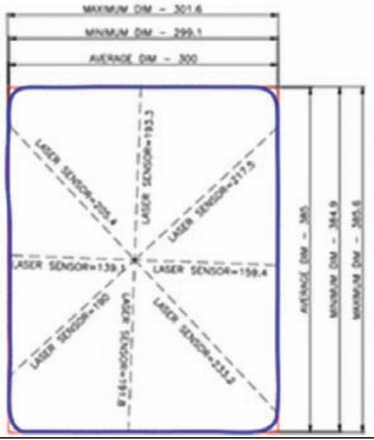

Fig. 3: Rectangular Profile Scan using Laser Sensor in bore dimension measurement system

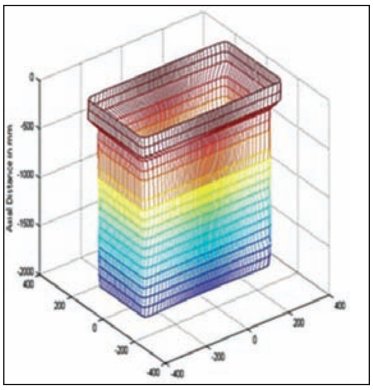

Fig. 4: 3D reconstructed inner surface profile of 152° ISI port

II.09 Development and Remote Handling Trials of In-Service Inspection Compliant Anti-Convection Barrier (ACB) Plug in PFBR using a Passively Actuated Gripper

Periodic in-service inspection (ISI) of Main Vessel (MV) and Safety Vessel (SV) of PFBR is important to assess their structural integrity. The MV is surrounded by SV forming an annular space (MV-SV interspace). Six rectangular access chutes are provided on the reactor vault for deploying the robotic devices to carry out the inspection. Below the ISI chutes, the MV-SV interspace is separated at the bottom of the roof slab level by an anti-convection barrier (ACB) which has six rectangular openings corresponding to the ISI chutes on the vault for the robot to pass through to the interspace. During the reactor operation, the ISI access chutes and ACB openings are normally closed with plugs (Fig. 1).

Prior to commencement of the ISI campaign, it is required to remove the Shield cum Seal Plug (ISI Plug) from the ISI chute first and then, the plug resting in the ACB opening (ACB Plug) to facilitate the deployment of the robotic inspection devices, namely, DISHA and MSISC. Remote handling of the ACB plug requires a special-purpose gripper while removing and replacing.

Dissimilar Metal Weld Inspection Device (DISHA), is used for the visual and volumetric examination of dissimilar weld between the roof-slab (RS) and main vessel of PFBR during pre-service inspection (PSI) and in-service inspection (ISI). DISHA is designed to be deployed on to the anti-convection barrier (ACB) and moving over the ACB for the inspection of the dissimilar weld. The ACB plug [Figures 2(a) & (b)] is designed to facilitate the trouble-free maneuvering of DISHA over ACB. The inspection of the dissimilar weld will be conducted with the ACB plug in the ACB opening.

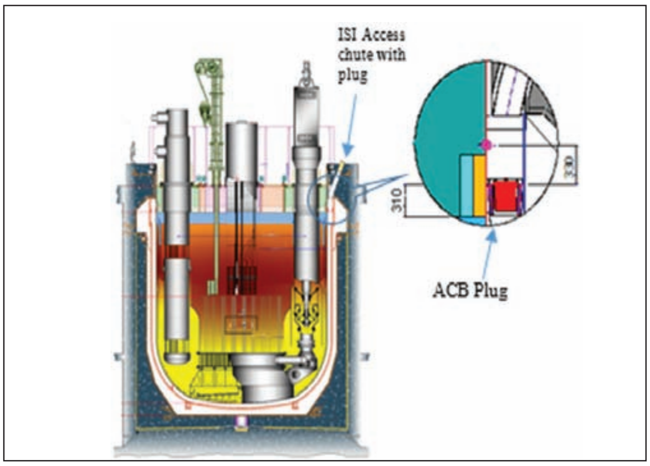

Fig. 1: Schematic of reactor assembly

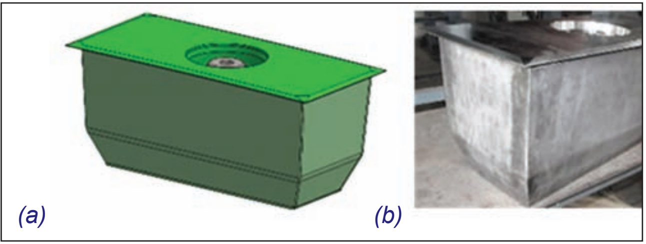

Fig. 2: (a) CAD Model of in-service inspection compliant ACB Plug and (b): Fabricated in-service inspection compliant ACB Plug

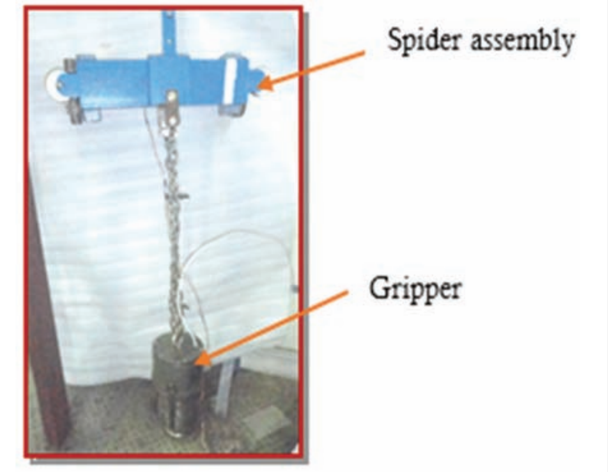

Fig. 3: Photograph of Gripper Assembly

For the remote deployment and retrieval of ACB plug into the ISI location in reactor vault, a special gripper assembly (Fig. 3) has been designed and developed. The salient feature of the gripper is its passive gripping in one downward stroke and in next stroke the load

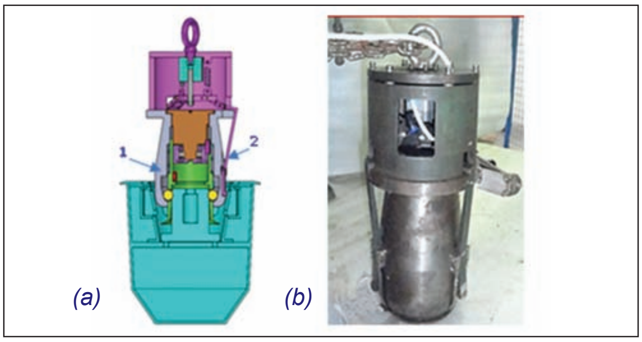

Fig. 4 :(a) CAD Model of the special gripper assembly with ACB plug showing Primary gripping [1] & Secondary gripping mechanisms [2] and (b) Photograph of the Gripper assembly: The gripper with ACB plug was inserted into the ISI opening, for ACB plug deployment

is released [Figs.4(a) & (b)]. Further, the passive gripping has a redundant gripping mechanism aided by pneumatic actuation. Before the deployment of ACB plug in the reactor, remote handling procedure of the plug has been qualified in the mock-up. The mock-up simulates ISI duct on the reactor Vault, ACB sector and MV-SV interspace above ACB.

Assisted by the load cell and camera visuals, the ACB plug was remotely placed on the ACB port. Then the ACB gripper was retrieved. Further, the gripper was lowered through the ISI duct/port and inserted in to the ACB plug, for ACB plug retrieval. The ACB gripper was hoisted along with ACBplug. The retrieval of the ACB plug was done remotely with primary gripping actuation. Further the secondary gripping mechanism was also tested and qualified.

Fig. 5: (a) Photograph ACB plug installed in 152° ACB opening and (b) ACB Plug at 152° ACB opening as seen by DISHA during inspection in PFBR

Fig. 6: Photograph of ACB plug installed in 218° ACB opening

After the successful qualification of remote handling of the ACB plug in the mock-up as per the approved procedure, the deployment and retrieval of ACB plug through all the six ISI access chutes at 33°, 96°, 152°, 218°, 276°& 333° orientations on the reactor vault in PFBR has been successfully demonstrated [Figs.5(a), (b) & 6] using the special gripper assembly.

Presently, the ISI-compliant ACB plug has been fabricated for one ACB opening and based on the successful remote deployment of the plug, clearance has been given for the fabrication of remaining five ACB plugs at Central Workshop Division, IGCAR.

II.10 Qualification of Steel Structures to Support Additional Snubbers Installed in Sodium Piping System of PFBR

Different sodium piping systems are available in PFBR, viz., primary purification piping system, secondary piping system, initial sodium filling piping system, and Safety Grade Decay Heat Removal (SGDHR) piping system. Piping layout and support configurations were decided based on the analysis at the design stage. Minor modifications in the piping layout and support were done during the piping systems fabrication and erection due to site constraints and the higher weight of valves. The piping systems were re-analysed for the as-built configuration. Additional 44 snubber supports at various locations are required to qualify the dynamic load case for the as-built configuration. These additional required snubbers are installed in the piping systems.

Fig. 1: FE model of steel structures to support additional snubbers

The additional snubbers needed in the piping system are supported by different steel structures at various elevations/locations inside the SGB. The steel structures to support snubbers are connected to the SGB through embedded plates (EPs). Considering the functionality of the steel structure, it is categorized as Design Class 3 and Safety Class 2, and the structure is qualified for seismic category-1 loadings. The structural members' design strength checks are carried out as per the allowable stress design method of the American Institute of Steel Construction (AISC) as per the AERB safety code.

FE Modelling and analysing of the snubber support steel structure is carried for Steel structures qualification. The structural members are discretized into finite elements model beam elements. Structural member-to-member and end connections are modelled to capture the connection behaviour in the Finite element model. Fig. 1 illustrates FE models of few typical steel structures. Initially, static analysis of structures has been done for the dead loads. Further dynamic analysis is performed to obtain the stresses under seismic loading. Response Spectrum (RS) method is followed for performing the dynamic analysis.

Modal analysis has been carried out to obtain the natural frequencies and mode shapes of the FE model of the structure. Three independent peak-broadened floor response spectra (two horizontal and one vertical spectrum) at the respective mounting location of the structure for OBE and SSE events are used as seismic input for the dynamic analysis. The analysis is performed separately for each component of earthquake motion, and the combined response for all three directions is obtained using SRSS. The design check of the steel structure is carried out, and the necessary retro-fittings for stiffening in structural members for qualification are suggested.

The steel structures are connected to the concrete elements through Embedded Plate (EP) fisher anchor bolts; hence, qualification of EPs is also essential. The reaction loads from the steel structure analysis are used as input for EP qualification. Support capacity checks of the EP arrangement are carried out as per ACI 318.t

II.11 Performance Testing of Cell Transfer Machine Gripper in Air using Spare Gripper

The Cell Transfer Machine (CTM) plays a critical role in the transfer of spent and fresh core Subassemblies (SAs) within the Fuel Transfer Cell (FTC). Two CTMs are placed inside FTC, each dedicated to handling either fresh or spent SAs, although both CTMs possess the capability to approach all ports. Each CTM is equipped with 9m long gripper subassembly designed for the handling of core subassemblies. Components of gripper hoisting mechanism are mounted on the top part of CTM (crab structure). CTM Gripper finger operation is provided with dual drives viz. pneumatically operated primary drive and an electrical (secondary) drive. In addition, manual drive is also provided for the gripper finger operation.

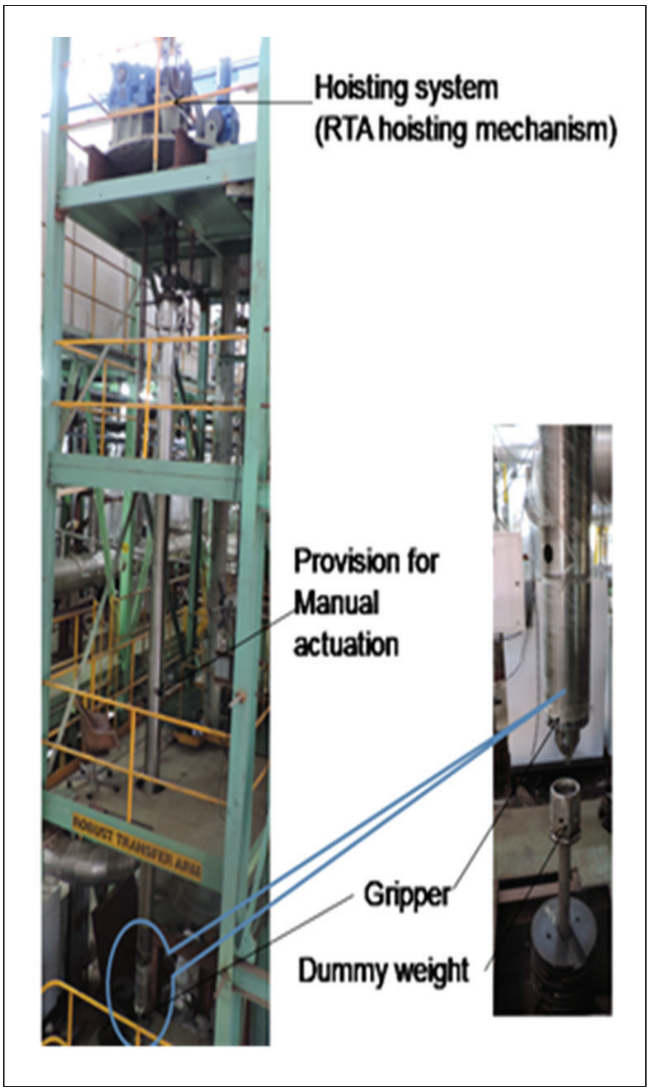

Fig. 1: Photograph of CTM gripper test setup

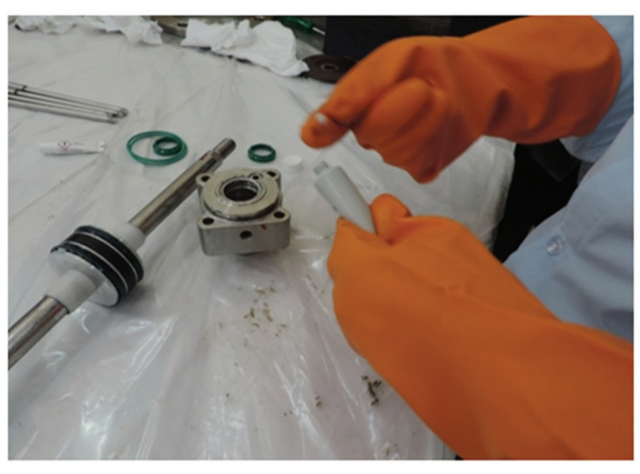

Fig. 2: Photograph of Reconditioning of pneumatic actuator

It was planned to test and demonstrate the performance of CTM gripper in air on an identical spare gripper in Hall-1 for 10% of envisaged life in reactor. The spare CTM gripper was integrated with a hoisting mechanism available in Hall-1 for the air testing as shown in Fig. 1. During testing, the gripper with load is hoisted up / down by 200 mm height at a speed of 0.5m/minute. Gripping/releasing of the SA (350kg)/Container (700kg) is simulated by a dummy load with handling head. Each cycle of CTM consists of open fingers on the load, hoisting by 200mm, closing fingers and empty gripper hoist by 200mm. The test plan was: 40 cycles with manual fingers actuation, 10 cycles with fingers actuation by electrical drive and 600 cycles with fingers actuation by pneumatic drive. Envisaged testing of 40 cycles and 10 cycles with fingers actuation by manual and electrical actuation was completed and parameters such as fingers open/close dimensions, reed-switch indications, torque for fingers actuation were consistent.

However, during testing with pneumatic actuation of fingers, after 10 cycles, it was observed that the fingers actuation became jerky due to a leak in the pneumatic actuator. Subsequently, a comprehensive dismantling procedure was prepared. CTM gripper was dismantled and the pneumatic actuator was reconditioned with new seals (Fig. 2). In the second phase, testing with pneumatic actuation of fingers was completed successfully for 600 cycles, demonstrating smooth and reliable performance.

II.12 Integrated Sodium Testing of Failed Fuel Location Module

Three identical Failed Fuel Location Modules (FFLMs) are housed in the control plug of PFBR and designed to identify the failed fuel sub-assembly after getting an indication from global Delayed Neutron Detector monitors. During the commissioning phase of these FFLMs, it was observed that their rotational torque was higher than the nominal values. Consequently, FFLMs were removed from the reactor pile for further investigation at IGCAR. The identified root cause of the torque deviation was the eccentric loading of the DC Conduction Pump (DCCP) on the guide. Subsequent to this investigation, design modifications were implemented. FFLM-1 was then integrated with the DCCP, Permanent Magnet Flow Meter (PMFM) and Positional Drive System (PDS), and the satisfactory performance of integrated FFLM was subsequently verified through testing in an air environment. Fig. 1 depicts the integrated FFLM as well as the FFLM within its selector valve housing. The primary objective of sodium testing was to validate the performance of the FFLM integrated with the DCCP, PMFM, and PDS. As part of the testing 1:1 model of the FFLM's non-removable parts of the control plug, like selector valve housing (SVH), guide sleeve, base plate, etc., were manufactured and assembled, and air testing of integrated FFLM-3 was successfully completed prior to sodium testing.

Fig. 1: Photograph of Integrated FFLM and FFLM with selector valve housing

Fig. 2: Photograph of FFLM installed in TV-5

Sodium testing was carried out inside Test Vessel-5 (TV-5) in Engineering Hall-3. After confirming the leak tightness of the assembled system, the FFLM and SVH were positioned in TV-5 as depicted in Fig. 2. The performance of FFLM was tested under simulated reactor conditions, and nominal torque was consistently maintained, with rotational torque values ranging between 6 to 8 Nm, well within acceptable limits during the testing period. PDS and the Advanced Positional Drive System (APDS) functional testing was accomplished successfully. The pump was operated for over 100 hours. Several challenges were encountered during this phase, all of which were effectively resolved. These challenges included an increase in DCCP resistance, power supply module failures, fluctuations in PMFM readings, and flow rate reductions. Remarkably, the nominal flow rate of 100 cc/s was consistently achieved for a 2000A current at 362°C. In summary, all envisaged objectives were accomplished, and the sodium testing phase was completed successfully.

II.13 Endurance Testing of Test Back-Up Seal of SRP / LRP

A pair of back-up seals between SRP & LRP and LRP & roof slab act as secondary leak-tight barriers for Prototype Fast Breeder Reactor (PFBR) cover gas during normal reactor operating conditions. As part of spare management for PFBR, an indigenous development of large diameter seals was initiated. In line with the above, the indigenously manufactured back-up seals of the same cross-section as in PFBR but of a reduced diameter of 1m are tested on a priority basis in the back-up seal test facility in Engg. Hall-I. The back-up seal cross-section and seal test facility are shown in Fig. 1. The seal is held by a seal holder, which is pressed against the sealing surfaces by clamping mechanisms and arranged circumferentially at regular intervals to obtain the seal's uniform compression.

Testing for performance evaluation involves dimensional inspection, fitment trials, room-temperature & high-temperature performance testing, high-temperature endurance testing and post-test inspection. One endurance test cycle involves loading the seal with 5 mm compression (maximum compression allowed in PFBR), pressurising the inter-space with 250 mbar (g) and then holding at 120°C for two weeks, followed by unloading and cooling to room temperature in 2-3 days.

Initially, four developmental seals were tested and the feedback from the tests was shared with the industry. Based on feedback from developmental seals testing, the industry fine-tuned the manufacturing and supplied one test seal of 1 m diameter (1st test back-up seal) that was joined in-situ in Engg. Hall-I and was subsequently tested for 7 cycles. Though the testing of 1st test back-up seal showed a permanent set-in seal height in every cycle, but the seal met the leak-tightness requirement and no material damage was observed. Feedback from the endurance testing of 1st back-up seal was communicated to the supplier for further improvements related to permanent set. Also, a purchase order of back-up seals for SRP and LRP of PFBR was placed.

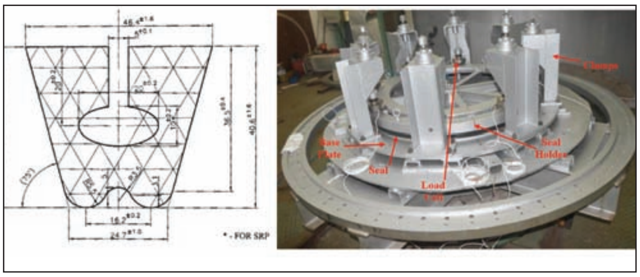

Fig. 1: Back-up seal cross-section and Photograph of test setup

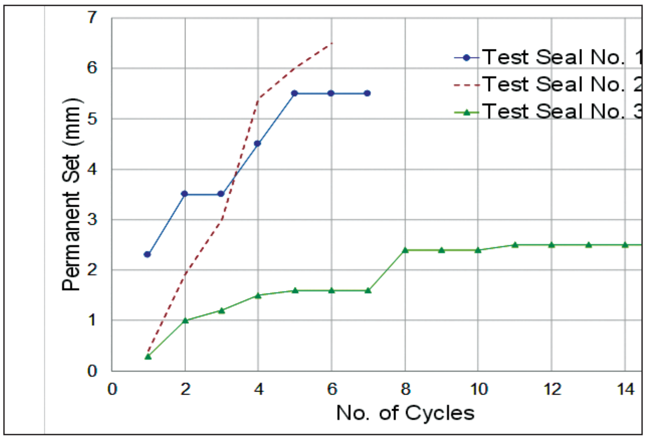

Fig. 2: Variation of permanent set with respect to number of cycles

Afterwards, the industry supplied back-up seals for SRP and LRP in the form of cords with extra length. 2nd and 3rd test back-up seals were extracted from the SRP seal cord and joined in-situ at the PFBR site during SRP back-up seal replacement. Testing of these 'test back-up seals' were prioritised to check the seal's performance. Second test back-up seal has undergone a total of 6 test cycles. This seal has also undergone the permanent set in the height of the seal, but the seal was maintaining the leak-tightness and no material damage was observed.

Based on the test feedback of all previously tested seals, it was inferred that the seal material is qualified, as no material damage was observed. Therefore, it was decided to test the 3rd test back-up seal with the minimum seal compression required to achieve the leak-tightness. Required leak-tightness was achieved with a compression of 3 mm (approx.). The 3rd back-up seal was tested for 15 endurance test cycles. During testing, the permanent set was observed during initial cycles only and the cumulative value was less. This reduction in the permanent set may be due to reduced applied compression. The seal could hold the leak-tightness and no material damage was observed. A comparison of the permanent set with respect to number of cycles tested for different test back-up seals is presented in Fig. 2.

Hence, a similar methodology is recommended during compression of the back-up seals in PFBR. The seal testing has given confidence in the operation of indigenous back-up seals in the reactor.

II.14 Manufacturing and Sodium Calibration of Spare ECFM

The Eddy current flow meter (ECFM) placed at the impeller outlet of the Primary Sodium Pump (PSP) measures the pump flow rate and provides one of the SCRAM signals for the event of primary pipe rupture. The output from ECFM can also be used for estimating the core flow. As part of spare management for PFBR, it is planned to keep few spare ECFM probes ready for reactor use. Accordingly, a purchase order was placed with an Indian industry for the manufacturing and supply of ECFM probes.

Fig. 1 shows the assembled view of ECFM sensor. The sensor consists of a bobbin made of Midhani Soft iron, over which one primary and two secondary coils were wound. MI cable is used for making primary and secondary coils. The primary coil consists of 205 turns and each of the secondary coils consists of 310 turns. The two secondary coils are wound symmetrically around the primary coil.

The sodium calibration of the spare ECFM probe was done in a dedicated test section, located in Steam Generator Test Facility (SGTF) loop, ref. Fig. 2. The main components of this test section are the inner guide tube assembly, flow straightener and magnetic shield. The inner guide tube assembly is supported by flow straightener at the bottom and is welded at the top to 2" pipe. It has two straighteners separated by a SS 410 tube by a distance of 384 mm. This SS 410 tube acts as a magnetic shield which minimizes the leakage of magnetic flux. A permanent magnet flow meter with known sensitivity is used as reference flow meter for calibration. During the testing, the temperature of the sodium was varied from 250°C to 450°C in steps of 50°C & flow through the sensor was varied from static to 25 m^3/hr in steps of 5 m^3/hr. Fig. 3 shows the obtained sensor characteristics of ECFS at various test temperatures. The response of the sensor is linear within the test conditions. It was observed that sensitivity, which is represented by the slope of the characteristics, vary slightly with the temperature.

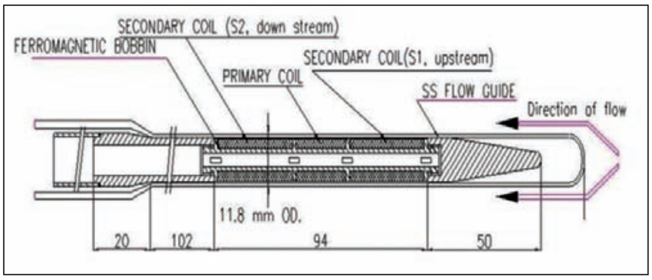

Fig. 1: Assembled view of ECFM sensor

Fig. 2: ECFM Test section in SGTF

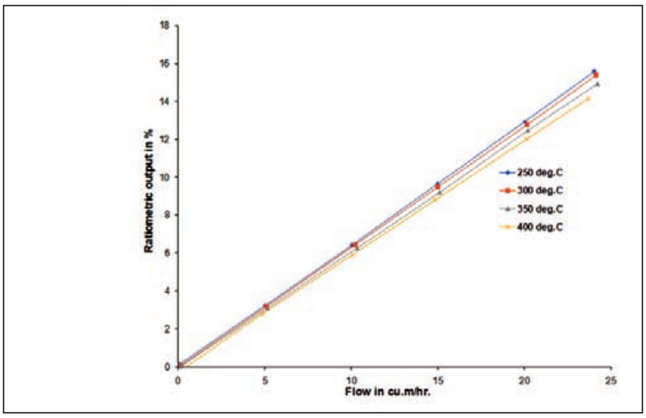

Fig. 3: Photograph of Sensor characteristics of ECFS at various temperatures (with zero correction)

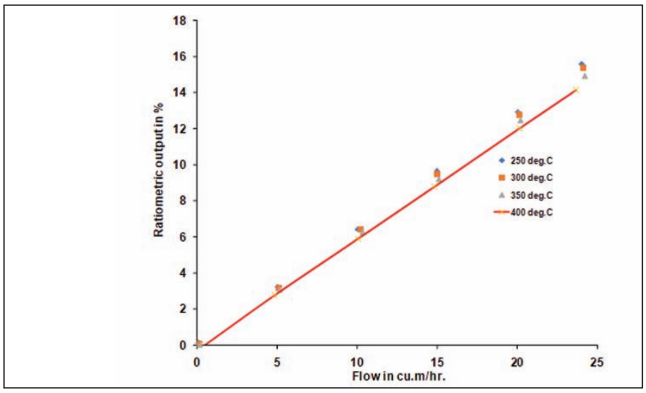

Fig. 4: Sensor characteristics of ECFS with calibration at 400ºC

In PFBR, the normal operating temperature of ECFM is 400°C, even at part load conditions. Hence, it was recommended to calibrate the ECFM at 400°C and the corresponding sensor characteristics with calibration at 400°C are shown in Fig. 4. The error in the output of ECFM sensor is less than ± 1.5% for 400°C. The spare ECFM probe met the design requirements and cleared for deployment in PFBR, if necessary.

II.15 Performance Evaluation of CSRDM With Bowed CSR SA

Initially, the Control and safety rod Subassembly (CSR SA) is straight and is offset (called initial offset) with respect to CSRDM. As the sodium filling and the operation of the reactor continue, temperature and irradiation induce additional offset and bowing of the SA. The offset and bowing of CSR SA result in interaction of mobile CSR with its outer sheath. The imposed displacements result in higher frictional forces and thus higher drop times during scram action. Thus, evaluation of the performance of CSRDM with bowed CSR enhances the confidence in the performance of CSRDM and CSR in PFBR.

The required bowed shape of CSR SA is achieved by pulling/pushing the CSR hexcan at pre-determined elevations. Initially, two rigid support columns were erected on either side of the hexcan. Three sets of holes were drilled in these columns at the given elevations. Rigid clamps were fixed to hexcan at these three elevations. The clamps mainly facilitate for pushing / pulling using tie rods. Studs fixed to the clamps act as tie rods and required pulling / pushing force was achieved by tightening the nuts, which were fixed to these studs, against the support columns. By properly adjusting the tie-rod deflection at given elevations, required bowed profile of DSR SA could be achieved. Fig. 1 shows the photograph of the bowed CSR SA in the test station.

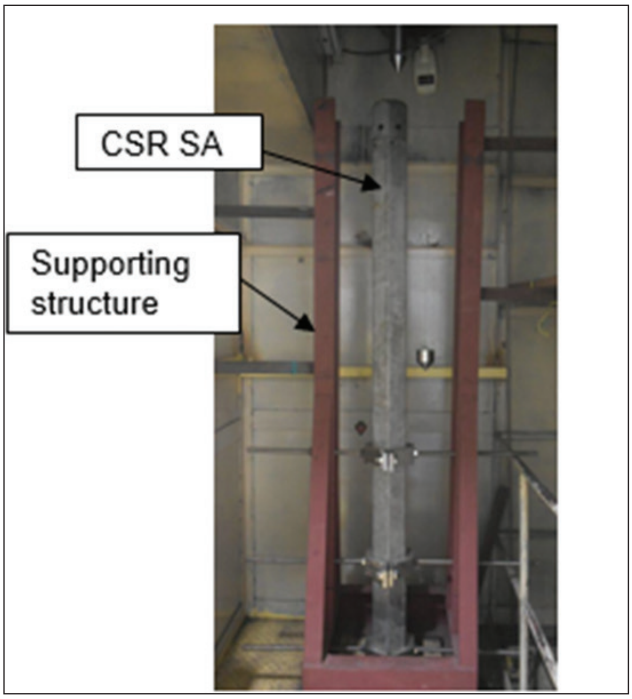

Fig. 1: Photograph of bowed CSR SA with its supporting structure

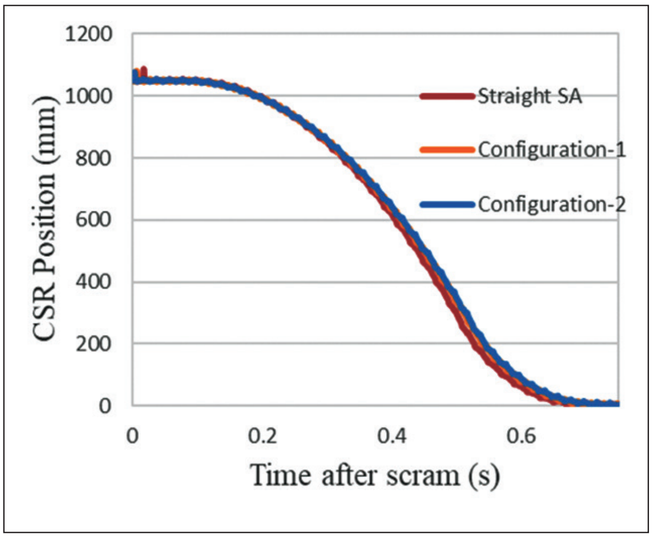

Fig. 2: Displacement characteristics of mobile assembly of CSRDM under various test conditions

The experiments were carried out in ARDM test facility in Engineering Hall-III. A spare CSRDM of PFBR was used for testing. Initially, tests were done with straight CSR SA, which is used as reference case.

The frictional force on mobile CSR, EM minimum holding current, EM response time and the drop time of mobile assembly were measured in each trial. The in-built load cells and potentiometer were used for measuring load on the mobile assembly and the position of the mobile assembly. Experiments were done in two different configurations of CSR SA. The first configuration (Configuration-1) corresponds to the anticipated bowing in PFBR and in the second configuration (Configuration-2), additional 3 mm bowing (at top) was simulated. Totally 30 scram operations were carried out, in both the configurations put together.

The peak frictional force was found to be 550 N for Configuration-1 and 650 N for Configuration-2. EM minimum holding currents and response times are found to be 0.48 A and less than 100 ms respectively. Fig. 2 shows typical displacement characteristics of mobile assembly during scram action for the given test conditions. Marginal increase in the free fall time and braking time compared to the straight SA can be seen. No change in the performance was observed after the endurance testing of 30 scram cycles.

The experiments demonstrated the satisfactory operation of CSRDM with bowed CSR SA and have given confidence in the design and safe operation of CSRDM and CSR in PFBR.

II.16 Vibration Testing of PFBR Dummy SA With Increased Foot Clearance

Fuel Subassembly (SA) is an essential component of a fast nuclear reactor. The SA is free-standing and supported at the bottom by a sleeve/guide. The radial clearance at support location strongly influences the resulting SA vibration, and it is necessary to understand its effect on the resulting vibrations. The designed foot clearance for dummy subassembly is 60-120 microns. This clearance at the foot is fixed considering the required leakage flow as well as the ease of subassembly insertion and removal during fuel handling. However due to functional requirements this clearance has been increased by 100-150 microns. In order to study its effect on dynamic behaviour of SA, flow induced vibration testing of full scale PFBR dummy fuel subassembly with increased clearances was carried out in water.

During this test campaign, test was done on two subassemblies with foot clearance of 286 and 347 microns. Fig. 1 shows the schematic of PFBR fuel subassembly.

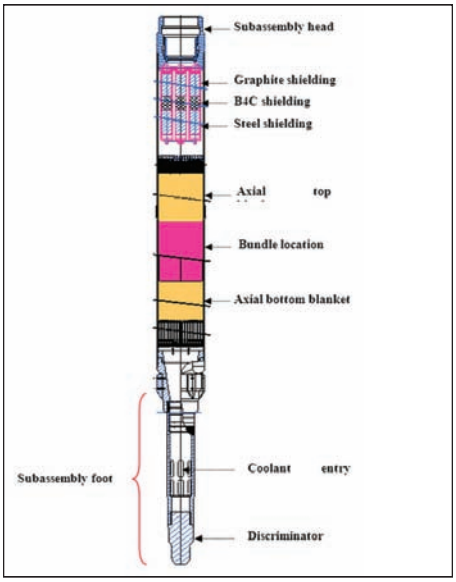

Fig. 1: PFBR subassembly schematic

The FIV test loop consists of grid box assembly and four inlet water connections. Full scale model of Zone-1 grid plate sleeve was used for mounting the test dummy SA. This arrangement simulates the support condition and flow path for subassembly as in the reactor.

The maximum sodium flow through the central subassembly is 36 kg/s and the flow is in turbulent regime. The flow through the fuel subassembly is parallel flow and the main excitation mechanism is turbulence. In the case of axial flow with turbulence as the main excitation mechanism, the simulation criterion from water to sodium is established from the Burgreen correlation. The test flow was thus derived as 185 m^3/h in water at 60 °C.

Initially, natural frequency measurement of dummy SA is carried out by exciting the subassembly using an electro-dynamic exciter in air. The first mode natural frequency of subassembly is found to be around 3 Hz. Then testing of SA is carried out in water at 60 °C.

Test flow is varied from 20% to 100% of rated flow and vibration signals are recorded using underwater accelerometers. Fig. 2 shows a typical vibration acceleration spectrum for the maximum flow rate condition.

In the acceleration spectrum, the frequency peak at 3 Hz corresponds to the first natural frequency of the SA and 19 Hz, 50 Hz etc. represent higher modes. Fig. 3 shows the variation of vibration displacement with flow.

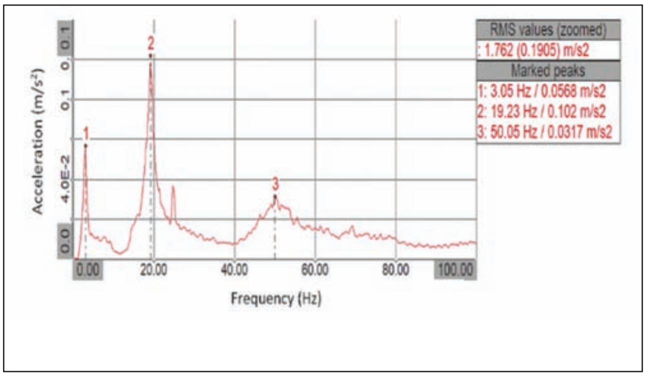

Fig. 2: Vibration frequency spectra

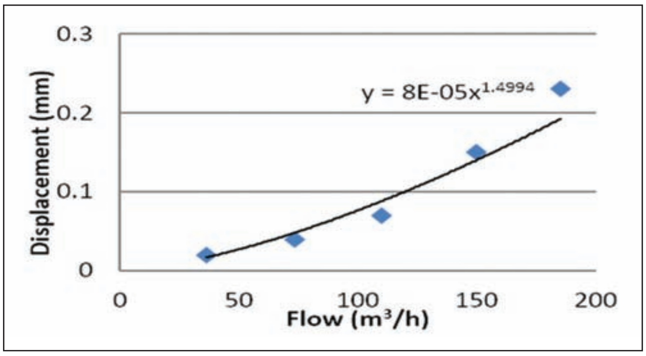

Fig. 3: Vibration displacement vs flow

The amplitude of vibration is found to be increased with flow as expected. The maximum amplitudes of vibration displacement (rms) are 0.15 mm and 0.23 mm for subassemblies with foot clearances 286 and 347 micron respectively.

II.17 Investigation of Flow Fluctuations In Secondary Sodium Main Circuit of PFBR

PFBR consists of two Secondary Sodium Main Circuits (SSMC) and each SSMC consists of two Intermediate Heat Exchangers (IHX), one Surge Tank (ST), four steam generators (SG) and one secondary sodium pump (SSP). The sodium flow rate in SSMC is measured by using a By-Pass flow meter installed at the 800NB suction pipe line of SSP. In By-pass flow meter, a 25NB line samples out a stream of flow from suction line and measures by a Permanent Magnet Flow Meter (PMFM). The flow in SSMC is estimated based on the measured sample flow.

During commissioning of SSMC, the sodium flow rate measured by the By-pass flow meter was observed to be fluctuating. The flow fluctuations were ± 7 % and ± 5 % for SSMC-1 and SSMC-2 respectively with 95% confidence level (± 2σ). In certain instances, the amplitudes of flow fluctuation are in the range of +15% to -30%. These fluctuations were not with any characteristic frequencies and distributed with the range of 0 to 1Hz.

Since By-pass flow meter is the only device available for measurement of flow in SSMC, alternate techniques are considered for the investigation of flow fluctuation. In a hydraulic system, if the flow fluctuates, the pressure at various locations of the system and pump developed head and power of the pump will also fluctuate. The flow through Steam Generator Leak Detecting System (SDLDS) of SSMC is governed by the pressure at the junction (suction side of SSP) of tapping of SGLDS line. Hence, to investigate the reason for flow fluctuation and confirm the presence of flow fluctuation as measured by By-pass flow meter, the following indirect techniques have been used in SSMC 1,

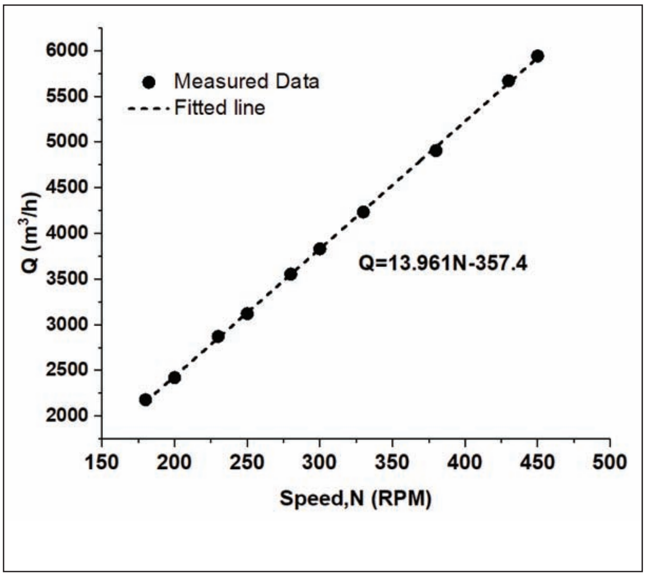

Fig. 1: Mean flow rate of SSMC with respect to SSP speed

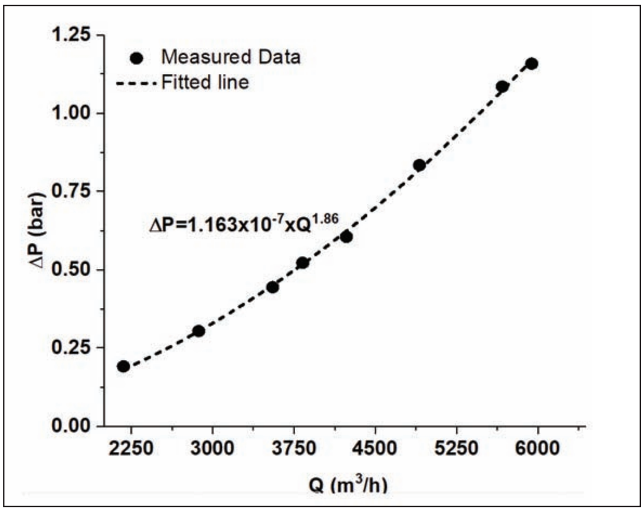

Fig. 2: Mean value of pump developed head with respect to flow rate

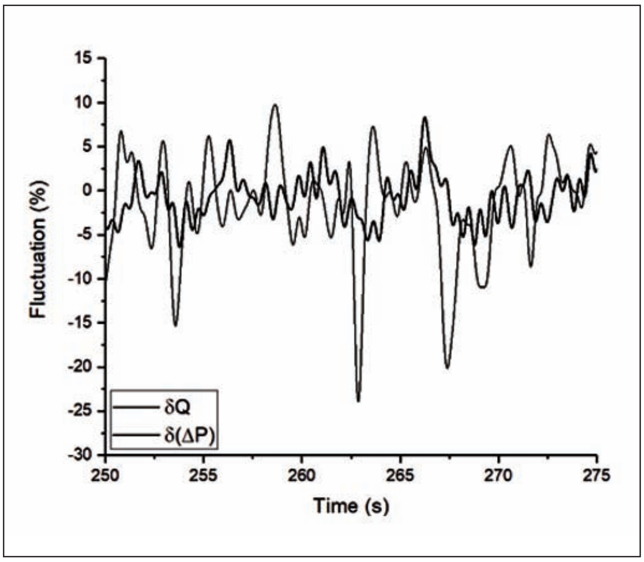

Fig. 3: Percentage of fluctuation in flow and pump developed head

a) Simultaneous measurement of SSMC flow, pressures at suction and delivery side of SSP.

b) Simultaneous measurement of SSMC flow and power and speed of SSP.

c) Simultaneous measurement of SSMC flow, SGLDS-5 flow and suction pressure of SSP.

The measurements were taken for SSP 1 for a speed range from 180 rpm to 450 rpm. From the mean value of flow through SSMC, pump developed head and motor power of SSP, it confirms that the design of SSMC, selection of SSP and By-pass flow meter system are performing as intended other than the indicated flow fluctuations over the mean value. The mean value of flow generated by SSP with respect to pump speed and pump developed head with respect mean flow rate are shown in Fig. 1 and Fig. 2 respectively. For all cases the fluctuation in level and cover gas pressure in surge tank is negligible and hence the loop is free from any large amount of locked cover gas.

To measure the suction and delivery point pressures of SSP, the newly developed and qualified Sodium Pressure Measurement Devices (SPMD) were used. From the simultaneous measurement of flow and pressures, the observed fluctuations in SSMC flow rate are in the order of ± 7.5% to ± 10% and the fluctuations in the pump developed head are in the order of ± 4.5% to ± 5% as shown in Fig. 3. No coherence between the measure flow and pressures are observed for all cases as shown in Fig. 4.

Further for the measured flow data, the pump developed head and the hydraulic resistance of the loop can be estimated based on the momentum equation and these values are supposed to be unrealistically fluctuated in the order of ± 150% which is impossible. The estimated flow fluctuation based on the pressure measurement is in the order of ± 1% only.

The By-pass flowmeter reading shows the fluctuation even during pump coast down as shown in Fig. 5, where the flow fluctuation is not expected in any closed loop.

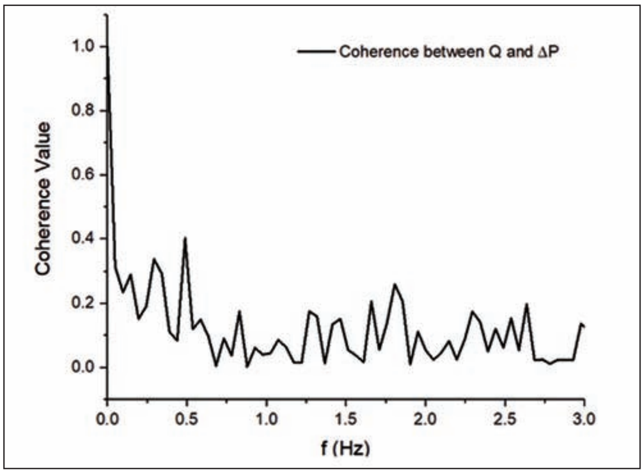

Fig. 4: Coherence between Q and ΔP

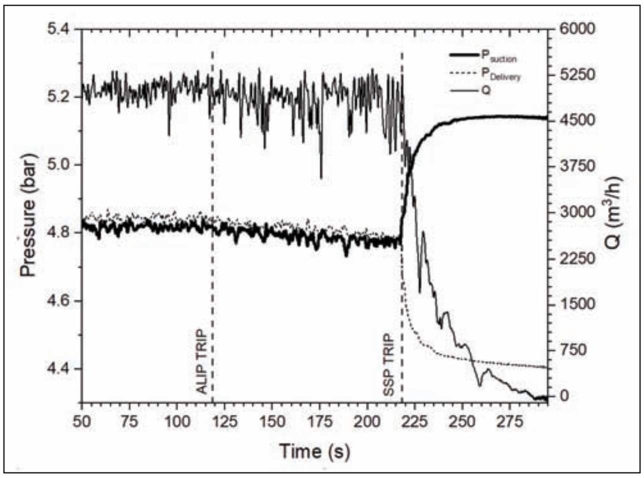

Fig. 5: Time history of flow and pressures in SSMC during SSP coast down at 380 rpm

From the pump coast down experiment, the possible causes for flow fluctuation due to variable speed driven motor is ruled out.

From the simultaneous measurement of flow and motor power, the observed fluctuations in fluid power are in the order of ± 6 to ± 6.5%. No coherence between the measured flow and power is observed and the fluctuation in power less than that of measured flow which is not possible in any system. The estimated power fluctuation based on the measured flow is supposed to be unrealistically in the order of ± 120%. Hence it is conformed that the flow fluctuation measured by the By-pass flow meter is not representing the actual flow rate fluctuation in SSMC. Further based on fluctuation in pump developed head and power, the flow fluctuation is expected in the order of ± 1.5% only.

From the simultaneous measurement of SSMC flow and SGLDS-5 flow, it is observed that the percentage of fluctuation in SGLDS-5 flow (1-2%) is much lesser than that of SSMC flow. SGLDS-5 flow is also not coherent with SSMC flow but it completely coherent with suction pressure measured by SPMD. From the analysis, it is found that measured flow fluctuation is not representing the actual flow rate fluctuation in SSMC and it is supposed to be in the order of 1.5% estimated based on the SGLDS-5 flow measurement.

Hence from the all observation, it is confirmed that flow fluctuations measured by By-pass flowmeter is not coherent with other measured parameter of system and it is not representing the actual flow rate fluctuation in SSMC. However, the mean value of flow measured by the flow meter is correct and matches with other parameters like pump developed head and pump power. The estimated flow fluctuation in SSMC is only in the order of ± 1% to ± 1.5%.

II.18 Hydraulic Characterization of PFBR Plugging Indicator Circuit

Plugging indicator (PI) is an inevitable instrument in sodium systems that indicates the level of dissolved impurities in sodium which has a temperature dependent solubility. Plugging temperature is used for setting the cold trap parameters such as sodium inlet temperature and cold point. PFBR sodium circuits have individual and identical PI systems.

During a plugging run, a part of sodium from the main flow (3.2m^3/h) is passed through plugging indicator circuit which branches into two lines; a line with orifice (0.2 m^3/h) and another parallel line with a float valve (3m^3/h). Pressure drop of float valve is independent of the flow rate within a certain range. Purpose of the float valve is to maintain a constant back–pressure in the upstream of orifice so that the plug formed would not be sheared off by flowing sodium. During operation of PIs in PFBR, chattering of float valve was observed. Concerning the plugging indicator in the SGDHR purification circuit, the flow developed is found to be less than the designed flow. Flow fluctuations were observed in plugging indicator of secondary sodium purification circuit (SSPC). Hydraulic experiments were carried out to study the hydraulic characteristics of PFBR plugging indicator circuit with a full scaled model.

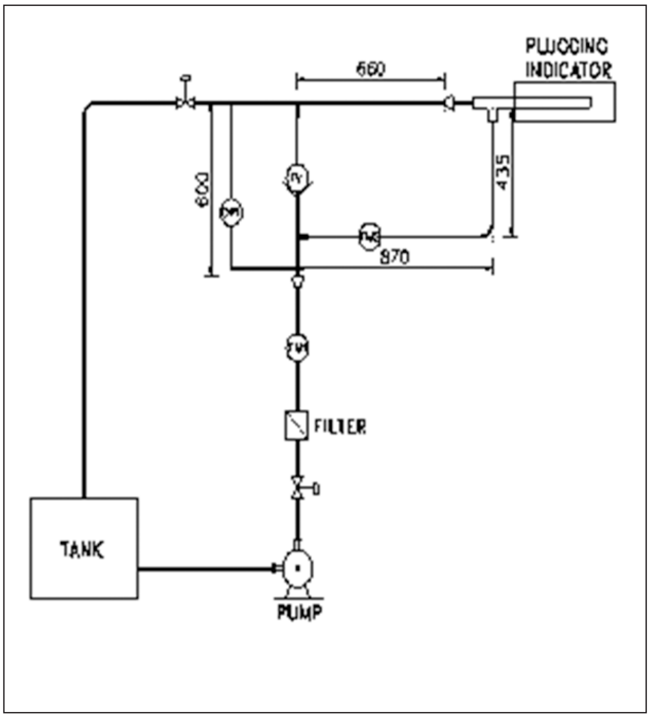

Fig. 1: Schematic of the Experimental setup for plugging indicator hydraulics studies

Experimental setup for plugging indicator hydraulics study is shown in Fig. 1. It consists of a pump of nominal capacity of 5 m^3/h at 4 bar head., a valve, filter and flow meters. An EM flow meter (FM1) is connected in the main line of the plugging indicator circuit and another EM flow meter (FM2) is connected to measure flow through orifice. Remaining flow shall pass through the float valve. FM1 is calibrated for a flow range of 0-8 m^3/h. FM2 is calibrated for a flow range of 0-0.4 m^3/h. Differential pressure transmitter was connected to measure the pressure drop across PI line. Dynamic pressure sensors were connected at inlet and outlet line of float valve and PI to record pressure fluctuation in the circuit as a result of flow. For hydraulics study a full scaled model of plugging indicator of SS 304 material was fabricated without cooling jacket and with removable orifice plate. A full scaled model of PFBR float valve was connected in parallel line. Internals of float valve and PI were manufactured in close tolerances to replicate the hydraulics. Water is used as the simulated coolant.

The experiment was started at rated flow rate of PFBR plugging indicator circuit (3.2 m^3/h). Water flow rate in the main line was varied by throttling the discharge valve of pump. The experiment was performed at different flow rates from 1 to 7 m^3/h. For each set of flow conditions, the pressure drop across plugging indicator circuit was recorded.

To investigate the root cause of problem the following experimental studies were carried out.

Case I: Hydraulics study at rated flow Initial study was performed at rated flow conditions of PFBR PI circuit. At total flow rate of 3.2 m^3/h, through plugging indicator circuit, a flow rate of 0.205 m^3/h was observed through plugging indicator. Pressure drop across the plugging indicator was 25.23 kPa. Dynamic pressure sensors were employed for indirect measurement of flow fluctuations in the plugging indicator circuit. Since the experimental loop is high pressure drop system, 4 bar pressure is being dropped across pump discharge valve during normal operating flow. Flow fluctuation in a system is function of overall loop resistance and experimentally obtained flow fluctuations will be much lesser than actual PI circuit hence, the pressure

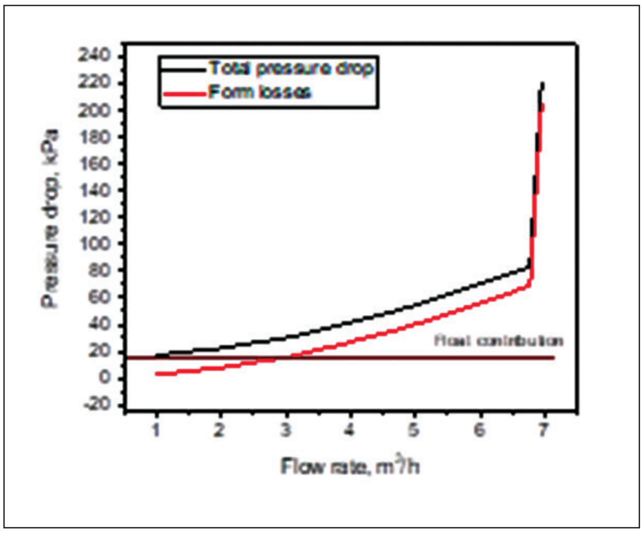

Fig. 2: Pressure drop characteristics of plugging indicator circuit

fluctuations are considered as indicating parameter for flow fluctuations in this study. Pressure fluctuations at rated flow of 3.2 m^3/h is within range of ± 0.5 kPa. A 5 Hz low pass filter was used to eliminate noise. Pressure variations in the upstream and downstream line are in phase which indicates that there are no abnormal eddies formation due to changes in flow path of the fluid. Chattering sound was observed from the float valve which indicates instability in float valve. In phase pressure variation indicates that the chattering sound observed in the float valve is due to lateral movement. There is no detectable vertical movement of the float at rated flow condition. Fast Fourier transform (FFT) of the experimental data was carried to observe the frequency domain of the pressure variation. No major frequency of oscillation was observed. Amplitude of pressure fluctuations in the experimental setup is insignificant. It is concluded from this study that the fluctuations in the plugging indicator circuit at rated flow is insignificant. Hydraulic design of plugging indicator circuit is adequate for rated flow case.

Case II: Investigation of low flow and flow fluctuation

Hydraulic design of plugging indicator circuit is adequate to allow a flow rate of 0.2 m^3/h across plugging indicator. Therefore, flow reduction observed in plugging indicator of SGDHR purification circuit may be due to increase in the hydraulic resistance across plugging indicator. It is anticipated that PI orifice may get chocked by foreign particles/ debris while fabrication or operation. Flow through PI is governed by orifice performance, chocking of orifice will lead in reduction in size of grooves which will affect the flow distribution. Due to increase in hydraulic resistance across plugging indicator, flow of 0.2 m^3/h across plugging indicator will be possible by increasing the main flow above rated flow. Pressure drop in parallel path of plugging indicator i.e. float valve will increase for higher flow rates due to change in flow geometry (form losses). To confirm this phenomenon an experiment was carried out in which the grooves of orifice were partially plugged with solid particles. Main flow was set at 3.2 m^3/h. In this condition the maximum flow observed through plugging indicator was 0.16 m^3/h. In order to get a flow of 0.2 m^3/h through the plugging indicator main flow had to be increased. Flow rate of 0.2 m^3/h through plugging indicator was achieved at main flow of 5 m^3/h. For higher blockage, main flow requirement will increase proportionately. When the main flow was increased above 7 m^3/h, a loud metallic sound was observed from the float valve. Main flow rate instantly reduced to 0.8 m^3/h and flow rate through plugging indicator was 0.75 m^3/h. Pressure drop in the circuit increased to 221 kPa. Entire flow was passing through the plugging indicator which indicates that the float valve got hydraulically stuck. It was observed that plug of float valve got lifted away from spherical seat and the bottom weight attached to plug got stuck at the bottom of seat. The pressure acting across plug weight is sufficient to push the plug out of seat region and hydraulically suspend the weight in such position. This indicated instability in the float valve at main flow rate higher than 7 m^3/h. Installed characteristics of the float valve is shown in Fig. 2.

Pressure drop across the float valve has two contributions; float contribution due to float weight and form losses. The contribution due to float shall remain constant and the form losses increases with flow. Above 3 m^3/h flow rate form losses contribution is found more than float contribution. At 6.8 m^3/h, form losses are sufficient to generate enough lift force to lift the float and make it hydraulically stuck below the valve seat.

From all of the above observations, it is concluded from the study that low flow observed in SGDHR PI circuit could be due to flow blockage in orifice. Flow fluctuation observed in the SSPC PI circuit is due to instability of float valve at higher flow rates for chocked condition.

II.19 Demonstration of Gas Release Performance of Purger Subassembly During Filling as well as Normal Operation

Purger subassemblies (PSA) are provided in the reactor core to ensure purging out of accumulated argon cover gas in the grid plate during filling of main vessel. An experiment is conducted in water using a simplified model to study the performance of PSA in releasing / purging the gas entrapped in liquid.

This model approximately reproduces the grid box geometry from centre of the grid box to periphery with 3 row slab configurations. The model bottom vessel simulates the grid box with all the sleeves, inlet water provision and angular viewing windows to enable observation of bubble entry through sleeve holes. In this model, total number of sleeves simulated are 48 flow subassembly, 1 Purger subassembly and 21 non flow subassembly. The Fig. 1 below shows the model after its erection.

The study is carried out in a 1:1 scale model with velocity similitude. This simulation required a maximum model flow rate of 3646 m^3/h.

The experiments were carried out to observe (i) gas locking phenomenon during simulation of initial filling of the reactor vessel (ii) release of these trapped gases during filling flow rate (iii) purging of entrapped gases during filling operation and (iv) purging performance during the normal flow condition. From experiments it is seen that a small layer of gas is getting accumulated in the slopping region of grid box top once the model is fully filled. Once flow is sent, this small amount of trapped gas layer disappeared and no gas bubbles of observable size were seen exiting from fuel and blanket SA. This experimental observation clearly shows that the purger subassemblies are effective towards purging trapped gas bubbles during simulation of filling operation. It is also observed that, gas bubbles are getting accumulated and released through purger SA up to water inlet flow rate corresponding to 2.5% of the nominal flow condition. Up to these flow rates, all the gas bubbles are exiting through Purger SA and no gas bubbles (that can be visually detected) are exiting from the other FSA and BSA sleeve as shown in Fig. 2.

Fig. 1: Photograph of Slab model scheme of sleeves

Fig. 2: Top surface of model showing no bubble from fuel and blanket SAs.

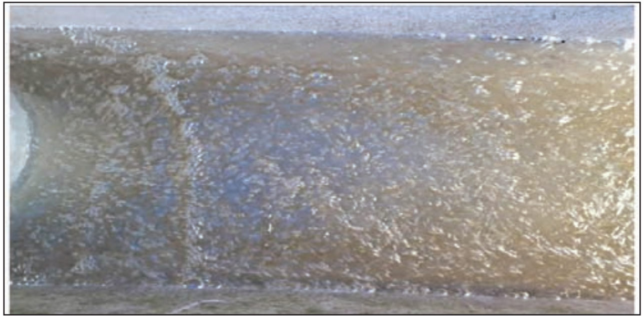

Fig. 3: Top surface of model showing bubble from fuel and blanket Sas at higher flow.

However, when the inlet flow rate increases above this flow rate the bubbles are seen to be exiting from all subassemblies. When the flow rate is increased further, the bubbles are mixed with the flow (with sizes up to 5mm) and exiting from all the subassemblies as shown in Fig. 3.

Hence it can be concluded that purger subassemblies are effective during the filling condition and not effective when flow rate increase above 2.5% of nominal flow rate of primary circuit.

II.20 Design and Development of Target Plate Holder Assembly for Material Research Beam Line of Medical Cyclotron

The Medical Cyclotron Facility, at VECC Kolkata has two dedicated proton beam lines for research experiments in the fields of material sciences. These consist of two sub-beam line having proton beam of low current (up to 50 μA) as well as high current (up to 200 μA). The maximum energy of the proton beam available in the facility is 30 MeV. Irradiation studies on different material using high current proton beams are planned using these beam lines.

One of the main challenges for carrying out the irradiation experiments with proton beam is to develop a suitable target holder so that the deposited energy (induced heat) on the target due to proton beam can be properly removed without causing failure of the target. The material of construction of the target holder is selected as aluminum alloy from induced activity point of view. The irradiation chamber has high vacuum inside (in the order of 10^{-6} mbar) and therefore the target holder assembly needs to be vacuum tight in order to maintain high vacuum inside the chamber. Moreover, the target needs to be inserted inside the chamber through respective nozzle for proton irradiation experiments. The overall size of the target holder assembly is limited by the size of nozzle (internal diameter of 95 mm) through which the same will be inserted in to an irradiation chamber.

The design of target holder assembly has been carried out through an iterative method combined with both analysis and testing. SS 304 has been considered as reference material for thermal analysis of target plate. The thickness of target plate is from 1 – 2 mm. The incident proton beam diameter on target plate is 20 mm. It is assumed that, the incident proton beam is uniform over the irradiated area. As a conservative approach, the total heat generation in the target plate is assumed as surface heat generation on the exposed surface of target plate. Since the heat flux on the target plate is very high, direct jet cooling by water is preferred for heat removal from opposite surface. In order to hold the target plate inside the irradiation chamber and to provide sufficient cooling for target plate, a target holder assembly has been designed. The design of target holder assembly is shown in Fig. 1. The outer shell of target holder assembly has been made as trapezoidal shape. The dimension of trapezoidal shaped chamber is such as that it is inscribed (ref top view, Fig. 1) in a circle of 93 mm diameter (with 1 mm radial clearance). An inlet and two outlet pipes have been provided from the top of trapezoidal chamber. Inlet pipe has a smooth bend (1.5D) to deliver water jet for cooling. An orifice with 37 nos. of 2 mm holes at triangular pitch of 3 mm is provided at the end of inlet pipe line to achieve higher water jet velocity.

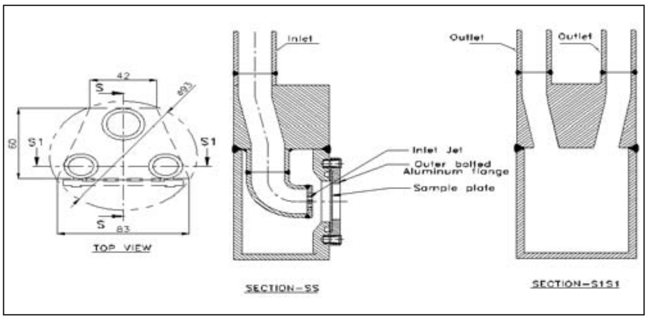

Fig. 1: Design of target holder assembly

The target plate needs to be easily removable from the target holder because of radiation concerns (remote operations). Moreover, the joint between target plate and target holder wall needs to be vacuum tight joint. A Viton O-ring along with bolted aluminum flange is selected for vacuum tight joint between target plate and target holder wall. The size of the O-ring is decided such that O ring is well away from the proton beam area (20 mm dia.) and the radial temperature distribution on target plate near the O-ring location is < 50°C. The outer aluminum flange of thickness 4 mm eliminates the direct irradiation of O-ring and extends the life of O-rings. The compression of O ring, target plate and outer aluminum flange with the wall is achieved using Titanium bolts.

Further, a thermal-hydraulic analysis of 3D model of target holder assembly is carried out and verified the design. The present model is capable of maintaining the mixed mean temperature of 1 mm thick target plate holder with in 200°C for the design heat input of 1.5 kW. A demo piece of the target holder assembly has been fabricated and tested for helium leak test. The test has qualified for leak of 10^{-9} mbar.L/sec. Actual target plate holder assembly will be manufactured as per the final design. Heat transfer capability of the target holder assembly will be demonstrated using the actual target holder assembly at VECC

II.21 Quality Assurance and Inspection Activities during Modification of Transfer Arm of PFBR

Transfer Arm (TA) is an offset arm type machine, employed for the in-vessel manipulation of core subassemblies (SAs).The lower segment of the TA includes guide tube and gripper assemblies, partially submerged in sodium, while the corresponding drive mechanisms are positioned above the biological shield of the reactor. The gripper subassembly undergoes vertical movement within a range of 4.6 meters relative to the guide situated in the shielding sleeve during the hoisting process. To mitigate wear/galling, the outer tube (OT) of the gripper assembly undergoes hard chrome plating, and the guide in the shielding sleeve is hard-faced with NiCr-B.

During pre-commissioning trials, excessive frictional loading and jamming of the gripper within the shielding sleeve observed. Visual inspection revealed some score marks spanning a length of 1.5 meters at the mid-portion of the 14.5-meter-long outer tube. Subsequent dismantling of the machine exposed corresponding scoring marks on the hard-faced guide in the shielding sleeve. Hence, a modification activity planned and executed and all the quality requirements, stated in quality assurance plan (QAP), are assured to meet PFBR specifications. Consequently, QA activities like qualification of welding, NDE, hardfacing of Colmonoy-5 by Manual TIG on Inner Diameter side for Top and Bottom bush. To standardize Chrome plating parameters, carried out using mock ups having Outside diameter 137.61 mm and length of 500 mm with simulated surface profiles and monitored all electric, chemical and mechanical parameters. On successful test results of coating thickness, hardness, qualified the procedures and personnel. New stainless steel pipe was machined to dia of 137.9 mm & length of 3.6 m representing Outer tube no2 (OT2) for replacement. To ensure the required quality, a production test coupon is attached with newly machined OT2 [Fig.1]. During hardchrome plating [Fig. 2], quality checks such as bath chemical composition, electrical and temperature control parameters were monitored and maintained with the limits. After hardcrome plating, OT2 is inspected and measured for diameter (137.58/137.60 mm), coating thickness (80 ± 5 μm), run-out, surface finish (0.3 to 0.5 μm) at equal intervals of 500 mm at four orientations and straightness using methods that meet to the precisions stipulated in PFBR documents. Production test coupons (PTC) ensured the performance of activities based on satisfactory results (No micro fissures [Fig. 3]) of adhesive test [Fig. 4] and surface hardness of 980 to 990 Hv of as per PFBR specification. The challenges faced during all the QA activities were systematically addressed and reported.

To replace the top & bottom bushes of shielding sleeves, weld joints of bushes and various pins (Pin1 -12 Nos. and Pin 2 -5 Nos. and Pin 3- 1 No) in shielding sleeve were detected using Ultrasonic examinations., Hard facing of refurbished bushes using qualified WPS & PQR and ensured soundness of hard facing using NDE techniques like VE, LPE and UT. The pre and post hard facing hardness survey was conducted on PTC and achieved 48 HRC for the overlay thickness of 2 mm. The OT2 is integrated with main outer tube assembly (15m) and top & bottom bushes with shielding sleeve of TA as per approved QAP and examined for straightness [Fig. 5] and concentricity respectively using optical jig transits and levelling methods and accepted for further assembly & testing.

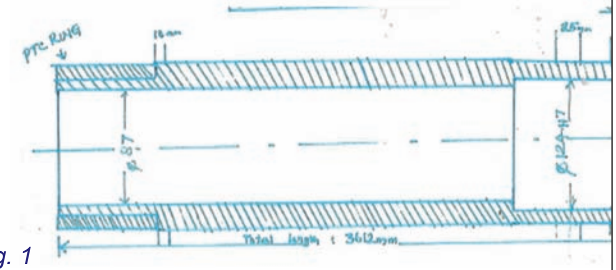

Fig. 1

Fig. 2

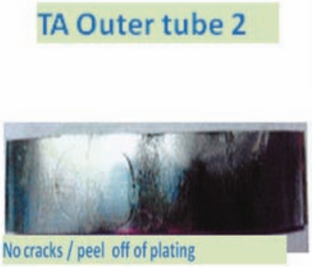

Fig. 3

Fig. 4

Fig. 5

II.22 Manufacturing and Inspection of Components for PFBR Main Vessel Pre-Heating and Sodium Filling

Preheating and sodium filling of PFBR main vessel (MV) was scheduled without the 4th intermediate heat exchanger (IHX), which was dismantled for repairs. The IHX opening in the MV had to be closed for pressure hold test and subsequent pre-heating. Central Workshop Division (CWD) manufactured the following three critical components on mission mode for PFBR MV pressure hold test, pre-heating and sodium filling:

1. Stiffened Carbon Steel S Dummy Flange to close IHX opening for PFBR MV pressure hold test.
2. SS support flange with holes and spacers for closure of IHX opening and to support the pre-heating spools.
3. 61 hole Orifice Plate used as IHX equivalent device for PFBR-Secondary Sodium Main circuit.

This articles details manufacturing and inspection aspects of the above.

1. Stiffened carbon steel dummy flange:

A 20mm thick, 2520 mm diameter stiffened carbon steel dummy flange (CS) was fabricated for closure of the PFBR IHX opening to conduct main vessel pressure hold test. Due to non-availability of full size plate, the required size was realized by long seam welding of two plates. Edges of both the plates were beveled in the plate beveling machine for double 'V' butt weld. Such long double V butt welding was indeed a challenging task considering inevitable weld distortion and specified tolerances, which were mitigated through restraints and sequence welding. The resulting weld distortion was corrected by re-rolling of the welded plate in plate bending machine. After joining the two plates, the 2520 mm diameter circular flange was cut using CNC water jet cutting machine. 42 Nos. of diameter Φ35 mm equally spaced holes were drilled on 2456 mm pitch circle diameter (PCD) using the RM 65 radial drilling machine (Fig 1). For strengthening the flange, a pre-fabricated hexagon shaped Rib Stiffener (ISA50 angle) was welded using Shielded Metal Arc Welding (SMAW) process to the top side of the Flange. Four numbers of 16 mm thickness lifting lugs were cut by plasma cutting machine and fillet welded to the top side of the flange at 90˚ apart on Ø1200 mm PCD.

Fig. 1: Photograph of Drilling with 42 Nos. Dia. 35mm holes

Fig. 2: Stiffened 20 mm thick carbon steel flange for PFBR MV pressure hold test.

Stage-wise inspection was carried out during fabrication of the flange. The first step involved Material Identification followed by marking inspection as per drawing. Marking, layout and component inspection was done using trammel tools, measuring tape and Vernier to measure flange diameter, hole locations, distance between holes and PCD of holes. The angles between stiffeners were determined using a 45° template. All the welds were subjected to visual and Liquid Penetrant Examination (LPE) to ensure defect free weld joints for holding leak tightness during pressure hold test. The stiffened dummy flange was fabricated to meet the drawing specification, coated with Red-oxide paint and delivered (Fig.2).

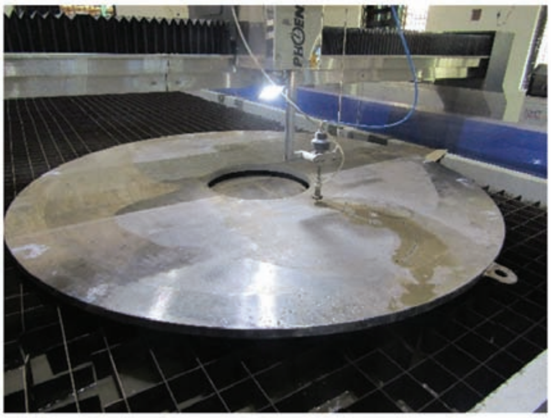

Fig. 3: CNC Abrasive Waterjet Cutting of holes for preheating spool pipes

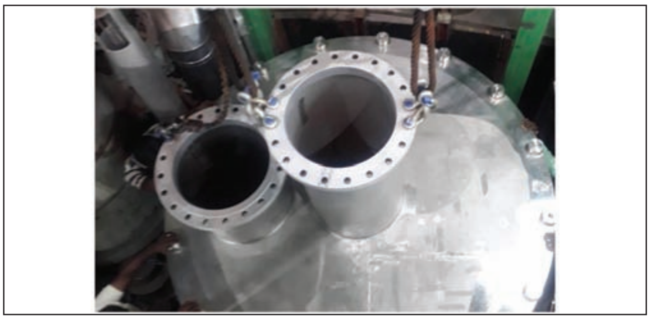

Fig. 4: 40 mm thick SS Flange with spacers and preheating spool pipes

2. 40mm thick SS support flange:

A Ø 2336 + 3.0/-0.0 mm outer diameter, 40mm thickness SS 304L flange was fabricated for leak tight closure of the PFBR IHX opening and to support the main vessel preheating spool pipes. Due non-availability of full size plate, three plates were welded to achieve the required size. Weld edge preparation was done using portable plate beveling machine for Double "V" weld joint configuration and subjected to LPE followed by weld fit-up to integrate all three plates. Root pass was welded using Gas Tungsten Arc Welding (GTAW) process and subsequent passes were welded with SMAW process and sequence welding technique was adopted to control weld distortion. The outer diameter and two holes of Ø562mm at 680mm pitch with 10mm offset on the 0°-180° line were cut by CNC abrasive water jet cutting machine (Fig. 3) using optimized cutting parameters.

8 Nos. of solid spacers and 8 Nos of M30 x 3.5 blind threaded Φ86 mm spacers were precisely machined, inspected and fillet welded equidistance on PCD of 2250mm on one face of the flange. The spacers were specified with surface roughness within 1.6 µm on both flat faces, flatness tolerance of 20 µm and 3 x 45° chamfer on the welding face. The spacers and the threaded lifting bushes were matched with corresponding hole locations in intermediate connecting piece of the PI Flask, which is used to handle Primary Sodium Pump and IHX for repairs/replacements, transport to storage locations and decontamination pits.

Stage inspection was done during welding of spacers.

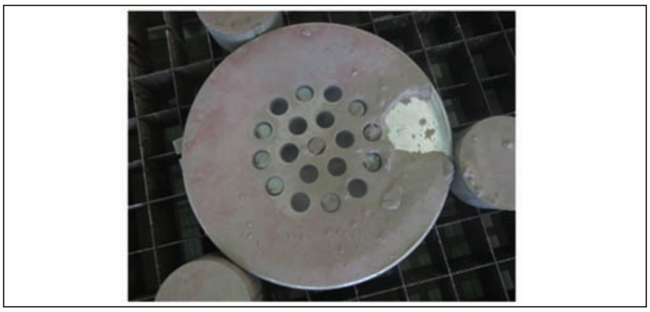

Fig. 5: CNC Abrasive water jet cutting of near-net shape holes on IHX equivalent device

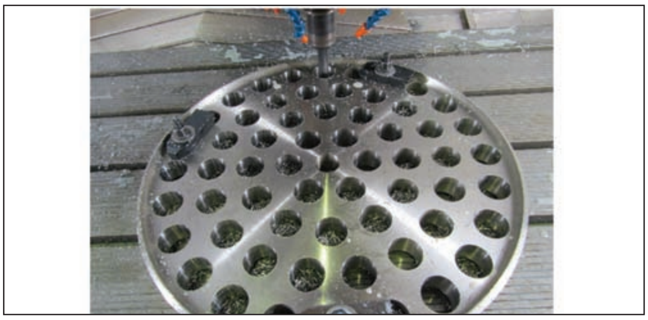

Fig. 6: Precise machining of 61 Nos. of dia.45mm holes using CNC -VMC

Solid spacers were intermittently welded, while the threaded spacers were welded all round. The height of the spacers was measured after final machining of the flange to ensure equal 90 mm height with unilateral tolerance of 500 µm on the negative side. All the above mentioned critical dimensions were inspected using various measuring instruments like digital Vernier caliper, Contour measuring machine, CMM, Electronic height gauge.

The SS flange with spacers and handling nuts was successfully fabricated, inspected and delivered to site in shortest possible time. The preheating spool pipes were welded to the flange at site by BHAVINI and the integrated flange was installed on PFBR for preheating of the main vessel (Fig. 4).

3. IHX equivalent device - Orifice Plate

The IHX equivalent device consists of an Orifice plate designed for flow balancing in PFBR. The SS 316LN orifice plate is of Φ559 mm outer diameter with 59mm edge, 35mm thick with center hole of Φ38.5mm and 60 holes of Φ43mm arranged in 4 concentric PCDs. The orifice plate is designed to generate pressure drop equivalent to that of one IHX thereby ensuring the required pressure drop in the respective sodium pump. Tolerances of the holes is +100 µm / -50 µm.

The holes were cut to the near net shape and dimensions using CNC abrasive water jet cutting (Fig. 5) followed by machining to the required outer dimensions in lathe and finish machining of the 61 holes in the CNC vertical machining center (VMC) (Fig. 6).

Thorough inspection was carried out including material composition using XRF analyser, ultrasonic examination and tensile testing. During marking / machining of the plate and drilling of holes, each stage was dimensionally inspected. The orifice plate has a centrally placed hole, which is reference for establishing centers for all other holes and PCDs. CNC Coordinate Measuring Machine (CMM), which has the capability to establish an imaginary center, was used for inspection of all the holes and groove dimensions. The machined orifice plate was delivered to BHAVINI on time.

II.23 Manufacturing of Container for PFBR Canned Sub Assembly Storage

Central Workshop Division (CWD) executed manufactured two containers to store the neutron source sub-assemblies in PFBR canned SA storage vessel location at BHAVINI. Overall size of the storage container is OD 219.1 & 114.3 x 4755 mm and material of construction is SS 304L. The container is a slender assembly comprising of 10 Nos. of different components including machined components, seam welded pipes and formed cones. Joints are made by butt welding using GTAW process and achieving the overall straightness requirement of 3.0 mm was highly challenging task. Manufacturing acceptance criteria is ASME Section III.

200 NB sch #40 seamed pipes were initially subjected to ultrasonic inspection to ascertain seam weld integrity and then the pipes were cut to the required length using Fabmax split frame cold pipe beveling machine (Fig. 1). Parts 1A, 1C,ID, 1F,IG and 1K was precisely machined to the required linear and geometrical tolerances as per drawing. Machining of components named 1G, with two different spherical radius R100 and R50 were very critical requirements and it was successfully achieved by using CNC Lathe machine. IDs of two components, namely 1C and guides (Fig. 2), where the Sub-assemblies rest were Hard chrome plated with 50 microns thickness through outsourcing. Scratch and bend test was conducted in the respective product test coupon to ensure the quality of chrome plating and found satisfactory.

Concentric tapered cone having dimension OD 175 and OD 114.3 mm (Fig. 2) with 55 mm height respectively was fabricated into two equal halves and L-seam welded using Single "V" butt joint. Controlling ovality and maintaining dimensional accuracy in the tapered cone was highly challenging task. Plate was cut CNC abrasive water jet to required dimensions and the segments were formed by progressive punching using 90 T capacity press brake machine.

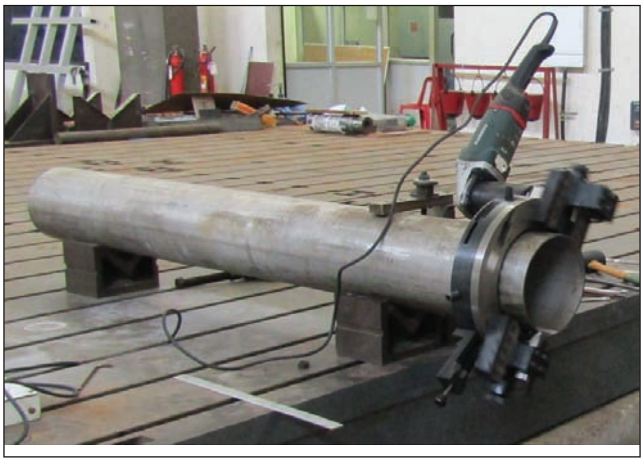

Fig. 1: Pipe (200 NB sch # 40) cutting using FABMAX split frame cold pipe beveling machine

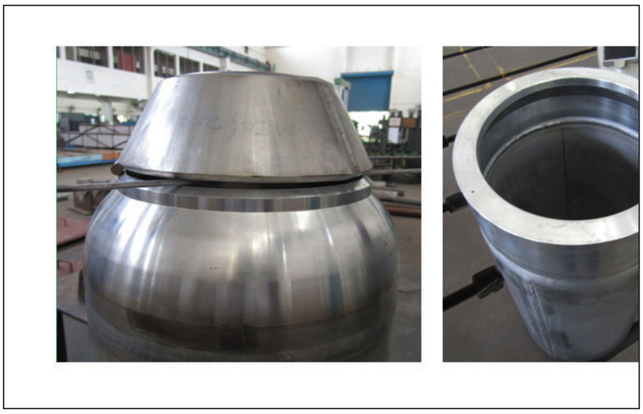

Fig. 2: Concentric tapered cone with component namely "IG" (Left side) , Hard chromed Guide (Right side)

To facilitate the assembly and welding, total assembly was divided into six subassemblies, assembled, and welded using GTAW process. Weld distortion was controlled using mechanical spiders and sequence-welding. All welds were subjected to Liquid Penetrant Inspection (LPI) on root and final pass. Butt welds were subjected to 10% double wall single image radiography testing.

The straightness of the containers (Fig. 3) was checked optically, using a calibrated JIG TRANSIT and optical scales (attached to the container horizontally) and the straightness achieved was 1.6 mm against the specified value of 3mm and delivered to BHAVINI in time.

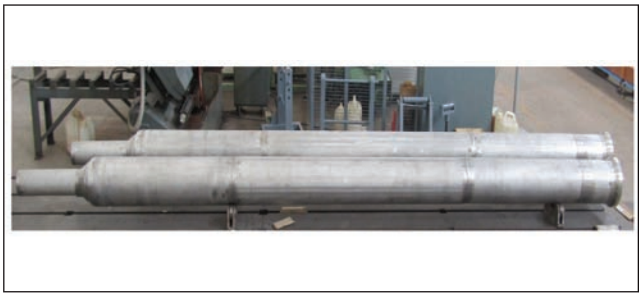

Fig. 3: Fabricated storage containers for PFBR

II.24 Repair/Refurbishment of PFBR Transfer Arm

Transfer Arm (TA) is a critical component of Prototype Fast Breeder reactor (PFBR) and is used for facilitating handling of various Subassemblies (SAs) in and out of the main vessel. Primary part of TA is the very slender hard Chrome plated outer tube (OT) of dimensions OD137.75 x ID124 x length 14545 mm, which slides vertically inside the shielding sleeve through two Colmonoy 5 ID hard faced bushes. Both OT and shielding sleeve are made of 316LN stainless steel. This offset arm type machine maintains a fixed offset length of 572.5 mm. The Transfer Arm is installed over the pile, and conducted numerous SA handling operations since its installation. However, the TA faced issues during operation manifesting as increased force due to high friction. Subsequently, the outer tube and shielding sleeve were dismantled from the lower section of the TA, transported to CWD, IGCAR for comprehensive inspections, root cause analysis and refurbishment. The 14.545 m long outer tube has varying internal cross sections and is made by connecting four tubes through pin joints and guided butt welding. The four individual tubes are named as Outer Tube No. 1, 2, 3 and 4, which itself are welded tubes of different cross sections.

To identify the root cause of the problem, several inspections were carried out. Scoring marks on the hard chrome-plated surface of the outer tube and the bottom/middle guide of the shielding sleeve were observed. Straight edge method for local bends followed by optical measurement method were employed for straightness measurement. Analysis concluded that the straightness of individual portions of the outer tubes were maintained within 0.1 mm. Combining optical measurements and verification with the straight edge method revealed a bend of around 7.2 mm from the top flange of the outer tube. According to design specifications, the outer tube was intended to be straight within 5 mm for its entire length and 0.5 mm/m locally.

Significant scoring and bend were noticed on the outer tube no.2 (OT 2) of 3.7 m length and it was decided to replace it with a new tube of identical specifications. The OT 2 was dismantled from the OT by cutting the seal welds and removing the locking pins. A new OT 2 was manufactured from fresh raw materials supplied in the form of SS 316LN Dia 150 mm rod and 125 NB Sch 80 pipe. The overall dimensions of OT 2 are OD 137.75 g6 and length 3600 mm. The new OT2 consists of five parts of different cross sections and end conditions, namely A1, A, B, C & D connected by guided butt welding. End to end concentricity requirement is 0.5 mm and straightness tolerance is within 0.3 mm/m, which are critical and functional requirements. Considering the

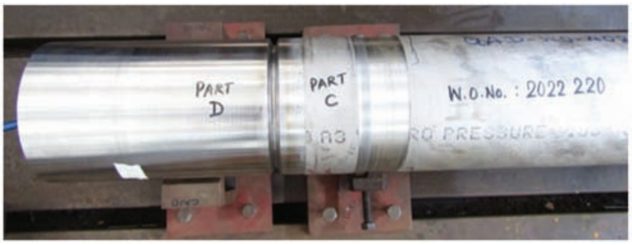

Fig. 2: Outer tube 2 Assembly and Welding

Fig. 1: Outer tube 2 Part machining

Fig. 3: Final machining of outer tube 2

Fig. 4: Match Drilling of transfer arm

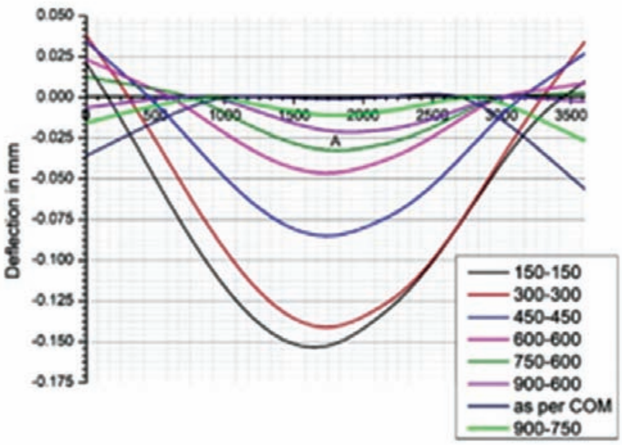

Fig. 6: FEM results - Deflection vs length of the Outer tube with varying distance of roller support from the ends

final assembly requirements, part drawings covering the pre-machining, stage assembly, welding and final machining stage details were prepared. Unique process plan sheet and micro schedule were prepared and executed.

Parts A1, B and D were pre-machined from 150 mm dia solid, while parts A and C were pre-machined from 125 NB sch 80 pipe (Fig. 1). Total length of pipes were 1752 and 1198 mm respectively. ID of the either end of pipe was machined to dia 124 mm H7 tolerance to 100 mm length to suit the mating parts. Reference cut was taken on OD to facilitate steady rest support, machining, assembly and welding. Machining was carried out using the facing lathe with three point steady rest support. ID 87 mm and 88 mm were machined to final dimensions.

The pre-machined parts were guded but welded (Fig. 2). To control the welding distortion and also to achieve the assembly straightness requirement, optimum assembly and welding sequence was prepared and executed in phased manner. Parts B, C and D were assembled and welded into one sub-assembly and Parts A1 & A were assembled and welded into another sub-assembly. Finally, the both the welded sub-assemblies were further connected and welded as per drawing.

Final machining of the fully welded OT2 assembly of 3.7 m length was carried out in the L45 lathe (Fig. 3) and OD was machined to dia 137.92 / 137.83 mm over the entire length. One end ID was machined to dia 124 mm H7 up to 100 mm length and on the other end OD was machined to dia 124 mm g6 to length of 90 mm as per drawing to integrate with the other parts of the OT. Final assembly was subjected to QAD inspection and found satisfactory.

The job was very challenging considering the long length, slenderness and stringent concentricity and straightness tolerances and successfully achieved within the tolerances specified through meticulous process planning, execution and control. The finish machined

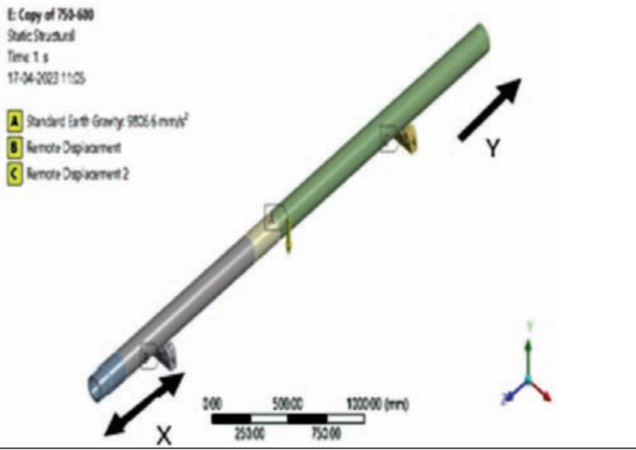

Fig. 5: FEM model of PFBR OT Assembly

Fig. 7: Final QA Check of the Refurbished 14.5 m long PFBR TA Outer Tube

Fig. 8: Completed transfer arm being shifted to BHAVINI

OT2 was delivered for final finish grinding and hard Chrome plating on OD to an outsourced vendor.

The newly machined, welded and hard Chrome plated OT 2 was match drilled to integrate with the other existing parts of the OT, which were also match drilled (Fig. 4). The OT pieces were joined by radially arranged cylindrical pins. Before match drilling, the individual tube's straightness was ensured and the final joints were subjected to seal welding and concentricity measurement. Thermal corrections were done to restore/ achieve the specified straightness.

The long outer tube passes through two cylindrical bushes, which act as guides, in the shielding sleeve of the TA. The sharp edge located at the base of the shielding sleeve possesses a radius of 0.3 mm, while the upper edge of the middle guide bush features a radius of 2 mm. The presence of such sharp edges results in exceptionally high contact stresses at the junction between the outer tube and its guide bushes in the shielding sleeve. To reduce these high contact stresses, the cylindrical guide bushes were replaced with new ones of modified design, which provided convex spherical curvature of 500 mm on the ID of the bush in place of the existing cylindrical surface. Colmonony 5 hard facing was provided on the convex ID surface of the bushes followed by precise machining to the specified spherical curvature. The finish machined guide bushes assembled, fastened and integrated with the shielding sleeve.

To ensure the straightness during assembly and welding of the transfer arm outer tube, it is imperative that the deflection between the rollers and at the overhanging ends is either identical or nearly identical. This uniformity is crucial for maintaining straightness during assembly & welding in horizontal position. Achieving this warranted thorough examination of the roller positions to ensure that the deflection between the centre of the rollers and at the extreme overhanging ends is consistent with both rollers. To optimize the roller support positions during assembly and welding, a full scale FEM model of the long OT and the rollers was developed and executed a quasi-static structural analysis software (Fig. 5). Extensive parametric studies by varying the roller support positions were carried out to study deflection at the specified points mentioned below and optimum roller support locations were determined. The deflection of the bottom most fibre was plotted against the length of the TA outer tube at varied distance between supports (Fig. 6).

Given the variable cross-sectional geometry of the TA along its length, a series of graphs were generated using various (X, Y) combinations, where X and Y represent the distances of roller support from the free ends. The graph depicting the (X, Y) combination of (900,750), shown in green, is found to be the most suitable. In this configuration, the deflection at the centre of supports is nearly equal to the deflection at the ends of the TA outer tube. A similar analysis was conducted for Outer Tubes 1, 3, and 4 to ensure the desired performance and characteristics.

Overall straightness of ~1.4 mm over the entire length of 14.545 m was achieved against the specified value of 3mm or less in the refurbished outer tube of PFBR TA (Fig. 7). The refurbished outer tube and shielding sleeve were delivered to BHAVINI (Fig. 8) and were installed on the reactor pile.

II.25 Design, Development and Testing of Subassembly Flow Measurement Instrument

As a part of surveillance, coolant flow (liquid sodium) exiting through selected subassemblies (SA) in the core and blanket region is envisaged to be measured using an Eddy Current Flow Sensor (ECFS) prior to every reactor startup. The ECFS is part of Core Flow Monitoring Mechanism (CFMM), which helps in positioning the ECFS at the exit of the subassembly. The ECFS consists of a primary coil at the centre and secondary coils on either side of the primary coil. The primary coil is excited with a sinusoidal constant AC at a fixed frequency and the difference in the voltages induced in the secondary coils is proportional to the flow. As the flow measurement is carried out under a constant sodium temperature of ~200˚C, temperature compensation is not required.

For the above purpose, a readout instrument namely Core Flow Monitoring Electronics (CFME) was developed. Refer Fig. 1 for the block diagram of the CFME. The instrument has been designed in a modular manner and realized in a 3U chassis, which can be accommodated in CFMM control panel.

The functions of the various modules are briefly described below:

Waveform Generator (WFG) – The sinusoidal waveform of required frequency is generated using a Numerically Controlled Oscillator implemented using Field Programmable Logic device. The frequency is selectable between 100 Hz to 1000 Hz with 1 Hz resolution.

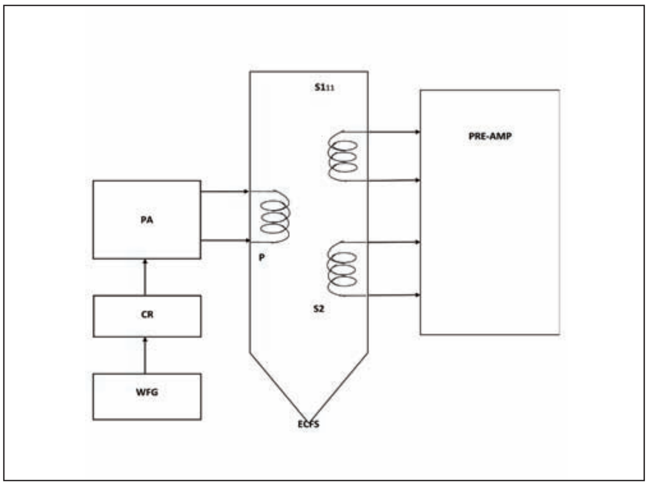

Fig. 1: Block Diagram of CFME

Fig. 2: Photograph of CFME Unit under test in Hall-3

Current Regulator (CR) – The output of WFG is used by this module to adjust the excitation current through the primary coil of ECFS in the range of 100 mA – 220 mA and regulate it with ± 1 mA of the adjusted value.

Power Amplifier (PA) – A Class AB amplifier stage is used to deliver the required current through the primary coil of the ECFS.

Pre Amplifier (Pre Amp) – The signals from the secondary coils of the ECFS are amplified, filtered and rectified for further processing.

ADC (ADC) – Digitizes the conditioned signals from the Pre Amplifier.

Microcontroller Unit (MCU) – The flow value is

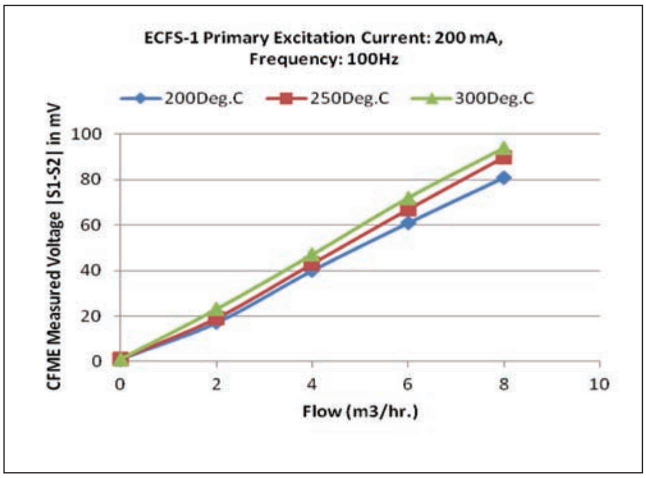

Fig. 3: Flow vs. Voltage – ECFS1

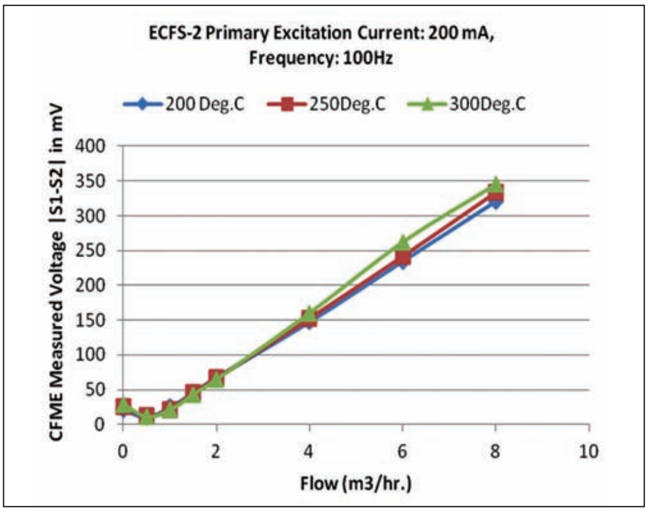

Fig. 4: Flow vs. Voltage of ECFS2

computed from the digitized data obtained from ADC. The Flow value is displayed to the operator and also transmitted over serial port for logging on a PC/Laptop.

Based on error budget analysis, the error in measurement is estimated to be ≤ ± 2 % of the span. The temperature stability of the instrument was evaluated using a test sensor in the temperature range of 10˚C – 60˚C @ 50% RH. It was observed that the excitation current and frequency was within ± 1 mA and ± 1 Hz respectively of the set value.

Subsequently, CFME was tested (Refer Fig. 2) with ECFS-1 and ECFS-2 sensors in a test loop in Hall-3, FRTG. ECFS-1 is used for flow measurement in core region and ECFS-2 is used for flow measurement in blanket region. The flow measurement was carried out for sodium flow in the range of 0 – 8 m^3/hr. and at 200˚C, 250˚C and 300˚C temperature.

During the test, the excitation to the primary coils of the sensor was maintained at 200 mA and the frequency used was 100 Hz for ECFS-1; ECFS-2 was tested with excitation frequencies of 100 Hz, 200 Hz and 300 Hz. Fig. 3 and Fig. 4 provide the results for ECFS-1 and ECFS-2 respectively at various sodium temperature. The sensitivity of ECFS-1 and ECFS-2 are provided in Table-1 and Table-2 respectively.

Table 1: ECFS-1 Sensitivity

Sodium Temperature (˚C)	Sensor Primary Coil Excitation Frequency (100 Hz) mV/(m^3/hr.)
200	0.310
250	0.345
300	0.361

Table 2: ECFS-2 Sensitivity

Sodium Temperature (˚C)	Sensor Primary Coil Excitation Frequency (Hz)mV/(m^3/hr.)		
	100 Hz	200Hz	300Hz
200	1.308	0.920	0.646
250	1.381	1.018	0.739
300	1.447	1.111	0.817

II.26 Multi-NDE Inspection of IHX Tubes of PFBR

NDE investigations of the intermediate heat exchanger (IHX) tubes of PFBR was envisaged, subsequent to the identification of sodium deposits in the shell side from the tube side in IHX-1 and 2. Multi-NDE investigations of the tubes using eddy current (EC), visual and ultrasonic based internal rotary inspection system (IRIS) techniques was carried out. Visual inspection was carried out prior to sodium cleaning at the inlet and outlet windows of the IHXs using an industrial videoscope. Inspection revealed sodium signatures such as aerosols, speckles, patches leak lines etc.at various locations in the shell region. Further cleaning in the shell and tube sides was done in both the IHXs for removal of sodium and a comprehensive multi-NDE inspection of the tubes was carried out.

EC inspection of the entire length of the tubes excluding the tube-sheet regions was carried out using dual frequency mixing technique to eliminate support plate signatures. The sensitivity of the EC technique was optimised for a 0.8 mm diameter hole and equivalent volumetric defects. The probes and procedure for testing was developed in-house.The EC data of the inspected tubes were analysed manually and using a software specifically developed in Python for automated analysis and visualization of the indications.Fig. 1shows the distribution of indications observed in the mixer channel by automated analysis of the EC data acquired in the tubes of IHX-1 &IHX-2. The colour map provides approximate distance of the maximum EC amplitude indication from the bottom tube sheet and the size of the markers is proportional to the maximum amplitude of the indication observed in the corresponding tube.

Visual examination and IRIS techniques were employed at locations where EC testing showed recordable indications.Visual examination revealed anomalies like a few scooping marks, rust marks, pits and sodium deposits at the ID locations and denting in few support plate (USP) locations.Stereoscopic imaging was performed to identify the depth of the scoop marks. Further, visual examination of an IHX-2 tube having localized noisy EC signal revealed multiple pits at the location with a white deposit patch. Fig. 2 shows the EC signals and visual images of the corresponding location.

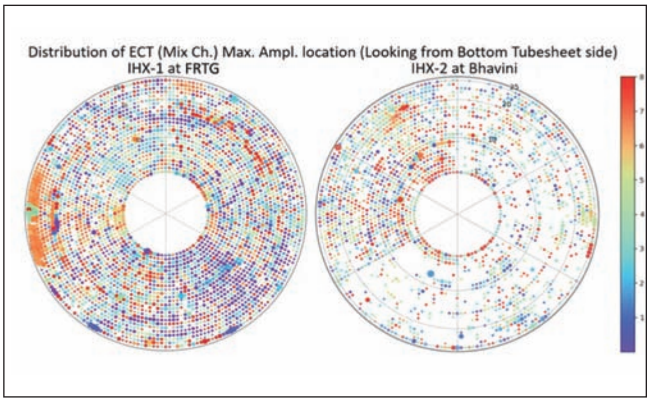

Fig. 1: Distribution of indications observed in the mixer channel by automated analysis of the EC data of IHX-1 and 2

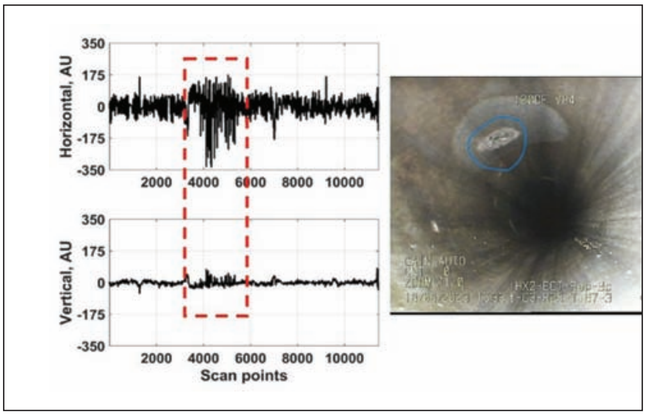

Fig. 2: EC response and videoscope image of IHX-2 tube (Row no. 25, Tube no. 50) having multiple pits.

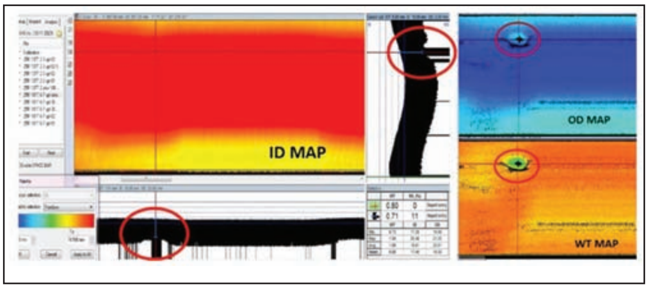

Fig. 3: IRIS response of IHX-1 tube (Row no. 25, Tube no. 101) having OD indication

Detailed IRIS examination of selected USP locations confirmed denting which might have occurred during fabrication. Further, IRIS examination of locations where ECT showed OD indications, wall thickness reduction from OD to was observed.Fig. 3 shows IRIS response of a typical OD indication observed in IHX-1. A 0.2 mm deep pit like OD indication was observed at the corresponding location.

Based on the observations from all the NDE techniques, potential leaky tubes of IHX-1 & 2 were identified and recommended for plugging. Complimentary nature of different NDE techniques has been utilized in Multi-NDE characterization for improved sensitivity in addition to accurate sizing of flaws in IHX tubes.

Back to Main

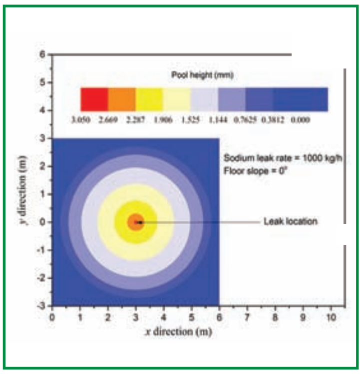

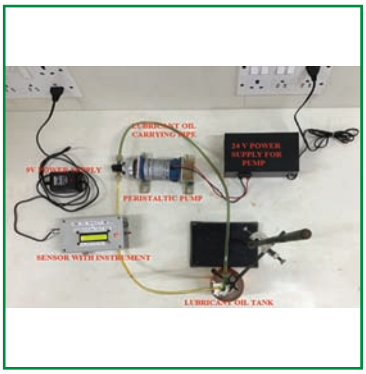

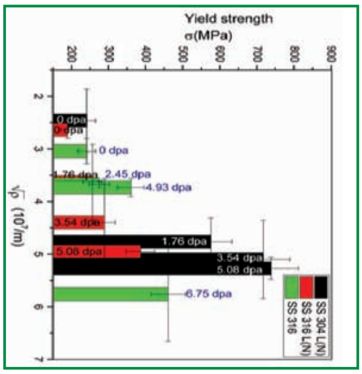

CHAPTER
III

R&D for Fast Breeder Reactors

III.01 General 2D Code Development for Computing Static and Dynamic Characteristics of Bearings for Sodium Pumps

In PFBR, PSP and SSP shafts are supported by oil lubricated hydrodynamic radial bearings at top and sodium lubricated hydrostatic radial bearing at bottom. Various performance parameters like load bearing capacity, stiffness and damping coefficients are required for enhanced performance assessment of PSP & SSP. Hence, a general 2D code development is carried out for computing performance parameters. The code developed solves the Reynolds Equations using Finite Difference Method (FDM) with appropriate boundary conditions for each bearing. The outcome of this study will help in enhancement of input data for rotor dynamic and seismic analysis of pumps and towards further study on optimization of bearings.

Top Radial Bearing

From the FDM formulations, pressure distribution in the bearing for given geometric parameters is obtained. Applying infinitesimal perturbation method, the formulations for pressure gradients are obtained and solved. Static and dynamic characteristics of journal bearing with axial groove (Fig. 1) are studied and the results obtained are validated with the literature. PFBR pumps have radial bearing which are pocket type bearing. The effect of variation of geometric parameters like pressure, groove geometry, groove angle, etc on the rotordynamic parameters are studied. The load direction in a vertical shaft will vary continuously with reference to housing in the bearing. Hence, orbit plots were generated for bearings of PSP / SSP operating at 200 rpm, 590 rpm and 900 rpm (Fig. 2).

Hydrostatic Bearing

Pocket type hydrostatic bearing used in PFBR pumps are modelled with pocket and land regions. With assumed pocket pressure, the Reynolds equation is solved in the land region. Pocket pressure is then iteratively corrected such that flow continuity in the pocket is satisfied (Fig. 3). The optimum resistance of flow restrictor to attain maximum load capacity for a given bearing configuration is estimated and results are validated with literature. The dynamic coefficients are estimated using finite perturbation method and validated with literature. The effect of turbulence in the flow is implemented by using bulk flow theory and the reduction in the load bearing capacity is estimated.

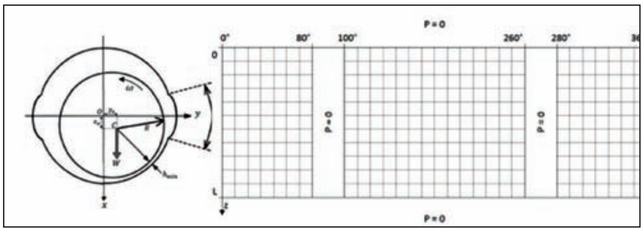

Fig. 1: Schematic of axial groove journal bearing and developed view with discretization

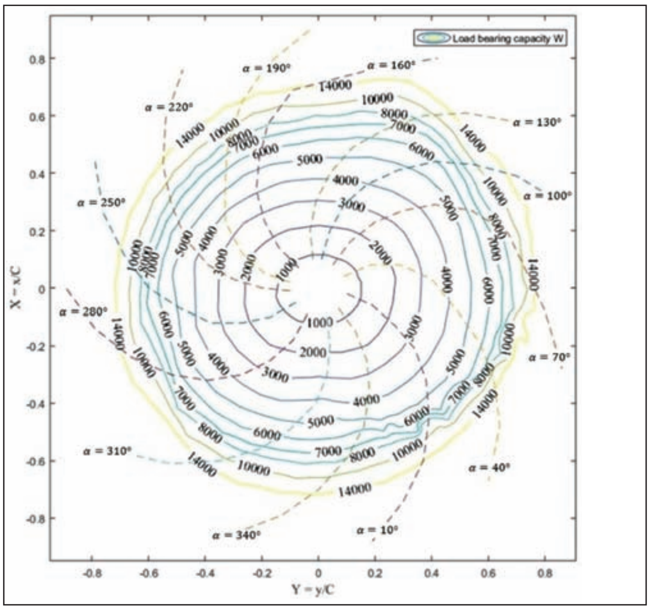

Fig. 2: Orbit plot of load bearing capacity of PFBR pump's top radial bearing at 900 rpm

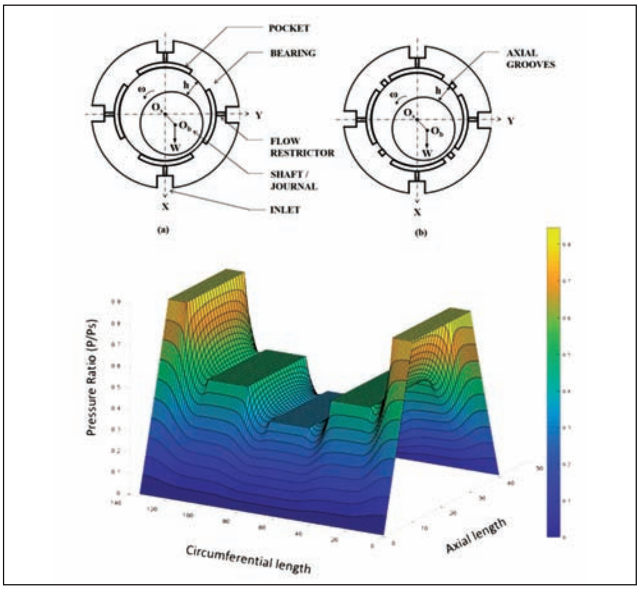

Fig. 3: Geometry and typical pressure distribution in hydrostatic journal bearing

III.02 Investigation of Small Leak Scenario in Steam Generator of Future FBR

Water leaks in tubes of steam generator (SG) will lead to sodium water reactions, resulting in release of hydrogen gas. Some of the major reactions between sodium and water/steam are given below.

$Na + H_2O \rightarrow NaOH + ½ H_2$

$Na + NaOH \rightarrow Na_2O + ½ H_2$

$Na + ½ H_2 \rightarrow NaH$

Early detection of small leaks and isolation of the concerned steam generator is important to prevent large accidents. Hydrogen produced during sodium water reaction is detected using hydrogen in sodium detector (HSD) or hydrogen in argon detector (HAD). Estimation of hydrogen concentration for different leak rates and at different temperatures are useful for design of leak detection system.

A computer code ‘Chyled’ is used to carry out the analysis for small leaks in SG. Chyled code models hydrogen and NaOH production, transport, distribution and dissolution in sodium. General transport equation is used to model transport of NaH and NaOH throughout the circuit. Various components of secondary sodium main circuit (SSMC), viz., pipes, IHX (intermediate heat exchanger), SG, tee junctions, HSD etc., are modeled in Chyled code. Hydrogen bubble radius is given as input in the code. Fig. 1 shows the bubble radius for various flow rates and at various temperatures. It can be seen that, the bubble size increases with decrease in sodium temperature for a given flow rate.

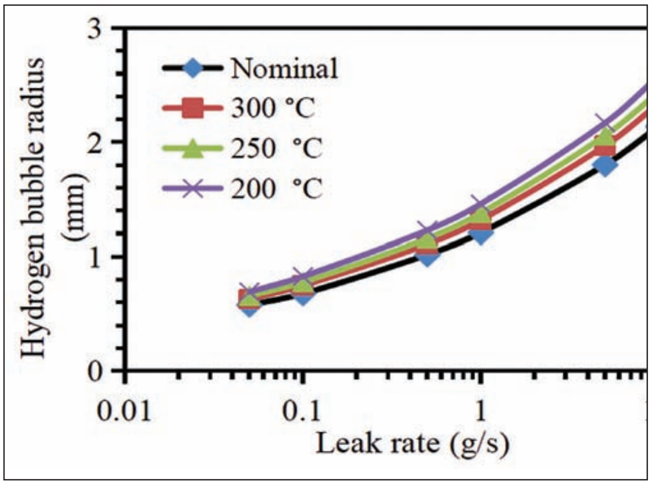

Fig. 1: Hydrogen bubble radius for various leak rates at different sodium temperatures

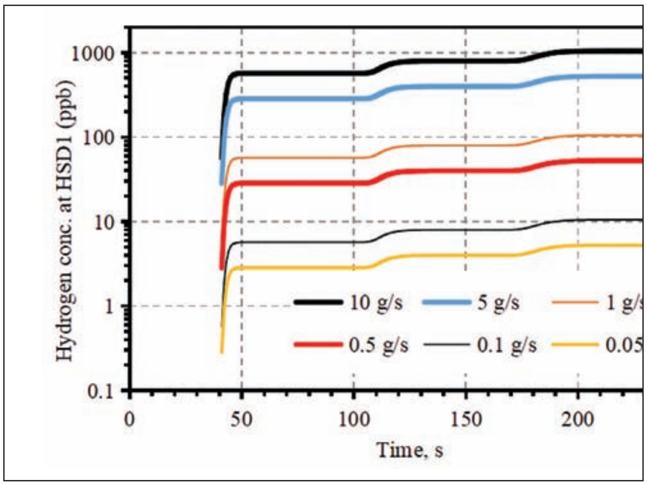

Fig. 2: Hydrogen concentration at HSD for various leak rates at normal operating temperature of SSMC

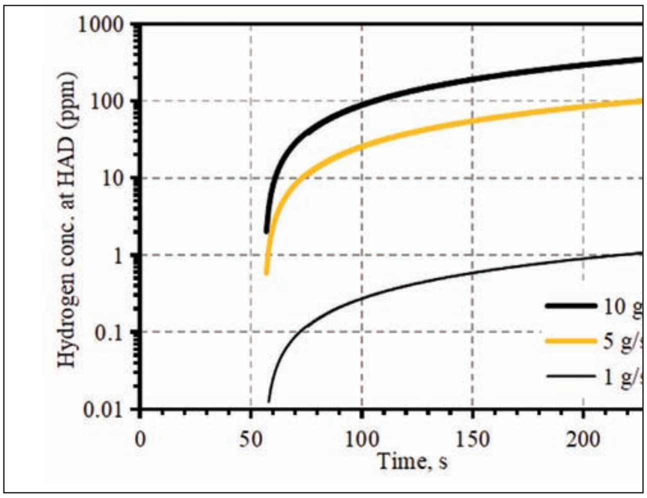

Fig. 3: Hydrogen concentration at HAD for various leak rates at 300 °C temperature of SSMC

Figure 2 shows evolution of hydrogen concentration at HSD for various leak rates during normal operation of SSMC. Following the leak, hydrogen concentration at HSD rises at 41 s. Then the concentration increases steeply and reaches a value of 571.1 ppb at 50 s for 10 g/s leak rate. Hydrogen concentration increases with leak rate.

Hydrogen concentration in HAD is shown in Fig. 3 for 300 °C temperature. The concentration starts rising 57 s onwards. For 10 g/s leak rate, the concentration is estimated as 353 ppm at 230 s. Hydrogen concentration at HSD and HAD are also estimated for other sodium temperatures and leak rates. These results will be used for design of leak detection system and early detection of leaks, which will help in preventing large accidents.

III.03 Development of CFD Code for Simulating Melting and Solidification Phenomenon in Sodium Systems

Most FBRs use liquid metal as coolant. This coolant is stored in large storage tanks in solid state before initial filling. In order to effect initial filling of primary or secondary systems, the solid metal needs to be liquefied and subsequently pumped into heat transport systems. During melting, convection increases the overall transport rate and, hence, the growth rate of the new phase, which is desirable. On the other hand, during solidification convection decreases the growth of the new phase and also seems to affect the morphology of the solid-liquid interface adversely. The morphology of the solid is largely determined by what occurs in the vicinity of the solid-liquid interface. The heat release (absorption), density change and other processes that take place in the vicinity of the transformation front result in non-uniformities along the front that cause its shape to change. The resulting density gradients in the liquid generate buoyancy-driven convection that can affect the transport of heat, constituent chemicals, and the growth rate. To simulate such a moving boundary problem, enthalpy-porosity technique of modeling phase change is implemented for simulating melting of pure metals. The present work will give insights for the determining the most optimal method for melting solidified sodium in storage tanks.

The enthalpy-porosity methods accounts for the melting (or solidification) by assigning a nodal latent heat value (ΔH) to each computational cell according to the temperature of the cell. Upon changing phase, the nodal latent heat content of the cell is adjusted to account for latent heat absorption or release, this adjustment is reflected in the energy equation as either a heat source or sink term.

Nodal latent heat value (ΔH) of zero indicates fully solid cell and of value L (latent heat of solidification) indicates fully liquid cell. Computational cells that are undergoing a phase change (i.e., $0<\Delta H<L$) are modeled as pseudo-porous media, with the porosity, $\varepsilon = \Delta H/L$, being a function of $\Delta H$and ranging between 1 (fully liquid cell) and 0 (fully solid cell). The present work involves the application of this enthalpy-porosity technique to the two-dimensional melting of a pure metal in a rectangular cavity. Fig. 1 shows the comparison between the results predicted by this method and experimental results of Gau and Viskanta and numerical results of Brent et al.available in the literature in order to validate the applicability of this technique for metal systems.

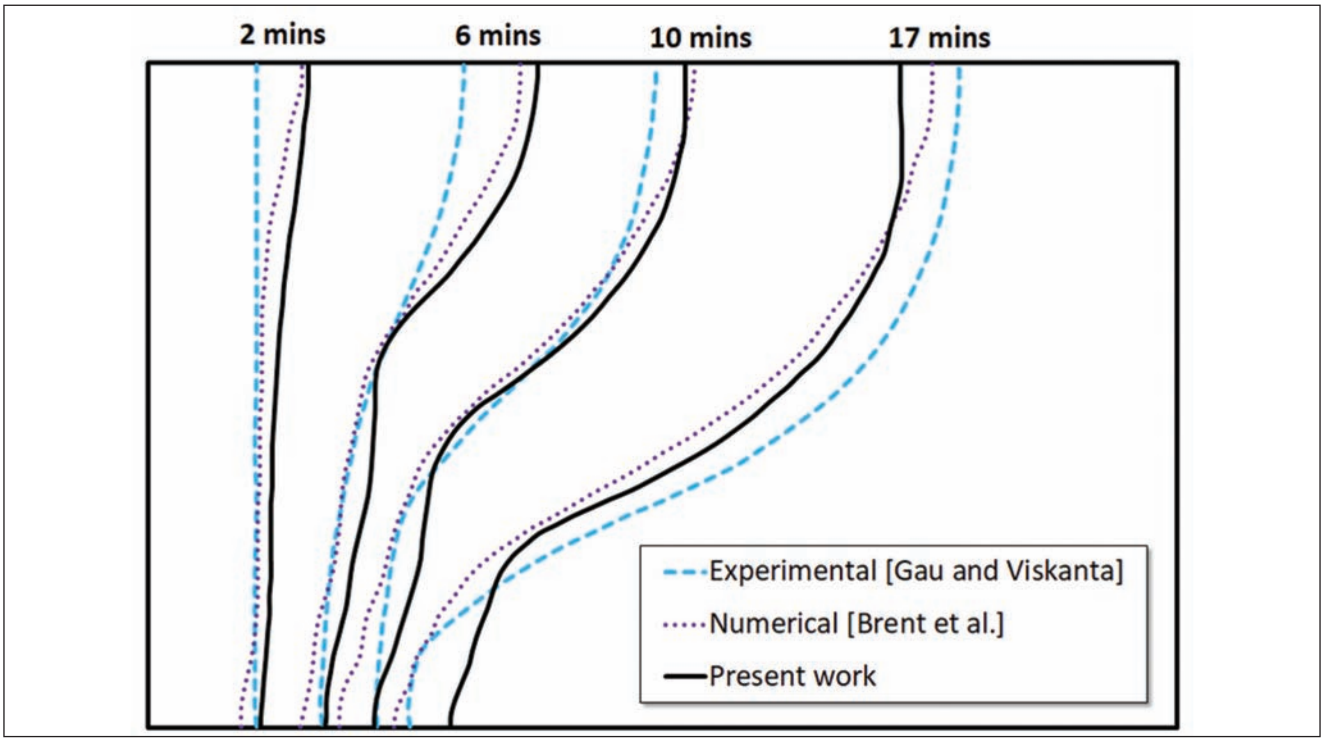

Fig. 1: Comparison of melt fronts as computed by code with the experimental (Gau and Viskanta) and numerical (Brent et al.) data available in the literature

III.04 Numerical Modeling of Accidental Sodium Leaks Spreading on the Sloped Floor Surface in SFR Cells

The accidental breach in pipelines and components of heat transport circuits in Sodium-cooled Fast Reactor (SFR) can create sodium leak that eventually reaches the cell floor, spreads gradually, and forms a burning pool. In order to prevent the occurrence of sodium fire and to minimize its consequences, adequate safety measures have been incorporated in the SFR systems.

The leak rate of sodium released in an accidental event can vary widely and it mainly depends on the size of the leak path created. Large-scale leak is possible due to guillotine rupture of sodium pipelines (of size 100 NB or below). For this purpose, sloped floors are provided in reactor cells for guiding the leaked sodium towards the drain lines through which a large fraction of spillage can be drained out to a collection tank and minimize the consequences of sodium fire.

In this context, it is necessary to understand the flow pattern and spreading dynamics of sodium pool on the sloped floor surface for the effective design of draining systems in SFR cells. Towards this, numerical investigation has been carried out on the spreading behavior of burning sodium pool on the sloped/plane cell floor by developing a 3-D numerical model based on the viscous-gravity current equation of the shallow layer model. The governing equations of the model have been solved numerically by implementing the Finite Volume Method. The model developed has been validated with the experimental results in the literature for the liquid spreading process on the plane and sloped floor surfaces for different leak rates ranging from few tens to few thousands kg/h.

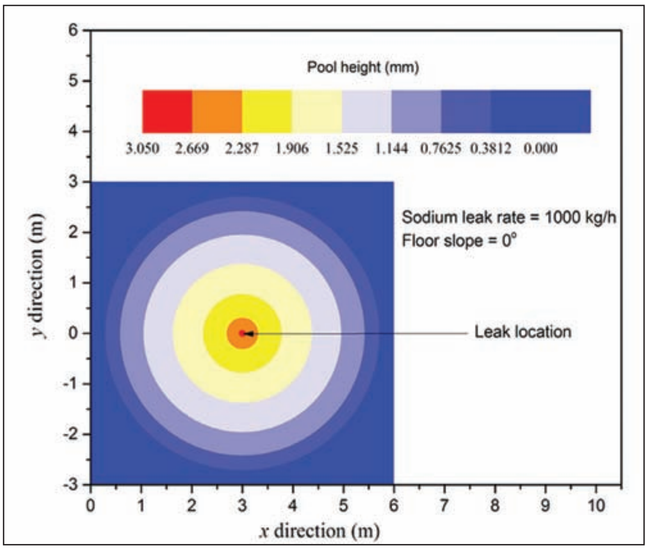

Fig. 1: Equilibrium pool shape for 1000 kg/h sodium leak rate on plane surface

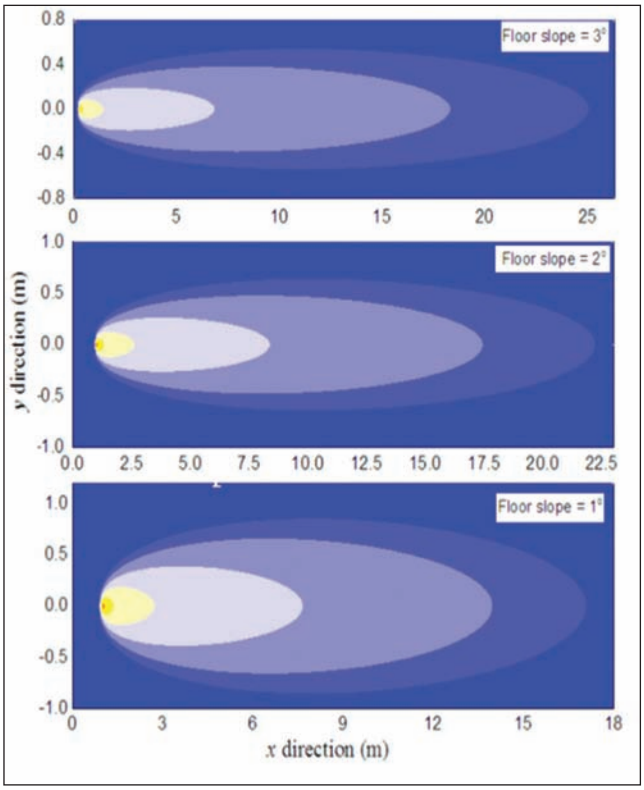

Fig. 2: Spreading behaviour of sodium on the sloped floors (equilibrium pool shapes for 1000 kg/h)

Using this model, numerical simulations were carried out on sodium pool spreading based on the leak events that occurred in the fast reactors and also for various postulated leak scenarios envisaged in SFR systems. The time-varying pool size and shape, pool height profile, maximum pool area, and pool mass inventory have been estimated for a range of sodium leak rates and typical floor slopes of interest to nuclear power plants. The model predictions revealed that the floor slope alters the shape of the equilibrium pool and decreases time for pool formation. The increase in floor slope increases the extent of spreading in the down-slope direction and decreases the spreading in the upslope and cross-slope directions (Figs 1 and 2).

The analysis results contribute towards the assessment of SFR safety against the postulated sodium fire events.

III.05 Numerical analysis of sodium-argon flow in narrow channels under severe accident conditions in pool type SFR

During the postulated energetic core disruptive accident (CDA) in a pool-type SFR, the formation and expansion of a large (~ m) two-phase fuel bubble (with work potential) can occur in the disrupted core. The fuel bubble expansion into this overlaying liquid sodium pool and the compression of argon cover gas results in the reactor vessel pressurization. Under this condition, the sodium pool-cover gas interface undergoes churning, forming a sodium-argon two-phase mixture at the interface vicinity. This sodium-argon mixture can be released to the reactor containment building (RCB) due to the pressure difference between the reactor vessel and RCB (i.e., driving pressure). The release takes place through the opened vessel head (top shield) penetrations. Fig. 1 shows the schematic of the sodium-argon release process through a vessel head leak path.

The sodium fire in RCB, which follows the sodium-argon release under energetic CDA, decides the RCB thermal loading, pressure rise and the resulting leak rate. The sodium fire depends on the total sodium mass in the sodium-argon mixture. Therefore, the total sodium mass released from the reactor vessel (primary containment) to RCB (secondary containment) is an essential parameter in the SFR safety analysis. In this context, a two-phase flow model is developed to estimate the total sodium mass in the sodium-argon release through the top shield penetrations. The model considers the two-phase frictional and local pressure drops to evaluate the sodium-argon transient flow.

The model is validated with the benchmark experiments from the literature. The experiments used a high-pressure source inside the water pool to investigate the sodium-argon release phenomenon.

Model predictions for total release mass and the water release velocity are compared with the experimental results, and good agreement is observed. Fig. 2 and 3 show the comparison of model predictions and experimental observation for transient water release velocity and release mass, respectively.

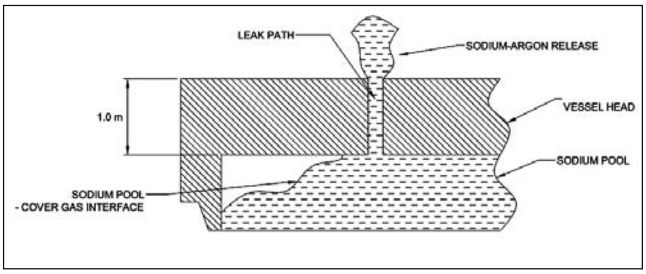

Fig. 1: Sodium-argon release through the vessel head under energetic CDA conditions

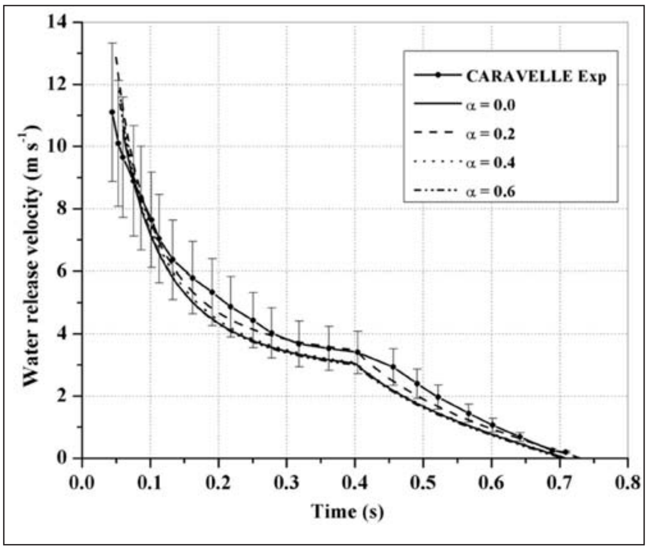

Fig. 2: Comparison of model predictions and experimental observation for transient water release velocity (α = air volume fractions)

The numerical analysis of sodium-argon flow in a typical reactor-scale geometry shows that the acoustic impedance of the sodium-argon mixture is lesser than that of single-phase sodium, which mitigates the sodium release process during the slug impact phase. Similarly, the frictional pressure drop and the entry loss decreases the total release mass to RCB by 25%.

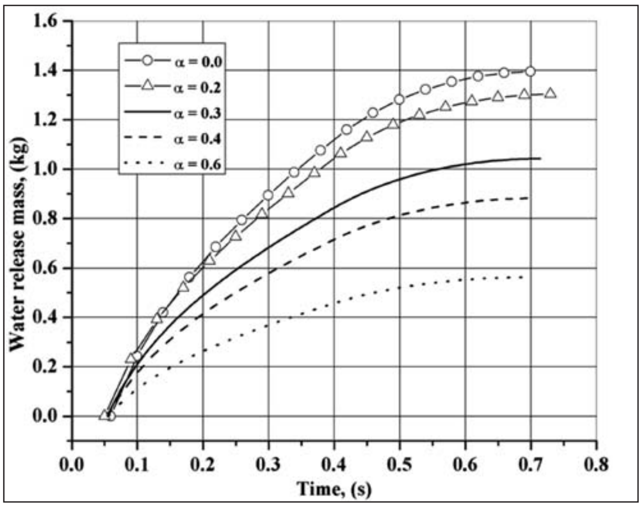

Fig. 3: Total mass of water released for air volume fractions up to 0.6

III.06 Life-Estimation of Labyrinth Type V-Ring Seal Used in Shut Down Mechanisms of PFBR

An in-house designed and developed labyrinth type V-ring seals are used as dynamic seals in Control and safety rod drive mechanism of PFBR. The main design objectives of the seal are to provide leak-tightness and offer low frictional resistance. The photograph of the seal is shown in Fig. 1.

During the seal development stage, the prototype seal was tested for 1000 cycles of scram operations in simulated conditions. Later, the qualification testing of prototype CSRDM and DSRDM served as a platform for integrated qualification of the seals. Qualification testing was carried out under simulated operating conditions. Duty cycle on seals encompasses nearly 1500 fast drop cycles and equal number of translations for CSRDM and nearly 1000 translation cycles for DSRDM. Seals in both the mechanisms were found meeting operational requirements even after this duty cycle, validating the suitability of the seals.

As a next step in demonstrating the reliability and robustness of these seals, the ageing studies of the seals were taken up.

The ageing studies were carried out in a dedicated test facility, in Engg. Hall-I. The test set-up simulates the geometric features of the CSRDM. Provisions were made for raising / lowering and for fast dropping the central mobile shaft. There is provision to keep two seals in series in the seal holder and test them simultaneously. Test set-up consists of heaters for heating it to 200 °C. The test set-up is also provided with necessary instrumentation.

Ageing studies were carried out at three different temperatures, viz., 150 °C, 180 °C & 200 °C. At each temperature, characterization tests such as friction force measurement, leak rate measurement and fast drop tests were carried out.

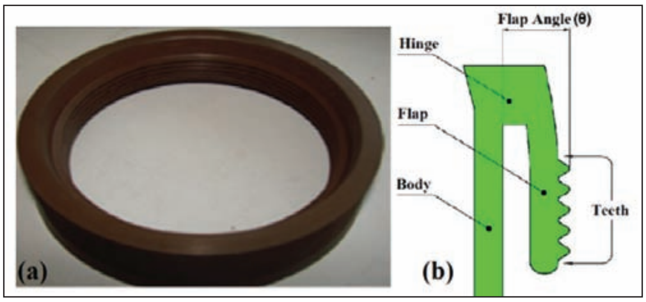

Fig. 1: (a) photograph of labyrinth type V-ring seal and (b) schematic diagram of V-ring seal

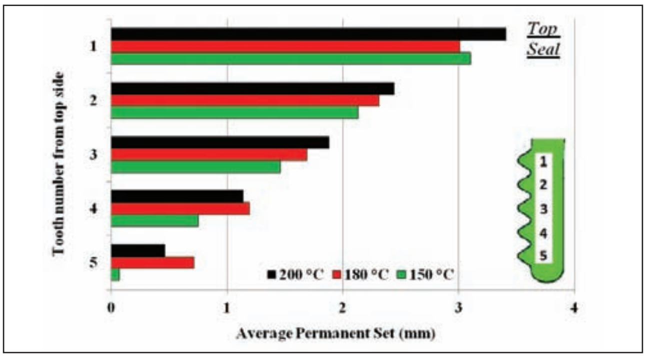

Fig. 2: permanent set on the teeth of failed seal at different temperatures

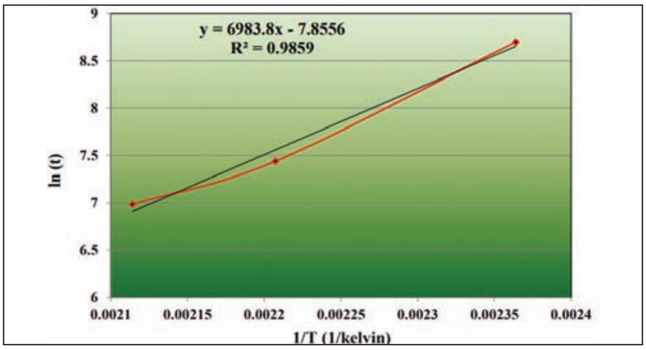

Fig. 3: seal-life estimation using the Arrhenius- plot

The leak rate and friction force measurements were done periodically. Fast drop testing was carried out in 10 days intervals. Similarly, ten translations were also done along with fast drop testing. The translation operation is found satisfactory.

It was found that the leak-rate was higher after 6000 hours, 1704 hours & 1080 hours of ageing at 150°C, 180°C and 200°C respectively. In the visual inspection of the seals after the above testing, no cracks or blisters were observed and no cut was found in the teeth of the seals. No signs of structural damage to the seals were observed after both the campaigns. Dimensional inspection revealed that the permanent set of the teeth is the root cause of increased leak rate. The 'average permanent set' of each of the teeth at 150 °C, 180°C & 200°C are represented in Fig. 2.

The life of the seal is calculated by using data of time-temperature at 150°C, 180°C and 200°C in Arrhenius equation and extrapolating the curve for working temperature of 110°C as shown in Fig. 3. Based on ageing studies, the life of the seal is estimated as ~ 3 years and 8 months at nominal operating temperature (110°C). Presently, studies to optimise the seal design for improving the seal life are under progress.

III.07 Design & Sodium Calibration of ECFM With Higher Size MI Cable

Measurement of sodium flow plays a major role in Fast Breeder Reactors (FBR), as the reduction or absence in sodium flow may lead to severe accidents. Various types of flowmeters such as Eddy current flowmeter (ECFM) or Permanent magnet flowmeter (PMFM) are deployed in primary as well as secondary circuits of FBRs for estimating the sodium flow rate. In certain applications where outside of the sodium pipes is not accessible to exterior-type flowmeters, it is desirable to use a probe type flowmeter. ECFM probe is a one such kind of that category.

ECFM probes use Eddy Current Flow Sensor (ECFS) for flow measurement in Primary Sodium Pump (PSP). A variant of ECFS is used in Core Flow Monitoring Mechanism (CFMM), which is used for measuring coolant flow exiting from Core sub-assemblies. Valuable experience is gained in manufacturing and in-sodium testing of these two designs of ECFS. The feedback experiences show that the manufacturability, availability, handling and coiling with 0.75 mm diameter MI cable is easier than that with 0.5 mm MI cable.

In this context it is proposed to explore the feasibility of re-designing the ECFS of PSP with higher size i.e., 0.75 mm diameter MI cable. A detailed design study was carried out to accommodate the ECFS with 0.75 mm diameter MI cable, while respecting the dimensional restrictions in the pump. Since the dimensions of inner guide tube couldn't be changed, the size of ECFS bobbin also couldn't be altered. Hence, the same bobbin was proposed to be used. Consequently, no. of primary and secondary turns of the sensor got reduced with 0.75 mm MI cable.

All the cables (12 nos.) of two sensors shall be routed through the bobbin, which is of 3.5 mm in internal diameter. Trials with 0.75 mm MI cables revealed that only 8 cables can be routed through ID of the bobbin. This challenge was overcome by routing the remaining 4 cables on the outside surface of the bobbin. The design solution proposed to meet the constraints is shown in Fig. 1(a). Coils of the bottom secondary (S2) are routed through the ID of the bobbin, while those of primary & the other secondary coil (S1) of the top sensor are routed over the OD. The length of the bobbin is increased to accommodate the cables routed over the bobbin. These cables are routed into the probe assembly through the slots provided near the top step of the bobbin. Based on the experience with PFBR probes, the connection between the probe and the bobbin was changed from screwed joint to the snap-fit, as shown in Fig. 1(b). This change was mainly aimed to prevent the loosening of the bobbin in advertently during reactor assembly/disassembly.Later, a probe was manufactured and feasibility of the coil winding & routing was demonstrated, ref. Fig. 1(c). The sodium calibration of thus manufactured probe was done in a dedicated test section, located in Steam Generator Test Facility (SGTF) loop.

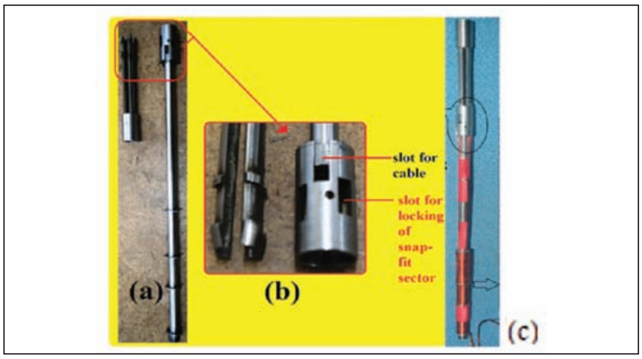

Fig. 1: Proposed solution to meet the design constraints

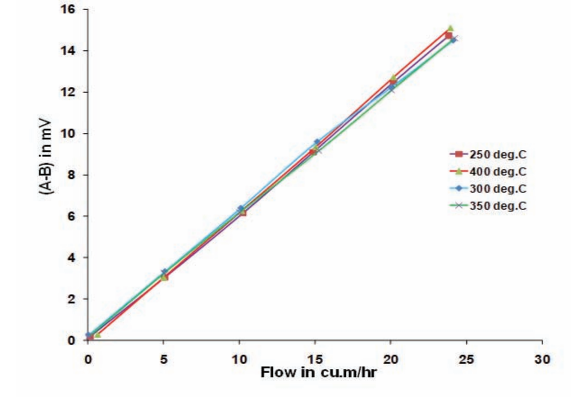

Fig. 2: Sensor characteristics of ECFS at optimum frequency (80 Hz)

During this testing, the temperature of the sodium was varied from 250°C to 450°C & flow through the sensor was varied from static to 25 m^3/hr. From the frequency response characteristics, it was found that 80 Hz is the optimum frequency for this sensor. The output graphs between the sodium flow and sensor output at 80 Hz are depicted in Fig. 2.

Thus, the feasibility of manufacturing and sodium operation of ECFS with 0.75 mm MI cable has been demonstrated. It is planned to manufacture and test few more sensors before deployment in FBRs.

III.08 Sodium Testing of Dismountable Type Ultrasonic Transduce

In PFBR, Under Sodium Ultrasonic Scanner (USUSS) is used to view the internal components of reactor and in-house developed 1MHz and 5MHz ultrasonic transducers (UT) are used for this purpose. These transducers are welded at the bottom end of the scanner, in the transducer holder. Mineral Insulated (MI) cables (~7.5 m length) carrying signals of UTs are routed through a spinner tube and taken out from the top of the spinner tube.

Replacement of a transducer of USUSS in case of any damage / non-functioning is difficult as the UTs are welded with its transducer holder and it requires disassembly of the scanner. Studies were done to identify techniques that facilitate easy replacement of transducer in USUSS. In this regard, Dismountable type UT was found to be more suitable for FBRs.

Dismountable type UT consists of two parts, namely - male part, and female part. Photograph of Dismountable type UT before and after assembly are shown in Fig. 1 and Fig. 2 respectively. Male part consists of MI cable, male Lemo connector and its mounting arrangement. MI cable and SS bush are welded with top of the male assembly and the male Lemo connector is mounted using nut arrangement. Copper conductor of MI cable is soldered with the male lemo connector's pin. Female part consists of UT, SS nut & ferrule arrangement, female lemo connector and SS washer. Female part of the lemo connector is brazed with the SS washer, which in-turn is welded to the housing. UT assembly's SS wire is soldered with the female lemo connector's pin.

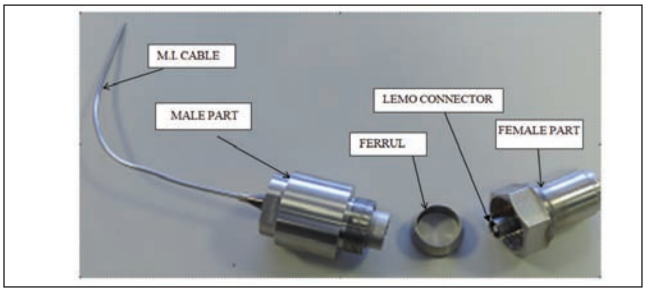

Fig. 1: Parts of Dismountable type ultrasonic transducer

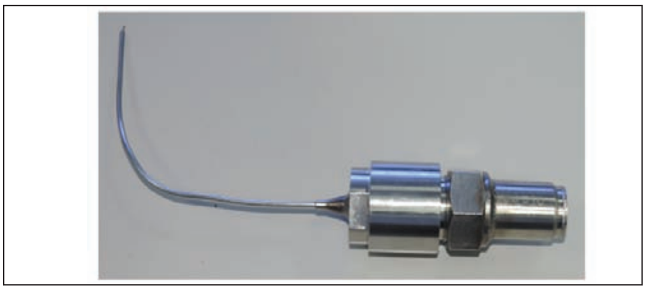

Fig. 2: Dismountable type UT assembly

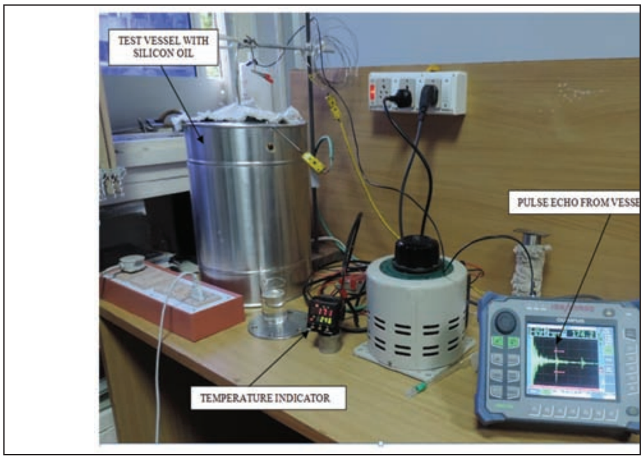

Fig. 3: Silicone oil experiment test setup

Fig. 4: Typical healthy Pulse echo signal observed during sodium testing.

One such UT of 1 MHz frequency was fabricated, assembled and qualified (weld qualification) for functionality testing. Initially, the transducer was tested successfully in water and in high temperature silicone oil (upto 225 °C). The silicone oil test setup is shown in Fig. 3. Pulse echo signal of the transducer was monitored and found to be healthy throughout the experiment. Later, the UT along with a SS target was installed in a sodium test vessel and was successfully tested in sodium for temperatures up to 225 °C and with dwell period of 1 month to check its integrity. Throughout the testing, Pulse echo signal of the transducer (Fig. 4) was monitored, and the estimated value of distance of SS target was observed to be matching with its actual distance, indicating satisfactory performance of the UT. UT retrieved after sodium testing was observed to have no sodium ingress into the transducer assembly.

A dismountable type transducer was developed, qualified and successfully tested for its performance in sodium.

III.09 Manufacture of Electromagnetic Pumps of Different Capacities in Collaboration with Indian Industry

Annular Linear Induction Pump (ALIP) is a type of electromagnetic pump widely used in the auxiliary circuits of fast reactors to pump the liquid metal under hermitically sealed conditions. Two ALIPs (Table-1) were required for the sodium facilities in FRTG. The 50 m^3/h and 18 m^3/h ALIP are planned to be used in SFCT and LCTR loop respectively, whereas, the 150 m^3/h ALIP is for future study on large annular gap pumps. In-house design of these pumps was carried out and thereafter detailed drawings were prepared. Subsequently, these pumps were manufactured by two Vadodara based firms as per the drawings and specifications provided by FRTG.

An ALIP mainly consists of an austenitic steel duct assembly and an electrical winding assembly. The duct assembly (Fig. 1) consists of inner and outer ducts. Supporting buttons have been provided on the inner ducts in all the pumps. The reflux type ALIP has been provided with colmonoy coated spacers. Proper material identification procedures were followed at various stages of manufacturing – from material procurement to final component assembly. The components were fabricated using modern, high precision instruments in clean workshops. Inspection of the manufactured components and manufacturing procedures was carried out in coordination with TC&QMD-IGCAR following an approved QAP. Quality checks were carried out by adopting proper NDE techniques. Pneumatic test and helium leak test were carried out to check the integrity of the ducts. Thermocouples were provided on the ducts.

The electrical winding assembly (Fig. 2) consists of insulated copper coils which were skilfully inserted in the slots formed from stacked CRGO laminations. Coil to Coil connections were made by silver brazing. Resistance and inductance of the coils and insulation resistance of the winding assembly were measured for each phase. The values were found to be in acceptable range. High Voltage test and surge test were also performed. To test the winding before final assembly, the coils were excited with three phase voltage. A block of copper was found to move across the pump, confirming the generation of linearly travelling magnetic field and Lorentz force. The stator winding and duct were assembled (Fig. 3 & 4) and various quality checks were performed. The ALIPs were subsequently received in FRTG. Some more electrical and mechanical checks were performed before accepting the pumps at site.

Fig. 1: Typical Duct of an ALIP

Fig. 2: Typical Electrical Winding of an ALIP

Fig. 3: Assembling of Duct & Winding

Fig. 4: Typical Full Assembly of an ALIP

Table-1: Ratings of three ALIPs

Flow Rate	Type	Designed Head
50 m^3/h	Reflux	4 kg/cm^2
18 m^3/h	Once Through	4 kg/cm^2
150 m^3/h	Once Through	4 kg/cm^2

III.10 Transient Analysis of SGDHR System with DHX -B During Station Black Out Event

In PFBR, Safety Grade Decay Heat Removal system (SGDHR) is employed as a safety feature for removal of post shutdown decay heat in the case of non-availability of Operational Grade Decay Heat Removal System (OGDHR). SGDHR system consists of four independent loops of 8 MWt individual heat removal capacities. Each loop consists of a sodium to sodium heat exchanger (DHX) immersed in the hot pool of reactor, secondary sodium loop, sodium to air heat exchanger (AHX), chimney which generates required air flow across the AHX tubes and air side isolation dampers. DHX picks up the decay heat from hot pool and transfer to secondary sodium loop which transfers the heat to AHX. The secondary sodium gets circulated by natural convection in loop due to the temperature difference in hot and cold legs of the loop. From AHX, the decay heat is released to atmospheric air as the ultimate heat sink. This system will be in poised state during nominal operating condition and it will be put on action against demand by opening air dampers. Out of four independent loops of SGDHR system, two loops are of type-A design and other two are of type B design. DHX type-A is vertical counter-flow shell and tube heat exchanger consisting of straight tubes. DHX type-B is vertical, U- tube shell and tube heat exchanger. AHX type-A has sodium inlet and outlet headers which are connected by serpentine shaped finned tube bundle with four passes. AHX type-B has ring type sodium headers which are connected by straight vertical finned tube bundle. The difference in design imparts diversity in the SGDHR system and avoids common cause failure.

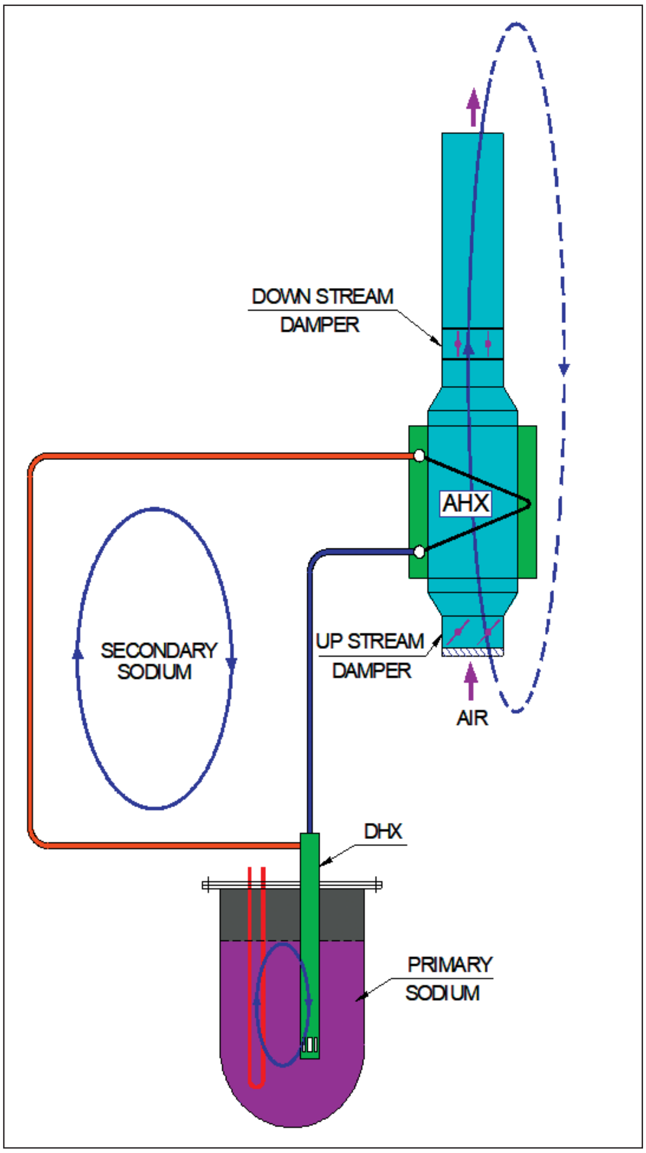

Fig. 1: Schematic of SADHANA facility

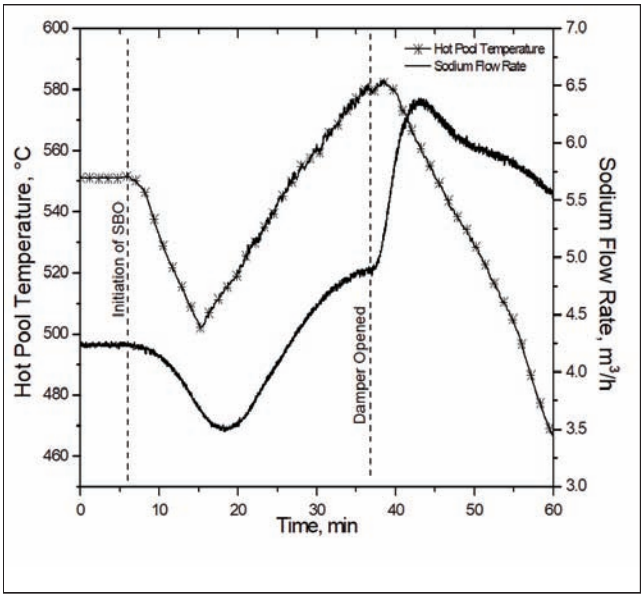

Fig. 2: The response of secondary sodium flow during station black out

To study the thermal hydraulic behaviour of SGDHR of PFBR, a 1: 22 scaled down model in power by simulating Richardson number, SADHANA (Safety Decay Heat removal loop in natrium) was established in Engineering Hall-III, IGCAR. The schematic of the facility is shown Fig. 1. Nominal heat removal capacity of SADHANA loop is 355 kW. In SADHANA loop, hot pool of PFBR is

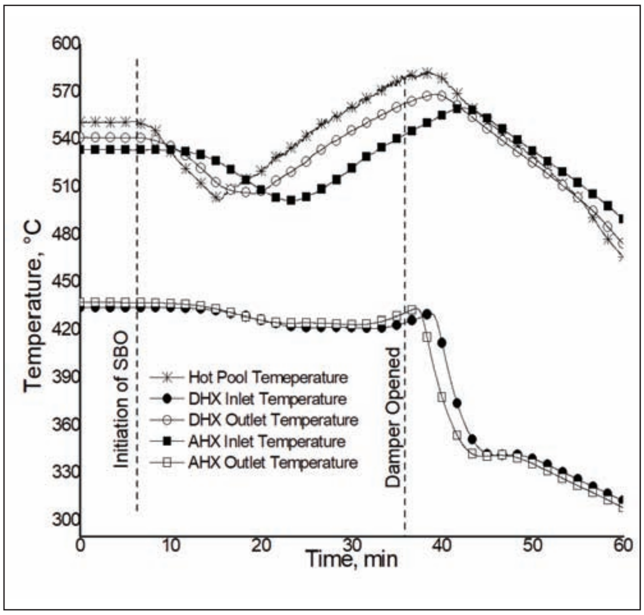

Fig. 3: The response of temperature during station black out

simulated by a test vessel. Sodium in the test vessel is heated by immersion electrical heaters. In SADHANA facility, various experiments were planned with different combination of DHX and AHX. Now the performance of system with combination of DHX type-B and AHX type-A has been experimentally demonstrated during Station Black Out (SBO) event. The role of DHX is expected to be more dominant compared to AHX. This is primarily due to fact that both shell and tube sides of DHX interact with transient temperature conditions due to SBO, whereas the conditions of air side of AHX is not much changed. Hence simulation of SBO with above said heat exchanger combination, simulates the behaviour of SGDHR type-B system during SBO event.

During SBO, the worst-case scenario is considered as OGDHR systems and one SGDHR circuit are not available and other three SGDHR circuit operations are initiated after a delay of half an hour. The heat removal from the core is ensured by three SGHDRs only. Hence the simulation of SGDHRS behaviour during SBO with 30 min delay in damper opening was considered for transient experiments in SADHANA facility.

During SBO, as per analysis the hot pool temperature falls from 547°C to 508°C (ΔT = 39°C) in first 420 seconds and rises from 508°C to 556°C (ΔT=48°C) in next 2000 seconds. This temperature fluctuation in hot pool may lead to flow instability and reversed flow condition in the intermediate loop which reduces the heat removal capacity of the system. Thereafter, for reproducing the temperature profile as in the reactor transients during station black out, the sodium pool temperature was reduced by injecting cold sodium and the required rate of heating was achieved by immersion type heaters.

The dampers were in crack opened position. The cold sodium was injected to reduce the pool temperature from 550°C to 510°C within 10 minutes and pool temperature was raised to 570°C by electrical heaters.

The sodium flow in secondary circuit was reduced initially as sodium pool temperature was falling and started to increase along with pool temperature raises. After half an hour of initiation of transient, the dampers were opened.

The air flow reached maximum in a minute and the sodium flow reached maximum corresponding to the pool temperature within 7 minutes after opening of damper. Then the sodium flow followed the pool temperature. Evolution of secondary sodium flow and temperatures are given in Fig. 2 & 3. The pool temperature was always higher than secondary circuit temperatures and the hot leg temperatures were higher than cold leg temperatures. Hence the secondary sodium flow was followed the pool temperature. No flow oscillations were observed.

In comparison with DHX type A- AHX type-A configuration, the behaviour of the present system is similar in terms the evolution of sodium flow and temperatures. Due to different tube configurations, the system with DHX type-B attains maximum flow in shorter time than the system with DHX type-A where the time taken was 9min.

From the experiments, it is demonstrated that SGDHR system with DHX type-B are stable during the transient even of SBO without any flow reversal and instability.

III.11 Experimental Study on Establishing of Sodium Frozen Seal with Indigenously Developed 450 NB Butterfly Valve

Frozen Seal Butterfly Valves (FSBVs) with backup gland packing are used in PFBR for isolation of Steam Generators (SG) modules. Leakage of sodium to ambient environment is prevented by frozen seal of solid sodium itself. Liquid sodium rises in annular space between bonnet and stem and solidifies at 98°C by losing heat to atmosphere. Fins are provided on bonnet to enhance the heat transfer. Graphite asbestos gland packing is used as secondary seal.

Total 16 numbers of such valves are used in both of the secondary sodium loops of PFBR. All the valves used in PFBR were imported. It was envisaged to improve the valve design and indigenously develop it for future FBRs. The valve design was optimized with enhanced thermal hydraulics & mechanism. Various design features introduced in indigenously made valve are; provision of cover gas port in the annular space of stem and bonnet, replacement of integral finned bonnet with welded fin type bonnet design, optimizing the bonnet thickness, number of fins and the actuator size. Incorporating all these modifications a prototype valve of 450 NB size was manufactured for the first time in India with one quarter of cost of an imported valve. Fig. 1 shows schematic of indigenously made FSBV. An instrumented bonnet assembly representing 450 NB FSBV was also made for experimental characterization of frozen seal behaviour in valve bonnet at operating temperature. Valve along with the instrumented bonnet assembly were tested in an experimental facility up to the design temperature of 550°C, to validate the design for sodium applications. Experimentally obtained height of frozen seal for various temperatures is shown in Fig. 2. At 550°C, frozen seal height was established between 3rd & 4th fin for ambient air condition of 35°C. Total seventeen numbers of fins are provided as margin in case of upset events such as loss of ventilation or local fire. Functionality of valve at design temperature was demonstrated by performing cyclic test. After each valve operation, sodium frozen seal get sheared off and liquid sodium seeps upwards and gets solidified again. Integrity of frozen seal after the valve operation was demonstrated experimentally. The study concludes, indigenously developed 450 NB FSBV is fit for sodium applications.

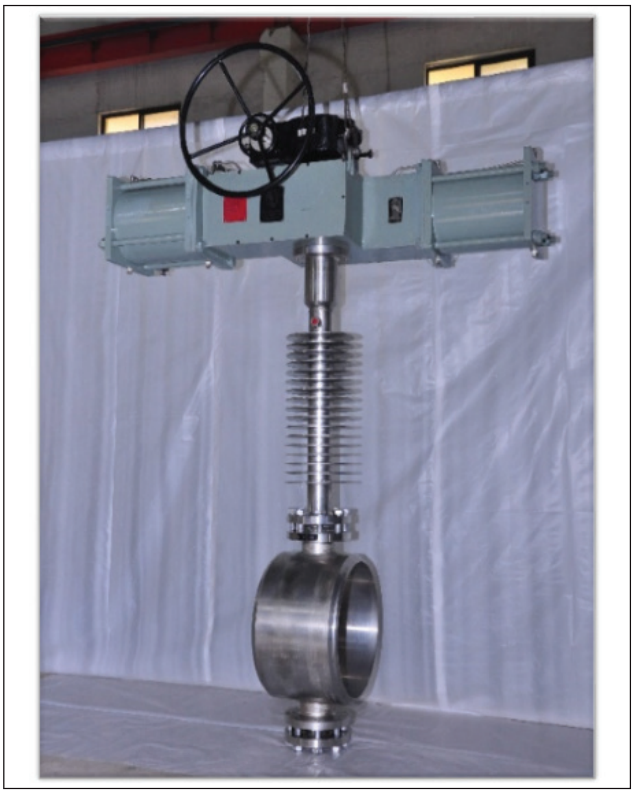

Fig. 1: Indigenously developed 450 NB FSBV

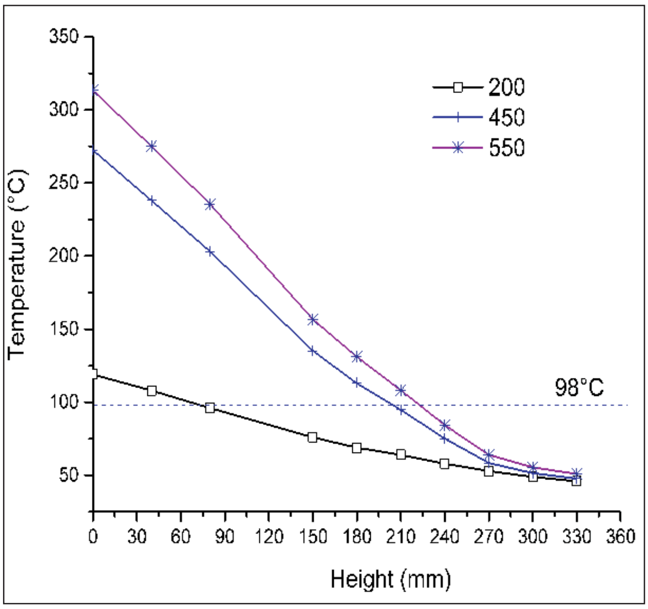

Fig. 2: Sodium temperature variation inside bonnet assembly

III.12 Experimental Studies on Dispersion of Sodium and Fission Product Aerosol in a Confined Environment

As a part of fast reactor safety analysis, aerosol studies pertaining to severe accident conditions are carried out using sodium and non-radioactive fission product (FP) aerosols in a medium-scale test facility. The study aims to generate an experimental database for the evolution of aerosol dynamics during severe accidents inside containment and validate the numerical models. The experiments were carried out at the MINA facility, which consists of a rectangular steel chamber (6.0 m x 5.45 m x 4.6 m)with a volume of 150 m^3 designed to withstand an internal pressure of 1 bar at 300ºC. The facility has state-of-the-art equipment for generating sodium and FP aerosol, monitoring gas and wall temperature, a data acquisition system, aerosol metrological instruments and a high-speed video imaging system. The non-volatile FP aerosol (SrO) is generated by vaporization and condensation routes using a 40-kW thermal plasma torch aerosol generator (PTAG). The PTAG best simulates the aerosol characteristics generated during an accident because of the high temperature at which the materials vaporize. Experiments were conducted with aerosol concentration simulating the CDA condition, i.e., 4 g/m^3 (sodium aerosol) and ~ 10 mg/m^3 (SrO aerosol) in containment. The evolution of aerosol characteristics (concentration, size distribution and growth)was analyzed.

Before conducting the experiment, a 40-kW thermal PTAG, power supply, control console, chiller unit, and powder feeder were installed at the MINA facility. The operational parameters of PTAG have been optimized by conducting a series of experiments, operated at 25-30 kW power, 45 - 55% electro-thermal efficiency and 25 lpm flow rate of plasma forming gas for the generation of aerosols. The aerosol was generated for about 12 min using non-radioactive SrO_2 powder. The sodium aerosol was generated from a sodium pool fire by using 2.0 kg of sodium spreading in a catch tray with an area of 0.25 m^2. The aerosol sampling was done at multiple locations using real-time and offline aerosol metrological devices.The spatio-temporal temperature evolution has been recorded using 40 numbers of thermocouples. The turbulent natural convective velocity was also monitored during the experiment.The evolution of aerosol number concentration and mean size growth is shown in Fig. 1. The average suspended number concentration reached a maximum of 4.2*10^{11} #/m^3 during the generation period. After aerosol generation ceased, the concentration decreased and was reduced by one order of magnitudes from maximum concentration in about 5 hrs. The aerosol count median diameter (CMD) for initial size distribution is 0.18 μm with σ_g–1.5,and CMD increases with time and reaches a saturation value of 0.38 μm. The observed aerosol median size doubles from the initial median size in ~ 5 hrs. The suspended mass concentration increased during the generation period and reached a maximum of ~ 8.1 mg/m^3 and started decreasing and reduced to about 45% from the maximum concentration in ~ 5 hrs. A comparison of the evolution of normalized suspended aerosols(SrO and sodium) mass concentration is shown in Fig. 2.

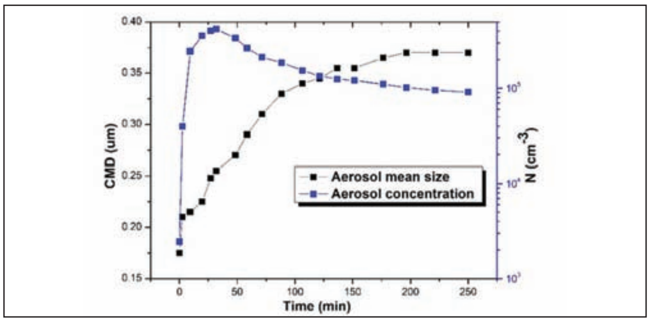

Fig. 1: Evolution of average aerosol number concentration and size growth.

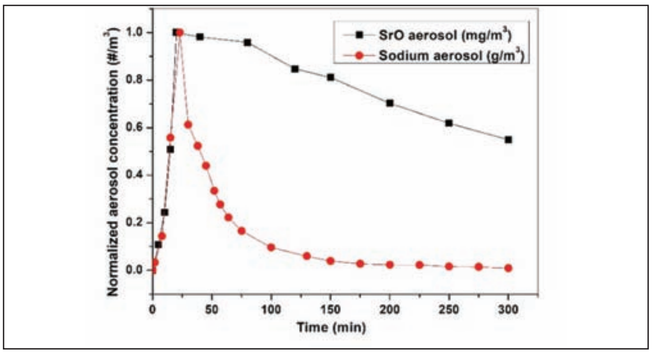

Fig. 2: Comparison of SrO (FP) and sodium aerosol concentration evolution.

The sodium pool temperature was increased to a maximum of 685 ºC, and peak convective velocity observed in the rising plume above the pool is ~ 0.95 m/s.SrO aerosol concentration halving time is more than 5 hrs.; however, for sodium aerosol, it is less than a hr. The faster reduction of suspended aerosol concentration in the case of sodium aerosol is due to faster size growth by various processes like coagulation and hygroscopic growth and higher concentration of aerosol, which enhances faster deposition. The size growth factor is 2 for SrO aerosol; however, it is ~ 25 in 5 hrs for sodium. A few more experiments with mixed aerosols are planned, and the data will be used to validate numerical models.

III.13 Determination of Effective Density Corrected Size Distribution of Sodium Aerosol and Evaluation of RCB Aerosol Dynamics Under CDA Condition of a SFR

The Reactor Containment Building (RCB) is the final barrier containing radioactivity and preventing its release to the environment during Core Disruptive Accident conditions (CDA). During CDA, RCB gets bottled up with sodium combustion aerosol, fission product aerosols, fission gases, and highly volatile fission products. Sodium aerosol dynamics plays a crucial role in scavenging radioactive core material aerosols. It also controls the releases through leakage paths in RCB by plugging the narrow capillary-like leakage paths. Realistic estimate of suspended aerosol concentration particularly during the sodium fire duration and subsequent phases is very essential for source term estimation. Towards this, a polydisperse aerosol dynamics model has been indigenously developed based on nodal method approach and validated with spherical non porous PAO aerosol dynamics tested in 1 m^3 chamber. This report demonstrates the methodology of ascertaining the effective density corrected actual number size distributions of sodium aerosols through test chamber experiments at ATF and in association with the estimates using the aerosol dynamics model. These validated parameters are used to estimate the sodium aerosol mass concentration decay in RCB of Prototype Fast Breeder Reactor (PFBR) during CDA condition with envisaged initial concentration (M_0) of 4.0 gm^{-3}, including the effects of varying containment temperature, pressure with time and also turbulence parameters.

Experiments on sodium aerosol dynamics at ATF

Experiments are conducted inside a 1 m^3 cylindrical aerosol chamber of 1.5 m diameter and 0.6 m height at 47 ± 3% RH with the initial sodium combustion aerosol concentration M_0 of 2.9 ± 0.25 gm^{-3}. The real-time aerodynamic number particle size distribution (APSD) measurements with time are carried out using an Electrical Low-Pressure Impactor ELPI+ with a reference particle density of 1 gm^{-3}. The initial APSD of sodium aerosol measured within 1 min after its generation is shown in Fig. 1. This is polydisperse with the count median aerodynamic diameter of CMAD=0.66 µm and σ_g=1.96. The APSD is corrected with different effective density ρ_e values to arrive at the respective Mobility Equivalent PSDs (MEPSD) in the case of porous sodium aerosol, which could be non-spherical based on humidity levels. The MEPSDs are also shown in Fig. 1. The sodium aerosol concentration increases nearly three times, and the median diameter decreases by almost half if the ρ_e increases from 0.61 gcm^{-3} to 2.27 gcm^{-3} for the given tested concentration, as listed in Table 1. It is also observed that the σ_g of derived mobility equivalent distributions considerably increases as the ρ_e increases. The actual initial size distributioncould be among the APSD or MEPSDs. Sodium aerosol behavior is modeled from the completion of generation using four types of distributions listed in Table 1 and the corresponding morphological parameters are analyzed for realistic estimates.

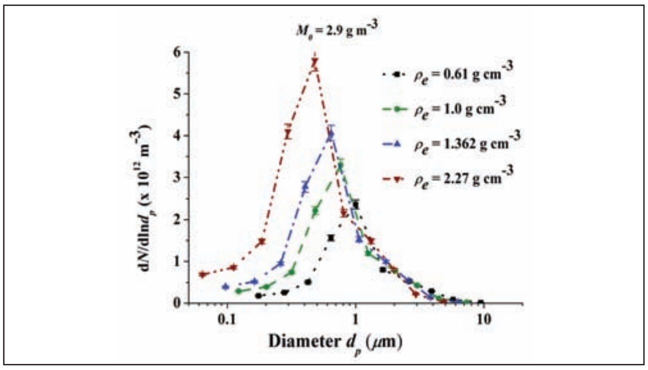

Fig. 1: Initial aerodynamic and the corresponding mobility equivalent number size distributions.

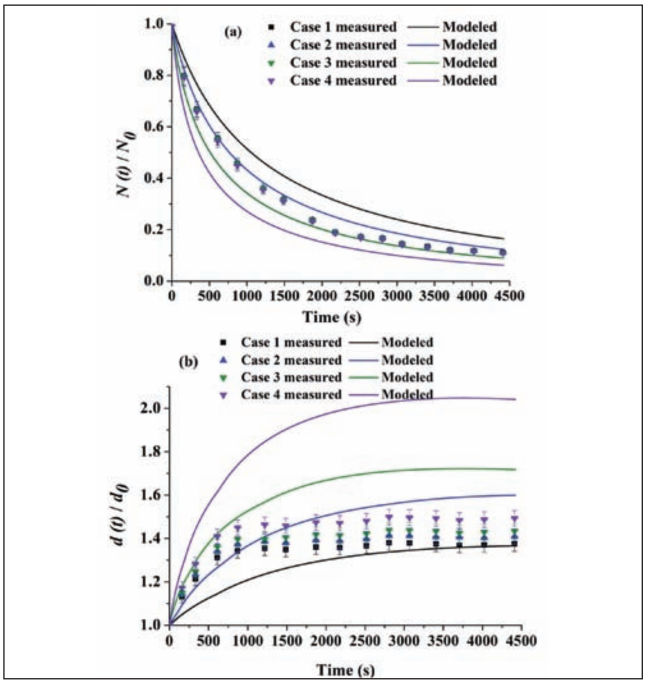

Fig. 2: Measured and modeled sodium aerosol a) concentration decay (top), b) size growth (bottom).

The patterns of measured and modeled concentration decay and size growth with time are compared up to 4400 ± 10 s in Fig. 2. (a) and (b). Based on the equivalent diameter concept, the gravitational settling rates are the same for these four sets in the tested concentration level. Diffusion, thermophoresis, and electrostatic coagulation due to charges obtained from combustion processes are observed to be insignificant. So, the Brownian coagulation gets influenced by changing the equivalent size distributions.

Table 1 Properties of equivalent distributions in the modeled cases

Case no.	ρe (g/cm³)	χ	Number conc. N_{t0} ($x10^{10}/m^3$)	Initial CMAD/ CMMED d_0 (μm)	Average initial σ_g0
1	0.61 (MEPSD)	1.37	148 ± 7.4	0.87 ± 0.04	1.89 ± 0.1
2	1 (APSD)	1	213 ± 10.6	0.66 ± 0.03	1.96 ± 0.1
3	1.36 (MEPSD)	1.05	270 ± 13.5	0.55 ± 0.03	2.27 ± 0.1
4	2.27 (MEPSD)	1	400 ± 20	0.4 ± 0.01	2.13 ± 0.1

The MEPSDs correspond to ρe of 2.27 cm^{-3} (Case 4) overestimates the coagulation as the particle sizes are significantly smaller than the actual one. This causes a more significant deviation of 40% for number concentration decay and 33% for size growth. The MEPSD corresponds to ρ_p=0.836 gcm^{-3}, Χ of 1.37 (Case 1) underestimated the coagulation up to 50%. Both the APSD with CMD=0.66 μm, σ_g=1.96, ρ_p=1 gcm^+, Χ=1(Case 2); and MEPSD with CMD=0.55 μm, σ_g=2.16, ρ_p=1.43 gcm^{-3}, Χ of 1.05 (Case 3) cases provided good agreement between the measured and modeled dynamics within 11.1% to 15.45% for number concentration decay and 11.5% to 17.5% for size growth respectively. The enhanced aggregation process causes the particles to be porous. Further, the pores of the particles get filled with moisture and tend to become colloidal, and this causes a reduction in the actual density of particles from material density. These factors caused the particles' effective density to reach about 1 gcm^{-3} by the initial PSD measurement. It is inferred that case 2 parameters of Table 1 represents the actual values. The analysis also shows that suspended sodium aerosols are spherical at 50% RH as reported in literature.

Estimation of RCB aerosol dynamics during CDA

The dimension of RCB is 35 x 40 x 54.5 m. It is assumed that sodium fire is instantaneous, and the temperature, pressure, and mass concentration simultaneously reach a maximum level at the same time under CDA condition. The validated number size distribution parameters at 2.9 gm^{-3} with CMD=0.66 μm and σ_g=1.96 (mass median diameter=2.61 μm) are used to fit the log-normal size distribution for the higher concentration of 4 gm^{-3}. Validated ρ_e of 1.0 gm^{-3} and χ of 1 are considered in the model. Spatial homogeneity of concentration is assumed despite the significant spatial in homogeneity of concentration in the large containment. The temperature gradient between the air medium and the inner wall surface of 700 Km^{-1} is used. The estimated time-varying temperature T and pressure P during CDA condition are incorporated in the model. The changes in RCB air properties such as air density, dynamic viscosity, and mean free path, with respect to temperature and pressure are included. The turbulence effect is incorporated for two different turbulence energy dissipation rates ε_T found in literature i) ε_T=0.02 m^2s^{-3} and ii) ε_T=0.3 m^2s^{-3}.

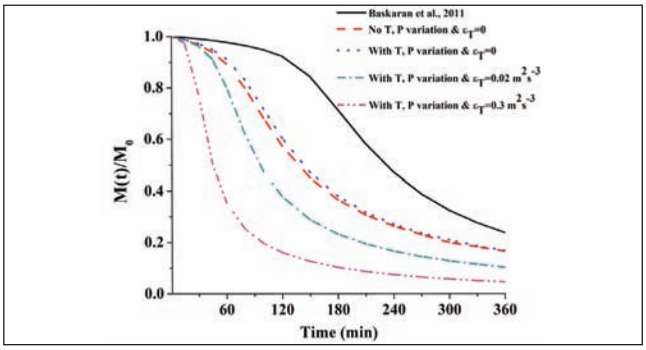

Fig. 3: Normalized mass concentration decay with time under different condition

Modelled normalized mass concentration decay is shown in Fig. 3. The aerosol dynamics modeled with constant ambient T and P values and no turbulence conditions are modeled initially as a reference. Compared to the mass concentration decay reported in the literature (Baskaran et al., 2011) for 4 gm^{-3} with the usage of mono disperse PSD parameters of MMD=1.0 μm and σ_g of 1.2, this study shows the concentration decay enhancement is more by 8.5% at 60 min, 37% at 120 min and 30% at 360 min. The poly disperse nature of sodium aerosols causes enhanced size growth in the early periods after the source's termination, guiding the settling phenomenon in the later stages.It is observed that the simultaneous variation of both the temperature and pressure with time does not significantly influence the aerosol dynamics. Gravitational settling is the dominant deposition process compared to diffusion and thermophoresis. In the absence of turbulence, it is observed that 91% of mass remains suspended at 60 min and it decreases to 60% at 120 min and 17% at 360 min. If the turbulence condition with ε_T=0.02 m^2s^{-3} is considered, 80% of mass remains suspended in 1st hour, decreasing to 38% in the second hour and 10% in the 6th hour. If the turbulence condition with ε_T=0.3 m^2s^{-3}, 35.4% of mass remains suspended, decreasing to 16% in the second hour and 5% in the 6th hour. The aerosol size is grown up to the maximum of 4.9, 5.09 and 8.03 μm at 60 min with the ε_T of 0 (no turbulence), 0.02 and 0.3 m^2s^{-3}, respectively. This study has revealed that aerosol dynamics phenomenon is more sensitive to turbulence effects which enhance the size growth and mass concentration decay.

III.14 Discrete-Sectional Method Based Computational Model for Nuclear Aerosol Dynamics in a Chamber

In the Sodium-cooled Fast Reactor (SFR), sodium combustion products aerosols are produced along with fission product aerosols during a sodium fire in the Reactor Containment Building (RCB) following a CDA, when a small fraction of liquid sodium leaks through the top shield of the reactor main vessel. A realistic estimate of the in-containment source term due to suspended aerosols in RCB is crucial for estimating the Environmental Source Term (EST). The analysis of in-containment aerosol transport also helps in developing accident management strategies. A computational model has been developed for assessing the dynamics of fission products and sodium combustion aerosols in a closed chamber or containment by solving the General Dynamics Equation (GDE) using the discrete-sectional method. The model is validated with experimental results from the AHMED facility (Finland) and is used to predict aerosol dynamics in the MINA chamber at IGCAR.

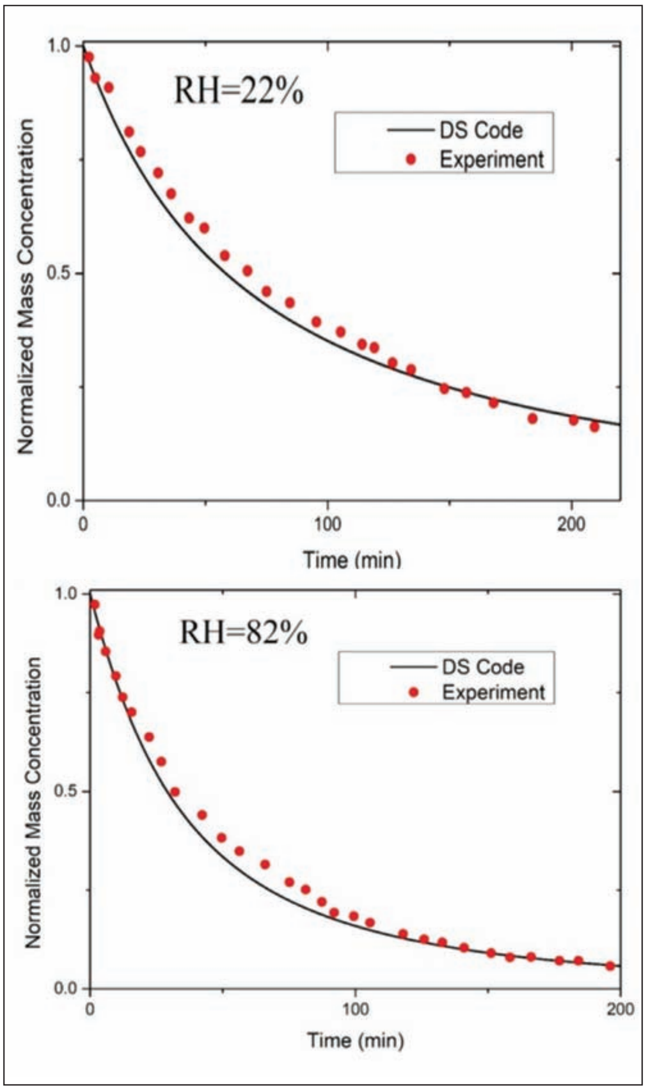

Fig. 1. Suspended Mass Concentration of NaOH aerosols in AHMED Facility at different RH.

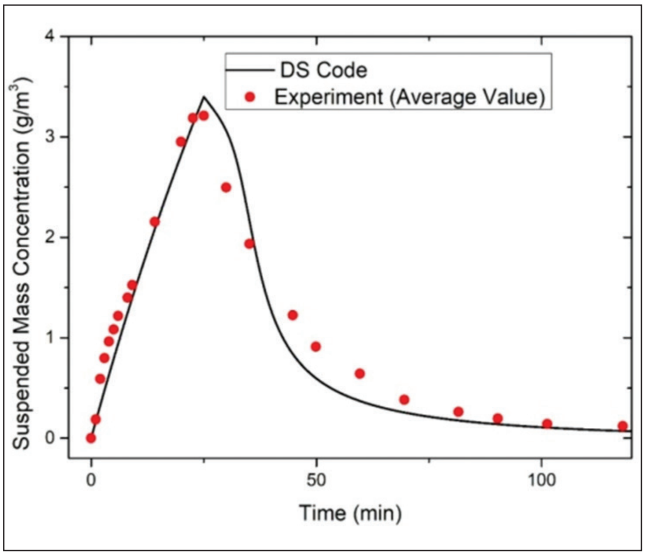

Fig. 2: Suspended Mass Concentration of sodium aerosols in MINA chamber

Validation with AHMED Experiment:

The experiments conducted in the AHMED facility of volume 1.81 m^3 consider the dynamics of NaOH aerosols at different humidity levels. Fig. 1 compares normalized aerosol concentration calculated by the DS code at 22% and 82% RH for the AHMED experiment. The water-soluble NaOH aerosol displayed hygroscopic growth within the chamber as humidity increased. The NaOH aerosol continuously absorbed moisture, causing an enlargement of particle size and a hastening of gravitational deposition in the experiment. Cooper's relation is used to account for the hygroscopic aerosol size growth in the model.

The root mean square error values were 1.3% and 1.65% for the RH values of 22% and 82 %, respectively, indicating excellent agreement with the experimental data.

Prediction for MINA Experiment:

The validated model is then used to predict the aerosol dynamics following a sodium pool fire in the Mini Sodium

Fire Facility (MINA), IGCAR. The MINA chamber is a rectangular steel chamber with a volume of 150 m^3 and 2 kg of sodium was burnt in a steel tray during the experiment. The sodium fire produced sodium aerosols at the rate of 0.24 g/s from the surface of sodium. It also generated large temperature gradients within the enclosure and turbulence in the airflow. These phenomena are taken into account in both the coagulation and deposition of aerosols in the code. Numerically predicted sodium aerosol concentration is given in Fig. 2, and it is compared with the average concentration value within the MINA chamber at different instants of time in the experiment.

The DS code results show that the suspended mass concentration increases up to the first 25 minutes when aerosol generation occurs due to the sodium fire, reaching a peak concentration of 3.5 g/m^3 and decreasing thereafter as the sodium fire ceases. The experiment also follows a similar trend where the maximum aerosol concentration at the end of 25 minutes is 3.2 g/m^3. After the fire ceases, aerosols are not generated further, resulting in concentration decay due to deposition. The DS code prediction and experimental results are well in congruence with each other, with a root mean square error value of 5.6%, proving the model's capability to study aerosol transport following a sodium fire.

Further work is in progress to enhance the code to address the multi-component aerosol population in the SFR reactor containment following a sodium fire.

III.15 A Comparative Study on Residual Stress of SS 304L Welds using X-ray Diffraction Technique (XRD)

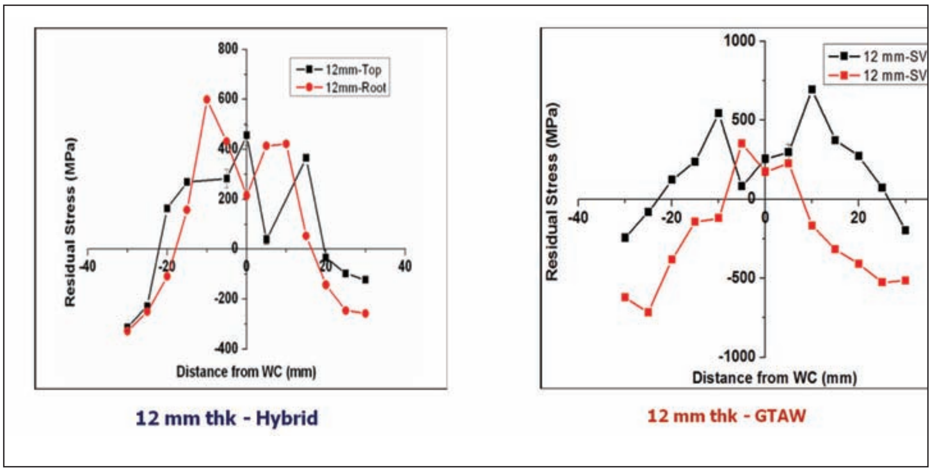

12 mm thk - Hybrid

12 mm thk - GTAW

Fig. 1 : Residual Stress in 12 mm Hybrid and GTAW weld

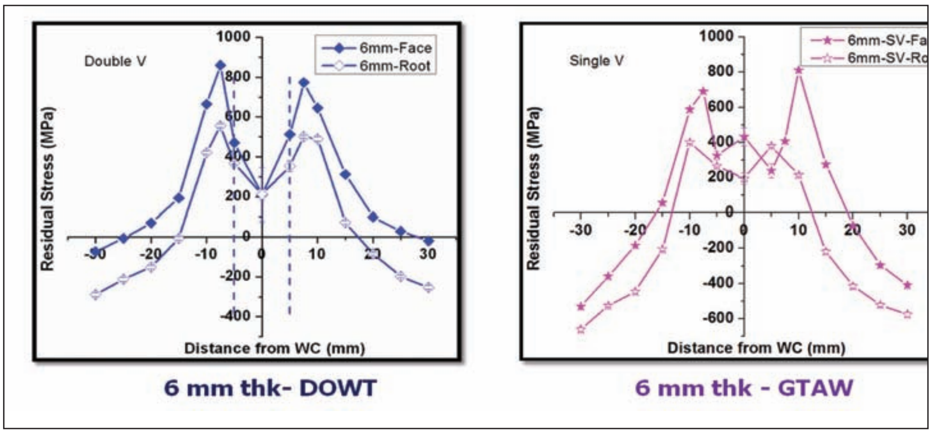

6 mm thk- DOWT

6 mm thk - GTAW

Fig. 2 : Residual Stress in 16 mm Hybrid and GTAW weld

Introduction: In Demonstration Fast Reactor Fuel Reprocessing Plant (DFRP), more than 200 Process vessels & 64 km length of piping is used for reprocessing of Spent Fast Reactor Fuel. Nitric Acid of varying concentrations, such as 4 to 11.5 N in Boiling condition is used as Process Fluid. AISI 304L is the workhorse material due to its excellent corrosion resistance in highly oxidizing atmosphere and better amenable to fabrication. Gas Tungsten Arc Welding (GTAW) is used for welding of process vessels and piping. Commonly used thickness of process vessels in this facility are 6 mm, 12 mm & 16 mm. Gas tungsten Arc Welding (GTAW) is widely used in nuclear industry owing to its better root quality and greater control of weld pool in real time. However, the process is quite slow (75-100 mm/min) compared to other slag based processes. This is a disadvantage especially when thicker sections need to be welded. Newer welding techniques such as Hybrid Weld (Combination of GTAW & Flux Cored Arc Welding) and Doubler Operator Welding techniques has been attempted to improve the productivity without offsetting the quality requirements. Stress Corrosion Cracking (SCC) is a life limiting factor during service of these process vessels due to synergic presence of residual stress of the weldments in the as-welded condition and Corrosion species. This report mainly discusses on measurement of Weld Residual stress in SS 304L weldments of 6 mm, 12 mm & 16 mm thickness plates, welded by different welding techniques. Surface residual stress is measured using X-ray Diffraction (XRD) technique. The results are discussed in comparison with the conventional GTAW practices.

Method: 12 mm & 16 mm thickness SS 304L plates has been welded using Root & Hot pass with GTAW and rest of the fill passes with FCAW (Flux Cored Arc Welding). Single “V” weld joint configuration is used for 12 mm thickness and Double “V” configuration is used for 16 mm thickness for Hybrid Weld. 6mm & 12 mm.

Thickness SS304L coupons are welded using Double Operator Welding Technique (DOWT). In both coupons Double “V” configuration is employed. Simultaneously, 6 mm (Single “V” & Double “V”), 12 mm (Single “V” & Double “V”) & 16 mm thickness (Double “V”) coupons are also welded using GTAW. All these coupons in as welded condition has been experimentally analysed for the presence of Surface residual stress using X ray Diffraction (XRD) technique.

Results:. Hybrid Weld is having close to 30% (12 mm thick) & 40% (16 mm thick) saving in Arc on time as compared to that of GTAW Welds DOWT welds are having close to 36 % (6 mm thick) and 33% (12 mm thick) saving in Arc on time as compared to that of GTAW Welds Unsymmetrical “M” curve observed in 12 mm & 16 mm thick Hybrid Welds. Peak stress at Weld center is around 200 MPa (R) and 400 MPa (F) in 12 mm thick Hybrid Welds and & 500 MPa (R) and 280 MPa (F) in 16 mm thick. Residual stress values in Hybrid welds are seemingly higher than Conventional GTAW Welds due to higher current and voltage used for FCAW welds. Symmetrical “M” curve in 6 mm & 12 mm thick DOWT welds has been observed. Peak stress values in DOWT welds are comparable to that of GTAW welds. However, DOWT Values are closer to GTAW welds in Weld Centre line region. Pictorial comparison of RS values are depicted in Fig. 1 to 4.

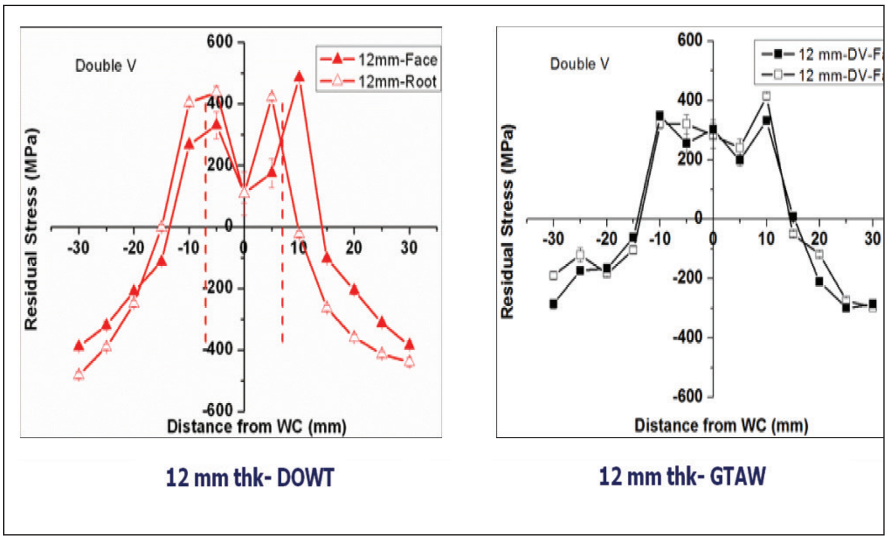

12 mm thk- DOWT

12 mm thk- GTAW

Fig. 3: Residual Stress in 6 mm DOWT and GTAW weld

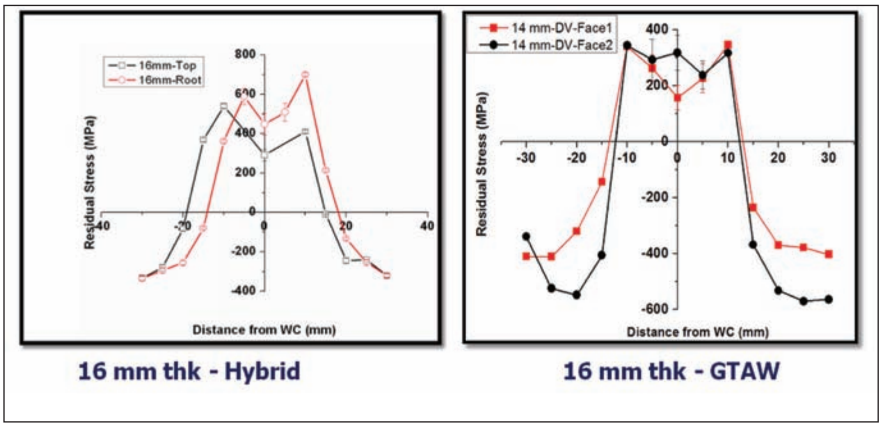

16 mm thk - Hybrid

16 mm thk - GTAW

Fig. 4: Residual Stress in 12 mm DOWT and GTAW weld

III.16 Challenges in QA during Leak Testing of SS 316L Pipe Weld Joints of Sodium Technology Complex using MSLD

Introduction

To facilitate sodium experiments and sodium testing of future FBR components, Sodium Technology Complex (STC) has been constructed. The sodium loop is integrated with system of fittings, valves, equipments and vessels spanning across elevations between -2m to +12m as shown in Fig. 1. ASTM A312 Type 316LN pipes size ranging from DN 20 to DN 200 Sch40 has been used as the material of construction. The sodium facility is designed for 40 years of life span in STC. All equipment and associated piping are to be designed for 40 years continuous operation. The facility operates at temperatures of 800-950 K with a pressure of 1.1 Mpa. Sodium is filled under vacuum at 473 K in STC. Due to prevailing high pressure, temperature & Sodium bearing environment, Entire piping system shall be ascertained for leakage rate by Helium Mass Spectrometry. This particular report addresses the development, implementation and validation of Helium Leak Testing (HLT) procedure for entire piping and associated Systems, Structures & Components (SSC) in erected condition at STC.

Method:

Tracer probe technique with Hood Method has been used to ascertain local as well as Global leak rate of each weld joint in STC. 350 nos of Butt welded joints are existing in the entire loop of STC.

a) Vacuumization

Entire piping loop are vacuumized with 80 m^3 Rotary pump is fitted to top of the loop (+12 m) to ensure the background vacuum pressure below level of 5x10^{-2} mbar to perform HLT. The absolute vacuum pressure is measured at far end of loop by employing pirani gauge as shown in Fig. 2. Desired vacuum of 5x10^{-2} mbar is achieved after 4 days.

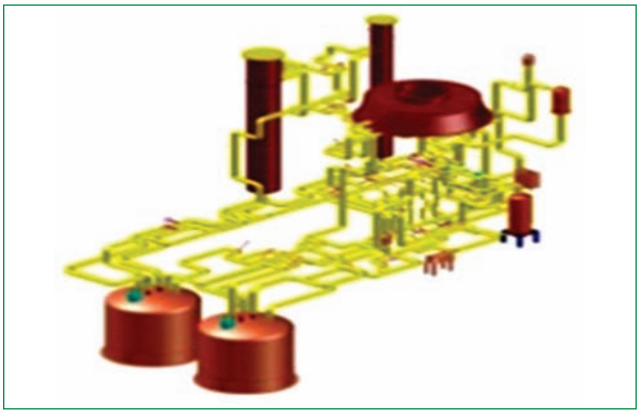

Fig. 1: Typical STC Piping loop

Fig. 2: Pirani Gauge

b) Instrument Calibration

Adixen Pfeiffer make ASM 340 MASS SPECTRUM HELIUM LEAK DETECTOR(MSLD) is employed to carry out the leak testing. The MSLD is calibrated with an internal standard leak of 2.7x10^{-7} mbar l/s and also to ensure required sensitivity.

c) Preparation of weld joints for testing

Since it is very difficult to connect the entire system with one single loop for testing, local hood is formed in all weld joints as shown in Fig. 3 using polythene bag wrapped around the entire circumference. Helium

Fig. 3: Local Hood around Weld Joint

Fig. 4: Std Leak with System

is injected while maintaining minimum of 50% helium concentration inside hood for finding leakage.

d) System calibration

Since the entire loop is spanning across 14 m height, it is essential to ensure response time for the system to improve the probability of detection. To establish response time, the component is evacuated to an absolute pressure sufficient for connection of the helium mass spectrometer to the system. Calibrated Std leak is connected to other end of system as shown in Fig. 4.

Fig. 5: MSLD and Piping Loop during testing

Response time is established by sensing of Helium by MSLD by opening std leak. Response time is observed as 25 minutes. Corresponding, the stable instrument reading is noted as M1. The background reading after closing standard leak is recorded as M2. The preliminary system sensitivity is calculated as per Equation-1.

e) Leak detection

After completing primary calibration, the space between the pipe surface and the hood is filled with helium. The MSLD output reading is noted as M3, after waiting for a test time equal response time from any leak. Since trace probe and local hood technique adopted for testing, the testing performed from top weld joints to bottom side as shown in Fig.5. Upon completing the test of the system, the standard leak is closed. The final reading is noted as M4.

To check the reliability of testing, the final correction factor is calculated as per Equation-2. The value of the FSCF (expand) is well within ± 30% of the PSCF (expand) . The final leakage quantity is calculated by using Equation-3.

$$PSCF=CL/(M1-M2) \text{ - Equation 1}$$

$$FSCF=CL/(M4-M3) \text{ - Equation 2}$$

$$Q=FSCP \times (M3-M2)/\%TGx100 \text{ - Equation 3}$$

Conclusion

Leak detection and quantification of leakage rate of entire STC piping system has been developed and implemented using Tracer probe with local hood method. Each weld joint has been successfully assessed; local (1 X 10^{-8} m.bar.l/Sec) & global (1 X 10^{-7} m.bar.l/Sec) leak rate.

III.17 Manufacturing of Nickel Coil Assemblies for FBR Steam Generator Tube Leak Detection Circuit

During start-up and low power operation of fast breeder reactor, the sodium temperature is maintained below 250°C. In case of sodium leak in the steam generator, resulting sodium- water reaction and hydrogen evolved due to this reaction escapes to the argon cover gas plenum present over sodium. Cover Gas Hydrogen Meter (CGHM) with built-in Nickel Coil Assembly (NCA) is used for continuous monitoring and detection of hydrogen in argon cover gas, thus detecting steam generator leaks. The hydrogen diffusing in through the thin walls of the pure nickel tubes is swept out using argon carrier gas and hydrogen concentration is measured using a thermal conductivity detector (TCD).

Central workshop division (CWD) was entrusted with the manufacturing of NCAs to be used in the CGHMs for PFBR. The overall size of the nickel coil assembly is Dia.168.3 x 567mm height and material of construction is SS 316L. The high precision components were precisely machined using the state of the art CNC machine tools to achieve the dimensional and geometrical tolerances.

The butt weld joint between central pipe and the bottom dished end/cup was qualified by 100% radiography testing. The thin walled (250μm) nickel tubes (Ni 222, ASTM B163) were highly ductile in nature, hence meticulous care was taken during the forming process using a specially fabricated tube bending fixture. Precisely machined SS 316L sleeves were autogenously (without using filler wire) welded to the formed nickel tubes and subjected to Helium Leak Testing. All the seven nickel tubes with sleeves were assembled and fillet welded to the top header flange using gas tungsten arc welding process followed by HLT. The Top header flange was split into two segments using wire EDM cutting process for ease of assembling around the central pipe. The nickel tubes welded to the top header flange were attached to the central pipe using 100 μm thick x 5 mm width stainless steel straps spot welded to keep them intact with the central pipe.

Fig. 1: Nickel Coil Assembly

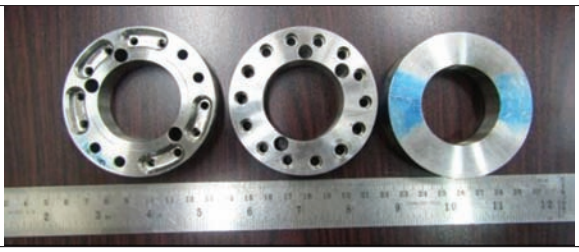

Fig. 2: Precisely machined Top header flange

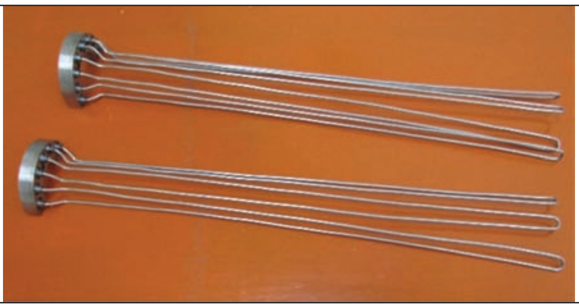

Fig. 3: Formed Ni tubes welded to Top header flange

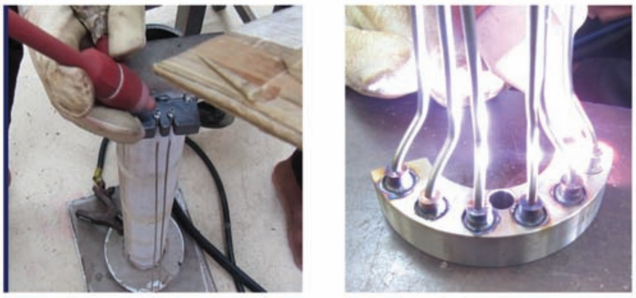

Fig. 4: Welding of Nickel tubes to SS316L sleeve and top header flange by GTAW process

Considering the manufacturing feasibility, the 90 degree bend profile of the interconnecting Stainless Steel tube (OD 3.2 x ID 1.6 mm) meant for carrier gas transport was simplified/modified to hemispherical profile, formed, inserted and fillet welded to the carrier gas inlet tube (OD 6.3 x ID 3.2 mm). The horse-shoe shaped pockets in the top header flange were closed using the identical closure plates and fillet welded followed by liquid penetrant inspection and HLT.

The NCAs were successfully fabricated as per drawing and in accordance with the ASME Section VIII Division 1 manufacturing code. Quality of the NCAs was ensured by adapting good engineering practices and seamless quality surveillance as per the approved quality assurance plan (QAP).

III.18 Robust Fault Tolerance for Critical Industrial Motor Drives: VFD Hot Standby Redundancy with Seamless Switchover

In fast breeder nuclear reactors and their reprocessing facilities, numerous critical applications important to safety—such as fuel handling machines and pump drives—depend on Variable Frequency Drives (VFD)-fed Induction Motor Drives, where the dependability and availability of the latter are of utmost importance. Consequently, stringent regulatory requirements are in place. Since VFDs are primarily of commercial nature, meeting regulatory compliance and the single failure criteria as mandated by regulator for safety class 2 instrumentation and control (I&C) systems poses a significant challenge. To address such issues, a method was developed using a real-time VFD Supervision and Safety (VSS) System, combined with dual redundant VFDs, to achieve robust fault tolerance for critical industrial motor drives.

In light of the aforementioned reasons, the developed approach incorporates autonomous real-time supervision of VFDs for independent failure identification, departing from sole dependence on the built-in diagnostics output (Fault Output) of the VFD. The two fault detection mechanisms operate in a 1002 voting fashion to initiate switchover. This strategy prioritizes guaranteed switch over to maximize safety and availability, over the probability of spurious switch over. The design also ensures online maintainability of failed VFD and least transients in drive system during switch over event.

The block diagram of the developed method and system is shown in Fig. 1. As shown, in a typical application, the real-time computer (RTC) supplies the speed set-point to the VFD, and the latter, in turn, delivers the controlled electrical output to the induction motor, resulting in a sinusoidal current of a specific frequency in the stator. Consequently, the speed is effectively controlled. In this case, the RTC provides identical speed set-points to both redundant VFDs (VFD1 and VFD2) also shares the copies of these set-points with the VFD Supervision System (VSS).In addition, the VSS independently supervises the dual redundant VFDs by monitoring the output frequency of the stator current. It compares the set-point speed with the output frequency of each VFD and detects faults such as over speed, under speed, over-acceleration, under-acceleration, direction of rotation fault, and overload fault.

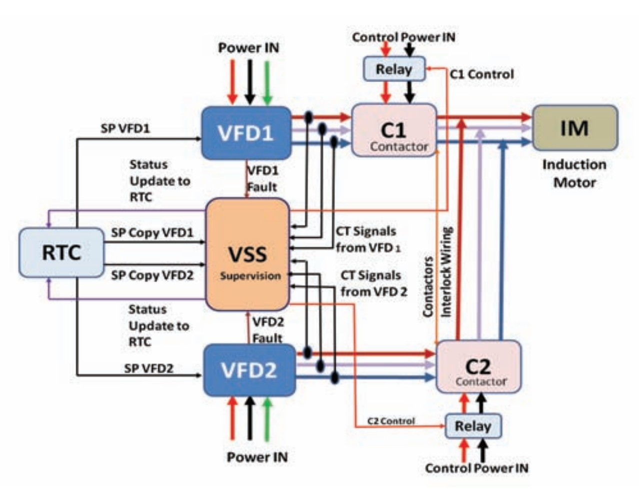

Fig. 1: Block diagram of System

The VFDs also perform internal diagnostics and relay fault outputs to the VSS. These faults along with VSS fault detection undergo a 1-out-of-2 voting process, dictating the control of contactors C1 and C2. These contactors feature interlock wiring, ensuring connection of only one VFD to the induction motor at a time. The VSS also updates the RTC regarding online/offline status of VFDs.

The method successfully achieves a fault detection time of less than 500 ms and switchover with minimal transients. In the future, the system will undergo further functional, environmental and EMI/EMC qualification testing for reactor deployment.

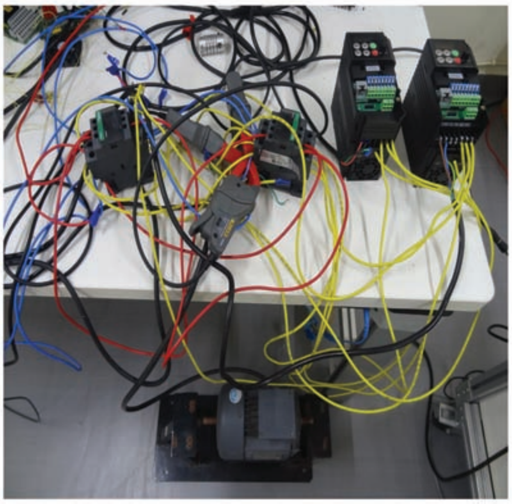

Fig. 2: Test Setup

III.19 Data Exchange Unit for Reliable Information Exchange Among Real-time Control Systems of Nuclear Reactors

To address the formidable qualification challenges associated with Linux based commercial equipment such as servers and operating consoles involved in distributed control architectures of Nuclear Power Plants; without compromising on useful capabilities in terms of HMI interface & data logging, a novel verifiable hardware capable of handling the safety-related data routing & processing functionalities was designed & developed. This hardware is referred as Data Exchange & Processing Unit (DEPU), capable of supporting multiple concurrent TCP sessions for connecting to various end control systems, and facilitating reliable data exchange among them. A set of such hardware shall perform all safety-related operations of a typical COTS servers and can also act as a gateway interface for isolating non-verifiable components and certified field-level control systems. This development shall bring down the safety dependency on COTS equipments, and hence the qualification requirements can be subsequently relaxed.

A multiport data exchange & processing unit (DEPU) is designed to facilitate TCP data exchange among 80 control nodes. The block diagram & fabricated unit is shown in Fig. 1. ARM microcontroller is interfaced with ten independent network modules for TCP/IP over ethernet communication. Each network module consists of a hardwired TCP/IP offload engine for independently providing stable data communication capabilities to the master controller with simple memory-like controls, which eventually leads to simpler, predictable, and deterministic software architecture.

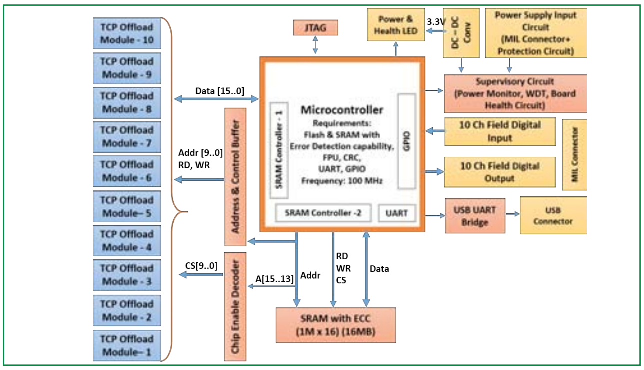

Fig. 1: Block Diagram of DEPU

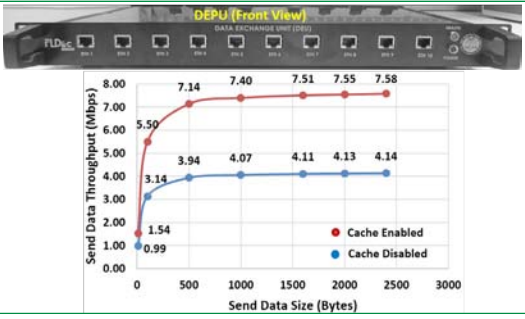

Fig. 2: Fabricated DEPU & Send data throughput achied with a single TCP socket with Eight live concurrent sessions

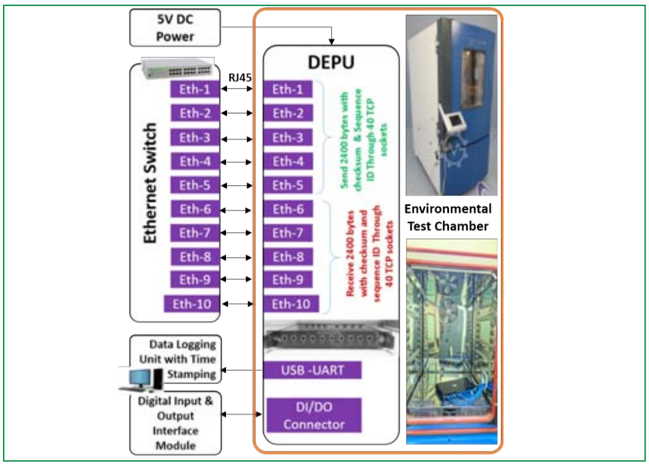

Fig. 3: Environmental Qualification Setup

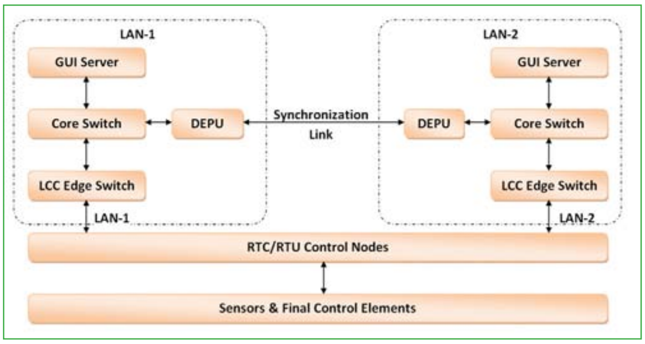

Fig. 4: Distributed Control Architecture with DEPU

The fabricated Unit and send data throughput from a single TCP socket is shown in Fig. 2. Environmental qualification (Fig. 3) is carried out for evaluating performance up to ambient temperatures of 55°C and 95% relative humidity.

Seismic qualification was performed with zero anomalies for 5-OBE & 1-SSE tests. EMI/EMC qualification tests were carried out as per Indian NPPs requirements for Safety class-2 systems and Class-A performance was achieved except the surge test with Class-B performance which is acceptable for Safety related systems. MTBF of 2,60,484 hours is estimated based on reliability estimation in line with MIL-HDBK-217-F. The proposed I&C architecture based on DEPU, along with the industrial servers & display components, is illustrated in Fig. 4.

III.20 Analysis and design of a self-oscillating opto-resistive type quasi-digital sensor to check the quality of lubricant oil

In the context of large rotating machinery, lubricant oil plays a vital role. Its primary purpose is to minimize friction between metallic surfaces that come into contact, ensuring smooth operation. Additionally, it effectively removes foreign particles and debris that can contaminate the surfaces. Moreover, as the machinery operates, the lubricant oil also functions as a coolant, efficiently dissipating heat generated by the moving surfaces of crucial components like bearings and gears. Maintaining the in-service lubricant oil in optimal condition is crucial, as it plays a vital role in determining the longevity of essential components such as bearings and gears in rotating machinery. Sensors designed for online monitoring of lubricant oil can alert operators to maintain the oil in optimal condition.

Self-oscillating type opto-resistive quasi-digital sensor has been developed at ISS to detect the quality of lubricant oil. Its working principle is illustrated in Fig. 1. Light transmission principle is applied to detect the quality of the lubricant oil.The light transmission reduces with decrease in the quality.

Two sensors with different dimensions were designed, fabricated and tested using laboratory made experimental set up. A testing platform fabricated to assess the sensor's detection capabilities concerning lubricant oils of varying ages.To assess the sensor's detection capability, a testing apparatus is constructed.

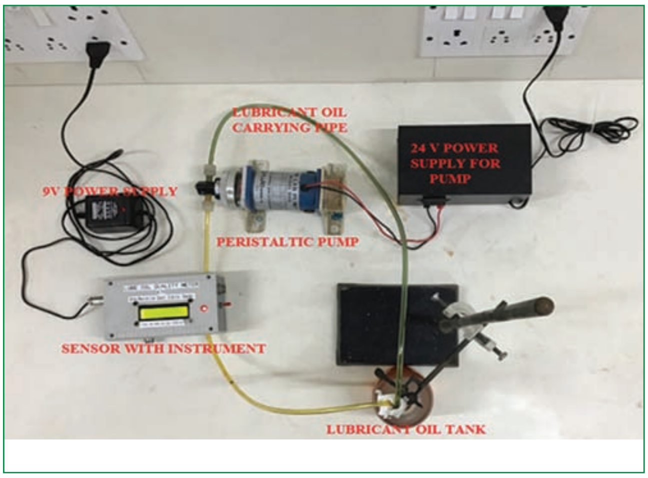

Fig. 2: Testing platform to validate the Sensors and instrument.

Fig. 2 illustrates the test platform, comprising the power supply, sensor module, instrument, peristaltic pump, lubricant oil tank, serial communication, and LCD. Lubricant oil samples are circulated through the sensor using a peristaltic pump and recorded by the instrument. A PIC18F4550 microcontroller based instrument was designed, developed and fabricated to read the sensor output. It reads the sensor output and transmits the data to computer through serial communication and display on LCD.

To calibrate the sensor and instrument, service oil samples spanning from fresh to aged were gathered and utilized in the experiment. The instrument was calibrated using samples with ASTM D 1500 color codes ranging from 0.5 to 8. A plot depicting the relationship between the color code and sensor output is shown in Fig. 3.

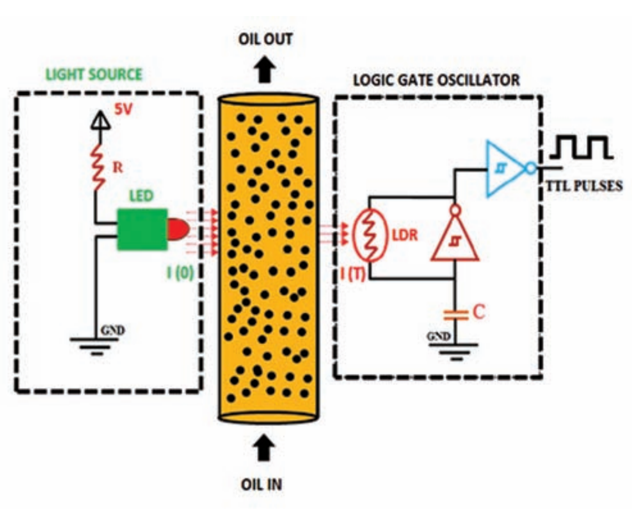

Fig. 1: Principle of opto-resistive type quasi-digital sensor.

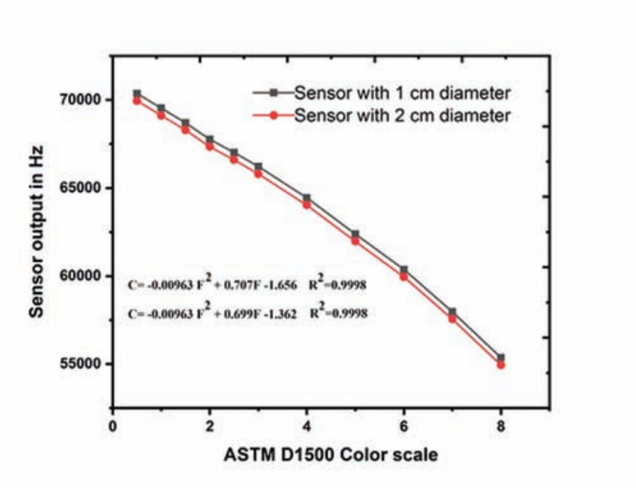

Fig. 3: Testing platform to validate the Sensors and instrument.

III.21 Development of Sensor for Detection of Onset of Boiling in Sodium

Sodium is the metal used in liquid form in fast reactors for cooling the reactor core. There are possibilities where boiling of sodium may occur locally or globally. In this scenario we need to detect on set of boiling of sodium in order to take necessary action to curtail any untoward incident in the reactor. Various other methods to detect voids in sodium are using eddy current based void detection, capacitive based sensor and neutron based imaging techniques. We have developed a technique to detect onset of boiling using an inductance based pulsating sensor here after named as onset of boiling detector for sodium (OBDS). In order to demonstrate the working of the developed sensor in sodium we have done lab scale experiments using alternate liquid medium at room temperature. The equivalence of using the alternate liquid medium is discussed subsequently.

OBDS has a specific behavioral pattern which can distinguish between diamagnetic (Mercury, Tin, Lead) and paramagnetic (Sodium, Aluminum, Lithium) materials. During ingress of air in the mercury medium through the sensing electrodes the output of pulsating sensor decreases and will increase for paramagnetic material like sodium. Taking advantage of this behavior of inductance based pulsating sensor, and to overcome the difficulties in handling liquid sodium towards demonstrating detection of onset of boiling, lab scale experiments have been carried out using mercury instead of sodium. Thus the results can be correlated if we extract the behavioral pattern of the sensor in mercury.

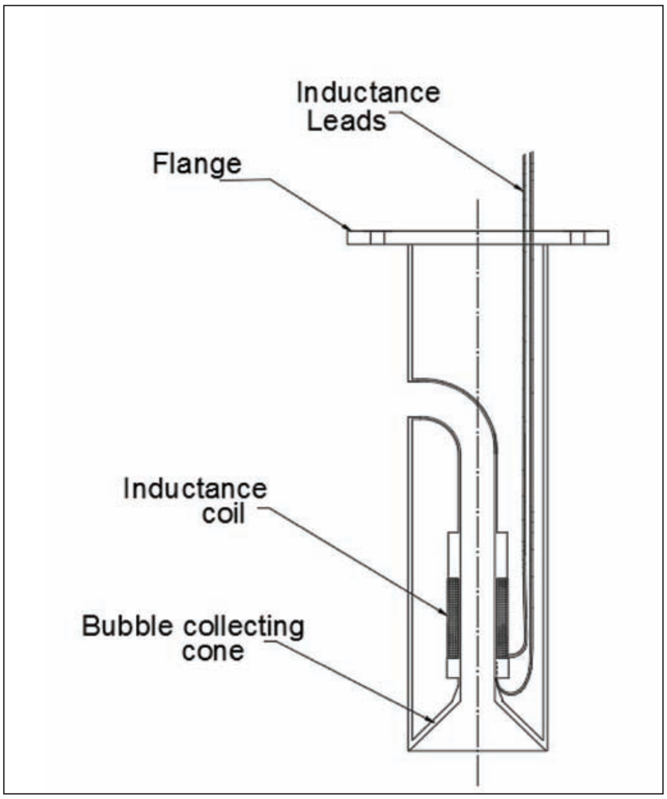

Fig. 2: Sensor probe for sodium

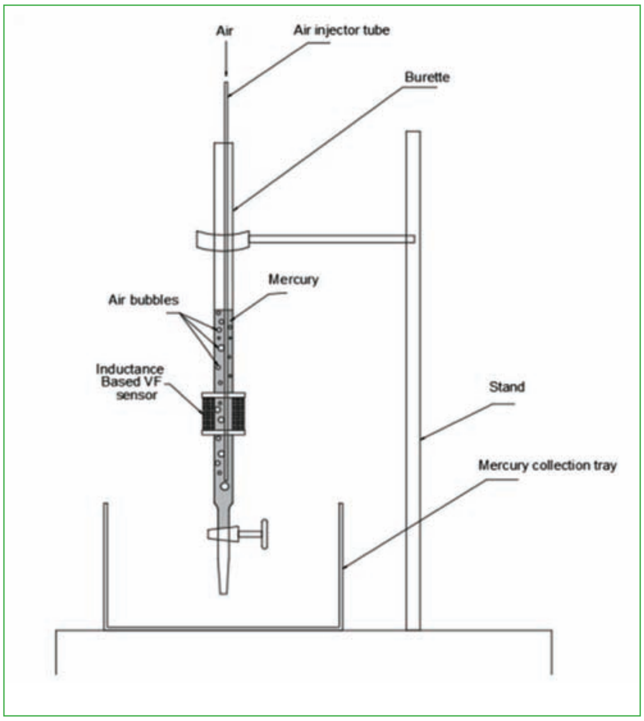

Fig. 1: Lab scale experimental setup

Mercury Experiments to demonstrate working of OBDS:

Prior to deploying the fabricated probe and the sensor in sodium facilities we attempted to test the sensor in mercury medium so that the feasibility of the sensor working in sodium can be demonstrated. Fig. 1 shows the schematic of the experimental setup. Since the actual probe is designed such that the ID of the probe is exposed to the working medium (sodium), similar condition is maintained in the lab scale experimental setup. In the lab scale experiment the ID of the electromagnetic coil is wetted by the working medium (Mercury). The experimental setup consists of a burette filled with mercury to a height of 400 mm. At half the height of mercury, an inductance coil bobbin with enamel coated copper as the lead is fixed on the burette. A Teflon tube is inserted from the top to inject voids which rises through Mercury column inside the burette. Two modes of injection of voids were done in the experiment. One mode of injection was constant volume injection through a syringe and a height gauge, in which a syringe of volume 50ml was fixed to height gauge. Height gauge was moved to a constant displacement thus a constant volume air injection was made. The other mode of injection was using a pump and a rotameter in which a mini air pump was used to pump air which was regulated by a rotameter(0-5LPM). Maximum of 2.5LPM of air was injected in the mercury column with an increment of 1ml.

Sensor design and construction for Sodium application:

The OBDS is designed to detect the onset of boiling in sodium pool. The sensor is basically an electromagnetic coil which is wound over a hollow pipe with a conical end at the bottom. The ID of the pipe is exposed to the medium in which void is to be measured and the liquid is free to rise through the pipe. The conical end at the bottom of the sensor is to facilitate maximum number of voids, to pass through the sensor, formed during boiling.

The sensor is designed as a passive sensor with no moving parts. An outer sheath is provided in order to prevent the wetting of the electromagnetic coil and to allow the sodium and voids entering the sensor back to the Sodium pool. The outer sheath is in turn welded to a flange which will be mounted on the sodium tank. The schematic of the sensor probe and its construction is shown in the Fig. 1. The number of turns, length of the coil and wire thickness is determined and optimized based on numerical analysis and experimental trials. Since the actual probe have to withstand high temperatures MI cable with Nicrome core was selected. SS 316 is the material of construction of the probe.

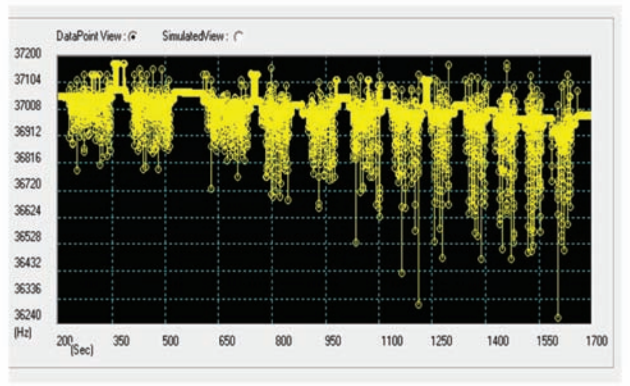

Fig. 3: Typical sensor output showing change in frequency

Results and Discussion:

The results were analysed for resolution, sensitivity and response of the sensor. Both the injection methodology yielded the same change in output parameter.

A typical sensor output showing change in frequency with time is shown in Fig. 3. Average change in frequency for volume based injection through syringe and flow based injection through pump setup is 50Hz for 0.00066 LPS and 200Hz for 0.0025 LPS respectively. Our pulsating sensor electronics is capable of measuring ± 1Hz with 99% confidence which leads to detection of voids equivalent to 26.4 μLPS(approximately 2mm bubble). Hence this methodology can be used to detect onset of boiling in sodium medium.

III.22

Design and Testing of Feasibility Models of Inherently Safe Portable Micro SMR for Vehicles & Captive Power Plants towards Defence Low Power Applications

There is heavy demand for electricity in isolated and deserted places such as islands, deserts and mountains for military people for living infrastructure and maintaining artillery. Similarly the transport of fuel and delays for refueling are very intricate issues in the operation of patrolling vehicles either on land or water.

Salient Features:

- Reactor is Inherently safe as absence of heat removal shuts down the reactor.
- No additional nuclear fuel type, fabrication, shielding-cooling-moderator material and spent fuel storage facility is required, than what is presently available.
- No moving parts are present inside the reactor.
- Double containment can be provided around the fuel with –ve pressure in the vessel gap.
- Heat energy is taken from the core directly to drive the shaft to increase the efficiency.
- Spent fuel pin/subassembly also can be used for the heat source, for low power requirements, to avoid criticality related issues and neutron radiation.
- Beyond DBE also, decay heat can't heat the core beyond 100 degrees, increasing the fuel integrity and mechanical strength.

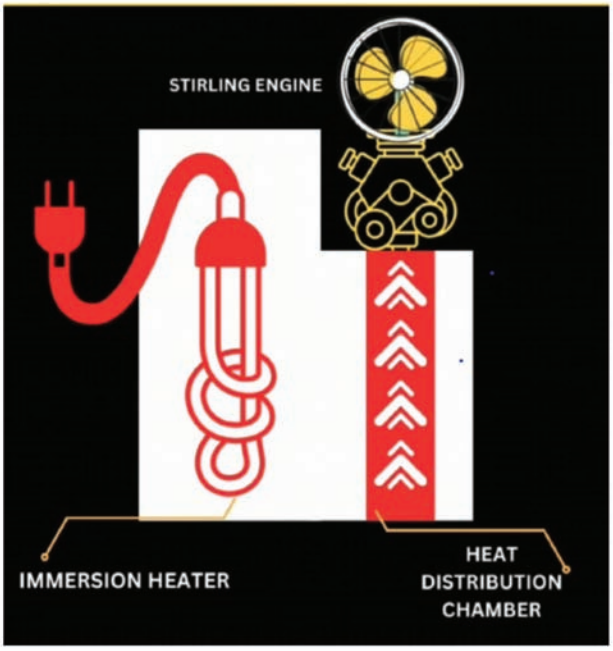

Fig. 1: Simulation

Fig. 2: Working model

- If heat removal is absent when spent fuel is used as heat source, there can be mechanism to remove the heat through surface convection to avoid over heating
- The fuel breeds during its operation
- There is no requirement of exclusion zone and sterilized zone.
- It is possible to use the module as captive power plant to supply ~kW power capacity
- It does not require any special vehicle for transport.
- Exclusive installation, radiological training and maintenance are not required.
- No radioactive gas will be released to atmosphere during reactor operation.
- Can be easily installed and operated in moving vehicles on land, water and air.
- Do not require large water bodies near by.
- No necessity of grid connectivity.
- Except enough security measures, there is no need of any dependent factor/parameter for installing this reactor, such as pressure, temperature, humidity, altitude.
- Stringent codal requirements such as voting logic,redundancy diversity, fail safe and single failure concepts may not be needed.

- No fuel handling is envisaged at the utility. Only the reactor module to be replaced with new one, possibly every 5-10 years.
- System works at ambient pressure & temperature (<100ºC)
- Ultimate passive safety measure of introducing neutron poison into the core can be provided incase needed, i.e. if pressure and temperatures are crossing beyond limit.
- Manual mechanism can be provided to start the reactor after the above incident.
- Passive temperature and pressure sensors can be provided.

Working Principle Of The Feasibility Prototype 1:

Fuel pins of FBTR/PFBR can be placed in core support structure in subcritical configuration with air medium. Once minimum water is filled in the shielded reactor vessel (~20 mm thick SS vessel), reactor becomes critical and coolant gets heated up. The Engine takes the heat from the water in the reactor vessel and converts to mechanical, electrical & kinetic energy. Power can be controlled from the water inlet and drain valve, if required. Reactor will be shutdown even if some water is converted to steam or water is not sufficient, due to the absence of moderation. In case of any untoward incident temperature and pressure going beyond limit, manually the boron carbide shutter can be inserted. Same thing can be taken back for restarting the reactor.

In the feasibility model shown in Fig. 2, the heat from the fuel pins is generated from immersion heater as per the simulation shown in Fig. 1. The rotating wheel is not having physical contact with the coolant. i.e. the energy from the water coolant at ambient pressure is taken by conduction and coolant is not exposed to outside environment. It is also checked that, the trapped heat in water is converted to rotational energy for a long time even after switching of the heat source The rotational energy from the wheel can be connected with gears and dc generator to make a moving platform with electrical load. The system is operated for more than 100 hours successfully.

Fig. 4: Working prototyp

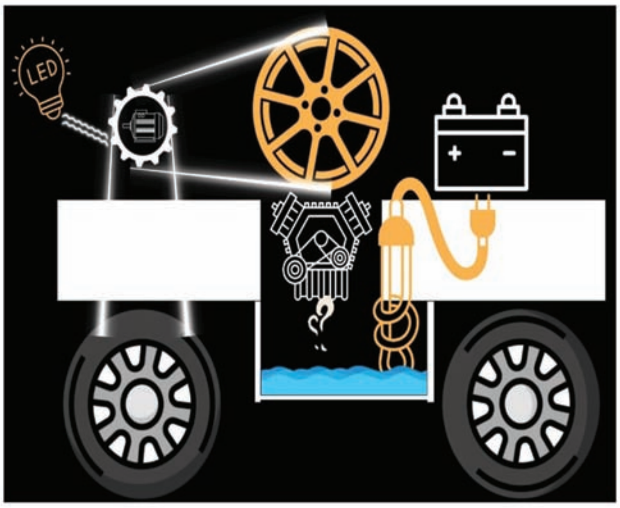

Fig. 3: Simulation

Working Principle Of The Prototype 2 Moving Vehicle With Electrical Load:

In this model shown in Fig. 4 also the heat from the fuel pin/storage pin is produced from immersion heater as per the simulation shown in Fig. 3. The energy is transferred in similar manner without the necessity of the coolant having contact with the rotating wheel. The rotational energy is converted to mechanical energy for the moving platform through gear mechanism. DC generator is also coupled to this gear mechanism to generate electricity to power an LED.

Future work:

In the next model, design of the water tank, heater, air chamber and piston will be modified to increase the efficiency.

Applications:

- Captive power plants with operational cycles in islands, deserts and mountains (eg. Siachin) for defence and strategic purposes.
- Low Power source without the need for refueling for years, for army/defence trucks.

References are taken from national and international released reports to validate and ensure the functionality of actual prototype and the correctness of fuel configuration, moderator, neutron flux, temperature, power and shielding calculations.

III.23 Interaction of Air Plasma-Sprayed Spinel and Yttria Coatings With Ultra-High Temperature Ceramic-Metal Hot-melt

Air Plasma Sprayed (APS) ceramic coatings are conventionally used for protecting metallic parts of hot section components in aero- and land-based gas turbines. Owing to their capability to withstand very high temperatures, high specific heat capacity, and thermal shock resistance, such APS coatings are also investigated for the potential to protect the core catcher in nuclear reactors during the high-temperature core-meltdown accidents resulting in corium hot-melt. Several sacrificial oxide ceramics were investigated for such applications due to their miscibility with molten oxide fuels, low thermal conductivity, high melting points, high irradiation stability, and excellent chemical stability in liquid-sodium coolant. Sintered rare-earth oxides and magnesium aluminate ($MgAl_2O_4$) spinel single crystals were found to have satisfactory chemical stability in liquid-sodium environments. In this study, candidate plasma-sprayed spinel and yttria (Y_2O_3) coatings on SS 316LN substrates were subjected to an ultra-high temperature (UHT) ceramic-metal hot-melt generated by thermite reaction (spontaneous exothermic reaction) between Fe_2O_3 and Al metal to generate a molten mixture of Al_2O_3 and Fe metal at ~2800˚C as a simulant to corium.

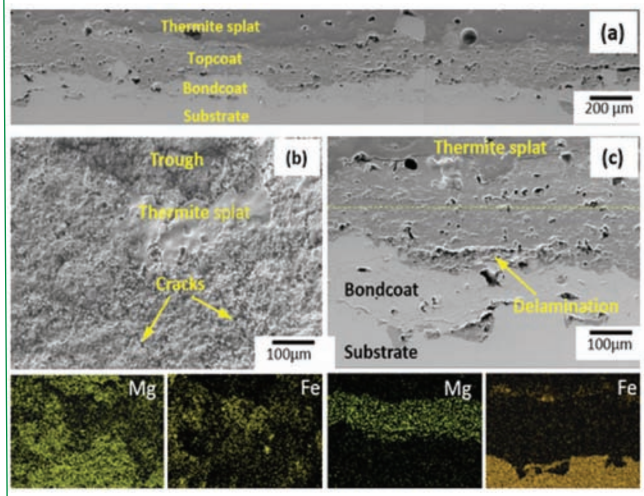

Fig. 1: (a-c). SEM and EDS analysis of spinel coating after thermite exposure

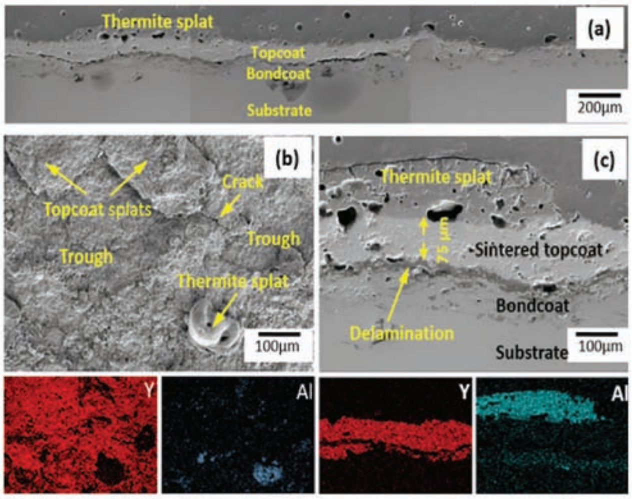

Fig. 2: (a-c). SEM and EDS analysis of yttria coating after thermite exposure

The surface and cross-section SEM analysis of spinel coatings after UHT melt interaction with corresponding EDS is shown in Fig.1(a-c). The micrographs reveal slight thickness loss after removal of thermite splats (Fig.1a), intermittent delamination cracks were seen at topcoat/bondcoat interface (Fig.1c). The surface micrographs reveal densification due to sintering effect (Fig.1b). Phase analysis by XRD reveal stability of spinel phase after exposure. The similar surface and cross-section analysis for yttria is shown in Fig. 2(a-c). The remnant top coat layer is shallow and irregularly distributed (Fig. 2a).

Surface analysis reveal severe damage with presence of thermal shock induced cracks and completely densified due to sintering (Fig. 2b) and phase analysis confirmed the formation of new $Y_3Al_5O_{12}$ after UHT melt exposure. The evolution of interfacial fusion was observed in the case of yttria coatings due to the formation of primary YAG and Al_2O_3-YAG eutectic at the interface. Spinel coatings with a comparatively lower thermal conductivity could generate a higher ΔT across the thickness with limited grain growth in the substrate.

This study provides critical inputs on the interaction of coatings on a SS substrate when subjected to UHT melt towards assessment of the applicability of TBCs to the core catchers of future SFRs.

III.24 Lattice and Bulk Thermal Expansion Coefficients of Enriched Boron Carbide

As a part of the core modification programme to attain the design power output of 40 MWt, 50% ^{10}B enriched B_4C (50E-B_4C) was recently introduced as a burnable poison in Fast Breeder Test reactor (FBTR). B_4C with 90% ^{10}B enrichment (90E-B_4C) and natural ^{10}B isotopic composition (N-B_4C) are also used in FBTR for the absorber rod and neutron shielding applications respectively.

As the two isotopes ^{10}B and ^{11}B in B_4C differ in mass by ~10%, the coefficient of thermal expansion (CTE) is anticipated to undergo significant change due to ^{10}B enrichment. In this regard, both the lattice and bulk thermal expansion coefficients were measured in the temperature range of 298-1273 K using high temperature X-ray diffraction (HTXRD) and dilatometry techniques respectively for N-B_4C, 50E-B_4C, and 90E-B_4C.

Fig. 1a and b show temperature dependence of lattice parameters along –a and –c axis (a_T and c_T) estimated from HTXRD and Fig. 2 shows the bulk dilatational strain $(^{\Delta l}/l_{298})$ measured using dilatometer.

The lattice (LTE) and bulk (BTE) thermal expansion coefficients were estimated from these measured values of aT, cT and $(^{\Delta l}/l_{298})$ using standard procedures and their variation with temperature is shown in Fig. 3(a)-(c). The parameter (α_l^{avg}) stands for the average linear lattice thermal expansion coefficient and (α_b^{avg}) represents the average linear bulk expansion coefficient of natural and enriched B_4C.

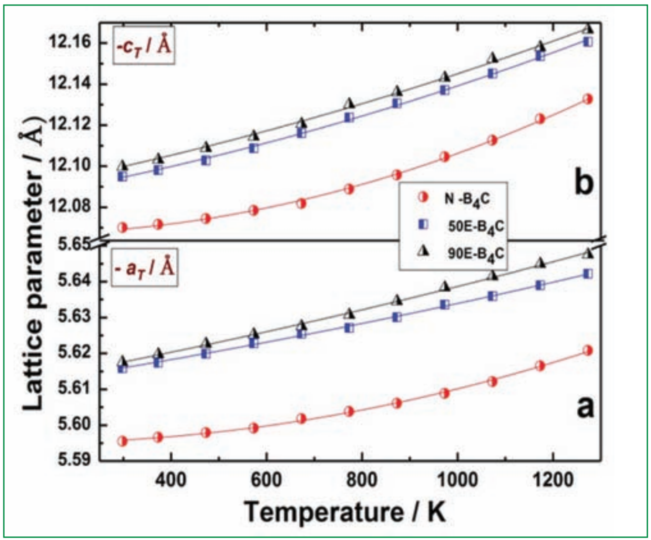

Fig. 1: Lattice parameters for N-B4C, 50E-B4C and 90E-B4C

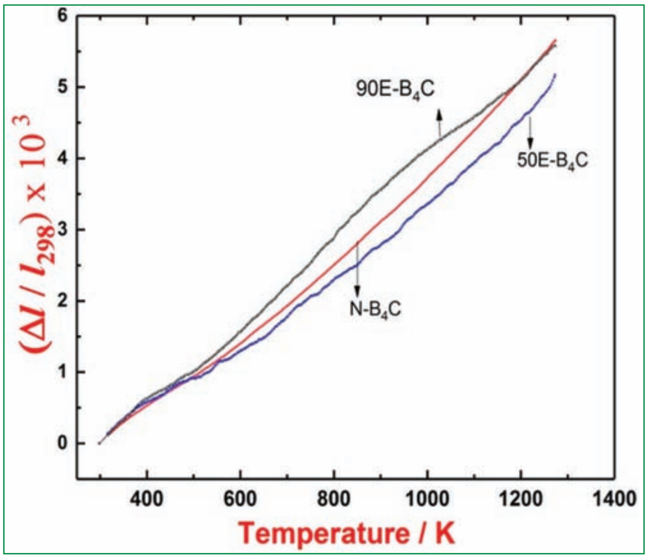

Fig. 2: Dilatational strain measured as a function of temperature for N-B_4C and enriched B_4C

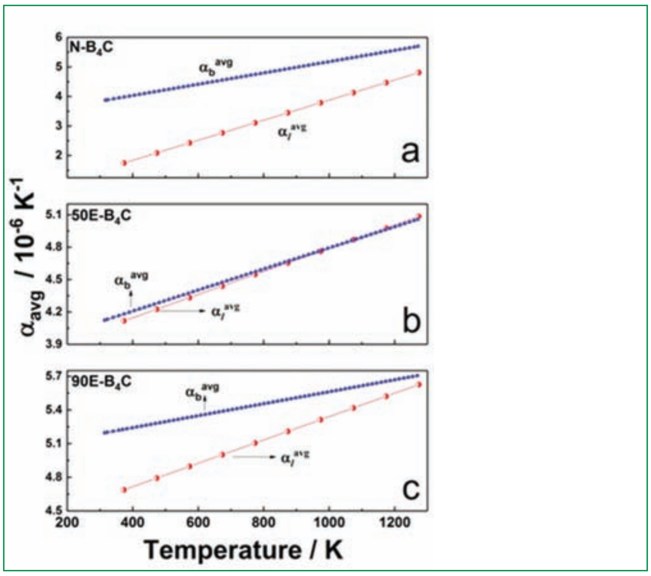

Fig. 3: Comparison of LTE (αlavg)with that of the BTE (αbavg) for N-B4C, 50E-B4C , 90E-B4C

The results show that, (i) the average CTE increases with increase in ^{10}B enrichment for polycrystalline B_4C (ii) bulk expansion is always higher compared to the lattice expansion (iii) the difference in bulk and lattice expansion is minimum for 50E-B_4C whereas it is significant for N-B_4C and 90E-B_4C and (iv) the difference in bulk and lattice expansion gradually comes down with increase in temperature.

The 50E-B_4C specimen with density close to the theoretical density shows minimum difference between BTE and LTE. In essence the significant difference in the lattice and bulk expansion coefficients in boron carbide is attributed to the density deficit in the material caused by defects and impurities.

III.25 Interaction of Zr with FBR Cladding Materials

In metal-fueled reactors Zr is used as the liner to reduce fuel clad chemical interaction. Due to lack of literature information, diffusion couple experiments were carried out under identical experimental conditions to understand the interaction of Zr with the clad materials: alloy D9 and P91 ferritic/martensitic (F/M) steel. Fig. 1 shows the sandwich type diffusion couple which was heat treated in the temperature range of 973-1273 K up to 24 h. Evolution of interface microstructure with thermal exposure, phase stability of the reaction zones and their growth kinetics were studied and compared with literature information to understand the role of alloying elements and crystal structure on interdiffusion behavior.

At all temperatures below β-transus (<1173 K) a reaction layer with ~300 HV0.1 hardness formed at the interface of both the couples. Fig.s 2(a) and (b) show back scattered electron (BSE) images and superimposed concentration profiles obtained using Electron Probe Micro Analyzer (EPMA). Based on microchemistry and XRD analysis, the reaction layer at the interface having a composition of 52.8Fe-8.8Cr-38.4Zr (at.%) was found to contain Fe_2Zr intermetallic phase. After heat treatment, the interaction zones were wider in P91/Zr diffusion couple, their width increasing with both temperature and time of heat treatment. Above β-transus there was significant increase in the width of the zones. In addition to Fe_2Zr, stabilized β-Zr formed at the interface with a width of ~300 µm (at 1173 K; 24h) for P91/Zr couple.

Growth kinetics of the interdiffusion zones was studied by monitoring the change in thickness (x) with T and t. 'x^2' vs 't' had a parabolic behavior indicating volume diffusion to be the rate controlling process. Calculated growth parameters are given as insert in Fig. 3.

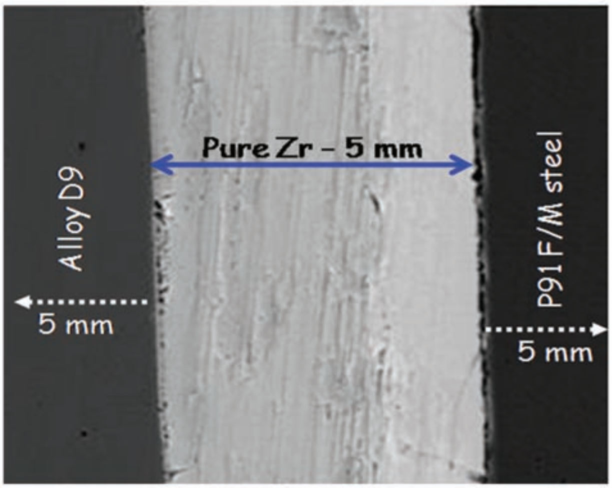

Fig. 1: Representative image of sandwich type diffusion couple

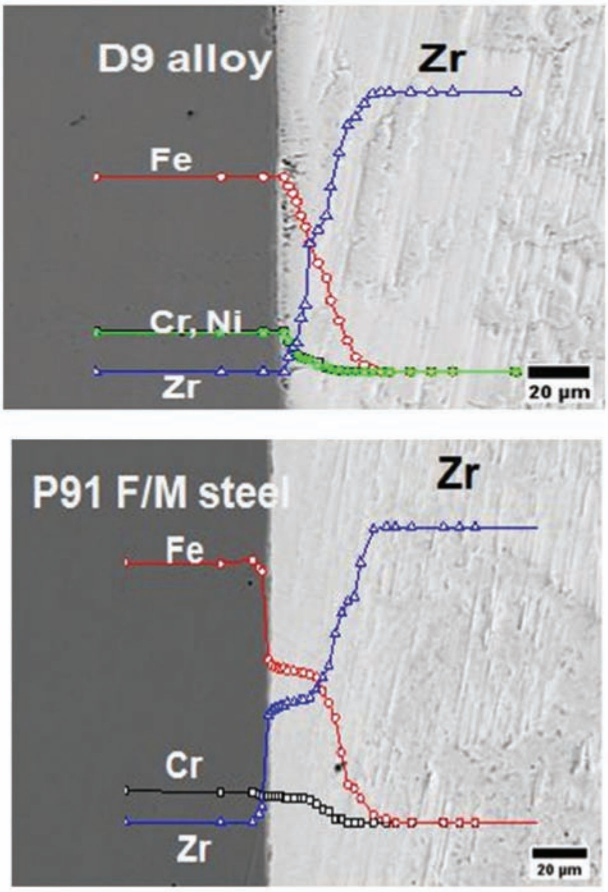

Fig. 2: (a) and (b) BSE images obtained from the cross section of the diffusion couples with superimposed EPMA concentration profiles

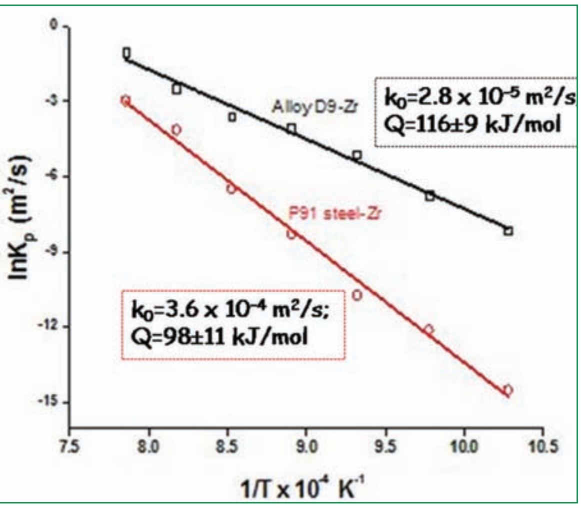

Fig. 3: Arrhenius analysis of effect of temperature on the rate of the reaction

III.26 Generation and Detection of ultrasonic High Frequency Guided Waves (HFGW) in Complex Structure

Generation and detection of ultrasonic high frequency guided waves (HFGW) have been studied in a complex weld structure that is similar to the main vessel core support structure (MV-CSS) of PFBR. To verify this, a complex plate structure with a tri-junction weld was fabricated using 15 mm thick austenitic stainless steel plates as shown in Fig. 1(a), as part of an IGCAR-CEA collaboration. The HFGW was generated by using an edge-mounted transducer i.e., normal to the edge surface at 2.25 MHz. To understand the physical features of HFGW in this complex geometry, a series of 2-D finite element simulations were performed using the ABAQUS explicit method. The results obtained from these models were analyzed and compared with experimental measurements. Fig. 1(a) compares the experimental and simulation results.

These wave modes are considerably less dispersive over a scan distance of a few meters. Both simulation and experiment show that the multiple wave modes in HFGW are formed due to mode conversion at high fxd product (above 30 MHz-mm) i.e., a nearly longitudinal mode pulse is generated followed by several trailing pulses. During the propagation of HFGW, the maximum energy is transferred from the leading pulse to the following trailing pulses. The potential of HFGW has been examined for the detection of artificial notches of 50%WT made near the weld zone. It is observed that the HFGW is reflected or transmitted through the notches without significant mode conversion. Fig. 1(b) show the time domain signals of HFGW obtained from the 50% WT notches made near the weld.

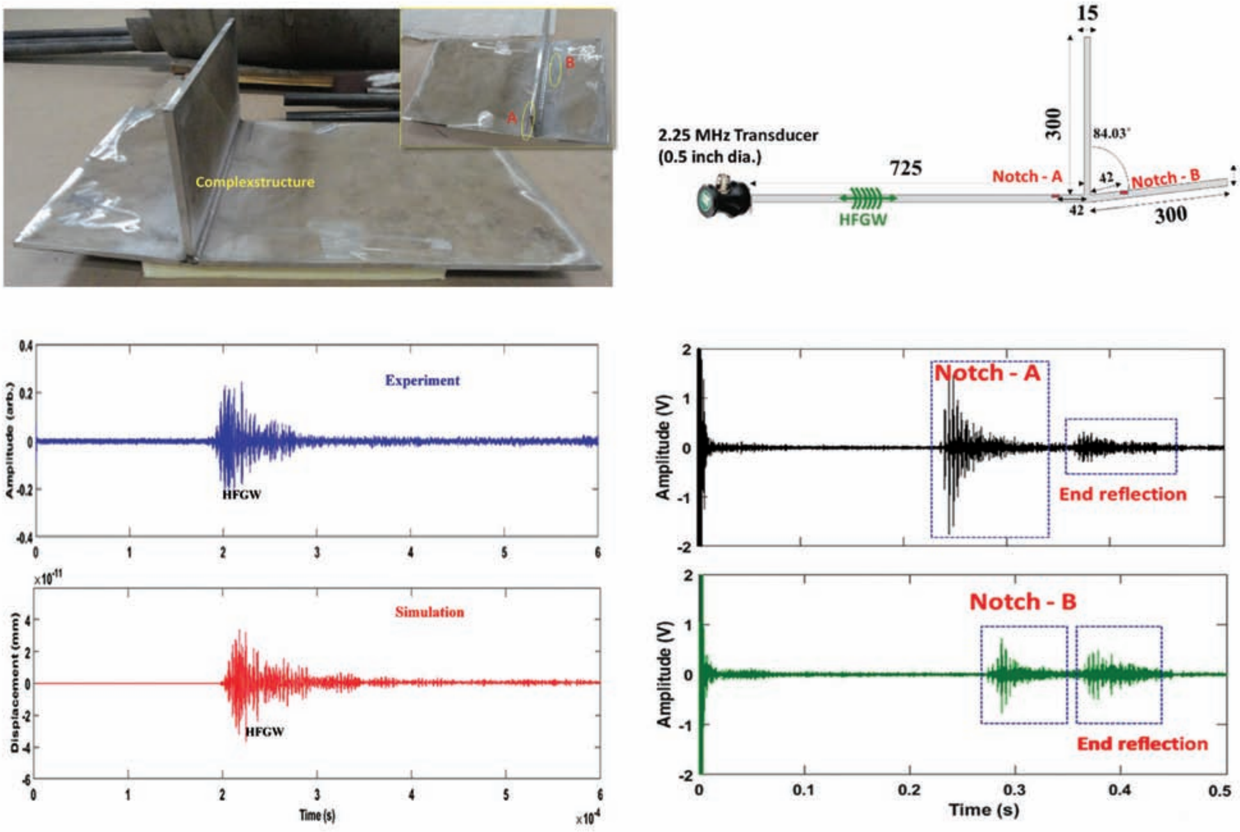

(a) (b)

Fig. 1: (a) Photograph of the complex weld structure and the signals obtained from the measurement and simulation and (b) the schematic for the interaction of HFGW with defects and the corresponding A-scan signals.

III.27 Short-term Aging Effect on Creep Properties of Alloy D9I SS

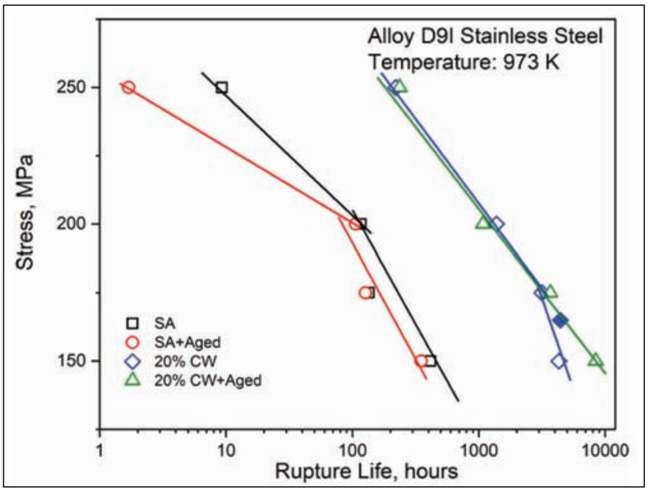

Fig. 1: Variation of rupture life in the stress range of 150 to 250 MPa at 973 K.

Alloy D9I austenitic stainless steel (Titanium added 14Cr-15Ni SS) in 20% cold worked (CW) condition is a candidate material for future cores of oxide-fuel based sodium cooled fast reactors of India (SFRs). Precipitation of fine secondary TiC in this material during service enhances the resistance to both the void swelling and creep deformation. As secondary TiC precipitates nucleate only on dislocations, prior cold work level of 20% is mandated for core components (clad, hexcan & spacer wire). However, transient conditions such as failure of coolant pumps, power ramps during operation etc. result in inadvertent thermal excursion that can reach the clad hot spot temperature of 973 K. Though such exposures are likely to be of a brief duration, substantial microstructural changes can occur thereby influencing the creep performance. In order to comprehensively understand the effect of thermal exposure on the creep performance of this alloy, short-term aging was carried out on D9I SS at 973 K for 40 hours after imparting a prior cold work level of 20%. Additionally, three more conditions of this alloy were investigated for establishing the reduction factors with respect to rupture life for creep tests carried out in the stress range of 150-250 MPa at 973 K. The four conditions investigated in this study were: a) Solution annealed (SA) condition, b) Solution annealing followed by aging (SA+Aged) condition, c) Solution annealing followed by 20% cold work (20%CW) and d) Solution annealing followed by 20% cold work and aging (20%CW+Aged).

The rupture lives for the SA condition were marginally higher than those of the SA+Aged condition at all the stress levels as shown in Fig. 1. However, the rupture lives of these two conditions were considerably lower compared to their cold worked counterparts (Fig. 1). The rupture lives were comparable between the 20%CW and 20%CW+Aged conditions at all the stress levels except 150 MPa. The higher rupture life of the 20%CW+Aged condition tested at 150 MPa is attributed to the stability of the CW induced dislocation structure. On the other hand, extensive dislocation recovery was evident in case of 20%CW variant. Thus, short-term aging supported retention of CW-induced dislocation structure that sustained TiC precipitation, in turn enhancing the creep strength and rupture life. Inferior creep strength of SA and SA+Aged conditions is attributed to the extensive precipitation of $M_{23}C_6$ in preference to TiC during creep exposure.

In order to examine the difference in creep life with reference to the standard condition viz., 20%CW, creep life fractions were estimated for three material conditions (Fig. 2). Rupture lives of SA & SA+Aged steel were 0.2 times that of the 20%CW at all testing conditions. For 20%CW+Aged condition, the life variation is within ± 22% of that observed for 20%CW condition, except at 150 MPa wherein significant life improvement is observed after aging. Further, the creep rupture elongation of 20%CW+Aged steel is within 20% of that of the 20%CW condition. The above observations indicate that short-term thermal excursions would not result in significant deterioration in the creep properties of Alloy D9I SS

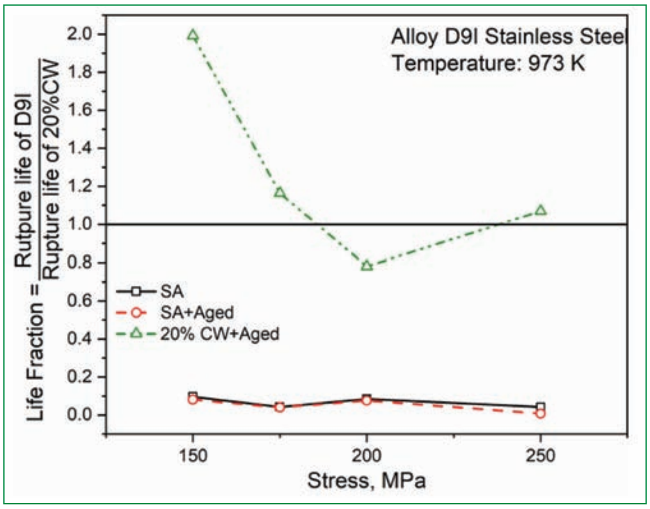

Fig. 2: Creep life fraction with reference to 20%CW Alloy D9I SS.

III.28 Influence of prior tensile deformation on creep properties of Grade 91 steel

The elevated temperature strength/softening of Grade 91 (Gr.91) steel results from alloying elements, dislocation structure, boundaries (lath, packet, block, sub-grains) and precipitates. The evolution of these microstructural features during high temperature exposure significantly influences the material behavior. It is therefore important to examine how prior microstructural hardening or softening influences the creep deformation and damage behavior of Gr.91 steel. In order to study this, distinct initial microstructures (with different degrees of softening and hardening) were obtained by subjecting the material to various strain levels in tensile deformation at 873 K and a strain rate of 5×10^{-5} s^{-1}, namely 0.2% (yield strength), 0.4% (slightly above the yield strength), 1.7% (ultimate tensile strength, UTS), 5.3%, 8%, and 13%. Creep tests at 873 K and 170 MPa were then carried out on prior deformed samples. According to the Considère criterion, the necking instability occurs when the rate of change of stress with respect to strain (dσ/dε) equals the stress (σ) at the maximum load (Ultimate tensile strength). Interestingly, necking was not observed in Gr.91 steel even at the UTS, but appeared at a strain >13%, which is far beyond the strain corresponding to the UTS (Fig. 1). An increase in dislocation density contributes to strain hardening up to UTS beyond which dislocation annihilation and substructural coarsening lead to a progressive reduction in the load-carrying capacity of the steel. Creep curves presented in Fig. 2 reveal prolonged secondary creep regime and ~35% reduction in the secondary creep rate of prior deformed samples (with 0.2% to 5.3% strain) compared to the as-received sample. In contrast, samples with prior deformation levels of 8% and 13% exhibited an increased secondary creep rate above 80% with respect to the as-received sample.

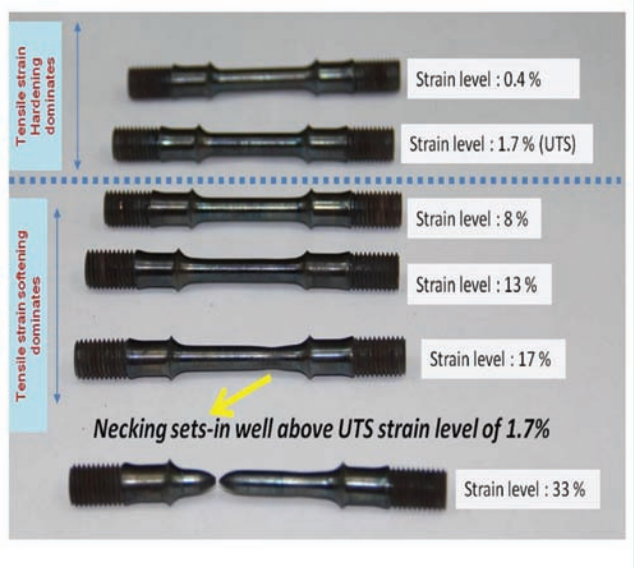

Fig. 1: Tensile specimens at different interrupted strain levels. Necking instability sets in well above UTS strain level (1.7%). Dominance of hardening and softening is marked, based on the instantaneous strain-hardening analysis for the steel.

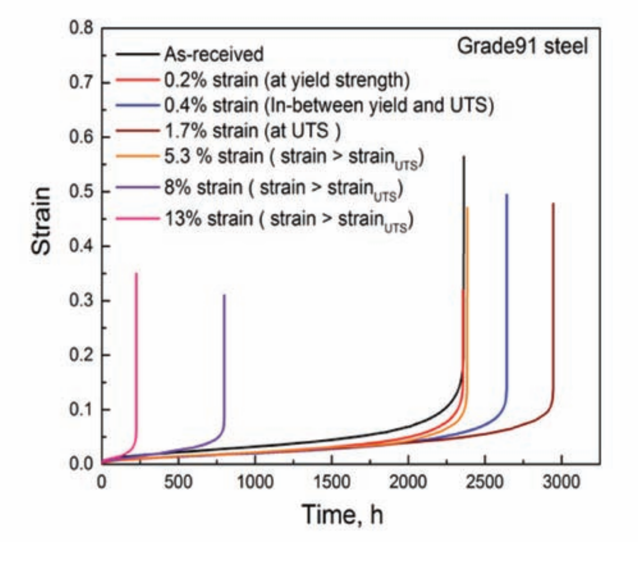

Fig. 2: Creep curves corresponding to different prior strain levels.

The rupture lifetimes of samples with prior plastic strain levels of 0.2% and 5.3% closely matched those of the as-received condition. Gr.91 steel with prior deformation levels of 0.4% (slightly above the yield strength) and 1.7% (UTS) displayed a higher creep life compared to the as-received condition. In fact, the steel demonstrated the highest creep life at the prior-deformed level of 1.7% strain (UTS). On the other hand, the steel with higher prior strain levels (8% and 13%) showed nearly 66% and 90% reduction in creep rupture lifetime respectively, compared to the as-received condition.

The investigation distinctly reveals that the extent of initial strain hardening and softening stemming from prior tensile deformation significantly influences the resultant creep deformation and rupture lifetime of Gr.91 steel. The study provides vital information of relevance to the understanding of material behavior under sequential tensile and creep loadings.

III.29

Welding of FeNiCo alloy to AISI 316L(N) Steel for Temperature Sensitive Magnetic Switch Application of DSRDM

Temperature sensitive magnetic switch (TSMS) is a safety feature in Diverse Safety Rod Drive Mechanism (DSRDM) of FBR. TSMS is made of soft magnetic material (NiFeCo alloy having Curie temperature of 625 ± 2°C), which operates as a sensor based on demagnetization occurring above Curie temperature. This material is under development in the tube form and stringent magnetic as well as mechanical properties and weldabilityof the alloy tube need to be ascertained. The TSMS application involves dissimilar welding between the NiFeCo alloy and AISI 316L(N)SS tube. A study has been taken-up for development of the NiFeCo alloy tubes and study of weldability of the alloy with 50 mm diameter, 2 mm thick AISI 316L(N)SS tube as it was not successful in earlier occasion.

The quality of the NiFeCo alloy tube is investigated by radiography (Fig. 1). Microstructure and hardness of the NiFeCo alloy is studied. Tensile properties are assessed at room temperature, 500 and 580°C. Creep tests are performed at 580°C at stress levels of 25 and 45 MPa. Dissimilar weld joints between NiFeCo alloy and AISI 316L (N) SS tubes are prepared.

Single phase austenitic microstructure with average grain size 2950 μm is observed in the NiFeCo alloy. Hardness of the alloy is measured as 138 ± 2. A typical engineering stress-strain plot for the alloy is shown in Fig.2. The tensile strength and ductility of the alloy at room and high temperature is higher than pure nickel, Table1 indicating solid solution strengthening of alloy. Creep test of the alloy, performed at 580°C indicates 51 and 1243 hours of rupture lives at applied stress level of 40 and 25 MPa respectively. Direct joint between the tubes is prepared by GTAW process with alloy 82 filler wire as shown in Fig. 3. The weld quality is confirmed through LP and radiography. Sound weld joint could be made first time from this tube join indicating improvement in quality of cast product compared that prepared to earlier. However, as distortion is noticed in the welded tube, residual stress is measured at 0, 90 and 180° interval in axial and hoop directions. It is observed that axial residual stress is tensile within the NiFeCo alloy side at 90 and 180° with reference to bend in the welded tube (Fig. 4). On the other hand, hoop stress is compressive in the NiFeCo alloy side and tensile in the AISI 316L (N) side. Further improvement in the quality of NiFeCo alloy is under progress. alloy tube and mechanical property determination of the weld joint is in progress.

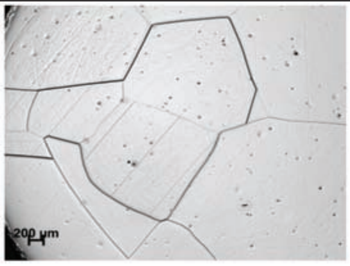

Fig. 1: Photomicrograph of NiFeCo alloy

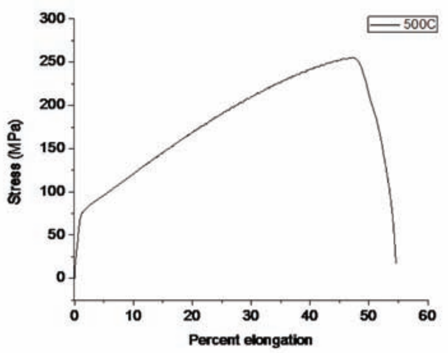

Fig. 2: Engg. stressvselongation plot for NiFeCo alloy at 500°C

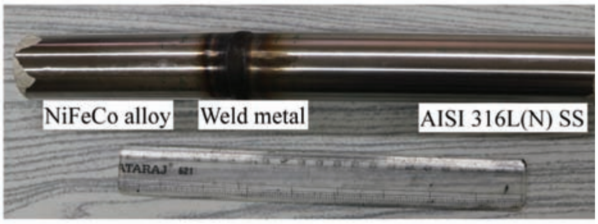

Fig. 3: Weld joint of NiFeCo alloy to AISI 316L(N) SS

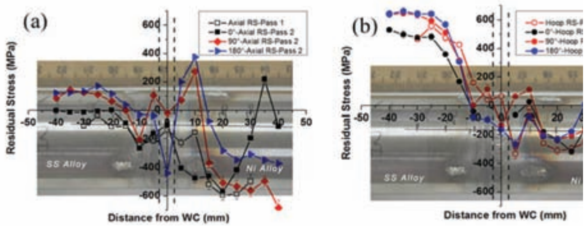

Fig. 4: Residual stress distributions in NiFeCo and AISI 316L(N) SS dissimilar weld joint in (a) axial and (b) hoop direction

Table 1: Tensile properties of NiFeCo alloy

Temp (°C)	YS (MPa)	UTS (MPa)	Ductility (%)
RT	132	319	33
500	72	238	49
580	52	152	33

III.30 Weldability assessment of AISI 316L(N) steel hybrid weld joint

Austenitic stainless steel of grade AISI 316L(N) is the major structural material for PFBR due to adequate high temperature mechanical properties, corrosion resistance and compatibility with sodium. Tungsten inert gas (TIG) and Shielded metal are (SMA) are the welding processes used for fabrication of nuclear components. Activated TIG (A-TIG) process, which uses small quantity of surface active flux, produces a weld joint having higher penetration in a single pass than in TIG and better mechanical properties than SMAW techniques. Combination of TIG with A-TIG techniques (hybrid process) can be useful for welding of thicker sections for higher productivity and to improve mechanical properties. A study has been undertaken to weld 10 mm thick AISI 316L(N)SS plates by combination of A-TIG and TIG processes with 316L filler wire and microstructure, mechanical properties of the weld joint is compared with that of A-TIG and TIG weld joints of AISI 316L(N) SS.

The microstructure of the weld metal (Fig. 1) reveals vermicular ferrite in austenite matrix and ferrite content in the weld is 8FN, which is permissible for this grade of steel to diminish the hot cracking susceptibility of the weld. Average hardness of hybrid weld metal is 190 VH0.5 as compared to 180, and 210 VH0.5 of TIG and A-TIG joint. Tensile strength and impact toughness of the hybrid weld metal (Table 1) is higher compared tothat of A-TIG joint and comparable to that of TIG weld joint of AISI 316L(N) SS. Fractographic study (Fig. 2) reveals ductile fracture. Oxygen content within the hybrid weld metal is low (200 ppm)which improves impact energy. The propensity for crack propagation within the weld metal is assessed by compact tension testing (Fig. 3) and it is observed that fracture toughness (J_{1C}) of the hybrid weld metal at room temperature is higher than TIG and A-TIG weld metal and the crack propagates preferably from TIG to A-TIG weld metal. Fracture toughness of TIG weld metal is comparatively higher at high temperature (550˚C) (Table 2).

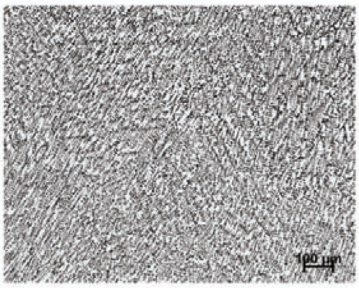

Fig. 1: Optical microstructure of TIG+A-TIG weld joint of AISI 316L(N) steel

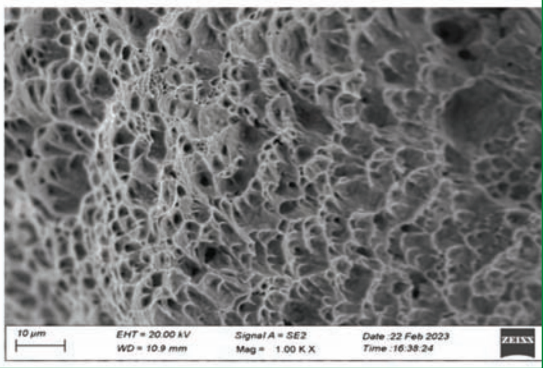

Fig. 2: Fractograph ofTIG+A-TIG weld joint after impact testing

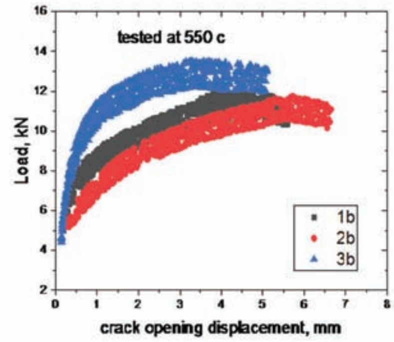

Fig. 3: Load-vs-crack opening displacement for different weld joints

Table 1: Tensile properties of the weld joints

	Y.S (Mpa)	UTS (Mpa)	Elongation (%)	Impact Energy (J)
TIG weld	400	600	30	155
A-TIG weld	325	545	37	140
TIG+A-TIG weld	360	575	32	150

Table 2: Fracture toughness of the weld joints

	J_{1C} at room temp (KJ/m^2)	J_{1C} at 550˚C (KJ/m^2)
TIG weld	300	170
A-TIG weld	395	165
TIG+A-WTIG weld	410	155

The study indicates that microstructure and mechanical properties of TIG+A-TIG hybrid weld joint of AISI 316L(N) SS meet PFBR specification. Successful implementation of this hybrid welding technique will be a novel approach for joining of thicker structural components of future FBR application. This will allow using multiple processes for the same weld joint.

III.31 Tribological Behaviour of Self-mated Alloy D9 Steel

Alloy D9 stainless steel (SS) is the material for the fuel clad, spacer wire and wrapper due to its good tensile, creep properties and void swelling resistance. The above-mentioned components come in contact with each other during the service or handling. The contact stress at the mating surface is generated due to various reasons such as flow-induced vibrations, self-weight, irradiation induced growth and fluctuating temperature, which causes differential thermal expansion etc. As a result, the material is subject to tribological degradation. This study focuses on understanding the tribological degradation mechanism in Alloy D9.

To generate the experimental data for the study, self-mated tribo-pairs of Alloy D9, in ball-on-disc form was used on a Tribometer. Experiments were conducted in a vacuum with a pressure of 6×10^{-6} mbar with a sliding velocity of 50mm/s over a total sliding distance of 500 m. To understand the effect of temperature and load on the tribological properties, experiments were carried out using loads 2N and 5N at temperatures-room temperature (RT, 23˚C), 200˚C, 500˚C, and 550˚C.

Figure 1 shows the variation of coefficient of friction (COF) with sliding distance at various temperatures for load of 2N. At room temperature, a stable COF with minimal variation is observed. Such behaviour is indicative of an abrasive wear mechanism. However, at elevated temperatures, variation in values of COF represents stick and slip motion. Such behaviour is associated with the adhesive wear mechanism. From Figure 1, it can be seen that coefficient friction is the lowest at the room temperature As the temperature is elevated from RT to 200ºC, a rise in COF was noticed which reduced at 500ºC and 550ºC. However, the COF values at 550ºC remained higher than that was obtained at RT. Similar pattern was noticed for a load of 5N. However, with raising the load from 2N to 5N, the COF increased for all test temperatures.

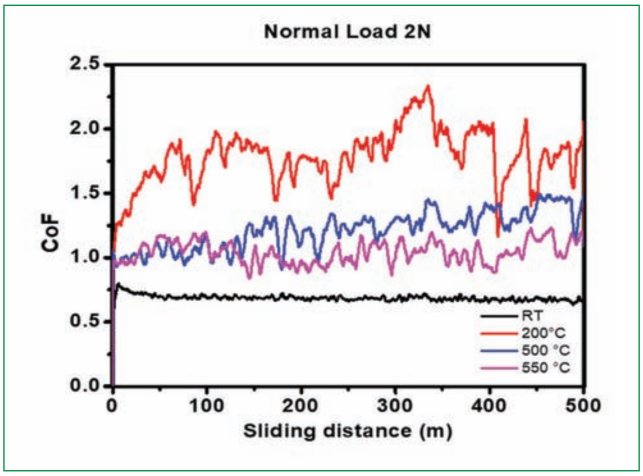

Fig. 1: Coefficient of Friction Vs. Sliding distance for a load of 2N

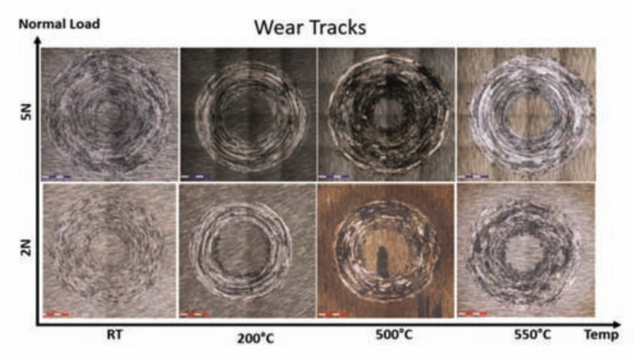

Fig. 2: Disc wear tracks at various temperatures

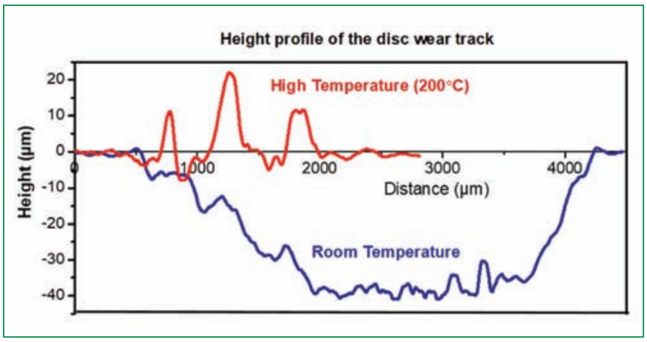

Fig. 3: Representative Wear track profiles

Substantial wear is evident within the tested domain, and the distinct characteristics of wear track signatures are depicted in Figure 2. The physical features of the disc wear tracks and wear of the ball suggest that increase in loading leads to more wear. At room temperature, the wear profile exhibits a broader width and deeper valleys without ridges, indicating the presence of an abrasive wear mechanism (Figure 3). In contrast, at elevated temperatures, the predominant adhesive mechanism leads to a reduction in wear, resulting in a narrower track width. Notably, the wear tracks at higher temperatures show the formation of small valleys with ridges. Alloy D9 pair demonstrates a lower COF and experiences severe wear at room temperature. Conversely, at 200ºC, there is an observed increase in COF and lower wear within the tested domain. The wear mechanism is predominantly adhesive at 500ºC and 550ºC.

III.32 Defect analysis of Neutron Irradiated Austenitic stainless Steels using XRD

Austenitic stainless steels namely 304 L(N), 316 L(N) and SS 316 were irradiated to 1.76 – 6.75 dpa in FBTR at 380-400˚C with peak neutron flux in the ranges of 1.0-1.7×10^{15} n/cm^2/s. Defect analysis of these neutron irradiated SS grades was carried out using Synchrotron X-Ray Diffraction (XRD) line profiles recorded at the beam line-12 of Indus-2, Raja Ramanna Centre for Advanced Technology (RRCAT), Indore

Synchrotron radiation energies used were 14.968 keV (wavelength ~0.82833 ˚A) and 17.185 keV (wavelength ~0.72146Å) in the angular range 20˚-50˚ and 18˚-45˚ respectively. Diffraction data were recorded using a MYTHEN detector in a step scan mode with a step size of 0.0029˚. Unirradiated sample was used as the reference and 'Si' standard sample was used for subtracting the instrumental broadening.

Fig. 1 shows the normalized X-ray diffraction profiles recorded for the neutron-irradiated SS 304 L(N), SS 316 L(N), and SS 316 samples. The prominent peaks were indexed to the fcc (face centred cubic) austenite phase (γ) and weak reflections to the bcc (body centred cubic) ferrite phase (α) of SS 304 L(N) and SS 316 L(N).

The individual peak profiles are fitted with the split Pseudo-Voigt function of the Fityk software (version-1.3.1) to determine the broadening in the reflections. Peak broadening was determined by the integral breadth method. Assuming microstrain is entirely contributed by dislocations, the contrast effect of dislocations on the XRD line profiles was utilised to determine the dislocation density using the modified Williamson-Hall method. Fig. 2 shows the dislocation density determined as a function of irradiation dose.

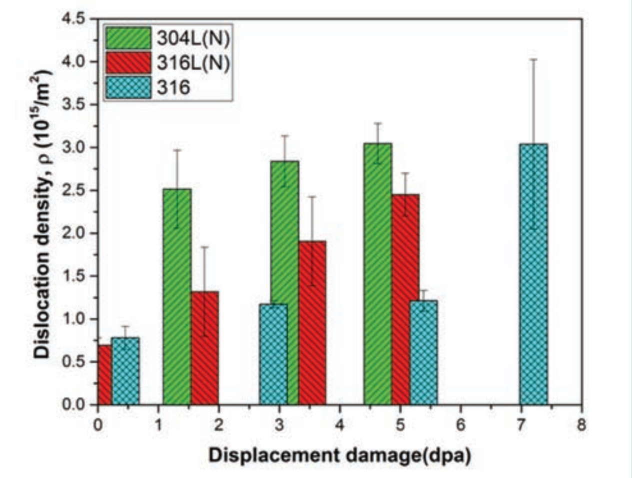

Fig. 2: Dislocation density estimated for neutron-irradiated (a) SS 304 L(N), (b) SS 316 L(N), and (c) SS 316 respectively.

The dislocation density is found to increase with displacement damage for all the three variants of austenitic stainless steels with SS304 L(N) showing the highest value at a given dpa level. The dislocation density tends to saturate beyond 2 dpa for SS 304 L(N) whereas for SS 316 L(N), a linear behaviour is exhibited up to the highest dpa. Fig. 3 shows the plot of yield strength as a function of the square root of dislocation density.

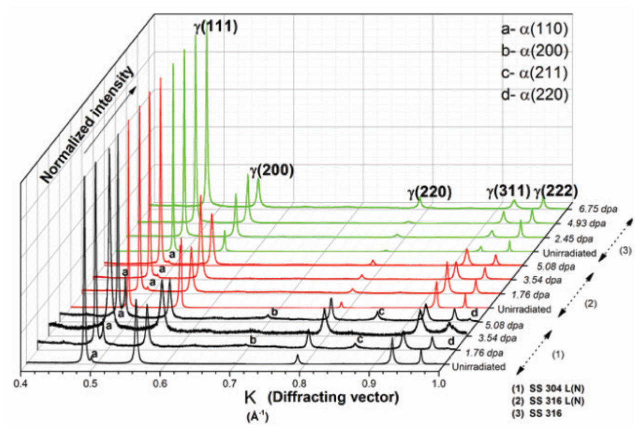

Fig. 1: X-ray diffraction profiles of neutron-irradiated (a) SS 304 L(N), (b) SS 316 L(N), and (c) SS 316 samples.

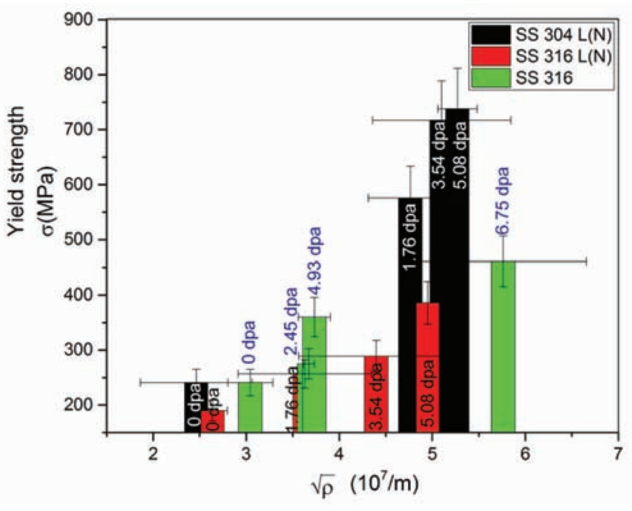

Fig. 3: Irradiation hardening as function of square root of dislocation density.

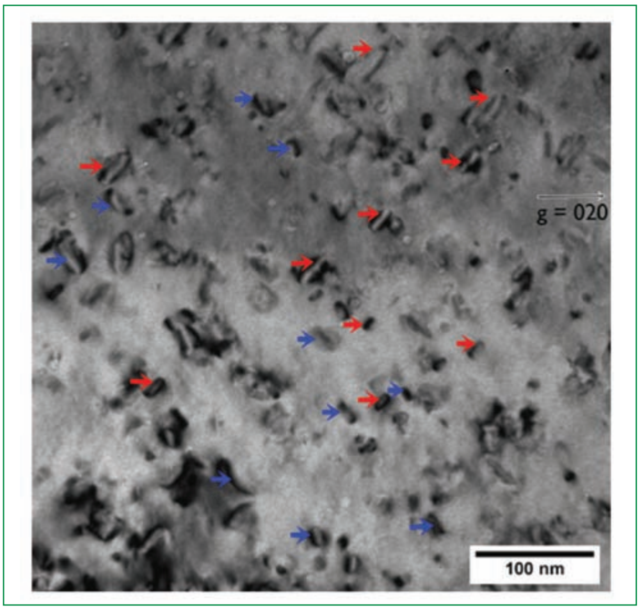

Fig. 4: TEM bright-field image of SS 316 (6.75 dpa) sample near [001] zone axis showing voids and two variants of faulted loops. Average loop diameter is 20.4 nm (standard deviation 5.3 nm) and the number density is 2×10^{22}/m^{3}.

In SS 304 L(N), there is a higher rate of hardening for 1.76 dpa and beyond this, the hardening effects tend to saturate. However, in the case of SS 316 L(N) and SS 316, there is a continuous increment in the irradiation hardening as a function of displacement damage. Intrinsic stacking fault probability (α_{sf}) has been calculated from the shifts in the position of the (111) and (222) reflections with respect to the peak position of the un-irradiated (reference) material using Balogh's method. Negative values α_{sf} in the material denotes the formation of extrinsic stacking faults due to irradiation. The increase in yield strength due to the interaction of moving dislocations with the existing defects has been correlated to the square root of the dislocation density (Fig. 3).

In SS 304 L(N), due to the low SFE, high number density of faulted dislocation loops produced at 1.76 dpa causes higher rate of hardening. Beyond this dpa the hardening effects tends to saturates. In SS 316 L(N) and SS 316, being high SFE materials, fewer defects are produced during irradiation. Hence there is a progressive increment in the yield strength without saturation effects.

TEM analysis indicated that Frank dislocation loops are the major irradiation-induced defects present in these materials (Fig. 4).

Apart from the increment in the dislocation density, a systematic rise in the phase fraction as a function of irradiation dose is seen in the case of both SS 304 L(N) and SS 316 L(N), as shown in Fig. 5 with SS304 L(N) exhibiting a greater propensity for the phase change. However, detectable amount of irradiation-induced ferrite is not observed in the case of SS 316.

Present study of XRD line profile analysis clearly corroborates the defect microstructure of the neutron irradiated austenitic stainless steels with the mechanical properties.

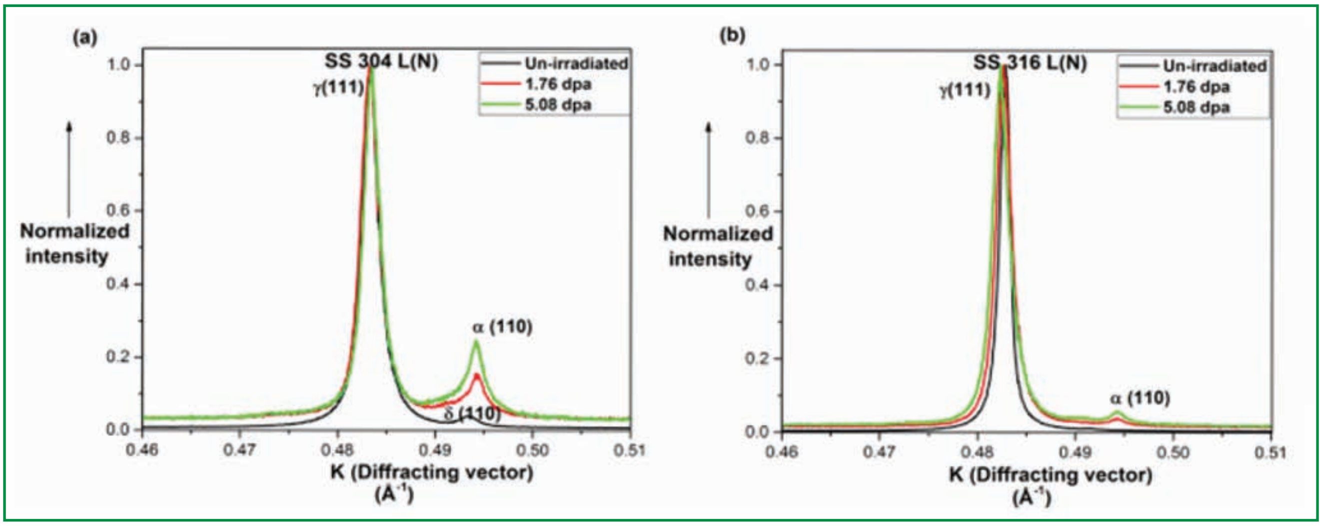

Fig. 5: Principal austenite and ferrite peaks for neutron irradiated (a) SS 304 L(N), and (b) SS 316 L(N). SS 304 L(N) showing the higher propensity for phase change.

III.33

Development of a Novel Method for Hardening Large Bearing Balls

Large rotating components are vital for heavy machinery used in various industries, including power generation. As example, rotating plugs for rotation and transfer of core subassemblies are a critical part of fast breeder reactors. Similarly, mining and earth moving industries regularly utilize equipment containing large rotating parts. Each of these applications depends on optimal performance and reliable performance of rolling elements, such as bearing balls.

Although the above applications are crucial for the progress of developing economies, the current approach to manufacturing is limited by fundamental factors. The limiting factor is the inadequate hardenability of the predominantly used bearing steel, AISI 52100. Bearing balls made of AISI 52100 steel can be hardened only to small depths of 10-15 mm. At higher depths, such bearing balls cannot meet service requirements of 55-60HRc hardness. This limitation forces Indian heavy industries to import bearing balls made of new materials for which adequate know-how is often unavailable.

With a view to develop an in digeneous solution to the manufacturing of these critical components, efforts were undertaken to develop a novel method for hardening large bearing balls made of AISI 52100. The method was developed keeping in view the metallurgical fundamentals needed for hardening, as well as the ease of adoption by Indian industries, including small and medium scale enterprises. Consequently, efforts were directed towards minimizing process complexity and eliminating the need for additional capital investment by the industry.

Through metallurgical analysis, it was established that the through-thickness hardening can only be achieved through a relatively severe quenching process involving use of a water bath. Such severe quenching treatments have rarely been applied to AISI 52100 steel due to its tendency for quench cracking. However, laboratory experiments, coupled with computer simulations revealed that quench-cracking could be avoided through careful design of the prior heat treatment and by control of the quenching process parameters.

A novel heat treatment, involving two stages of austenitization under specified heating rates was developed and validated using laboratory-specimens. This heat treatment was then adapted for full-size balls, and eventually was converted into a batch process for industrial applications. The hardened balls so produced were subjected to an extensive property evaluation process, including measurements of surface hardness and internal (through-thickness) hardness, wear resistance, fracture toughness, residual stress measurement, retention of hardness after exposure to service temperatures, and corrosion resistance. In all evaluated properties, the balls produced through the novel hardening method were superior to the balls hardened by conventional methods. Critically, the conventional method only yields a hardness of 55-60HRc up to a depth of 10-15 mm, whereas the novel hardening method yields a hardness of 55-60HRc up to a depth of 40mm.

The novel method for hardening large bearing balls has been assigned Indian Patent application number 202421000643 on 04 January 2024, titled 'A method for hardening a bearing ball'. Efforts are being made towards commercialization of this technology through technology transfer.

Conclusion:

A novel method for hardening large bearing balls made of AISI 52100 steel was developed at IGCAR. The method leads to production of bearing balls with superior properties relative to conventionally manufactured balls. correlations for future technology development. The method has been formalised through Indian Patent application number 202421000643.

III.34 Drop Time Measurement of Hydraulically Suspended Absorber Rod in Water

Hydraulically Suspended Absorber Rod (HSAR) is a passive reactor shut down device. It is raised to its operating position with the help of HSAR drive mechanism. After establishing the nominal mass flow rate through HSAR, the drive mechanism will be detached from the HSAR. HSAR will be suspended in its top position due to the drag forces generated by the flowing sodium. In case the coolant mass flow rate reduced below the predetermined value of the nominal mass flow rate, the HSAR will fall by gravity. At the end of free fall, HSAR is decelerated by a sodium dashpot inside the subassembly and brought it to rest. In case of SCRAM or Primary Sodium Pump (PSP) trip event, the flywheel provided in PSP slowly reduces the coolant flow through the core and increase the pump cost down time. The PSP flow halving time is 8s. Therefore, HSAR shutdown device will take minimum 8s to trigger in case of SCRAM or PSP trip. However, it is vital that the HSAR shutdown system should take minimum possible time to shutdown the reactor, once its activation mechanism is triggered. It is also mandatory for the design qualification to estimate the time taken by the HSAR to detach from its seat and deposited in the dashpot. Therefore, an experimental study has been carried out in water to estimate the drop time of HSAR. The results obtained from the experiment can be used to estimate the drop time of HSAR in reactor condition. Dynamic Pressure Sensors (DPS) with response time (<5μS) are used to detect the pressure variation in water due to the movement of the HSAR. Charged accelerometers are installed on the dashpot to detect the low frequency hitting sound of mobile HSAR with the dashpot. The schematic of the drop time measurement test setup is shown in Fig. 1. The initiation of the HSAR fall time T1 is taken from the indication of DPS (1), which is installed just below the top seating position of the HSAR. The completion of the HSAR fall time T2 is taken from the highest peak recorded by the accelerometer installed in the dashpot region. A typical plot of measurement is shown in Fig .2. This experiment was repeated more than 100 times to determine the drop time of HSAR with statistical estimation of measurement uncertainty. It is found that the average drop time of HSAR in flowing water with 99.7% confidence level is 1.5 ± 0.06 s.

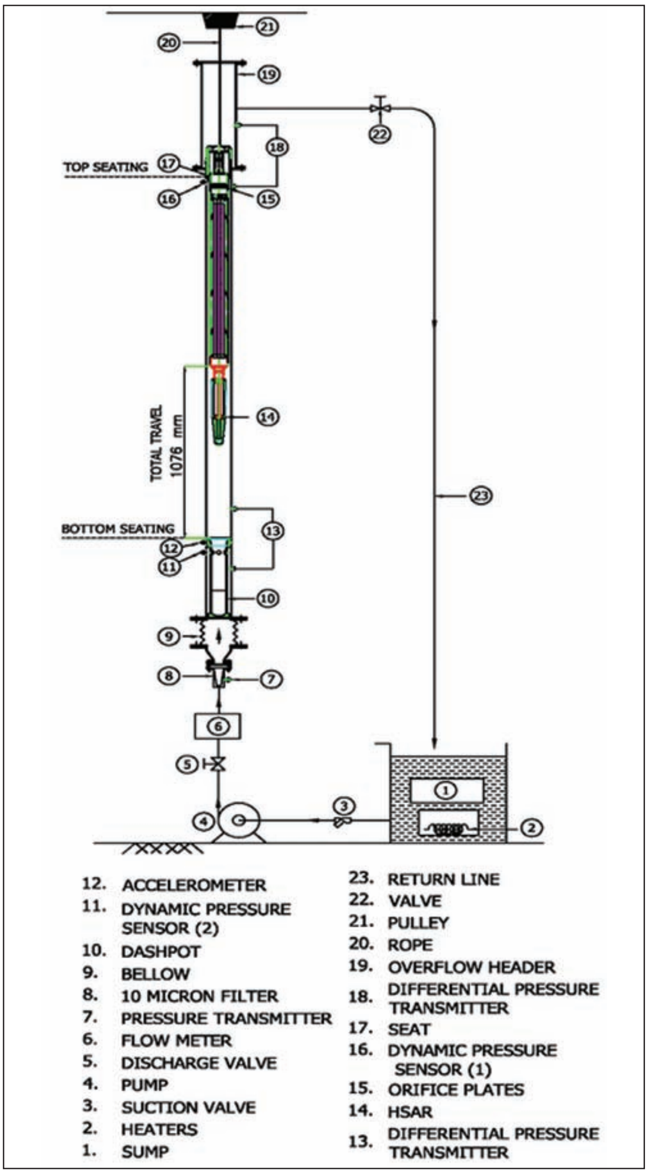

Fig. 1: Schematic of test setup

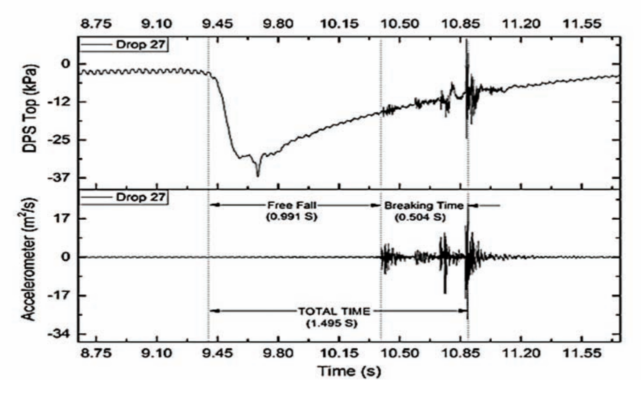

Fig. 2: Typical plot for HSAR drop in time domain

III.35 Design, Fabrication, Installation and Commissioning of Mini Mono-rail hoist for Injection Casting Operation

Injection casting is a well-established technique for producing fuel slugs (U-Zr) for fabrication of metallic fuel pins. Injection casting was chosen, as this method is suitable for remote operation and is capable of mass production with minimum radioactive waste generation in the glove box. Fuel slug of large length to diameter ratio (~64) can be cast with injection casting method.

Double walled water-cooled process chamber (vacuum chamber) with induction heater and mould heater assembly are housed inside the glove box to carry out the casting process under high purity inert atmosphere. Lifting mechanism was designed and installed adjacent to process chamber to lift the top chamber during loading of charge and for moving up/down the ram rod with quartz tube bundles during casting process (Fig. 1). Functioning of lifting mechanisms is crucial to continue the casting process in the event of mal-functioning of lifting mechanism by failure of electrical motor (or) mechanical components. Hence, for redundancy a mono-rail mini crane was designed with safe working load of 100 kg to perform the chamber movement/lifting and to assist in maintenance of process chambers. In addition, for fail safe operation, an additional ram rod drive mechanism was designed & installed on the chamber for moving ram rod during casting process.

Major challenge in design of mono rail crane is to size the system to accommodate inside the glove box & compactness for easy maintenance. Due to head room limitation, the hoist was made modular in construction for dismantling the crane components.

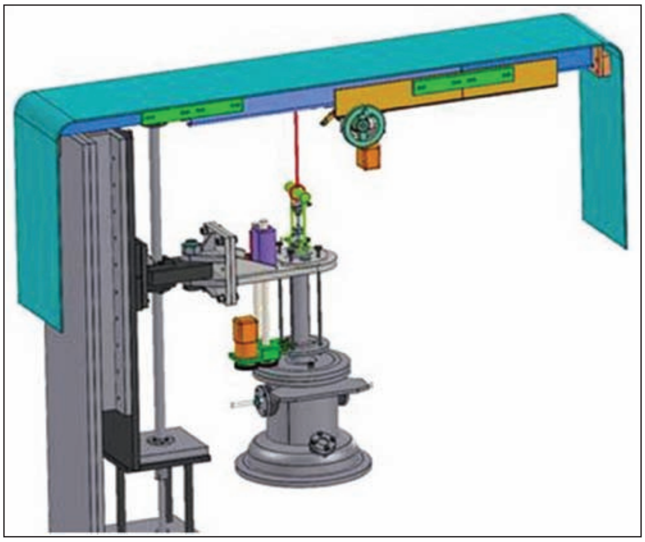

Fig. 1: Solid model of mono-rail & ram rod mechanism

Fig. 2: Mono Rail Mini crane installed inside the IC GB

Monorail crane supporting boom structure is constructed with ISA 80 x 80 x 6 mm for safe working load of 100 kg and they were assembled with linking brackets to form platform for long travel of trolley. Long travel length of the crane is 500 mm. Long travel trolley is designed to support the wire rope drum, worm & worm wheel drive for lifting top chamber using stepper motor. Rack and pinion gear assembly is mounted on the boom and connected to trolley for smooth movement of trolley with load (top chamber).Locking assembly mounted on the pinion shaft has locking latch with indexing plate to position trolley at desired location. Stopper assembly is mounted on boom structure to position the trolley with rope drum exactly at the center of process chamber. Stainless steel hook at the wire rope of diameter-5 mm is tested with load of 150 kg before installing in the crane (Fig. 2). Alignment of supports on both side of glove box is checked and then crane boom was installed along with trolley. Functionality check of both mini crane and ram rod drive mechanism was completed by lifting the top chamber assembly and operating the ram rod up & down.

III.36

Design, Fabrication and Testing of Wire Wrapping Machine for Sodium Bonded Metal Fuel Pins of Length- 932 mm

Setting up of lab scale facility for fabrication of sodium bonded metal fuel pins of length -932 mm for test sub-assembly irradiation in Fast Breeder Test Reactors is under progress. Metal fuel pins after fabrication and qualification are to be wrapped helically with spacer wire. The wrapper wire provides inter-elemental gap for coolant flow as well as facilitates proper mixing of the coolant with nearby sub-channels for better heat extraction inside the sub-assembly.

In the wire wrapping process, the bead end of the wire is entangled inside a groove on the bottom end plug, subsequently wrapped helically by simultaneous rotation of the pin and forward movement of the wire under a tension at 6 kg(f). Once the wire reaches the top end plug, it is welded with the top end plug. The wire may lead to failure if fusion welding is done under tension of the wire, as the molten pool does not have sufficient strength to endure the tension. The tension on the wire is restrained before welding by crimping it with the plug. The wire beyond the crimping point is thus relaxed. Crimping is done by placing the wire inside a groove provided on the top end plug and by applying sufficient force by a motorised tool to deform the plug such that it holds the wire firmly and limits the tension on the wire .

After crimping, the wire is welded with the top end plug by Tungsten Inert Gas (TIG) spot welding few millimeter away from the crimping point. After welding, the extra length of the wire is trimmed. In this process, a proper orientation between the bottom end plug groove and the top end plug groove is required so that after wrapping, the other end of the wire ends up in perfect alignment with the top end plug groove for crimping. The orientation between the bottom and top end plugs is ensured during top end plug welding during fuel pin fabrication (Fig. 1).

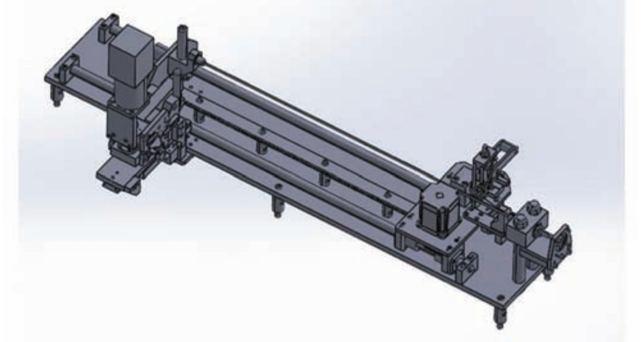

Fig. 1: Wire wrapping Equipment model

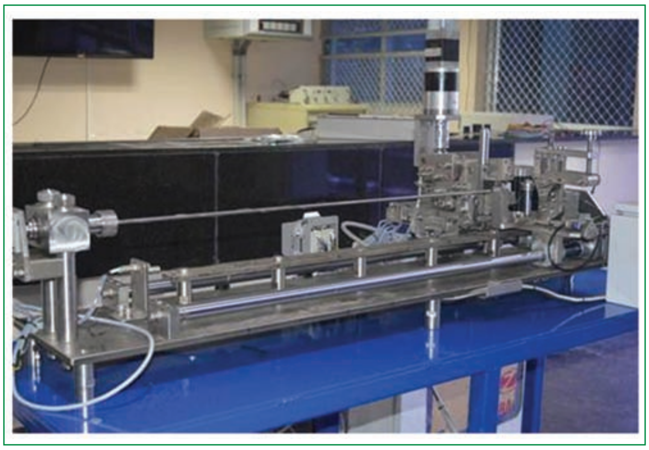

Fig. 2: Installed wire wrapping equipment

Maintaining the orientation during top end plug welding becomes critical, as mis-orientation of the top end plug by few degrees with respect to bottom end plug causes rejection of the fuel pin.

Wire wrapping equipment was designed for wrapping SS wire of dia-0.95 mm over sodium bonded metal fuel pin of length -932 mm.

It consists of fuel pin holder using manually operated chuck with stepper motor on left side (drive end) and spring loaded collet on right side (non drive end). Wire tensioning device is designed to apply tension of 8 kg(f) on spacer wire. The spacer wire is inserted inside the groove on rollers surface and pulling/tension load was applied by tightening the spring connected to top rollers. Tension on the wire is continuously measured by using a load cell. Linear motion drive for carriage assembly for guiding the wire over fuel pin surface during wrapping is achieved by using rack and pinion with motor assembly. Crimping assembly has hinged lever jaw with crimping tool operated with geared motor to generate the load for local deformation of the end plug groove with spacer wire after positioning manually. Entire operation was carried under manual assistance and end limits were controlled with proximity switches (Fig. 2).

During testing functionality of the equipment, the wire pitch of 90 mm is arrived by optimizing the rotary speed of fuel pin and linear speed of wire wrapping carriage assembly. Crimping load for deformation of top surface of the groove is arrived by optimizing the torque generated by the motor.

Back to
Main

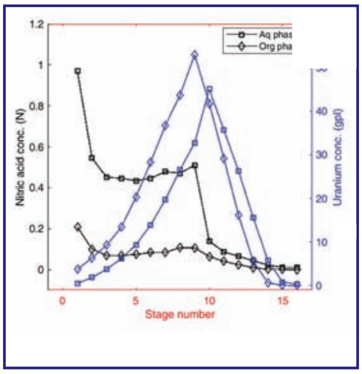

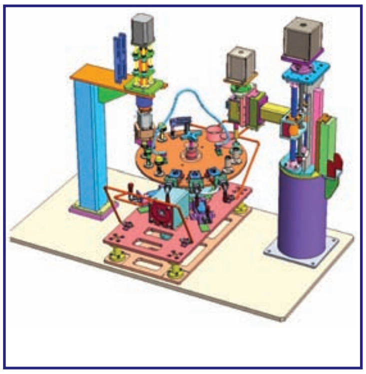

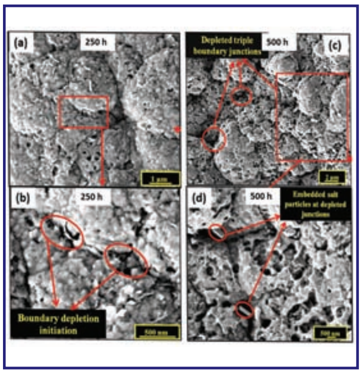

CHAPTER
IV

Fuel Cycle

IV.01 Performance Analysis of International Benchmarks on MOX Fuel Pins as a Part of IAEA CRP

IAEA has initiated a Co-ordinated Research Project (CRP) on "Fuel Materials for Fast Reactors (FMFR)" with different member states to carry out fuel performance analysis of various international benchmarks on MOX fuel pins and compare the results of various codes. Towards this, fuel pin performance analysis of (1) Phenix MOX (SANTANEY), (2) MOX FFTF (FO2) & (3) MOX –SUPERFACT pins were carried out using in-house fuel performance code (CAMOX) and the salient results are discussed below.

(1) SANTANEY MOX Fuel pin was irradiated in Phenix reactor up to a peak dose ~ 74 dpa. The peak Linear Heat Rating (LHR) was 585 W/cm and the active core length was 850 mm. The in-house analysis results indicate that the maximum fuel centerline temperature (~2623°C) occurs at End of Life (EOL) due to the maximum operating LHR and also due to the absence of Joint Oxide Gain (JOG) modelling in CAMOX. The fuel and clad temperatures at the Peak Power Location (PPL) are shown in Fig. 1. The radial gap between fuel and clad was closed near to the middle of life. The fission gas release is estimated as 72.4% and fission gas pressure is estimated to be 2.56 MPa.

(2) FO-2 MOX Fuel pin was irradiated in Fast Flux Test Facility (FFTF) reactor up to a burn-up of ~ 6 at%. The peak LHR was 425 W/cm and the fuel column height was 914 mm. The in-house analysis results indicate that the fuel centerline temperature at Beginning of Life (BOL) is 2332°C and at EOL, it has reached 2207°C. The radial temperature distributions in the fuel pin (at 401 mm) at BOL & EOL are shown in Fig. 2. The decrease in the fuel centerline temperature at EOL is because LHR itself is less when compared to BOL, even though the temperature drop in the gap is increased due to the fission gas dilution. The fission gas release reaches a maximum of 78.5% and the fission gas pressure is estimated to be 2.38 MPa at EOL.

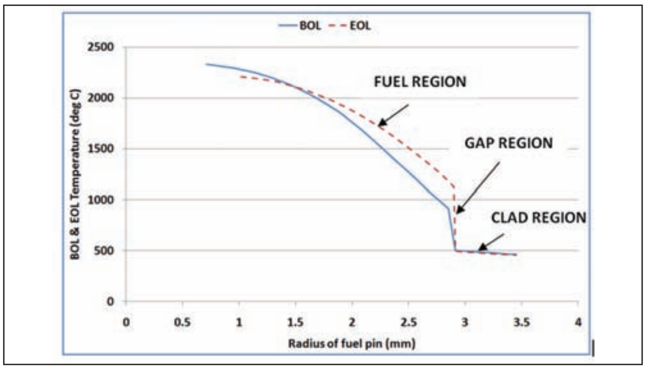

Fig. 2: BOL & EOL temperature distribution at 401 mm axial location

(3) SUPERFACT MOX Fuel pin was irradiated in Phenix reactor up to a burn-up of ~ 6.4 at% and a peak dose of ~ 52 dpa. The peak LHR was 413 W/cm at BOL and the active core length was 850 mm. The in-house analysis results indicate that the maximum fuel centerline temperature (~2459°C) occurs at BOL due to the maximum operating LHR and then decreases to ~ 1970°C at EOL as LHR is decreased. Central hole diameter started forming at BOL and reached 0.696 mm at the end. The radial gap was closed near to the end of life. The fission gas release is estimated as 52.4% and fission gas pressure is estimated to be 1.54 MPa.

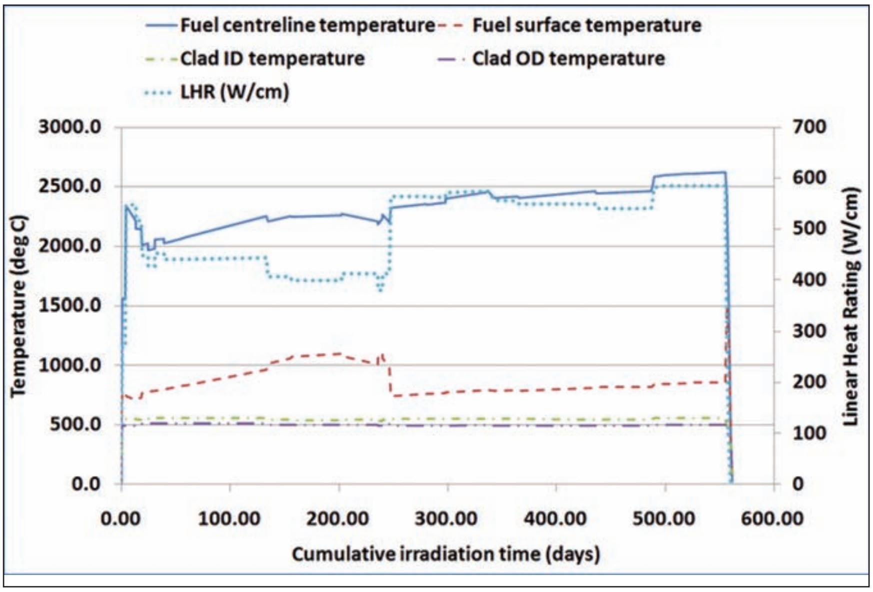

Fig. 1: Fuel and clad temperature & LHR variation with irradiation time at PPL

The results of all the benchmark analysis reasonably matched with the PIE data and with the results of other fuel performance codes. This exercise has helped in identifying the areas/ models, which need to be further improved / fine tuned in CAMOX code. In addition, this exercise has increased in-house capability in fuel performance prediction for MOX fuel pins.

IV.02 Distribution Behaviour of Uranyl Ions in Presence of Di-butyl Phosphate in PUREX Stream

During the reprocessing of spent nuclear fuel from fast reactor, the solvent (1.1 M TBP/n-DD) comes in contact with highly ionizing radiation and nitric acid leading to the radiolytic and hydrolytic degradation of the solvent. Di-butyl phosphate (HDBP), the major degradation product of TBP being complexing in nature, shows high affinity for metal ions. Hence, during the recovery of metal ions from organic phase, the presence of HDBP along with TBP/n-DD can alter the distribution behaviour of the actinides. In this context, the distribution behaviour of U (VI) as a representative of the actinides in TBP/n-DD solvent was investigated in the presence and absence of HDBP.

The variation in the distribution ratio for U(VI) in 1.1 M TBP/n-DD in presence and absence of HDBP (0.014 M) as a function of equilibrium nitric acid concentration in aqueous phase is plotted in Figure 1.The variation in distribution ratio of U (VI) in 1.1 M TBP / n-DD containing HDBP (0.5 to 3 g.L-1)as a function of equilibrium aqueous.

Phase acidity (0.01 to 0.5 M HNO_3) is shown in Figure 2 For the 1.1 M solution of TBP in n-DD, the D value increases with aqueous phase acidity. A similar trend was observed for the TBP/n-DD containing HDBP but with increased D value at all equilibrium acidities. This could be due to the synergic participation of HDBP in the extraction of U(VI) by 1.1 M TBP/n-DD as shown in equation 1.

$$\overline{HDBP} + \overline{TBP} + UO_{2\ aq}^{2+} + 2NO_3^- \Leftrightarrow \overline{UO_2(NO_3^-)_2(TBP)_x(HDBP)_y}\ \mathrm{org} \qquad (1)$$

Similarly, from Fig. 2 it could be seen that, the distribution ratio of U(VI) increases with increase in HDBP content in TBP/n-DD as well as aqueous phase acidity.

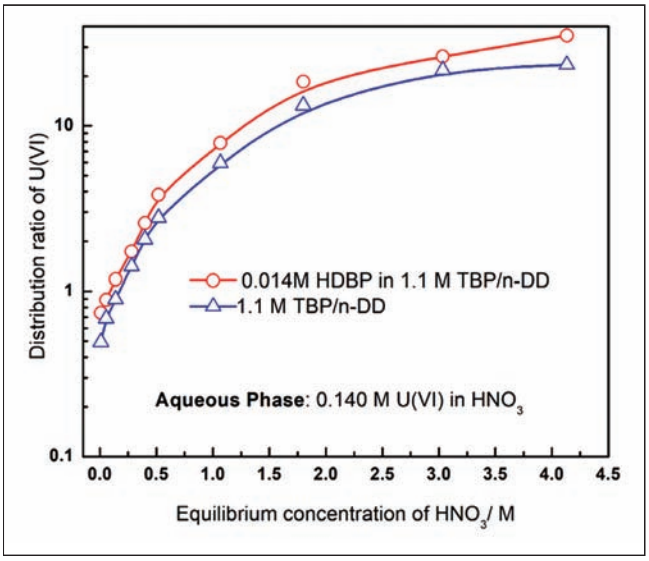

Fig. 1: Distribution behaviour of U(VI) in TBP/n-DD in presence and absence of HDBP w.r.to equilibrium aqueous phase acidity

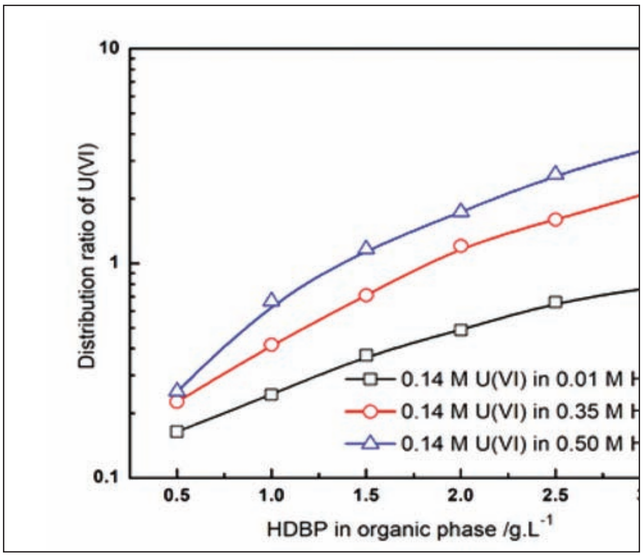

Fig. 2: Distribution behaviour of U (VI) in TBP/n-DD with different HDBP content at different equilibrium aqueous phase acidities

IV.03 Mass Transfer Performance of 16-stage Annular Centrifugal Extractor during Extraction and Stripping of Uranium

Annular centrifugal extractors (ACE) are widely used in the fast-breeder nuclear reprocessing industries. The main advantages of ACEs are a) low residence time, which reduces the radiolytic degradation of solvent, b) compact size (critically safe geometry), and c) high throughput, etc. ACE bowls of 30mm diameter were under operation for more than two decades in the CORAL facility. Also,ACE bowls (40mm diameter) were installed in the DFRP to separate the U and Pu from FBTR and PFBR spent fuels. Extraction and stripping experiments are conducted with low uranium concentration feed to understand the performance of the multistage ACE. In this work, the above experiments were performed in the 16 stages of the ACE (25 mm dia bowl) setup (Fig. 1).

During the extraction experiment, 30% TBP in n-Dodecane pre-equilibrated with 3N nitric acid is used as an organic phase. One gram per liter of Uranium in 4.5 N nitric acid (feed), 6N nitric acid (high acid scrub), and 3N nitric acid (low scrub acid) are used as an aqueous phase. During the stripping experiment, 30% TBP in n-Dodecane loaded with uranium is used as an organic phase. Dual strip is provided with nitric acid of which, 4N acid is used as srtip1 and 0.01N acid is used as strip2. The extraction experiment was conducted for two and a half hours and stage samples (both aqueous and organic) were collected at the end of the experiment. Similarly, the stripping experiment was conducted around 10.5 hrs and stage samples (both aqueous and organic) were collected at the end of the experiment. Uranium and acidity concentrations in the above samples were measured.

From the extraction stage profile it was found that, three counter-current stages are enough to complete the uranium extraction for the given operating condition. During the stripping experiment, 1 gpl U loaded 30% TBP is used as an organic phase. The stage profile shows the maximum U concentration in the aqueous phase and organic phases are ~ 45 and 53 gpl respectively. From the results, it is concluded the ACE setup has not reached the steady stage condition even after 10.5 hours of operation. It may be due to the back extraction of U and stripping inside the setup due to dual-acid stripping conditions and the availability of free TBP. Theoretical calculation shows that about 24 hours are required to reach steady state for this stripping operation.

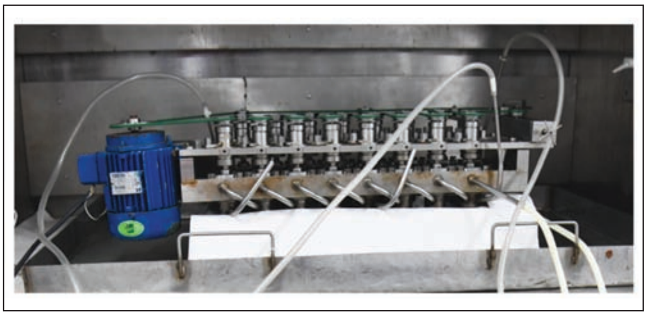

Fig. 1: Photographic view of 16 stages 25 mm ACE bank inside fume hood

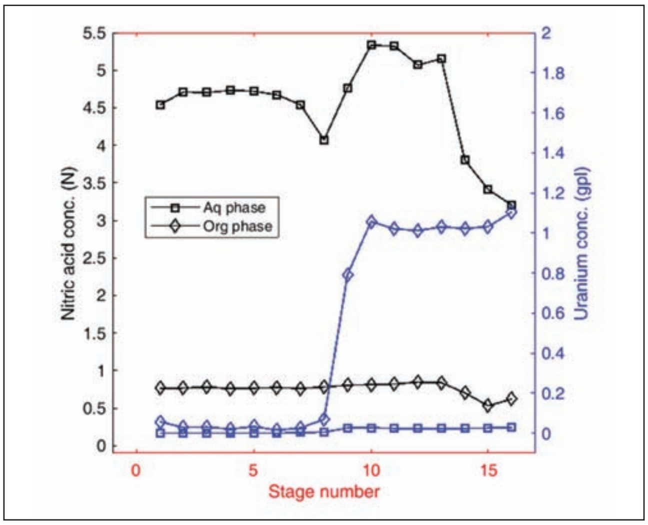

Fig. 2: U and acid con. in the aqueous and organic phases with respect to stage numbers during the extraction experiment

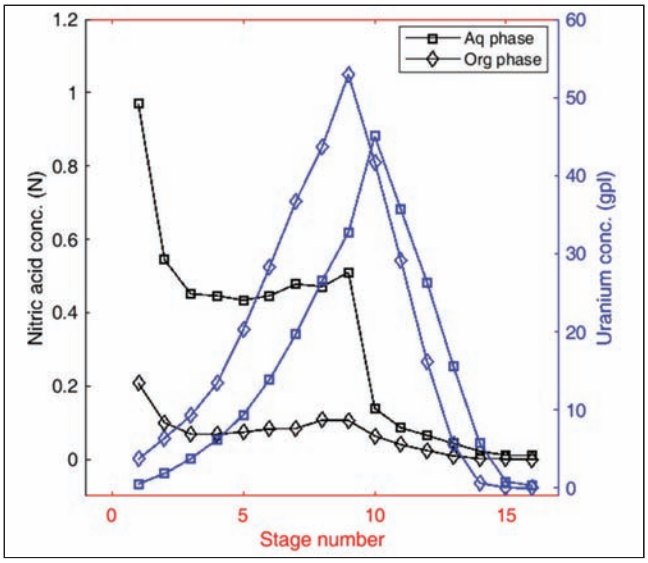

Fig. 3: U and acid conc. in the aqueous and organic phases with respect to stage numbers during the stripping experiment

IV.04 Machining Learning Model for the Prediction of Distribution Coefficient of U(VI) Extraction in 1.1M TBP

The solvent extraction operation is one of the important unit operations in nuclear fuel reprocessing. Distribution coefficient of the solute of our interest,defined as the concentration of solute in organic phase to the aqueous phase at equilibrium, is an important parameter in the design of the solvent extraction flow sheet. Computer simulation is often employed in the design and optimization of solvent extraction flow sheet.

In this, the stage concentration profile of the solute is calculated by solving the multistage mass balance equation coupled with mass transfer of the solute between the aqueous and organic phases. The mass transfer in each stage is governed by the distribution coefficient of solutes. Therefore distribution coefficient is essential for the accurate simulation of solvent extraction flow sheet. During simulation,this is estimated using distribution coefficient model. The models were often developed based on the first principles. The first principle based models are computationally more expensive and slower. Hence empirical models are used which best fit the experimental data over the desired concentration range and takes less computational time in flow sheet simulation.

In the present work machine learning methods were employed to fit the distribution coefficient of U(VI) and HNO_3 in 1.1M Tri-n-Butyl Phosphate (TBP) to Artificial Neural Network (ANN) model. ANN model was constructed with 2 input and 2 output nodes. The typical neural network with 2 hidden layer is shown in Fig. 1. The number of neurons in the 1st hidden layer is varied from 5,7,10 and 2nd hidden layer is 3, 5 and 7. The learning rate is fixed at 0.001 for all the runs. The inputs are molar concentration of HNO_3 and U(VI). The outputs are the distribution coefficient of HNO_3 and U(VI). The input data for training the ANN is generated from our in-house code SEESPEC which is derived from the first principles based on thermodynamic model. Totally 10,000 input data were generated for various HNO_3 and U(VI) concentrations. Off these, 80% of the data were used for training the model and the rest is used for validation. The neural network model available in the pytorch module in the PYTHON programming language was used. The weightages in the neural network model were estimated by minimizing the mean squared error using Adam optimization routine available in pytorch library. The neural networks with 10 and 7 neurons in the 1st and 2nd hidden layer gave the lowest error between the input and output data. The Root Mean Square Deviation (RMSD) of validation data set for the estimation of distribution coefficient of HNO_3 and U(VI) is 0.8 and 1.64% respectively. The comparison between the input and output data is shown in Fig. 2. The ANN model with 2 hidden layers gave good accuracy for the prediction of distribution coefficients as shown in Fig. 2.

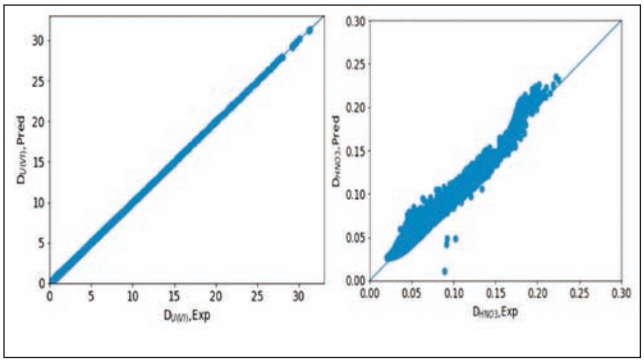

Fig 2: The comparison between input and predicted distribution coefficient a) HNO_3 b) U(VI)

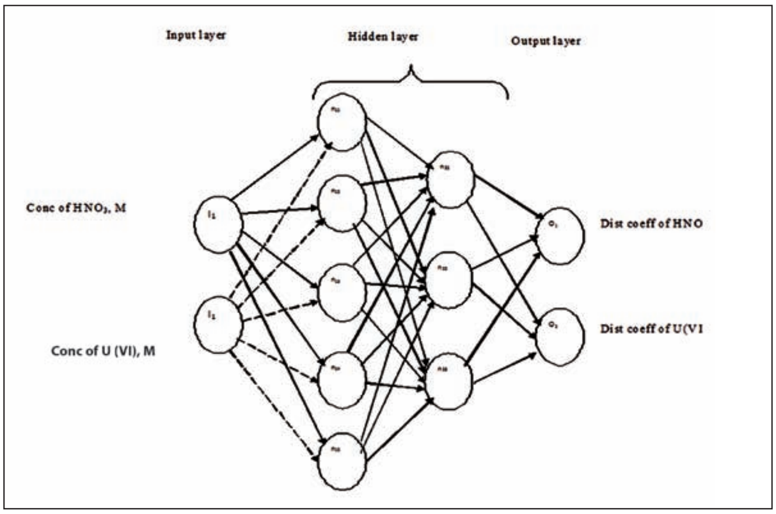

Fig 1: The typical neural network with 2 input , 2 output layers and 2 hidden layers

IV.05 Experimental investigation of Axial Mixing in Taylor Couette Solvent Extraction Contactor

The solvent extraction in nuclear fuel reprocessing is carried out in liquid-liquid contactors. They are broadly classified in two categories such as stage wise contactor and differential continuous contactors. In nuclear fuel reprocessing where high mass transfer stages are required, differential contactors such as pulsed column are mostly preferred due to its compact foot print. However in fast reactor fuel reprocessing stage wise equipment such as centrifugal contactor was used due to its low liquid holdup and low residence time.Taylor Couette (TC) contactor, though being a differential contactor, offers high mass transfer efficiency with low liquid holdup. Hence TC contactors have application potential in fast reactor fuel reprocessing. In TC contactors, liquid-liquid contact takes place in the annulus formed between the two concentric cylinders where Taylor vortices are formed when the rotational speed of the inner cylinder reaches beyond the critical value. These vortices enhance mass transfer and minimize the axial mixing. TC contactor with 25 cm mixing length and 2 cm annular gap between the stationary outer cylinder and rotating inner cylinder was fabricated in SS 304L.

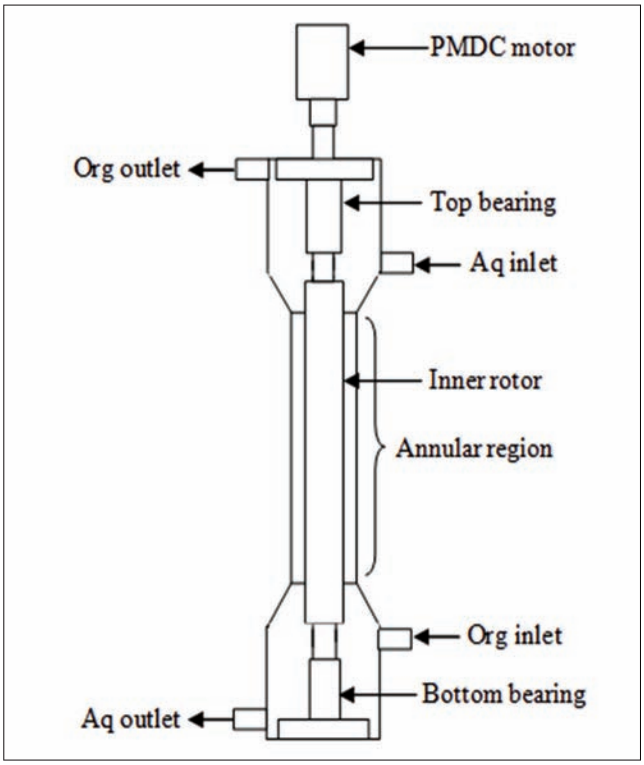

Fig. 1: The schematic of Taylor Couette contactor

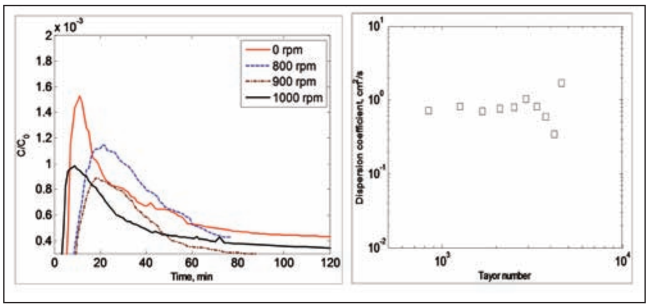

Fig. 2: a) The exit concentration measured over time for various rotational speeds and b) The dispersion coefficient as a function of Taylor number (Ta)

The schematic of TC contactor is shown in Fig. 1. The enlarged top and bottom portions are settlers which collects organic and aqueous phase respectively. The contact between the aqueous and organic phase occurs in the middle annular portion formed between the two concentric cylinders. The inner rotor is connected to the PMDC motor at the top. The rotational speed of the rotor is controlled by the speed controller. The inner rotor is supported by top and bottom bearing.

The aqueous and organic phase enters from top and bottom respectively. The single phase axial mixing in the contactor was measured by Residence Time Distribution (RTD) studies using an online fiber optic method. In all the experimental runs, $KMnO_4$ solution was used as the tracer. The tracer was injected at the aqueous phase inlet and the concentration was measured in the aqueous phase outlet. The concentration in the aqueous phase outlet was measured for every 2 minutes using online fiber optic method as shown in Fig. 2a. Experiments were performed for various rotational speeds (0 to 1100 rpm) and fixed aqueous phase flow rate of 15 ml/min. From the RTD studies,dispersion number was estimated as a function of rotational speed . The estimated dispersion number is plotted as a function of Taylor number(Ta) in Fig. 2b. From Fig. 2b , the dispersion number starts decreases after crossing the critical Ta where tayor vortices starts forming and decrease the axial mixing. Further increase in rotational speed the dispersion increases as shown in Fig. 2b. This may be due to the disappearance of Taylor vortices and transition of flow regime to turbulent Taylor vortices regime. The estimated dispersion number will be useful for the design and scale up of TC contactor.

IV.06 Synthesis and Evaluation of Diglycolamic Acids for the Mutual Separation of Lanthanides and Actinides from Nitric Acid Medium

The separation of lanthanides from actinides is essential for the effective transmutation of the actinides in advanced facilities like fast reactor and accelerated driven subcritical system. In this context, the digly colamic acid (HDRDGA) based extractants such as *N*, *N*-dihexyl diglycolamic acid (HDHDGA), *N*,*N*-dioctyl diglycolamic acid (HDODGA), *N*,*N*-didecyl diglycolamic acid (HD^{2}DGA) and *N*,*N*-didodecyl diglycolamic acid (HD^{3}DGA) were synthesized and studied for the mutual separation of trivalent actinides and lanthanides from dilute nitric acid media. The general structure of diglycolamic acid is shown in Fig. 1. Since these diglycolamic acids are strongly polar, and not soluble in traditional diluent (*n*-dodecane), isodecyl alcohol (IDA) was added to the solvent phase as phase modifier. Since HDHDGA and HD^{3}DGA were sparingly soluble even in the presence of 30% (v/v) IDA in *n*-dodecane, the solvent extraction studies like the extraction behaviour of Eu(III) and Am(III) was studied only in a solution of HDODGA or HD^{2}DGA present in 30% (v/v) IDA/*n*-dodecane. The cation-exchange mechanism of extraction and the stoichiometry of trivalent f-ion to these diglycolamic acids were elucidated from the slope analysis of the extraction data. Since the stoichiometry of metal to ligand complex in organic phase was unusually varying from 1:3 to 1:6 depending upon the Nd(III) loading in the organic phase, the reverse micellar aggregation behaviour and the coordination chemistry of Nd(III) in organic phase were probed by dynamic light scattering and visible spectroscopy, respectively. The results revealed that three molecules of anionic DRDGA$^-$ were coordinated to Nd(III) in the inner-sphere at lower metal concentrations, and also three more neutral molecules of HDRDGA co-ordinate in the outer-sphere at higher metal concentrations as shown in Fig. 2. Coordination of Nd(III) with HDRDGA induced significant changes in the hypersensitive band of UV-visible spectrum of Nd(III) observed at 580-610 nm. All the absorption bands of Nd(III) were shifted to lower wavelength region due to inner-sphere coordination of anionic DRDGA$^-$ species with Nd(III). The studies clearly indicated that good separation factor can be achieved with the use of these ligands. Based on the extraction, aggregation, and spectroscopic studies, it can be concluded that HDODGA and HD^{2}DGA ligands are promising candidates for the mutual separation of lanthanides and actinides from dilute nitric acid solution.

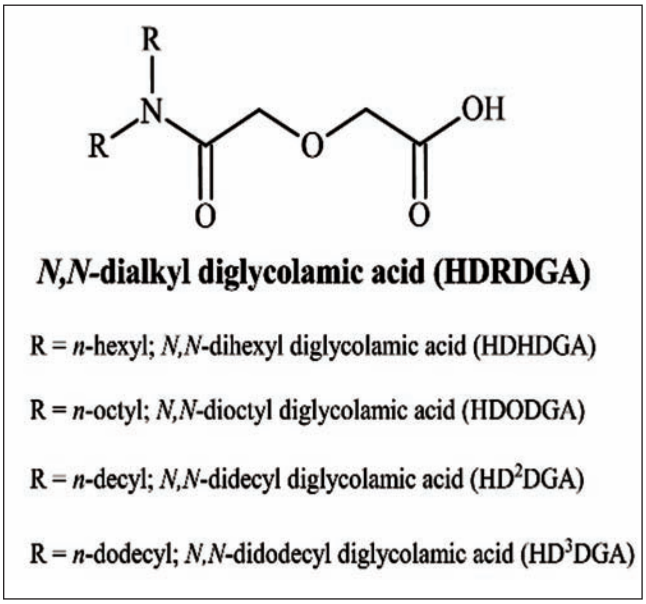

Fig. 1: The general structure of diglycolamic acid

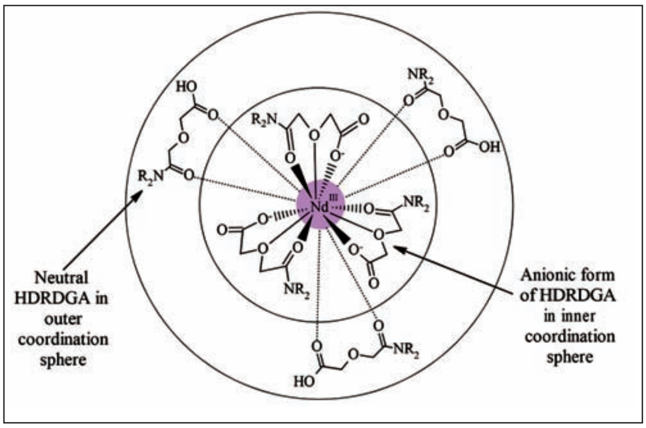

Fig. 2: Schematic illustration of Nd(DRDGA)$_3$.(HDRDGA)$_3$ complex in the organic phase.

IV.07 The Effect of Catalyst Support on the Reduction of U(VI) to U(IV)

In PUREX process, uranous nitrate has been employed for partitioning of U(VI) and Pu(IV). At present, the U(IV) is being generated electrochemically, which has the limitations of poor kinetics, less efficiency (50-60%) and frequent maintenance of the electrodes. Therefore, there is a need to develop suitable alternate methods for the preparation of uranous nitrate. In our laboratory, we are working on the development of catalytic methods for the production of uranous nitrate. Various types of platinum-based catalyst material was synthesized in-house and were evaluated for the reduction of U(VI). Two methods are employed for the reduction of U(VI), viz, by employing H_2 and N_2H_4 as reducing agents. The platinum impregnated catalyst material was synthesized by impregnating H_2PtCl_6 on various types of support materials like SiO_2, Al_2O_3, CeO_2, C (activated carbon), ZrO_2, SBA-15, TiO_2. After impregnation, the catalyst material was calcined in air followed by reduction in flowing 8% H_2/Ar gas mixture. In all the catalyst materials, the amount of platinum loaded was estimated to be approximately 1%. After the synthesis, the catalysts were evaluated for U(VI) reduction in nitric acid medium. All the experiments were carried out in a stainless steel autoclave. The experimental conditions employed for U(VI) reduction in each method are shown in Table 1 . The effect of support material on the reduction of U(VI) is shown in Fig. 1.

The percentage (%) of U(VI) reduced was calculated at 6 min in H_2 method and 15 min in N_2H_4 method. It can be seen from Fig. 1 that among all the catalysts, Pt/C gave near 100% conversion at faster rate in both the methods. The higher catalytic activity of Pt/C could be due to the high surface area of activated carbon employed in the present study. These studies indicates Pt/C can be employed as a potential catalyst candidate over other tested catalyst for the reduction of U(VI) employing both H_2 as well as N_2H_4 method.

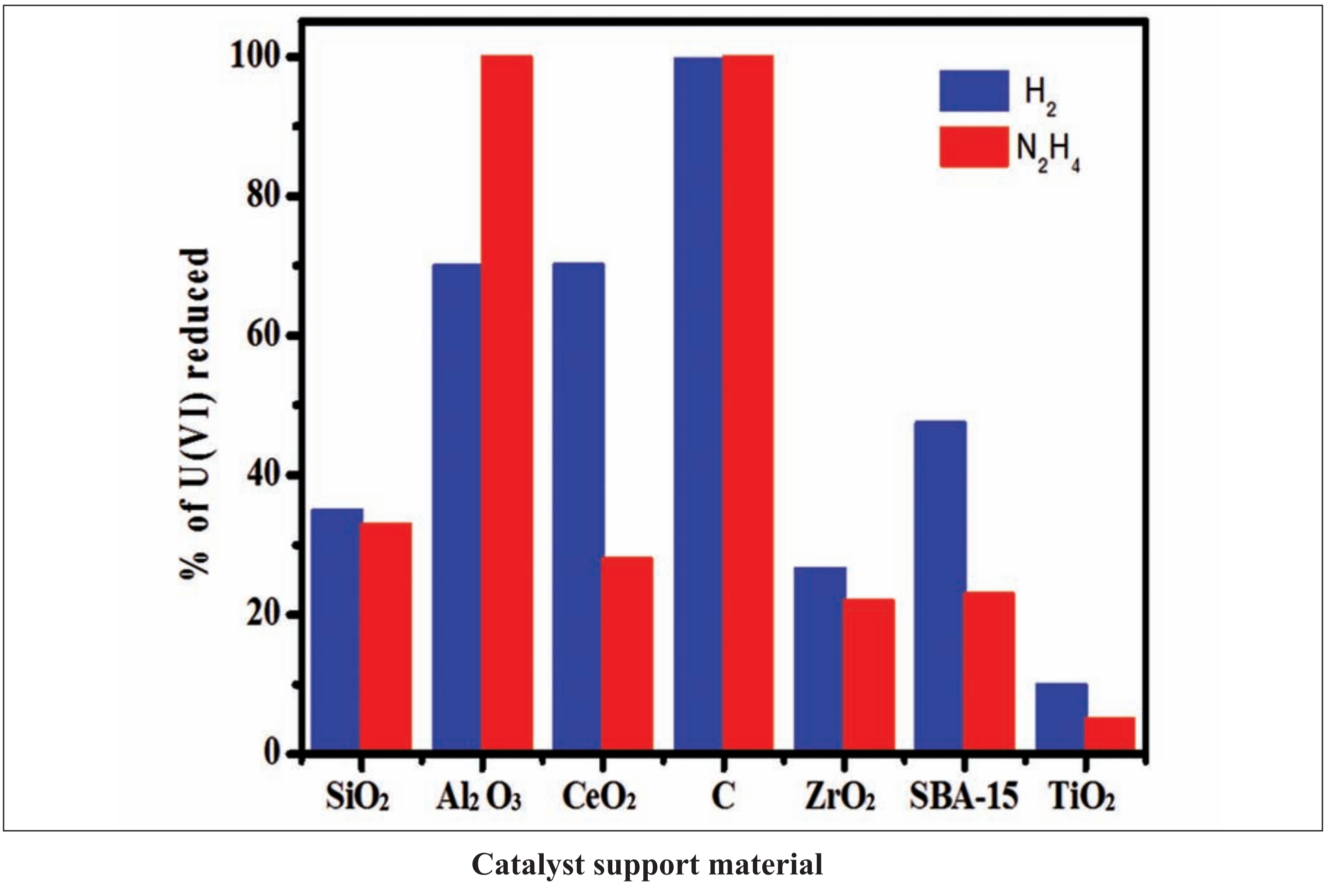

Fig. 1: Catalytic reduction of U(VI) over Platinum based catalyst material

IV.08 Management of Spent Solvent Treatment and Actinide Recovery in Fast Reactor Fuel Reprocessing

The recovery of nuclear materials from the Pu rich mixed carbide spent fuel discharged from FBTR is carried out in CORAL facility by deploying the modified Purex process with 30 vol% tributyl phosphate (TBP) in a hydrocarbon diluent as the solvent. The solvent undergoes degradation due to radiolysis (from Pu and fission products) and hydrolysis (by nitric acid). In fast reactor fuel reprocessing at CORAL facility, the extent of the solvent-diluent degradationis enhanced due to short cooling period of the spent fuel, high plutonium and fission product content and high acid flow sheet. The degradation products such as HDBP and H_2MBP holds appreciable amount of Pu, U and fission products in the organic phase and reduces the solvent extraction efficiency and decontamination factor. This necessitates a solvent treatment for the removal of degradation products and the recovery of actinides before being reused or discharged as a waste.

The treatment of the spent solvent is generally carried out by sodium carbonate scrubbing for the removal of primary degradation products. In CORAL, usage of sodium carbonate scrubbing lead to formation of emulsions due to the interaction of diluents degradation products like long chain fatty acids with sodium. Hence, alternative scrubbing agents like hydrazine carbonate and ammonium carbonate were tried. Though these reagents could address the problem of emulsion formation, subsequent recovery of actinides from the aqueous stream is a major challenge. Processing of the aqueous carbonate solution resulting from spent solvent treatment by acidification leads to the formation of Pu-U-DBP sticky solids. This requires an extended boiling acid hydrolysis for the destruction DBP to yield a solution suitable for recycling by solvent extraction. Vigorous frothing, dilution of product concentration, incomplete metal ion recovery and generation of more secondary waste volume are some of the other added disadvantages expected during metal ion recovery from carbonate scrub solution. In this context, reagents such as oxalic acid, sodium oxalate and ammonium oxalate which possess acidic or near neutral pH have been investigated for spent solvent treatment.

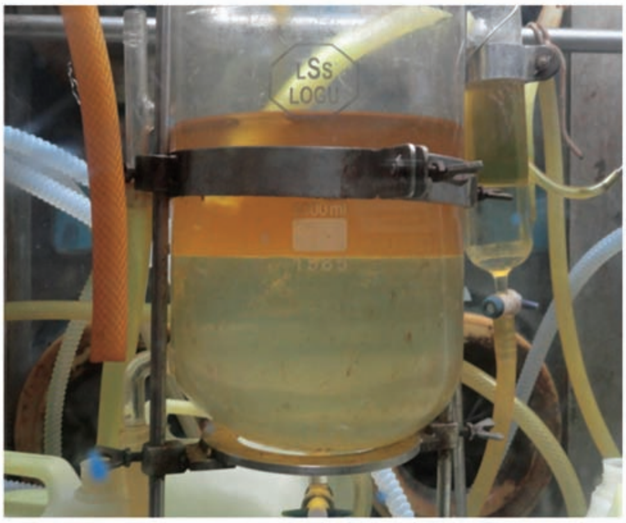

Fig. 1: Used solvent treatment in glass mixer settler unit inside a at CORAL

From the lab scale followed by plant scale trial runs, sodium oxalate solution (pH adjusted to 11-12 by adding NaOH)was found to be a potential candidate. It offers the least retention of metal ions and degraded products in the treated solvent without any crud formation and with excellent phase separation. Plutonium and HDBP concentrations in the treated solvent was reduced to well below their allowed limits in single contact with an aqueous to organic ratio of 1:1. The plutonium concentration was measured by alpha radiometry while HDBP content in the organic phase was determined by plutonium retention method. Oxalate based reagent is chosen in contrary to the conventional carbonate reagents as Pu(IV) oxalate solids are highly unstable in the near neutral and alkaline conditions and are readily hydrolysed to form complexes that are readily recovered.Plutonium recovery from the oxalate scrub solution was carried out by carrier precipitation using uranous nitrate solution and the mixed oxalate cake was calcined to oxide. The mixed oxide was further dissolved in nitric acid and partitioned by selective precipitation of uranium as ammonium uranyl carbonate.

IV.09 Platinum Loaded Reduced Graphene Oxide for U (VI) Reduction

Platinum loaded reduced graphene oxide (GO) was synthesized with varying the Pt loading from 2.5 to 10 wt%. For this initially graphene oxide (GO) was synthesized from graphite precursor by improved hammers method. Finally, the washed dried GO powder was dispersed thoroughly in 80% ethylene glycol-water medium in an ultrasonic bath for 6 h subsequently required amount of Chloroplatinic acid solution was added and the solution was transferred into a Teflon lined hydrothermal autoclave. Finally, the autoclave was heated at 120 °C for 12 h. for the in-situ reduction of graphene oxide and Pt (IV) to obtain Pt loaded reduced graphene oxide (GO). The product was separated from the medium by centrifugation and washed several times with water followed by ethanol, before drying it in a vacuum oven for over night.

All as-synthesized materials were characterized by XRD, Raman, FTIR and HR-TEM.

The XRD pattern was recorded using Co K-alpha (wavelength 1.79 Å) as X-Ray source. Recorded XRD patterns shows sharp peaks at 2θ of~46°, ~55°, ~82° and ~100° which corresponds to metallic Pt state. This confirms the complete reduction of Pt(IV) to Pt(0). Moreover the characteristics peak of GO at 2θ of 10.72° does not appear in any of these Pt loaded samples, instead a broad peak does appear at 2θ of 27.45° which indicates the reduction of GO to RGO.

Raman spectra of the samples shows two sharp peak corresponding to the Raman Shift at 1350 cm^{-1} 1600 cm^{-1} which are typical characteristics of the defect containing graphitic materials. The ID/IG ratio of the RGO and Pt loaded RGO was found to be comparable, concluding that the Pt loading does not add any additional defects to RGO.

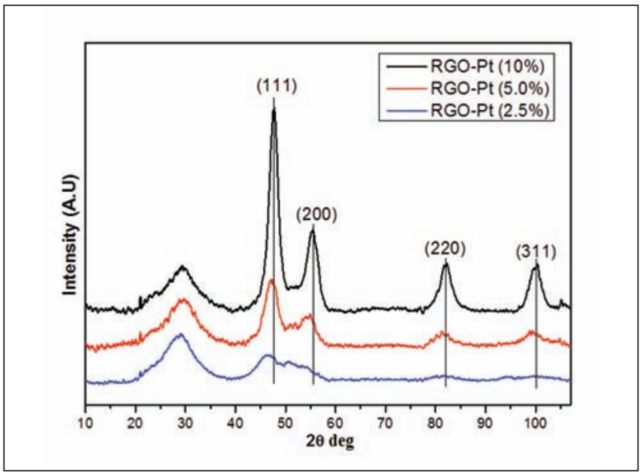

Fig. 1: XRD Pattern of RGO-Pt (2.5%), RGO-Pt (5%) RGO-Pt (10%)

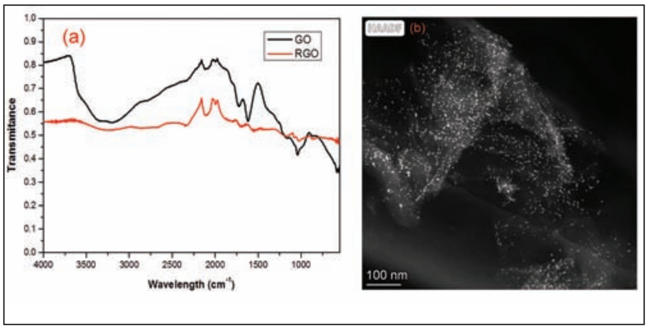

Fig. 2: (a) FTIR spectra of GO and RGO (b) HADAF immage of RGO-Pt (2.5%)

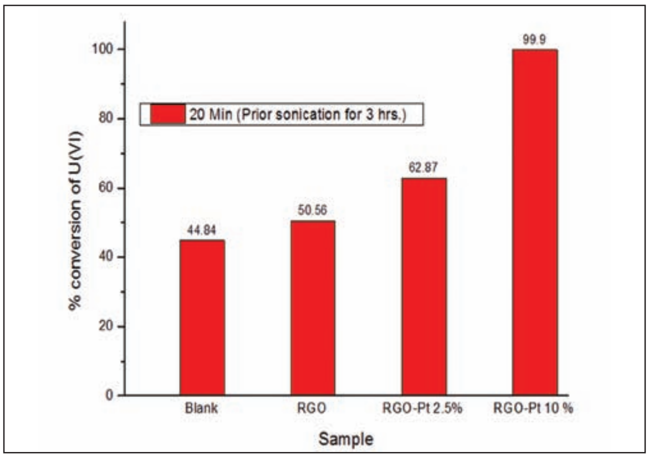

Fig. 3: U (VI) to U (IV) conversion in 20 min

Several peaks corresponds to the oxygen containing functional groups appear in the FTIR spectra of the GO. However, in case of RGO most of these peaks disappears or the intensity comes down drastically, indicating a drastic reduction of the oxygen content in the sample and the effective reduction of GO to RGO by ethylene glycol at 120 °C.

The microscopic structure clearly shows the dispersion of the small (3 to 7 nm) Pt particles over the RGO sheet.

All the above samples were subjected to the reduction of U (VI) to U (IV) under hydrogen as a catalyst in a nitric acid- hydrazine medium. The highest catalytic efficiency was obtained with RGO-Pt (10%) due to the improved dispersibility of the catalyst material with the increase of Pt loading.

IV.10 Reprocessing of High-burn Fuel Discharged from FBTR at CORAL

CORAL (COmpact Reprocessing of Advanced fuels in Lead cells, earlier known as Lead mini cells), located at the Reprocessing Development Laboratory, houses the equipment and systems for the demonstration of reprocessing of FBTR fuel. The primary objective of the CORAL plant was to process the irradiated mixed carbide fuels with varying degrees of specific activities to gain operating experience with Pu-rich carbide fuels through an aqueous reprocessing route. It is a unique facility dedicated to innovative research, design, development, and deployment of closely guarded reprocessing technology required for higher capacity plants like DFRP to demonstrate recycling mixed-oxide FBR fuels and the FRP of FRFCF. CORAL is the hotbed for evolutionary technology and related equipment research for fast reactor fuel reprocessing. Fig.1-4 shows the different perspectives of CORAL.

CORAL had initially reprocessed the low burnup spent fuel discharged from FBTR. Progressively higher burnup fuels were taken up by obtaining necessary regulatory approvals from AERB. The spent Pu rich mixed carbide fuel from FBTR with 25, 50, 100, and 155 GWd/t burnup has been reprocessed as per approved technical specifications and license conditions. Currently, 155 GWd/t burnup fuel is being reprocessed on campaign mode.

CORAL has completed its initial design mandate of reprocessing 14 subassemblies of FBTR in February 2017 over an extensive run of 44 campaigns. As per AERB norms, the relicensing of the CORAL plant has to be carried out once in five years. After carrying out intensive refurbishment works, detailed in-service inspections of the waste vault, and regulatory inspections, CORAL was relicensed for five years since September 2018 by the regulatory agency.

Fig. 1: A view of CORAL Operating Area

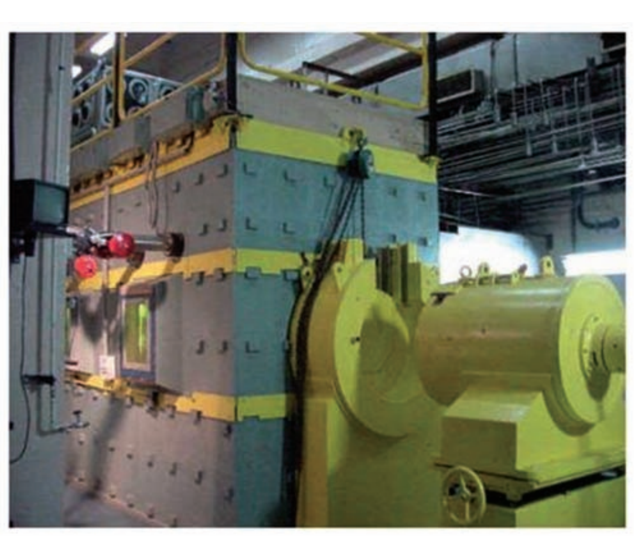

Fig. 2: A view of CORAL Fuel Charging area

During this period, CORAL reprocessed 21 campaigns successfully, and then, the prerequisites for relicensing activities were carried out, and all required documents were submitted to the Regulatory Agency. In-service inspection of critical components such as Dissolver, in-cell tanks, and underground waste tank farms have been carried out and found to be healthy. Remote thickness measurement of the Dissolver was carried out for the first time, and it was observed that there is no notable change in thickness even after a service life of 20 years. As part of aging management, the active area exhaust duct has also been replaced with minimal plant downtime. The Class 4 Electrical Power Supply System has been revamped, and the old HT cables and the transformers have been replaced with LT cables from the new substation. CORAL facility has been relicensed by AERB for a further period of 5 years since September 2023. Till now, 65 reprocessing campaigns have been completed with high recovery and decontamination factors.

Fig. 3: A view of Equipment inside CORAL hot cell

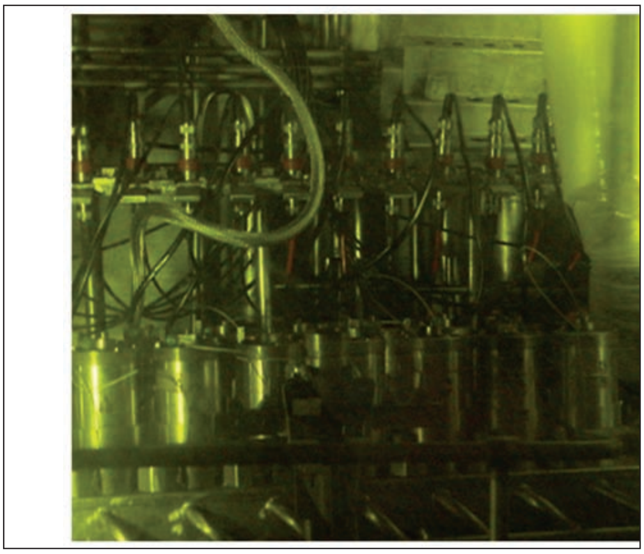

Fig. 4: A view of centrifugal extractors installed in CORAL

During the reprocessing campaigns, CORAL had implemented critical improvements in process, equipment, and operating procedure to meet the desired objective of developing the fast reactor fuel spent reprocessing technology for future plants such as DFRP and FRP. These operations gave vital design inputs and valuable operating experience for future plants. Fine-tuning of some of the process parameters/equipment was carried out primarily to minimize the radioactive waste generation with minimum downtime in future plants. CORAL is the only plant that can carry out such advanced research on FBR fuel reprocessing. Moreover, CORAL also provides the necessary operator training for FBR reprocessing. The CORAL plant continues to operate with an excellent recovery factor and radiation safety record.

IV.11

Spectrophotometric Technique for the Determination of Uranous Nitrate Concentration in Plant Samples

The PUREX process is employed for the recovery of plutonium and depleted uranium from the spent fuel discharged from nuclear reactors. In this process, the uranium and plutonium are coextracted into organic phase for their purification followed by their mutual separation using uranous nitrate stabilized with hydrazine as the partitioning agent. The concentration of uranous nitrate solution in hydrazine nitrate plays vital role in PUREX process during partitioning.

Conventionally, uranous nitrate is estimated by volumetric titration with potassium dichromate. Since, hydrazine is employed as the stabilizing reagent whose reduction potential is -0.22V (Vs SHE), the interference of hydrazine in the estimation of uranous nitrate cannot be eliminated. Therefore, it is necessary to develop a suitable alternate method for the determination of uranous concentration in the presence of hydrazine.

The uranous nitrate exhibits some characteristic absorption bands in UV-visible absorption spectrum, which can be exploited for the direct spectrophotometric determination of uranous nitrate concentration. In this method, the optical density of U(IV) at 660 nm was measured. The UV-Visible absorption spectrum of uranous nitrate in nitric acid concentration range of 0.5-2.0 M is provided in Fig.1. The effect of hydrazine nitrate and uranyl nitrate on the absorption spectrum of uranous nitrate was investigated and the results revealed no significant interference.

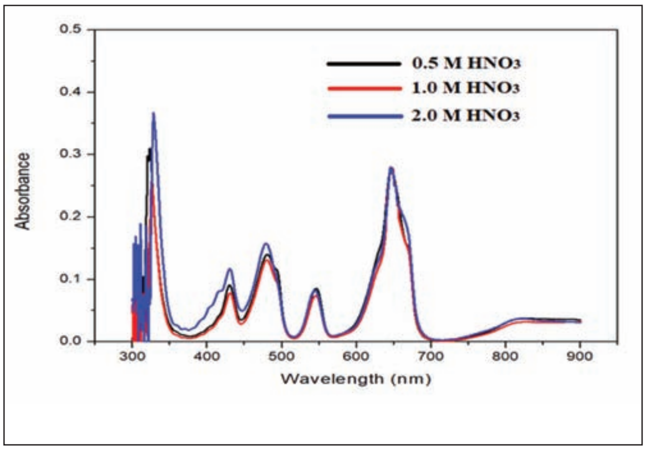

Fig. 1: Effect of free acidity on UV-Visible absorbance spectra of Uranous Nitrate; [U(IV)] = 2.13g/L; [N_2H_5+ NO_3-] = 0.5 M

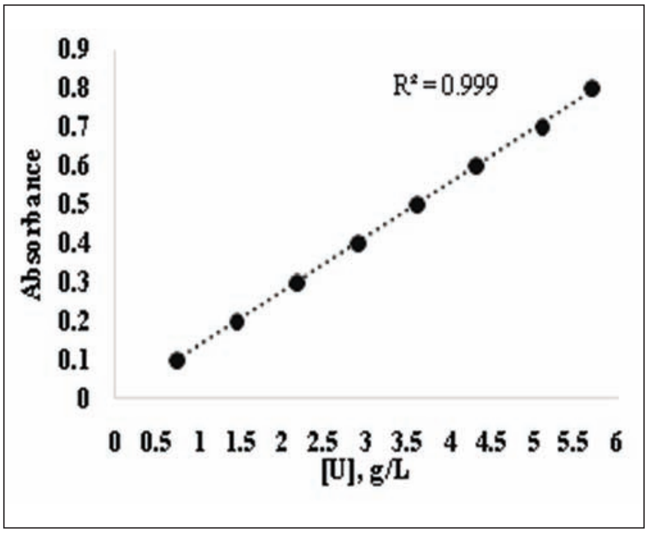

Fig. 2: Calibration plot of determination of [U(IV)] in 0.51 M nitric acid medium in the presence of 0.5 M Hydrazine nitrate

Since the U(IV) could vary from 0.5 to 6 g/Lboth in 0.5 M nitric acid and hydrazine, the absorption spectrum of U(IV) was recorded in this concentration range and the calibration plot is presented in Fig. 2. It can be seen that that there was a linear relationship between the absorbance and U(IV) concentration with correlation coefficient of 0.999. The molar absorptivity of U(IV) was determined to be 33 $Lmol^{-1}$ cm^{-1}. The advantages of the method are simplicity, amenability for online monitoring and generate of no analytical wastes containing corrosive chemicals. This method has been successfully employed for analysis of uranous nitrate in the CORAL plant samples and the results obtained are in good agreement with the concentrations determined by conventional method with a precision and accuracy of ± 3.0%.

IV.12 Development of an Improvised and Modular Analytical Sample Handling Robot for DFRP

The Demonstration Fast Reactor Fuel Reprocessing plant (DFRP) is a facility for reprocessing of spent fuel discharged from Fast Breeder Test Reactor (FBTR) in regular plant scale and a demonstration facility for processing the spent fuel discharged from Prototype Fast Breeder Reactor (PFBR). The spent fuel with high burn-up (155 GWD/T) with a cooling period not less than 2 years discharged from FBTR is envisaged to be reprocessed in DFRP. The chemical laboratory plays a vital role in monitoring the performance of process equipment as per design intent by analyzing the samples drawn at different steps of the process. due to the nature of the spent fuel, the plant samples received in DFRP control lab would be associated with high level of radioactivity. Hence, the handling of the samples would be very challenging. Therefore, analysis of the high active samples inside hot-cell would minimize the man-rem expenditure and maintain ambient dose in laboratory with in the permissible levels. In view of the above, an analytical handling robot (AHR) was designed, fabricated and erected in analytical hot cell of DFRP. The AHR has provision to take suitable volume of aliquot from 0.100 mL -1.00 mL with high level of precision and accuracy (< 1%), delivering to the titration vessel followed by carrying out titration. The capper/de-capper system available in AHR facilitates the changing of inner lid with punctured inner gasket thereby avoiding manual handling of high active sample bottles.

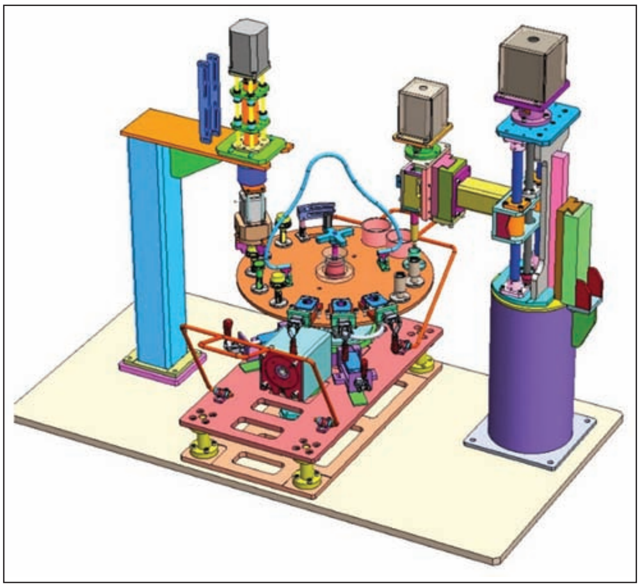

Fig. 1: Model of analytical handling robot

Fig. 2: Modular analytical sample handling robot in DFRP

Customized AHR for the application of handling analyzing samples from various locations of hot cells was designed, developed, functional tested and installed in sampling cell of DFRP. The unit is designed with minimum number of maintainable parts & drive units as an alternate to complex Robot, which had the difficulty in accessing most of the parts vulnerable for maintenance and at a cost less than 1/10th of cost of conventional Robot. The design is modular enabling replacement of any maintainable parts remotely in short time. The assembly & disassembly of the entire unit takesless than an hour. The 3D model sketch and the actual equipment installed in DFRP are given below.

IV.13 Development of Silicon Photo-multiplier Based Combined Alpha & Beta Counting System for Spot Contamination Monitoring

Portable Alpha & Beta combined counting system for spot contamination is required for monitoring the particulate alpha & beta radioactive contamination on a small or narrow area as on the inner surface of a pipe. The contamination monitor contains a detector, pre-amplifier placed very close to the detector, counting electronics and readout electronics with display unit. Conventional detectors with PMT cannot be used for this application due to its large size. Hence, a new detector with Silicon Photo-multiplier (SiPM) was developed to meet the requirements.

Unlike the conventional PM tubes, the SiPM is compact and is an active semiconductor device consisting of multiple Avalanche Photo Diodes (APD) arranged as an array. For detecting the radiation, 0.25 mm thick dual phosphor scintillator detector was used. SiPM with a photo sensitive area of 6x6 mm was used as the photon detector. The dual phosphor detector was optically attached to the SiPM covering the sensing area. The detector and photon sensor were covered with Mylar sheet to arrest the light leakage. The biasing voltage of SiPM was 58V DC. And the gain is 7x10^5.

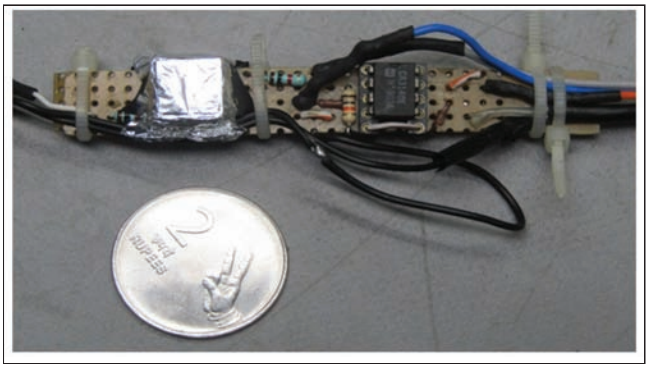

Fig. 1: Detector and Pre-amplifier

Fig. 2: Contamination detection system

The Pre-amplifier circuit was assembled on a PCB of dimensions 85 x 12 x 10 mm.

The output from the preamplifier was fed to the signal processing circuit. The alpha and beta discrimination was done based on amplitude and pulse width. The pulses due to Alpha and Beta were separated and counted. The same was displayed on a HMI. The system was tested using various standard radioactive sources. On testing with Pu 239 alpha source, efficiency was found to be 20%. On testing with Sr90-Y90 beta source, efficiency of 22% was obtained. A natural Uranium source of 7 Bq also used to test combined Alpha & Beta response of the system, the alpha efficiency was found to be 30% and beta efficiency was found to be 45%. The average background was found to be 0.8 cpm for alpha and 2.8cpm for beta. The corresponding MDA values are 0.22Bq/cm^2 for alpha and 0.24Bq/cm^2 for beta. The system is satisfying the required criteria for contamination measurement.

IV.14 Revamping of the Class 4 Electrical Power Supply System of CORAL

The electrical loads of the CORAL Reprocessing facility were catered by 415V power supply and it was fed by the 11kV / 415V RDL substation. This substation had an 11 kV HT switchboard with Minimum Oil Circuit Breakers (MOCB) which received the 11kV Class IV power supply through two numbers of 11kV cable feeders. The 11kV is stepped down to 415V by two numbers of 750 kVA, oil cooled Transformers and distributed by a 415V Power Control Centre (PCC). The system was more than 45 years old getting the spares was difficult. Hence, it was difficult to maintain the 11 kV systems in RDL Substation.

Design

The new 11kV/415V substation (PDC-III) was utilized to provide Class 4 power to CORAL. The total installed capacity of the substation is 6 MVA and has the spare capacity to meet the maximum demand of CORAL. Hence, it was proposed to feed 415V LT power supply directly to CORAL PCC from PDC- III PCC through two LT cable feeders. Thereby, the 11 kV systems in RDL Substation can be dispensed with. The existing electro-mechanical relays on 415V PCC was also replaced with Numerical relays for enhanced reliability of the Class IV power supply system.

The Challenge:

As in the case with any operating nuclear plant, the availability of electrical power is essential for normal operation as well as for operating the safety related systems. This imposed a challenge to carry out the modification activities without interrupting power supply the safety related systems.

To overcome the above challenge, meticulous planning was done to ensure that the safety related equipment is always running. This was achieved by carefully implementing various schemes of power flow route by operating specific circuit breakers and minimizing the unavoidable power interruption to non-essential systems by scheduling shutdown of one section at a time while maintain power supply to other sections continuously.

Result:

The revamping was carried out safely and the new Class 4 system is operating continuously and reliably.

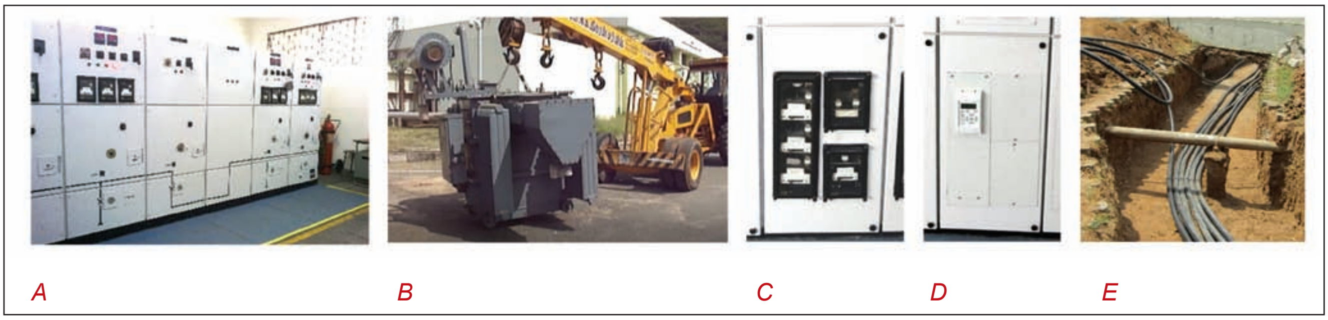

Fig. 1 : (A) Old 11kV HT Switchboard, (B) Old Transformer being removed, (C) Old Electro-Mechanical protection relays at 415V PCC, (D) New numerical protection relays has been installed, (E) New LT cable being laid underground.

IV.15 Design of Induction Motors for Centrifugal Extractors of Various Capacities

Centrifugal extractors are unique and critical equipment in fast reactor spent fuel reprocessing plants and they are used for solvent extraction. At present, they are used in CORAL and DFRP Plants. Each stage of the centrifugal extractor is driven by a custom-made three-phase squirrel cage induction motor. Centrifugal extractors of various higher capacities are required for FRP-FRFCF. The higher capacity centrifugal extractors need higher capacity motors.

The higher capacity electrical motor is designed using OCTAVE software. Modelling and simulation of the design is done in FEMM software. Static analysis and Nodal analysis of the system are done by applying suitable boundary and load conditions and results of simulation are analysed and data is compiled for motor fabrication.

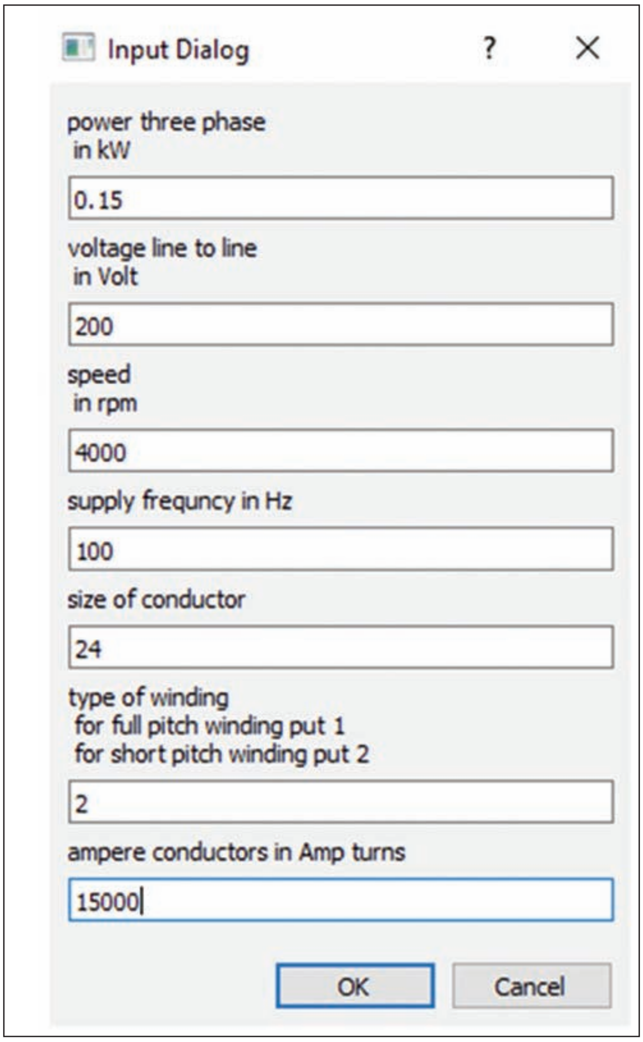

power three phase in kW: 0.15

voltage line to line in Volt: 200

speed in rpm: 4000

supply frequncy in Hz: 100

size of conductor: 24

type of winding
for full pitch winding put 1
for short pitch winding put 2: 2

ampere conductors in Amp turns: 15000

Fig. 1: Inputs window for the design of an induction motor

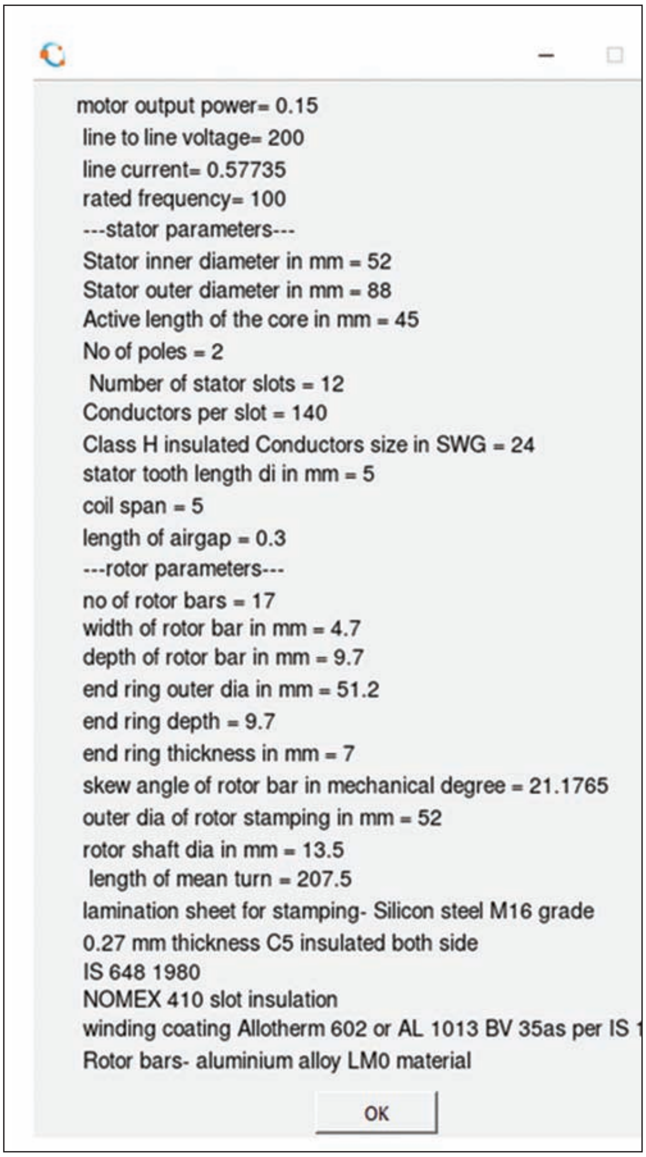

motor output power= 0.15
line to line voltage= 200
line current= 0.57735
rated frequency= 100
---stator parameters---
Stator inner diameter in mm = 52
Stator outer diameter in mm = 88
Active length of the core in mm = 45
No of poles = 2
Number of stator slots = 12
Conductors per slot = 140
Class H insulated Conductors size in SWG = 24
stator tooth length di in mm = 5
coil span = 5
length of airgap = 0.3
---rotor parameters---
no of rotor bars = 17
width of rotor bar in mm = 4.7
depth of rotor bar in mm = 9.7
end ring outer dia in mm = 51.2
end ring depth = 9.7
end ring thickness in mm = 7
skew angle of rotor bar in mechanical degree = 21.1765
outer dia of rotor stamping in mm = 52
rotor shaft dia in mm = 13.5
length of mean turn = 207.5
lamination sheet for stamping- Silicon steel M16 grade
0.27 mm thickness C5 insulated both side
IS 648 1980
NOMEX 410 slot insulation
winding coating Allotherm 602 or AL 1013 BV 35as per IS
Rotor bars- aluminium alloy LM0 material

Fig. 2: Outputs window motor dimensions

Design

The purpose of induction motor design is to obtain the physical dimensions of all the parts of the machine to meet the requirements of load and operating conditions. The parts of the motor to be designed are: stator, stator windings, rotor, rotor bars and enclosure.

The design of three phase induction motor is governed by specified equations for which inputs are to be provided. These equations were used for building a basic computational tool using the OCTAVE software, which allows the users to choose the inputs. The software gives the main dimensions of the motor as output.

Analysis

After the motor dimensions are calculated, the next step is to simulate the design in FEMM which is a software tool used for electromagnetic simulation and analysis. The motor design is imported into FEMM, and the magnetic field is analyzed using the software. The simulation provides insights into the motor's performance, including its efficiency, torque, and power factor. The performance characteristics of the motor are obtained from the design.

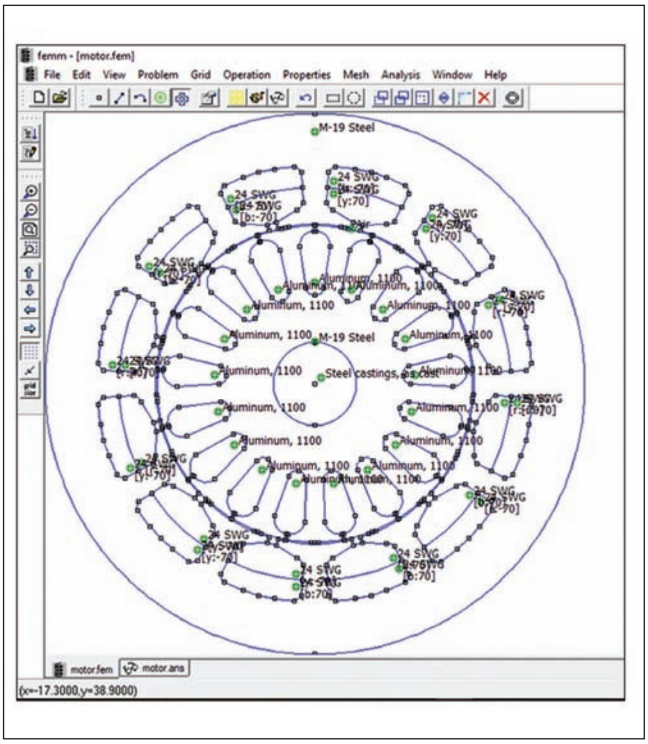

Fig. 3: Middle cross section of FEMM model of 150 W, 200V 2 pole motor

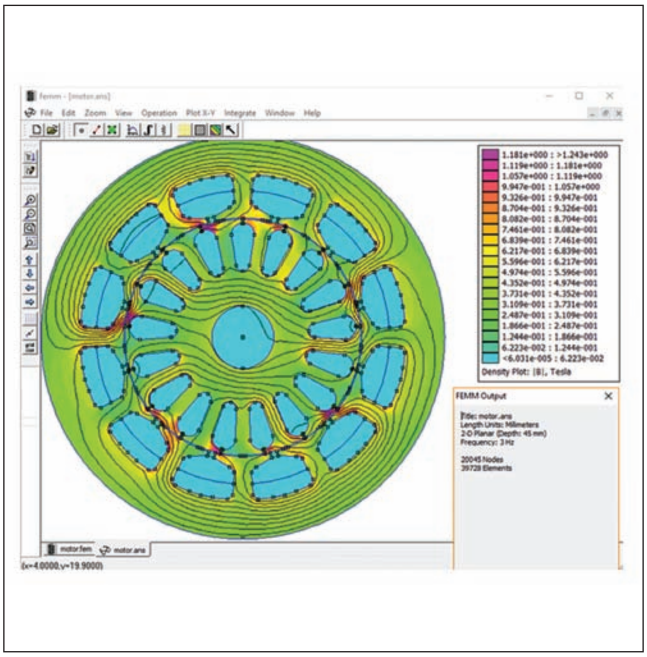

```
Title: motor.ans
Length Units: Millimeters
2-D Planar (Depth: 45 mm)
Frequency: 3 Hz

20045 Nodes
39728 Elements
```

Fig. 4: Magnetic field lines distribution in the middle cross section of the induction motor

Results

The design of a three-phase induction motor for a centrifugal extractor involves calculating the motor parameters using OCTAVE, simulating and analyzing the design in FEMM and finally optimizing the design based on the simulation results. This process ensures that the motor meets the required specifications and performs optimally for its intended application.

Squirrel cage induction motors of 150 W were designed for centrifugal extractors required for FRP-FRFCF.

IV.16 Field Evaluation of Indigenous Plutonium Continuous Air Monitor with Health Physicist Display Station Software

One of the major concerns in facilities handling large amounts of Plutonium (Pu), in powder form, is the potential inhalation hazard due to Pu airborne contamination. The prompt detection of Pu aerosols in air becomes a necessity to alert and evacuate the operating personnel so as to reduce the risk of inhalation.

A Plutonium Continuous Air Monitor (PuCAM) was indigenously developed, which has a dual Passivated Ion Implanted Planar Silicon (PIPS) detector to detect alpha, beta and gamma radiations. A System on Chip (SoC) Field Programmable Gate Array (FPGA) based custom built hardware provides the functionalities such as (i) multi channel analyzer for building the energy spectrum (ii) execution of algorithm on the spectrum for calculation of concentrations of isotopes in terms of DAC and DAChr (iii) comparison with the alarm thresholds and generating alarms (iv) communication to remote PC etc. The algorithm is custom designed and tailored to Indian reprocessing plants, for identification and quantification of airborne releases of alpha emitting ^{239}Pu along with beta and gamma releases. In-built background compensation of Radon and Thoron progenies reduces the occurrences of false alarms.

PuCAM was deployed in Compact Reprocessing of Advanced fuels in Lead cells for field evaluation by Health Physicist (HP). PuCAM is designed to work standalone as well as part of the plant network. It stores all the alarms/events, configuration data, estimated data and acquired spectrums in non-volatile memory. The instrument is connected to PC located in Control Room (CR) via Ethernet with an In-house developed Graphical User Interface (GUI) software viz. Health Physicist Display Station (HPDS) Software.

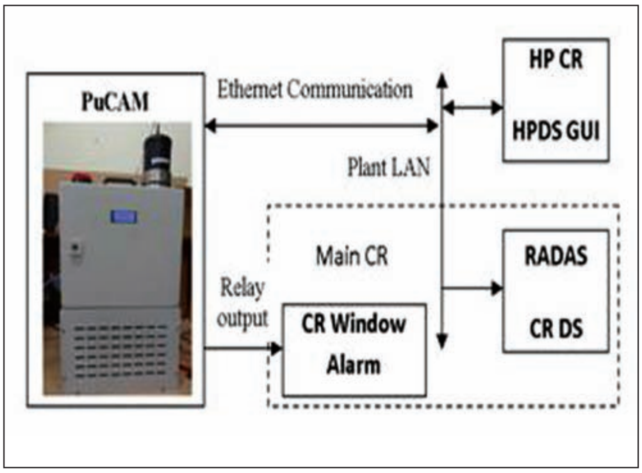

Fig. 1: PuCAM Connectivity in Plant

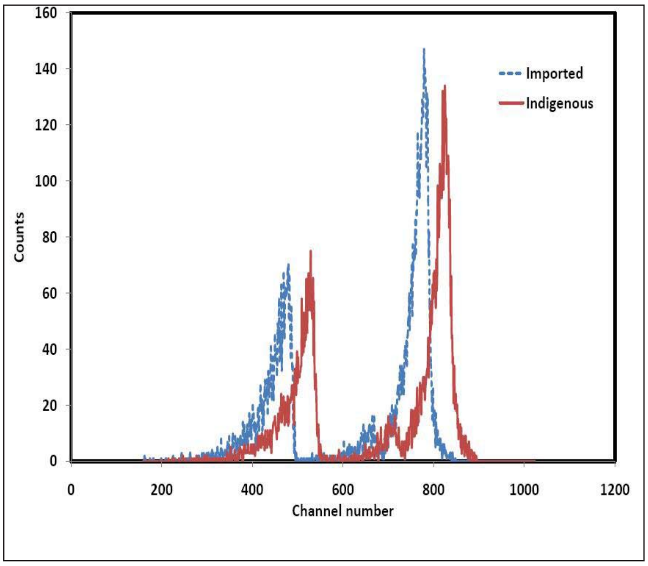

Fig. 2: Comparison of Energy Spectrums from Indigenous PuCAM and Imported Instrument

Software is designed and developed to operate in two modes: Normal and Admin modes. In normal mode software acquires and presents calculated parameters, alarm-events data, Natural & Spectrum Data (NSD), Real Time Spectrum (RTS), raw spectrum data, filter paper change detection, overall alarm status indication and history viewing. It also provides facility for buzzer & indicator testing and acknowledgement for alarm & reset remotely. PuCAM data is acquired periodically and presented in various formats such as mimic, trend graphs, table etc. on the GUI. The screen shot of main display is shown in Fig. 3. Admin mode requires an additional authentication, in which operator can perform calibration and remote configuration of PuCAM and the on board power relays for driving window alarm in Control Room. HPDS software logs all the data in PC which is further used for detailed analysis.

PuCAM is evaluated along with imported instrument at CORAL for a period of 45 days. The background counts are recorded and matching with imported instrument. Fig. 2

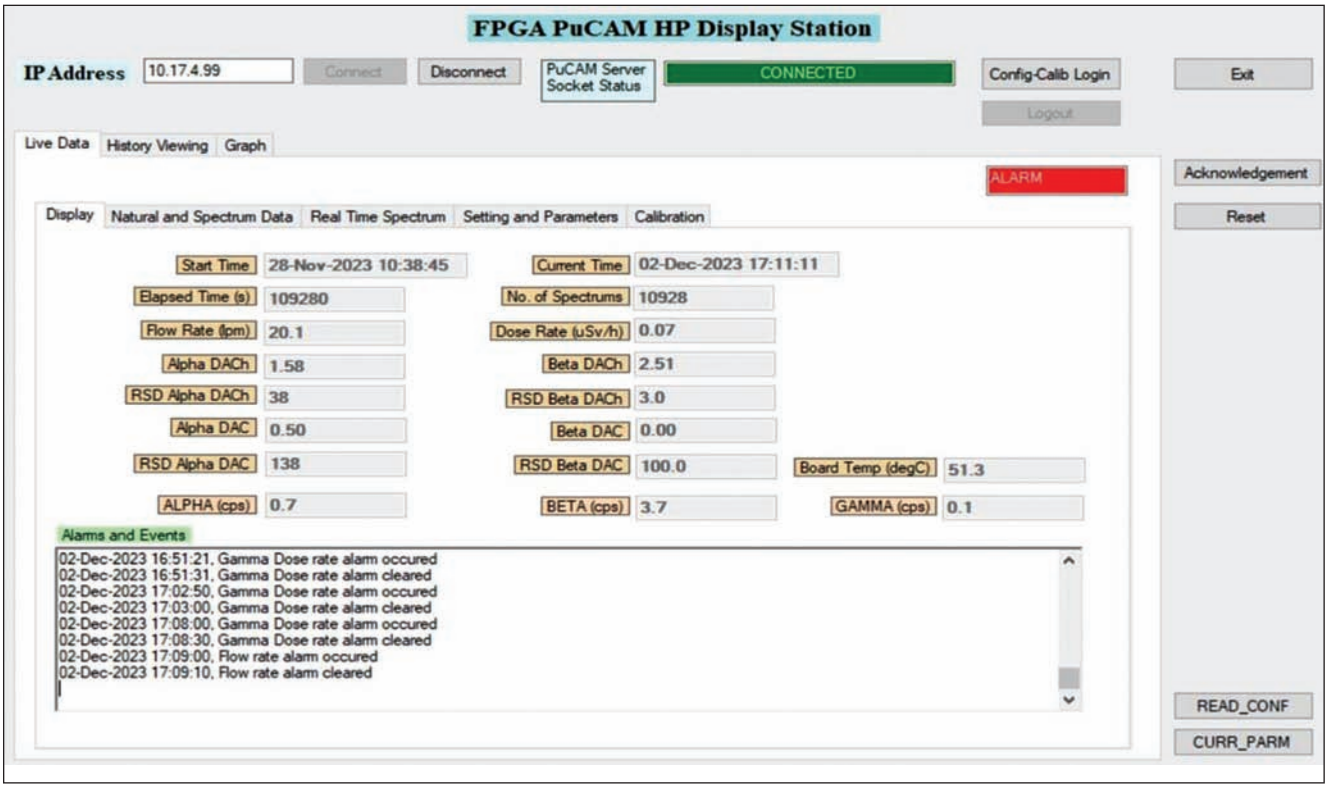

IP Address 10.17.4.99

Start Time 28-Nov-2023 10:38:45
Current Time 02-Dec-2023 17:11:11
Elapsed Time (s) 109280
No. of Spectrums 10928
Flow Rate (lpm) 20.1
Dose Rate (uSv/h) 0.07
Alpha DACh 1.58
Beta DACh 2.51
RSD Alpha DACh 38
RSD Beta DACh 3.0
Alpha DAC 0.50
Beta DAC 0.00
RSD Alpha DAC 138
RSD Beta DAC 100.0
Board Temp (degC) 51.3
ALPHA (cps) 0.7
BETA (cps) 3.7
GAMMA (cps) 0.1

Alarms and Events

```
02-Dec-2023 16:51:21, Gamma Dose rate alarm occured
02-Dec-2023 16:51:31, Gamma Dose rate alarm cleared
02-Dec-2023 17:02:50, Gamma Dose rate alarm occured
02-Dec-2023 17:03:00, Gamma Dose rate alarm cleared
02-Dec-2023 17:08:00, Gamma Dose rate alarm occured
02-Dec-2023 17:08:30, Gamma Dose rate alarm cleared
02-Dec-2023 17:09:00, Flow rate alarm occured
02-Dec-2023 17:09:10, Flow rate alarm cleared
```

Fig. 3: Main Display Screenshot of HPDS Software

shows the natural background energy spectrums of indigenous PuCAM and imported instrument operated for 8 hours. The spectrums of both the systems are comparable and shows that indigenous system performance was on par with that of imported instrument. The shift in the peak positions are due to the difference in distance between filter paper and detector in indigenous PuCAM and imported system.

IV.17 Pyrolytic Graphite as Anode for Direct Electrodeoxidation Process in Molten Salts for Pyroreprocessing Application

Pyrochemical reprocessing of spent mixed oxide fuels consisting of a mixture of actinides and rare earth metals oxides requires an additional head-end process to convert them into respective metallic forms. Electro de-oxidation process is a molten salt electrochemical process where solid oxides is directly reduced to respective metals with a low level of oxygen. Isostatic pressed high-density graphite (HDG) is used as an electrode in direct de-oxidation of metal oxides in molten salt medium. The lower stability of graphite in molten LiCl-Li_2O melt leads to the discharge of carbon particles; its accumulation leads to short circuit and increases the viscosity of the molten electrolyte. Also, the anodically released CO_2 leads to a chemical reaction with dissolved Li_2O to form Li_2CO_3, affecting its utilization and requiring recycling. Highly dense and oriented pyrolytic graphite (PyG) provides excellent sealing for HDG against molten salt corrosion. In this present study, PyG coatings are grown over HDG anodes by CVD route and its chemical cum electro-chemical response under simulated electro de-oxidation condition is investigated. The chemical compatibility of PyG-coated HDG is studied by static immersion in molten LiCl + 1 wt% Li_2O salt composition at 923 K. The surface morphology and microstructural changes in the specimens induced by molten salt corrosion were evaluated. Furthermore, the behavior of PyG-coated HDG as an anode in the direct electrochemical de-oxidation of uranium oxide pellets in LiCl + 0.1wt % Li_2O melt at 923 K was investigated.

The surface SEM micrographs after exposure to molten salt for 250 and 500 h are shown in Fig.1 (a-d). The long term chemical compatibility study reveals the selective molten salt attack initiated at the triple boundary junctions and other high-energy defective centers by the formation of pits (Fig. 1a,b). The normalized weight loss in PyG coating at the end of 250 h was 24%. With increasing exposure time to 500 h, the severity of pit formations i.e. the number density and its dimensions increased with pronounced triple boundary depletion by encompassing the adjacent areas through pore tunneling and widening mechanisms (Fig. 1c,d) producing a normalized weight loss of 38%. The molten salt corrosion of PyG is due to the chemical reaction between Li_2O and C, to the formation of lithium carbon oxides and the possible intercalation of lithium ions into the graphitic structure

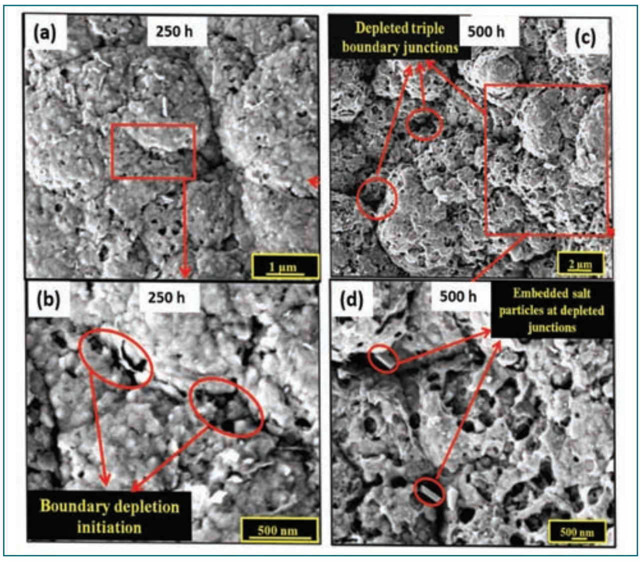

Fig. 1: (a-d). SEM micrographs of PyG surface after 250 and 500 h of molten salt (LiCl + 1% Li_2O) exposure at 923 K.

Furthermore, the anodic behavior PyG-coated HDG during direct electro deoxidation process was studied and compared with HDG. The PyG consumption from the electrode surface is mainly attributed to anodic polarization to reactively discharge O_2. In electrolytic cell, the carbon consumption from the surface of the electrode is uniform with no selectivity for preferred defective energy centers as shown in Fig. 2 as a schematic.

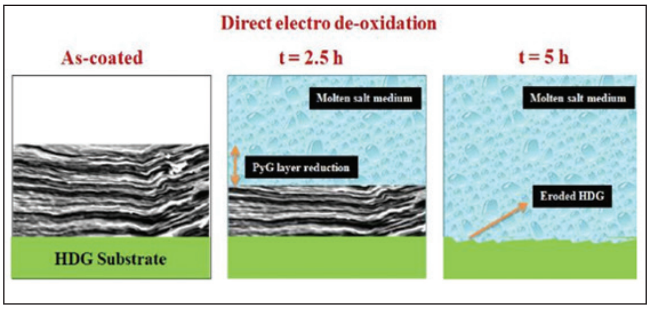

Fig. 2: Microstructural schematic of electrochemical consumption of PyG in LiCl + 0.1% Li_2O at 923K.

IV.18 Corrosion inhibition of service/fire water pipeline materials: Elucidating the efficacy of non-oxidizing biocides and Molybdate / Zinc/ Ionic liquid based corrosion

Synergistic enhancement of corrosion protection of carbon steel (CS) using biocides (BC) and corrosion inhibitor (CI) combinations of zinc chloride ($ZnCl_2$) in phosphoric acid (H_3PO_4) - Zn, sodium molybdate (Na_2MoO_4) – Mo and an ionic liquid, 1-Butyl-3-methylimidazolium chloride (IL) was demonstrated. 25 ppm of biocides such as benzalkonium chloride, bronopol, and isothiazoline showed an excellent antimicrobial activity against the slime formers and manganese and iron-oxidizing bacteria (Mn/IOB) as shown in the Fig. 1.

Electrochemical analysis (Fig. 2) showed nearly 98% corrosion inhibition efficiency of mixed CI at the concentrations of 100 ppm each of Mo & IL and 50 ppm of Zn. The anticorrosion mechanism of CI on iron was further studied by quantum chemical calculations and adsorption studies. Molecular adsorption studies with the inhibitors onto the Fe(110) surface modeled from the first principle calculations showed that adsorption energies of the $ZnCl_2$, H_3PO_4, Na_2MoO_4 and the IL inhibitor molecules were -1.94 eV, -9.73 eV, -2.14 eV and -2.46 eV, respectively. The adsorption energies in the order of H_3PO_4>IL>Na_2MoO_4>$ZnCl_2$ indicated the thermodynamically favorable interactions of inhibitors on the Fe surface confirming the theoretical model was in good agreement with the experimental data.

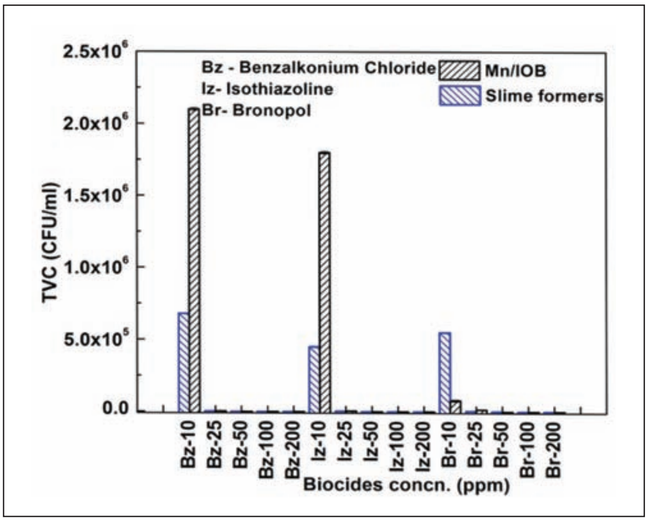

Fig. 1: Total viable count (TVC) measurement of planktonic cells of slime formers and Mn/IOB treated with different concentrations of biocides

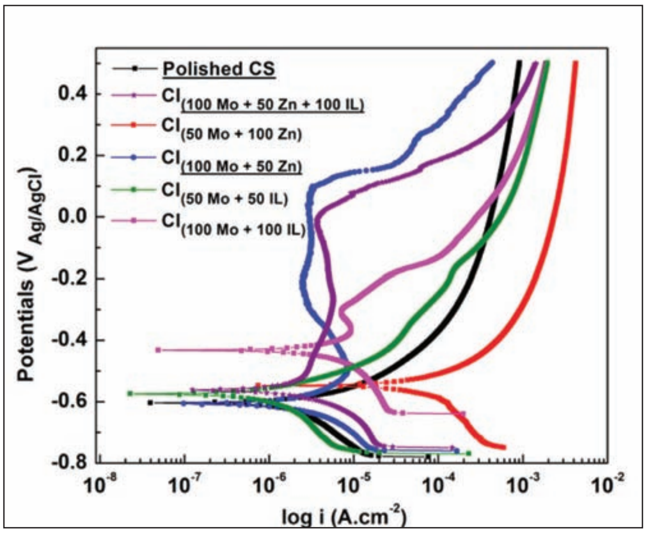

Fig. 2: Potentiodynamic polarization curves of as polished CS specimens exposed to cooling waters with combined corrosion

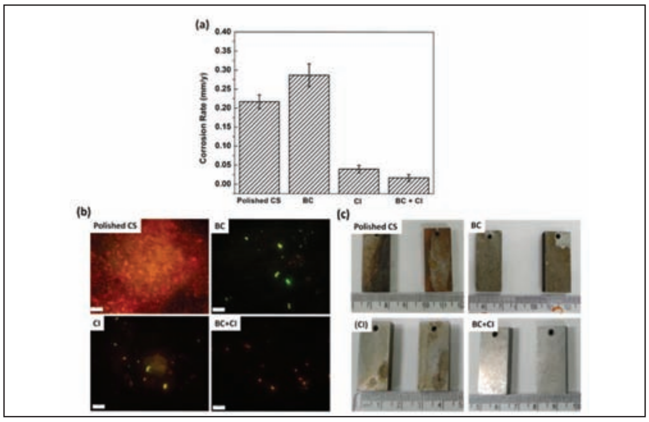

Fig. 3: (a) corrosion rate of carbon steel exposed to cooling loop water with and without biocides and corrosion inhibitors for 45 days each; (b) Epifluorescence micrographs of CS specimens exposed to cooling waters with and without biocides and inhibitors; (c) Photographs of CS specimens exposed to cooling waters with and without biocides and inhibitors

The long-term efficiency of BC and CI combinations evaluated under accelerated conditions in a pilot scale-cooling tower, indicated that nearly 92% corrosion inhibition efficiency was exhibited by a combination of all CI and BC when compared to corrosion inhibitors alone (81%) as shown in Fig. 3.

The study provides new insights into new types of corrosion inhibitors and biocides to combat corrosion issues of carbon steel water pipes used for service/fire water transport.

IV.19

Application of X-ray Computed Tomography for Assessing De-choking Behavior of Centrifugal Extractor bowls

Conditions to understand the interaction of Zr with the clad Centrifugal extractor (CE) bowls are used in the reprocessing of fast reactor fuel. When the centrifugal extractor bowl gets choked due to the deposition of chemical compounds, the bowl becomes inoperable for further processing of nuclear fuel. In order to reuse these bowls, de-choking using an ultrasonic method is being developed at PRCRRDD, Reprocessing Group in IGCAR. To visualize the pattern of de-choking, and to optimize the ultrasound bath conditions, CE bowls were choked with 147 g and 108 g of Zirconium Molybdate (ZM) slurry in laboratory.

These choked bowls were subjected to X-ray Computed Tomographic (XCT) studies using a mini-focus X-ray tube (320 kV) with a focal spot size of 0.2 mm and a PerkinElmer flat panel detector with pixel size of 200 μm. The bowl initially choked to 146 g of Zirconium Molybdate (ZM) was de-choked ultrasonically to 70 g and the 108 g choked bowl was de-choked to 60 g. The vertical cross-section (Fig. 1(a) and 2(a)) indicates that both the bowls followed a definite pattern of excess choking at bottom which gradually decreases towards the top. From the vertical cross-section shown in Fig. 1(c), the de-choking is observed to start from the top and progresses towards the bottom. Similar de-choking pattern is observed in Fig. 2(c) where in the bowl choked to 108 g is de-choked to 60 g. The horizontal cross-section (40 mm from the bottom) as shown in Fig. 1(b), 1 (d), 2(b) and 2(d), reveals that the ZM is removed in a few of the quadrants and gets accumulated in other quadrants. From these observations the pattern of de-choking with duration of cleaning in ultrasonic bath could be understood.

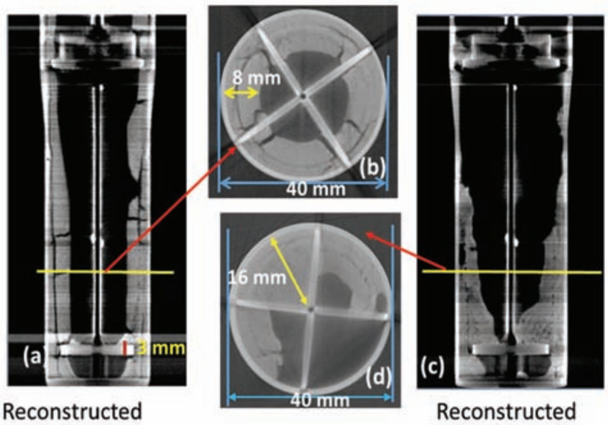

Reconstructed vertical slice of CE bowl choked to 147 g of ZM

Reconstructed horizontal slices at height of 40 mm from bottom as marked in vertical slices

Reconstructed vertical slice of CE bowl de-choked to 70 g of ZM

Fig. 1: Reconstructed vertical and horizontal slices of CE bowl choked to (a) 147 g and de-choked to (c) 70 g of ZM

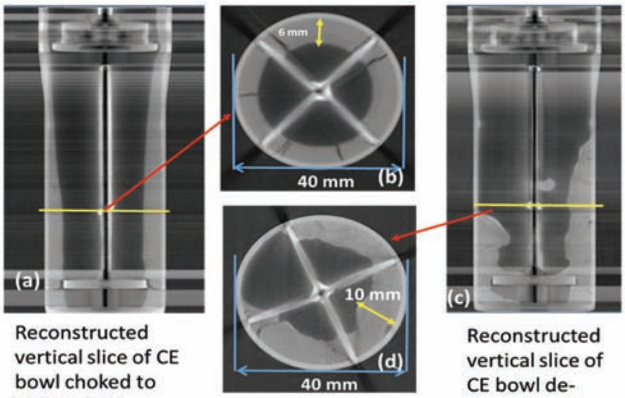

Reconstructed vertical slice of CE bowl choked to 108 g of ZM

Reconstructed horizontal slices at height of 40 mm from bottom as marked in vertical slices

Reconstructed vertical slice of CE bowl de-choked to 60 g of ZM

Fig. 2: Reconstructed vertical and horizontal slice of CE bowl choked to (a)108 g, de-choked to (c)60 g of ZM

From these CT cross-section images, a quantitative correlation between the number of pixels occupying the gray level value corresponding to ZM and the remnant ZM mass is being studied.

IV.20 Investigations on the Extraction Behavior of Zr with Phosphates and Phosphonate Based Solvents

Third phase formation is major concern during the extraction of tetravalent metal ion such as Pu(IV), Th(IV) and Zr(IV) with tri- n-butyl phosphate (TBP) based solvent extraction process. Our earlier studies on development of alternative extractant to TBP revealed that Tri-iso-Amyl Phosphate (TiAP) and phosphonate based solvent such as dibutyl butylphosphonate (DBBP) and diamyl amylphosphonate (DAAP) exhibit lower third phase forming tendency than TBP. The present study compares the extraction behavior of zirconium from nitric acid solutions using Tri-iso-Amyl Phosphate (TiAP) and Tri-n-Butyl Phosphate (TBP). The third phase formation of Zr was examined with TiAP and TBP based solvents using different A/O ratios. It was observed that TBP forms third phase with Zr when it was extracted from zirconium feed slurry with aqueous / organic ratio of 1:6; whereas third phase was not observed even in the case of 1:3 indicating that the third phase limits are higher in the case of TiAP system. Cross-current experiments were carried out with zirconium feed slurry using TiAP based solvent for quantitative extraction, scrubbing and stripping of Zr. Quantitative stripping of Zr from loaded TiAP solvent is possible using 0.01 M HNO_3 without emulsion formation.

The present study also compares the extraction behavior of zirconium from nitric acid solutions using DBBP and DAAP solvents with TBP. The major variables studied were concentration of nitric acid and extractant at a fixed temperature and phase ratio. Distribution ratios (D_{Zr}) for Zr were measured using DBBP and DAAP solvents as a function of nitric acid and extractant concentrations. Distribution ratios for Zr increases with increase in concentration of nitric acid and extractant. Solvent extraction studies in the cross-current mode were carried out to recover Zr from nitric acid solutions. Flow sheet for the extraction and stripping of Zr by 1.1 M DBBP and 1.47 M and DAAP in n-dodecane from Zr feed solutions in cross-current mode has been evaluated in the present study. The concentration of Zr in the organic phase decreases with stage number and the cumulative extraction of Zr was found to be about 97.7, 98.3 and 32.6%, respectively in the case of 1.1 M solutions of DBBP, DAAP and TBP in n-DD (Fig. 1).

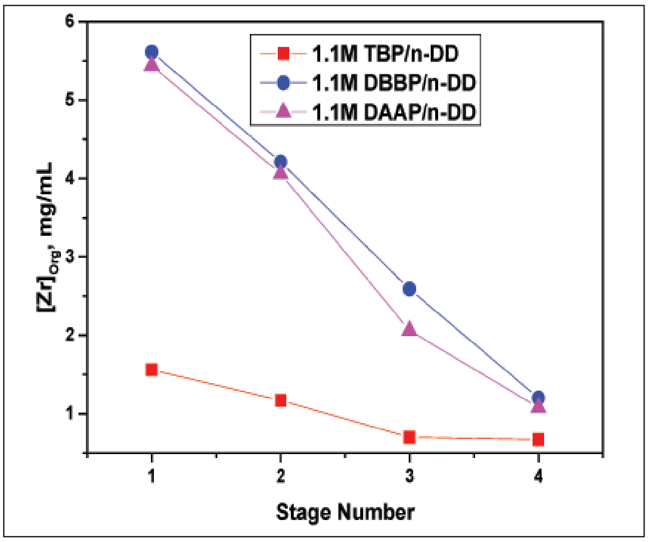

Fig. 1: Organic stage profiles for Zr during the extraction from 4 M HNO_3 by 1.1 M TBP, DBBP and DAAP at 303 K.

The aggregation behavior of TBP, DBBP and DAAP loaded with Zr(IV) was studied using DLS. Results of the study indicated that the aggregate size of the Zr-TBP formed was more widely distributed. However, DBBP exhibited a sharp peak of around 20 nm during the first extraction stage, and DAAP peaked at approximately 25 nm. It can also be seen that the aggregate sizes of Zr-DAAP and Zr-DBBP are more intense than the Zr-TBP complex, suggesting that Zr-DBBP and Zr-DAAP complexes are relatively more stable. Based on the Dynamic Light Scattering studies and the solvent extraction experiments on zirconium extraction, it can be concluded that DBBP exhibited superior Zr extraction behavior compared to DAAP and TBP.

IV.21

Miniature Table-top Module for the Treatment of Bulk Radioactive Organic Liquid Waste

The presence of radionuclides (U, Pu and Am) in organic liquid waste that are generated in radiochemical laboratories poses a serious challenge with respect to their disposal. To concede with the guidance of the regulatory agencies for smooth transport of organic waste to central waste management facility for the treatment and subsequent processing, the gross radioactivity of the organic liquid waste was suggested to be reduced to less than 5000 Bq/mL. Towards fulfilling this objective, a method was developed using an indigenous ion exchange based process and solid state complexant for complete removal of radionuclides. A novel diglycolamic acid anchored resin, prepared through chemical modification of the commercially available polystyrene-divinylbenzene (PS-DVB-DGAH) resin was studied to treat the alpha-bearing radioactive organic liquid waste by both batch and column modes of operation. Of different solid-state complexants studied, oxalic acid showed superior performance in reducing the activity of the organic waste.

To study the feasibility of the PS-DVB-DGAH resin towards the radioactive organic waste treatment, batch extraction studies (consisting of contacting approximately 0.5 g of resin with 5 mL of the waste), and a small-scale column experiment (by passing approximately 1 litre of waste through 5 g of resin loaded in a 8 mm dia. glass column) were performed. The efficiency of the process was assayed based on the analysis of the effluent samples using alpha and gamma spectrometric techniques.

To get the advantage of oxalic acid and PS-DVB-DGAH resin in efficient processing of the organic waste, both the methodologies were combined in the bulk treatment of the waste. As the required level of radioactive decontamination cannot be accomplished in a single contact for such a large volume of the waste, an automated closed-loop circulation system was devised to process the waste. The pumping of the organic fluid was designed using a valve less metering pump with SS316 housing that can endure harsh chemical environment. A special chemically resistant hose was used to prevent chemical reactions with the organic fluids. The first campaign of organic waste treatment was executed using a module consisting of four SS columns (450 mm length and 10 mm diameter) connected to the valve less metering pump. The first column was filled with glass wool for removing the solid waste if any that is present in the organic waste, the second with oxalic acid (10 g), and the last two with PS-DVB-DGAH resin (20 g in total). Almost 10 litres of waste was processed in this campaign.

(a) (b)

Fig. 1: Image of the waste treatment module used for campaign 2. SS column assembly (top: PS-DVB-DGAH resin, bottom: oxalic acid); (a) microprocessor control unit (top) and metering pump (bottom); (b): the treated organic waste (with <5000 Bq/mL activity) in a 50 litres carbuoy.

To miniaturize the design further, the second campaign was carried out by increasing the column diameter to 30 mm and the design was made compact. Fig. 1 shows the photograph of the organic waste treatment assembly utilized in campaign 2. This campaign employed two SS columns, with the first one filled with oxalic acid (60 g) and the second one loaded with PS-DVB-DGAH resin (50 g). The flow-rate of the valve less pump was adjusted with the help of a microprocessor based controller unit. The automated system controlled by microprocessor based control unit assures minimum radioactive exposure to working personnel. Using this module, approximately 60 litres of the waste was processed. Overall, the current development encapsulates the technological advancement of waste treatment to meet the demand for treating organic liquid waste in the bulk scale with minimum human intervention.

IV.22 Development of a Method for the Assay of Zirconium and Americium in the Irradiated U-Zr Metal Alloy Fuel Slug

U-Zr alloy based blanket fuel is proposed for advanced metallic fuel reactors in India along with the U-Pu-Zr core fuel. This report highlights the analytical estimation of Zr and Am (as ^{241}Am) in the irradiated U-6 wt.% Zr (U-Zr) fuel that has experienced a burn-up (~2000 MWd/t), for basic understanding of the fission and activation products in the fuel.

Sodium bonded U-6wt.% Zr fuel pin with ferritic steel cladding was irradiated in the Fast Breeder Test Reactor (FBTR), it was received from RML and was cooled for two years. A small portion of U-6 wt.% Zr slug weighing 1.1 g was cut from one of the fuel pin sections inside the hot-cell of Radio Chemistry Laboratory (RCL) at IGCAR and was dissolved in a mixture of 12 M HNO_3 and HF (~100:1) by heating under Infrared (IR) lamp. For complete dissolution, the solution was evaporated to dryness and the procedure was repeated four times, with only 12 M nitric acid in the fourth cycle. The dissolver stock solution was prepared by making up the dissolved concentrate up to 50 mL using 4 M nitric acid. The free acidity of the resulting solution was found to be 4.5 M. The above dissolver solution was used for further analyses.

2.5 mL of the above solution was transferred to a 10 mL vial and this was used as the feed for subsequent liquid-liquid extraction stages, conditioned by addition of 0.025 mL of freshly prepared saturated sodium nitrite solution. Four successive stages of liquid-liquid extraction were carried out using this feed solution, as described in Fig. 1. The extracting phase for stages 1 and 2 was 1.1 M (30 vol.%) TBP in n-dodecane, while 0.2 M TODGA in n-dodecane + 5 vol.% 1-octanol was employed as the extracting phase for stages 3 and 4.

For the analytical estimation of ^{241}Am, prior removal of the U and Pu was an essential step and it was carried out in two extraction stages using the PUREX solvent containing 30% TBP in n-dodecane. The extraction of ^{241}Am from the aqueous phase obtained from the above was achieved by two extraction stages using 0.2 M TODGA/ n-dodecane as the extracting phase medium.

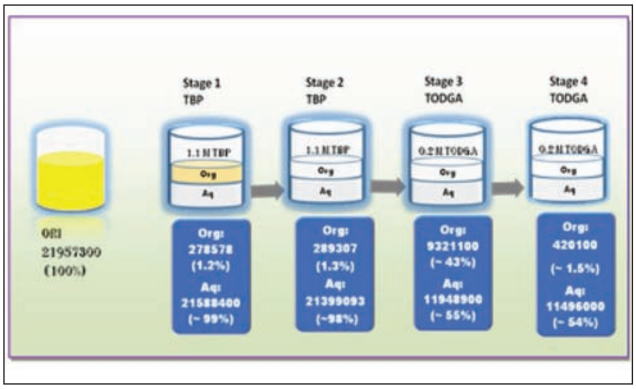

Fig. 1: Scheme of liquid-liquid extraction stages and results of LSC counting for each stage.

The amount of ^{241}Am extracted to the TODGA phase of extraction stage 3 was quantified by alpha spectrometry by comparing it with in-house prepared ^{241}Am standard. The quantity of ^{241}Am was then calculated as ~0.498 µg in one gram of the irradiated fuel, based on the specific activity of ^{241}Am (3.43 Ci/g). This amounts to 0.0000498 wt.% of the fuel. The above assumptions were validated by a separate study involving spiking of known concentrations of ^{241}Am tracer as well. Analysis of Zr by spectrophotometry was carried out with UV-2100 double-beam spectrophotometer, using Xylenol Orange (0.005 wt./vol%) as the complexing agent, following absorbance maximum at 514 nm. The analysis was carried out in presence of 0.25 wt./vol% of PVP in an acetic acid-sodium acetate buffered (pH 4.8) medium. Successive addition of boric acid (500 µg/mL, 0.1 mL), potassium carbonate (2000 µg/mL, 1 mL) and BmimCl (6000 µg/mL, 1 mL) to the samples enabled the masking of F^{-}ions. Ascorbic acid (1 mg/mL) was added to mask the interference of Pu. The percentage of Zr in the irradiated fuel was estimated from the sample absorbance, and it showed a zirconium composition of 6.08 %.

Overall, the composition of Zr and ^{241}Am in the irradiated fuel was estimated to be 6.08 wt.% and 0.0000498 wt.% (0.498 µg/g) by spectrophotometric and radiometric methods respectively.

IV.23 Ionic Liquid Mediated Zirconium(IV) Separation

Zirconium is an unwanted and important troublesome element present in High Level Liquid Waste (HLLW) solutions. During the partitioning of trivalent lanthanides and actinides, Zr(IV) poses numerous challenges to the safe and fission product free Ln(III)/An(III) partitioning and transmutation process. In addition, in case of the metallic fuels proposed for fast reactors, Zr(IV) plays a critical role in designing the fuel composition. The spent metallic fuel contains 5-10 times higher concentration of Zr(IV) in dissolver solution as compared to that present in the spent oxide fuel dissolver solution. Consequently, it is essential to separate Zr(IV) from Ln(III)/An(III) present in nitric acid phase for a smooth way of Partitioning and Transmutation (P&T) of minor actinides present in HLLW solution.

Among various solvent systems comprising of extractants and diluents designed for the spent fuel reprocessing application, ionic liquids (ILs) have shown tenacious potentiality due to their several appealing properties. In this context, a strongly hydrophobic phosphonium IL: Trihexyl (tetradecyl)phosphonium nitrate ($[P_{66614}][NO_3]$) was employed in its undiluted form for the separation of Zr(IV) from nitric acid medium containing Eu(III)/Am(III). The equilibrium concentration of Zr(IV) in IL phase showed an increasing trend with an increase in feed acidity. The corresponding extraction efficiency value increases from 60% to 96% in the studied range of nitric acid. In contrast to this, the extraction factors of Eu(III)/Am(III) were insignificant irrespective of the feed acidity leading to remarkable separation factors for Zr(IV) over the former.

The separation factors were significant even at high loading conditions of Zr(IV) over Eu(III). The coordination mechanism corroborated the uptake of Zr(IV) into IL phase through the formation of its anionic nitrato complex, which was not feasible for the trivalent metal ions under the same experimental conditions. Effect of IL anion inferred that Zr(IV) extraction is higher in IL containing NO_{3-} anion as compared to Cl- and NTf_{2-} ion.

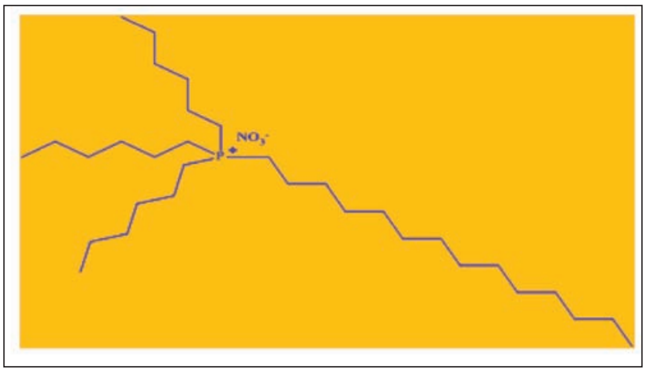

Fig. 1: Structure of Ionic Liquid ($[P_{66614}][NO_3]$)

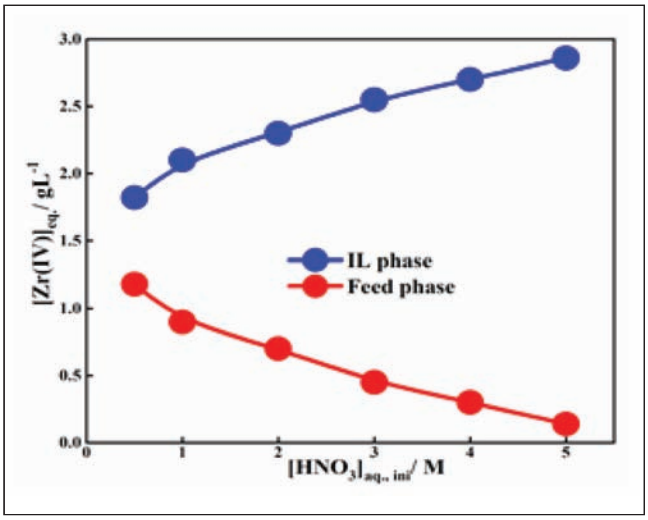

Fig. 2: Zr(IV) extraction in ionic liquid phase

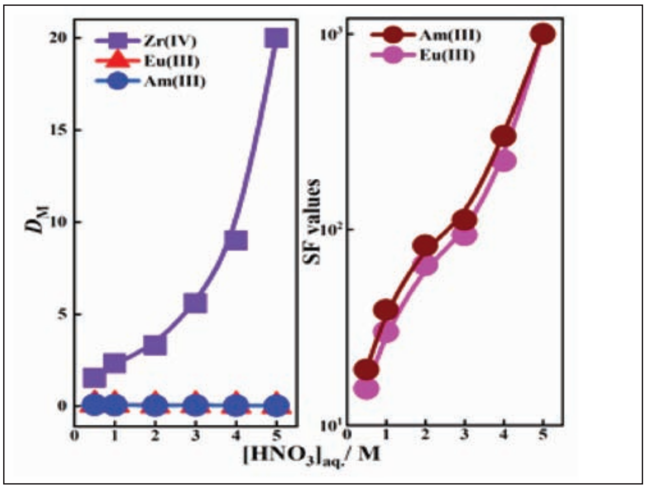

Fig.3: Separation factors of Zr(IV) over Eu(III)/Am(III)

Exceptional extraction factors obtained for Zr(IV) without using any added extractant in IL phase as well as without tuning the feed phase with any salting agent undoubtedly substantiate the robustness of $[P_{66614}][NO_3]$ for the metal ion extraction. Remarkable separation of Zr(IV) from Eu(III)/Am(III) even at high feed concentration indeed opens a new opportunity to address the efficient separation of Zr(IV) from spent metallic fuel solution, wherein Zr(IV) content is high.

IV.24 Off-line Estimation of Evolved Gases from RDL Waste Vault During Blackout by using Semiconducting Metal Oxide Sensors

Nitric acid is used as the primary medium for dissolution of spent fuel discharged from nuclear reactors for aqueous reprocessing. The dissolution of chopped fuel pins is carried out in hot nitric acid medium. Chemical separation is achieved by TBP-HNO_3 partitioning route to extract uranium and plutonium. The high-level aqueous waste containing organic compounds from CORAL is stored in the waste vault tanks having a storage capacity of around 9000 L. The raffinate during the dissolution of depleted fuel pins from FBTR is also stored as high-level waste (HLW). Hydrogen is continuously generated by radiolysis of water and its concentration gradually builds up in the storage tanks. Being an inflammable gas with an LEL of 4 %, hydrogen must be monitored to avoid its build-up in the storage tanks. Apart from hydrogen, evolution of NO_x can also occur, as the high-level waste is in nitric acid medium. Organic waste in the waste vault tanks may decompose to yield vapours of n-butanol, decomposed products of n-DD, etc. To avoid build up of all the vapours that includes H_2, NO_x, continuous air purging is done in the HLW tank during the regular operation using an exhaust system which dilutes their concentration. However, during station blackout, neither the exhaust system for continuous air purging nor the tank vacuum will be available, and this leads to a hydrogen concentration build-up which has to be monitored.

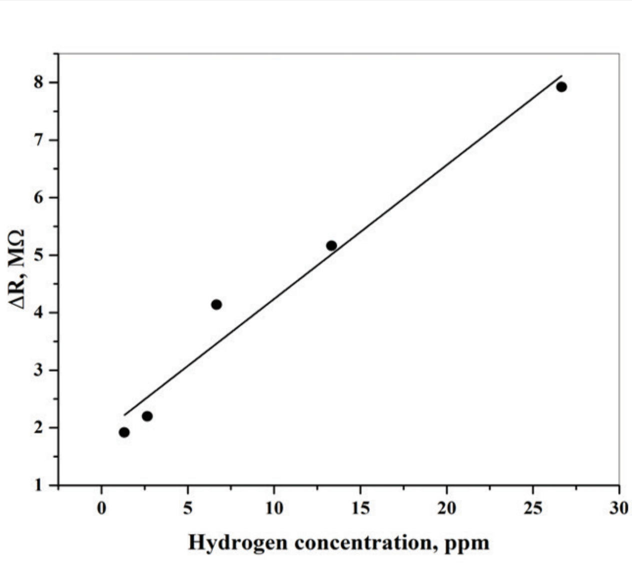

Fig. 1: Typying calibration plot SnO_2 at 623 K

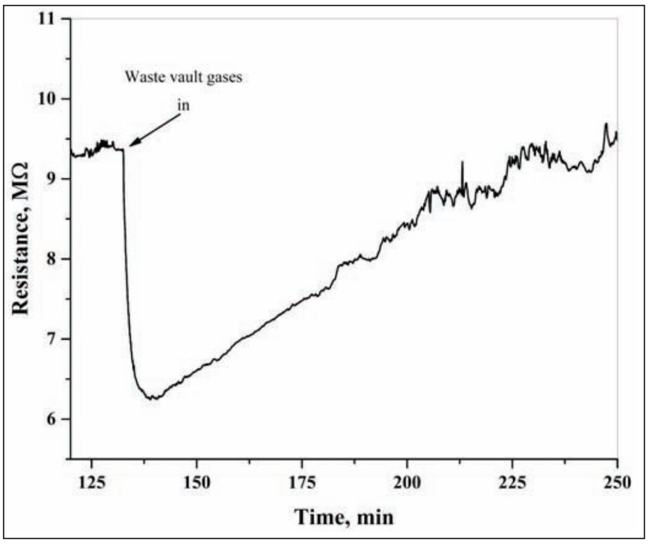

Fig. 2 Typical transient plot of SnO_2 at 623 K towrds RDL waste wait vault gases collected during blackout on 23rd Sep 2023

Assessment of evolved gases from RDL waste gases was carried out using a SnO_2 sensor on 23 September 2023 during a blackout. A set of calibrated SnO_2 (for H_2 sensing) and In_2O_3 (for NO_x sensing) sensors were used to check the evolved gases. The sensors have shown characteristics of transients for the presence of hydrogen. The typical calibration plot of SnO_2 sensor is shown in Fig. 1. From the fitting of calibration plot's fit, the hydrogen concentration in the evolved gases was deduced. A typical transient during the injection of sample gases into the SnO_2 sensor assembly is shown in Fig. 2. From the back-calculation of the concentration of hydrogen from the known volume of injections of the evolved gases trapped, the concentration of hydrogen was estimated to be around 400 ± 40 ppm. The study shows H_2 generation takes place and its concentration builds up during black out.

Table 1 Conclusions drawn from the present study

S.NO	Condition used	Concentration of H_2 obtained	Remarks
1.	EGA from RDL waste vault during blackout on 23rd Sep 2023	~400 ± 40 ppm	No additional characteristics for the presence of any other gases.

IV.25 High Pressure High Temperature Structural Investigations of Cs-loaded Nuclear Waste Host Matrix, Zeolite- A

Development of novel matrices (ceramic, glass glass bonded composites etc.) and their property evaluation for nuclear waste immobilization is very important for closing the fuel cycle and safe disposal of radioactive waste. Various matrices are being used to immobilize the radioactive waste. However, considering the type of fuel and spent fuel reprocessing technologies, the composition of waste matrices need to be changed to accommodate the fission products. In this context, ceramic matrices such as zeolites are being studied to immobilize fission products. Zeolite-A was synthesiszed using fly ash from the thermal power plants using hydrothermal technique. Cs- was loaded to the zeolite-A to simulate the behavior of Cs-137 in zeolite-A. In this report Cs-loaded zeolite-A was investigated under extreme pressure and at elevated temperatures to evaluate its performance for waste immobilization purposes.

The diffraction data of Cs-loaded zeolite-A collected at ambient pressure and room temperature indicates that they crystallize in the cubic structure (space group Fm-3c). Powder diffraction data has been collected using the Almax-made Helios diamond anvil cell (DAC) with a culet dimension of 600 μm at Elettra Sincrotrone beam line at Trieste, Italy. A 160 μm hole that was drilled at the centre of a pre-intended steel gasket was used as the sample chamber. Silicone oil was used as a pressure-transmitting medium in all the pressure runs. The pressure was calibrated using the equation of state (EOS) of gold. Three sets of data were collected during the beam time; the diffraction data at high temperatures at ambient pressure, the high-pressure diffraction data at 100°C, and the high-pressure diffraction data at 200°C.

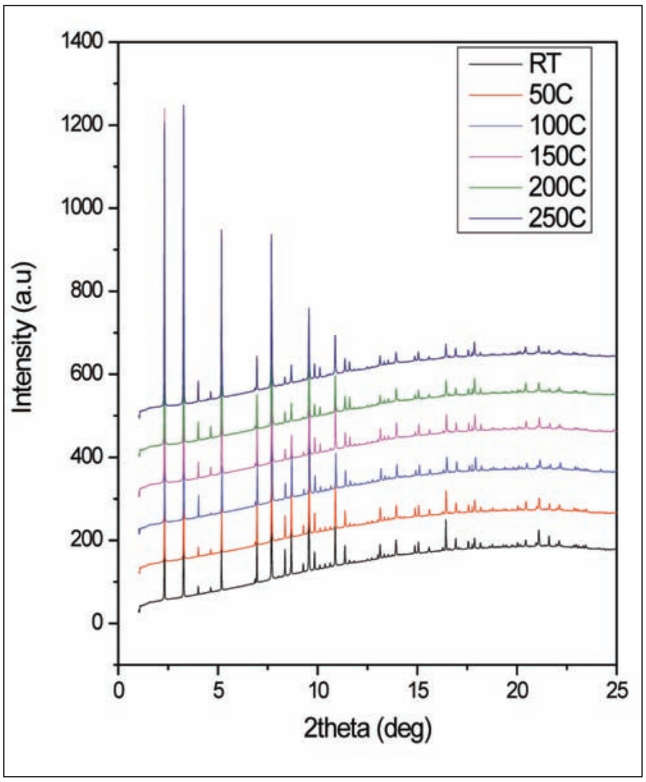

Fig. 1: XRD patterns taken at high pressure and high temperature under Sincrotrone

The diffraction data collected at high temperatures up to 250°C is shown in Fig. 1. The data indicate the absence of any structural phase transitions until the highest temperature studied in this experiment. This is consistent with the available reports in the literature. However, a clear shift of the diffraction peaks towards lower 2 theta below 150°C has been observed due to the expulsion of water molecules from the pores of the zeolite structure.

The data indicate the absence of any structural phase transformations. However, Cs-loaded zeolite-A undergoes a pressure-induced amorphization at both the temperatures studied.

On decompression, releasing the pressure to well below the amorphization pressure could not retrieve the ambient cubic phase of the zeolite-A. This indicates that the pressure-induced amorphization observed in the Cs-loaded zeolite-A is irreversible in nature.

IV.26 Resolving Isobaric Interference In-situ by Home-made Laser Ionization Mass Spectrometry – Towards Analysis of Irradiated Fuel

The determination of specific isotopes is very important for a nuclear fuel cycle. Among various isotopes, there are three crucial isotopes, namely, ^{148}Nd, ^{90}Sr and ^{137}Cs. ^{148}Nd is essential to evaluate fuel utilization and its performance inside a thermal reactor in terms of burn-up. ^{90}Sr and ^{137}Cs are of major concern in waste management point of view, as they are relatively long-lived isotopes, emitting high energy radiation and have environmental risk due to their chemical similarity to calcium and potassium. Mass spectrometry (MS) based methods are commonly used to determine all these isotopes. In any MS measurement, there will be isobaric interference at ^{148}Nd, ^{90}Sr and ^{137}Cs from ^{148}Sm, ^{90}Zr, and ^{137}Ba. Therefore, the MS analysis require a prior chemical separation of interfering isotopes or abundance correction at ^{148}Nd, ^{90}Sr and ^{137}Cs by using the abundance of non-interfering Nd, Sr and Cs isotopes, respectively. Therefore, there is a need for an alternative method, which can overcome the above shortcomings.

In the present study, laser ionization mass spectrometry (LIMS) was used to determine ^{148}Nd, ^{90}Sr and ^{137}Cs isotopes in simulated dissolver solution of nuclear fuel without any prior chemical separation and interference correction. The isobaric interference at ^{148}Nd, ^{90}Sr and ^{137}Cs was eliminated by optimizing laser fluence. Among the different MS techniques, LIMS has many advantages, namely, can be home-built, compact, simple, ease to couple with glove box or lead shielded mini-cell/hot-cell for radioactive sample, low cost, minimal sample requirement (~μg), simultaneous, negligible radioactive waste generation, lesser radiation exposure and hence suitable for handling highly radioactive samples.

Liquid sample was prepared by mixing their respective nitrate standard solutions having natural isotopic abundances. The sample solution was then mixed with tri-butyl phosphate (TBP) and methanol to improve mixing of analyte and complexing agent. About 60 μL of the solution was mixed with graphite powder and loaded onto a stainless steel (SS) disc that serves as a sample holder. The above sample slurry was applied in a thin layer to the SS sample plate, dried in open air, and loaded into the LIMS sample chamber. LIMS is a home-made Mamyrin type reflectron time-of-flight mass spectrometer with a Nd-YAG pulsed laser (M/s Litron,) with a 1064 nm wavelength and 4 ns pulse width.

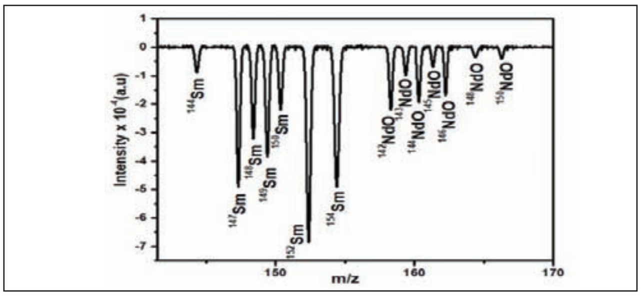

Fig. 1: Mass spectrum at a laser fluence of 0.026 J cm^{-2}

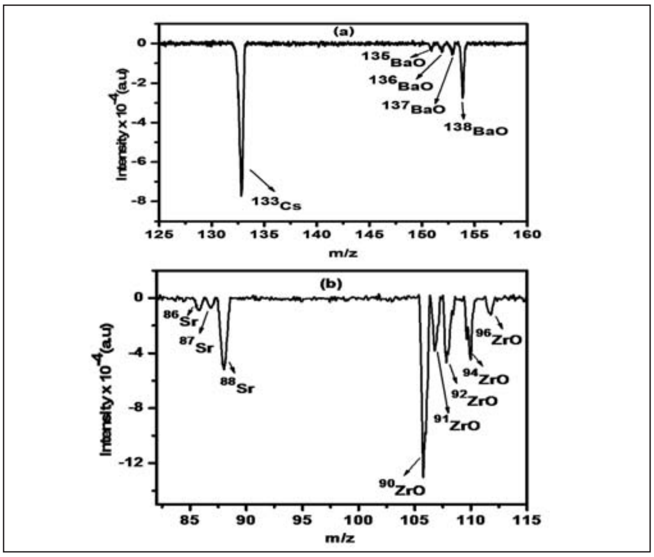

Fig. 2: Mass spectrum at a laser fluence of 0.0003 J cm^{-2}.

Fig. 1 is obtained at a laser fluence of 0.026 J cm^{-2}. It is clear from the mass spectra that Sm is present only in elemental form, namely Sm$^+$, while Nd present only as corresponding monoxide species, namely NdO$^+$. All natural abundance isotopic peaks for Sm$^+$ and NdO$^+$ are observed and all are well resolved. Thus, Nd isotopes can be well separated from Sm using LIMS at a laser fluence of 0.026 J cm^{-2}. However, when the laser fluence was increased by about four times (0.105 J cm^{-2}), both the elemental and corresponding monoxide peaks do appear for Nd and Sm. Fig. 2(a)-(b) is obtained at a laser fluence of 0.0003 J cm^{-2}. The spectra indicates that Sr and Cs appear only as their elemental form, namely Sr$^+$ and Cs$^+$; while Zr and Ba form their corresponding monoxide species, namely ZrO$^+$ and BaO$^+$. All natural abundance isotopic peaks for Sr$^+$, Cs$^+$, ZrO$^+$ and BaO$^+$ are observed and they are well resolved. When the laser fluence is increased by twenty times (0.006 J cm^{-2}), both elemental as well as their monoxide peaks do appear for Sr and Ba; but Cs and Zr appearance remains the same as Cs$^+$ and ZrO$^+$.

IV.27 Non-destructive Assay of U-Zr and U-Pu-Zr Metal Pins for Fuel Homogeneity by Gamma Scanning

India's future fast breeder reactors contain metallic fuel fabricated using slugs of binary or ternary alloys made with zirconium and fissile element viz. uranium and plutonium (U-Zr, U-Pu-Zr). Metallic slugs containing U-6wt.%Zr were prepared using injection casting method at IGCAR. As a quality control protocol, the fabricated sodium bonded metallic fuel pins using casted metallic slugs were subjected to an active gamma scanning (AGS) for assessing the fuel homogeneity using an attenuation source. The fuel pin scanning coupled with $LaBr_3(Ce)$ detector, its associated electronics and MCA acquisition software. The VB software was developed in-house & coupled with APTEC MCA to automate the gamma spectra acquisition at desired locations of fuel pin by moving it.

1 m fuel pins with 100 and 320 mm of U-Zr slugs used as blanket and fuel respectively were assayed by active gamma scanning method using ^{137}Cs source through 3 mm Pb collimation. The fuel pin was moved vertically and attenuated gamma spectrum was registered from bottom at every 3 mm step up to a total length of 537 mm. All the acquired spectra were analyzed and the net counts of attenuated photo peak of 661.6 keV as a function of scanned length of fuel pin was plotted. The system was used to scan several metal fuel pins successfully (Fig. 1a) to obtain the profile of fuel slug and determined the length of fuel and blanket about 420 mm. A discontinuity i.e., a gap of more than 1 mm between the blanket and fuel in one of the pins was identified (Fig. 1b) which can be attributed to the presence of sodium between the two slugs. Similarly, six nos. of enriched U-Zr (3) and U-Pu-Zr (3) of 0.5 m length were assayed by active & passive gamma scanning (PGS) methods (Fig. 2). In PGS, 185.7 keV (^{235}U) & 413.7 keV (^{239}Pu) gammas were used to profile the enriched U-Zr & U-Pu-Zr respectively. All the three 14.5% enriched U-Zr pins (E3, E4 & E6) showed a uniform distribution of fuel as well as similar fuel (~160 mm) and blanket (~50 mm) column length.

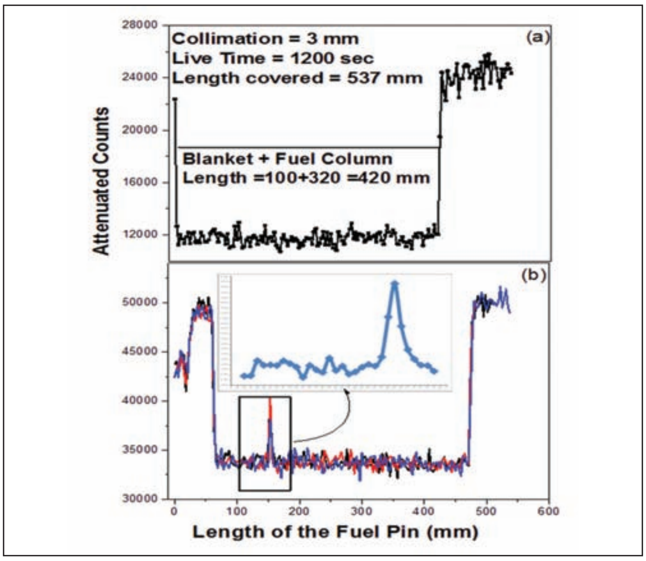

Fig. 1: Profile of fuel homogeneity in U-Zr metal fuel pin (a) and pin with gap between blanket and fuel in metal pin (b)

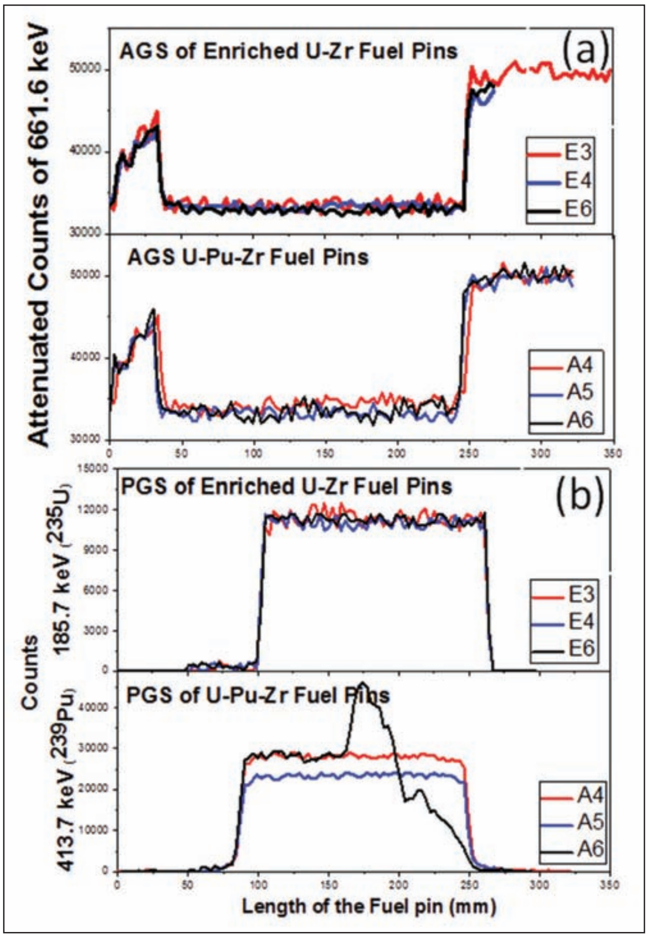

Fig. 2: Profile of fuel homogeneity in Enriched U-Zr and U-Pu-Zr metal fuel pin using AGS (a) PGS (b) techniques.

In the case of U-Pu-Zr fuel pins, A4 and A5 showed uniform distribution of fuel as well as similar fuel and blanket column lengths. However, pin A6 showed non-uniformity in Pu distribution in fuel slug.

Thus, the present study could non-destructively profile the length of the fuel slug (U-Zr or U-Pu-Zr) in both 0.5 and 1 m metal fuel pins along with non-uniformity and discontinuity between slugs.

IV.28 Electrochemical Dissolution of U-Mo-Zr Alloys in LiCl-KCl Eutectic Melt for Pyroprocessing Applications

Electrochemical dissolution of spent metal fuels in LiCl-KCl eutectic melts from anode basket is an important aspect of electrorefining process since it being facile or sluggish eventually decides the rate of electrodeposition of uranium. In order to achieve selectivity in dissolution in a narrow span of potential range, it is important that studies are carried out with metal alloys with simulated compositions of spent fuel constituents to establish the optimum potential for electrochemical dissolution during electrorefining operations. To initiate such an investigation, U-Mo-Zr ternary alloys were selected due to Zr and Mo being noble metal fission products. Two compositions, U-2Mo-4Zr and U-4Mo-2Zr (in wt.%) were prepared by vacuum arc-melting and they were further annealed at 1123 K. Both the alloys belonged to ternary phase field comprising of α-U+δ-$UZ_{r2}^{+}U_2M_o$. To establish the equilibrium potential of these alloys in LiCl-KCl eutectic melt, they were immersed in LiCl-KCl-UCl_3 melt and their potentials were measured against standard Ag+|Ag reference. It was established in this work that the equilibrium potential of both U-2Mo-4Zr and U-4Mo-2Zr alloys can be estimated with a maximum uncertainty of ± 3 from the respective equilibrium potentials and phase-fraction of α-U, δ-UZr_2 and U_2Mo recorded under similar conditions of temperature and melt characteristics. Equilibrium potential for the onset of dissolution of alloy was observed to be -1.31 and -1.29 V, respectively for U-2Mo-4Zr and U-4Mo-2Zr at 773 K. These potentials are only slightly more anodic (about 90 mV) to that of pure uranium electrode. Variation of electromotive force of alloys and their comparison with that of α-U, δ-UZr_2 and U_2Mo phases is shown in Fig. 1. Cyclic voltammograms recorded in potential region -1.50 to -0.50 V against Ag^+|Ag reference are characterized by an anodic peak at around -1.25 V followed by unlimited current up to -0.50 V suggesting a near continuous dissolution of alloy leading to maximum current density of 50 mA/cm^2, depicted in Fig. 2. Since Zr dissolves at potentials more anodic to -1.10 V and Mo at -0.40 V or higher, co-dissolution of U and Zr is possible up to potential of -0.50 V. In few voltammmograms, additional anodic feature at -1.11 V was observed signifying the limiting nature of Zr_2^+|Zr couple. Following the anodic dissolution of the alloys, the melt was subjected to cyclic voltammetry analysis, revealing the absence of redox features related to Zr and Mo. It is thus indicative from equilibrium potential measurements and chemical analysis of melt after dissolution experiments that noble metal dissolution could be prevented by controlling the anode potential in range of -1.25 V until up to -1.15 V, beyond which Zr could dissolve in melt. Since chlorides of Mo are less stable in melt, it needs very large anodic overpotential to dissolve Mo and thus in all likelihood, Mo will stay in anode basket during electrorefining conditions.

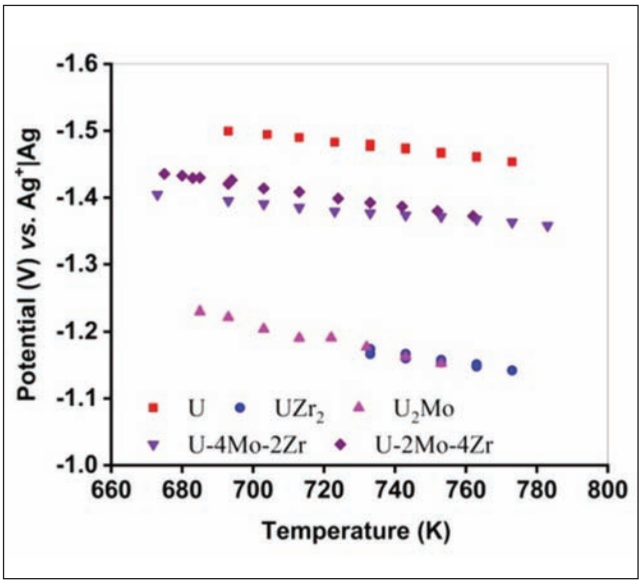

Fig. 1 Equilibrium potential of α-U, δ-UZr_2, U-2Mo-4Zr and U-4Mo-2Zr ternary alloys in LiCl-KCl-UCl_3 melt

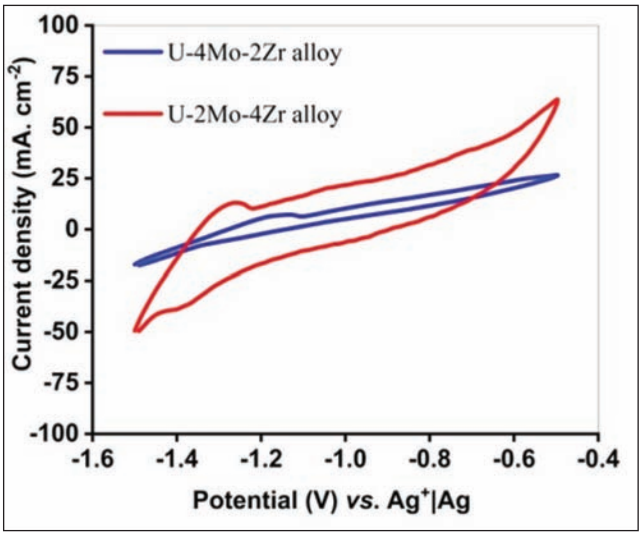

Fig. 2: Cyclic voltammograms of U-2Mo-4Zr and U-4Mo-2Zr ternary alloys recorded in LiCl-KCl eutectic melt at 773 K

IV.29 Direct Oxide Electrochemical Reduction of UO_2 to metal in LiCl-Li_2O melt

In recent times, the electrochemical reduction of solid metal oxides in a suitable molten salt medium has become an attractive method for the preparation of metals and alloys. In this high-temperature molten salt electrolysis process, the solid metal oxide cathode is directly converted to respective metal or alloys by electrons or in-situ electro-generated reductant metal, e.g., Ca, Li etc., under application of a constant cell potential or current between the cathode and the platinum or graphite anode. A programme has been initiated in MC&MFCG, IGCAR for the bulk scale (1-2 kg) conversion of uranium dioxide (UO_2) to U metal. Direct oxide electrochemical reduction (DOER) is proposed for the conversion process considering our rich experience in conducting high temperature molten salt experiments. In this context, a new molten salt experimental facility is set up for scaling up the process up to 2 kg of UO_2/batch. The essential equipment viz., electrolytic cell, rotary pellet press, mini hoist, are housed inside a glove box. A photograph of electrolytic cell inside the GB is shown in Fig. 1. The electrolytic cell is consisted of i) cathode assembly ii) anode assembly (two platinum cruciform anodes placed inside shrouds) and iii) other electrodes such as W wire, Pt coil, Mo coil and Ni|NiO reference electrodes. Initially, it is planned to demonstrate the conversion of 500 g of UO_2 pellets into U metal. Towards this, about 18 kg of LiCl was dried under vacuum and melted. After melting, decomposition potential of LiCl was determined by I-V curve. The DP was found to be 3.44 V at 650°C. The molten LiCl-1.5wt.% Li_2O was prepared by adding the required quantity of dried Li_2O. Cyclic voltammetry experiments were performed to determine oxygen evolution and Li deposition potentials. About 500 g of UO_2 pellets (6 mm dia, 1.5 g each, 8 mm length, sintered at 1500°C under Ar-H2 mixture) were loaded into a perforated cathode basket and immersed in LiCl-1.5wt.% Li_2O melt at 650°C. Fig. 2 shows the photographs of salt loading, platinum electrodes, and sintered UO_2 pellets in cathode assembly. Electrolysis of 500g sintered UO_2 pellets was conducted in constant current mode of 50 A using DC power supply for about 10 h and continued till the deposition of excess Li onto the cathode. After electrolysis, the reduced pellets (Fig. 2) were retrieved and examined. The metallic texture and electrical continuity confirmed the reduction of UO_2 to U metal. The distillation of LiCl from reduced product was carried out at 875°C under vacuum. The reduced products were characterized by density, XRD analysis, oxygen analysis and chemical analysis. The conversion ratio was found to be > 95%.

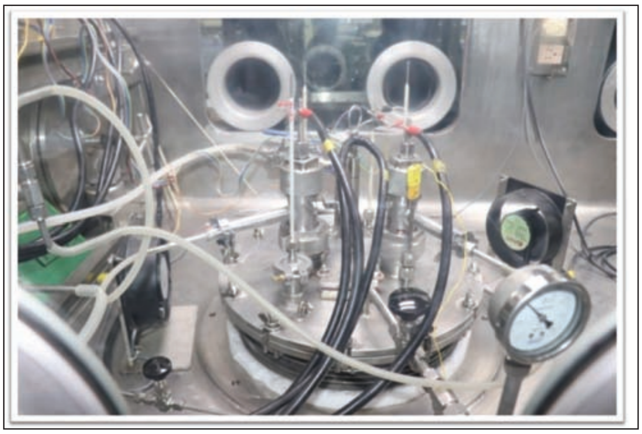

Fig.: 1. Photograph of electrochemical cell inside GB

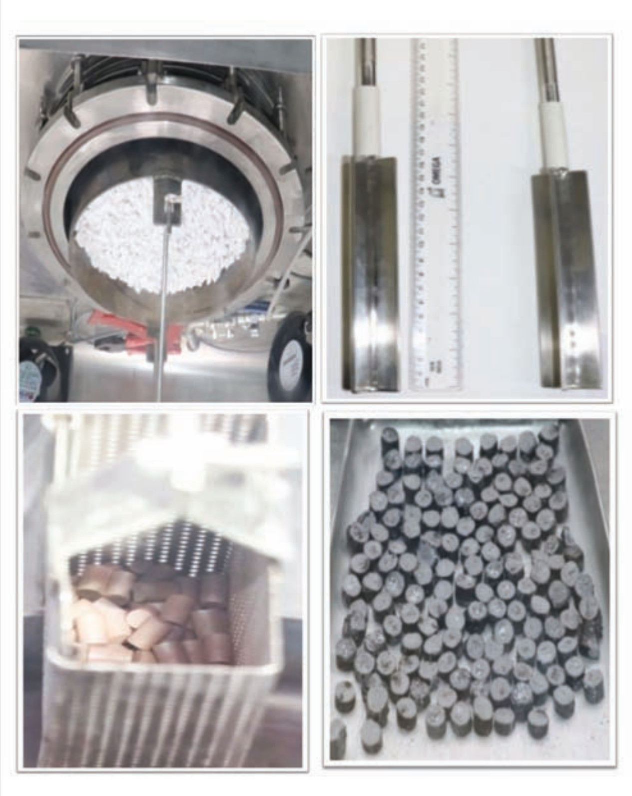

Fig. 2: Loading of salt, platinum electrodes, sintered UO_2 pellets in cathode assembly, and reduced pellets.

IV.30 Production of Uranium Metal Ingots by Pyroprocess Technology

Pyro Process Research and Development Facility (PPRDF), an Engineering scale facility commissioned to demonstrate high temperature electrorefining and cathode consolidation of uranium and uranium based alloys. This facility is established to demonstrate metal fuel pyro processing flow sheet at 10 kg of U alloys per batch. A High Temperature Electro Refiner (HTER) and an Automated Vacuum Distillation and Melting System (AVDMS) (Fig. 1) are housed inside a 500 m^3 Containment Box (CB). High temperature electrorefining of uranium metal was conducted in two steps. Accordingly, 4.0 kg and 1.9 kg uranium dendrites were obtained. The electrodeposited uranium dendrites were collected in a high density graphite crucible and loaded into AVDMS. The vessel was evacuated to 10 torr and heating by induction was initiated. At 200°C, the vessel was purged with argon and vented to remove the moisture. At 1000°C, occluded salts on the deposits were distilled off.

The system was held at this condition for 30 minutes to ensure completion of distillation. Subsequently, the induction power was raised to attain 1250°C in the charge to melt the left over uranium metal. Completion of uranium melting was ensured by holding the vessel at this temperature for 45 minutes.

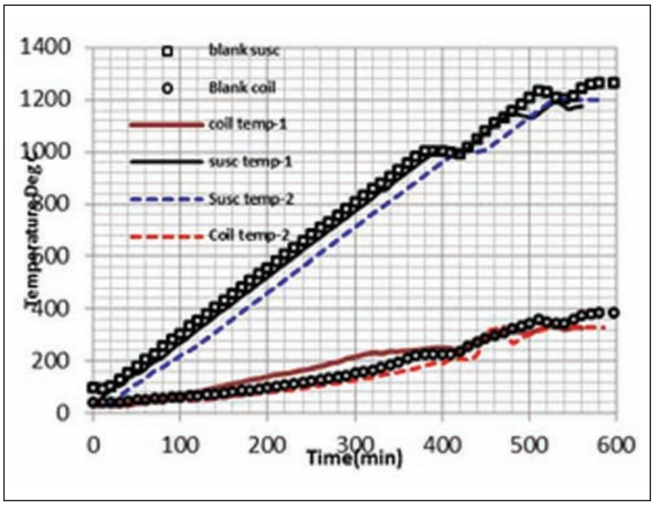

Fig. 2: Temperature profile of susceptor and coil during the campaigns

A blank run with empty graphite crucible was initially carried out in the same sequence. The temperature variation in the susceptor and the solid induction coil is shown in Fig. 2. Subsequently, the heating was switched off and the system was allowed to cool to ambient temperature.

The crucible was shifted to a glove box and the solid uranium ingots weighing 3.56 kg and 1.78 kg were recovered as shown in Fig. 3.

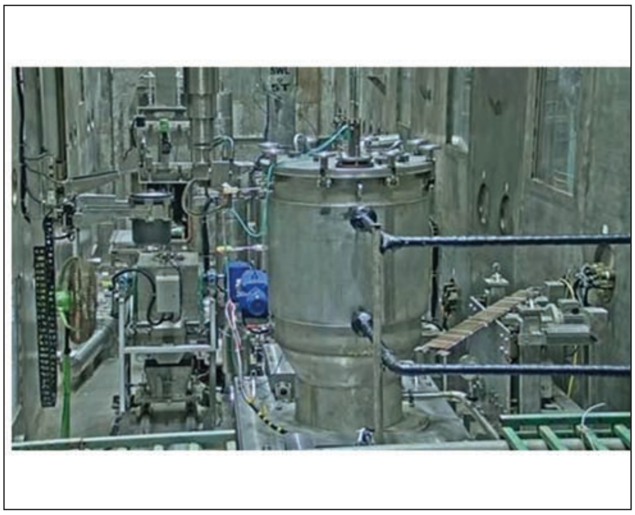

Fig. 1: Automated Vacuum Distillation and Melting System inside containment Box

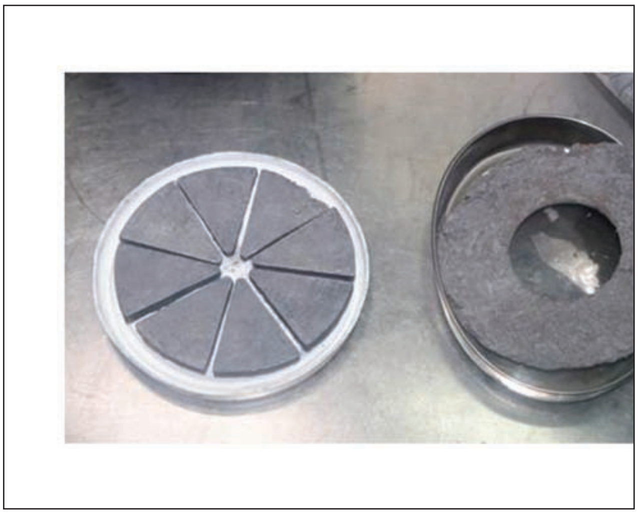

Fig. 3: Uranium ingots recovered after two melting campaigns

IV.31 Microscopic Analysis of Uranium Deposit from 10 kg Scale Electro-refining at PPRDF

In the context of pyro-chemical reprocessing of metallic fuel, uranium metal was electro-deposited in an electro-refining experiment at 10 kg scale in LiCl-KCl-UCl_3 at 773K in 500 m^3 argon atmosphere glove box at PPRDF. Electrodeposited uranium metal was distilled to separate adhered electrolytes and consolidated by melting in graphite and yttria-coated graphite crucible at around 1523K in two separate runs. After cathode consolidation about 3.32 kg (U-I) and 1.79 kg (U-II) uranium metals were obtained from graphite and yttria-coated graphite crucible. Scanning Electron Microscopy (SEM) and Energy Dispersive X-ray (EDX) analysis are non-destructive analysis methods to characterize the surface for morphology and chemical analysis in a semi-quantitative manner.

Samples of U-I and U-II were cleaned to remove surface impurities (oxide, carbon, etc.). SEM-EDX analysis of samples was carried out by using Cross beam 340 (Focussed Ion Beam-Scanning Electron Microscope, M/s Carl Zeiss, Germany) and X max-50 (EDS, Oxford Instruments, UK). Samples were loaded in a special type of sample holder. Microscopic analysis was performed by placing the sample at a 5 mm working distance, 8-15 KV beam energy, and 0.5-1 kX magnification range with a live time of 30-60s.

Fig. 1 shows cleaned uranium metal pieces (U-I, U-Ia and U-II). It is exhibiting a rough surface due to the melting of flakes and dendritic electrodeposit of uranium at 1523 K in graphite/yttria coated graphite crucible. SEM analysis reveals that the surface is not planar and porous around the sample piece. A piece was cut from U-I (Fig. 1) and polished to study the morphology and composition inside the sampler named as U-Ia.

Fig. 1: Uranium metal before and after cleaning

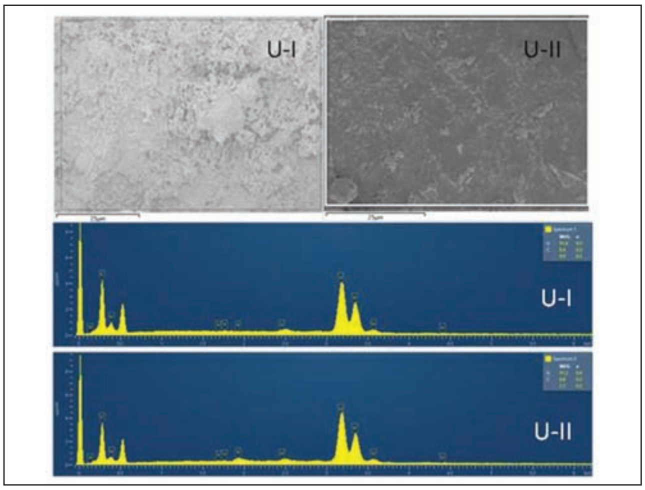

Fig. 2: SEM-EDX analysis of U-I and U-II

It exhibited planar non-porous morphology. All the samples were subjected to chemical analysis by EDX methods and observed compositions are tabulated in table-1

Table -1- EDX analysis for uranium deposit

Elements (Wt.%)	U-I	U-II	U-Ia
U	91.6	91.2	91.6
C	8.4	6.8	8.4
Y	0	2.1	0

The surface composition for the U-I sample shows the uranium matrix (91.6 wt.%) along with carbon (8.4 wt.%) and the U-II sample shows the uranium matrix (91.2 wt.%) along with carbon (6.8 wt.%) and yttrium (2.1 wt.%) in Fig. 2. Morphology and chemical analysis of U-Ia match well with U-I confirming the homogeneity of the uranium sample. The presence of carbon is attributed to the graphite crucible and yttrium to yttria coated graphite crucible. Impurities present are within the acceptable limit for metallic fuel fabrication. Impurities of salt, cadmium, and structural material were not observed at any location of the consolidated uranium sample (U-I, U-Ia, and U-II) confirming the appropriate execution of the involved process steps resulting in a viable method for uranium metal separation.

Back to Main

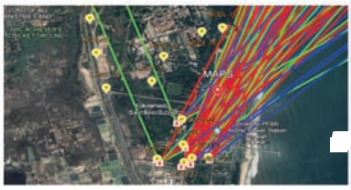

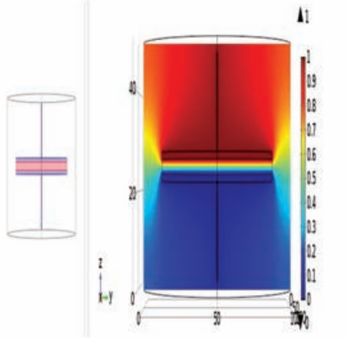

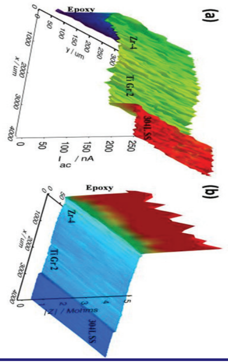

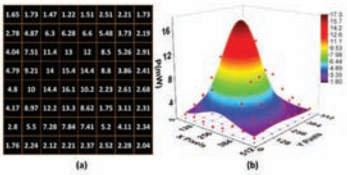

1.65	1.73	1.47	1.22	1.51	2.51	2.21	1.73
2.78	4.87	6.3	6.28	6.6	5.48	3.73	2.19
4.04	7.51	11.4	13	12	8.5	5.26	2.91
4.79	9.21	14	15.4	14.4	8.8	3.86	2.41
4.8	10	14.4	16.1	10.2	2.23	2.61	2.68
4.17	8.97	12.2	13.3	8.62	1.75	3.11	2.31
2.8	5.5	7.28	7.84	7.41	5.2	4.11	2.34
1.76	2.24	2.12	2.21	2.37	2.52	2.28	2.04

CHAPTER
V

Basic Research

V.01 Convection-Permitting Numerical Weather Forecast Model Implementation with Sensitivity Studies for Online Nuclear Emergency Response System (ONERS)

The Online Nuclear Emergency Response System (ONERS) is crucial part of emergency preparedness and it is operational at IGCAR. The base component of ONERS i.e. numerical weather forecast model is updated with Convection-Permitting model (CPM) Weather Research Forecast (WRF). We conduct the sensitivity of new conFig.uration with respect to horizontal grid resolution, Land-use/Land-cover, Land Surface Model and Planetary Boundary Layer (PBL) physics by performing a series of 3-day forecast for 7 Nuclear Power Plant sites. The model outputs are compared with site specific meteorological tower and Radiosonde data.

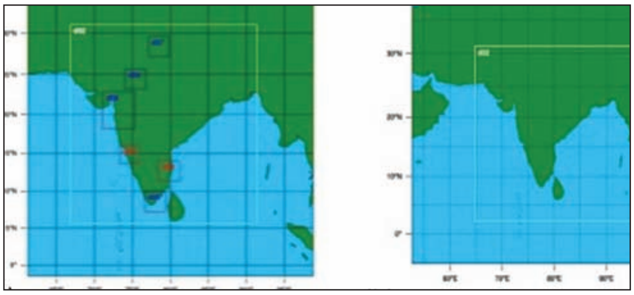

Fig. 1: Domains with (a) 2km (b) 3km grid resolution

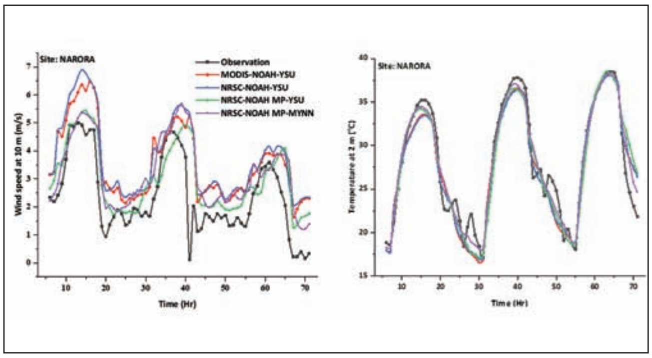

Fig. 3: Surface Observation of wind speed at 10m (left) and temperature at 2m (right) at Narora

Methodology

Model sensitivity to horizontal resolution is studied using two model configurations [3-domains 18, 6, 2 km; 2-domains 9, 2 km resolutions](Fig. 1). Further sensitivity to land cover using MODIS and NRSC data, land surface physics using NOAH and NOAHMP and PBL physics using YSU and MYNN 2.5 scheme are performed. Initial data by Global Forecast System on

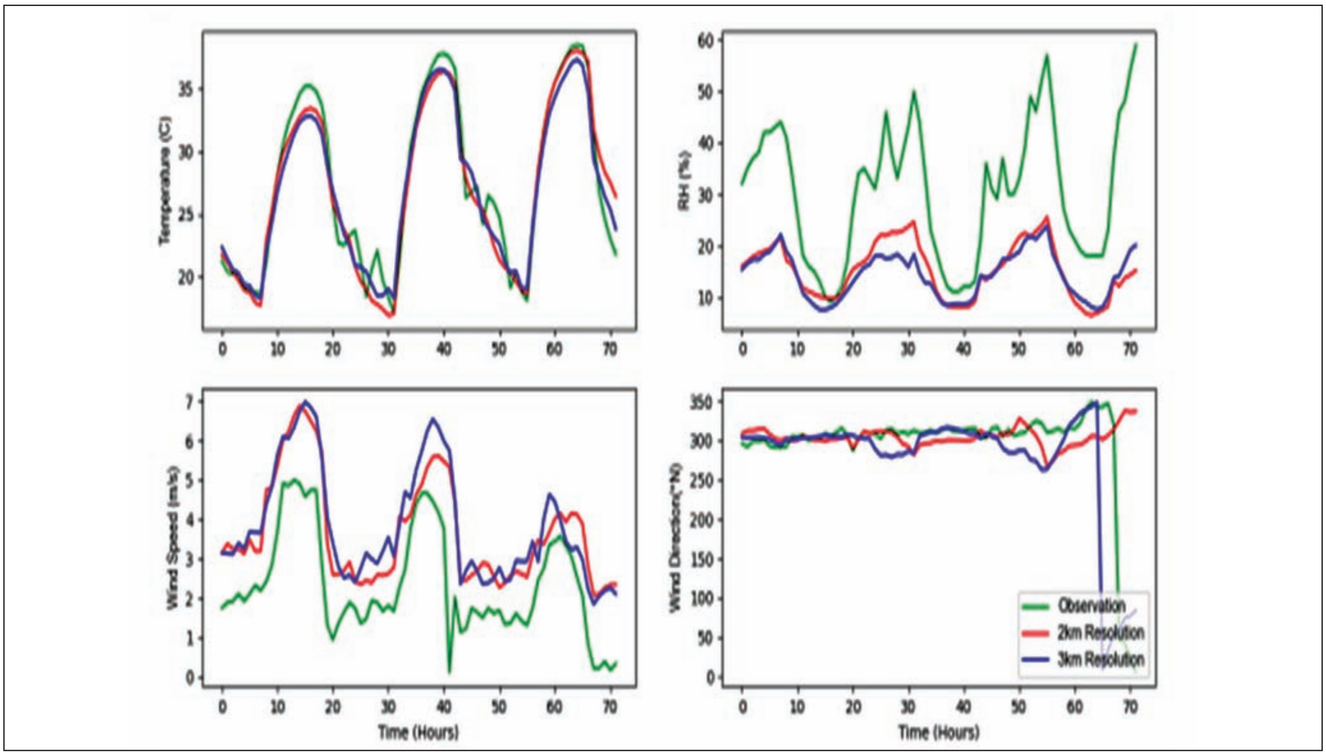

Fig. 2: Surface Observation at Narora for horizontal grid resolution sensitivity

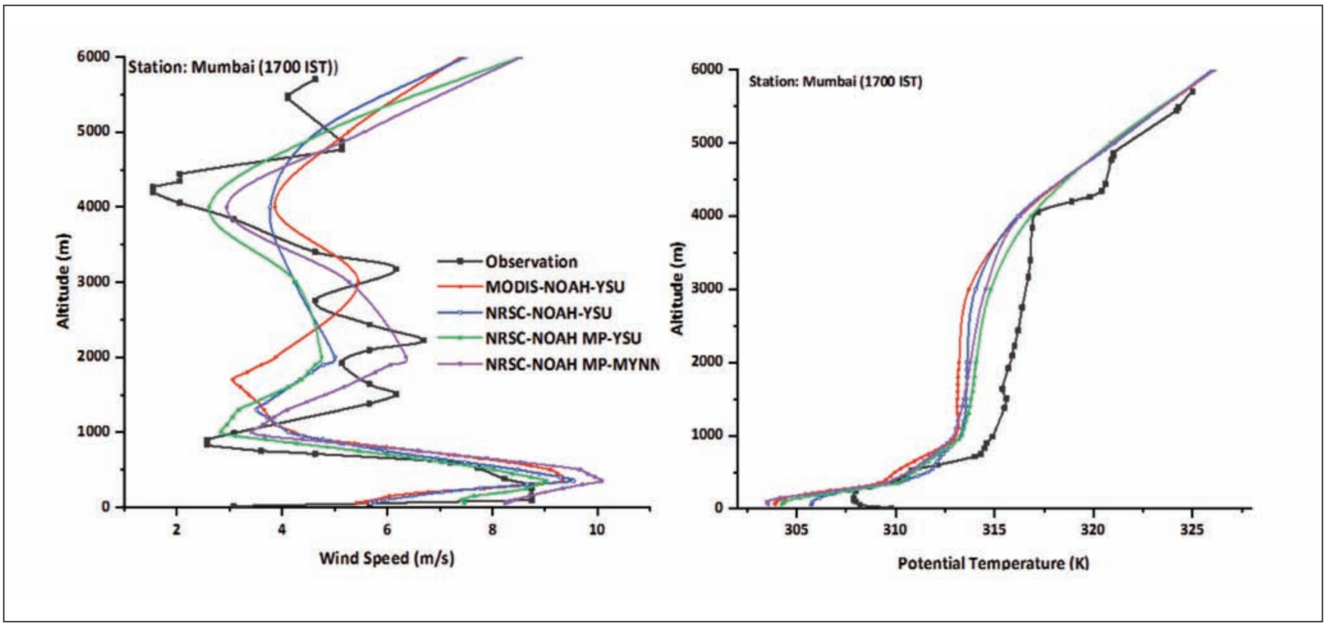

Fig. 4: Radiosonde Observation of wind speed (left) and potential temperature (right)

10th April, 2017 at 0.5°×0.5° and 3 hr resolution is used in the WRF model. The model physics includes WDM6 microphysics, Kain-Fritsch convection scheme in parent domain, MM5 Surface layer and RRTM/Dudhia for long wave/shortwave radiation scheme.

Results and Discussions

Table 1. Statistical Estimates				
Stat	Temp		Wind Speed	
	2 km	3 km	2 km	3 km
MB	-0.41	-0.51	1.33	1.37
RMSE	1.69	1.59	1.51	1.65
CC	0.97	0.98	0.86	0.86

Diurnal temperature trend and winds from NW and WNW at Narora in during April agree well (Fig. 2, Table 1) indicating both 2 km and 3 km resolution domains produce close forecast values.

Further sensitivity tests conducted with 3 km domain suggests that NRSC-NOAHMP-YSU (green line) combination better simulates the variation in both wind speed at 10 m and temperature at 2 m (Fig. 3). It also better simulates the vertical structure up to ~6 km among other combinations (Fig. 4).

The configuration (NRSC-YSU-NOAHMP) with NRSC land cover with more India specific land categories, NOAHMP which includes additional land physics such as dynamic vegetation, ground hydrology, canopy layer effect on rain and radiation transfer etc, and YSU which considers nonlocal turbulent eddies under convective atmospheric regime are found to yield better performance. Based on these results the WRF model with NRSC-NOAHMP-YSU with 3 km domain is implemented in the ONERS.

V.02 Soil - rice transfer (F_v) of Radionuclides in Local Rice Variety: A Site - Specific Observation from IGCAR Experimental Field

Information on soil-rice radionuclide transfer factors (F_v) in India is scarce. Site-specific soil-rice radionuclide transfer factor (F_v) is essential for public dose assessment. The objective of the study is to establish a database on site-specific transfer factors (F_v) as per IAEA-472 (2010) guidelines for natural and manmade radionuclides concerning the terrestrial environmental pathways for the Kalpakkam region. The results obtained will form the first-hand information from the Kalpakkam site. Soil to rice F_v for natural (^{40}K, ^{238}U, ^{232}Th, and ^{210}Po) and artificial (^{137}Cs and ^{90}Sr) radionuclides in rice grown in the experimental field at IGCAR are presented here.

Soil, and different parts of the rice plant (root, stem, leaf, and grain) in the log phase of growth and the matured stage were collected and analyzed. ^{137}Cs was below the detection limit in the soil and plant samples and hence the F_v could not be calculated. Among the natural radionuclides, ^{40}K was the most predominant and had higher activity in the harvested stem (609.95 ± 2.8 Bq/Kg). The matured grain had the lowest activity concentration (50.84 ± 9.1 Bq/Kg). In the log- phase different parts of the plant and the early grains (30 days old) had a relatively high ^{40}K as compared to the harvested grains except the stem. The root of the rice plant had a higher ^{238}U content (134.15 ± 3.8 Bq/Kg) followed by the stem (2.54 ± 1.4 Bq/Kg) and matured grain (1.52 ± 0.93 Bq/Kg). The early grain had a lower ^{238}U (0.19 Bq/Kg) as compared to the matured grain. Higher ^{232}Th (^{228} Ra) activity was observed in the root (48.63 ± 1.4 Bq/Kg) when compared to the stem and leaf. In the early grain ^{232}Th was 7.91 Bq/Kg and that of mature grain was 3.84 Bq/Kg (Fig. -1).The activity of ^{137}Cs and ^{90}Sr was below the detection limit (0.2 Bq/Kg) in 90% of the soil samples and all the rice grains.

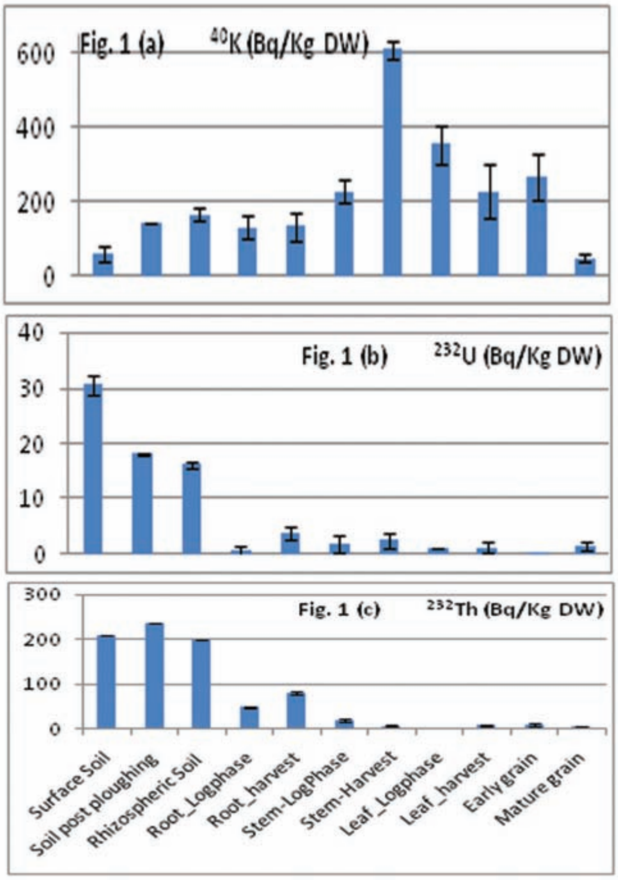

Fig. 2: Activity concentration of radionuclides in Rice

From the data obtained, it was observed that F_v of ^{40}K was highest in the stem (3.32) followed by the leaf(1.63) and root (0.95). F_v of ^{40}K in the mature grain was 0.036 and that of the early grain was 1.9. F_v of ^{40}K in Kaiga was reported as 1.5 in the grains, 4.9 in the straw, and 2.0 in the roots (Karunakar et al., 2013). Soil to rice F_v of ^{238}U in Kalpakkam was recorded at 0.008 in mature grains and 0.001 in early grains (Table1).Stem, leaf, and root had F_v values of 0.14, 0.07, and 0.21 respectively. F_v of ^{232}Th was found to be much lower as compared to 40K and was recorded as 0.002 in mature grains and 0.03 in the early grains. Root had higher F_v of ^{232}Th (0.34) when compared with stem and leaf (0.03 each). F_v of ^{232}Th and ^{238}U at Kaiga was reported as 0.041 and 0.05 by Karunakara et al., 2013.

Table-1.Soil-rice F_v of radionuclides at Kalpakkam

	^{40}K	^{238}U	^{232}Th	^{210}Po
F_v in Soil to rice (Present study)	3.6 x 10^{-2}	8.0 x 10^{-3}	2.0 x 10^{-3}	1.3 x 10^{-2}
F_vA in Soil to rice (IAEA TRS-472)	1.8 x 10^{-2} to 7.8 x 10^{-1}	8.56 x 10^{-6} to 9.0 x 10^{-2}	2.2 x 10^{-5} to 3.0 x 10^{-2}	9.4 x 10^{-3} to 1.7 x 10^{-2}

The site - specific F_v values from Kalpakkam are one degree lesser than the reported values of IAEA TRS - 472. A database on site-specific activity conc. of radionuclides and F_v values were established. ^{137}Cs and ^{90}Sr were BDL (0.2 Bq/Kg) in all the rice samples and more than 90% of the soil samples.

V.03

Back Trajectory Technique for Identification of Radiation Source using Gamma Dose Monitoring Data

During the operation of nuclear plants radionuclides are released to the atmosphere in low and permissible quantities. Environmental radiation monitors are installed across the Kalpakkam site for surveillance. At a multi-facility site the dose registered by monitors can be originating from several possible sources within the site. Detection and characterization of radiation sources is crucial to ensure radiological safety during both normal operation and in the event of unlikely accidental scenarios.

Back-trajectory Technique

Radionculides released to atmosphere are transported and diluted by the wind. The source can be identified by tracing the path of radionuclides at the receptor location. Here backward trajectory analysis technique in HYSPLIT (Hybrid Single-Particle Lagrangian Integrated Trajectory) dispersion model is used to trace the paths of radionuclides backward in time from receptors to identify likely source location. The observed significant radiation measurements above background level are compared with calculated dose rates from first guess locations by combining onsite wind direction, wind speed, atmospheric stability, and mixed layer height. Cluster analysis is then performed by computing the total spatial variances (TSV) and optimizing the number of clusters to identify source regions from patterns within the trajectory data.

Analysis of backward trajectories

Wind speeds and directions are measured using an onsite 50m meteorological tower. Stability is determined by calculating the Bulk-Richardson number and the mixed layer height is estimated using onsite SODAR observations. Back trajectories are computed at hourly intervals during different seasons, each characterized by unique wind flow behaviors. On 9th February 2021, the predominant wind vectors at the site fall in the NNE, NE, and ENE wind sectors. Consequently, AGDL-12, 22, 23, 24 (during 10 to 23 IST) and AGDL-11, 21 (during 02 to 14 IST) exhibit significant radiation doses. Backward trajectories analysis (Fig. 1) indicates that the majority of back-trajectories originating from various AGDLs pass through the vicinity of MAPS.

Fig. 2: Backward trajectories on 10th March'2021

On 10th March'2021, significant doses were recorded at AGDL-05 (during 08 to 20 IST) and AGDL-18, 19 (during 00 to 23 IST) due to Easterly winds. While the majority of trajectories during this period pass through the vicinity of MAPS, it is observed that a few trajectories also converge near FBTR (Fig. 2).

Cluster Analysis

Through TSV analysis, the back trajectories have been categorized and optimize into 8 clusters (Fig. 3).

The cluster analysis indicates that MAPS has the highest percentage (39%) in the cluster-mean trajectory, establishing it as the primary source of radiation around the site. In contrast, FBTR makes a minor contribution to radiation, with 8% of cluster-mean trajectories passing through its vicinity.

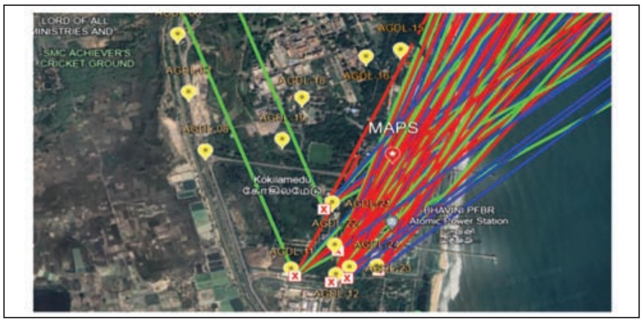

Fig. 1: Backward trajectories on 9th February'2021

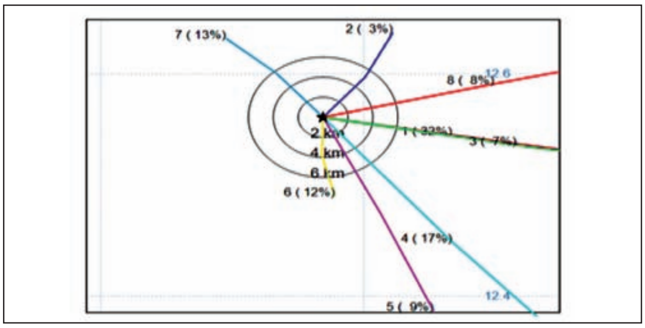

Fig. 3: Clusters of backward trajectories on March'21

V.04 Retrospective Dose Estimation from Tooth Enamel using EPR

Tooth enamel, mineralized in hydroxyapatite crystal, is a potential material for electron paramagnetic resonance (EPR) dosimetry. Radiation doses received by humans can be assessed retrospectively, if the patients provide extracted teeth. However, extraction of healthy tooth is invasive, thus not recommendable. So, animal teeth can be used as surrogate to human teeth. In this work, goat tooth enamel was taken and its dosimetric properties like of EPR signal analysis, dose response, fading, and dose reconstruction were studied using EPR.

Materials and methods: Goat molar and premolar teeth were collected from a local shop in Kalpakkam. The enamel was extracted from tooth using alkaline denaturation method and used in this work. EPR measurements were performed using a Bruker EMX X-band (9.8 GHz) EPR spectrometer. Gamma irradiations were performed at room temperature using ^{60}Co source calibrated in terms of air kerma.

Results and discussion

Various EPR parameters were optimized to avoid signal saturation, clipping, broadening and distortion and used in this work for irradiated tooth enamel. Fig. 1 shows the experimental, deconvoluted and fitted EPR spectra of irradiated (10 Gy) tooth enamel. The signal at g = 2.0043 is due to inherent native signal (NS). The signal at $g_\perp$ = 2.0018 and $g_{||}$ = 1.9974 is termed as dosimetric signal (DS) and is assigned to stable CO_2^- radicals.

The perpendicular component of DS is used for all quantitative dosimetric studies as it is dose sensitive. The EPR dose response curve for irradiated tooth enamel was established (Fig. 2). The response was found to be linear up to 100 Gy.

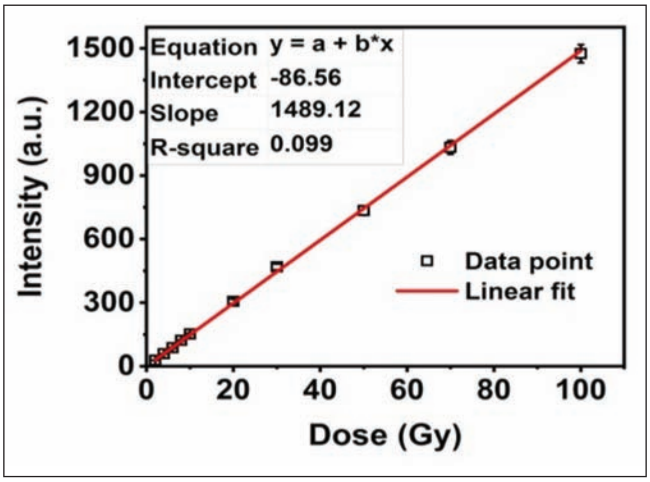

Fig. 2: EPR dose response of tooth enamel

The fading of DS was studied by measuring the EPR spectra of irradiated enamel at different storage time (Fig. 3). From the Fig., it is clear that the signal fading is within statistical fluctuation of ± 5 % up to 30 days of storage.

Single aliquot additive dose (SAAD) technique was used for dose reconstruction. The doses were found to be reconstructed with ± 2.5 % error, which is within the recommendation of IEC for radiation dosimeters. The validation of this technique with standard alanine/EPR dosimetry system showed satisfactory results.

The outcomes of this study suggest that animal tooth can be a good alternative to human tooth for retrospective dose estimation in accident dosimetry.

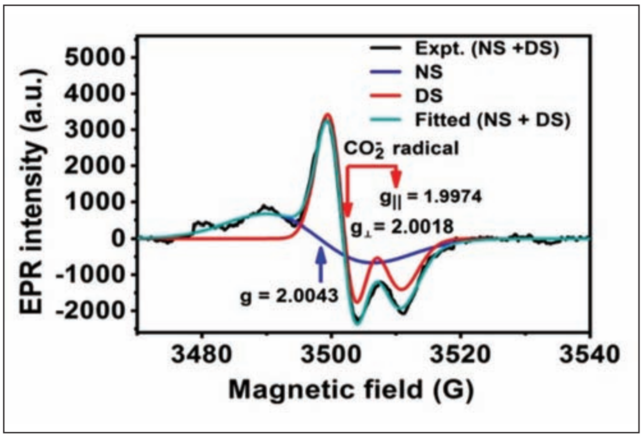

Fig. 1: EPR spectra of irradiated tooth enamel

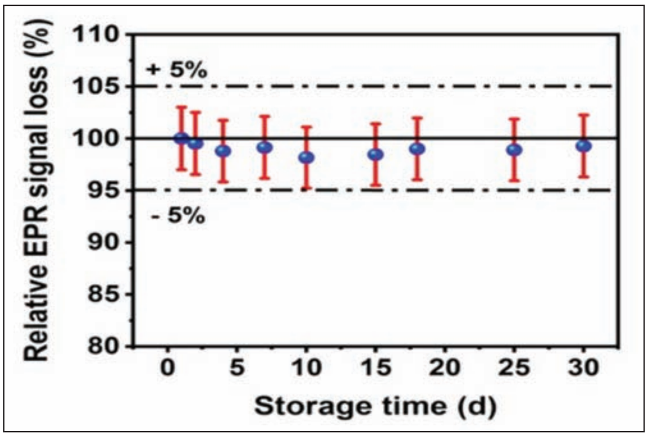

Fig. 3: Fading of DS of irradiated (10 Gy) enamel

V.05

Synthesis, Characterization and Dosimetry Studies of Metal Organic Framework

Metal organic frameworks (MOFs) are hybrid porous materials consisting of organic linkers and inorganic nodes. The periodic arrangement of inorganic nodes and bridging organic ligands results in crystalline framework materials with ultra-high porosity and enormous internal surface area. MOFs are used in gas storage, catalysis, thin film devices, luminescent materials, and biomedical imaging. MOFs are deployed in nuclear industry for radionuclide separation, radiation dosimetry, and detection. In the present work, the possibilities of using uranium MOF as OSL dosimeter are explored.

Synthesis and Characterization

Uranyl MOF $(UO_2)_4(C_2O_4)_4(C_4O_4)[N(CH_3)_4]_2$ is synthesized by hydrothermal method using uranyl nitrate, oxalic acid, succinic acid, tetramethyl ammonium bromide and dilute nitric acid. Uranyl ion reacts with oxalic acid and forms uranyl oxalate chains, which convert to uranyl oxalate carboxylate sheets by reacting with succinic acid and further extend to the 3D framework of Uranyl MOF. The formation of Uranyl MOF is confirmed by FTIR, XRD and photo luminescence analysis.

OSL decay curve of MOF

OSL measurements of irradiated and unirradiated MOF was carried out at room temperature using an automatic Riso TL/OSL reader (model DA-20) with blue LEDs (λ=470 ± 30 nm) as stimulation source. The recorded OSL signals of MOF are shown in Fig. 1. A negligible signal was found in unirradiated MOF, and significant increase in OSL signal was observed due to irradiation.

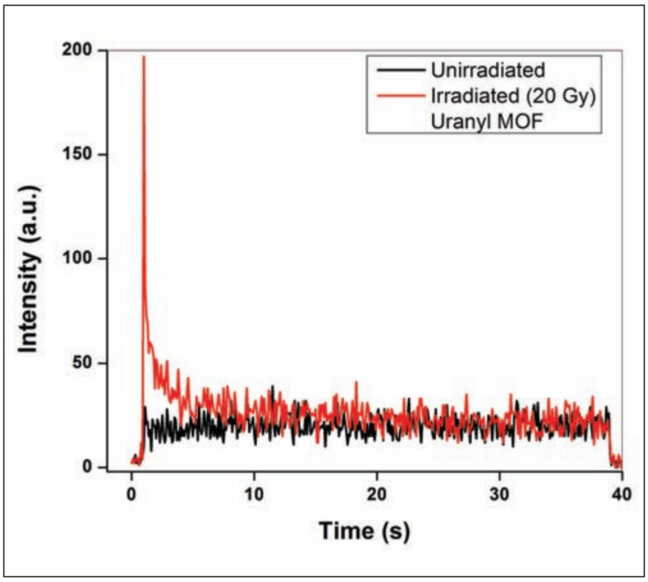

Fig. 1: OSL response of Uranyl MOF

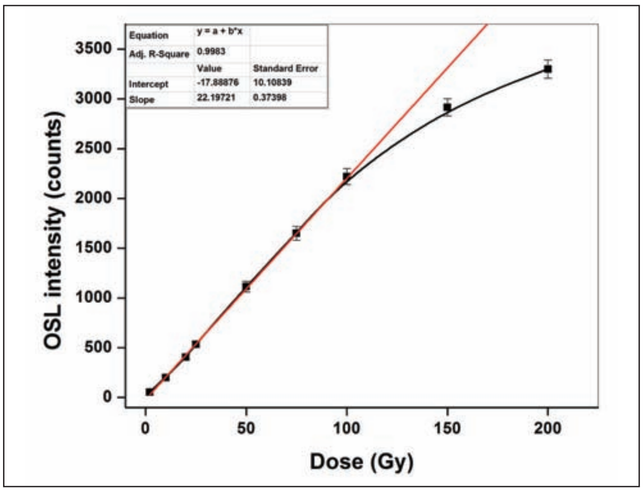

Fig. 2: Dose response of Uranyl MOF

Dose Response and minimum detectable dose

In order to check the OSL response of MOF, 3 samples of MOF (5 mg each) were irradiated to doses in the range of 1 Gy to 200 Gy using reader in built Sr^{90}/Y^{90} beta source (dose rate .1 Gy/s). The OSL signal intensity increases linearly from 2 Gy to 100 Gy, showing a sublinear behavior beyond 100 Gy.

The minimum detectable dose (MDD) is estimated from three times the standard deviation of the background OSL signal of unirradiated MOF samples. The estimated value of MDD for Uranyl MOF was 1.1 Gy.

Repeatability studies and fading studies

The repeatability of the OSL output of the MOF has been tested for 10 cycles of irradiation and OSL readout. The OSL output variation was ± 7 % relative to first cycle OSL output. The fading test was carried out by exposing multiple aliquots of MOF to 20 Gy of beta irradiation and OSL readout was recorded with different storage timings. The signal intensity of Uranyl MOF reduces to around 15% of the original value in thirty days of storage.

Conclusion

The Uranyl MOF displayed promising OSL dosimetric properties with linear dose-response up to 100 Gy with 1.1 Gy MDD, good repeatability, and decent radiation stability.

V.06 Installation and Commissioning of Dual Polarized C-band DWR at IGCAR

A C-Band Polarimetric Doppler Weather Radar (DWR) is installed at IGCAR, Kalpakkam in collaboration with ISRO Telemetry Tracking and Command Network (ISTRAC) Bangalore under the ministry interaction "Application of Space Technology in DAE" towards atmospheric modelling needed in the weather and plume dispersion forecasts for nuclear emergency response and disaster management applications. The continuous data from this instrument facilitates improved weather predictions with data assimilation techniques besides opportunities to undertake research on atmospheric phenomena.

Specific features of DWR

The RADAR was installed at Kalpakkam site along with Endurance test, Site Acceptance Tests and calibration completed during April-Sep 2023. DWR established at Kalpakkam is dual polarized pulsed Radar with operating frequency of 5.6 GHz. It can monitor weather systems in the range of up to 450 km around the Nuclear Power Plant (NPP) site. It employs 4 kW Solid State Power Amplifier (SSPA) based transmitter. Fig. 1 shows the Radar electronics rack (SSPA transmitter, digital receiver and power supply), servo sub-and antenna sub-systems. The Radar can be operated remotely through a web-based application called Radar User Control Application (RUCA). The radar can be operated in various modes such as sector, volume, designated. The system can cover 360◦ azimuthally and 0◦ to 90◦ vertically covering the entire troposphere to scan deep convective cloud systems.

Fig. 1: (a) Radar electronics with SSPA transmitter and Servo Sub-system, (b) Radar antenna

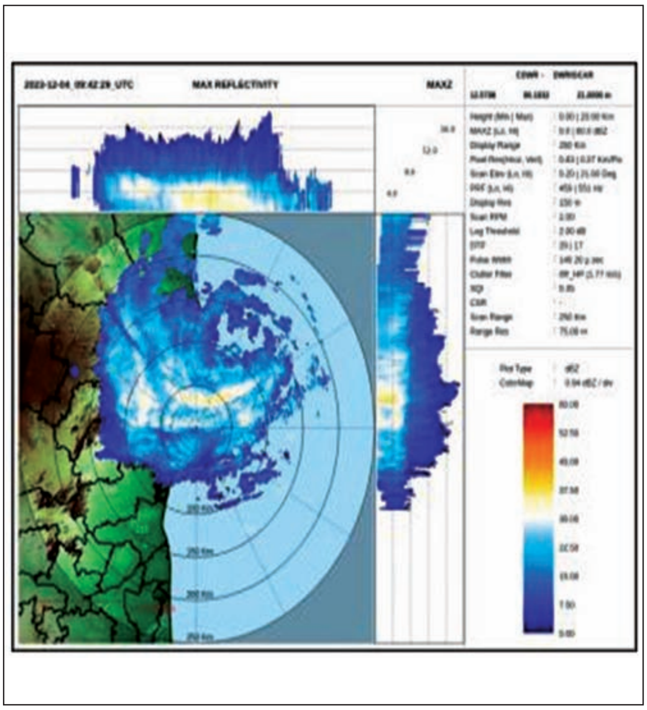

Fig. 2: Maximum Reflectivity(dBZ) as observed by Radar

Operation of radar and important results

DWR is operated for over 200 days since May 2023 to monitor the weather during SW/NE monsoon seasons and important events are analyzed. The movement of Michaung cyclone on 4th Dec'2023 is captured by the Radar. It shows comma type cloud structure with spiral bands. Observed cloud band structure and distribution of reflectivity (≤40 dBZ) is depicted in Fig. 2. Intense convective activity in the rear southwest sector of the cyclone, less cloud activity in the forward sectors and central eye region free from cloud is clearly visible from Radar images. Further analysis of weather events using radar data is in progress.

V.07 Thermal Diffusibility Measurement of Metal Plates Using Non-contact Flash Method

The knowledge of thermophysical properties of materials plays vital role in design, operation and life extension of nuclear power plants. Apart from temperature, thermophysical properties of a material depend on radiation exposure, porosity, thermal treatment, etc. Non-contact techniques are preferred for measuring thermophysical properties at high temperatures and harsh environments. One such method is being discussed in this article.

Thermal diffusivity (α) is one such important thermophysical property that indicates the ability of a material to conduct heat relative to its ability to store heat, as given by equation (1). Here, k is the thermal conductivity, ρ is the density, and c is the specific heat capacity of the material.

$$\propto = \frac{k}{\rho c} \qquad (1)$$

The laser flash method is the most widely used non-contact method for measuring thermal diffusivity. In this technique, a high-energy laser flash of short duration (typically a few milliseconds) is used to heat the front surface of the sample. The time-dependent temperature rise at the rear surface is recorded using a radiation-based detector. The thermal diffusivity can be calculated using equation (2) by measuring the time taken for the temperature to reach half of its maximum ($t_{1/2}$). Here, L is the thickness of the sample. In a nuclear reactor, measuring the thermal properties of irradiated materials is one of the challenging tasks. For this, a single-sided area based technique is always preferred. Hence, the flash lamp-based Pulsed Thermography technique in reflection mode has been adopted and the results are compared with values obtained using classic transmission mode. Equation (3) is used for thermal diffusivity calculation in reflection mode, where t_2 is the peak time in second the derivative plot of time-temperature in the log domain. The schematic diagram of the technique and the time-temperature response for transmission and reflection modes are shown in Fig. 1 and 2.

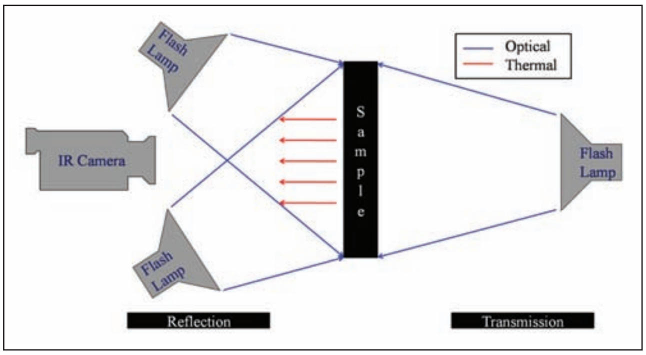

Fig. 1: Schematic Diagram of the Experimental Setup

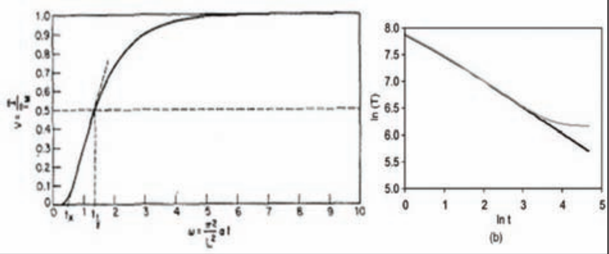

Fig. 2: Temperature response in transmission & reflection

$$\alpha = \frac{1.38L^2}{\pi^2 t_{1/2}} \qquad (2) \qquad \alpha = \frac{L^2}{\pi t_2} \qquad (3)$$

The experimental study was carried out using a Xenon flash lamp with a power of 3600 W and a cooled IR camera with a pixel resolution of 640 x 512 and a thermal resolution of 20 mK. A detailed experimental investigation was carried out on the effect of energy, frame rate, and coating thickness of the black paint applied on the surface (to improve the emissivity). It was observed that the error in diffusivity measurement was high for lower flash energy, while the surface coating thickness had least effect on the measurement. In addition, if the diffusivity of the inspecting material is high, one should use a higher frame rate to achieve accurate measurement.

The experiment was carried out on plates of SS 316 L, mild steel, and aluminum with a thickness of 3-mm. The actual thermal diffusivity values were taken from standards. Measurement was done using both reflection and transmission modes, and the results are tabulated in Table 1. From Table 1, it can be observed that the thermal diffusivity could be measured with good accuracy in reflection mode.

Table 1 Measured thermal diffusivity for different metals

Metals	Actual value (mm^2/s)	Measured Value (mm^2/s)			
		Reflection Mode	Error %	Transmission Mode	Error %
Aluminum	83	76.85	7.4	81.23	2.13
Mild steel	14	14.71	5.07	15.83	13.07
SS 316 L	4	3.59	10.25	3.76	6

The feasibility of Pulsed Thermography technique in reflection mode for thermal diffusivity measurement is successfully evaluated.

V.08 Investigation of Modified Fricke Dosimeter for Low-dose Irradiation Applications

The Ferrous and Ferric chemical dosimeter (Fricke dosimeter) is one of the most commonly used chemical dosimeters with acceptable accuracy in the 20–400 Gy dose range. The Fricke dosimeter is unsuitable for low-dose irradiation (1-10 Gy) applications. The modified Ferrous and Ferric chemical dosimeter with Benzoic acid is used for low-dose irradiation applications. This study evaluates the dosimetric parameters (molar extinction coefficient and chemical yield) of the FBX (Ferrous-Benzoic-Xylenol) dosimeter in low-dose irradiation applications.

The FBX dosimeter is prepared with the following chemical composition: 0.2 mol m^{-3} Ferrous Ammonium Sulfate, 5.0 mol m^{-3} Benzoic acid, and 0.20 mol m^{-3} Xyelnol orange (XO) in 40.0 mol m^{-3} Sulphuric acid. The molar extinction coefficient value of the FBX dosimeter is determined from the measured absorbance values at 548 nm for different Fe^{+3} ion concentrations. The absorbance values are measured using the UV-visible spectrometer. The molar extinction coefficient (Ɛ) is found to be 18753 ± 530 $M^{-1}cm^{-1}$.

The absorbed dose is determined from the established calibration curve between the absorbance values at different dose values. The FBX dosimeter is irradiated in the 1-7 Gy dose range and the color change before and after irradiation is depicted in Fig. 1. The Fig. 2 shows the absorption spectra of irradiated FBX dosimeter at different dose intervals. Fig. 3 shows the calibration curve between the absorbance values of the irradiated FBX dosimeter and absorbed dose values. The correlation coefficient is found to be 0.99. The radiochemical yield (G) is defined as the number of Fe^{+3} ions formed per 100 eV of energy absorbed in the chemical dosimeter after irradiation. The chemical yield (G) is determined from the calibration curve between absorbance and absorbed dose values. The average G value is found to be 4.7 ± 0.1 X 10^{-6} mol/J.

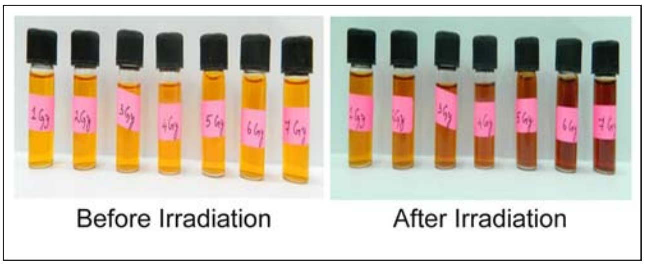

Fig. 1: FBX Dosimeter before and after irradiation

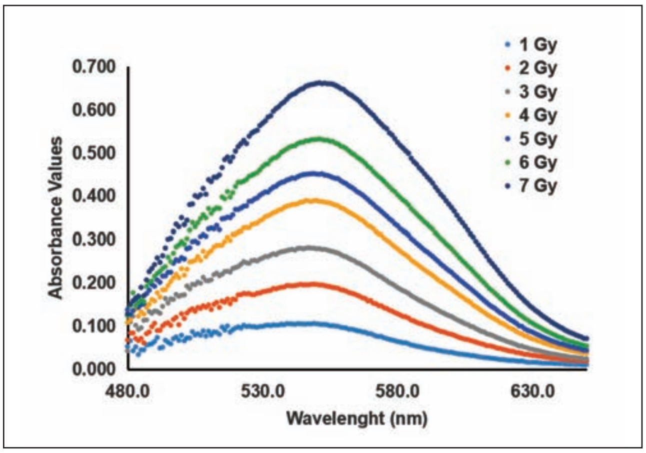

Fig. 2: Absorption spectrum of an irradiated dosimeter at different absorbed doses

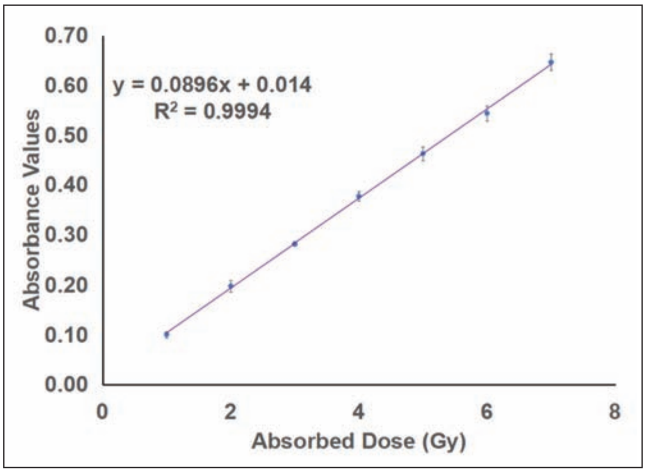

Fig. 3: Calibration curve of FBX Dosimeter

V.09 Modeling Parallel Disc Capacitor Probes using Algebraic Topological Method for Determination of Dielectric Permittivity of Solid Insulators as per IEC D150 Standard

In order to characterize solid and liquid insulating materials, parallel disc capacitor (PDC) probes are widely used. The non-destructive dielectric permittivity assessment of insulators in electrical systems is an example of this application. The dielectric constant and dielectric losses evaluation in solid insulating materials using parallel metallic disc probes is described in the ASTM D150 (IEC 60250) standard. Numerical modeling and simulation of such probes helps in interpreting the test results and understanding the physical principles involved.

This work presents the Algebraic Topological Method (ATM), an unconventional numerical technique that we use to model the geometry of parallel disc capacitors with various dielectric materials. The conventional numerical methods such as FDM, FEM and MoM use field formulation using vector variables for computations in electromagnetics. In contrast, the algebraic topological method offers computations in electromagnetics exclusively with scalar quantities. Hence ATM directly gives discrete algebraic forms of equations which can be solved with simple matrix solvers. This makes the computational algorithm simple and efficient in terms of computational resource requirements. We validate the results of the ATM with both experiment and Finite Element Model (FEM).

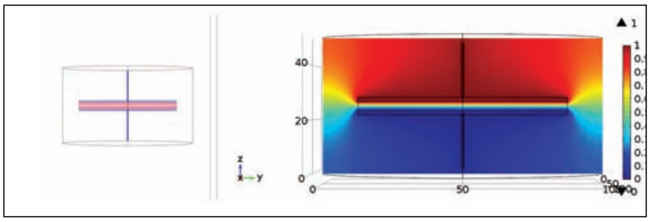

Fig. 2: Parallel plate capacitor model and electric potential distribution as numerical solution from Algebraic topological method

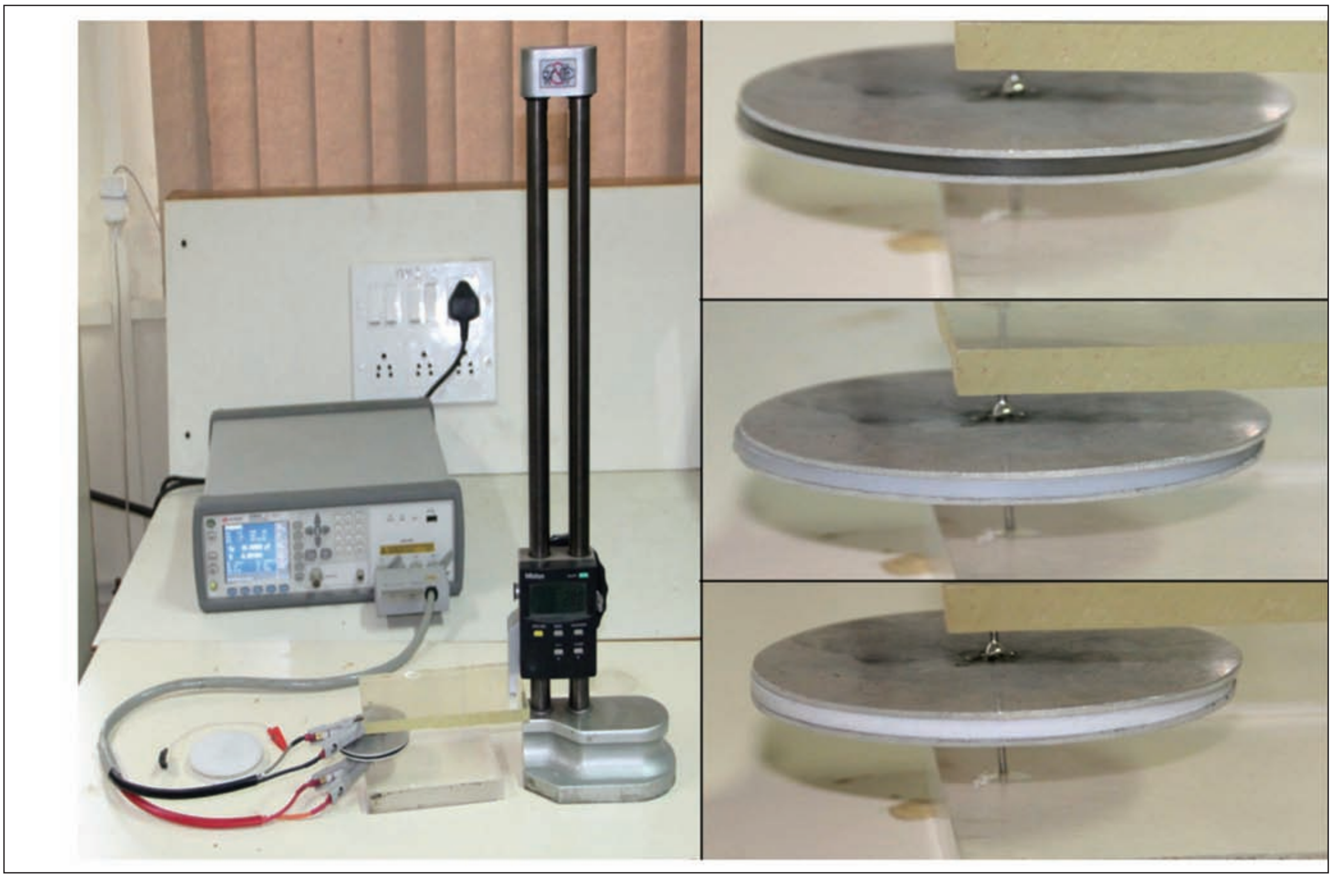

Fig. 1: Parallel disc capacitor probes with different solid dielectrics and the capacitance measurement using LCR meter.

Table 1: Dielectric constant measurement results for Teflon, Nylon and Perspex discs

Material	Density (kg/m^3)		Dielectric constant	
	Data sheet	Measured	Datasheet	Measured
Teflon	2200	2187	2	1.62
Nylon	1140	898	3-5	1.79
Acrylic(Perspex)	1133	1170	3-5	2.35

Table 2: Comparison of capacitance of PDC from measurement and computation

Dielectric material	C Measured (pF)	C using FEM (pF)	C using ATM (pF)
Air	13.706	14.979	13.769

Two metallic (Aluminum) discs measuring 75 mm in diameter and 1.5 mm in thickness make up the PDC probe under study. They are connected with SS terminals measuring 20 mm in length and 1.2 mm in diameter, and they are kept apart by a dielectric material.

The capacitance of the probe with Air, Teflon, Perspex and Nylon as dielectric materials was measured using LCR meter (Fig. 1). The dielectric constants of Teflon, Nylon and Perspex were calculated from the ratio of capacitance with air and the respective medium as per ASTM D150 standard. The values found to be lesser than the values mentioned in the datasheet of the dielectric material (Table 1). This is due to the density variation of material depending on manufacturing process and grade of the material. These dielectric constant values were used in the ATM numerical model. The PDC model is designed in an air region surrounding it with a diameter of 100 mm and a height of 50 mm (Fig. 2) to account for leak fields. The 3D capacitance was extracted by calculating the energy stored in the dielectric medium.

The ATM predictions were compared with the COMSOL Multi-Physics result and measurement for air capacitor. The results demonstrate that the ATM could predict the parameters such as electrostatic potential (Fig. 2), electric field including fringing fields, stored energy and 3D capacitance (Table 2), of the PDC model accurately and the predictions are in good agreement with FEM and experiment results. Further works are in progress to include inhomogeneous dielectric mediums in the capacitor models and solve it using the ATM scheme.

V.10 Optimising Parameters for High Contrast Corrosion Mapping of Zr-4-Ti-304L SS Weld Joint using AC-SECM

The localized electrochemical activity of individual material in multi-layer welded joints varies when immersed in an electrolyte, due to the difference in their electromotive force. The local electrochemical studies of such multilayer weld joints are rarely reported as the conventional potentiodynamic polarization, and electrochemical impedance spectroscopy studies provide averaged information from the entire surface of a heterogeneous sample. Intermittent contact alternating current scanning electrochemical microscopy (IC-AC–SECM) has been used to image the local electrochemical activity of Zr-4-Ti-304L SS dissimilar weld joint without a redox mediator at an open circuit potential. The schematic drawing depicting the experimental set up and scanned region of the sample is shown in Fig. 1a. The simplified equivalent circuit describing the IC-AC-SECM cell setup is shown in Fig. 1b. The potentiodynamic polarisation of the Pt UME in tap water was performed from –1.1 to +0.8 V with respect to its OCP at a scan rate of 0.1667 mV/s to determine the optimum DC bias potential for enhanced sensitivity of the Pt UME

The potentiodynamic polarization behaviour of Pt UME carried out in tap water revealed that the Pt UME biased with potential at –0.5 V was ideal for obtaining better sensitivity due to the maximum reduction of dissolved oxygen in the electrolyte.

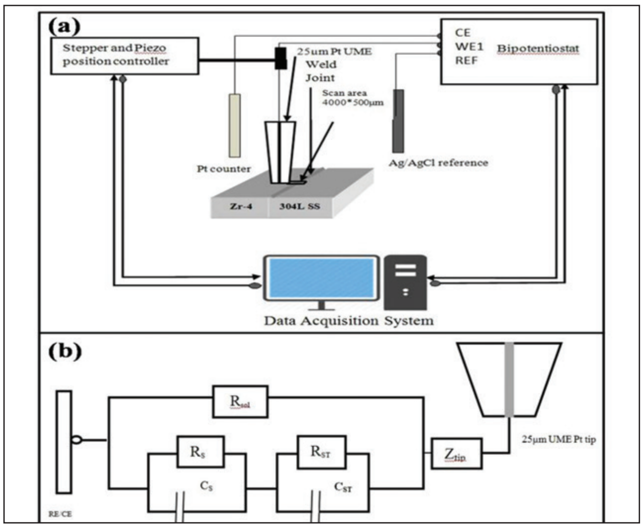

Fig. 1: (a) Schematic depicting dissimilar joint sample and IC-AC-SECM experimental setup (b) Equivalent circuit representing the Pt UME electrode in the proximity of an unbiased base electrode.

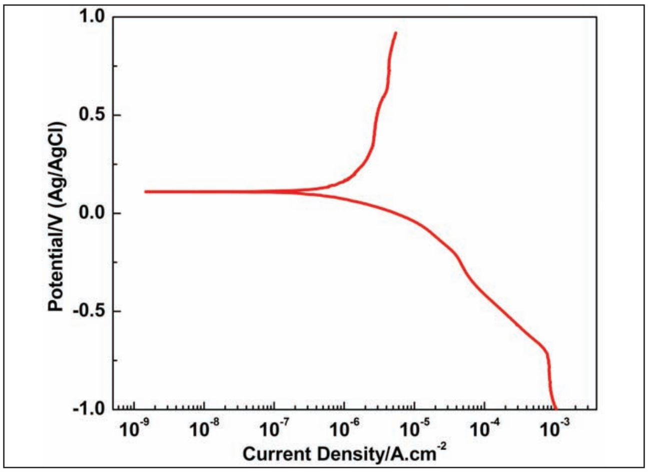

Fig. 2: Potentiodynamic polarization curve of 25 µm Pt UME in tap water.

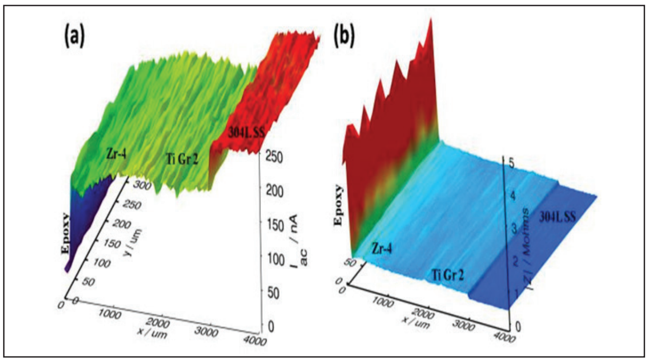

Fig. 3: IC-AC-SECM imaging of Zr-4-Ti-304L SS weld joint in tap water (a) current, (b) impedance magnitudes in 3D.

The polarization curve of Pt UME (Fig. 2) in tap water showed a significant difference in current density between the cathodic and anodic branch. The higher value of cathodic current density is associated with the dissolved oxygen reduction reaction (ORR) in the neutral tap water.The frequency dependent impedance behaviour of Pt UME, in the vicinity of a metal, revealed a maximum difference in the magnitude of current and capacitance values between 304L SS and Ti / Zr-4 at ~ 10 kHz. This suggests that, a perturbation frequency of 10 kHz could provide a maximum contrast in imaging the local electrochemical activity variation over the Zr-4-Ti-304L SS dissimilar metal weldment.

Fig. 3a and 3b represent the current and impedance magnitude map of 4000 × 300 µm area across the Zr-4-Ti-304L SS dissimilar weld joint.This study allowed better contrast in mapping local current and impedance magnitude across the weld joint by applying an optimum dc bias of –0.5 V to the Pt tip and perturbation frequency of 10 kHz.

V.11 A priori generation of defect signatures during magnetic nano-emulsion aided optical detection of defects in carbon steel components

Magnetic flux leakage (MFL) is one of the most common and economical techniques for non-destructive testing and evaluation of carbon steel components. When a ferromagnetic material containing a defect is magnetized, MFL occurs in the vicinity of the defects due to the magnetic permeability mismatch. Non-destructive evaluation of the defect is achieved by detecting the MFL using a suitable magnetic sensor (like magnetic particles, search coils, Hall probes, superconducting quantum interference devices, fluxgate sensors, etc.), and the experimental data are compared with various analytical or numerical models of MFL for interpreting the severity and locations of the defects accurately. For acquiring the MFL data, the above-mentioned sensors require time-consuming raster scans over the specimen surface. As an alternative, a magnetic nano-emulsion (MNE) based wide-area and non-contact optical sensor was developed earlier, where a visible optical pattern was discernible over the defect locations when the sensor containing the MNE was placed over the specimen surface, without the requirement of raster scanning or data processing (shown in Fig. 1a). The MFL, in the vicinity of the defects, causes an oriented linear arrangement within the MNE, which acts as a tunable 1D grating and generates optical contrast visible to the naked eye that indicates the presence of the defects. The detection of notches, rectangular and cylindrical defects were earlier demonstrated using the MNE-based sensors, where the generated optical contrast was qualitatively correlated with the severity of the defects. However, no studies were previously performed to theoretically predict the optical patterns, which is essential for the rapid evaluation of the defects.

A priori prediction of the optical patterns is extremely useful for optimizing the magnetizing field, lift-off distance, estimating the probability of detection, selection of suitable MNE sensor, and refining the inspection procedure without performing numerous time-consuming experimental trials. This is the primary objective of the present study. In the presence of a DC magnetic field (H_{DC}), the MNE droplets form a linear chain-like structure, parallel to the direction of the H_{DC}, where the inter-droplet separation decreases with increasing strength of the H_{DC}. This results in a blue shift of the wavelength corresponding to the maxima of the Bragg reflection profiles (λ_{max}), when exposed to a polychromatic light. Unique λ_{max}-H_{DC} calibration curves (shown in Fig. 1b) were obtained for various types of MNEs depending on the nature of the stabilizing moieties, like charged or neutral surfactants. Thereafter, the surface distributions of the MFL (shown in Fig. 1b) were obtained using a finite element model for various defects geometries. Here, the MFL, in the vicinity of the defects, acts as H_{DC}, and hence, utilizing the λ_{max}-H_{DC} calibration curves, the surface distributions of the MFL were converted to the surface distributions of λ_{max} values, which were then pseudo colour-coded to theoretically generate the optical patterns. The presence of the rectangular slots, double rectangular, cylindrical, and buried defects were clearly discernible from the simulated optical patterns, which were in good agreement with the experimentally recorded patterns (shown in Fig. 1a-b). Defect depth-dependent intensity variations and the defect widths estimated from the simulated images were in accordance with the data obtained from the experimental images, thereby validating the efficiency of the developed scheme for a priori prediction of the optical patterns. Further, the findings will be beneficial for the selection of appropriate MNE-based sensors, reducing inspection time, and developing automated inspection routines with enhanced detection capabilities.

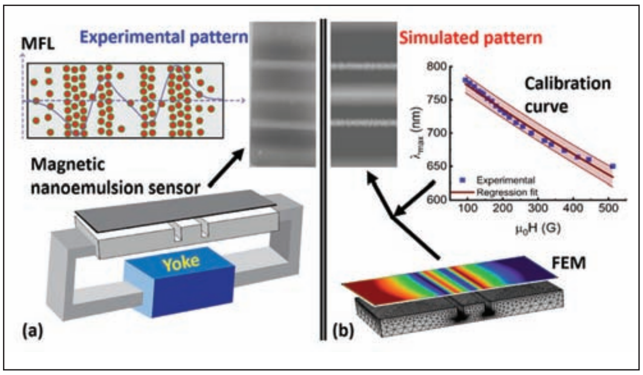

Fig. 1: (a) Magnetic nanoemulsion based optical detection of defects in carbon steel specimens. The experimentally recorded optical pattern and the experimental set-up are shown in the figure. (b) Theoretical simulations involving finite element model (FEM) and λmax-DC magnetic field (HDC) calibration curves for a priori generation of the optical patterns. The simulated optical pattern is shown in the figure

V.12 Development of Electrospun Superparamagnetic Fibrous Composite Nano-fiber Films for Enhanced Oil Sludge Recovery

Accidents and spillage of oil are causing an increase in oil pollution, impacting a serious concern to aquatic biota and the marine environment. This necessitated the requirement of cost-effective oil remediation with improved performance compared to traditional approaches such as skimmers and burners. In this context, superparamagnetic polyvinylidene fluoride (PVDF) composite nanofiber material was fabricated, which is suitable for enhanced oil sludge removal applications. The magnetic composite material was synthesized using an electrospinning technique by incorporating cellulose and manganese capped super-paramagnetic particles in the PVDF solution. Organic coating and inorganic capping of superparamagnetic magnetic nanoparticles(MNPs) are done to enhance the dispersibility of nanoparticles in the polymer solution using carboxymethyl cellulose and manganese oxide (MnO_x), respectively.

MNPs were synthesized using the oxidation precipitation method and hydrothermal method. The carboxymethyl cellulose and manganese oxide capping not only provided a homogenous dispersion, but also enabled interaction with poly(vinylidene fluoride) at the interface through H-bonding, thereby increasing the interfacial compa-tibility. Oil adsorption studies were carried out using oils with different carbon lengths and densities (octane, dodecane, kerosene, and oleic acid). An increase in sorption capacity with an increase in magnetic nanoparticle loading in PVDF is observed. The highest sorption capacity of 35.3 g/g for oleic acid was observed with 10 wt% loading of MNPs. The prepared fibers were hydrophobic with a water contact angle (WCA) between 119 and 128° as shown in Fig. 1(a).

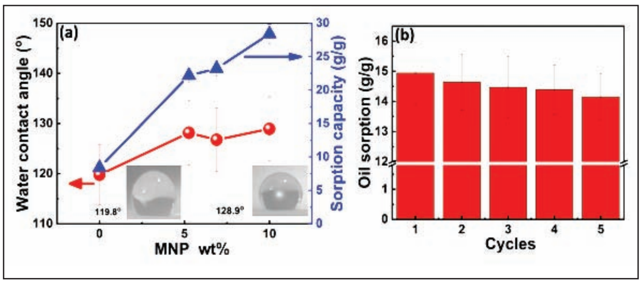

Fig. 1: (a)Water contact angle values and sorption capacity of octane using MNP/PVDF as a function of wt% of MNPs, inset shows the sessile water droplet of nascent PVDF fiber(119.8°) and 10 wt% MNP/PVDF(128.9°) (b) Regeneration studies for 5 cycles using 5.3 wt% MNP/ PVDF and dodecane

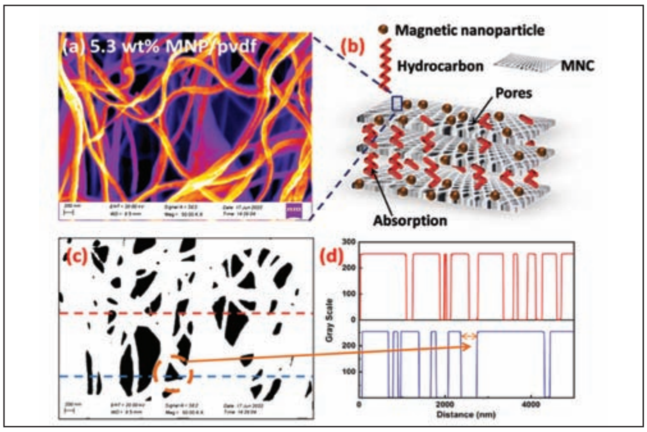

Fig. 2: (a)Pseudo-colored contrast SEM image of nanofiber (b) Schematic of oil sorption(c) The corresponding gray scale image showing the pores (shown as black spots)The orange circle in image (d) shows the size in the line profile in image

The feeble coercivities and remanence of superparamagnetic nanoparticles were ideal for regeneration.Only a very slight reduction in oil sorption capacity was observed after regeneration for five cycles (Fig.1(b)). Among various oils, oleic acid showed maximum sorption capacity. This may be due to the optimal pore size for the carbon length of oleic acid for the studied system. To have further insight into the number density and pores, pseudo-colored contrast images of 5.3 wt% MNP/PVDF was obtained and is shown in Fig. 2(a) and the schematic showing the hydrocarbon (oil) absorbed into the pores of the magnetic nanofibers followed by entrapment or retention due to the coalescence of oil in the rough and porous structure as shown in Fig. 2(b). The corresponding grayscale image (Fig. 2(c)) where the pores are shown as black spots. The line profiles of the images are shown in Fig. 2(d). Further, the fibers must have an optimum pore size to retain the oil without passing through the fiber. In the case of MNCs, the addition of MNPs lead to improved performance due to a decrease in the pore size and permeability of oil as compared to nascent PVDF. This is because the increase in the loading of MNPs resulted in an increase in the conductivity of PVDF and more discharge of solutions. This results in a higher number density of fibers and smaller pore size. This new procedure overcomes the problems of non-uniform anchoring on fibers, agglomeration of particles, and multiple steps involved in the fabrication process and shows the immense prospect of the prepared composite for oil sludge removal.

V.13

Unravelling the Complexities of $(Fe,Cr)_2B$ Structures in high B Content Steel using Ultra High Resolution Analytical TEM and Theoretical Modelling

High boron content steels (HBS) have generated significant interest to the nuclear scientist for spent nuclear fuel storage application owing to high neutron absorption cross section of B. Understanding the Cr distribution as well the formation of borides is quite important in order to assess the in-operando behavior of the high boron steel. Solubility of Cr in Fe_2B is thought to be responsible for the superior toughness of the material. In the present work, 5wt% Boron added Mod. 9Cr1Mo ferritic steel has been synthesized through vacuum arc melting of B and Mod. 9Cr1Mo steel. Thermodynamic calculations delve into the microstructure of modified P91 steel with 5 wt.% B (5B), consisting of relatively softer α-Fe and a hard/brittle $(Fe,Cr)_2B$ phase.

EBSD analysis confirmed the phase fraction of borides and ferrite as 62% and 38%, respectively (Fig. 1). Comprehensive analysis of the atomistic-level characterization of $(Fe,Cr)_2B$ phase shows that substitution of Cr atoms in Fe atom positions resulted in intensity variation of atomic columns of STEM-High Angle Annular Dark Field (HAADF) image. Image simulation has been carried out to understand this variation. Relative estimation of Cr atom substitution in Fe atom columns has also been quantified through analysis of changes in peak profile intensity ratio of STEM-HAADF image in comparison with simulated images. Variation in intensity peak profile ratio of two nearby atom column doublets can predict the position of the probable Cr atom substitution site as shown in Fig. 2.

STEM-based Integrated Differential Phase

Contrast (iDPC) provided an insight to the $(Fe,Cr)_2B$ structure (Fig. 3), revealing the simultaneous projection of Fe/Cr and B atom columns along [100]. However, the observed delocalization of B atom columns prompted scientific interest. To unravel this phenomenon, density functional theory (DFT) calculations were employed to analyze the effect of Cr substitution on B-B bond length, which indicates of having minimal impact. Theoretical calculations confirmed that energy imparted by incident electrons during imaging caused the observed B atom delocalization. This study provided a substantial insight on the impact of Cr on the atomic level structure of Fe_2B phase and elucidates B atom delocalization by high-energy electrons.

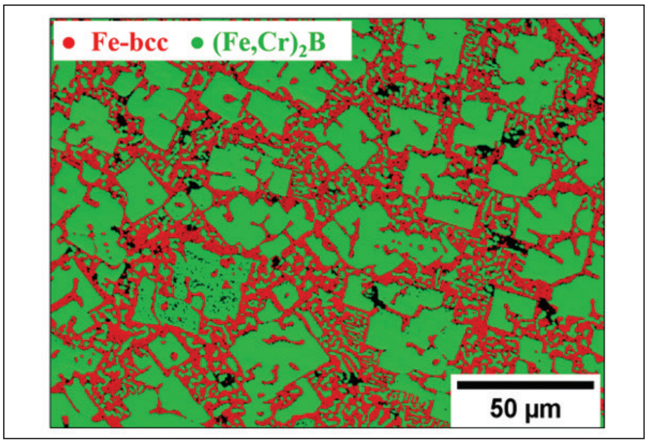

Fig. 1: EBSD map showing the ferrite and M2B distribution

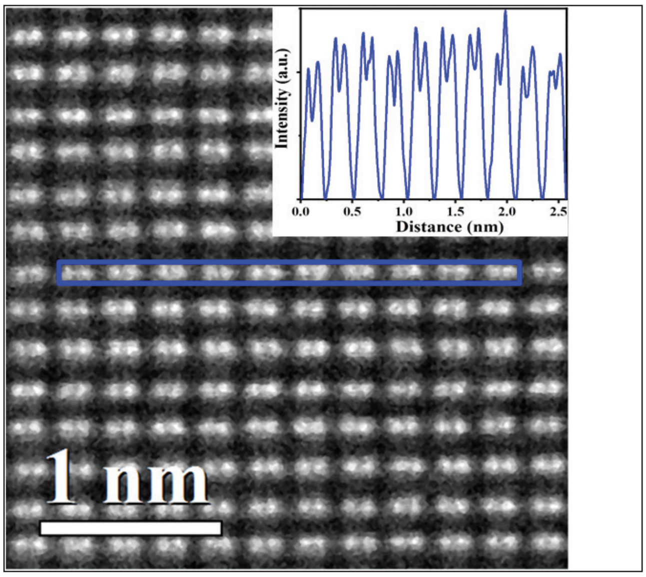

Fig. 2: STEM-HAADF micrograph and the corresponding intensity peak profile showing the probable Cr substitution sites

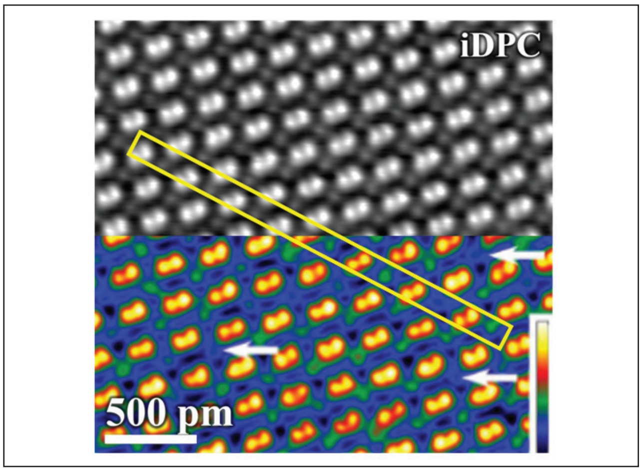

Fig. 3: STEM-iDPC image showing the B atom delocalization.

V.14

An Equivalent Circuit Approach for Flaw Sizing Using Pulsed Thermography

A novel equivalent circuit approach (ECA) has been developed to analyse thermographic data for flaw imaging and sizing. The ECA has been adapted for analyzing the temperature decay that occurs immediately after flash heating the front surface of a stainless steel (SS) specimen as a function of time. Thermographic data sequences fromthe flat surface of a specimen with fabricated flat bottom holes (FBH) (Fig. 1) were acquired after flash heating using a FLIR camera X6540sc with an indium antimonide (InSb) semiconductor detector sensitive in the 1.5-5.1 µm wavelength range for 5 seconds at 400 Hz.The flat surface of the specimen is black painted.

The temperature increase ΔT that occurs at the flat front surface of the paint layer immediately after the flash heating decays temporally as:

$$\Delta T(t) = T1 * exp\left(\frac{-t}{\tau_1}\right) + T2 * exp\left(\frac{-t}{\tau_2}\right) + T3 * exp\left(\frac{-t}{\tau_3}\right) \quad (1)$$

where T_1 is the increase in temperature of the front surface of the paint layer (P), T_2 is the temperature increase at the paint-SS interface, and T_3 is the temperature increase at the SS-air interface at the back surface of the specimen. The time constants, τ_1= R_P C_P' τ_2= R'C' and τ_3=R"C" are linked to the heat transfer time in the paint layer, SS with varying thickness, and in the air beyond the SS-air interface, respectively.

The decay of temperature with time at individual pixel locations were fitted to Eq. (1) based on the nonlinear least squares fitting method using the Levenberg-Marquardt (L-M) algorithm.

The decay constant, $\tau_2$is related to the thickness of the layer below the paint surface.Fig. 2(a) shows the map of the time constant τ_2, obtained for the SS specimen, wherein all the FBHs are visualized clearly. The line profiles of τ_2,corresponding to Row-1 and Column-4 are shown in Fig. 2(b) and 2(c), respectively. The systematic change in the values of τ_2 has been used for flaw depth determination.

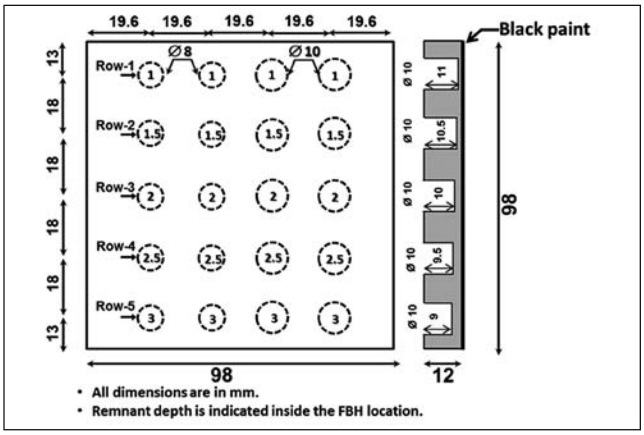

- All dimensions are in mm.
- Remnant depth is indicated inside the FBH location.

Fig. 1: Schematic of SS specimen with fabricated flat bottom holes.

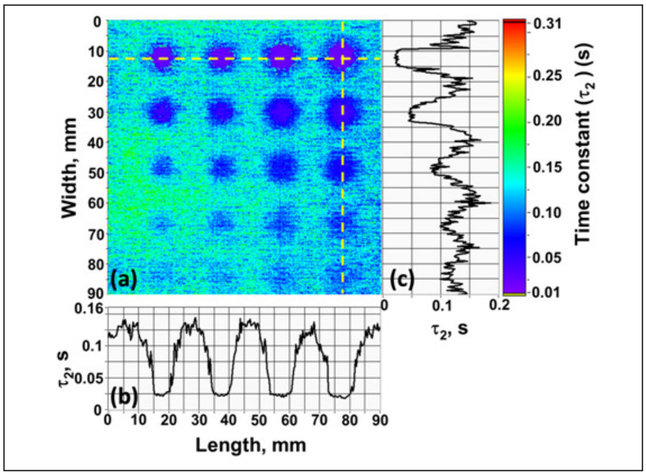

Fig. 2: Map of time-constant, $\tau 2$ for Specimen 2 and line profiles of $\tau 2$along (b) Row-1 and (c) Column-4 corresponding to horizontal and vertical dashed lines marked in yellow.

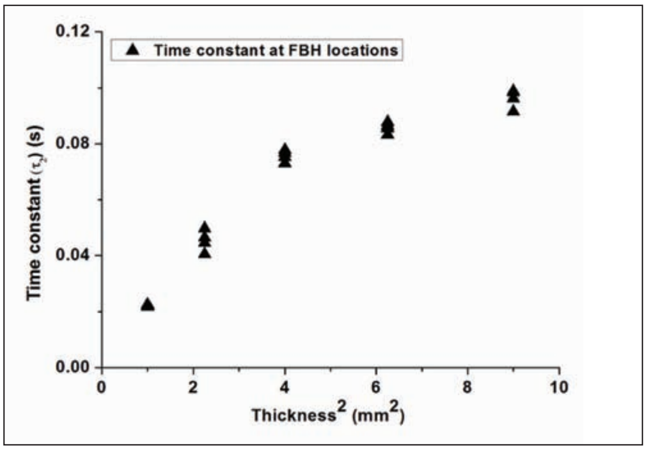

Fig. 3: Variation in time constant τ_2 with the square of thickness for specimen with flat bottom holes is shown.

Fig. 3 shows the variation in the values of time constant τ_2 with square of the remnant thickness at the center of FBHs obtained by Gaussian fitting. A good correlation is established consistent with the formalism adapted to arrive at the ECA.

This study proposes a new methodology for imaging and sizing flaws (FBHs) in stainless steel specimens based on the proposed equivalent circuit approach.

V.15 Development of a novel optical encoder for cable length measurement

Borehole logging system is used at AMD, Hyderabad for measuring the background radiation from inside the boreholes dug in Uranium mines by inserting a borehole probe containing dosimetric sensors using an armoured cable. In order to have information of the radiation data along the depth of the borehole, it is essential to accurately estimate the probe location inside the borehole by logging the length of the armored cable. A non-contact optical based encoder was developed for this purpose which overcomes the error inthe existing mechanical cable length encodersdue to mechanical slip of the cable.

Fig. 1 shows the schematic of an optical encoder. The encoder consists of a light source and lens for illuminating the surface of the object under motion and a camera for capturing the images of the moving surface. The images are processed using DSP algorithms to obtain the distance and direction of motion.

As the optical mouse used in personal computers tracks the physical movement of the mouse, a prototype non-contact cable length encoder was designed and developed using the PCB of an optical mouse. The PCB of the optical mouse houses an LED for the light source and a lens assembly along with a chip containing camera forimage capturing and an on-board DSP program for image processing. Fig. 2 the photograph of the optical mouse PCB along with the armoured cable assembled for measuring the cable movement shown in Fig. 2. The camera-lens assembly of the PCB is mounted such that it captures the movement of the armouredcable. The captured images by the camera are processed by the chipusingimage cross correlation algorithm and translates the cable movement to 3-bit data.

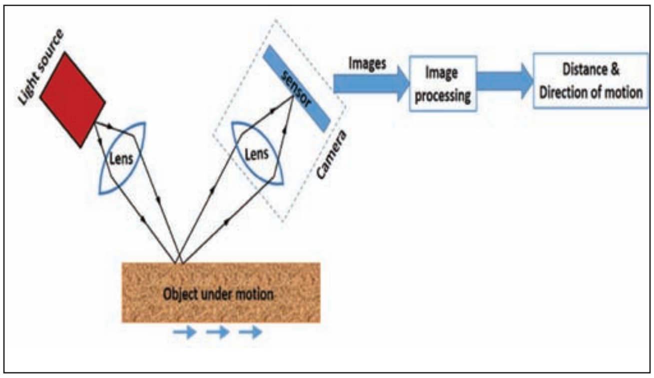

Fig. 1: Schematic of optical encoder.

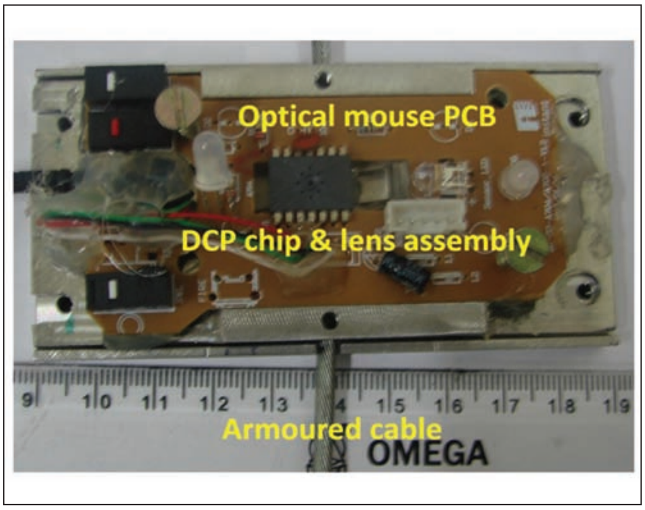

Fig. 2: Photograph of optical mouse PCB assembly for measuringmovement of the armoured cable

Fig. 3: Photograph of the Raspberry Pi based digital interface of the optical encoder.

Further, for control and data logging of the optical encoder,a Raspberry Pi based digital interface was developed using Python program. The program has provision for calibrating the encoder against a known length of armoured cable and for logging the movement. The photograph of the Raspberry Pi baseddigital interface of the optical encoder is shown in Fig. 3.

Extensive experimental trials were carried out for evaluating the performance of the optical encoder using a 20 m long armoured cable. The trials revealed a maximum relative error of the order of 1.3% in the length measurement. This can be further reduced by selecting optical mouse having higher DPI and by providing better mechanical fixtures for improving the alignment of the armoured cable with camera. Based on this development a prototype system is being fabricated for carrying out trials at site.

V.16 Development of Ultrasonic Velocity Correction Methodology for Reconstruction of Phased Array Ultrasonic Imaging in Anisotropic Material

For the narrow gap dissimilar weld between a ferritic steel and a nickel base superalloy used in Advanced Ultra Super Critical (AUSC) turbine rotor, a nickel base alloy buttering layer is deposited on the ferritic steel side as an intermediate layer. The bonding between the buttering layer and the ferritic steel is required to be inspected from the buttering layer side. The buttering layer exhibits very high elastic anisotropy due to elongated columnar grains with preferred orientations. The anisotropy in the buttering layer leads to distorted flaw images in ultrasonic testing (UT), which limits the lateral resolution and defect detection sensitivity. If any flaw goes undetected during the qualification of the buttering layer interface, it becomes critical due to the cyclic loading of the turbine rotor during its operation. The flaws, which are undetected during buttering qualification, may orient almost radially in the assembled rotor. Detection of such radial planar flaws in thick (~400 mm) as well as highly attenuating Ni base alloy using UT is difficult. Hence, it is important to detect the flaws during the qualification stage of buttering. A Novel method comprising of using two phased array ultrasonic probes in through transmission full matrix capture (TT-FMC) mode, is used to measure the angle dependent ultrasonic velocities due to anisotropy. The schematic of the phased array TT-FMC method is shown in Fig. 1.

The calibration block used for this study is shown in Fig. 2(a). The anisotropy in the buttering layer leads to distorted flaw images, which limits the lateral resolution and defect detection sensitivity as shown in Fig. 2(b).

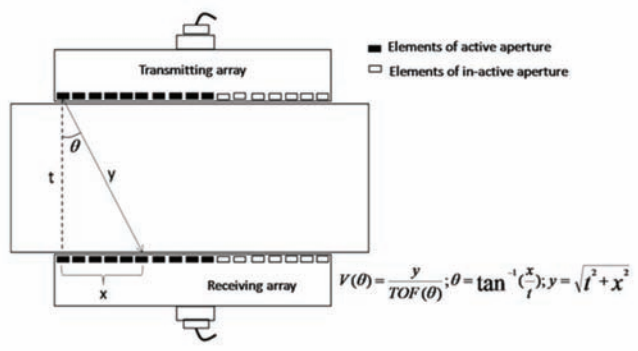

Fig. 1: Phased array ultrasonic TT method using FMC

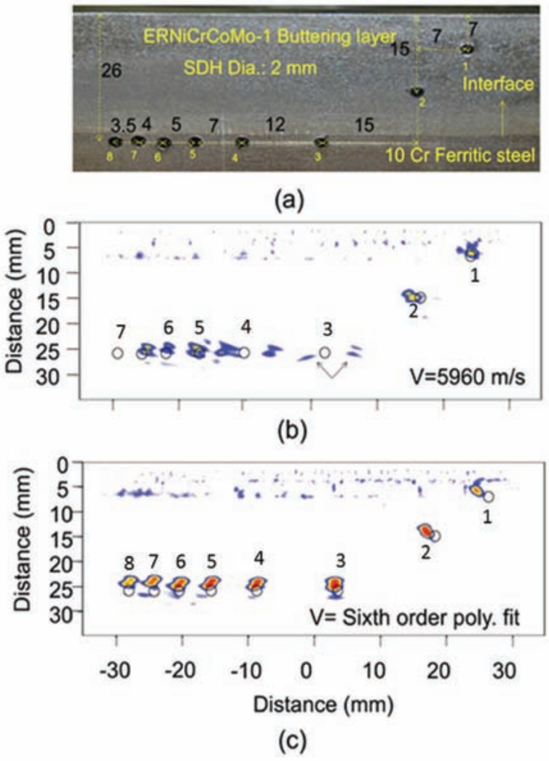

Fig. 2: Angle–depended velocity corrected FMC/TFM image.

The angle dependent ultrasonic velocity measured using theTT-FMC approach indicated a variation of about 600 m/s in ultrasonic velocity, with the minimum in the buttering thickness direction (0°) and the maximum at about 50°. The variation in ultrasonic velocity with angles in the range of ± 68° from the buttering thickness axis (0°) could be approximated with a simple 6th order polynomial curve against grain orientation. The fitted ultrasonic velocity was used to reconstruct the FMC data using Total Focusing Method (TFM) as shown in Fig.2(c). A significant improvement in the signal to noise ratio (SNR) of ~18 dB was obtained using the angle-dependent velocity corrected TFM images. Further, there was a significant reduction in distortion of flaw image in the buttering material. The development of this angle dependent ultrasonic velocity correction methodology, in phased array images show good promise in enhanced characterization of defects in anisotropic materials.

V.17

Generation of Constant Life Diagram for Alloy 617M Forge under Elevated Temperature Cyclic Loading Condition

The superior properties of Alloy 617 make it a favorable material of choice for the heat exchanger applications in Very High Temperature nuclear Reactors (VHTR) and Advanced Ultra Super Critical (AUSC) thermal power plants wherein fatigue damage is an important design consideration. The alloy has recently received endorsement by the Boiler and Pressure Vessel Code of the American Society of Mechanical Engineers (ASME) for nuclear applications. The alloy gains its strength from solid solution strengthening provided by Cr, Co and Mo, and precipitation strengthening imparted by gamma prime which forms g'upon exposure to elevated temperatures.

Present investigation deals with the elevated temperature high cycle fatigue (HCF) behaviour of Alloy 617M with a chemical composition (wt. %) of Ni-0.06C-9.26Mo-1.5Fe-12.09Co-22.19Cr-0.05Si-1.12Al-36ppm B. Tests were carried out on specimens machined from hot-forged block of 1000 mm diameter at a fixed temperature of 973 K using an electro-magnetic resonance based HCF machine operating at a nominal frequency of about 59 Hz. The tests were carried out with varying stress amplitudes (σ_a) and mean stresses (σ_m) for R-ratios ranging from -1 to 0.8 (R = $\sigma_{min}/\ \sigma_{max}$). The endurance limit of the alloy (S_e) was defined as the maximum stress below which the specimens went for run-out (defined as Nf > 10^7 cycles) under fully reversed (R = -1) stress cycling. The value of S_e was observed to be 330 MPa. The stress boundary defining the endurance limit of HCF life greater than 10^7 cycles for varying mean stresses is mapped as Haigh diagram, which defines the safe operating zone for the alloy. Fig. 1 shows a plot between σ_a and σ_m wherein the HCF lives obtained under varying conditions (cutting across different R-ratios) are superimposed. The 'run-out' stress conditions are shown as open symbols while the stress conditions which exhibited finite HCF life, defined as the finite life stress (FLS) are shown as closed symbols in Fig. 1 and 2. Various relationships such as Goodman, Soderberg and Gerber, have been proposed in the literature to analytically define the safe boundary in the Haigh diagram. Goodman equation is given as:

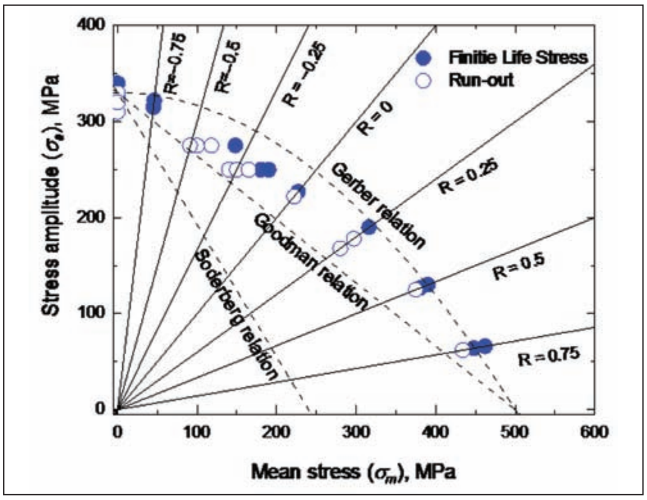

Fig. 1: Haigh diagram – demarcating the safe operating stress under HCF loading conditions.

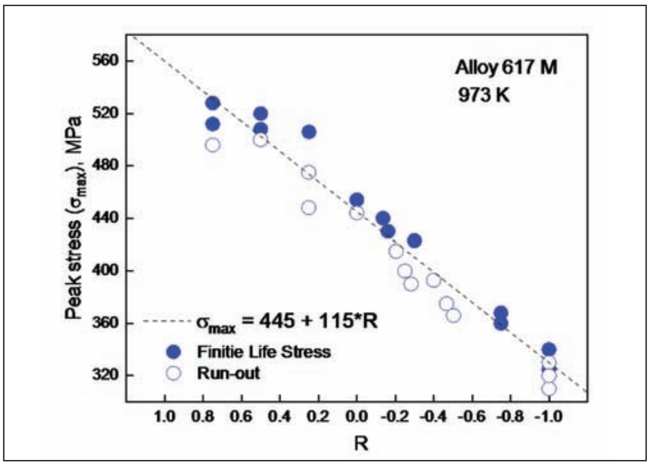

Fig. 2: Modified Haigh diagram in the form of peak stress vs. R plot.

$(\sigma_a/S_e)+(\sigma_m/S_U)=1$ (1)

where S_U is the tensile strength of the alloy at the test temperature. Replacing S_U with S_{YS} (yield stress) in the above equation gives the Soderberg equation which is expressed as:

$(\sigma_a/S_e)+(\sigma_m/S_{YS})=1$ (2)

Gerber equation is given as:

$(\sigma_a/S_e)+(\sigma_m/S_U)^2=1$ (3)

It can be observed that the Goodman, Soderberg and Gerber plots shown in Fig. 1 fail to represent the boundary between the FLS and 'run-out' conditions clearly. A novel method of plotting the Haigh diagram in terms of the peak stress (σ_{max}) as a function of R-ratio is presented in Fig. 2, wherein the boundary between the safe and unsafe regions is delineated more clearly by a single linear equation: σ_{max} = 445 + 115 * R.

V.18 Effect of Fracture Mode (I+II) Mixity on Deformation J-integral as a Fracture Parameter

To ensure the structural integrityof large size components with crack like defects under normal and accidental loads, itis important to analyze the cracks under mixed mode loading conditions. Due to complex loading spectra, the crack tip experiences a state of combined tension and shear. Under these circumstances, the applicability of Mode-I fracture toughness (J_{IC}) for structural integrity assessment cannot be justified as it will lead to unrealistic prediction of fracture behavior of components. Most of the existing literature is focused on effect of mixed mode loading on fracture behavior of high strength materials. To address this issue,coupled experimental-FEM analyses have been carried out to characterize the crack tip in SS 316LN material under mixed mode (Mode I+II)loading conditions.

Experiments

Asymmetric four point bend tests were conducted on specimens with notch at offset distance of 7, 14, 21, 28 and 34 mm from the centre of the specimen. This has led to mode-mixity (M_p)ranging from 0.1 to 0.85 at crack tip. As the M_p increases, the crack tip stress state changes from shear to bending.

$$M_p = {}^{2}/\pi \tan^{-1} (\delta I/\delta II) \qquad (1)$$

where δ_I and δ_{II} are the horizontal and vertical displacements of crack tip obtained from elastic-plastic FE analyses. The loading rollers at top and bottom were positioned asymmetrically at a distance of 34 mm and 51 mm from specimen centre. Experimental setup along with camera is shown in Fig. 1.

The experiments were conducted under displacement control and all the specimens were loaded up to an applied displacement of 1 mm. The plastic deformation around the crack tip was assessed using Digital Image Correlation (DIC) technique.

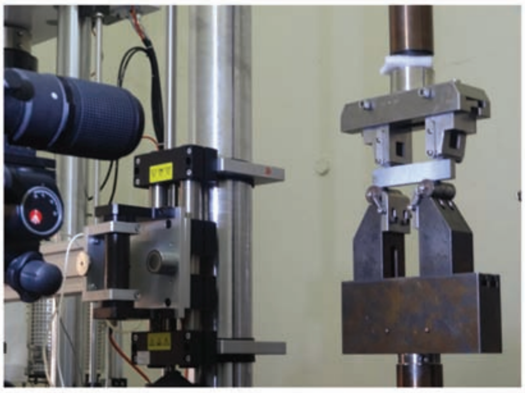

Fig. 1: Experimental setup with camera

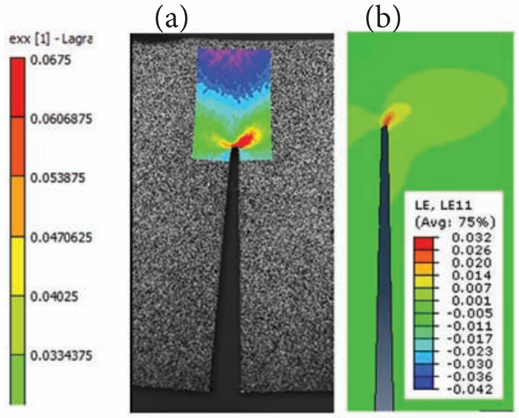

Fig. 2: Distribution of εxx at the crack tip for an applied displacement of 1 mm (a) DIC (b) FEM

FEM Analyses

Elastic-plastic FEM analyses were carried out to evaluate the load vs. displacement and distribution of normal and shear strains at crack tip. The distribution of strain obtained from DIC and FEM for a specimen with M_p= 0.23 is shown in Fig. 2.

Estimation of J-integral

DeformationJ-integral values for various M_p have been evaluated from experimental load vs. displacement curves and FEM analyses using plastic η factors. The values are shown in Table-1.

Table-1 J-values obtained from experiments and FEM

M*p*	J-Exp. (kJ/m^2)	J-FEM (kJ/m^2)
0.1	456	452
0.23	484	476
0.43	317	310
0.6	512	509
0.85	380	344

The deformation J integral and crack tip strain field predicted from FEM analyses are in close agreement with experiments.The deformation J for M_p= 0.43 is found to be lower than M_p = 0.85 which is closer to Mode-I.

V.19 Estimation of fracture toughness of austenitic stainless steel from tensile properties and validation with standard experimental data

Austenitic stainless steel SS 316LN is used for various high temperature structural components of fast breeder reactor. Many of these components are exposed to operating temperatures between 380 and 550°C. Determination of fracture properties (J_{1c} or K_{1c} or J-R curves) of SS 316LN at various temperatures (300-550°C including RT or room temperature) is essential to evaluate structural integrity of these components. It is well known that for determination of plane strain fracture toughness (either J_{1c} or K_{1c}) of various alloys requires that the test specimens satisfy minimum thickness criterion. It is difficult to determine fracture toughness when required material to fabricate specimens of minimum specified dimensions (thickness) is not available. In this study, an attempt was made to address this limitation by considering appropriate empirical method to predict K_{1c}.

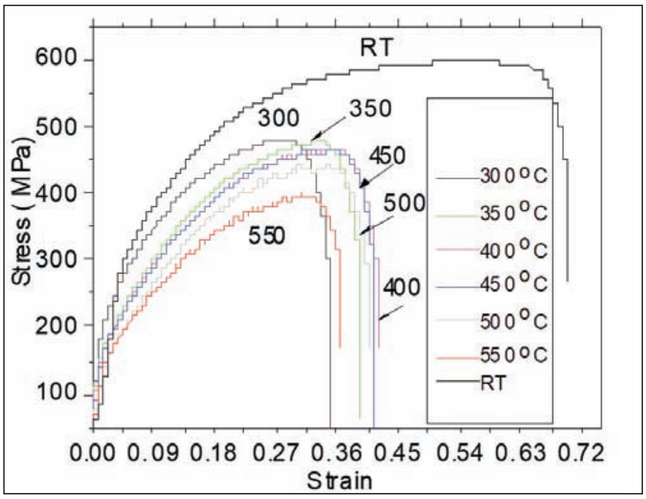

Fig. 1: Plot of Stress vs strain curves

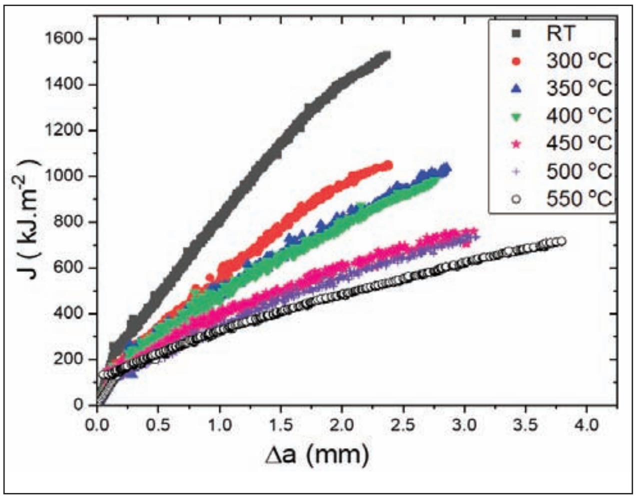

Fig. 3 : J-R curves at different temperatures

As a part of this objective, experimental data or fracture toughness or J_{1c} values were determined from J-R curves, tested in the temperature range of 300-550°C (including RT). Tensile testing was also carried out in this temperature range and tensile properties were determined. In this investigation, an attempt was made to estimate K_{1c} from tensile properties. The stress vs strain curves are plotted in Figure1. Modulus of toughness values were determined from the area under stress vs strain curves and are plotted in Figure 2. Additionally, Modulus of toughness values were estimated using equation 1 and are shown in Figure 2.

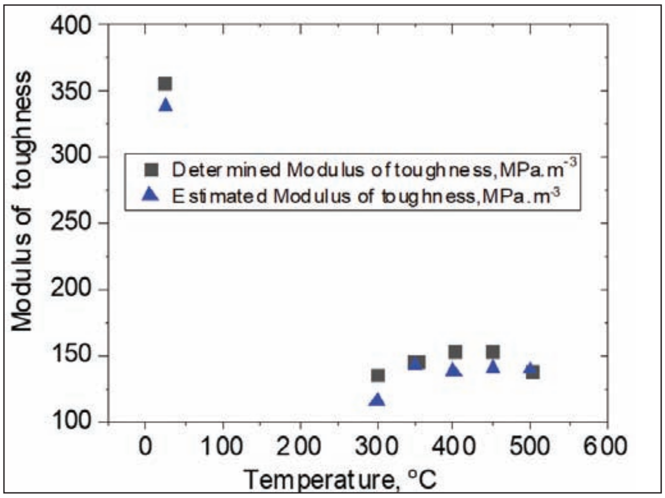

Fig. 2: Modulus of toughness results

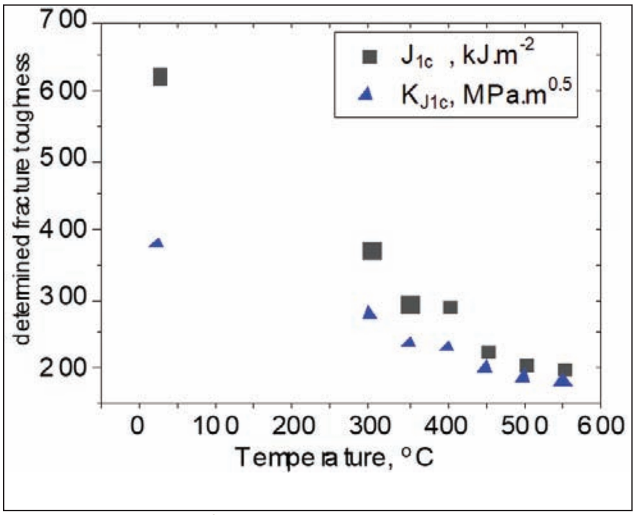

Fig. 4: Determined fracture toughness results

$$I = \varepsilon_f (\sigma_{ys} + \sigma_{uts}) / 2 \qquad (1)$$

Where I = Modulus of toughness, ϵ_f = total elongation, σ_{ys}= yield strength, σ_{uts}= ultimate tensile strength

J-R curves at various test temperatures are plotted in Fig. 3. From the J-R curves, fracture toughness values were determined (both J_{1c} and equivalent KJ_{1c}) and are plotted in Fig. 4. Estimation of fracture toughness (K_{1c} values) was carried out from tensile properties and based on a previously proposed empirical equation 2.

$$K_{1c} = \sqrt{\frac{2EI}{(1-v^2)}} \qquad (2)$$

Where K_{1c} = Fracture toughness, E = Youngs Modulus, I= Modulus of toughness determined from area under stress-strain curve, v = 0.3. The estimated K_{1c} values and determined K_{J1c} values, at different test temperatures are plotted in Fig. 5. The differences between estimated fracture results (K1c) and determined K_{j1c} values was within 15- 20%. Based on the estimated results, it is summarized that the proposed methodology (K_{1c} estimation) fairly holds good for SS 316LN.

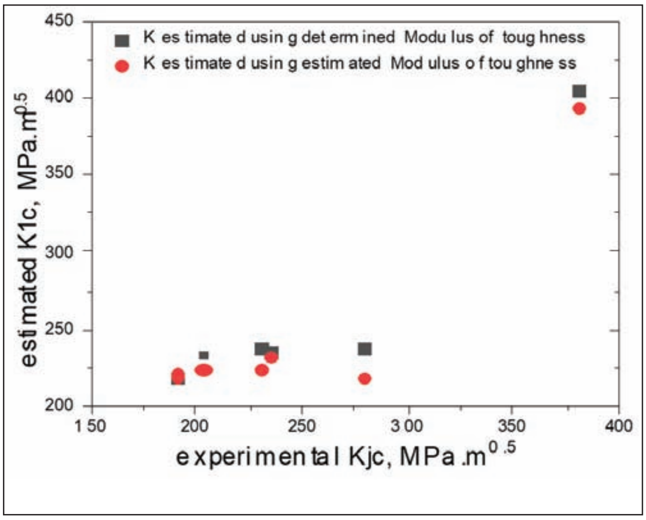

Fig. 5: Plot of estimated and determined fracture results at different temperatures

V.20 Irradiation-induced texture Development in Nanocrystalline Ni

The application of nickel coatings on structural materials in molten salt reactors for corrosion resistance is being researched. To resist corrosion, coatings must have a specific texture that remains invariant under irradiation. The majority of literature reports irradiation-induced textural changes occurring in the athermal regime (thermal effects are negligible, i.e., room temperature and low temperature). These changes are attributed to ion sputtering and differential damage in channeled and non-channeled grain orientations. There are no studies of irradiation-induced texture in the thermally-assisted regime, which is the operating temperature range of nuclear reactors. The study aims to clarify if the existing irradiation-induced texture mechanisms also apply to this range.

Pulsed electrodeposited nanocrystalline (NC) Ni samples with a grain size of 20 nm were subjected to 1.4 MeV Ni^+ ion irradiations up to 18.5 dpa at various temperatures, 250˚C, 350˚C, 450˚C and 550˚C. The irradiation-induced microstructures: the texture and recrystallized fractions are compared with the unirradiated counterpart that underwent similar thermal treatment as the irradiated, using Electron Back scattered Diffraction (EBSD).

Fig. 1 shows the texture intensities of the two prominent texture components <100> and <111> for unirradiated and irradiated regions.

At 250˚C, the unirradiated region displayed a strong <100>//ED texture value of 10.34 and <111>//ED less than 1. A decrease in <111>//ED, with a corresponding increase of <100>//ED texture, occurred during irradiation. To exemplify these changes, texture components of <100> and <111> with deviations of 15˚C were calculated. An increase in <100>//ED texture components in the irradiated area (74.6%) relative to the unirradiated area (67.6%) and a reduction in <111>//ED in the irradiated area (2%) relative to the unirradiated area (4.58%) are observed. Growth of <100>//ED grains at the expense of <111>//ED grains during irradiation could result in this effect. At 350˚C, a gradual declination of the <100>//ED fiber texture and an increase in the <111>//ED texture can be observed. This trend continues resulting in a double texture at 450˚C. However, at 550˚C, a texture reversal, i.e., an increase/decrease of <100>/<111>, is observed. Interestingly, irradiation at 350˚C and 450˚C progressively reduces the <100>//ED and increases the <111>//ED textures. Even at 550˚C, irradiation strengthens the thermal texture, i.e., increase in <100>//ED and decrease in <111>//ED. Therefore, irradiation accentuates the thermally-induced textures in the temperature range of 350˚C to 550˚C.

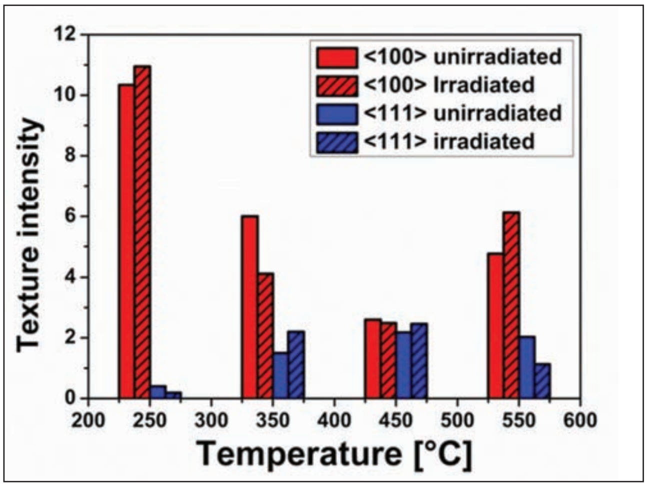

Fig. 1: The texture intensity variation as function of temperature for both unirradiated and irradiated areas

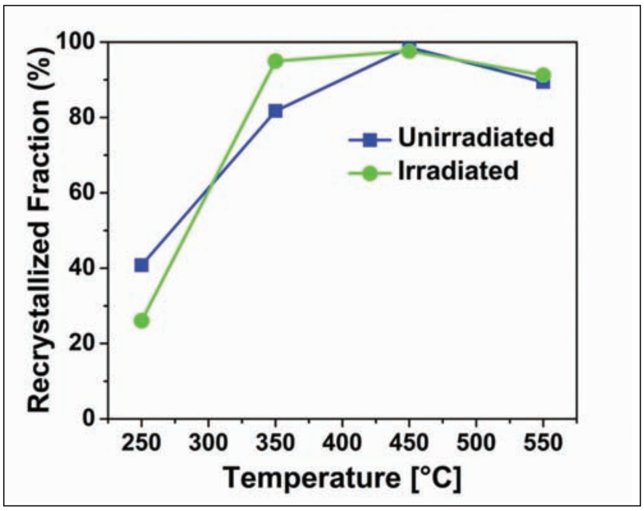

Fig. 2: The recrystallized fraction for unirradiated and irradiated areas at various irradiation temperature.

The recrystallized fraction obtained for unirradiated and irradiated areas at various temperatures is shown in Fig.2. The recrystallized fraction is computed from the Grain Orientation Spread (GOS). At 250˚C, the recrystallization fraction is lower in the irradiated area than in the unirradiated area. As the temperature increases, the recrystallized fraction in the irradiated area crosses over that of the unirradiated at 300˚C,

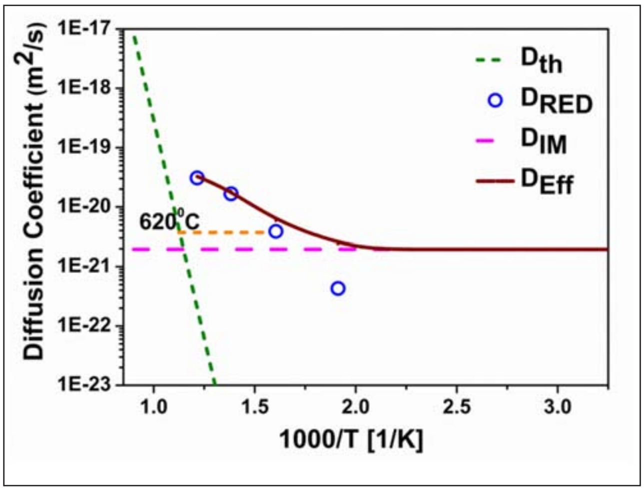

Fig. 3: Arrhenius plot of effective irradiation-induced diffusion coefficient (DEff). The DEff is the sum of RED calculated from rate theory and IM components. The diffusion coefficient Dth for thermally-induced induced diffusion is also plotted.

indicating that the irradiation-induced recrystallization kinetics occur at a higher rate. The fraction of recrystallized grains at 350˚C for unirradiated and irradiated regions is 81% and 95%, respectively. As the temperature increases to 450˚C, ~98% of grains are recrystallized in unirradiated and irradiated areas. In contrast to thermally-activated microstructure, a fully recrystallized microstructure developed during irradiation at 350˚C, and grains became nearly uniform. However, a marginal decrease in recrystallized fraction to ~90% is observed at 550˚C which may be associated with grain rotation and boundary migration.

The evolution of texture and recrystallization is related to atomic mobility, whose quantitative signature is contained in the self-diffusion coefficient. The atom transport during irradiation is achieved through two processes, ion mixing (IM) and radiation-enhanced diffusion (RED). The calculated self-diffusion coefficients for all temperatures with contributions from IM and RED are shown in Fig. 3.

At 250˚C, DRED (RED coefficient) is smaller than DIM (IM diffusion coefficient). Presence of nano-sized grains during the onset of irradiation at this temperature and the prevalence of DIM over DRED should resut in an increased probability of thermal spikes overlap on grain boundaries. Since the irradiations are carried out at normal incidences to the sample surface, the ion beam aligns with [100] and [111] axes. However, there are varying non-channeled fractions in grains with these orientations. Close encounter probabilities for <111> grains are twice that of <100>, resulting in more damage to <111> grains. Therefore, the volume free energy resulting from the steady state defect concentration is higher in the <111> compared to <100> orientations. Hence, the minimization of volume free energy is achieved through the growth of <100> orientations into <111> grains, thereby enhancing <100> texture. Irradiation at temperatures of 350˚C and higher strengthens the thermal texture, i.e., an enhancement of <111> and decrease of <100> up to 450˚C and enhancement of <100> and reduction of <111> at 550°C. At higher temperatures (>250˚C), RED contribution towards effective diffusion coefficient overwhelms IM (Fig. 3); since RED is thermally activated, the higher concentration of defects produced during irradiation accentuates the thermally-activated textures at respective temperatures, i.e., the <111> at 350˚C and 450˚C and <100> at 550˚C.

Irradiation renders fully recrystallized microstructure at 350˚C, downshifted by 100˚, relative to the thermal recrystallization temperature. The value of D_{RED} at 350˚C, is 3.8×10-^{21} m-^{2}. The self-diffusion coefficient for a thermally-activated process [2] in Ni is plotted in Fig. 3. The values corresponding to D_{RED} can be attained in a thermally-activated process at 620˚, signifying that fully recrystallized microstructure can be produced by thermal treatment at this temperature for the same duration as irradiation time. However, a fully recrystallized microstructure during thermal treatment occurs at a lower temperature, 450˚C (Fig. 3), which could be due to the high stored energies and nano-sized grains in the as-deposited samples. Therefore, the studies reveal that at temperatures greater than stage-III of recovery, irradiation accelerated the recrystallization kinetics, resulting in a fully recrystallized microstructure at temperatures down-shifted by 100˚C compared to thermally activated recrystallization.

V.21 Effects of Grain size in Radiation-Induced Segregation of Cr in Fe-Cr alloy.

Nuclear reactor environments are extreme in nature, due to the combination of exposure to corrosive coolant, mechanical stress, and neutron damage. This environment can lead to irradiation-induced/assisted precipitation, segregation, embrittlement coupled with enhanced creep and stress corrosion cracking. Ferritic steels show high resistance to radiation effects, such as void swelling and damage accumulation compared to austenitic steels. One of the approaches to enhance the radiation resistance is to increase the volumetric density of defect sinks like phase boundaries and grain boundaries through nanostructuring. In this context, effects of variation in grain size on the radiation-Induced segregation of Cr in Fe-Cr alloy is studied. Fe-20%Cr alloy samples with grain sizes of 350 µm ($FeCr_{LU}$) and 300 nm ($FeCr_{SU}$) are irradiated at 500 °C with 225 keV Xe^+ ions at a fluence of $1×10^{16}$ ions/cm^2 corresponding to a peak damage of 100dpa.

Upon ion irradiation, Cr segregation is observed at the grain and sub-grain boundaries as seen as particles in SEM images (Fig. 1). In large grain samples surface craters, formed by blistering of Xe bubbles are seen. EDX analysis (not shown) gives higher surface concentration of Cr upon irradiation, with a larger variation corresponding to larger Cr segregation in small grained FeCr sample.

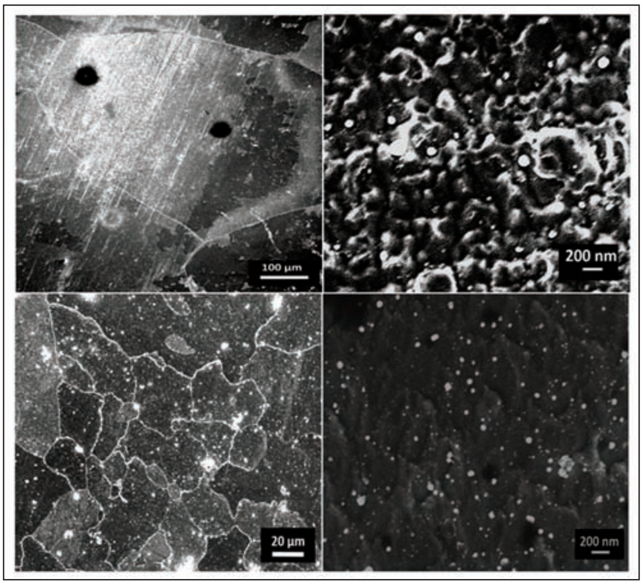

Fig. 1: SEM images of as prepared samples(a), (c) showing grain sizes, irradiated samples (b) FeCrLI with surface craters and (d) FeCrSI with Cr particles at sub-grain boundaries

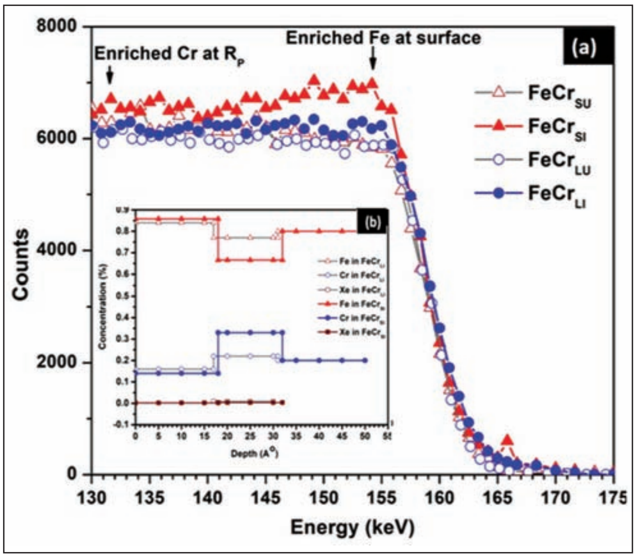

Fig. 2: (a) High Resolution RBS spectra from as-prepared and Xe- irradiated FeCr samples and (b) corresponding simulated concentration depth profile in the insert

High Resolution RBS measurements (Fig. 2) are carried out in these samples using 200 keV He^+ ions and are simulated with MEISWIN software. Upon Xe ion irradiation, enrichment of Fe is observed at the surface while segregation of Cr is observed deeper at the projected ion range, with a larger variation observed in small grained FeCr. The estimated Xe concentration is found to be $1.16×10^{15}$ atoms/cm^2 and $7.88×10^{14}$ atoms/cm^2 in $FeCr_{LI}$ and $FeCr_{SI}$ samples respectively, indicating outdiffusion and loss of Xe. Higher is the Xe outdiffusion, there is lesser probability of growth of Xe bubbles in small grained sample. Fe enrichment at 550°C which is greater than 0.5 Tm and at Cr concentration more than 15%, is due to inverse Kirkendall effect. Small grained sample with higher density of grain boundaries is aiding Cr-segregation as well as outdiffusion of Xe atoms. Cr, having higher binding energy with interstitials, segregates around the implanted defective region. XRD measurements show decrease in crystal size and 10 times increase in microstrain and dislocation density in large grained samples upon irradiation. In small grained sample, grain size increases with no change in microstrain and 10 times decrease in defect density, indicating that it has higher radiation resistance

V.22

Electronics and Instrumentation Hardware Development for Indigenous Control System of 1.7MV Accelerator

A 1.7MV tandetron accelerator has been in use at MSG,IGCAR for the past two decades as a key tool and workhorse for our accelerator based materials research covering single and dual ion irradiations, ion beam analysis on a wide spectrum of materials ranging from reactor structuralalloys to2D materials. Due to irrecoverable failure of the imported control system of the accelerator, we have indigenously developed a complete control system for the accelerator without compromising the functionality and the performance of the accelerator. The accelerator is run by a centralized control system. All accelerator parameters needed for normal accelerator operation are interfaced with the control computer. The control system software was developed to run on Industrial PC with the latest Windows and LabVIEW version. Commercial off the shelf type 12 bit and 16 bit data acquisition cards, programmable logic controller, analog and digital telemeter units form the major hardware of the control system. The control system can handle tens of analog and digital I/O signals, and analyse and present large amount of data in a comprehensive yet user friendly graphical user interface.It acquires all the analog input signals (~100) in every 10-100milliseconds using data acquisition cards used with DAQ PC and/or PLC. It also the controls the analog output signals (~100) continuously when the user operate the controls. Controls can be adjusted by menu-driven restoration of stored values, increment/decrement buttons, keyboard input of the desired parameter value for analog mode adjustments. The application software in PLC acquires all the digital input signals (~100) at a rate of 100Hz/ signal and updates all the digital output signals (~100) once in 10milliseconds. Whenever the user changes a digital control in the DAQ PC, the corresponding digital output signals are changed immediately (<5milliseconds) and related digital input signals are updated in the DAQ PC. Using the PLC, the Safety & Interlock System is separated from theDAQ PC to perform the protective and preventive safety interlock actions without failures. A total of 60 interlocks (vacuum, radiation,cooling, pressure, spark, high voltage etc) are guarded by the PLC and incorporated into the control system to protect personnel, equipment and samples. Whenever the

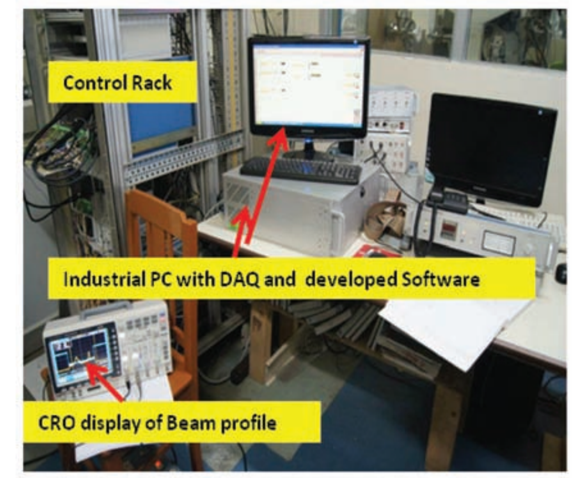

Fig. 2: Overall control system showing industrial PC, control cabinet and beam profile display during tests.

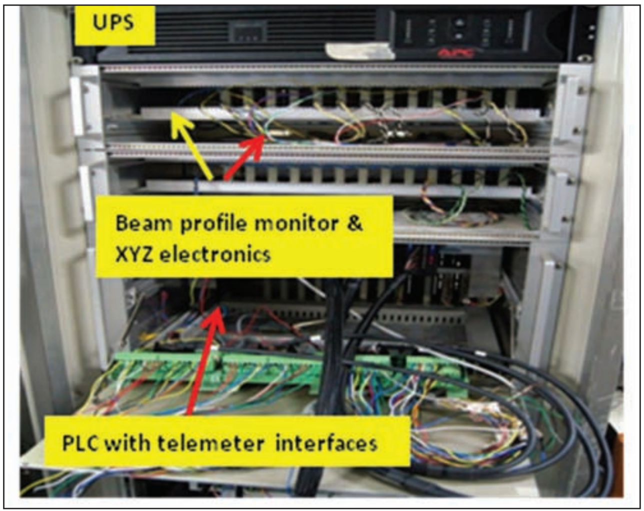

Fig. 1: Control cabinet of the new control system

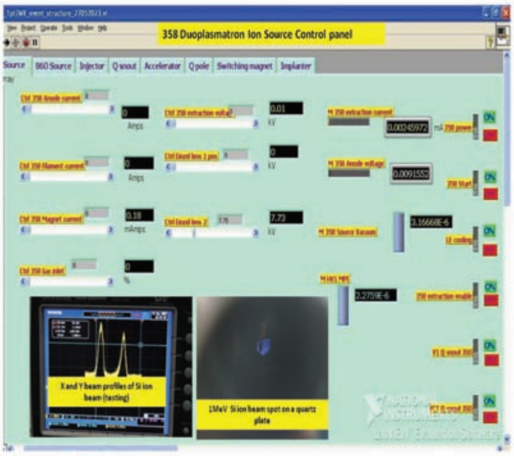

Fig. 3: Graphical user interface of 358 Duoplasmatron ion source with X and Y beam profiles and beam spot shown as insets

interlock conditions are satisfied,the necessary actions like setting digital outputs on/off,raising alarms are taken within an interval of1 millisecond.

The control system software design was made to meet the requirements of different groups of users categorized into operators, maintenance personnel, accelerator physicists and the users.The control software is modular designed, scalable, and easy to maintain. It provides user friendly interfaces. All the system parameters are controllable using computer mouse and/or keyboards. All the system readings are shown in an interactive sequential format or in a graphic format simultaneously as a function of time. The acquired machine data are displayed with a history of several hours. In addition, some data recorded in the kHz range are also to be displayed with a large history. The control software provides proper mechanism for accelerator diagnostics which requires intelligent data logging of the system. Operators may save and restore preferred system conFig.urations and setup preferences. This allows for an easy beam startup with little to no fine tuning needed. The overall response time to an operator's request is less than a few seconds, ideally 1second; unless progress of the process is indicated.

Assoftware is the most flexible part of the control system, the demands are very dynamic. Due to its modular nature, the control system software can be easily modified/reconFig.d as hardware is changed or added, paving way for easy tailoringto meet different experimental demands. New features that are required can be also added by the software. All the indigenously developed hardware and software were tested them using our own developed signal simulators in the lab and observed their functionalities. All required modifications/iterations were done till they functioned as expected and as required. Then we ported them to the accelerator, testing them for different stages of the accelerator starting from 358 duoplasmatron and 860 SNICS ion sources. Control and monitoring of all the subsystems of the accelerator (ion source, mass analysis, low energy negative ion injection, High voltage generation, stripping process (-ve ion to positive ion conversion), energy analysis, x-y raster scanning, neutral atom trapping) were successfully tested using the control system.

We could successfully initially obtain 295 keV Si ion beam at the zero port of the switching magnet. As a continuation of the testing, we could go ahead and successfully obtain 2 MeV Si ion beam at the target (irradiation chamber) of 10 degree beam line. The beam was raster scanned and with 2 uA current at the target. Since its development and incorporation into the accelerator, the control system continues to function satisfactorilywith the accelerator being used for various ion implantations using oxygen, silicon, hydrogen ions. The control system has been developed in a very cost-effective manner and without using much of the proprietary hardware and software. This indigenous development will help us to use the 1.7 MV accelerator trouble-free for next few decades. Further testing of the control system and the accelerator operation will provide critical inputs to the planned refurbishment of the other important systems of the accelerator leading to its enhanced performance and utilization.

V.23 Development of Iron Phosphate Glass Models using ab-initio Molecular Dynamics

One of the leading and most effective methods to immobilize nuclear waste is vitrification. It involves incorporating hazardous elements into a glassy matrix. Iron phosphate glass (IPG) having the composition of 40 mol% Fe_2O_{3-} 60 mol% P_2O_5 (Fe/P= 0.67) proved to be an excellent glass matrix for encapsulating high level nuclear wastes due to its exceptional chemical durability. So, we have attempted to obtain atomistic IPG models by the ab-initio molecular dynamics (AIMD) approach using the melt-quench procedure. Since the AIMD approach couples molecular dynamics (MD) with density functional theory (DFT), this method has higher accuracy as compared to the classical methods. In addition, the advantage of the melt-quench process is that it mimics the actual experimental procedure of manufacturing glasses but with a much higher melting temperature and faster quench rates compared to the experiments.

Born Oppenheimer molecular dynamics (BOMD)

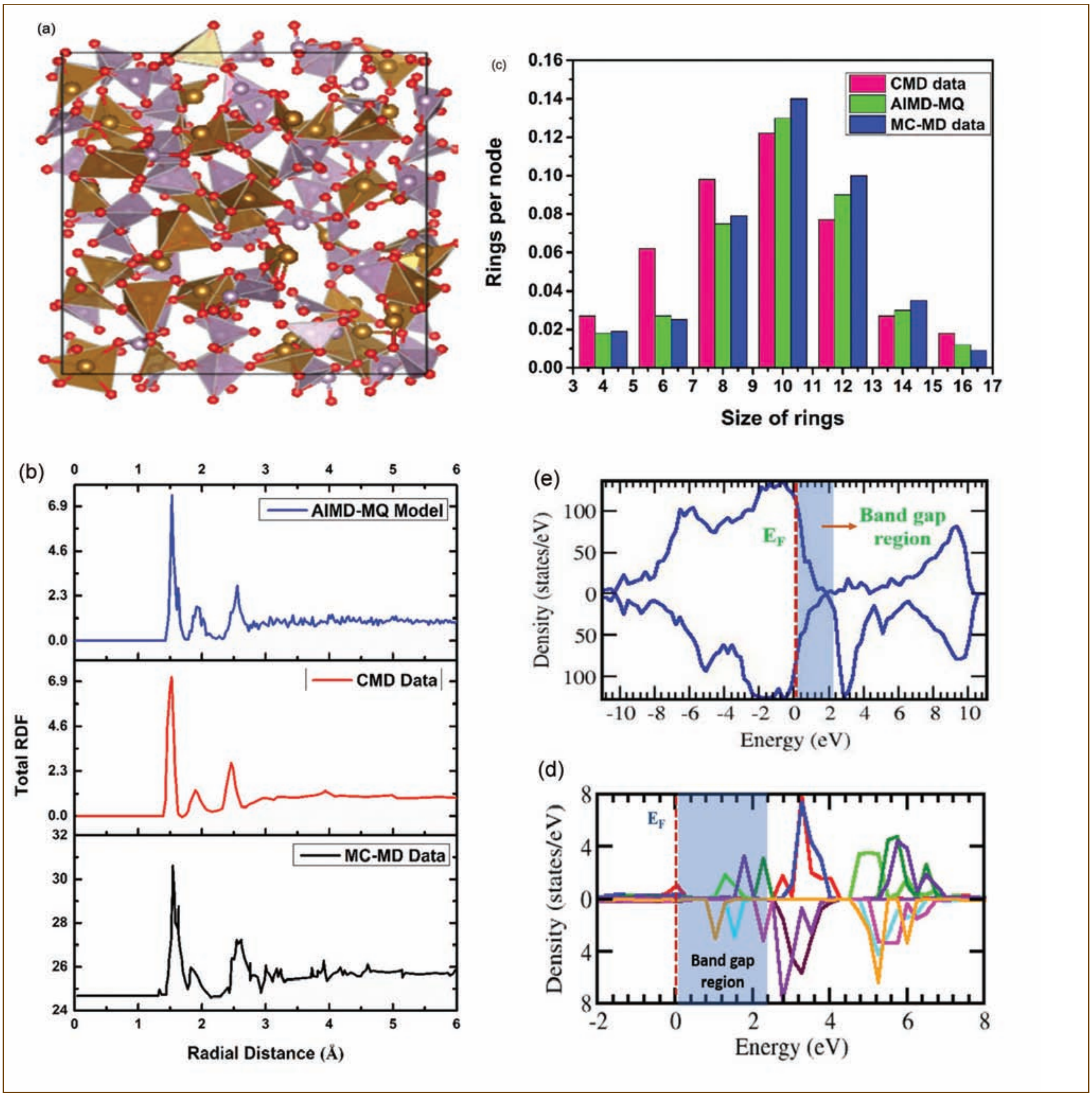

Fig. 1: (a) Atomistic conFig.uration of IPG, (b) Ring size distribution of the AIMD-MQ model, (c) Radial distribution function of the AIMD-MQ model compared with the other models, (d)Total electronic DOS of IPG showing the band gap, and (e) partial DOS for the Fe atoms with dangling bonds, showing their contribution to the defect states in the band gap.

simulations have been carried out using the VASP code on crystalline Iron Phosphate ($Fe_3(P_2O_7)_2$) to obtain its glassy counterpart. The exchange correlation potential in VASP is approximated using the Projector Augmented Wave (PAW) pseudopotentials in the generalized gradient approximation approach. Crystalline ($Fe_3(P_2O_7)_2$ is taken as the starting structure whose standard cell contains 84 atoms. The simulation cell used here is an orthorhombic 2x2x1 supercell containing 336 atoms (48 Fe, 63 P, and 225 O) and having the dimensions a = 18.16 Å, b = 20.65 Å, and, c = 12.39 Å. First, the temperature of the simulation cell is raised to 300 K, and the system is allowed to equilibrate for 1 ps. Following that, the temperature is raised to 2000 K and then to 5000 K, with the simulation box equilibrated at each temperature for 2ps. To reach the final configuration, the molten structure is cooled to 300 K in 7ps time, and is further equilibrated to lower the stress and interatomic forces for 3ps. The whole procedure is carried out under the Nosé-Hoover thermostat using the NVT ensemble. To reduce the pressure of the obtained model, the system is made to undergo further relaxation using the NPT ensemble for 2 ps. The pressure of the final configuration is about 0.01 kB and the final mass density is 2.97 gm/cc, in good agreement with the experimental value of 2.9 gm/cc.

One of the glass models obtained after relaxation is shown in Fig. 1(a). The model is characterized at different length scales. For short range, radial distribution function (Fig. 1(b)), bond angle distribution, and coordination numbers, which characterize the chemical order, are analyzed. There is an increased interest in studying the medium range order (MRO) as it tells us about the connectivity of the structural units and thus qualifies the structural stability in glasses. So, we study the ring size distribution (Fig. 1 (c)), neutron structure factor, and first sharp diffraction peak (FSDP). The structural properties of the current model (AIMD-MQ) are found to be in good agreement with previously reported experimental and computational data on large scale atomistic models of IPG (Classical molecular dynamics model, referred to as the "CMD" and MD equilibrated Monte-Carlo model referred to as the "MC-MD"). The similarity of these measures in the MRO means that our AIMD-MQ models are topologically similar to other larger structures. We have also studied the electronic density of states (DOS) of the AIMD-MQ models. The band-gap calculated from the DOS plot is found to be 2.25 eV which is smaller than the experimental value of 2.9 eV. Few peaks are also observed in the band-gap region of the plot due to the presence of the dangling bond defects in the system. Fig. 1(d) shows the plot for the total electronic DOS while the contributions to the partial DOS from the dangling bonds is shown in Fig. 1(e). In addition to the structural properties, electronic, elastic, and vibrational properties are studied as well. These quantities have been matched with literature results where available.

In any MD approach, faster quench rates are inevitable as the dynamics needs to be completed in a few pico to nano seconds. So, fast quench rates of ~10^{14} K/sec need to be used to form glasses, as slower quench rates can lead to local recrystallization. It's quite challenging to reproduce the medium range order in such small structures resulting from the AIMD technique. But by opting for an appropriate quench rate and a proper relaxation regime using the NPT and NVT ensembles we have successfully obtained the glassy structures which imitate the experimental models both at short as well as medium length scales.

V.24 Structural Evolution Mechanism of Detector Material $Cd_{0.9}Zn_{0.1}Te$ under High Pressure and High Temperature

CdTe, as a member of the II-VI semiconducting chalcogenide family has been of interest since five decades because of its important physicochemical properties and applications in different fields. With the substitution of Cd with Zn that has a smaller cationic radius, the energy gap, carrier concentration, activation energy and stability are observed to be affected to a great extent. Accordingly, a wide range of studies are being carried out on these compounds. In particular, the compounds with low zinc concentration are appreciated for their potential application in photovoltaic devices and radiation detectors. Recently, $Cd_{0.9}Zn_{0.1}Te$ (CZT) has gained immense interest as X-ray and γ-ray detectors. The structural behaviour of CZT was investigated under high pressure up to 22 GPa at beam line– 11 of the synchrotron facility at Indus-2, Indore using high pressure X-ray diffraction (HP XRD). Methanol-ethanol-water (MEW) in ratio 16:3:1 was used as pressure transmitting medium (PTM). High pressure-high temperature XRD studies were carried out up to 5 GPa-400 °C using a micro focus XRD setup (GENIX 3D, Xenocs, France) with a Mo target (λ = 0.711Å).

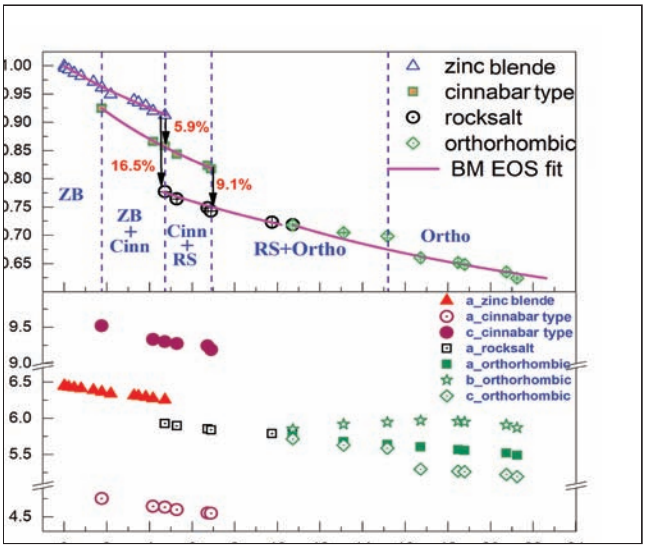

Fig. 1: Evolution of lattice parameters and unit cell volume under pressure. ZB – zinc blende, Cinn- cinnabar, RS – rocksalt and Ortho – orthorhombic structure.

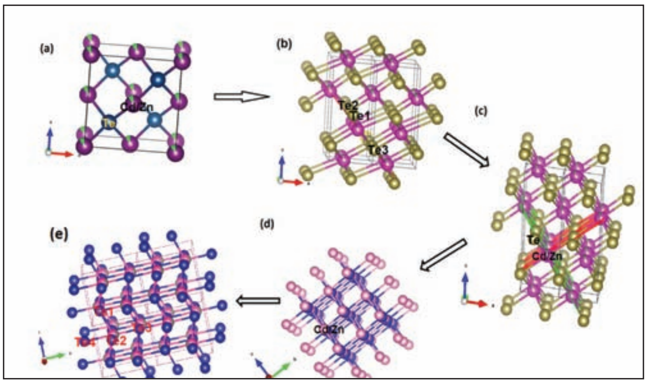

Fig. 2: (a)zinc blende type CZT at ambient, (b) cinnabar type CZT at 6.3 GPa, (c) cinnabar CZT identical with rocksalt structure, the (102) and $(\bar{1}04)$ are displayed in green and red respectively (d) rocksalt type CZT at 6.3 GPa (e) CrB type CZT at 16.7 GPa

CZT adopts zinc blende structure at ambient. At high pressures, the onset of transitions to cinnabar, rocksalt and orthorhombic Cmcm phases took place at 1.8, 4.7 and 10.7 GPa respectively. A left shift of one peak was observed under pressure for the Cmcm phase. The axial and volume compressibility of these phases are presented in Fig. 1. The lattice parameters of the zinc blende and cinnabar phases decrease monotonically. For the rocksalt phase, its axial length 'a' continuously decreases and merge with that of the orthorhombic phase while the parameter b increases initially and then decreases. The c axis initially decreases slowly when b is expanding and thereafter at a faster rate once the transition to orthorhombic phase is complete. The unit cells of different structures adopted by CZT at high pressure are shown in Fig. 2. In the zinc blende structure (Fig. 2a), the Cd/Zn layers and Te layers are present alternatively seen from any direction. Four Te atoms are placed equivalently around the Cd/Zn at a distance 2.793 A° with all the Te-Cd/Zn-Te angles as 109.47°. However, in cinnabar structure the individual Te layers and Cd/Zn layers are present parallel to the ab-plane or along the c axis. Upon a transition from zinc blende to cinnabar, the Te atoms move in planes parallel to ab-plane in such way that two Te atoms (Te1) come closer to Cd/Zn and the other two Te atoms (Te2) go farther as compared to that in zinc blende structure. Accordingly, the angles Te1-Cd/Zn-Te1 becomes larger and the angles Te2-Cd/Zn-Te2 become smaller. There are two more surrounding Te atoms (Te3) that are also

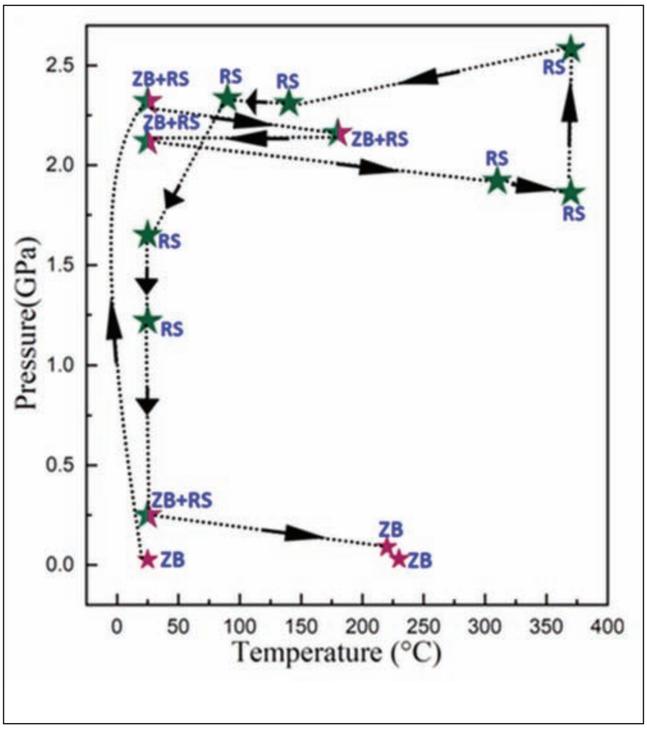

Fig. 3: The phases of CZT at HPHT. The arrows show the thermodynamic path. ZB- zinc blende, RS - rocksalt

placed in an equidistant manner little farther from Cd/Zn. On the other hand in the rocksalt phase, Cd/Zn atoms are surrounded by six Te atoms at equal distances with Te-Cd/Zn-Te angle as 90°. In rocksalt structure, both Cd/Zn and Te share the same plane.

In summary, cinnabar phase nucleates because of atomic displacement in the ab-plane of zinc blende type CZT resulting in a change of coordination number from 4 to (2+2+2). In the cinnabar phase it can be seen in Fig. 2b that Cd/Zn and Te do not exactly share the same plane. When both Cd/Zn and Te move along the a-direction of cinnabar type CZT to share the (102) and ($\bar{1}$04) planes (displayed in Fig. 2c), Cd/Zn gets surrounded by 6 equidistant Te atoms. Further movement of the atoms along the c-direction makes Te – Cd/Zn–Te angle as 90° just like the case in rocksalt structure. The (102) planes of cinnabar lattice are parallel to the (200) planes of the rocksalt phase.

In the bc-plane of the rocksalt phase, a Cd/Zn atom is orthogonally connected to 4 equidistant Te atoms (Fig. 2d). During the transition, the stack of ab-planes experiences more pressure along the c axis and the atoms move away from each other along the b axis. Accordingly, the c parameter decreases and b parameter (distance between two adjacent Te atoms) increases. In addition, the Cd/Zn atoms present in the alternate planes moves along the positive b axis that changes the straight Cd/Zn-Te chain to zig-zag as shown in Fig. 2e. Cd/Zn-Te bonds are of equal length along a or c axis. However, along the b axis alternative bonds are of same length due to the relative motion of Cd/Zn w.r.t. Te. The transitions to cinnabar and rocksalt phases were accompanied with volume collapses (Fig. 1). Therefore, though a material can undergo transition from cinnabar to rocksalt phase by following continuous atomic displacement, the observed transition in the case of CZT is of first order and hence involves reconstruction. In the case of transition to orthorhombic phase, the volume changed continuously from the rocksalt phase and is of second order that follows a displacive mechanism.

For HPHT studies, NaCl was used as PTM and pressure calibrant. Because of deviatoric stress on the sample in the nonhydrostatic condition, the transition to rocksalt phase occurred at a lower pressure of 2.3 GPa. Cinnabar phase could not be observed due to poor resolution of the lab source. A significant hysteresis in stability and transition was observed at HPHT during the reverse cycle and the P-T region explored is shown in Fig. 3. In the reverse P-T cycle, the rocksalt phase continued to be present till ~ambient implying the irreversibility of rocksalt phase at HPHT. However, further application of temperature resulted in zinc blende phase indicating that temperature helped in overcoming the kinetic barrier. .

No structural phase transition was observed up to 400 °C at ambient pressure. The high stability of the rocksalt phase as indicated by its irreversibility up to a low pressure of 0.2 GPa could have been induced by stress and/or temperature.

Corresponding email: sanju@igcar.gov.in

V.25

Development of IR Microscope to Characterize the Te inclusion Defects in CdZnTe-based Gamma Detectors

A portable and wireless gamma spectrometer was demonstrated with CdZnTe single crystals grown using the travelling heater crystal growth infrastructure established at MSG. In Dec.2021, we first resolved the photo peak of ^{137}Cs (662 keV) using a quasi-hemispherical geometry. However, the energy resolution was only 14%.

In the pursuit to improve the energy resolution, the growth parameters and post-processing procedures were further optimized. The defects in the crystals impedes the energy resolution and therefore a systematic study to tailor them is essential. The major defect in CdZnTe are Te inclusions. The size and density of these defect are the major component that decides the leakage current and energy resolution of the detector element. Commercial CdZnTe gamma detector elements are reported to possess Te inclusion of sizes < 5 micron. To yield CdZnTe single crystal with better energy resolution the inclusion defects have to be visualized using an microscopic technique to further optimize the growth condition.

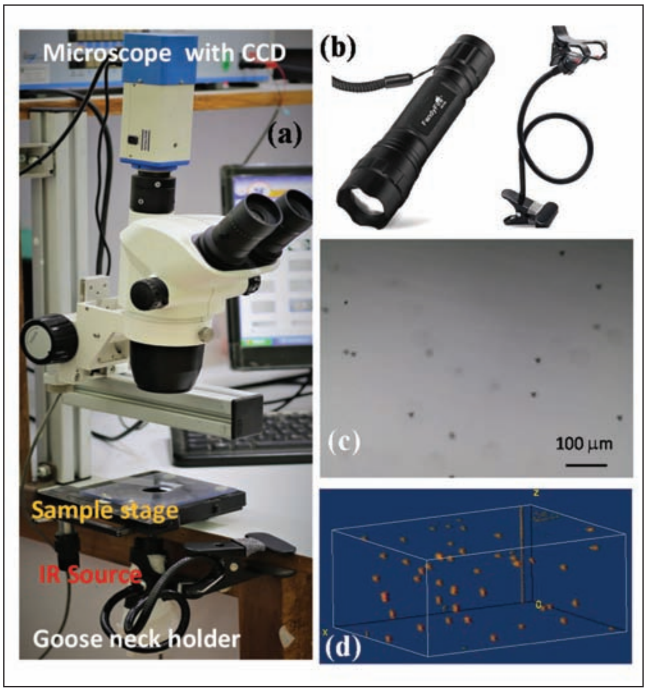

Fig. 1: (a) Assembled IR microscope (b) Commercial IR source and goose neck holder (c) representative2D IR image of Te inclusion in CdZnTe and (d) 3D reconstruction of multiple 2D imagesusing ImageJ.

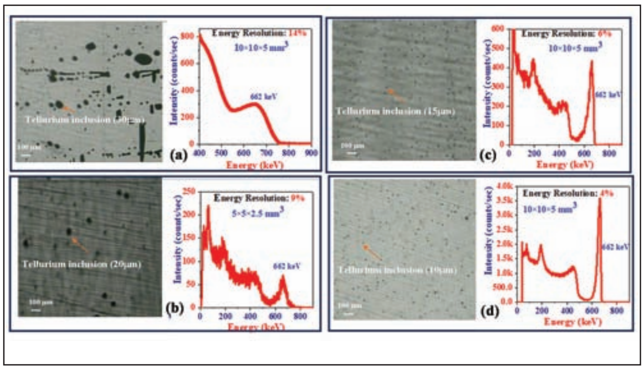

Fig. 2 : (a-d) IR microscope images of the tellurium inclusion in CdZnTe elements (left panel) and the corresponding gamma

CdZnTe is transparent in the IR regime of ~ 920 nm wavelength light due to the wide band gap of 1.5 eV.

The tellurium inclusion that are semimetal in the semiconductor CdZnTe matrix can be easily visualized using a transmission IR microscope setup.

Therefore, transmission IR microscope was assembled in-house using a stereo microscope with CCD camera, IR torch(940 nm),and micrometer sample stage as shown in Fig. 1 (a-b). The commercial IR torch (shown in Fig. 1 (b)) was held with the goose neck holder (Fig.1 (b))beneath the microscope stage. The signals from CCD camera were recorded by ImageJ software using Webcam Capture plugin.

A representative IR images of Te inclusionin CdZnTe samples and its 3D reconstruction using 3D volume viewer plugin in ImageJ is shown in Fig.1 (c and d).

As the detector's energy resolution strongly depends on the size and distribution of these tellurium inclusions, the growth rate, heater assembly and solvent ratio were further fine-tuned to reduce the size and distribution of inclusions. Fig. 2 (a-d) shows the IR microscope images of the tellurium inclusion in the detector elements from different growth runs with different growth parameters. The corresponding gamma spectrum of 662 keV of ^{137}Cs source is shown on the right panel. A systematic improvement in energy resolution is evident with corresponding reduction in the size of the tellurium inclusions from 20 micron to 10 micron. Efforts to further improve the energy resolution to < 2% are in progress.

V.26

Effect of Inhomogeneity on the Arrott Plots of First Order Magnetic Phase Transitions

Ferromagnetic materials exhibit ferromagnetic (FM) to paramagnetic (PM) transition at the critical temperature (known as Curie temperature, T_C). The FM to PM transition can occur as a first order or second order phase transition. The first or second order nature of transition influences the thermal/magnetic/physical properties of the material. Hence, proper knowledge of the order/nature of the magnetic phase transition is essential from both fundamental and practical application point of view.

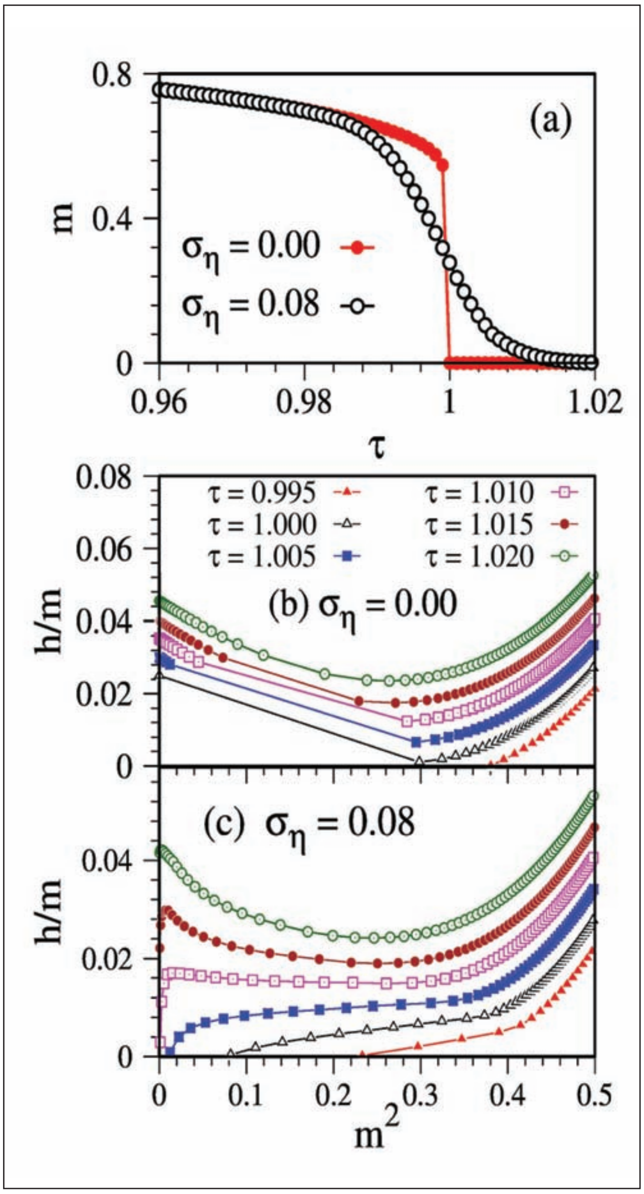

Fig. 1: (a) Reduced magnetization (m) vs. reduced transition temperature (τ) near the FM-PM phase transition for η = 1.5. Here τ is transition temperature normalized with the T_C *of the homogeneous sample (η = 1.5, ση = 0.00). The corresponding Arrott plots (h/m vs.* m^2*) for different values of τ, for (b) homogeneous (*σ_η*=0.00) and (c) inhomogeneous (*σ_η*=0.08) cases. Legends are common for both (b) and (c).*

From the experimental point of view, Arrott plots are generally used to study the nature of ferromagnetic phase transitions.

The Arrott plots are constructed as the h/m vs. m^2 plots, using the isothermal magnetization (m) vs. field (h) data. According to Banerjee criterion, the initial slopes of the Arrott plots will be positive for second order magnetic phase transitions and it will be negative for first order magnetic phase transitions. Various inhomogeneities found in real magnetic materials can cause local variations in the magnetic exchange interactions/environments in the material, resulting in local variations in T_C within the material, and consequently affects the nature of Arrott plots.

In the present study, inhomogeneous first order magnetic phase transitions are studied using the mean-field Bean-Rodbell model. Gaussian distributions in the Bean-Rodbell parameter (η) are considered to model the presence of inhomogeneities in the sample. The Arrott plots are generated with and without distributions in η and results are compared with each other.

Fig. 1 shows the main results of the study. Results indicate broadening of the FM to PM phase transition in the presence of inhomogeneities (Fig. 1a). Also the initial slope of Arrott plots changes from negative to positive values in the broadened transition regions (Fig.s 1b and 1c). In the paramagnetic regimes ($T >> T_C$) the initial negative slopes in the Arrott plots are preserved even in the presence of sample inhomogeneities.

In conclusion, the present results suggest that the Banerjee criterion on the Arrott plots will be valid only in the paramagnetic region, above the ferromagnetic to paramagnetic phase transition temperatures. Also, the change of slope of Arrott plots from negative to positive values in the broadened transition regions may be a signature of sample inhomogeneity.

V.27 Explicit Observation of Tertiary Magnetic Field in Geophysical Transient Electromagnetic Measurements

In time domain electromagnetic central loop sounding or coincidence loop measurements often a sign reversal is observed in the recorded decay transients. These negative decay transients are generally attributed to induced polarization effect. We observed a similar sign reversal in the decay transients recorded with SQUID (Superconducting Quantum Interference Device) as a receiver in central loop sounding measurements at later decay times. These experiments have been repeated by connecting a small resistor in series with the transmitter loop. To our surprise, the time at which the sign reversal occurred in the recorded decay transients with SQUID and across the resistor confirmed that the SQUID is recording the magnetic field produced by the flow of the induced current in the transmitter loop in addition to the decay of the secondary magnetic field from the ground.

A novel hypothesis has been proposed to explain the flow of induced current in the transmitter loop and extensive laboratory experimental simulations have been performed to prove it. The proposed novel hypothesis explains the occurrence of sign reversal in TEM (Transient Electro-Magnetic) systems not only in single loop but also in coincidence loop and central loop TEM conFig.urations. In all cases, the sign reversal is due to the self induced tertiary magnetic fields. In this work, a set of transient measurements have been carried out with different targets and different thicknesses. The experiments have been repeated by locating the targets at different depths in order observe the response of the tertiary magnetic field in the decay transients. The experimental data and subsequent analysis confirmed our hypothesis that the self induced tertiary magnetic field is responsible for the sign reversals rather than the induced polarization effects. Here, a set of three targets such as relatively thick aluminium foils (15 μm), ultra thin aluminized mylar foils (coating thickness of 50 to 100 nm) and thick copper sheets (0.2 mm) were used as targets.

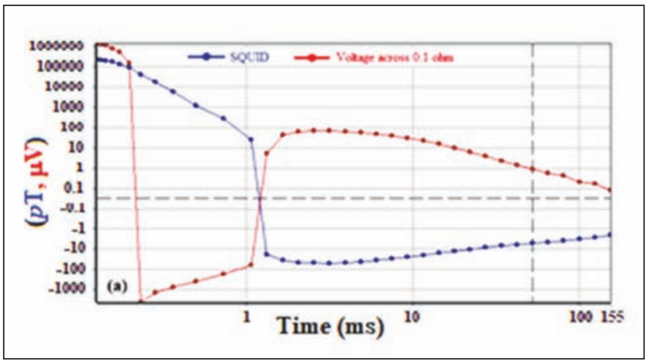

Fig. 1: The screen shot of the recorded decay transients with SQUID at the centre of the transmitter loop and the voltage measured across the resistor connected in series with the transmitter loop in the form of square with side length of 100 m.

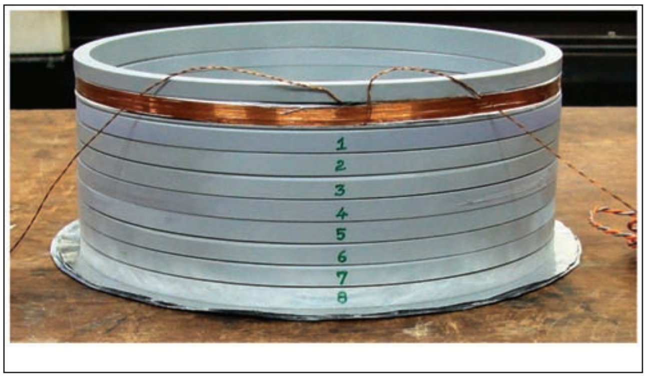

Fig. 2: Photograph of the transmitter and receiver in the form of coincidence loop configuration with spacers to locate the target at different depths.

The decay transients in Fig. 3 clearly show the tertiary response in addition to the secondary response. The above study confirms the existence of tertiary magnetic field in TEM measurements.

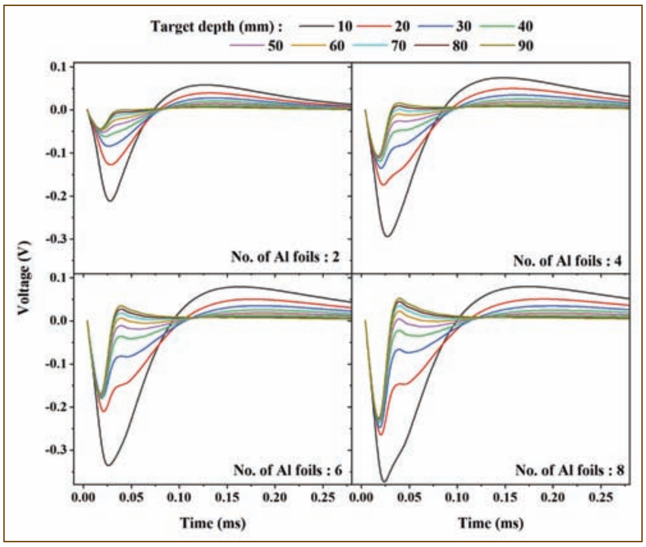

Fig. 3: The decay transients obtained for the aluminium foils with different depths and different thicknesses after subtracting the recorded decay transient without target

V.28 Positron Annihilation Spectroscopy Study of Irradiation-induced Defects in Tungsten

Tungsten and tungsten-based alloys have been considered as potential candidates for the application of plasma-facing components in magnetic confinement fusion reactors. The plasma-facing components should sustain high displacement damage induced by 14 MeV fusion neutrons along with high amount of transmuted gases such as H and He. The accumulation of irradiation-induced defects deteriorates the desirable properties of the plasma-facing components, which shortens their service life. Being a non-destructive defect characterization technique with atomistic resolution, positron annihilation spectroscopy (PAS) techniques have been widely used to investigate the microstructural changes induced by irradiation in nuclear reactor core structural materials.

In the present study, a 99.95% pure tungsten sample was well polished and annealed at 1273 K for 2 h in a dynamic vacuum of 1×10^{-6} mbar. The sample was then irradiated with 9.1 MeV $Au5^{+}$ ions to a peak dose of 1 dpa using 1.7 MeV Tandem accelerator. The irradiated sample was then isochronally annealed from RT to 1273 K in steps of 100 K to investigate the thermal evolution of point defects. The samples were characterized at each annealing step using positron annihilation Doppler broadening spectroscopy based on a variable low-energy positron beam.

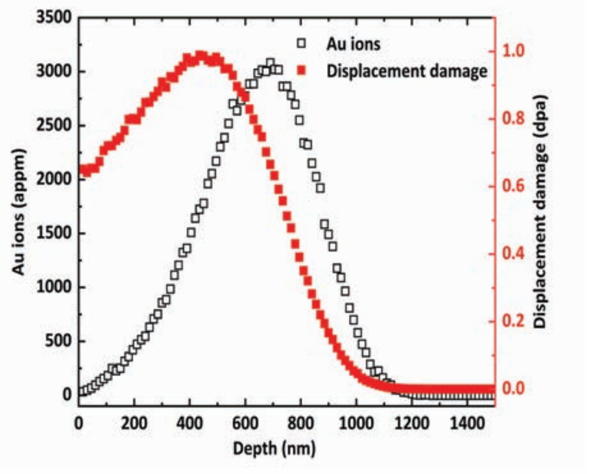

Fig. 1: The distribution profiles of Au ions and displacement damage calculated using SRIM-2013 code.

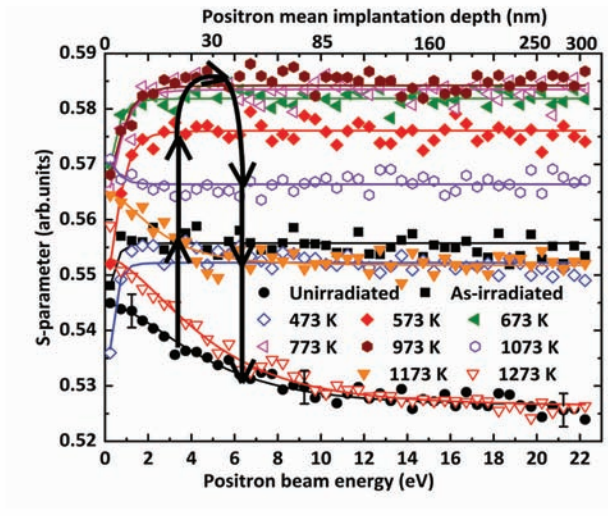

Fig. 2: S-parameter vs. positron beam energy plots of irradiated samples annealed from RT to 1273 K.

The distribution profiles of Au ions and displacement damage calculated using SRIM-2013 code are shown in Fig.1. The distribution peaks of Au ions and displacement damage occur around a depth of 700 nm and 440 nm, respectively. The variations of positron S-parameter as a function of positron beam energy (or positron implantation depth) at different annealing temperatures are shown in Fig. 2. The S-parameter increases upon irradiation due to the presence of irradiation-induced vacancies.

The S-parameter variations with respect to the annealing temperatures correspond to different stages of defect annealing viz. 1) stage III from 473 to 673 K, where the S-parameter increases because of the migration and clustering of vacancies, 2) stage IV from 673 to 973 K, where the S-parameter stood stable due to the growth of nanovoids during which the decrease in S-parameter due to the reduction in the concentration of vacancy clusters compensate the increase in S-parameter due to the increase in size of nanovoids and 3) stage V from 973 to 1273 K, where the S-parameter decreases due to the dissociation of nanovoids is observed in the study. The complete defect recovery occurred in the sample at 1273 K.

V.29 An Innovative Technique for Identifying and removing Noisy Signal Components in the Analysis of Single-variate Signal Amid the Overlapping Frequency Ranges of Signal and Noise Subspace

The Magnetocardiogram (MCG) serves as a non-invasive, non-contact modality to measure subtle magnetic fields associated with the heart's electrical activity. However, challenges arise due to interference from chest movement during respiration/breathing, which disrupts MCG data, impeding accurate interpretation, as depicted in Fig. 1. Conventional filtering techniques, such as high-pass filters and wavelets, face limitations due to the overlapping of low-frequency cardiac signal components and those of these artifacts. To address this issue, an automated algorithm is devised for identification and removal of noisy component from signal subspace. This approach employs empirical mode decomposition, a data-adaptive technique, to decompose the contaminated MCG signal into intrinsic mode functions (IMFs). These IMFs decompose the original signal into signal components with descending frequency contents.

Principal Component Analysis (PCA) is subsequently applied to these set of IMFs, transforming them into orthogonal principal components capturing the most significant variations in the data. The selection of principal components is based on their contribution tothe signal associated with breathing activity. The selection of the principal component hinges on the components' influence on the variance explained by the data.In our study, considering the substantial magnitude of respiration activity, the first few principal components effectively capture the breathing signal, resulting in the retrieval and removal of breathing activity to obtain the clean MCG data, as illustrated in Fig. 2.

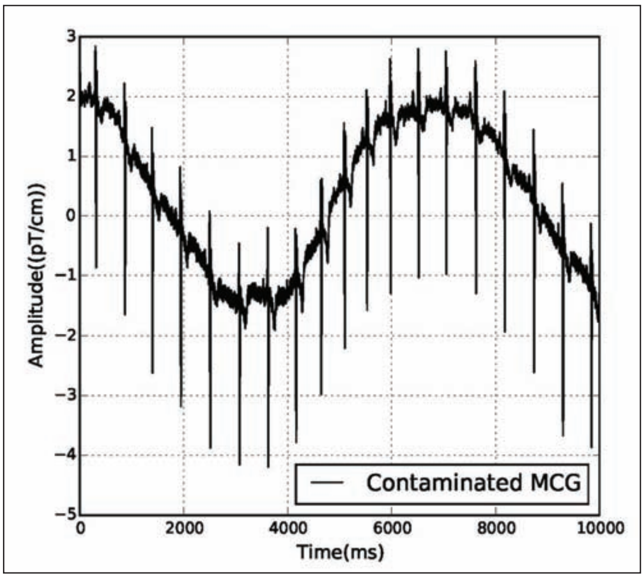

Fig. 1: Contaminated MCG data by respiration activity

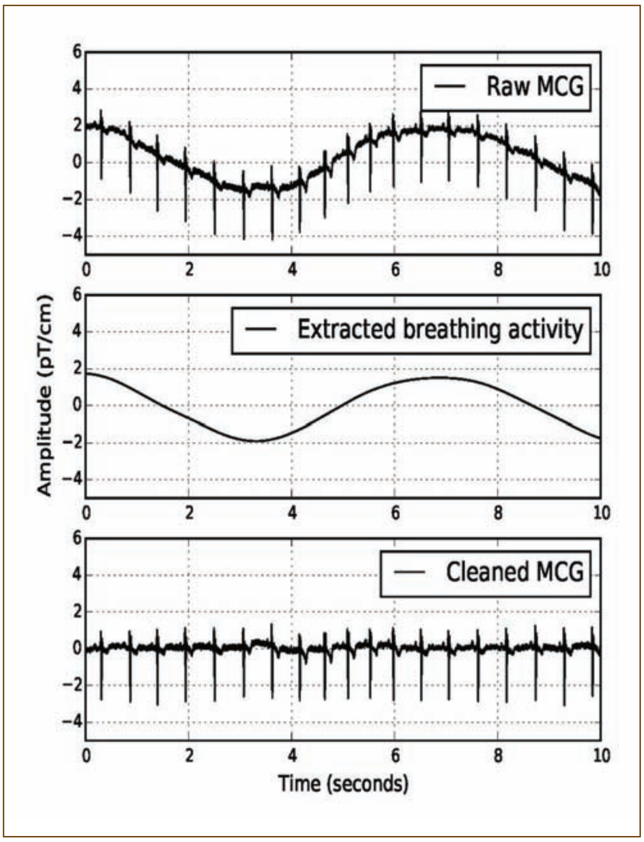

Fig. 2: Extraction of breathing activity from raw MCG to obtain clean MCG using the presented technique

This research establishes the foundation for various promising avenues of investigation. To begin with, there is potential for expanding the suggested technique to handle multichannel data scenarios. This extension would allow for an examination of its performance and adaptability in extracting signals when noise and signal share a common subspace in multichannel measurement. Additionally, this methodology can be further extended to acquire clean data in a wider range of experimental conditions where such overlappingartifacts are expected to be predominant, such as in stress ECG/MCG.

V.30 Defect-bound Exciton Emission in CVD-grown Monolayer MoS_2

Semiconducting two-dimensional transitional metal dichalcogenides have attracted significant attention because of their fascinating optical properties. Chemical vapor deposition (CVD) is one of the prominent techniques to realize the device-grade monolayer MoS_2 (1L-MoS_2). In this context, CVD-grown 1L-MoS_2 is more susceptible to interface defects than exfoliated 1L-MoS_2. Thus, it is important to understand the defects in CVD-grown 1L-MoS_2. The exclusive substrate effect can only be delineated by transferring the CVD-grown 1L-MoS_2 to another substrate. However, the conventional transfer methods may modify the 1L-MoS_2 inherent properties. Thus, a true dry transfer method is required to avoid any polymer-induced effects.

We established the origin of defect-bound exciton emission in CVD-grown 1L-MoS_2 using low-temperature photoluminescence (PL) spectroscopy. The defect analysis was conducted on 1L-MoS_2 flakes grown by CVD at 700 ^oC using MoO_3 and S as the precursor materials. The Typical PL spectrum of the 1L-MoS_2 grown on SiO_2 substrate are was shown in Fig. 1. Inset figure shows optical micrograph of the monolayer flake The PL spectrum was dominated by exciton (1.90 eV) and defect-bound exciton (DBE) (1.74 eV) emission. So far, the origin of DBE was attributed to free excitons bound to S vacancies and the role of substrate-borne impurities was overlooked

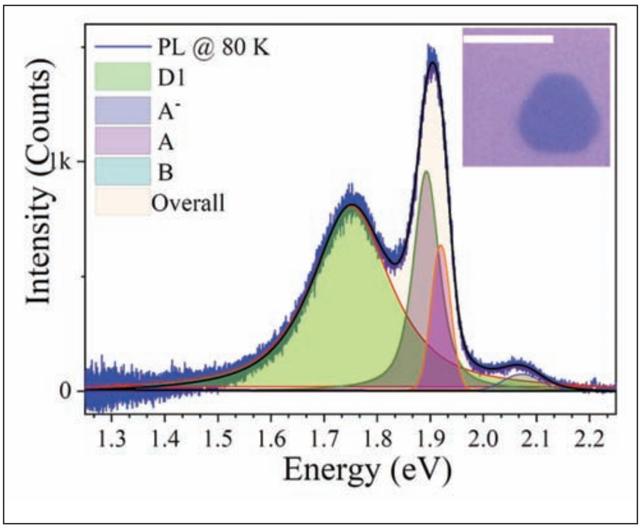

Fig. 1: PL spectrum of monolayer MoS_2 recorded at 80 K. Inset figure shows the Optical micrograph of flake grown on SiO_2 substrate

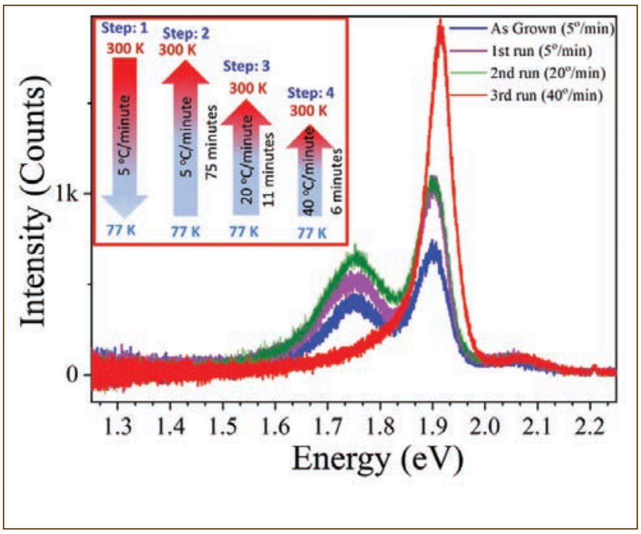

Fig. 2: PL spectra recorded at 77 K after each step. The inset figure shows the schematic scheme of the detachment process.

Here, we adopted an innovative dry detachment method to delineate the effect of substrate-borne impurities on bound exciton emission (Inset of Fig. 2). Initially, the sample was cool down to 77 K and bring to room temperature with different ramp rates. Figure 2 shows the PL spectra recorded at 77 K after each step. The defect bound exciton emission was intact up to the 3rd step (20 oC/min.) The defect-bound exciton emission was completely absent after the step 4 (40 ^oC/min.).

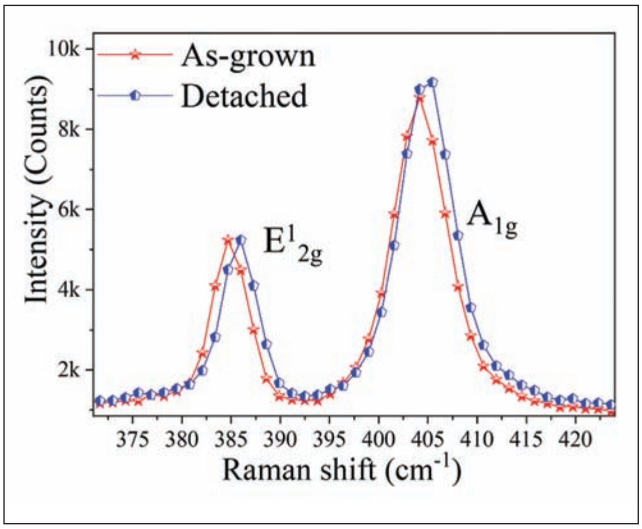

Fig. 3: Raman spectra of 1L-MoS_2 before and after detachment of flake.

The absence of defect bound exciton emission was attributed to detachment of flake from the SiO_2 substrate. The high ramp rate induces the sudden expansion of monolayer MoS_2 and negligible expansion of SiO_2 which leads to detachment of flake. Thus, the bound exciton emission must be originated from the free excitons bound to substrate-borne impurities rather than the sulfur vacancies. The qualitative carrier density analysis was carried out using Raman spectroscopy (Fig. 3). The A_{1g} phonon mode was blue shifted after detachment which indicates the reduced electron carrier density. It also indicates that the substrate-borne impurities acting as n-type dopants.

The typical SiO_2/MoS_2 interface defects are O-dangling bonds and H and Na charge impurities. Among these, Na charge impurities acts a n-type dopant to MoS_2. Thus, bound exciton emission is caused by the substrate-borne impurities like Na not because of S vacancies. Thus, origin of defect bound exciton emission in CVD grown 1L-MoS_2 is different from the exfoliated 1L-MoS_2 flake.

V.31 Nanomechanical Characterization of Sc doped AlN Thin Films

Group III nitrides such as AlN, GaN, InN are widely used in electronic industries due to their wide band gap energy. Among these nitrides, AlN shows the highest piezoelectric coefficient (d_{33}= 5 pC/N) and also has some excellent properties, such as a wide band gap (6.2 eV), high thermal conductivity (300W/mk), high electrical resistivity (10^{16} ohm m), high melting point (2400ºC) and refractive index (1.8), etc. AlN is one of the nitrides which has a good compatibility with CMOS (Complementary Metal Oxide Semiconductor) among other piezoelectric materials such as PZT, BTO, etc., and can exhibit piezoelectric property up to 1200ºC. When AlN is doped with transition metals, these dopants occupy the lattice sites of wurtzite structure of AlN crystal and induces specific properties like dilute magnetic semiconductor in the case of Cr, Ti, Fe, Mn, V, piezoelectricity when doped in the case of Sc, Y and increases the hardness in case of V, Ti and Cr.

In this report, we discuss the structure and nanomechanical characterization of $Al_{(1-x)}Sc_xN$ thin films synthesized with different Sc at%, using magnetron sputtering technique.GIXRD profile of these thin films are shown in Fig. 1, where the basal planes (100), (110) and (101) are seen to shift towards lower angles,depicts that the basal planes expand with the addition of Sc. We can see a systematic increase in the basal plane lattice parameter a, decrease in c (fig. 2) with the addition of scandium up to Sc 40 at%.

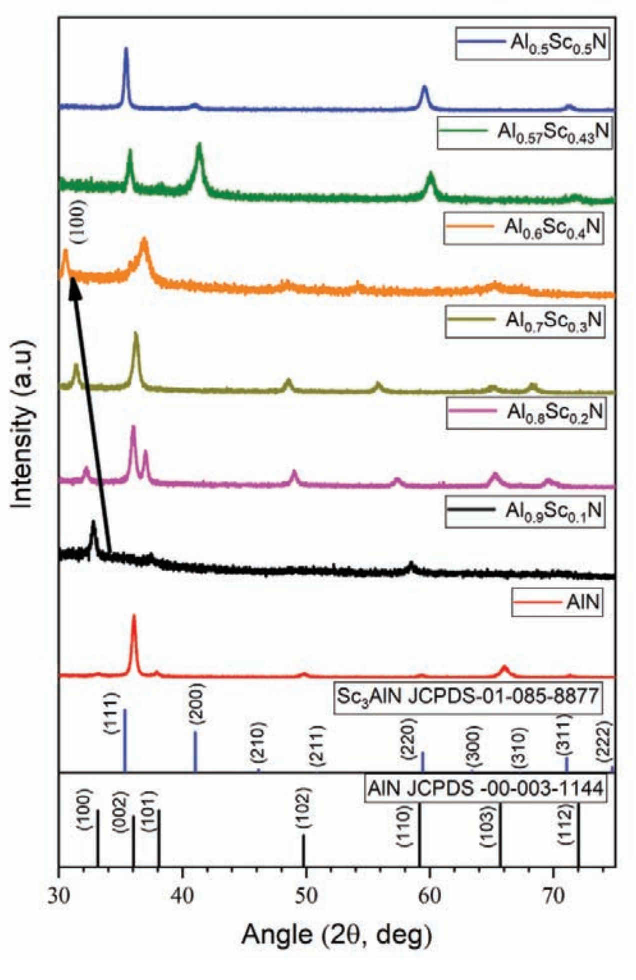

Fig. 1: GIXRD profile of Sc doped AlN thin films along with JCPDS profiles

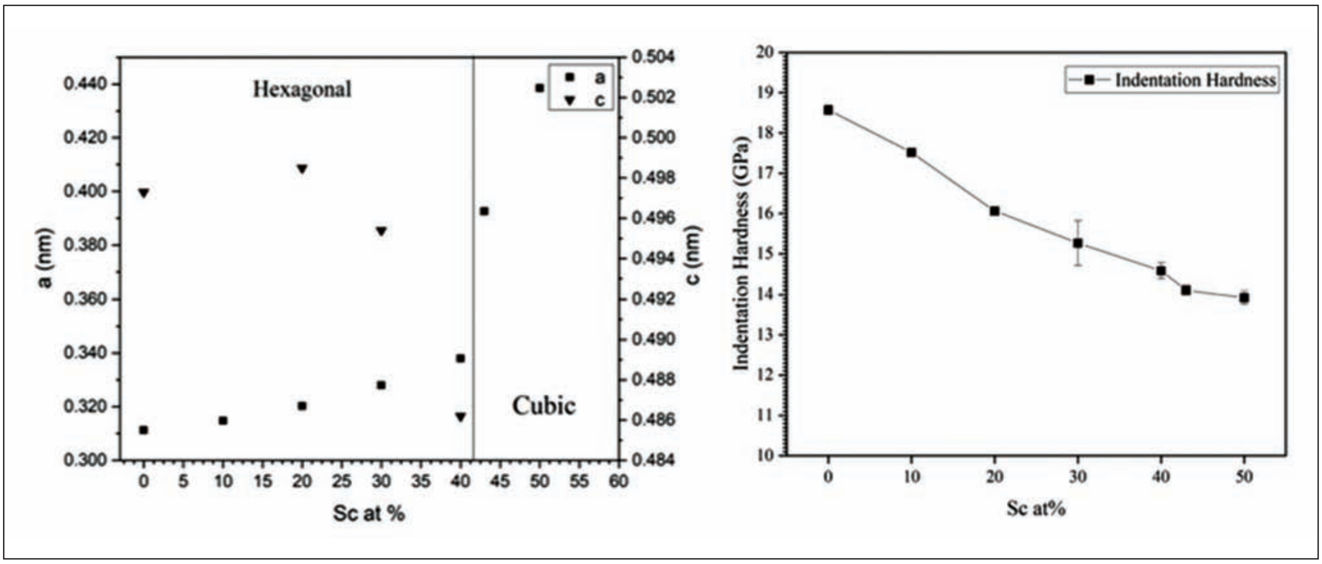

Fig. 2 and 3: Lattice parameters of Sc doped AlN thin films (a and c) and Nanoindentation hardness of pure AlN and doped with Sc

The pristine AlN shows hexagonal phase with highly oriented (002) plane, however for 50% Sc doped films exhibited profile corresponding to cubic Sc_3AlN and theymatch withJCPDS cards of respective compounds. With the addition of Sc, the c-axis plane (002) slowly disintegrates, combines with (101) plane and transform to (111) plane of Sc_3AlN, a new cubic phase emerged. The dislocation density calculation using W-H method clearly shown a decrease in the value with the addition of Sc.(from $1.3852^{17}$for pristine AlN to 2.2835^{16} m-2 50 at% Sc doping).

The hardness values were extracted for all these thin films using CSM technique (shown in Fig. 3) at a depth of 20 nm, since the total thickness of these films were ~200 nm, to avoid the substrate effect. The hardness of pristine AlN was 18.57 ± 0.11 GPa. However, with the addition of Sc to AlN decreased the hardness and the lowest was obtained for 50% Sc, 13.93 ± 0.16 GPa. The decrease in the dislocation density is the reason behind a systematic decrease in the hardness of these thin films.

V.32 Confinement of Light in Dielectric Mie Voids for Reflective Color Filters

Visible light interaction with subwavelength nanostructures could produce vibrant colors if resonant scattering of light occurs with the nanostructures. Vibrant colors are attractive for several applications including displays and imaging. The colors could be harvested in transmission or reflectance mode depending on the device structure and material type. These artificial colors could be primarily tuned via geometry of the nanostructure. Designing the nanostructure should ensure the purity and efficiency of the resonance peaks in the visible spectrum to realize a wide color gamut. Color generation and tuning by this way is therefore is referred as structural colors. Compared to the methods produce colors with active components (like LEDs), the structural colors produced via light-matter interactions from the passive components are more durable. Pigments and dyes are well known materials for rendering passive colors. However, as most of these materials are composed of toxic components, they are not environment friendly. Plasmonic and Mie resonance based dielectric materials are the preferred choices for this purpose in terms of environment friendly, durability and high resolution. As the plasmonic nanostructures suffer from considerable optical losses due to Ohmic heating that arise from the oscillating free electrons. In contrast, the dielectric meta surfaces composed of high-index materials with low optical losses are considered as potential alternatives. Si is one of the preferred choice of materials as it has been the core of the semiconductor devices and it less expensive. Sub wave length nanostructures fabricated on Si are shown to demonstrate the structural colors and demonstrate the possibility of tuning the spectral response via the structural parameters. In this piece of work, we have fabricated two dimensional array of nanovoids onto the surface of Si using a focused ion beam (FIB) lithography technique. FIB nanolithography isa single-step technique, emerging as one of the powerful tools in the field of nanofabrication. The advantage of controlled Ga ion beam milling at nanoscale was utilized to fabricate the 2D array patterns.Cone-shaped nanoetchpits (referred as nanovoids) milled by Ga ion beam were the basic elements of the subwavelength nanostructures. Dimensions and spatial arrangement of these elements were controlled directly by the FIB patterning parameters. This is one of the advantages of FIB nanopatterning compared to the other methods. Color filtering properties were studied in reflection mode

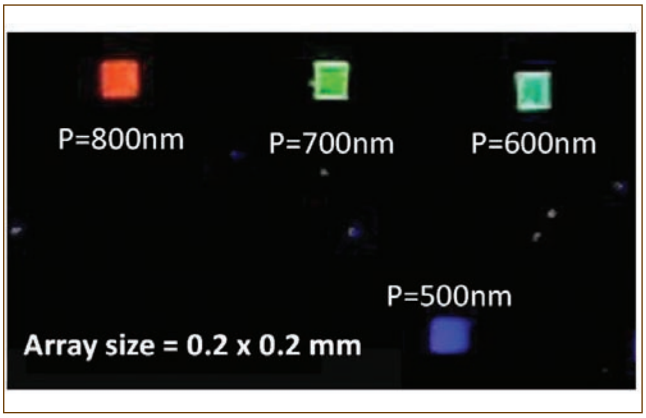

Fig. 2: Optical micrograph of the surface of Si with various nanovoid patterns reflecting various colors

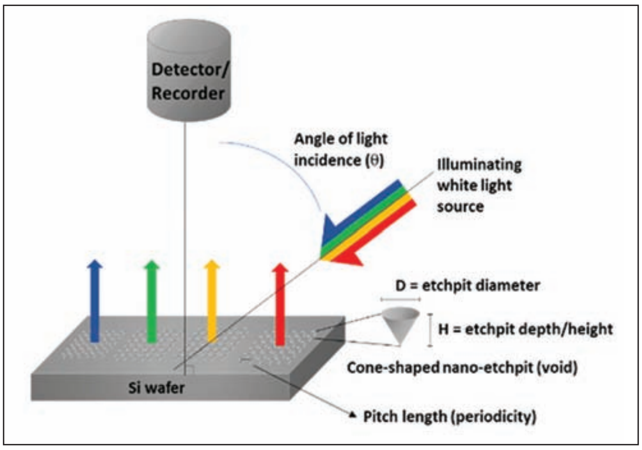

Fig. 1: Experimental setup for recording reflectance spectra and bright-field optical micrographs.

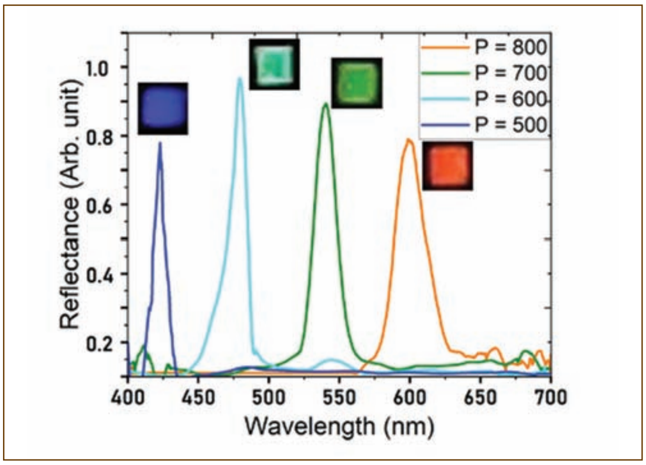

Fig. 3: Reflectance spectra of the patterns with various periodicities

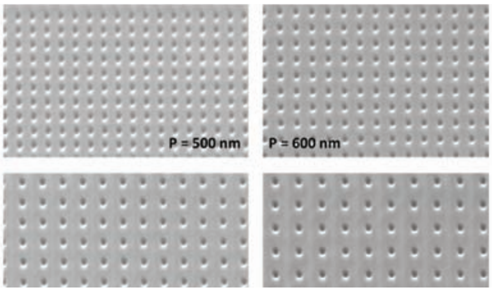

Fig. 4: SEM images of the nanovoid patterns with various periodicities

by recording the reflectance spectrum. We show that the reflected color could be tuned via the periodicity of the pattern, which in fact, could be varied via the beam overlap function of the FIB nanopatterning procedure. Color filtering phenomenon could be understood from the multipole (electric &magnetic) resonance of the periodic nanohole array. In principle, each nanohole is a resonator interacting with visible light that could be manipulated if the structure geometry and material type are tuned such a way that visible light could interact with the resonance modes. Electric and magnetic field intensity distribution, confinement over the nanohole resonators and their lattice effect determine the resonant wavelengths.

V.33 Room Temperature Humidity Sensor at Low Pressure with SnO_2 Quantum Dots

Ceramic and metal oxide based resistive and capacitative sensors are usually used for monitoring the relative humidity (RH) at standard atmospheric conditions. However, humidity sensors operating at low pressure are in demand in processing industries, space applications, and vacuum coatings. So, it is imperative to develop sensors to measure a very low level of humidity in a vacuum domain (<150 mbar). Earlier research indicated that large surfaces with surplus hydroxyl groups can be a suitable candidate for a viable humidity sensor operating under vacuum. In this direction, SnO_2 quantum dots (QD_s) provide sufficient scope for further investigation.

Fabrication of Sensor

SnO_2 QD_s are prepared without a surfactant so that a large active surface results. For synthesis of SnO_2 QDs, $SnCl_4.5H_2O$ and NH_4OH were used. For the sensor study, the interdigitated electrode (IDE) was prepared by depositing a thin gold film (100 nm) on SiO_2 (300 nm)/Si surface using a DC sputtering system. Dispersed SnO_2 QD_s in ethanol were dropcasted on IDE to make the sensor. Fig. 1 shows broad diffraction patterns of tetragonal rutile phase of SnO_2 (ICDD No. 41-1445) and TEM image of it. The average size distribution is 2.4 ± 0.2 nm which is close to the Bohr exiton radius of SnO_2. FTIR and TGA studies have confirmed the presence of water and hydroxyl groups in SnO_2 surfaces. Throughout the sensor experiment, the chamber pressure is maintained by a pump with a vent valve. The resistance change of the sensor is monitored against pressure of the chamber. Investigation reveals that moisture in the chamber responds to the resistance change.

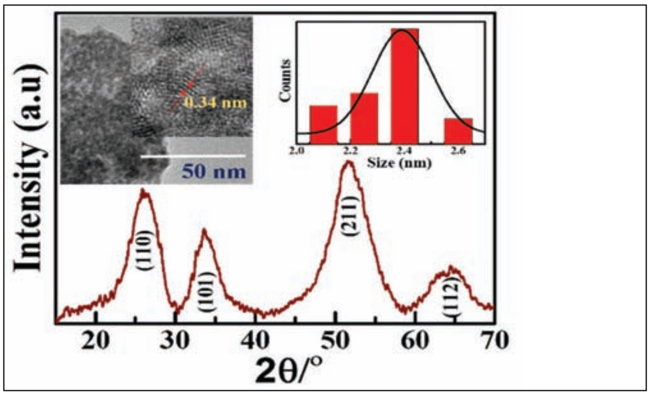

Fig. 1: XRD patterns of SnO_2 QD_s. The inset depicts TEM image and the distribution of particle size.

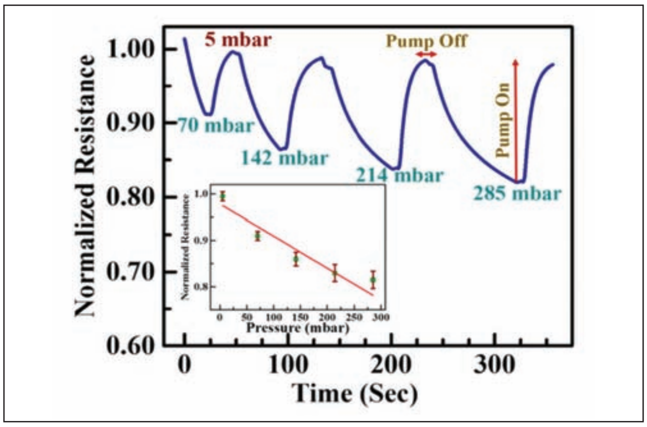

Fig. 2: Normalized resistance change with different chamber air pressure. Linear variation of sensor resistances with air pressure is depicted in the inset.

Sensing performance and mechanism

Clear change in resistance with various air pressure in the chamber is seen in Fig. 2. Obviously, low humidity exists in the chamber air at the low pressure. While the humidity level is high, the more water molecules are physisorbed at the surface of the nanoparticles ,the higher the electron flows at the surface by the proton hopping mechanism. So a decrease in the sensor resistance is observed. The above demonstration shows the potential of SnO_2 QD_s as a humidity sensor in the vacuum domain.

V.34 Understanding of water vapor adsorption kinetics on Si surfaces using MEMS based microcantilever sensors

Si is by far the most important semiconductor material for broad range of applications which include electronic devices/sensors, microelectromechanical systems, nano-manufacturing, and nano-mechanics. Understanding the nature of adsorption of water molecules on the Si surface is of interest in many of the above said applications as it influences the device performance and reliability.

Adsorption of water molecules on Si surface is governed by hydrogen bonding between water-Si, water-water as well as dispersive interactions. Surface chemistry and morphology of the Si surfaces are therefore, crucial as they decide the kinetics of the adsorbed water layer. For instance, if a Si surface is hydrophilic, strong interactions between the solid surface and water molecules may result in the formation of a strongly H-bonded water layer known as ice-like water. In sharp contrast to this, on hydrophobic Si, which is H-terminated, the adsorbed water layer consists predominantly of the weakly hydrogen-bonded structures. Traditionally adsorption of water molecules on solid surfaces is studied using contact angle measurements and Infrared spectroscopic techniques. In the present work an innovative gravimetric technique using microcantilevers is proposed for studying the water adsorption kinetics on hydrophilic and hydrophobic Si surfaces.

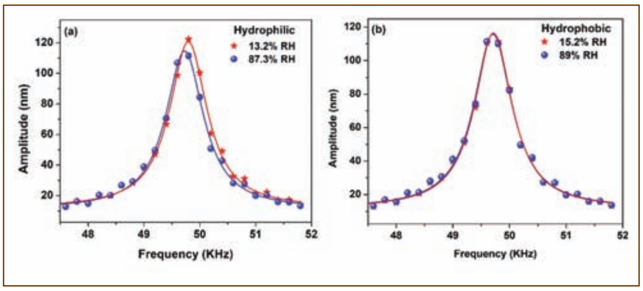

Fig. 2: Resonance spectra in hydrophilic and hydrophobic Si microcantilevers recorded at low and high RH values. Data was fit to Lorentzian

Si microcantilevers with hydrophilic and hydrophobic surfaces were synthesized using chemical route (H_2SO_4+H_2O_2 - Piranha and buffered hydrofluoric acid dip). The adsorption of water molecules on them was studied by measuring the shift in the resonance frequency while Relative Humidity (RH) is varying between 10 and 90%. Block diagram of the experimental setup is shown in fig.1. Microcantilever was placed inside an air tight chamber and its resonance frequency was measured using a Nano Vibration Analyzer (NVA). RH inside the chamber was varied using a bubbler setup. Energy for cantilever excitation was provided by a piezo actuator.

Fig. 2(a) and (b) shows the resonance spectra of hydrophilic and hydrophobic microcantilevers recorded using NVA at a typical low (~10%) and high (~90%) RH values, respectively. From these figures it is evident that in the case of hydrophilic Si surface, resonance frequency is shifting to a lower value at higher RH, whereas it remains the same in the case

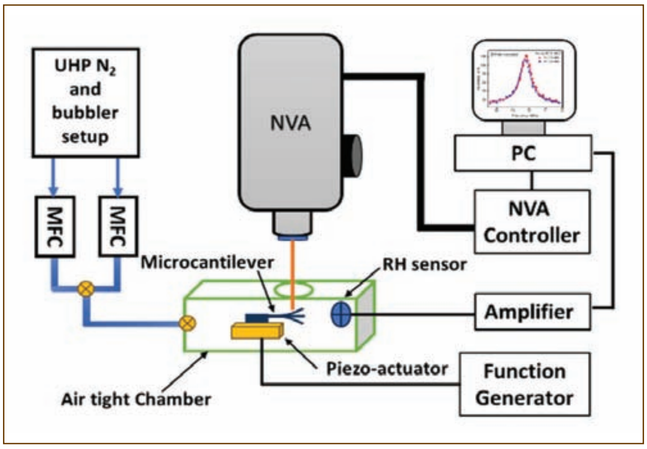

Fig.1: Experimental setup for studying the water adsorption kinetics on Si microcantilevers

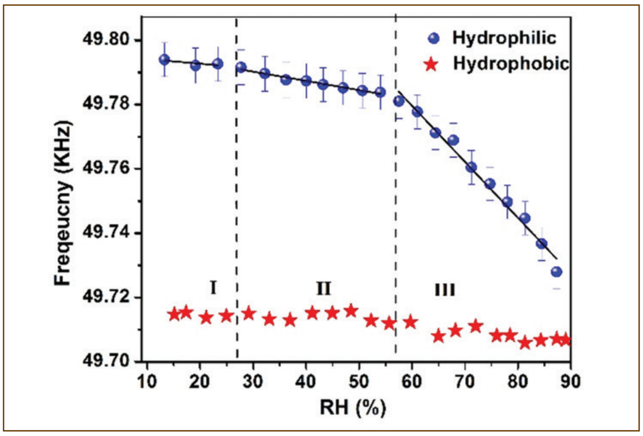

Fig. 3: Variation of resonance frequency with increasing RH in Si microcantilevers with hydrophilic and hydrophobic surfaces.

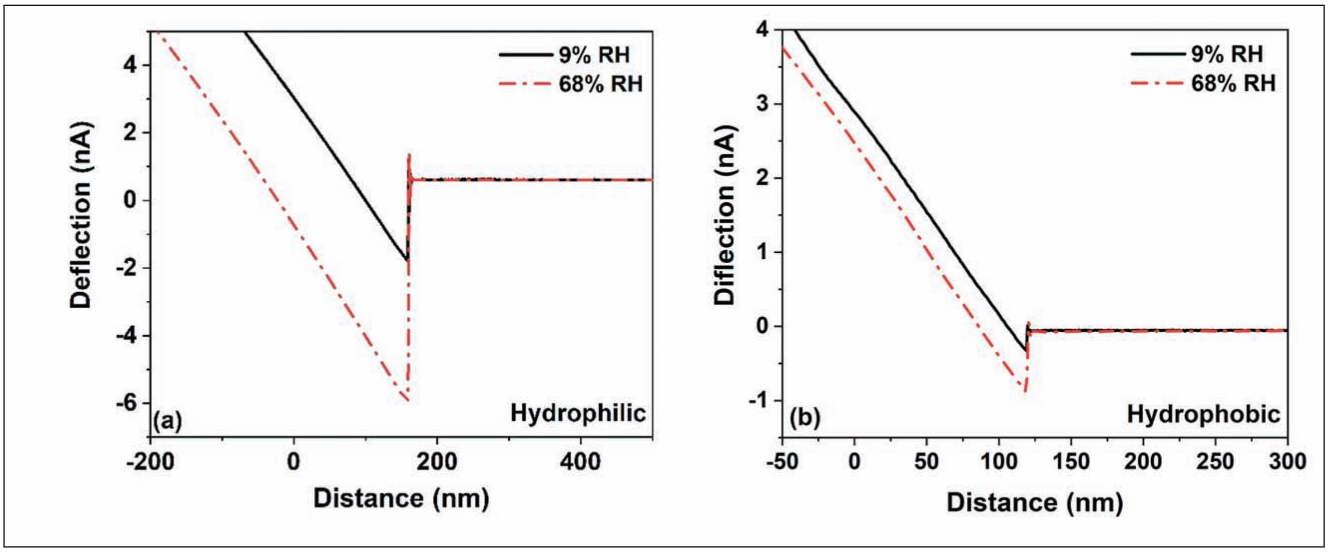

Fig. 4: Force distance curve recorded on hydrophilic and hydrophobic Si microcantilever surfaces at low and high RH values.

of hydrophobic cantilever. Similar experiments were performed at various RH values and Fig. 3 shows the variation of resonance frequency with increasing RH in both the cases. From this figure it is evident that in the case of hydrophilic cantilever, resonance frequency is decreasing with increasing RH and the rate of decrease is more at higher RH values. Decrease in resonance frequency clearly indicates mass loading and is attributed to physisorption of water molecules on its surface. Moreover, it has three different slopes, indicating different adsorption mechanisms operating at these regions as predicted by spectroscopicmethods. In a sharp contrast to this, resonance frequency was almost independent of RH in the case of hydrophobic Si surfaces (see Fib. 2b) implying no water molecules are adsorbed on its surface.

To further understand these results, force-distance curve measurements on the MC surfaces were performed using an atomic force microscope. Fig. 4 shows the force distance curve measured at low and high RH values in hydrophilic and hydrophobic Si microcantilever surfaces. From these figures, adhesion force at higher RH value was estimated and was found to be 55 nN and 8 nN, respectively. Higher adhesion force on hydrophilic surface confirms the presence of thin water layer, sufficient to form a capillary neck.

These results clearly demonstrate that resonance frequency shift in microcantilevers can be effectively used for studying the water molecule adsorption and its kinetics on the Si surface in real time. These results will be of value for designing microcantilever based sensors with improved characteristics and humidity tolerant gas sensors.

V.35

A Technique to Determine the Laser Beam Profile Across a Spatial Light Modulator in Holographic Optical Tweezers to Generate Quality Optical Traps

Holographic optical tweezers (HOTs) combine the technique of dynamic beam shaping with the optical manipulation system and can trap multiple particles at different locations in three-dimensional space. HOTs enable to create any desired discrete or continuous pattern of light. HOTs find application in various fields of science because of its ability to probe higher-dimensional structures in more than one direction, measurement of forces of order of pico-newton, and non-invasive probing down to nanometers. The dynamic beam shaping is accomplished by using a spatial light modulator (SLM) which modulates the phase of light in the optical manipulation system with a spatial resolution of ~ 10-15 µm (pixel pitch of SLM). Each pixelated region of SLM behaving as an independent scatterer enables the creation of the desired pattern of light in its Fourier plane and hence the multitude of optical traps. The phase of light is modulated by displaying suitable holograms, which change the refractive index across the pixels of SLM and hence the optical path leading to modulation of the phase of light traversing through the pixels. There are various trap-generating algorithms for the creation of holograms such as random superposition, weighted Gerchberg-Saxton iterative algorithms etc.

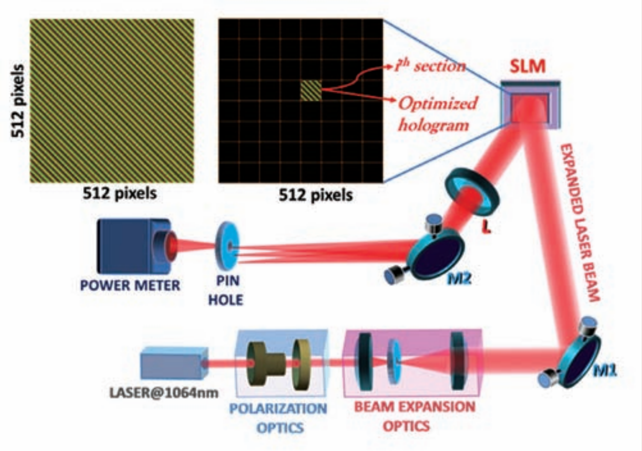

Fig. 1: Schematic of the diffraction based set-up within the HOTs set-up to measure the beam profile, showing a blazed hologram (grating period: 20 pixels in x-direction;20 pixels in y-direction) to generate a first order diffraction spot and a hologram with blazing only at the ith sub-section with other sub-sections kept blank. (Reprinted from Opt. Commun. 530 (2023) 129187, D.K. Gupta, T.R. Ravindran, Laser intensity mapping across a spatial light modulator to generate uniform and aberration-free focal spots, Page No.3, Copyright (2022), with permission from Elsevier)

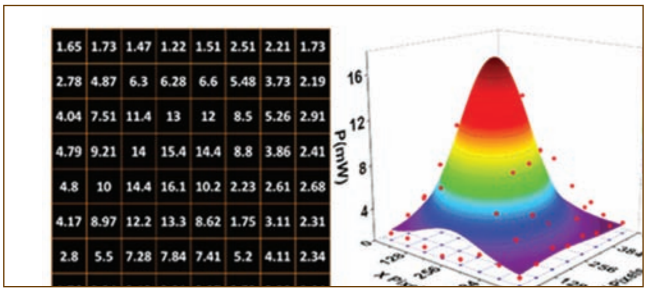

1.65	1.73	1.47	1.22	1.51	2.51	2.21	1.73
2.78	4.87	6.3	6.28	6.6	5.48	3.73	2.19
4.04	7.51	11.4	13	12	8.5	5.26	2.91
4.79	9.21	14	15.4	14.4	8.8	3.86	2.41
4.8	10	14.4	16.1	10.2	2.23	2.61	2.68
4.17	8.97	12.2	13.3	8.62	1.75	3.11	2.31
2.8	5.5	7.28	7.84	7.41	5.2	4.11	2.34

Fig. 2: (a) Table showing the maximum power (mW) diffracted off each of the 64 subsections into which the SLM is divided, with each of the subsections displayed with a blazed grating with other subsections kept blank, (b) The measured laser beam profile across the spatial area of SLM fitted to a Gaussian function. (Reprinted from Opt. Commun. 530 (2023) 129187, Page No.4, Copyright (2022), with permission from Elsevier)

The laser beam profile as incident over the SLM is taken as an input to those algorithms in the creation of holograms. In general, it is assumed to be a Gaussian laser beam profile being centered on SLM. However, in experiments, it is very difficult to ensure the laser beam is centered to the SLM center with a resolution down to ~ 10-15 µm (pixel pitch of SLM). Further, the use of IR laser (wavelength 1064nm) for most of the trapping experiments and the angle of incidence of laser on SLM ~10° it is very difficult to map the laser beam profile onto the SLM although it can be measured anywhere in the optical path by the use of beam profilers.

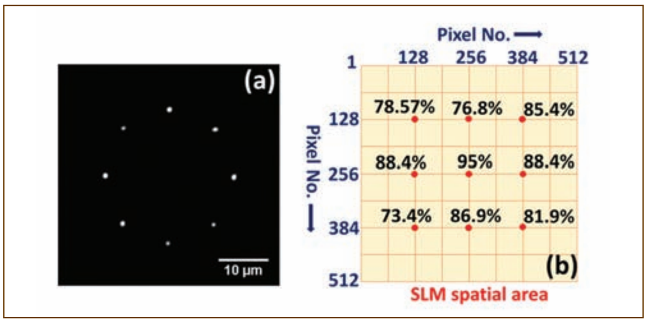

Fig. 3: (a) Circular array of eight spots generated using modified WGS algorithm [4] with laser beam profile programmed at the (256,256)th pixel of SLM (image processed to show only first-order diffraction spots); (b) Uniformity level in the trap spots in a circular array created as that of (a) with laser beam profile center programmed at different locations on the SLM as indicated with pixel numbers. (Reprinted from Opt. Commun. 530 (2023) 129187, Page No.4, Copyright (2022), with permission from Elsevier)

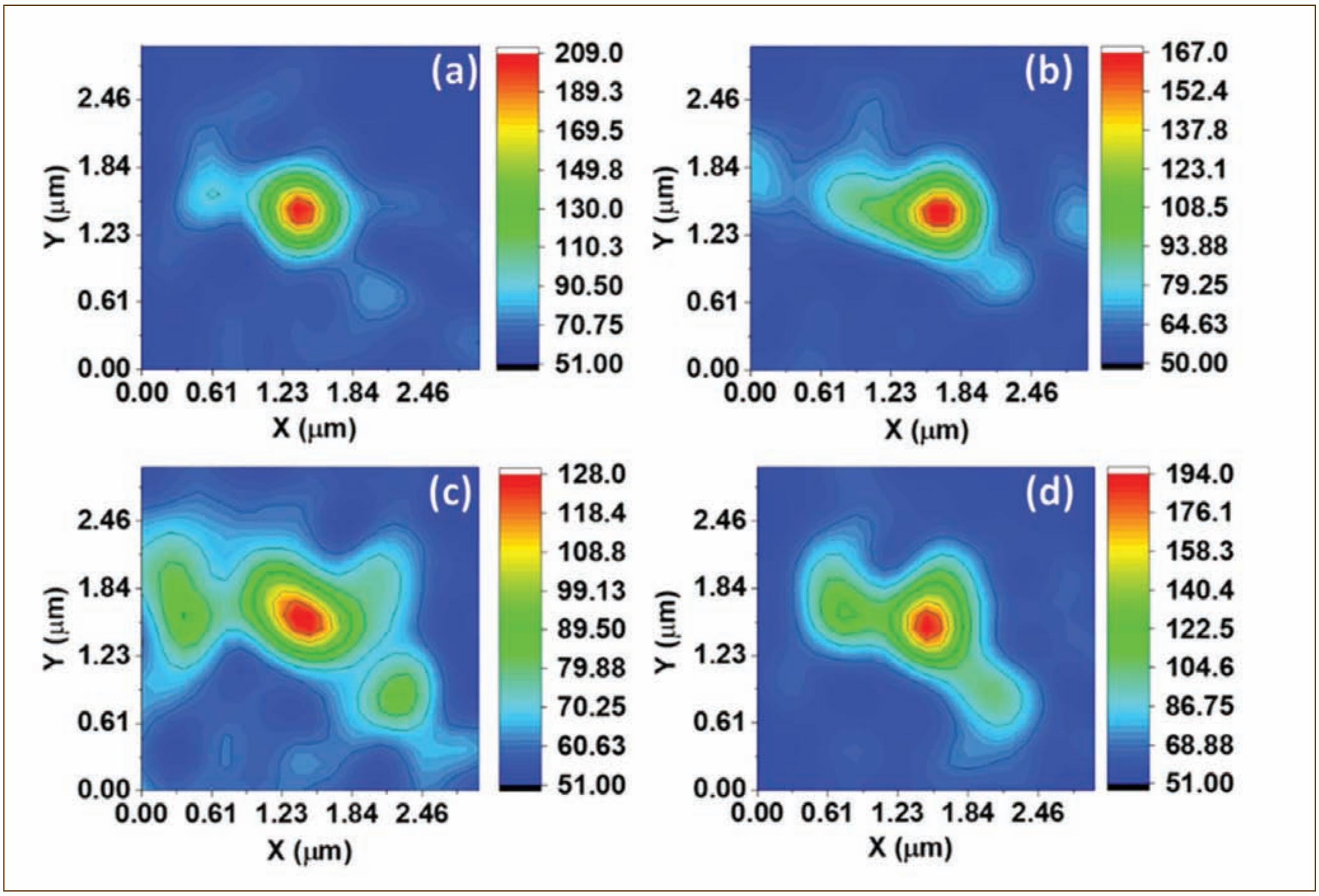

Fig. 4: Intensity plot of a typical trap spot from the circular array (Fig. 4(a)) showing the quality of the trap spot with laser beam profile center; (a) at the center of the SLM (256,256)th pixel; (b) displaced in X-direction at (256,384)th pixel; (c) displaced in Y-direction at (128,256)th pixel and (d) displaced in a diagonal direction at (128,384)th pixel in modified WGS algorithm. (Reprinted from Opt. Commun. 530 (2023) 129187, Page No.5, Copyright (2022), with permission from Elsevier)

We developed here a novel and direct technique to map the intensity of the laser beam onto the spatial area of SLM through a diffraction-based experiment as shown in Fig. 1. The SLM is divided into 64 sub-sections and each subsection is displayed with a blazed hologram (grating period: 20 pixels in X-dir. and Y-dir.) with other subsections being kept blank. This ensures the contribution is from only the sub-section under consideration displayed with the hologram. The power of the first-order beam is measured at the Fourier plane of the SLM with a power meter. The process is repeated for each of the sub-sections. However, before doing this measurement it is ensured that the SLM is corrected for spatially varying phase response as reported by us earlier (Appl. Opt. 57 (2018) 8374), to ensure the contribution to the first order diffraction spot from a given sub-section is proportional to the incident intensity in the given sub-section. The first-order diffracted power from each of the 64 subsections is the relative incident intensity of the laser beam and is fitted to a Gaussian function to map the laser intensity to each of the pixels of SLM (Fig. 2).

We further study the effect of the mismatch of the center of the laser beam with the SLM center by programming the laser beam center at different locations on SLM in the algorithm generating the holograms. An array of eight spots in a circle is created using the holograms with laser beam center coinciding with the SLM center and at different displaced locations in different directions. The uniformity in the intensity of the array of circular spots is maximum when the laser beam center coincides with the center of SLM and is degraded with displaced laser beam centers (Fig. 3). The effect of displaced beam centers on the quality of the optical spots is also studied. Fig. 4 shows the effect of displaced beam centers on the spot sharpness measured as in (Opt. Commun. 530 (2023) 129187). The spot is tightly focused when the laser beam center coincides with the SLM center and deteriorated by ~32% with the beam shifted in X-dir, ~60% in Y-dir and ~47% in a diagonal direction (Fig. 4). This highlights the importance of mapping the intensity of the laser beam onto the spatial area of SLM. Further, the method enables the use of any arbitrary laser beam spatial profile deviating from ideal Gaussian in HOTs with mapping of laser intensity over the spatial area of SLM in place.

V.36 Investigation of Phase Equilibria in LiCl-KCl-$LaCl_3$ Ternary System

LiCl-KCl eutectic melt is used as the liquid electrolyte medium in the pyrochemical reprocessing of spent metallic fuel, known as electrorefining process. In this process, spent metallic fuel is anodically dissolved in the LiCl-KCl melt and fuel elements like uranium and plutonium are selectively electrodeposited at the cathodes leaving the fission product in the melt. Lanthanum is one the rare earth fission products. In order to understand the interaction of $LaCl_3$ with LiCl-KCl melt, LiCl-KCl-$LaCl_3$ ternary phase diagram is being investigated by differential thermal analysis (DTA) and X-ray diffraction (XRD) methods.

DTA samples were prepared by mixing high pure LiCl, KCl and $LaCl_3$ at 10 mol% interval over the whole phase field inside an inert atmosphere glove box. Sufficient amount of the sample mixtures were loaded inside iron crucibles which were sealed by welding and tested for leak tightness. The samples were studied for DTA by Setsys Evolution 16/18 equipment from 250°C to 750°C at slow heating and cooling rates. Further, equilibrated samples were loaded in specially designed XRD sample holder and analyzed by XRD using CuKα radiation.

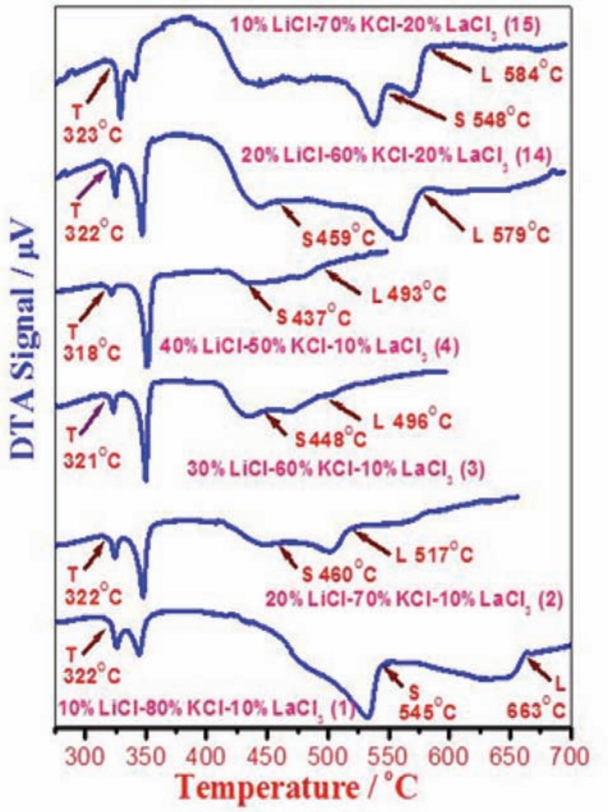

Fig. 1: DTA traces of the samples lying in the LiCl-KCl-K_2LaCl_5 composition triangle (T→Ternary eutectic, S→Secondary crystallization, L→Liquidus temperature).

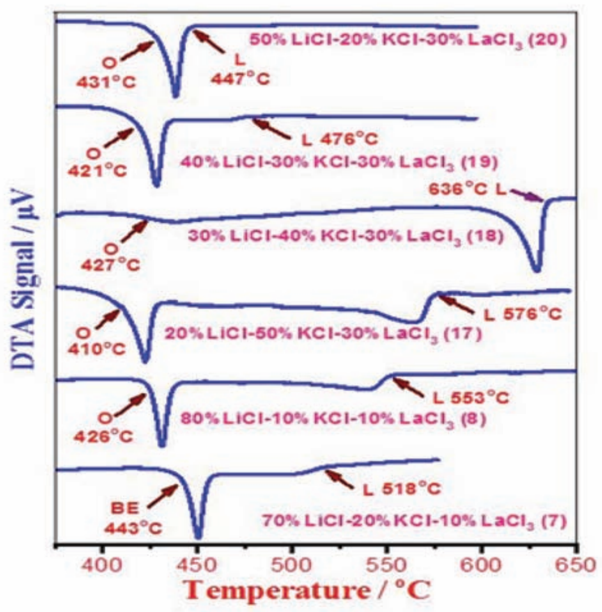

Fig. 2. DTA traces of the samples lying in the LiCl-K_2LaCl_5-$K_3La_5Cl_{18}$ composition triangle (O→ Solidus temperature L→ liquidus temperature)

The ternary eutectic temperature was observed at 323°C for the samples whose compositions were lying in the LiCl-KCl-K_2LaCl_5 composition triangle (Fig. 1). LiCl, KCl and K_2LaCl_5 were identified as coexisting phases in XRD analysis of samples lying in this composition triangle. K_2LaCl_5 is a congruently melting compound. LiCl-K_2LaCl_5 quasi-binary eutectic temperature was observed at 443°C (Fig. 2). $K_3La_5Cl_{18}$ is a non-stoichiometric compound having solid solubility of K_2LaCl_5. The solidus temperatures of the samples were observed from 410°C to 431°C having compositions lying in the LiCl-K_2LaCl_5-$K_3La_5Cl_{18}$ composition triangle (Fig. 2). Wide variation of solidus temperature is indicative of solid solution formation.

V.37 Development of Highly Efficient Bimetallic Metal Organic Frameworks for the Extraction of Pd(II) from Aqueous Solutions

The advent of widespread globalization has lead to increase in consumption of platinum group metals (PGMs) due to their unique role in catalysis, pharmaceuticals, automobile industries, etc. Palladium is one of the PGMs that is in great demand and is used extensively in electronic and electrical equipment. Despite its high demand and large-scale consumption, availability of palladium in earth's crust is sparse($<10^{-6}$ %), due to which there is a need for alternative sources of palladium other than naturally occurring ores. In this context, nuclear industry provides an unique solution, where nuclear waste having a plethora of elements, can be used as an alternative source of palladium.

There has been various reports where Metal Organic Frameworks (MOFs) have been used for the extraction of palladium from slightly acidic solutions with pH ranging from 2 to 6. In this context, we synthesized bimetallic MOFs, using Zn and Zr in various molar ratios with 2-amino benzene dicarboxylic as linker. We used FTIR and Powder XRD to characterize the synthesized MOFs, and TGA was performed to the check the thermal stability of the MOFs. We also employed PSM strategy to modify the parent MOF, UiO-66-NH_2 with glutaric anhydride and pyridine dicarboxylic acid to form UiO-66-GA and UiO-66-PDCA, respectively. The synthetic scheme is shown in Fig. 1.

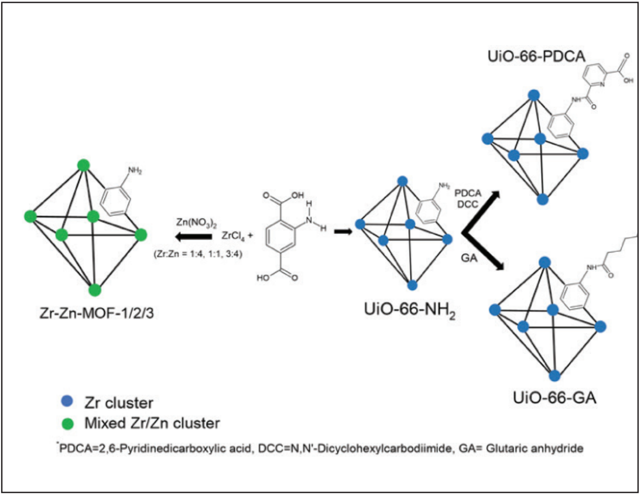

*PDCA=2,6-Pyridinedicarboxylic acid, DCC=N,N'-Dicyclohexylcarbodiimide, GA= Glutaric anhydride

Fig. 1. Synthetic scheme for MOFs

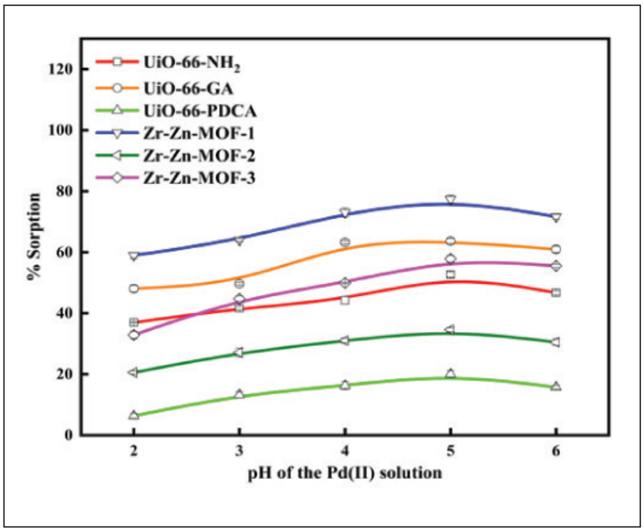

Fig. : 2 Variation of % sorption with pH

The XRD patterns of the PSM MOFs and bimetallic MOFs retained peaks at comparable positions as the parent MOF, confirming that the structural topology of the parent MOF is retained even after post-synthetic alteration and inclusion of Zn in the metal organic framework. The MOFs were used as adsorbent material for extraction of Pd(II) in the pH range of 2-6 (Fig. 2). Zr-Zn-MOF-1 have Zr:Zn in the molar ratio 1:4 exhibited maximum sorption of 77.37% at pH 5. The bimetallic MOF, Zr-Zn-MOF-1 showed high sorption capacity of around 129 mg g^{-1}, which is much higher than the parent MOF, UiO-66-NH_2 showing maximum sorption capacity of about 96 mg g^{-1} at pH 5. To understand the impact of contact time and sorption rate on various MOFs, Pd(II) from the aqueous solution was sorbed at various time intervals. The sorption capacity is greatly influenced by time. The amount of Pd(II) adsorbed on the MOFs initially showed an increment with the increase in contact time and saturated beyond 180 min and this time was determined to be the ideal time for equilibration. The thermally stable and highly efficient Zn doped Zr MOFs synthesized from robust parent MOF, UiO-66-NH_2, can be used as an excellent candidate for the sorption of highly valuable PGMs like palladium for sustainable applications.

V.38 Determination of Thermochemical Properties of D-9 & T-91 Alloys using Knudsen Effusion Mass Spectrometry

Austenitic stainless steel (type D-9) and Ferritic steel (type T-91), the multi-component alloys, are envisaged as clad and subassembly wrapper materials for Liquid Metal cooled Fast Breeder Reactors (LMFBR) in India. Thermochemical properties of these alloys are of significance to predict the interaction of clad with the fuel under normal and off-normal conditions during irradiation. The chemical activity data of clad constituents would be useful for the prediction of threshold oxygen levels in liquid sodium for the formation of corrosion products. Commercial grade D-9 and T-91 alloy samples received from M/s Nuclear Fuel Complex, India were used for the vaporisation experiments. These samples were subjected to XRF technique for semi-quantitative analysis. High temperature vaporisation thermodynamic studies were carried out in the temperature range 1202-1529 K and 1232-1530 K respectively, by using Knudsen Effusion Mass Spectrometry (KEMS). Seven lots of samples (designated as Lot-1 to Lot-7) from each alloy composition (D-9 and T-91) with approximately ~500 mg in each lot were used for the vaporisation studies. Alumina Knudsen cell having a knife edged orifice with a diameter of 0.5 mm at its centre was used in the present study. During the vaporisation experiments, the Knudsen cell and source chambers were evacuated to and maintained at vacuum levels of 3 x 10^{-7} Torr. The cell assembly was heated by electron bombardment furnace. The temperature was measured by employing a disappearing filament optical pyrometer. Mass Spectrometer procured from M/s Hiden Analytical, UK was employed in the present study. The molecular beam of equilibrium vapours, effusing from the orifice was ionized using electrons of energy 28.8 eV (at an emission current of 100 μA). The ions thus produced were mass analysed by quadrupole triple filter and detected by secondary electron multiplier (SEM) operating in pulse counting mode.

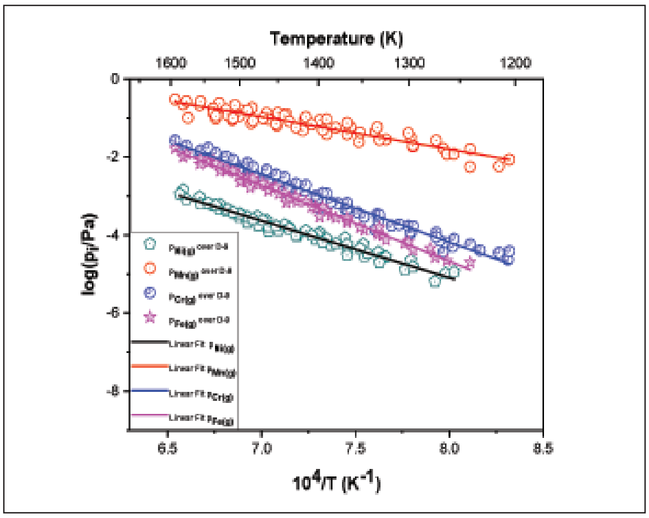

Fig. 1: 2^{nd} law plot of log(p_i/Pa) vs 1/T (K^{-1}) of Cr(g), Mn(g), Fe(g) & Ni(g) obtained over D-9 alloy.

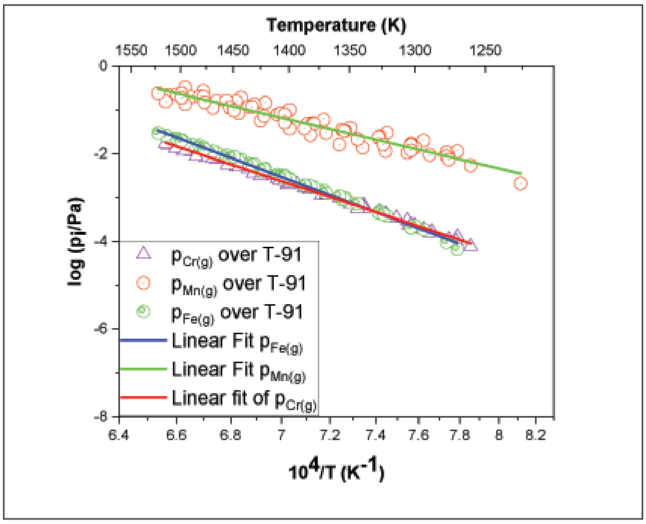

Fig. 2: 2^{nd} law plot of log(p_i/ Pa) vs 1/T (K^{-1}) of Cr(g), Mn(g) & Fe(g) obtained over T-91 alloy.

These studies revealed that both the alloys undergo incongruent vaporisation. Cr(g), Mn(g), Fe(g) and Ni(g) were the neutral vapour species observed over the D-9 alloy. Cr(g), Mn(g) and Fe(g) were the neutral vapour species observed over the T-91alloy. Partial pressure-Temperature relations were derived using KEMS for the first time. Apparent enthalpies of vaporisation data were deduced by second law method (Fig. 1 & 2). Chemical activities of all the major metallic elements (Fe, Cr, Ni and Mn) in the commercial grade D-9 austenitic stainless steel were determined in the temperature range of 1202-1529 K. In case of T-91 ferritic steel, chemical activities of Fe, Cr and Mn were determined in the temperature range of 1232-1530 K.

V.39 Thermochemical Properties Over LiCl-KCl-UCl_3 Ternary Salt System by using High Temperature Mass Spectrometry

Studies on pyro-metallurgical processes dealing with molten salt medium has been difficult because of corrosive nature of the medium which is highly aggressive to process equipment. Vaporisation studies over LiCl-KCl-UCl_3 with 4.46 wt.% UCl_3 (58.1 mol% LiCl - 41.2 mol% KCl - 0.7 mol% UCl3) ternary salt system are of fundamental importance to the pyro-metallurgical reprocessing of spent metallic nuclear fuel by employing molten salt electro-refining process, for the separation and recovery of precious actinides from the fission products. Nature and composition of vapour phase and partial pressure data over LiCl-KCl-UCl_3 ternary salt system are relevant for the cathode-processing step. Partial pressure data are essential for the effective removal of electrolyte salt from uranium metal (deposited onto solid cathode as “dendrite-deposit”).

LiCl(cr) (purity > 99%, M/s Fluka, Switzerland), analytical grade KCl(cr) (purity > 99.8%, M/s Glaxo Laboratories, India) and uranium metal of nuclear grade (BARC, Mumbai, India) were used for the preparation of LiCl-KCl-UCl_3salt. LiCl-KCl eutectic was purified by passing chlorine gas at 673 K and was melted subsequently under chlorine atmosphere. The purified salt was loaded with UCl_3 by equilibrating the salt containing $CdCl_2$ with uranium metal at 773 K in an argon atmosphere glove box. Fig. 1 shows the typical ionization efficiency curve recorded over KCl for K^+ ion.

Vaporisation studies were carried out over solid region of LiCl(cr), KCl(cr) & liquid region of LiCl-KCl-UCl_3 salt system in the range of 715 – 913 K. Monomeric & dimeric species were observed in the vapour phase in equilibrium with their respective salts, LiCl(cr) and KCl(cr). LiCl(g), Li_2Cl_2(g), KCl(g), K_2Cl_2(g), and UCl_3(g) were the neutral species observed in the equilibrium vapour over ternary salt. Partial pressure - temperature relations for vapour species were derived using in-situ calibration from pressure dependent equilibrium constants as well as using pure silver as external calibrant. Using p-T relations (Fig. 2), various heterogeneous reaction equilibria that exist between condensed phase-gas phase and the dissociation equilibra of following gas phase reactions: $Li_2Cl_2(g) = 2LiCl(g)$; $K_2Cl_2(g) = 2KCl(g)$ were evaluated by using 2nd and 3rd law methods. Also, the enthalpies of pressure-independent reactions: $LiCl(cr) + LiCl(g) = Li_2Cl_2(g)$; $KCl(cr) + KCl(g) = K_2Cl_2(g)$ were evaluated by using 3rd law method. Knudsen effusion mass spectrometric studies on LiCl-KCl-UCl_3 ternary salt system were carried out for the first time.

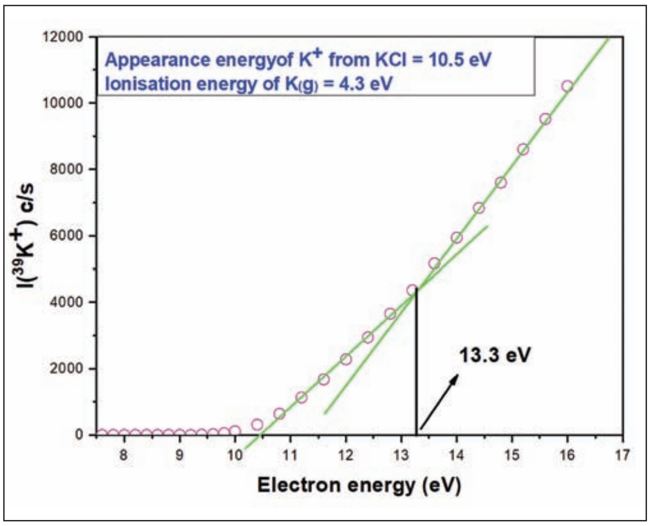

Fig. 1: Ionisation efficiency curve of K^+ recorded over KCl(cr).

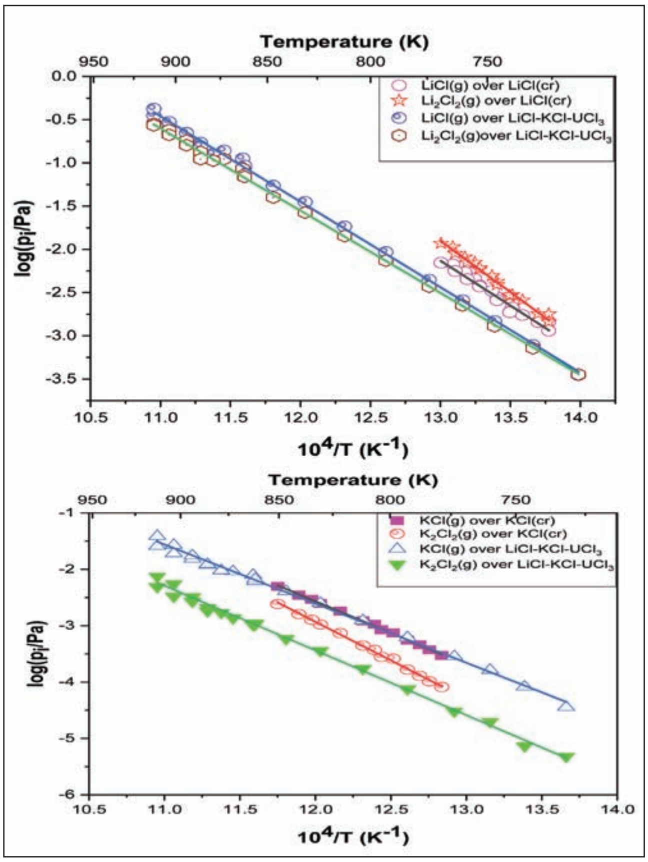

Fig. 2: 2nd law plots of log(pi) vs 1/T for all species recorded over LiCl(cr),KCl(cr) & LiCl-KCl-UCl_3.

V.40 Evaluation of Green Separation Process using Supercritical Carbon Dioxide Containing Ionic Liquids

Supercritical fluid extraction (SFE) based techniques are considered as green alternative to the conventional solvent extraction methods and results in minimum generation of secondary liquid waste. Ionic liquids have attracted considerable interest over the last few years and have already successfully been applied for the extraction of metal ions from aqueous solutions. Supercritical fluids and ionic liquids are green solvents and each of them has its own set of unique properties. Combination of these two is a new and interesting topic that can be successfully employed for the recovery of actinide species from variety of matrices.

The measurement of solubility of these ionic liquids in supercritical carbon dioxide ($SCCO_2$) medium is the fundamental step in development of a supercritical fluid extraction method for recovery of actinide species. In this regard, the solubility of a task-specific ionic liquid, 1-butyl-3-methyl imidazolium chloride (BMIMCl) was evaluated to check its applicability as ligand in supercritical phase. The influence of temperature (313-323 K) and pressure (10-20 MPa) on the solubility behavior was examined using a dynamic flow technique. The solubility of BMIMCl varied from 0.06×10^{-3} to 3.46×10^{-3} mol·mol^{-1} in the evaluated region.

The influence of temperature and pressure on the solubility of BMIMCl is depicted in Fig. 1. At constant temperature, with increase in the pressure, density of $SCCO_2$ increases and the intermolecular distance between CO_2 molecules decreases. This leads to better intermolecular interactions between CO_2 and BMIMCl, resulting in an enhanced solubility at higher pressures. At isobaric conditions, the solubility decreases with rise in the temperature. The reduction in solubility of BMIMCl DAHP at higher temperatures is due to decrease in the density of $SCCO_2$ and the phenomenon is known as retrograde solubility behavior. Retrograde solubility behavior shown by BMIMCl is due to its lower vapor pressure in the temperature of interest. The self-consistency of the experimental data was verified using Mendez-Teja model. The experimental solubility data was correlated using different empirical, semi-empirical and equation of state based models to predict the solubility at different conditions. The model predictions based on Chrastil equations are represented in Fig. 1. The performance of these models is compared with average relative deviation, correlation coefficient and Akaike Information Criteria. Among the models employed in the present study, association theory coupled with model found better for prediction of solubility of BMIMCl with an average deviation of 10%.

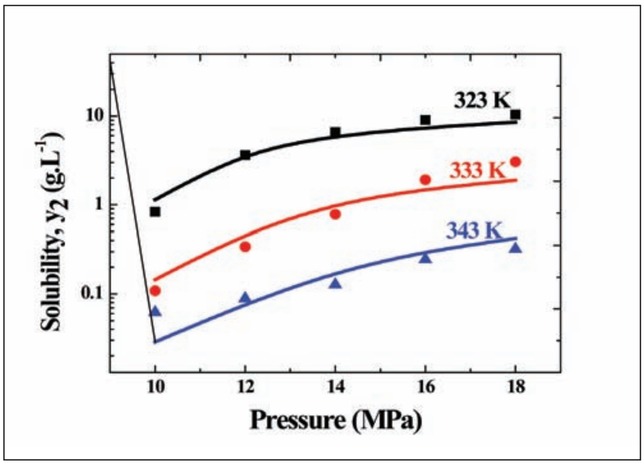

Fig. 1: Influence of temperature and pressure on the solubility of 1-buty l-3 methyl imidazolium chloride in $SCCO_2$ medium; scattered data is of experimental solubility; solid line represents Chrastil model predictions

These results have suggested that, BMIMCl has reasonable solubility in $SCCO_2$ and could be employed as a ligand for recovery of actinide species from different matrices. Future endeavor includes the effect of solvents on the solubility of ionic liquid and development of SFE methods for recovery of actinide ion with $SCCO_2$ containing ionic liquids.

V.41 Enhancing Extraction Efficiency by Fine-Tuning Phosphoryl Binding Strategies: Insights from Theory

The enhanced metal extraction ability of ligands, progressing from phosphate to phosphonate, phosphinate, and phosphine oxides, was initially attributed to the increasing electronegativity of the oxygen atom binding to the metal. This notion evolved, and for a substantial period, the prevailing belief linked the trend in D values to the basicity of the phosphoryl oxygen, defined as the availability of electrons on the phosphoryl oxygen atom.

If this hypothesis proves correct, the charge on the phosphoryl oxygen within these ligands is expected to follow the order phosphate<phosphonate<phosphinate <phosphine oxide, similar to the trend observed in D values. However, the computed electron density at the phosphoryl oxygen was found to be identical, despite an increasing positive charge on the phosphorus atom along the series. Conversely, during complexation with metal ions, the energy difference between the ligand donor and metal nitrate acceptor orbitals progressively decreases from phosphate to phosphine oxide. This facilitates enhanced metal–ligand orbital overlap and stable MOs, identified as a reason for strong metal–ligand interactions in phosphine oxides (Fig. 1). This suggests a need to refine the conventional definition of the "basicity of phosphoryl oxygen" as "the basicity of the phosphoryl group," which serves as the foundation for enhanced extraction behavior.

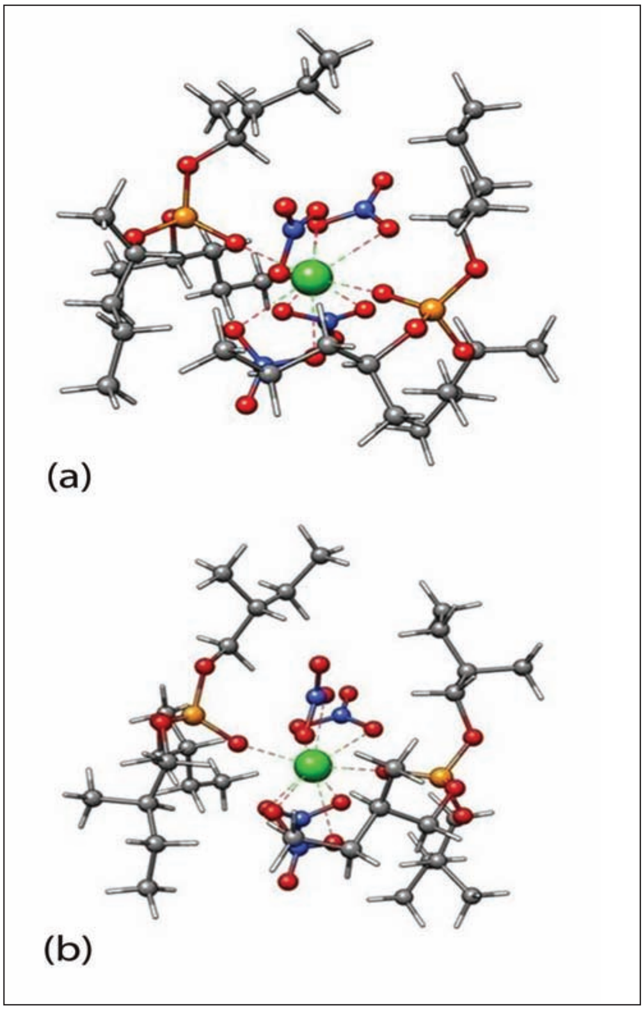

Fig. 2: Optimized geometries of (a) $Zr(NO_3)_4.2TsAP$ and (b) $Zr(NO_3)_4.2T2MBP$ established at DFT level.

This understanding is extended to fine-tune the extraction behavior of amyl phosphates with troublesome fission products, such as Zr. Four representative ligands – TsAP, T2MBP, TiAP, and TAP – differing in the position of the branching methyl groups, are considered during this step (Fig. 2). The computed complexation energies indicate an increasing extraction tendency in the order TsAP → TAP → T2MBP → TiAP. The derived electronic charges show no significant change in the P=O group electronic environment. However, the ligand donor orbital energies increase as we move from TiAP to T2MBP to TsAP. This implies an increase in the basicity of the phosphoryl group, facilitating enhanced metal-ligand charge transfer interactions in accordance with the derived complexation energy values. The contribution from dispersion energy is minimal, as the number of carbon atoms in all ligands is the same.

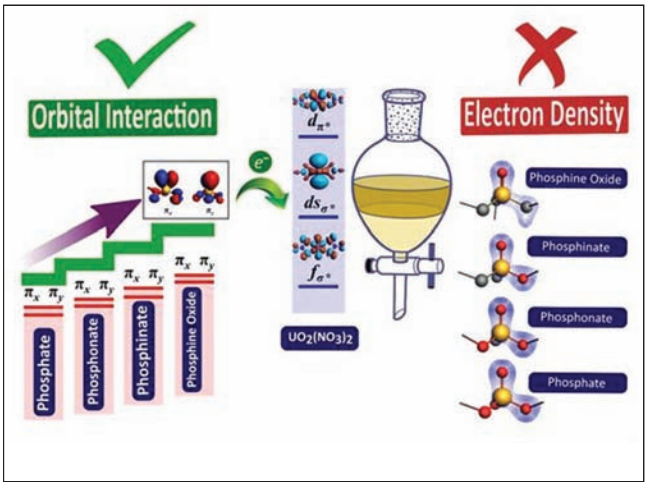

Fig. 1: Schematic Representation of the significance of increased orbital interactions in phosphine oxide ligands.

V.42

Evaluation of Dispersion Energies for Am(III) and Eu(III) Complexes

There is a growing demand for the selective separation of Am(III), an important minor actinide, present in spent nuclear fuel. Due to the similarities in the chemistry of trivalent lanthanides and actinides, these metal ions are expected to exhibit analogous complexation behavior with ligands, posing potential challenges in extraction and separation processes. Conversely, in designing a ligand for the selective separation of a metal ion, understanding the electronic structure and complexation behavior of such ligands with the metal ions is crucial.

In this regard, density functional theory (DFT) calculations offer an excellent accuracy-to-cost ratio for modeling the complexation behavior of realistic ligand molecules with lanthanides and actinides. However, they fall short in accounting for physically and chemically significant London dispersion interactions, crucial for evaluating intermolecular interaction energies that hold importance in chemistry. Technical challenges in parametrization have led to the unavailability of many popular dispersion energy correction schemes (e.g., Grimme's method, etc.) for Am and later actinides. Due to these reasons, energy corrections are frequently omitted from calculations for post-plutonium actinides. Nevertheless, such approaches result in inaccurate predictions, as dispersion interactions play a decisive role in metal-ligand complexation.

Alternately, the overall London dispersion energy can be determined by solving coupled-cluster equations, eliminating the need for additional empirical parameters. This can be accomplished through the recently proposed HFLD (Hartree−Fock plus London dispersion) computational scheme, known for its efficiency even in the study of very large open-shell systems. During this step, interligand dispersive interaction energies were computed at the DLPNO−CCSD level using the HFLD open-shell variant, with the application of the Foster-Boys localization scheme and TightPNO setting.

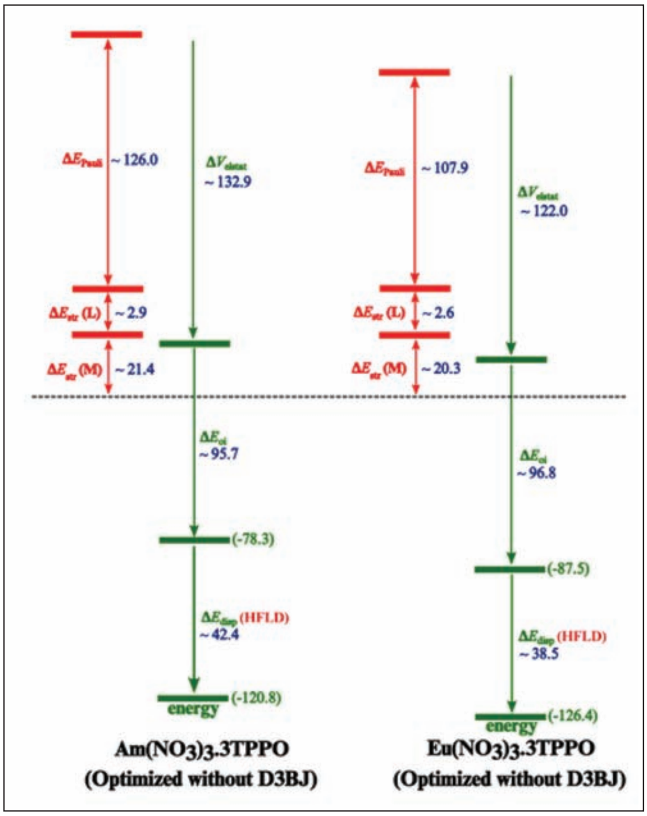

Fig. 1: EDA analysis of $Am(NO_3)_3$•3TPPO and $Eu(NO_3)_3$•3TPPO at DFT level along with the interfragment dispersive interaction energies computed at the RI-DLPNO−CCSD/def2-TZVPP-ZORA

In this context, dispersion energy contributions to the complexation energies were, for the first time, evaluated at the CCSD level for the 1:3 Am(III) and Eu(III) complexes with TPPO ligands, employing the HFLD method. The resulting interfragment dispersion energies were then incorporated into the energy decomposition analysis (EDA), facilitating a direct comparison of the complexation behavior between Eu(III) and Am(III) complexes (Fig. 1). Beyond energy corrections, the study underscored the importance of considering dispersion corrections during the geometry optimization of various lanthanide and actinide metal complexes. Additionally, the study emphasizes the necessity of scrutinizing theoretical predictions based on structures derived without considering London dispersion interactions during geometry optimization, as it may lead to discrepancies with experimental results.

V.43 High Temperature Mass Spectrometric Studies on Ce-Te Tystem using Knudsen Effusion Mass Spectrometry

Mass spectrometric studies was carried out for <$CeTe_2$ + Ce_4Te_7> two phase region using Knudsen effusion mass spectrometry (KEMS). The samples were taken in Mo Knudsen cell, which was placed in another tantalum outer cup. Heating of the sample was carried out by electron bombardment furnace. Temperature was measured by sighting a disappearing filament pyrometer to a black body hole drilled at the bottom of the outer cup. The vapour (in equilibrium with two phase mixture inside the Knudsen cell) effusing out of the orifice was ionised in the ion source of Quadrupole Mass Spectrometer (QMS) using energetic electrons. Ions thus produced were analysed by QMS and detected by Secondary Electron Multiplier (SEM) operated in pulse counting mode. Te^+ and Te_2^+ were the ionic species observed in the mass spectrum of equilibrium vapour over the above two phase region and were identified from the mass numbers and relative isotopic abundances. Subsequently, Ionisation Efficiency (IE) curves were recorded at the mass numbers of 130 and 256 to establish the neutral precursors of Te^+ and Te_2^+, respectively. The curve obtained for $^{130}Te^+$ is shown in Fig. 1. Time dependent intensities of ^{130}Te+ and $^{256}Te_2^+$ were recorded with electrons of 10.8 eV in energy over each lot of sample at various temperatures.

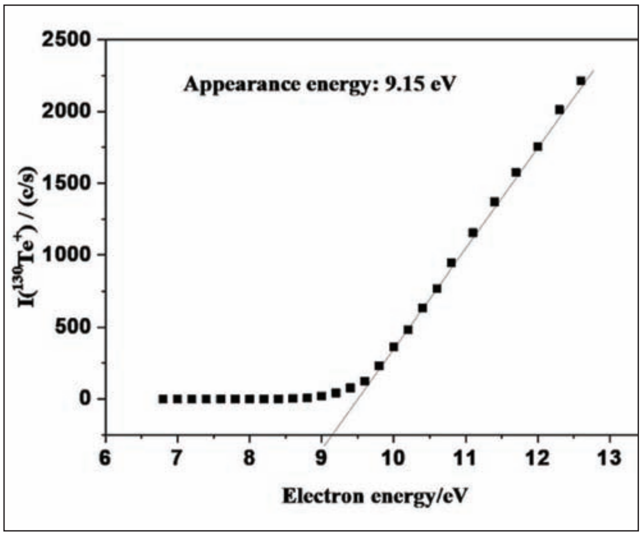

Fig. 1: Ionisation efficiency curve for $^{130}Te^+$

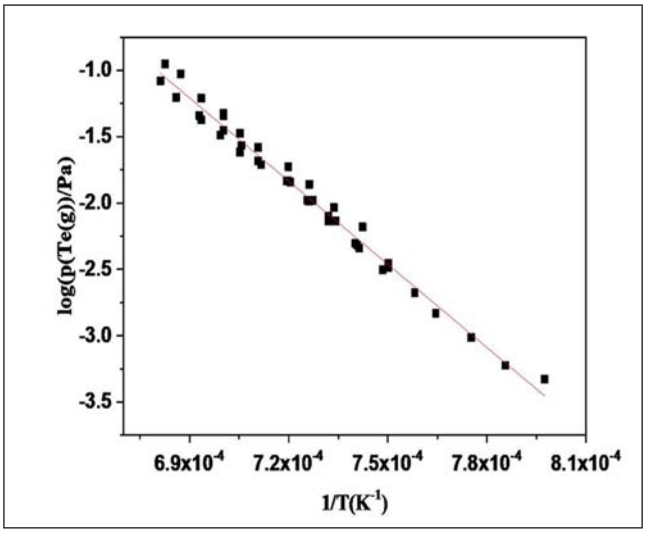

Fig. 2: Combined plot of log p(Te) vs 1/T over <$CeTe_2$ + Ce_4Te_7> two phase region.

It took long period for Te^+ intensity to become stable as the samples were maintained at various temperatures in the above temperature range, whereas Te_2^+ intensity disappeared completely during this period. Subsequently, $^{130}Te^+$ intensity was measured as a function of temperature in the range 1254-1468 K. Pressure calibration constant required for converting intensities of Te^+ into partial pressures of Te(g) was obtained from the pressure calibration experiments over pure silver taken in the same Mo Knudsen cell used for samples. Te(g) and Te_2(g) were ascertained as the neutral precursors of Te^+ and Te_2^+ from the respective IE curves.

The pressure data of Te(g) obtained from all the five runs were fitted in temperature to get pressure temperature (p-T) relation for Te(g) and the combined second law plot is shown in Fig. 2. From the p-T relation of each run,+$(\log(p/Pa) = -\frac{A}{T} + B)$, the enthalpy of decomposition of $CeTe_2$ [$4CeTe_2(s) = Ce_4Te_7(s) + Te(g)$] was derived from the slope. The mean enthalpy of reaction was deduced from the data from all four runs to be 389.2 ± 20.5 kJ.mol^{-1}.

V.44

IR Thermal Imaging Studies on Thin Film ITO and Thick Film Pt Heaters for use in Semiconducting Metal Oxide Sensors

Compact, energy efficient semiconducting metal oxide (SMO) sensors are promising for detection of trace levels of toxic gases in air/inert ambient. Thin films of tin oxide sensors are used for monitoring hydrogen in argon at FBTR and other sodium/steam handling facilities in IGCAR. The surface temperature of the sensing film is maintained around 300°C using a thick film platinum heater printed on the rear side of the alumina substrate. Pt being expensive, replacement of Pt heaters by alternate heating elements are considered. In the current study, conducting tin-doped indium oxide (ITO) is considered as a candidate. The temperature profiles of the Pt heater and ITO thin film heaters measured by IR thermograph are compared. Compact ITO thin film heaters of length about 7 mm, thickness 2 μm and width 300 μm were deposited by pulsed laser deposition using appropriate masks where as Pt thick films were screen printed by doctor blade technique. The surface temperature of the sensing film is maintained by passing appropriate current through the heater calculated from its calibration plot. In this study, temperature profile across the sensing film heated by both ITO and Pt heater is measured to the accuracy of ± 25 mK using Infrared thermography.

Fig. 1 shows the IR thermograph profile of the Pt thick film heater which can go up to 300 °C along with the current through the heater for maintaining different temperatures. Fig. 2 depicts the variation in the resistance of ITO film with temperature.

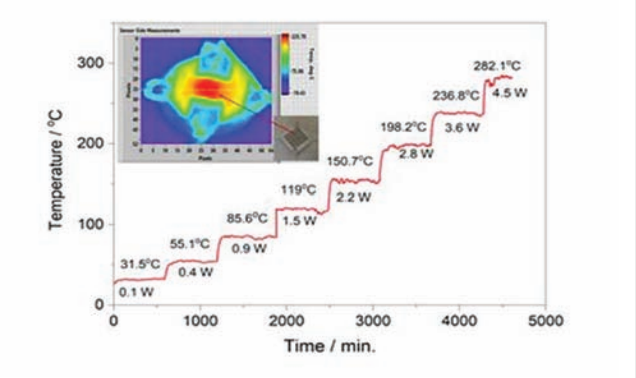

Fig. 1: IR thermal image & heating profile of Pt thick film

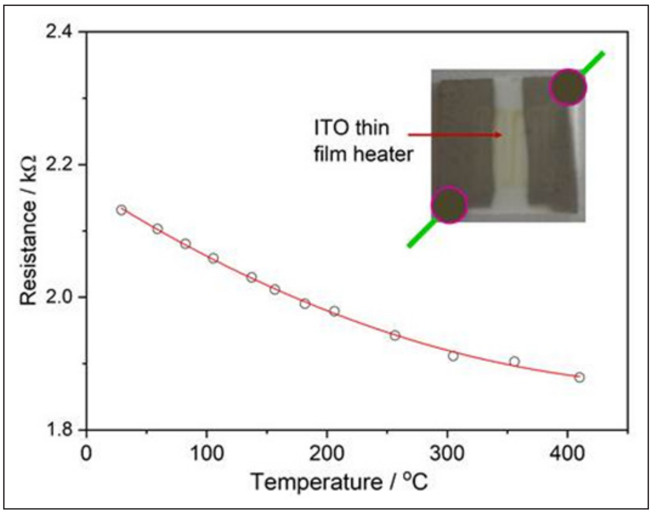

Fig. 2: Photograph of ITO thin film & resistance vs temperature profile of ITO

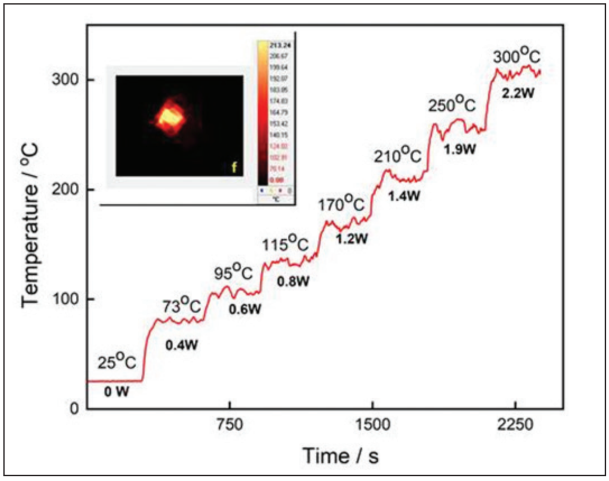

Fig. 3: IR thermal image & heating profile of ITO thin film

The inset shows the photograph of the thin film ITO heater. The IR thermograph in Fig. 3 displayed the variation in the surface temperature of ITO film maintained at different power levels by passing a known current through it.

The performance of ITO heater is comparable to that of Pt-heater except a higher noise level in ITO heater, which arises from the surface adsorption effects on resistance of ITO. It can be minimized by suitable overcoat on the ITO layer, which eliminates surface adsorption effects on ITO resistance. The first results show that the in-house developed ITO heater can be used for heating the sensing film provided the noise level is reduced. It is promising as it can offer considerable cost reduction.

V.45 Fabrication and Performance Testing of a Gas Cell for Estimation of Gaseous Samples by UV-Visible Spectroscopy

Quantification of gases has become an important area in the industrial and environmental research programs. For example; detection of toxic gases for health and safety, identifying volatile organic compounds, monitoring the greenhouse gases for environmental protection and indoor air quality, etc. Gas chromatography (GC) is widely used for the detection of various gases. GC is a time-consuming technique and it requires extensive sample preparation steps. Recently, there has been growing interest in the application of spectroscopic based methods due to their advantages such as compactness, rapid analysis, and selectivity. The possibility of UV-Vis spectroscopy for the detection of gaseous samples using a gas cell was explored

A stainless steel cavity of 1 m path length was used as a gas cell. Suitable stainless steel flanges equipped with quartz windows were mounted at both ends of the cavity. Collimating lenses were used to collimate the light from a deuterium lamp. The transmitted beam was collected using collimating lens and then focused to a fiber optic cable. Finally, the light signal was carried through the fiber optic cable and connected to a fiber optic spectrophotometer, model AvaSpec-2048. Fig. 1 shows the gas cell setup with spectrophotometer.

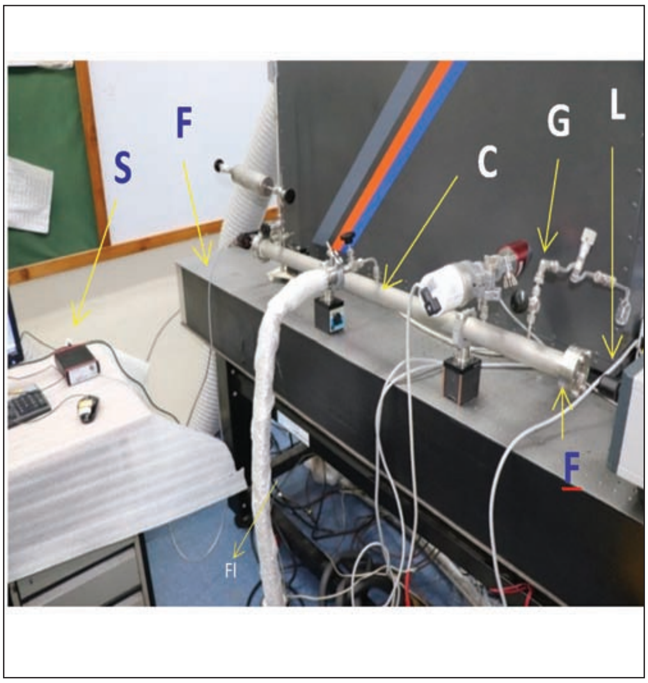

Fig. 1: Photograph of gas cell setup : C-gas cell; G- gas line; Fl- SS flange with lens; L-lamp; F-Fiber optic; S- AvaSpec-2048

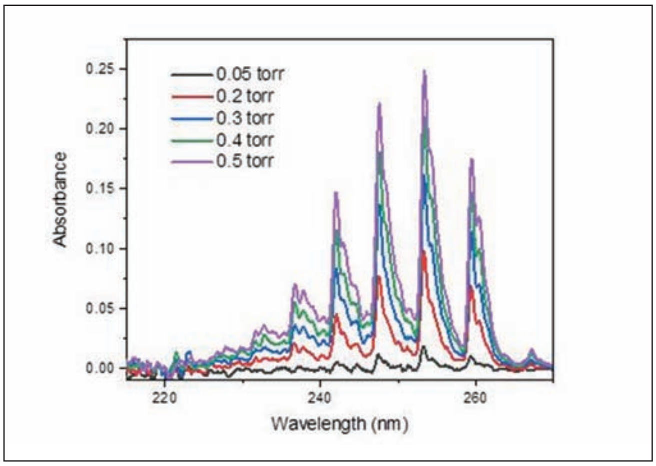

Fig. 2: Absorption spectra of benzene vapor at various pressures

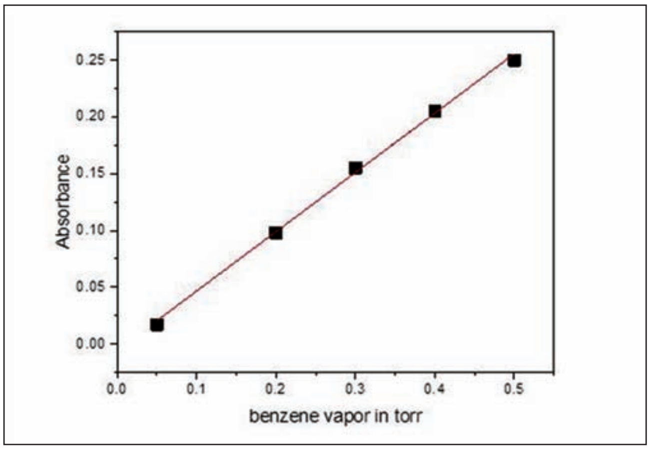

Fig. 3: Calibration plot for benzene vapor at various vapor pressures

After leak testing of the gas cell, benzene vapor, produced from liquid benzene taken in a glass bulb,was introduced in the cell. The vapor pressure was controlled through a vacuum valve. The benzene vapor was diluted with argon gas in the cell. Fig. 2 shows the absorption spectra of benzene at various vapor pressures (0.05 -0.5 torr). A fine structure of benzene in the wavelength range 230 - 270 nm is clearly observed.

The highest absorbance peak at 253.6 nm is used for calibration plot. As can be seen from Fig. 3, there exists linearity over 0.05 to 0.5 torr of benzene vapor pressure. These studies warrant the performance of the gas cell and utilization of UV-vis spectroscopy for the detection of gaseous samples.

V.46

Establishing a Test Facility for the Evaluation of Adsorbent Materials used to Trap Gaseous Iodine

A system for handling off-gas is necessary to manage and regulate the emission of radioactive gases into the site surroundings, with the goal of minimizing the exposure of individuals in unrestricted areas to radioactive gases to the lowest feasible levels. The objective is to uphold occupationally safe exposure levels without compromising plant operation or accessibility. The design of the off-gas system should aim to keep the dose from regular station releases well below the limits set by AERB for individuals outside the facility. Additionally, there is a need for a laboratory-scale testing facility to assess different solid adsorbent materials for gaseous iodine.

Several literature sources suggest that Ag-Substituted Zeolite stands out as a notable adsorbent material for iodine gas. This is attributed to the high affinity of silver (Ag) for Iodine, coupled with the porous nature of zeolites that offers a substantial surface area to facilitate the adsorption process. The efficiency of the adsorption process is notably high at 423 K, with the complete conversion of Iodine reacting with Ag to AgI occurring at 723 K. The data on equilibrium maximum sorption capacity of the adsorbent for iodine (in mg/g), may not be directly applicable to plant conditions where radioactive gaseous materials are released dynamically. For dynamic conditions, the literature proposes a new term, the sorption capacity index. This index is defined as the degree to which the gaseous iodine content in the gas flow decreases after 1 second of its presence in the sorbent's volume. Importantly, this property remains independent of the test conditions. To assess this property, experiments must be conducted under flowing iodine through the packed column of the adsorbent, moving from bottom to top.

By analyzing the amount of Iodine adsorbed concerning the axial distance in the column, as well as considering the flow rate of the carrier gas,packing density, and packing length of the adsorbent inside the column, the sorption capacity index can be determined.

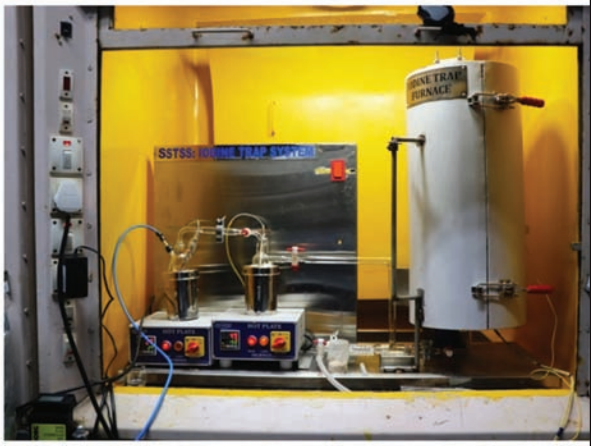

Fig. 1: Iodine sorption study facility commissioned

A laboratory scale facility to determine the sorption capacity index of various adsorbent materials (initial experiments with commercially available Ag-zeolite) was designed, fabricated, commissioned and installed in the laboratory. A photo of the lab scale facility that commissioned in the fume hood is shown in Fig. 1.

The facility is composed of an I_2 generator module, a pre-heating module, and a sorption module. Within the sorption module, there is a divided furnace where the sorption process occurs at 423 K within a distinct column containing the adsorbent. Following the completion of sorption, iodine is extracted from the specific ampule of the column through an optimized procedure involving a 0.1 M sodium thiosulphate solution. The concentration of iodine in the solution is determined using ICP-OES. The preliminary results of the sorption capacity index of the adsorbent is found to show sorption capacity index value of 47 S^{-1}. Further analysis is in progress.

V.47 Dehydration Behavior of Li and Na Tagged Zeolites

In spent salt treatment step in pyroprocessing flow sheet, spent LiCl-KCl eutectic melt, which gets loaded with fission products during electro refining, needs to be treated for removing the fission products for possible recycling of melt. This is essentially important since the melt can be loaded with fission products only to a limited extent as higher loading may increase the melting temperature thereby lessening the difference between melting and operating temperature also the presence of fission products especially lanthanides may reduce the purity of cathode product. Thus, the treatment step helps in purifying the melt as well as recycle the purified melt thereby reducing the volume of salt waste. In this step, melt is treated with zeolite that comprises of sodium or lithium as ion-exchangeable species that exchanges with fission products in melt and alumino-silicate framework where chloride salt gets occluded. It is observed that lithium-tagged zeolite could be more suited to spent salt treatment since its sodium counterpart could alter significantly the Li/K ratio in melt. However, zeolite has quite high moisture absorption capacity (in range of 20 g/g) and thus, efficient dehydration of zeolite in the head-end step of the treatment is essential, as moisture is detrimental to the performance of melt due to high hydrolysis tendency of LiCl. Dehydration behaviour of sodium and lithium-tagged zeolites were investigated by thermogravimetry to ascertain optimum temperatures for dehydration of zeolites. Lithium tagged zeolite was prepared by dynamically equilibrating 7 M LiCl aqueous solution with sodium zeolite in a column set-up at a flow rate of 1 mL/min. Average loading of lithium was estimated at 70-75%.

The lithium and sodium tagged zeolites were characterized by X-ray diffraction technique (Explorer System procured from M/s GNRsrl, Italy).The pattern of the dried powder samples is shown in Fig. 1. The peaks were indexed and the pattern was found to be similar to the pattern reported for aluminio silicates. Pattern indicates the presence of same phases in both the zeolites. No change in pattern was observed before and after drying the zeolites sample.

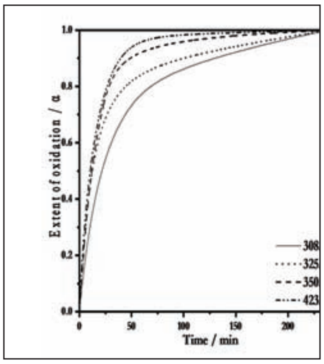

Fig. 3: A plot of 'α' with 't' at various temperatures for Li tagged zeolite (Isothermal experiments)

Both zeolites were first vacuum dried at 140 ^{o}C for about 72 h after which they were saturated with moisture by dynamically equilibrating them with distilled water in a glass column at 1 mL min^{-1} for about 96 h. They were then air dried and based on net weight increase, equilibrium moisture capacity for both zeolites were estimated at 18-20%.

This equipment had a mass sensitivity of 0.1 µg and a temperature sensitivity of 0.01 K. A platinum crucible of 70 µL capacity was used as the sample container. The inner muffle of the furnace was constantly purged with argon (20 sccm). A typical thermogravimetry curve for lithium and sodium tagged zeolite is shown in Fig. 2. A rapid loss in mass was observed till 500 K which continued till 800 K but with lower rate. No change in mass was observed beyond 800 K. For lithium tagged zeolite the total mass loss was ~ 27-29 mass % whereas it was 17-18 mass % for sodium tagged zeolite. The mass loss remained same for all the heating rates which showed completion of the dehydration reaction at the selected heating rates. The dehydration reaction appeared to be a two step process and these steps were not well resolved under the prevailing experimental conditions.

Isothermal experiments were conducted (for Li-tagged zeolite) at four temperatures (308, 325, 350 and 423 K). The variation of extent of reaction 'α' with respect to time is shown in Fig. 3. Higher extent of dehydration was achieved in a shorter time if high isothermal temperature was chosen for the experiment.

From the isothermal data it is inferred that complete removal of water could be achieved from the moisture saturated Li-zeolite after heating it at 423 K for 4 h in the flowing argon atmosphere. Similarly, it was observed that complete dehydration of the sodium tagged zeolite was achieved by heating the sample at 423 K / 472 K for 6 h. The difference in the drying time could be due to nature of bonding of water molecule in the zeolite matrix.

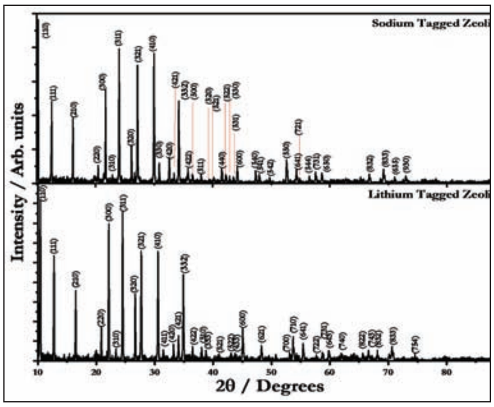

Fig.1: X-ray diffraction pattern of Li and Na tagged zeolites

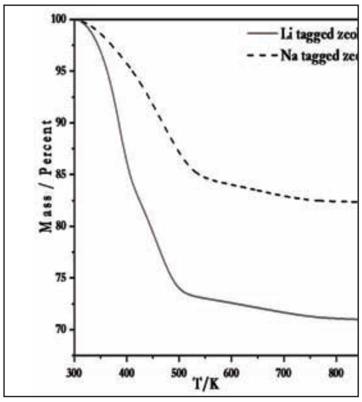

Fig. 2: Thermogravimetric curves for Li and Na tagged zeolite

V.48 Conversion of Contaminated De-moulded Quartz Coated with Y_2O_3 to Borosilicate Glass

Metal fuel (U-Pu-Zr) is chosen as a candidate driver fuel for future fast reactors and MC&MFCG is focusing on fabrication of sodium bonded metal fuel pins. Presently the blanket (U-6Zr) slugs were cast through injection casting route using quartz moulds coated with Y_2O_3. The coating provided on inner surface of the quartz mould is by chemical solution deposition route. This coating is essential to minimize the contamination of silicon in slugs during casting of molten metal alloy. The cast slugs were retrieved after de-moulding the quartz moulds and the broken quartz pieces are treated as contaminated solid waste, which needs to be disposed in a safe manner.

Fig. 2: Photograph of (a) BSG and (b) BSGQ

Borosilicate glass (BSG) is internationally accepted inert matrix for safe disposal of nuclear waste where, SiO_2 is used as a major glass former. Hence, the Y_2O_3 coated de-moulded quartz, being SiO_2 with trace levels of Y_2O_3 can be converted into BSG through melt-quench route. In addition, the interest also focused towards conversion of rejected / drained sodium to BSG. This drained sodium is discharged from defective sodium bonded metal fuel pins with the removal of metal fuel slugs. This drained sodium can be converted to its oxide, to be used as a glass modifier. Presently, Na_2CO_3 was used instead of drained Na during optimization of glass composition. Various BSG compositions were tried, the glass with the composition of 43.2 SiO_2 - 8 ZnO - 6.5 CaO - 12.3 B_2O_3 - 30 Na_2O (wt. %) was chosen as the base composition, labelled as BSG. The collected de-moulded quartz was crushed and ground using mortar and pestle. Preliminary experiment at 10 g level was carried out by replacing the SiO_2 with de-moulded quartz without altering Na/Si ratio and the molten mass was air quenched. After confirming its non-crystallinity by XRD, it was scaled up to 100 g level. The bulk BSG formed using de-moulded quartz was labelled as BSGQ, characterized for its non-crystallinity and found to be X-ray amorphous. Density measured by immersion technique was found to be 2.57 g/cc. Surface morphology analysed by SEM revealed the homogeneity of the product. Some of the essential thermo-physical-chemical properties such as glass transition temperature, specific heat capacity, linear thermal expansion and chemical durability were determined. BSGQ is found to be similar to that of BSG.

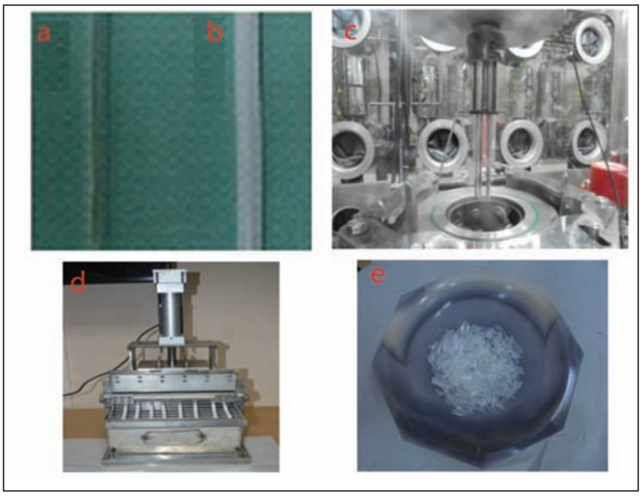

Fig. 1: Photograph of (a) Virgin quartz, (b) Coated (inner) withY_2O_3, (c) Slugs casted using quartz, (d) Demoulding System and (e) Broken quartz

V.49 Miniaturized Instrumentation for Semi Conductor Metal Oxide Sensor using Microcontroller

The semiconductor metal oxide (SMO) sensor construction involves a heater & sensor pattern integrated on a miniature alumina substrate and necessary electrical leads incorporated in it. For proper functioning of the sensor, the heater is maintained at a constant temperature of 623 K. Due to compactness, temperature sensor provisions on the heater surface is not provided. To measure sensor signal and to control the heater temperature, without temperature sensor, a Microcontroller based instrument miniature in size is developed.

The instrumentation consists of a pre-amplifier & display unit. The pre-amplifier unit interfaces with the sensor signal and transmits after appropriate conditioning. The display unit receives the sensor signal, processes the signal in the Microcontroller and displays the hydrogen concentration in ppm.

The pre-amplifier unit receives signal like a variable resistance from the sensor. Sensor resistance decreases with increase in the hydrogen concentration. The sensor resistance varies from 5 M Ohms to 10 K ohms corresponding to 3 ppm to 100 ppm of hydrogen concentration. This change in resistance is converted into current signal (4 to 20 mA) for long distance transmission up to 1 km. The pre-amplifier receives its power from the display unit. Fig. 1 shows the overall setup of sensor, amplifier unit and display unit.

Signal processing is done by in-built PSoC3 Microcontroller. Serial communication through RS232 is provided. Capacitive touch display is provided in the front panel of the unit for the complete interaction with the user and to display all parameters. Fig. 2 shows front panel of display unit. The sensor current signal transmitted from pre-amplifier unit is received and converted into corresponding voltage signal which is processed in the Microcontroller to display the corresponding hydrogen concentration in ppm. The required voltage and current for the heater is controlled from the display unit through Microcontroller. Fig. 3 shows the instrument connected to sensor and Fig. 4 shows the temperature and sensor signal stability. Fig. 5 shows the sensor response for hydrogen injection.

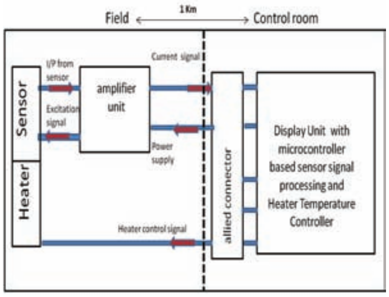

Fig. 1: Overall setup of sensor and instrument

Fig. 2: Display unit front panel

Fig. 3: Instrument connected to sensor.

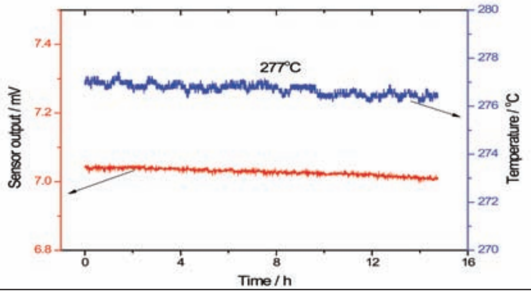

Fig. 4 : Heater temperature and sensor voltage stability

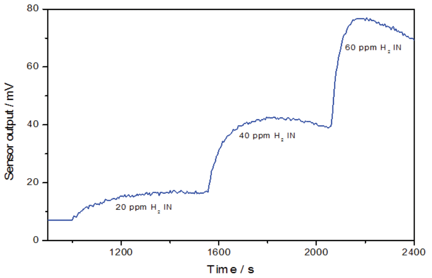

Fig. 5: Sensor response for hydrogen injection

V.50 Development of Soft Temperature Sensor using Artificial Neural Network

Soft Sensors are computer-based systems based mathematical models to estimate various process variables. They can be used for many process related applications like sensor validation, fault detection, customized sensing etc. A soft temperature sensor has been developed for estimating the liquid temperature of the dissolver based on vapor temperature data of dissolver from a thermocouple sensor.

Supervised machine learning methods like Feed Forward Neural Network (FFNN) and Time series prediction based on Nonlinear Auto-Regressive with Exogenous inputs (NARX) neural networks have been used to build a temperature estimation model. A large set of plant data has been used for validating the developed model and is shown as a plot in Fig. 1.

In FFNN, parametric studies with respect to number of Layers, number of neurons in each layer, type of activation function in the layer, Optimizer, learning rate etc. were done and Mean Square Error (MSE) for each combination was estimated. It was observed that NARX gave better results and a MSE of 0.1 ºC was obtained which is shown in Fig. 2.

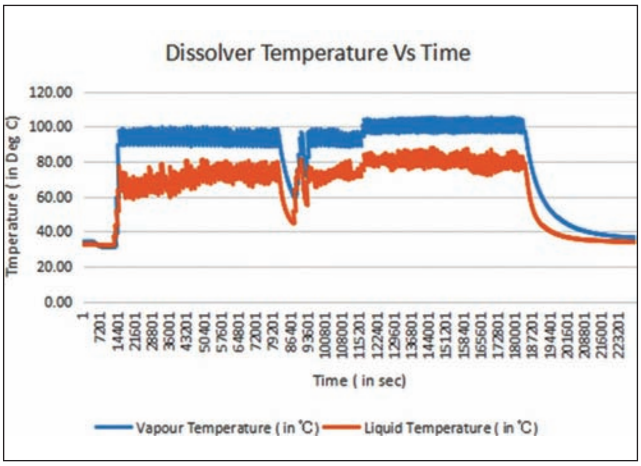

Fig. 1: Dissolver Temperature (Liquid and Vapour) Vs Time Plot – Data Set

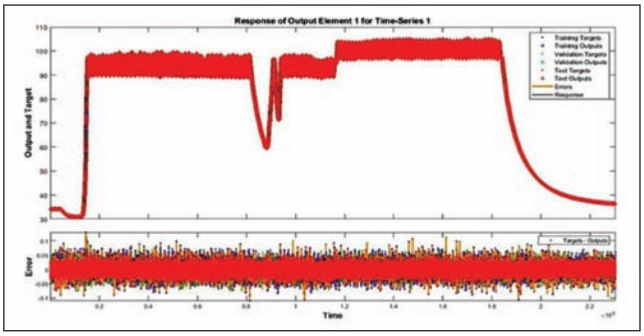

Fig. 2: Actual Vs Predicted Liquid Temperature, Error Plot

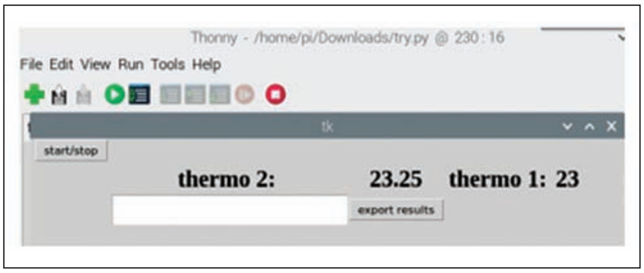

thermo 2: 23.25 thermo 1: 23

Fig. 3: GUI (thermo 1: Liquid Temperature and thermo 2: Vapour Temperature)

Tensor Flow, Keras, Fire TS, Pandas, NumPy library were some of the data analysis and ANN tools that were extensively used. The first version of the model was implemented on a Raspberry Pi SBC and tested using a K-type thermocouple with MAX 6675 interface module. Then actual Plant data has been used to test the model. GUI for the application has been developed using Tkinter library in python as shown in Fig. 3. Front end has integrated and tested on existing Plant Data Acquisition System.

V.51

Wireless Sensor Network for Water Quality Monitoring at 2MIGD SWRO Desalination Plant, IGCAR

Wireless Sensor Network (WSN) is one of the recent technologies with bounteous potential to cater innumerable applications. This technology has been utilized at IGCAR to provide a continuous, fully automated data collection with centralized monitoring and storage facility for various applications.

Sea Water Reverse Osmosis desalination plant (SWRO) with a capacity of 2 Million Imperial Gallons per Day (2 MIGD) is one of themain source of potable water in DAE complex. It is designed with state of the art Reverse Osmosis Technology(RO). For operation of the plant, the inlet sea water is received from the discharge point of Auxiliary Seawater System of BHAVINI. The RO process discharge brine is diluted in the BHAVINI discharge canal and delivered to the sea via MAPS outfall canal.

It is mandatory to monitor and maintain the delta difference between the inlet & outlet water quality parameters of the plant within the prescribed limits of TNPCB. As the inlet is at the in-feed tank inside Nuclear Demonstration Desalination Plant (NDDP) and outlet is the near seashore outside the IGCAR perimeter wall, it is difficult to establish a wired network for monitoring. Hence it was decided to utilize WSN to send the water quality parameters at inlet and outlet wirelessly to the control building of 2MIGD plant. The Architecture of WSN is shown in Fig. 1.

WSN Node and Data Acquisition

WSN Nodes were designed and developed with ARM Cortex-M0+ processor, ZigBee compliant transceiver, RS485 serial interface, power efficient regulator and power control circuitry. WSN Node was powered by solar panel with integrated power supply module, 11.1V, 2Ah Li-ion rechargeable battery and signal conditioning board to handle the Data Acquisition Unit.

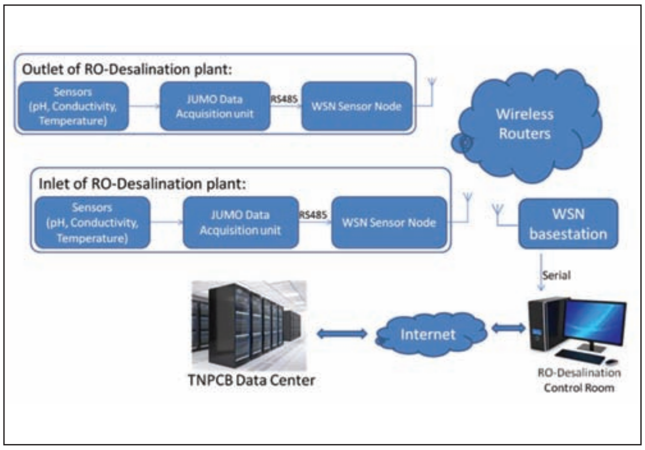

Fig. 1: Architecture of WSN system at Desalination plant

Fig. 2: WSN nodes installed at Inlet & Outlet of RO Desalination plant

Water quality parameters viz. pH, Conductivity and Temperature are measured at both inlet and outlet by a JUMO Data Acquisition Unit. The data acquisition unit senses the water quality parameters and displays the readings. It also provides facility to configuration sensors, and display settings. The in-house developed WSN Node has been programmed to acquire data from the JUMO DAC using Modbus over RS485 interface.

WSN Router Node

WSN Router nodes are designed with IP68 protection to withstand rain & dust and are powered with rechargeable battery. Battery capacity of 2AH & solar panel sizing of 10W has been chosen for WSN Router Nodes to have a backup for two dark days. These router nodes forward the data towards the destination and helps in expanding the network coverage and reliability.

WSN Basestation

Base stationis a network coordinator for the wireless network, which serves as the gateway between wireless network and Base station Server. The base station powered by USB receives data packets from routers and forwards to the base station server which runs a dedicated software to send the data to the TNPCB data server periodically.

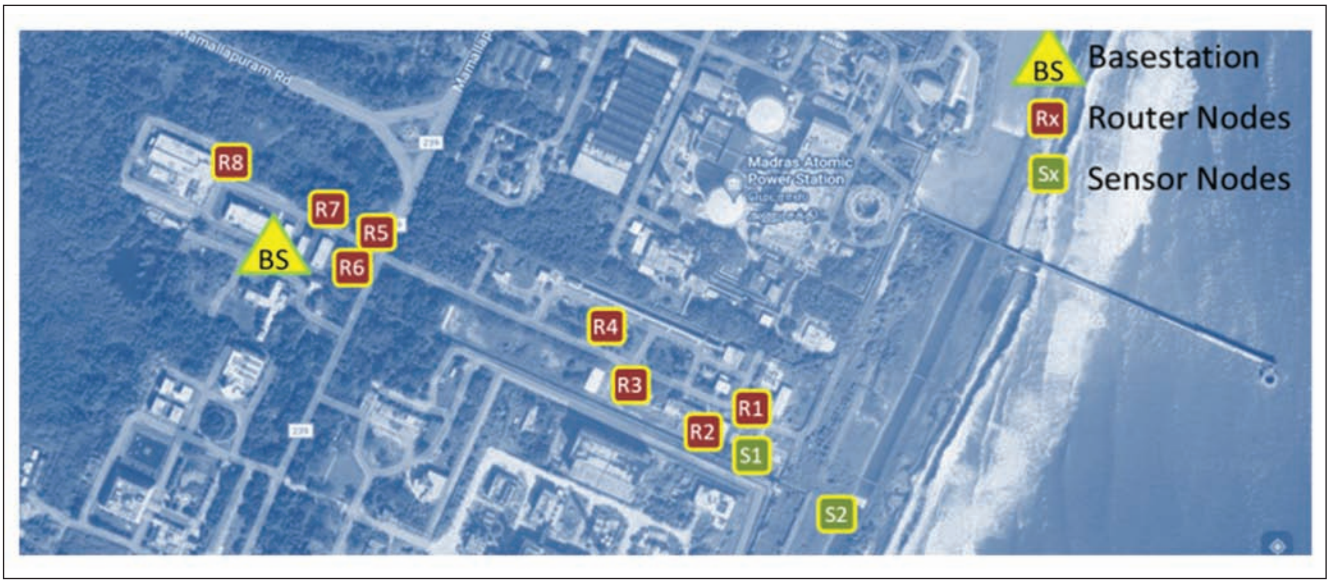

Fig. 3: Satellite view of WSN deployment at Desalination plant

WSN Deployment

RF Site survey was performed to identify the appropriate locations of router nodes for reliable communication. Each location identified has two more router nodes in its forwarding path. Solar Panel as well as street light supply have been utilized to power the router nodes.

The Wireless Sensor Network which spans for almost 1km has been successfully deployed with 2 sensor nodes, 8 Router nodes & 1 Base station at the control room. The deployed network transmits the water quality data once in a minute to the TNPCB server.

Deployed WSN nodes at inlet and outlet are shown in Fig..2. Fig. 3 gives the satellite view showing WSN layout with node locations. Periodic data uploaded at TNPCB server is shown in Fig. 4.

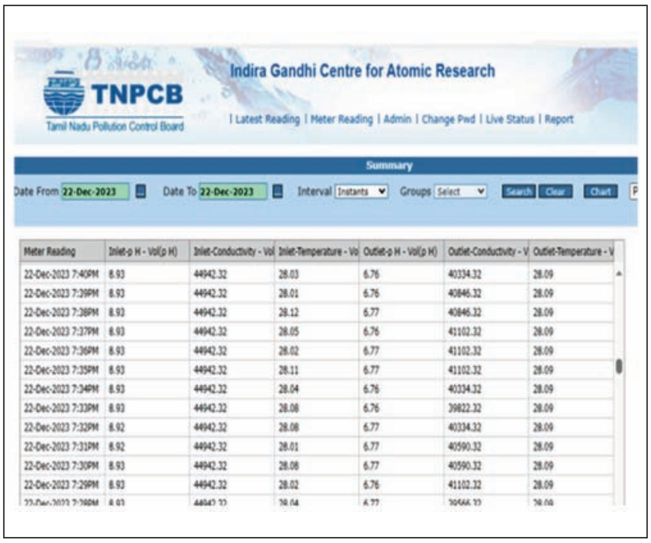

Date From 22-Dec-2023 Date To 22-Dec-2023 Interval Instants Groups Select

Meter Reading	Inlet-p H - Vol(p H)	Inlet-Conductivity - Vol	Inlet-Temperature - Vo	Outlet-p H - Vol(p H)	Outlet-Conductivity - V	Outlet-Temperature - V
22-Dec-2023 7:40PM	8.93	44942.32	28.03	6.76	40334.32	28.09
22-Dec-2023 7:39PM	8.93	44942.32	28.01	6.76	40846.32	28.09
22-Dec-2023 7:38PM	8.93	44942.32	28.12	6.77	40846.32	28.09
22-Dec-2023 7:37PM	8.93	44942.32	28.05	6.76	41102.32	28.09
22-Dec-2023 7:36PM	8.93	44942.32	28.02	6.77	41102.32	28.09
22-Dec-2023 7:35PM	8.93	44942.32	28.11	6.77	41102.32	28.09
22-Dec-2023 7:34PM	8.93	44942.32	28.04	6.76	40334.32	28.09
22-Dec-2023 7:33PM	8.93	44942.32	28.08	6.76	39822.32	28.09
22-Dec-2023 7:32PM	8.92	44942.32	28.08	6.77	40334.32	28.09
22-Dec-2023 7:31PM	8.92	44942.32	28.01	6.77	40590.32	28.09
22-Dec-2023 7:30PM	8.93	44942.32	28.08	6.77	40590.32	28.09
22-Dec-2023 7:29PM	8.93	44942.32	28.02	6.76	41102.32	28.09
22-Dec-2023 7:28PM	8.93	44942.32	28.04	6.77	39566.32	28.09

Fig. 4: View of water quality data logged in TNPCB server

Back to Main

CHAPTER VI

Infrastructure & Resource Management

VI.01 Building of State of Art Mid Tropospheric Radar Facility for Micro Meteorological Weather Surveillance

The state of art weather surveillance facilities Doppler Weather Radar (DWR) and Mid Tropspheric Radar Facilities (MTRF) are located in IGCAR near Edaiyur creek area. Both the systems are developed and installed in collaboration with ISTRAC –ISRO Bangalore. IGCAR has designed & constructed the buildings and provided technical services for installation and operation by ISTRAC. DWR building is completed and is operational. Now construction of MTRF is also completed.

Mid Tropspheric Radar are clear air doppler phased array radars that detect reflection from turbulence and eddies.It is an important research tool in the investigation of prevailing winds, waves (including gravity waves), turbulence and atmospheric stability inputs in atmospheric dispersion studies.

Fig. 2: Rear Side view of MTRF building

The MFTR is G+1 structure with an area of 630 m^2. and with the amenities like storage room, electrical panel room, shift in charge room with pantry area at ground floor. The instrumentation and Transmit & Receiver Module (TRM) room are located at first floor is supported with UPS and battery system. Control room of size 3.8 m x 3.8 m and electrical panel room are planned at this floor. A refuge platform is provided to cater to emergency. Special earthling is done for the building. Wind Arrays are installed in terrace. The RF cables from each antenna will be brought down to environmentally controlled room through a J shaped tube capable by avoiding rain water and dust entry to the room. Stainless steel railing on the ceiling to fix the TRM is provided galvanized steel cable tray to route the cables along the TRMs and control room and power distribution network is provided.

The faraday cage is provided during construction and it was earthed to protect the person in control room from Electro Magnetic Interference (EMI) radiation. The antenna arrays will be installed on the rooftop mounted on individual concrete pedestal and guarded by a M.S Fence. The TR module will be suspended from first floor ceiling. The antenna installation is in an area encircling a radius of 6.75 m

The most challenging part of the building involves construction of Roof slab at the terrace level of second floor. In conventional building roof slabs are intented to act as a shelter and designed to resist dead load, live load, seismic load, and wind.

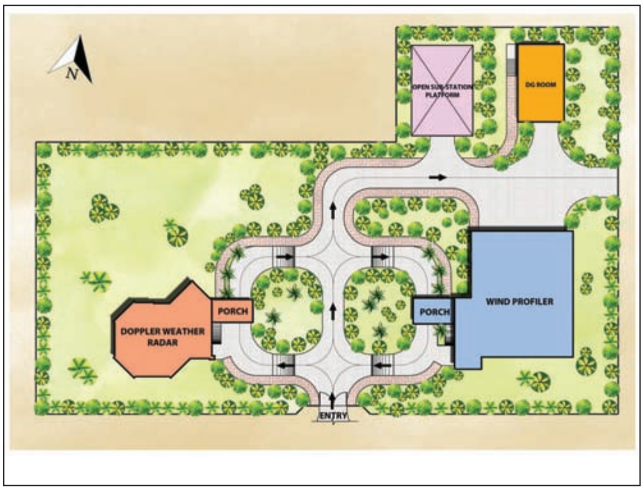

Fig. 1: Site Plan showing building Location

Fig. 3: Front Side view of MTRF building

Fig. 4: Roof slab with provision for holes and pedestal.

Fig. 6: Aerial View of the MTRF building

Whereas, in this building the roof slab was intended to support 135 nos of YAGI Antenna with structural steel fencing over the top surface of slab and support the 135 no's TRP Modules under the beam bottom of slab through structural steel channel, in addition with above loads mentioned for normal slabs.

In order to support the Antenna 135 no's of RCC pedestals of size 450x450x500mm are monolithically constructed over the terrace and each pedestal was provided with 4 nos. of SS bolts to fix the antennas with a tolerance of ± 1mm. Structural steel fencing made of 132 × 132× 6 mm hollow steel section is used in both the vertical and horizontal framing and it was welded with a 300 mm × 300 m × 16 mm base plate anchored on the beam at roof top, using four self-anchored anchor bolts. This structural steel framework encompasses with galvanized iron wire mesh to act as fencing.

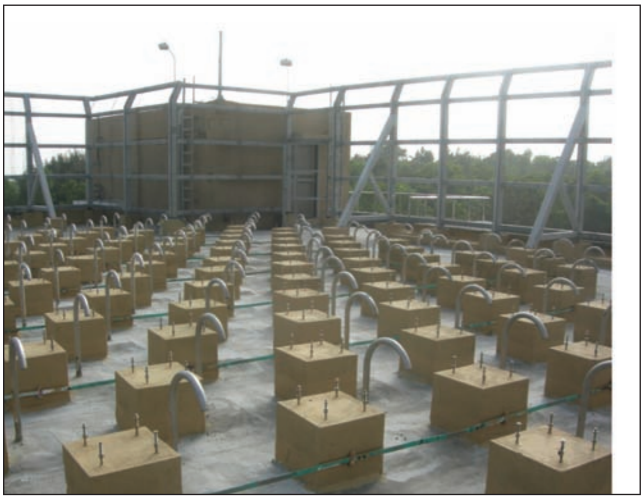

Fig. 5: Roof slab with pedestal and SS-J tubes penetrations.

135 Nos of TRP modules with high sensitive instruments are supported at the bottom of slab by using 14 no's of ISMC channel. Structural steel channel was supported on R.C beam bottoms along with necessary cable tray support.

Roof Slab of 170 mm thick is constructed with 136 Nos of through and through packet holes for fixing the stainless steel inverted J shaped tubes to route the high power RF cables from antenna to the TR modules which are fixed at soffit. The inverted SS- J tubes are fixed on the roof slab along the pedestals sides and through holes are grouted to prevent the ingress of rainwater and structural slope of 70 mm was provided to the slab to drain out the rainwater without stagnation on the terrace level. High performance elastomeric thin film water proofing technology was implemented with suitable protective screed concrete over the roof terrace as an additional preventive measure to stop the ingress of rainwater into the high sensitive instrumentation room. The construction of the building along with all utility & services are completed in all respect adhering time schedule.

Mid Tropspheric Radar Facilities (MTRF) will help us in weather monitoring, early detection of disaster and improve the weather predictions for emergency response decision support and will facilitate research activities in the field of metrology.

VI.02 Adoption of Least Invasive Technique within Cylindrical RC wall for restoration of safety related embedded piping

Due to corrosion of embedded pipe, a leak was detected at the drain of safety related piping system. It was decided to cut the corroded portion of pipe from main system and provide a bypass pipe to meet functional requirement.

The curved reinforced concrete wall is 1m thick and the pipe is embedded at 600mm from the outer approachable side. The grade of concrete is M45 and 36 mm diameter bars were provided in a dense mesh of 200 mm c/c along with shear links of 12 mm at 300 mm c/c vertical as well as horizontal. Corrosion was located at the pipe bend of 40NB, sch.80 carbon steel pipe through videoscopy. As the wall was heavily loaded and was part of leak tight boundary acting as biological shield ,least invasive methods were to be adopted for exposing the pipe bend .Further complexity was presence of one more pipe just above the corroded pipe and both pipes had channel sections enclosing them filled with asbestos wool for facilitating thermal movement of pipes. Due to this arrangement, barely 25 mm gap was there between the pipes as per drawing .The challenge was baring the pipe alround by removing concrete without damaging the healthy pipe above.

Static analysis of reinforced concrete wall was carried out to check the adequacy to meet the stresses arising due to static vertical loads at the temporary partial cut-out at repair location .

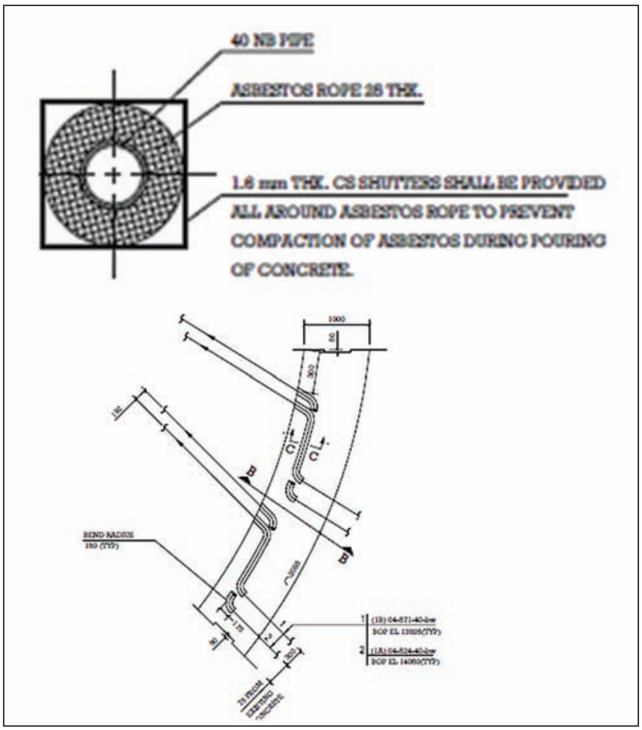

Fig. 1: Drawing showing the encased pipe and layout within wall

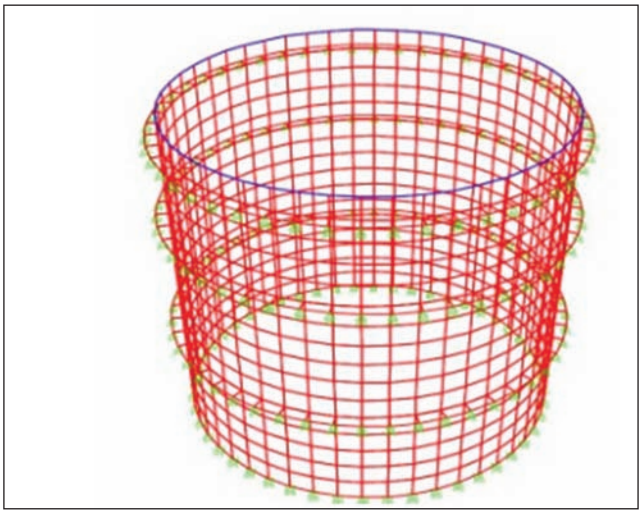

Fig. 2: Decoupled FE model of RV in NICB

In order to demonstrate the feasibility of concrete cutting, qualification of welding equipment, welding procedure and also to ensure the repeatability multiple mock up trials were held at the site.

Work was undertaken at actual site after successful trials. The approximate location of pipe bend was marked on the surface of the wall. Reinforcement mesh was identified through non destructive method using ground penetrating radar. The concrete in the cover zone to 90mm depth was removed through stitch coring ,for an area of 600mm x 600mm around the marked pipe

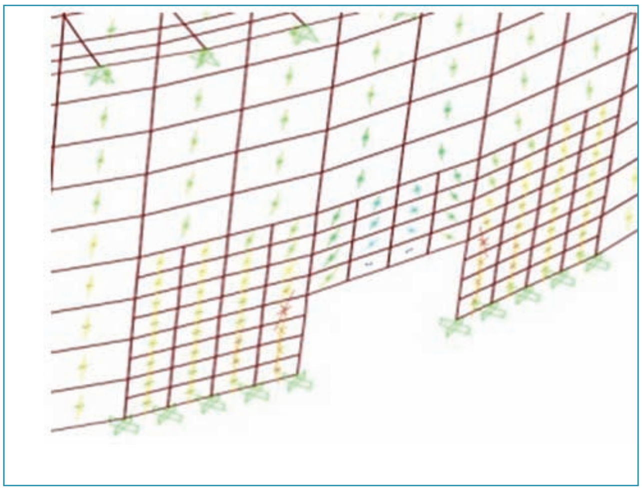

Fig. 3: Force Path around cut-out location

Fig. 4: Mockup

bend, and the rebars were exposed. Concrete between the rebars was removed through coring/drilling in a controlled manner, until the outer duct of embedded pipe was encountered, without cutting the rebar. Removal of outer envelope and chipping of concrete around the pipe was carried out until the required clearance of 50 mm is achieved all around the damaged pipe at the location of repair. Once the pipe was exposed, three rebars hindering the pipe welding was cut in order to facilitate the welding.

After the pipe welding ,an annular gap was formed using PVC pipe and new pipe to accommodate thermal expansion of pipe during operation. Provision was made to pour and fill the annular gap using Polyurathene with necessary venting. The reinforcement cut to facilitate pipe welding work was welded back in position as per the approved welding procedure. Further, bonding agent was applied on the existing concrete surface to receive fresh concrete. Hopper arrangement was made at the top of shutter to enable concrete pour and compaction with needle vibrator. Sealant was applied around the shutter and the PVC pipe in order to avoid slurry loss during concreting.

Fig. 5: Coring of concrete

Fig. 6: Exposing the embedded pipes through core cutting

Fig. 7: Welding of new pipe and rebars

Fig. 8: Application of bonding agent & shuttering

Fig. 9: Restoration of the system

N 45 concrete was poured through the hopper. The concrete was filled in layers till the top and compacted with needle vibrator without disturbing the pipe. Epoxy grouting was carried out around the construction joint between parent and the fresh concrete after 28 days of curing. Then the system was commissioned.

VI.03 Seismic Re-evaluation of RC Ventilation Stack in DFRP

Demonstration Fuel Reprocessing Plant (DFRP) 75m tall RC stack was designed & constructed in the year 1987 & was designed as per codes/ standards and guidelines prevailing at the time of its design. The purpose of the stack seismic analysis is to qualify or determine that the 75 m stack meets the safety criteria under high level of Review basis ground motion (SSE) with 10000 years return period, (0.22g) and undertake up-gradation of structure, if found necessary,

Re-evaluation is carried out based on IAEA Safety series 28. The seismic Margin is determined by HCLPF (High Confidence Low Probability Failure) capacity in terms of PGA (Peak Ground Acceleration).

Assumptions & method of analysis of structure:

Consideration of soil structure interaction and spring Stiffness based on impedance function approach [ASCE 4 -98] adopted. The uncertainty in the soil properties has been considered by varying shear Modulus G (0.5G, 1G& 2G).Averaged shear wave velocity $V_{S,30}$ considered for analysis Inelastic Absorption Coefficient is an multiplying factor to convert linear demand to nonlinear demand shown in Table 4.

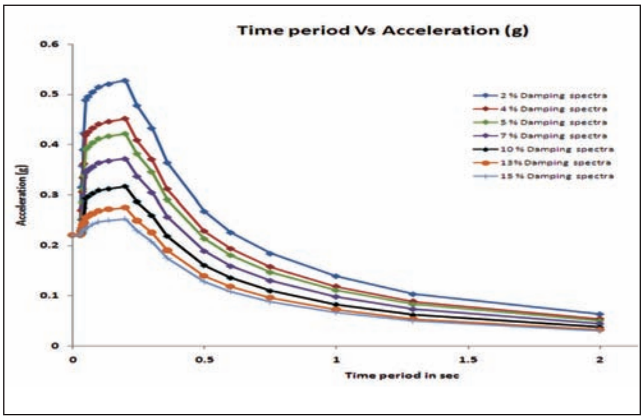

Fig. 1: RBGM Spectrum with 0.22 g PGA

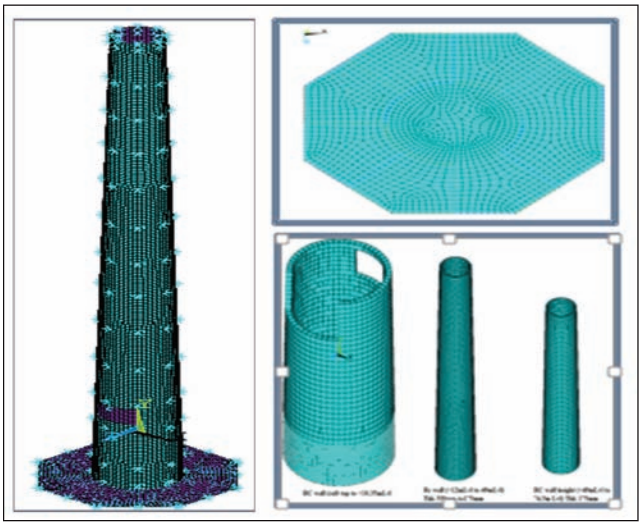

Fig 2 Lumped Mass Model and FEM Model of stack structure

Model Description:

The RC stack structure was modelled usingfour-node shell elements with element with six degrees of freedom at each node. The seismic response of structures is evaluated on the basis of dynamic analysis of appropriate structural models, taking into account Soil structure Interaction (SSI) effect staking account of uncertainty. The stiffness of embedded plate around the large opening has been accounted in the model by using equivalent beam elements. The geometrical specification, material properties and geotechnical properties for the finite-element analysis are described in following Tables 1 & 2

Table 1 Geometrical Specification of RC stack

Height of stack from FFL	*74.5m*
Outer Diameter at Base	*8m*
Top outer Diameter	*4.65m*
Wall thickness	*400 mm to 175 mm*
Duct opening size @ + 7.65m(bottom)	*4.7m(L) x 2.7m(H)*
Duct opening size @ + 8m(bottom)	*3 m(L) x 2 m(H)*
Stack Ep plate 6mm thick welded around the opening	*4.7m(L) x 2.7m(H) 1.5 m(W)*
Octagonal Raft	*1.5 m Thickness, 6.628 m side*

Table 2 Material property & Geotechnical property

Grade of Concrete	*M25*
Shear Modulus(G) (Gpa)	*9.889Gpa*
Shear wave velocity (m/sec)	*2223.7 m/sec*
Damping	*7%*

Seismic Re-evaluation Methodology:

The approach recommended may be summed up by the main following steps:

Table 3 Model statistics

Item.	*Attribute*	*Number*
Stack	*Number of nodes in the model*	*16871*
	Total number of elements	*16183*

Step 1: Calculate the elastic seismic demand in members by elastic seismic response analysis, using the elastic response spectrum with realistic damping and actual live load (Fig. 3 to 8).

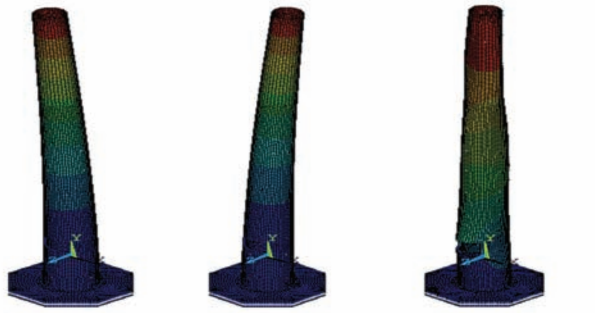

Mode 1=0.82 Hz (1.22 sec)

Mode 2=0.96 Hz (1.04 sec)

Mode 14=12.13 Hz (1.0813 sec)

Fig. 3: Mode shapes and frequencies for predominant modes

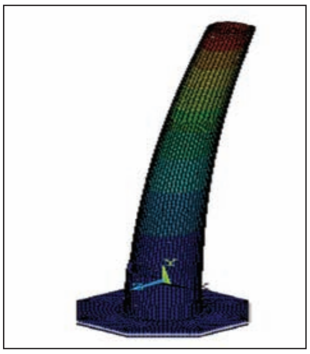

Fig. 4: Maximum Displacement under seismic X direction is 45.459mm

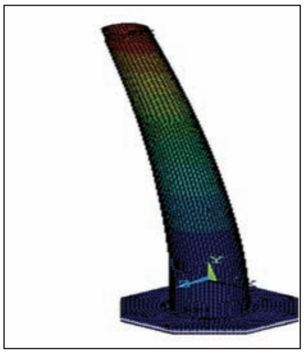

Fig. 5 Max Displacement under Seismic Z direction 54.7 mm

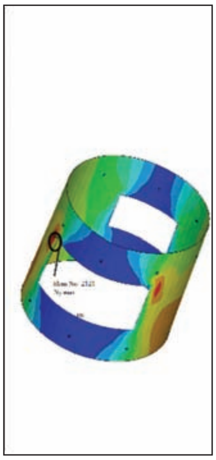

Fig. 6: Membrane Force in Y near cutout in Newton

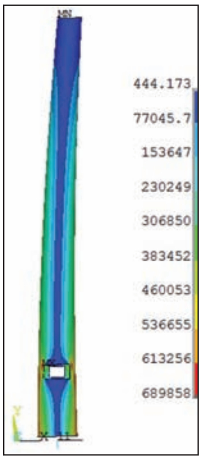

Fig. 7: Membrane forces in Y direction in Newton

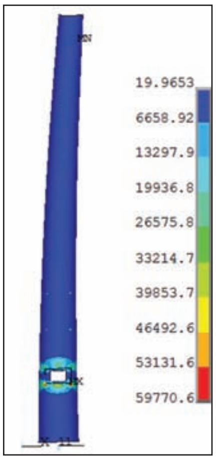

Fig. 8: Out of plane shear in X direction in Newton

Fig. 9: HCLPF value for RCwallRaft to 6.55m Lvl

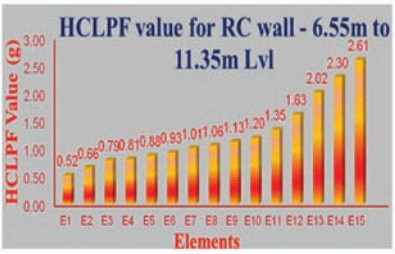

Fig. 10: HCLPF value for RCwall +6.55 m to 11.35 Lvl

Step 2: Estimate concrete capacity by limit strength according to the method IS codes (Fig. 9, 10)

Step 3: Calculate the strength factor by deducting the capacity for static demand and dividing the net capacity by Seismic demand

Step 4:Modify the Strength factor by taking into account the inelastic energy absorption. If the value is less than unity, strengthening measures should be considered.

Step 5: Evaluate HCLPF capacity by multiplying the strength factor with PGA (0.22g) and if the value is more than 0.22g ,the members are qualified.

The seismic re-evaluation methodology is shown in Figure 2

Table 4: Fμ - Inelastic Absorption factor	
Concrete shells where flexure dominates.	1. 5
Concrete shear where shear dominates.	1.25

Results of Response Spectrum Analysis:

Determination of Seismic Margin:

HCLPF= ((Capacity-Static demand))/(Dynamic Demand)*Fμ*0.22g

Based on deterministic assessment, it is concluded that the stack structure meets the RBGM demand with low probability of failure. The lowest HCPLF capacity of the stack structure, 0.32g, which is more than the nominal demand for the specified review level condition (i.e. 0.22g PGA). Hence the structure is considered adequate.

VI.04 Establishment of Tertiary Treatment Plant-A Green Initiative

Air Conditioning and Ventilation Services Division (AC&VSD) has undertaken a pioneering green initiative with the establishment of a Tertiary Treatment Plant. This project signifies a step towards sustainable water management by harnessing sewage treated water for air-conditioning applications. The primary objective of this initiative is to reduce dependence on fresh water resources and promote eco-friendly practices in the operation of air conditioning and ventilation systems.

In IGCAR, the central air conditioning plant currently relies on approximately 300-400 cubic meters of fresh water per day for the makeup of its condenser cooling water system. Meanwhile, the Sewage Treatment Plant (STP) in IGCAR processes an average of 600-700 cubic meters of water daily, primarily serving the watering needs of plants within the Centre's premises.

Fig. 1: View of Tertiary Treatment Plant

In an effort to reduce the dependence on fresh water and to promote more sustainable practices, a study was undertaken to explore the feasibility of utilizing the treated water from the STP for condenser cooling water system. To facilitate this, a tertiary treatment plant (TTP) was established near central air-conditioning plant (Fig. 1). The Tertiary Treatment Plant features state-of-the-art technologies, including an ultra-filtration (UF) membrane module and a Reverse Osmosis (RO) membrane module.

The process ensures that the treated water's quality aligns with the requirements for the cooling towers as shown in process flow diagram (Fig. 2). The RO membrane module will significantly reduce the Total Dissolved Solids (TDS) in the water, while the UF module will effectively eliminate total suspended solids (TSS). This plant has no imported components and hence is 100% Atmanirbhar. The project will save fresh water to the tune of the water requirement of 3000 urban citizens of India at the current consumption level. The successful implementation of this green initiative is poised to set a precedent for similar projects across the organization, fostering a culture of environmental responsibility and sustainability. The establishment of the Tertiary Treatment Plant by AC&VSD is a testament to our commitment to green practices, environmental stewardship, and the pursuit of sustainable solutions. This initiative not only addresses immediate water needs but also sets the stage for a more environmentally conscious future in air conditioning and ventilation operations.

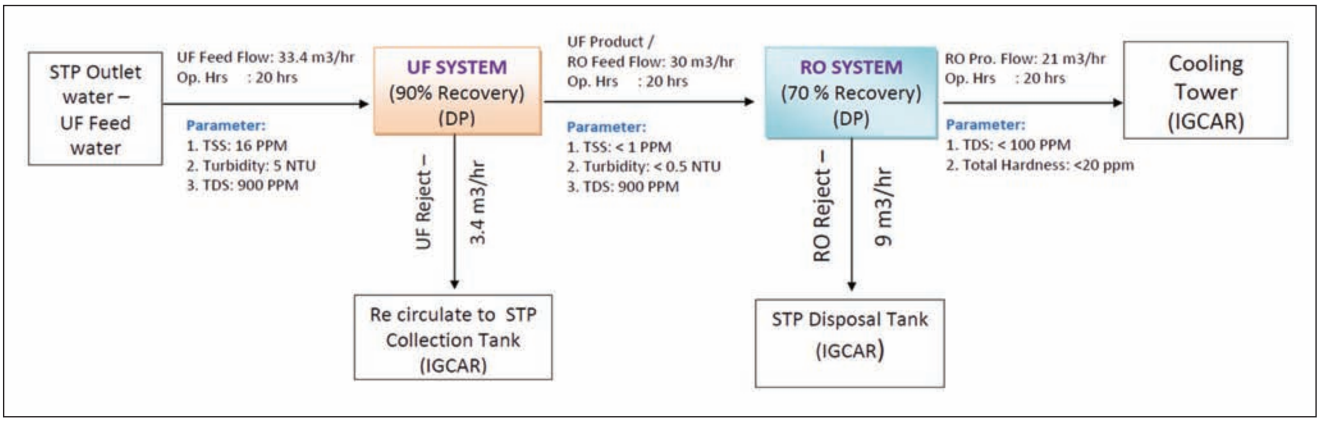

Fig. 2: Process flow diagram of Tertiary Treatment Plant

VI.05 Performance Enhancement of 2 MIGD Desalination Plant at IGCAR

2 MIGD Sea water Reverse Osmosis Desalination plant of IGCAR is in 24X7 operations to meet the growing need of potable water for all DAE units including IGCAR, BHAVINI, NRB, BARCF at Kalpakkam for the last 8 years. Reverse Pumping Provision from IGCAR reservoir is also available to feed potable water to DAE Township at Anupuram, if needed. The Desalination plant is designed with the state of art two pass Reverse Osmosis Technology to meet the variable operational requirements of 25 %, 50%, 75% and 100% of the plant capacity with a 4 skid arrangement of 0.50 MIGD capacity each.

Several up-gradations and modifications were carried out in the plant to enhance its performance. A few of the most highlighting modifications are presented below.

1.0 Capacity Boosting:

The foremost performance of the Desalination plant is its output flow. Each skid is provided with 22 vessels in parallel with 7 membranes in series each to deliver 0.50 MIGD. 95 m^3/hr is the 2^{nd} Pass output with 105 m^3/hr first pass output flow. Each vessel delivers around 4.77 m^3/hr. During the design of the skid itself, there was a provision made to upgrade the no. of operating vessels by two more vessels i.e from 22 vessels to 24 vessels with the existing capacity of pumping systems.

After 8 years of continuous operation, this 2 vessels addition was taken up to boost the plant output flow. Two vessels with 7 membranes each were added to four skids. This upgradation has boosted the flow by 9.54 m^3/hr. Plant Capacity boosting by 9% without any other component modification.

2.0 Intake Bye-Pass System:

For operation of the plant, the inlet raw sea water is received from the discharge point of Auxiliary Seawater System (ASW) of BHAVINI. Due to the elevation differences in en-route of the intake seawater tapping pipeline, high turbid & pipe septic water enters our intake sump on every ASW start up time. Fig. 2 shows the condition.

Fig. 2: Intake Seawater condition on every start up of ASW

We are forced to shut down the plant and unable to restart for minimum 8 hours to clear this high turbid water at every start up of ASW.

To take up the periodic intake sump maintenance also, we are depending on the ASW shut down. Without ASW shutdown, we are unable to empty the intake sump. This dependency does not allow timely cleaning of our intake sump. This leads to heavy accumulation of turbid sledge at the bottom of intake sump along with high biological growth.

To overcome the above difficulties without much modification in present setup, a 500 NB by-pass line (Fig.4) at a lower elevation to sump overflow point was established in 1000 NB inlet line near to the in-take sump with a by-pass valve control.

After establishing this In-take Bye-Pass System, whenever ASW restarts, the bye-pass control valve is

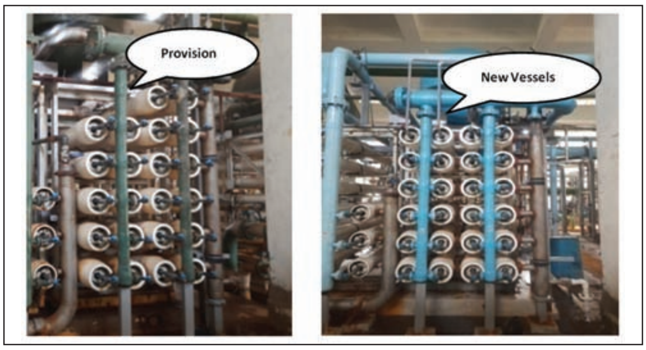

Fig. 1: 22 vessels & 24 vessels

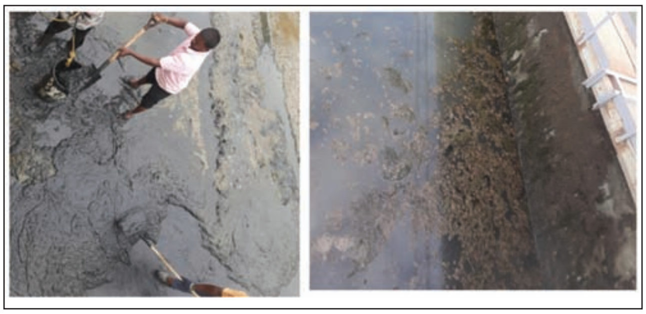

Fig. 3: Accumulated Sledge & Sump Biological growth

Fig. 4: A 500 NB by-pass line at a lower elevation to sump overflow point was established in 1000 NB inlet line near to the in-take sump with a by-pass valve control

operated by us and the muddy/pipe septic seawater will be let out to canal. After 20-30 minutes, the clear water will be allowed to enter our intake sump. This prevents entry of high turbid/pipe septic seawater to intake sump.

The intake sump cleaning is also now taken up on-time periodically irrespective of shut down of the ASW and hence no accumulation of sledge or accelerated biological growth at intake sump. This enhances the quality of pretreatment.

3.0 Identical Membrane Cleaning Facility:

On continuous operation, Membrane choking, scaling, bio-fouling are the normal degradation phenomena. This reduces the flow, increases Differential Pressure and reduces the quality.

Cleaning in place (CIP) is the available system to clean the membranes periodically. Membrane chemical cleaning will be performed in in-vessel skid arrangement (24 pressure vessel x 7 elements) to restore the performance of the membrane. This in-vessel cleaning method was found inadequate for retrieving the original flow / quality / differential pressure. Only partial cleaning of membrane was happening and performance of the membrane was also restored partially as they are in series of 7 membranes in a vessel.

Fig. 5: Seawater after 30 min. bye-pass on every start up of ASW

Fig. 6: Membranes in series in a vessel

Fig. 7: Identical Membrane Cleaning Facility

On detailed analysis, we found that the lead membranes which were heavily fouled, reduces the cleaning flow and not allowing the chemical solutions to the subsequent membranes inside the vessel while cleaning. The cleaning was not uniform to all the 7 membranes in a vessel. So, to improve the cleaning method and in order to ensure the full and fresh flow of cleaning chemical solution individually, we developed this seven array identical membrane cleaning facility (Fig. 6) with existing pumps in CIP line itself.

The advantages of this identical membrane cleaning facility are,

1. All the membranes will get the fresh and full flow of chemical solution uniformly.
2. The impurities removed from one element will not travel to the next element like in the in-vessel cleaning method.
3. The required number of membranes i.e only lead membranes can alone be cleaned. No need of exposing all the elements to the harsh chemical solutions.
4. Reverse cleaning of membrane is also possible.
5. The membrane performance getting restored to its original performance in terms of flow by 5-10% and differential pressure by 30% in turn sustains Specific Energy Consumption also.

This identical Membrane Cleaning Facility is being utilized for the periodic cleaning of lead membranes which are prone to be fouled heavily.

The modifications in the plant are being taken up continuously to enhance the plant performance as a continuous process.

VI.06 Energy Conservation – ESG Strategy

Energy Conservation (EC) is a theme that Engineering Services Group (ESG) has adopted well in advance. In the light of the country giving its attention to the looming climate crisis, the EC activities are accelerated and major steps are under way. The steps initiated have already delivered considerable savings in energy. This article provides the details of EC works ESG has completed, the benefit accrued and the way forward.

EC Activities initiated by ESG

ESG has identified many areas with Energy saving potential and is in the process of implementing EC steps in various systems. List of activities identified and in various stage of implementation are given below:

1. Conversion of conventional lamps to LED lamps
2. Plugging the chilled water leakage
3. Establishing Solar PV plants
4. Indoor Lighting control by Occupancy sensors
5. Automatic control of street lights
6. Conversion of packaged AC unit to centralized AC
7. Capacity optimisation of pumps
8. Conversion of aged unitary ACs with energy efficient invertor ACs
9. Use of weekly timer for exhaust fans to optimise the running time.

1. Conversion of conventional lamps to LED lamps

IGCAR was having close to 50,000 Nos. of conventional lamps primarily of gas discharge type. Conversion of LED installation was started as per OM No. DAE/HNCPW/E-6.12/2017/10471 dated 16.08.2018. The approach adopted is phased conversion utilising the conventional lamps to its full life. In this, conversion is carried out in a specific location. The conventional light fittings removed would be used as spares for other areas. This was necessitated on account of the massive investment required for enmasse replacement. After the OM mentioned above no conventional lamp or its spares are procured and all new buildings are provided with 100% LED lamps.

Present status of conversion is 55% which has resulted in a monthly energy saving of 2,03,220 units.

Fig. 1: First solar PV plant in Kalpakkam in 2015

2. Plugging the chilled water leakage

Centralised Air conditioning of IGCAR buildings is achieved by Air handling Units (AHU) placed in the building that gets chilled water supply from the CWCP (Centralised Chilled Water Plant). Chilled water is extended by underground (UG) insulated pipe lines which runs throughout the campus. These pipes are installed 4 decades back and aging resulted in pipe corrosion and leakage of chilled water. There is a very large network of UG pipes and 90% of the pipes are replaced with pre-insulated UG pipes.

By revamping of underground chilled water pipelines, the chilled water loss from the system brought down from 10 m^3/h to 1.5 m^3/h. (Note: A small amount of leak is permitted for gland cooling purpose)

On this account the monthly energy saving achieved is 20,000 units.

3. Establishing Solar PV plant

ESG has commissioned the first solar PV plant in Kalpakkam in 2015. The first plant was of capacity 30 kWp. Subsequently multiple plants are commissioned taking the total solar power capacity to 850 kWp providing 1 Lakh units of electricity every month. ESG is currently working on a mega scale PV project which will take the total installed capacity at IGCAR to 3 MWp. All major equipment has arrived and installation is in progress and is expected to be on grid in a few months.

Solar modules mounted on four wheeler parking structures

4. Indoor Lighting control by Occupancy sensors

Use of Occupancy sensors for lighting control is an established method for energy saving and longer lamp life. At IGCAR it was first introduced in the corridors of UGC - DAE – CSR building. All the buildings constructed during XI plan were provided with Occupancy sensors. From then onwards all newly constructed buildings are provided with Occupancy sensors for lighting control. Some time back it was extended to common areas of IGCAR. The savings in energy by this method is of the order of 65%.

5. Automatic control of street lights

Automatic control of outdoor lights using light sensitive switches was introduced in IGCAR long ago. Recently it is identified that level of lighting can be brought down in certain areas during late hours without affecting security. These areas are attended to and action taken to reduce lighting level after 10:30 PM. Since the basic system is established decades back, the savings is not projected in this case.

6. Conversion of packaged AC unit to centralized AC

Considering the limited capacity of CWCP, some of the buildings were provided with standalone Packaged AC units. In 2021, IGCAR commissioned CWCP2 and part load of CWCP is transferred to CWCP2. Also the packaged units of cumulative capacity 400 TR is removed and chilled water from CWCP or CWCP2 is extended to meet the AC needs. Centralised AC is much more efficient than standalone packaged units. This transition resulted in a monthly energy savings of 22,000 units.

7. Capacity optimisation of pumps

Most of the pumps in the centralised chilled water system are 4 decades old. As part of aging management, many units were required to be replaced. During this process a review of the capacity of pumps also was carried out. This resulted in capacity down grading of many pumps. Major change was in 3 Nos. condenser water pumps where the 70 HP pumps were replaced with 50 HP pumps. The monthly energy savings in these 3 condenser water pumps alone is 28,000 Units.

8. Conversion of aged unitary ACs with energy efficient invertor ACs

This was taken up as part of aging management. Split air conditioners of 2 Ton and 1.5 Tons which are more than 15 years were identified. About 130 such units are replaced with energy efficient split ACs. The monthly savings gained by this activity is 5000 Units of electricity.

9. Use of weekly timer for exhaust fans to optimise the running time

All units of DAE provide exhaust fans in all toilets. Though 1 No. is sufficient, generally 2 Nos. are provided to meet the functional requirement even when one is under repair. A common sight is that both the exhaust fans thus provided will be running 24 x 7. Though the fans provided are of industrial grade which are more rugged and have better design margins, they are not designed to run continuously. This type of operation leads to frequent failures, winding burn out etc. In addition to such losses, it will also result in huge energy loss in terms of the total energy used for this purpose.

Identifying the scope for energy savings, a weekly timer was introduced for each fan. The timer is programmed in such way that any time only one exhaust fan will be operating and it operate only during office hours. This has resulted in 70% energy savings compared to full time operation. The step also brought down failures drastically and no winding failure since then. Total of 150 Nos. of exhaust fans are provided with weekly timer which resulted in a monthly energy savings of 11,000 units.

By the steps taken so far as explained has resulted in an energy savings of 3 Lakhs units per month apart from 1 Lakhs units per month of solar PV generation. It is targeted to complete all the activities listed which will save 5.5 Lakhs units of electricity in a month and 4.9 Lakhs units of monthly solar production. Once completed the energy requirement for lighting and air conditioning from grid will reduce by 50%.

VI.07 Public Awareness Activities in 2023

As part of 'Azadi Ka Amrit Mahotsav' the advancement in Science after the Independence was the chosen theme of our awareness activities. Awareness Progarmmes were planned and organized at different places. The awareness Programme consisted of various competitions held for the students and a technical exhibition showcasing the societal benefits of nuclear energy in addition to power generation.

National Mathematics and Science day celebration was held at Nethaji Subbash Chandra Bose College of Arts and Science, Thiruvarur in association with Tamil Nadu State Council for Science and Technology ,Govt of TN, from 31st -01st February 2023. 2500 School and college students visited the exhibits.

One day workshop and Technical exhibition "Walking with Atom" was held on 2nd Feb 2023 at DG Govt. college for women , Mayiladuthurai. – 150 college students and around 50 faculty members from neighbouring colleges attended the workshop

International Business Leaders meet (iBLME) and Exhibition (iCURE) was held from 4-6th Feb 2023 at Madurai Kamaraj University. The International Business Leaders Meet and Exhibition was a three day program alongside the International Conference on Consortium of Universal Research Erudition - 2023. It was inaugurated on 04 February 2023 by Hon'ble Minister of Commercial Taxes and Registration, Tamil Nadu , Shri P. Murthy, in the presence of the Vice Chancellor, Dr J Kumar and the Registrar, Dr.K Sadasivam, , Madurai Kamaraj University. Around 2500 of students and general public visited the exhibition.

State level science exhibition as part of National Science Day celebration was held on 14th Feb 2023 at Chennai DG Vaishnava college, Chennai - The Science Exhibition was inaugurated by Dr. N. Sivaraman, Director, MCMFCG, IGCAR, Kalpakkam. 700 students from various schools and colleges visited the exhibition.

National Science Day celebrations at Sri Vidya Mandir Arts and Science college, Uthangarai, Krishnagiri was held from 16th and 17th Feb 2023. Around 5900 students from various schools and colleges visited the exhibition.

National Science & Mathematics day celebration was held on 16-17th February 2023 at Sri Sankara Vidyalaya Matriculation higher secondary school, Urapakkam in association with TNCST, Govt of TN. Around 1500 school students visited the exhibition and interacted with the volunteers.

Dr. A. P. J. Abdul kalam Satellite Launch Vehicle Mission – 2023 was held on 18-19th Feb 2023. At TTDC-Ground, Devaneri village, Mamallapuram. The Exhibition was inaugurated on 18th February 2023 by Dr Sultan Ahmed Ismail, presently Member, State Planning Commission, Government of Tamil Nadu . Dr. Anand Mogalingam, Space Zone India Foundation, presided over the programme. Dr.Tamilisai Soundararajan, Telangana Governor was the chief guest for the satellite launch and Dr Mayilsamy Annadurai, former director ISRO & Dr B Venkatraman , Director IGCAR were the guest of honour. Around 5000 School students from all over India participated in the event and visited the IGCAR exhibition.

National Science Exhibition cum workshop – at Adhiparashakthi college of Engineering college, Chennai. The event was inaugurated on 22nd February 2023 by Smt. S. Rajeswari Head, SIRD, IGCAR, Dr. G.B Senthikumar, Correspondent, Adhiparasakthi Engineering College. Ms.S.Santhi, District Educational Officer, Madhurantagam was the Guest of Honors. Around 5000 college and school students visited the exhibition.

Chennai Science Festival 2023 at TNSTC campus held from 28th Feb – 1st March 2023. On 28th February 2023 Tmt. S. Malarvizhi, IAS Vice Chairperson, Science City and Dr Sultan Ahmed Ismail, presently Member, State Planning Commission, Government of Tamil Nadu inaugurated the Chennai Science Festival. Around 4000 General public, students from various colleges and schools visited our exhibition and interacted with the volunteers.

International Engineering Sourcing Show (IESS) held at Chennai from March 16-18, 2023 – EEPC India the apex body under Department of Commerce, Government of India is engaged in promoting exports, investments and trade for the engineering and manufacturing sector. In this regard, EEPC India organized the tenth edition of International Engineering Sourcing Show (IESS X) from 16th to 18th of March 2023 at Chennai Trade Centre, Chennai, India. Around 3000 college students, exhibitors, delegates and general public visited the exhibition. IGCAR-DAE won the best Pavilion award in the PSU category.

Indian Analytical Science Congress-2023 held at IMA House, Kochin Kerala, During 23-25th March 2023. The Indian Analytical Science Congress (IASC) Series is a grand Annual Land Mark Event of ISAS. The IASC-2023, scheduled during 23-25, March, 2023 at the IMA House, Kochi was themed, The Role of Analytical Science in Achieving India's Centenary Sustainable Development Goals . Around 200 registered participants of the conference visited the exhibition. IGCAR had participated as an exhibitor and had won the best Exhibition award for the display and the interactions with the visitors during the Conference.

National Technology Day celebration was held at Pragathi Maidan, Delhi for a week from 11th to 14th of May 2023. 4000 visitors interacted with IGCAR stall in the DAE pavillion

Exhibition on 'The Fourth State' - Plasma & 'Atoms in the service of the Nation'

Institute for Plasma Research, Ahmedabad, Gujarat, & Tamil Nadu Science and Technology Centre, Chennai, in association with Indira Gandhi Centre for Atomic Research (IGCAR), Kalpakkam, organised a 5-day exhibition on 'Nuclear technologies and its applications' at Birla planetarium, Chennai, from July 3 to 7, 2023. The objective was to create awareness about the key role of nuclear energy in the energy security of the nation and applied research in Plasma Science and Technologies. The mandate was to develop expertise for Nuclear Fusion, a source of energy with two major TOKAMAK experiments, including India's First Indigenous TOKAMAK 'Aditya'.

The exhibition was inaugurated on July 3 by Prof. Nilesh J. Vasa Dean, Indian Institute of Technology (M), Chennai. It saw a footfall of 2,741 till July 7.

Anu Awareness Yatra 2023

An awareness programme named 'Anu Awareness Yatra – 2023' with the theme 'ATOMS IN THE SERVICE OF THE NATION' was organised by IGCAR in association with the National Council of Science Museum (NCSM), Ministry of Culture, Government of India, Vigyan Bharathi - Arivial Sangam, Tamil Nadu, and Indian Association for Radiation Protection. The programmes were organised in nodal institutions in seven districts in Tamil Nadu and three in Kerala as part of Azadi Ka Amrit Mahotsav, to showcase the indigenous progress in science and technology. The objective was to highlight (i) the progress in nuclear science and technology in India, popularise technologies developed by the Department of Atomic Energy (DAE) for societal application, and application of ionizing radiation in various walks of life; (ii) to create an interest among the youth in science subjects and to explore opportunities in DAE; (iii) Dispelling myths on nuclear energy.

The curtain raiser was organised at IGCAR, Kalpakkam, on July 24, 2023. The yatra was flagged off by Ms. K. A. Sadhana, Director, Visvesvaraya Industrial & Technological Museum (VITM), and Shri Gopal Parthasarathy, State Secretary, VIBHA, (Tamil Nadu Arival Sangam), in the presence of Director, IGCAR and senior officials. Dr. Ajit Kumar Mohanty, Chairman AEC & Secretary DAE, addressed the gathering through a message. The yatra culminated at IREL, Aluva, travelling more than 1,000km, covering Kancheepuram, Thiruvannamalai, Salem, Erode, Karur, Coimbatore, Palakkad, Thrissur and Kochi. In each of these places, a nodal institution was chosen in association with Vigyan Bharathi – Tamil Nadu Ariviyal Sangam and an awareness programme was organised in that institution for two days. The nodal centres coordinated with regional institutions of each district to ensure the active participation of about 2,000 students and the public in each venue. The programme comprised lectures, quiz competitions, art competitions, creative writing competitions, conceptual orations, and exhibitions showcasing nuclear reactor models and the application of ionising radiation in medical, engineering, and agricultural fields. This Yatra was unique in that a mobile science exhibition named "Science on Wheels" from VIT-M showcased working models on societal application of space technology. A total of 25,720 people visited the 10 venues. Photographs showing the highlights of the events are presented here.

Inter school science exhibition by Bala Vidya Mandir Senior Secondary School, Adyar, Chennai, was organised on August 12, 2023, with the participation of IGCAR & MAPS, highlighting 'Atoms in the service of the Nation'A footfall of .

A workshop on "Radiation Technology and its Applications " and "Exhibition on Nuclear Energy" was organized at Anna University, in association with Science and Technology centre, Chennai & Centre for Materials at Informatics, Anna University Chennai from 04.10.2023 –06.10.2023.

The exhibition had a footfall of 1500 comprising of school and college students"The Grand Odyssey", CPS expo 2023 was held at Chennai Public School Anna Nagar on 17.10. 2023. IGCAR has put a stall to create awareness among school students on the use of nuclear Energy.

Target Audience		
School	College	Public
37150	19366	13195

Programmes in collaboration with

In Collabration with TNSCT	4
Colleges	12
Confrences	4
State Govt	3
Central Govt	2
Schools	3
DAE units	2

The exhibition had a foot fall of 1000 comprising of students and general publicA Two-day ANU Awareness program – 2023 was organized in association with the Academy of sciences, Chennai & St Joseph's college, Tiruchirapalli at St. Joseph's college, from 30.11.2023-01.12.2023. The exhibition had a footfall of 2400 comprising of school students and college students.

A Three-day ANU Awareness program - 2023 was organized in association with Academy of sciences, Chennai & PSGR Krisnammal College for women at PSGR Krishnammal College, Coimbatore From December 20 to 22, 2023. There was a foot fall of 2300 students from schools and colleges .

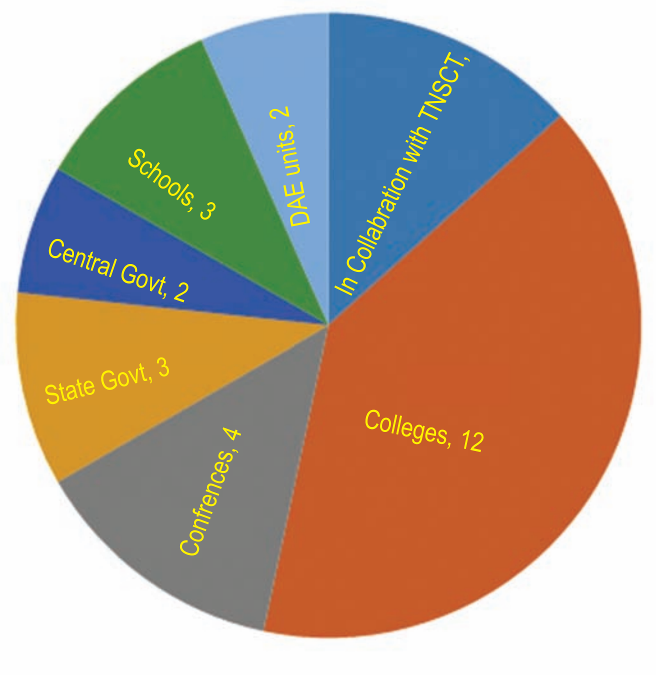

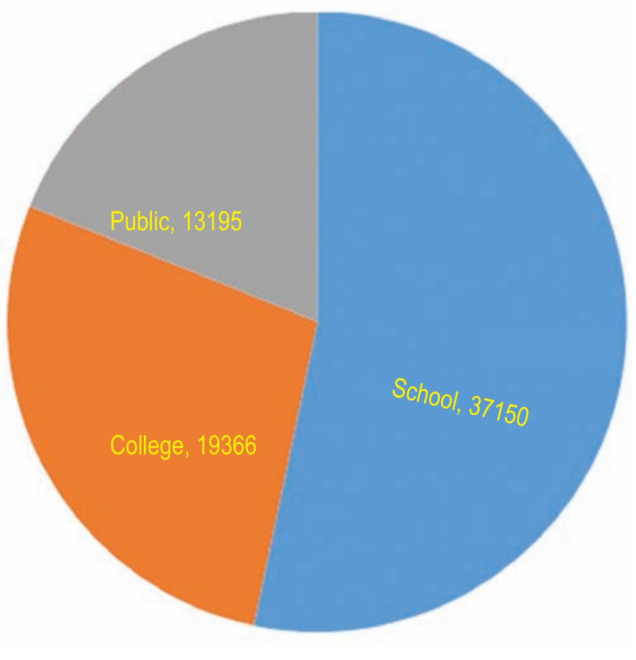

Indira Gandhi Centre for Atomic Research (IGCAR), Kalpakkam on 24 .07. 2023

Sri Sarada Nikaten College of Arts and Science, Karur during 04.08.2023-05.08.2023

Sri Sankara Arts And Science College, Kanchipuram during 25.07.2023-26.07.2023

Kumaraguru Engineering College, Coimbatore, during 07.08.2023-08.08.2023

Arunai Engineering College, Thiruvannamalai during 27.07.2023 – 28.07.2023

NSS College of Engineering, Palakkad during 09.08.2023-10.08.2023

AVS College of Arts & Science, Salem during 31.07.2023-01.08. 2023

Christ College Lringalakuda during 11-12. 08.2023.

Erode Sengunthar Engineering college, Erode during 02.08.2023-03.08.2023

IREL (India) Limited, Aluva on 14.08.2023

VI.08

Leveraging AI and Data Analytics for Visualizing HPC Job Scheduler Data & Predictive Analysis of Run Times

High Performance Computing (HPC) utilizes advanced computing infrastructure to tackle scientific and engineering problems that demand significant computational resources. Within HPC clusters, job schedulers organize parallel jobs submitted by users, prioritizing them based on a scheduling policy before assigning them to available processors for execution.

Data analysis and visualization tools have been developed to scrutinize historical data derived from HPC job scheduler logs. Data spanning eight years has been collected from 400-node HPC cluster operational at IGCAR. With around 100 active users, the cluster supports a diverse array of scientific applications including weather forecasting, molecular dynamics, computational fluid dynamics, and finite element analysis.

This initiative aims to enhance understanding of system functionality and optimizing scheduling policies through analysis of job execution and wait times, rate of system errors and job failures, load on job queues, patterns in user behavior and other pertinent metrics. Fig. 1 shows CPU allotment distribution for the jobs and Fig. 2 depicts the distribution of job run times.

Predicting job run times is one of the most challenging research problems in HPC due to multitude of factors such as input characteristics, global load, unpredictable failures and complex scheduling policies. Accurate run time predictions can help administrators in making better resource allocation decisions and taking advantage of scheduling policies such as backfilling, resultingin better system throughput and lesser overall user response time. We have applied Artificial Intelligence (AI) techniques, namely, Lasso Regression, Ridge Regression, K Nearest Neighbours (KNN), Random Forest (RF) and Support Vector Regression (SVR) on job scheduler data to predict job run times. Details of the job such as user, group, queue, application, date and time of submission and requested CPUs are used as input to the models. The models are evaluated in terms of Mean Absolute Error (MAE), Root Mean Square Error (RMSE) and R2 Scores. The results are shown in Table 1. It can be seen that Random forest gives the best prediction results for job run times.

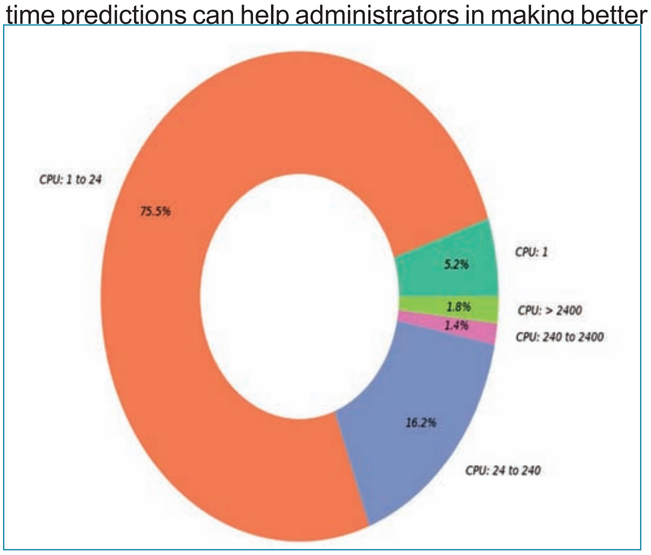

Fig. 1: Exploratory Data Analysis on Scheduler Logs: Distribution of CPU allotment

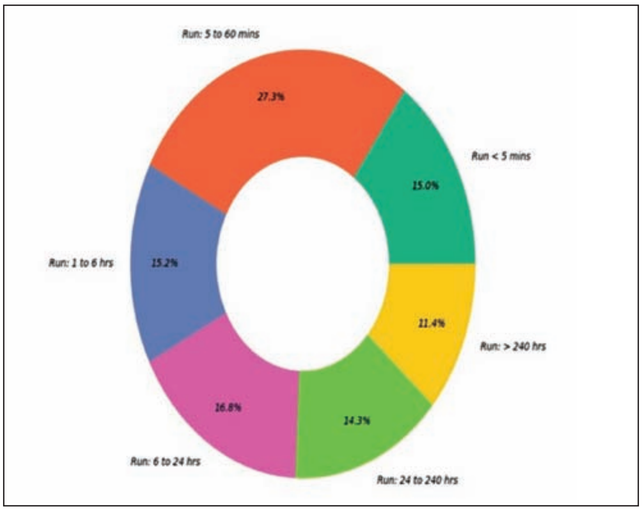

Fig. 2: Exploratory Data Analysis on Scheduler Logs: Distribution of Job Run times

Table 1: Results of applying AI models for job run time prediction

Model	R2 Score	MAE (min)	RMSE(min)
RF	0.370487	536.1439	1414.602
KNN	0.358954	545.425	1427.246
SVR	0.144268	565.7613	1649.803
Ridge	0.032165	773.2457	1754.891
Lasso	0.031573	766.3588	1755.192

VI.09 Prototype Mobile based Guard Tour monitoring system for Nuclear Facilities

In all the Nuclear plants of IGCAR such as FBTR,DFRP and CORAL, the security personnel has to perform a guard tour in every shift along the boundary wall of inner fence area to check any intruder is hiding in the area inside the double fence. Presently, in-house developed hand-held RFID readers are used for performing guard tour. Now, it is planned to replace the hand-held RFID readers with NFC based mobile system.

An exclusive mobile app, using NFC (Near Field Communication) protocol facility to communicate with the mifare card has been developed in java platform to read the information contained in RFID cards embedded on the various places of the boundary wall. This mobile application is currently designed for 12 Guard tour locations. The mobile application along with the SQLite database is developed to store the information about guard tour performed to the mobile locally.

Guard tour information is displayed on the mobile screen in both pictorial representation and tabular form (Fig. 1). Voice assist is one of the salient feature included in this application. Once the guard tour is performed, transactions are stored locally in mobile database then these transactions are transferred wirelessly using Bluetooth to the GTMS server.

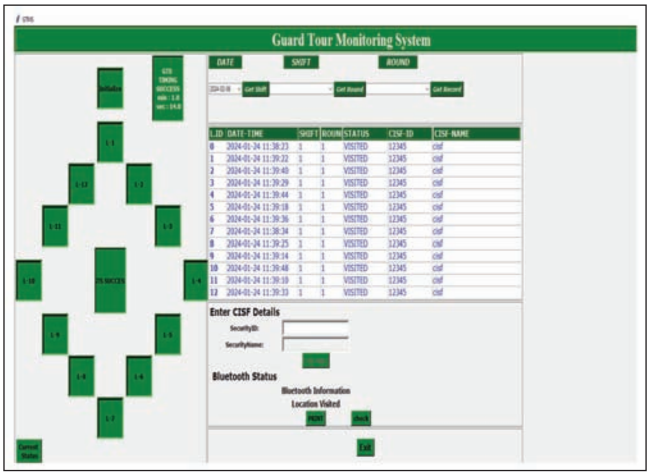

L.ID	DATE-TIME	SHIFT	ROUND	STATUS	CISF-ID	CISF-NAME
0	2024-01-24 11:38:23	1	1	VISITED	12345	cisf
1	2024-01-24 11:39:22	1	1	VISITED	12345	cisf
2	2024-01-24 11:39:40	1	1	VISITED	12345	cisf
3	2024-01-24 11:39:29	1	1	VISITED	12345	cisf
4	2024-01-24 11:39:44	1	1	VISITED	12345	cisf
5	2024-01-24 11:39:18	1	1	VISITED	12345	cisf
6	2024-01-24 11:39:36	1	1	VISITED	12345	cisf
7	2024-01-24 11:38:34	1	1	VISITED	12345	cisf
8	2024-01-24 11:39:25	1	1	VISITED	12345	cisf
9	2024-01-24 11:39:14	1	1	VISITED	12345	cisf
10	2024-01-24 11:39:48	1	1	VISITED	12345	cisf
11	2024-01-24 11:39:10	1	1	VISITED	12345	cisf
12	2024-01-24 11:39:33	1	1	VISITED	12345	cisf

Enter CISF Details
SecurityID:
SecurityName:

Bluetooth Status
Bluetooth Information
Location Visited

Fig. 2: GTMS Server Software

GTMS server software has been developed using python as front end along with Mysql database as back end for storing the information about the guard tour performed,once guard tour is completed by the security personnel. The details are received via Bluetooth from mobile application. Guard tour information is displayed on GTMS server in both pictorial representation and tabular form (Fig. 2). This software has the intelligence to make the decision whether GTMS has completed successfully as per the guidelines. GTMS server software has the capability to retrieve the tour records based on date and shift. It also has the facility to take the print of GTMS performed based on the search results (Fig. 3).

Moreover, this mobile-based system is user friendly. The security personnel can also ascertain location information with the voice message at the time of performing the guard tour. One CISF official is deployed on round the clock shift basis to perform guard tour.

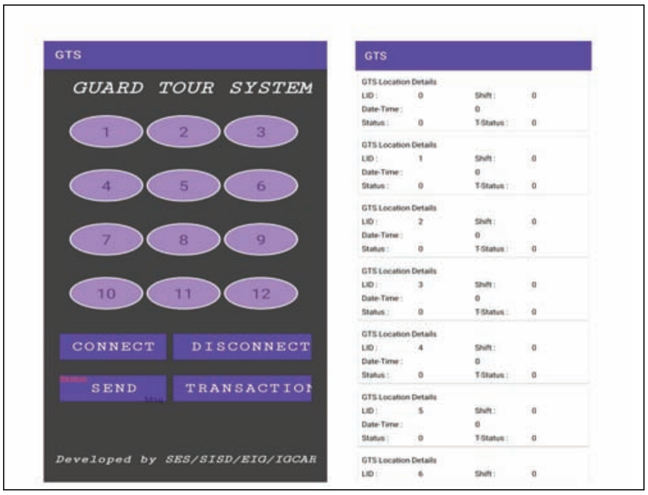

GTS Location Details
LID : 0 Shift : 0
Date-Time : 0
Status : 0 T-Status : 0

GTS Location Details
LID : 1 Shift : 0
Date-Time : 0
Status : 0 T-Status : 0

GTS Location Details
LID : 2 Shift : 0
Date-Time : 0
Status : 0 T-Status : 0

GTS Location Details
LID : 3 Shift : 0
Date-Time : 0
Status : 0 T-Status : 0

GTS Location Details
LID : 4 Shift : 0
Date-Time : 0
Status : 0 T-Status : 0

GTS Location Details
LID : 5 Shift : 0
Date-Time : 0
Status : 0 T-Status : 0

GTS Location Details
LID : 6 Shift : 0

Fig. 1: GTMS Mobile Application

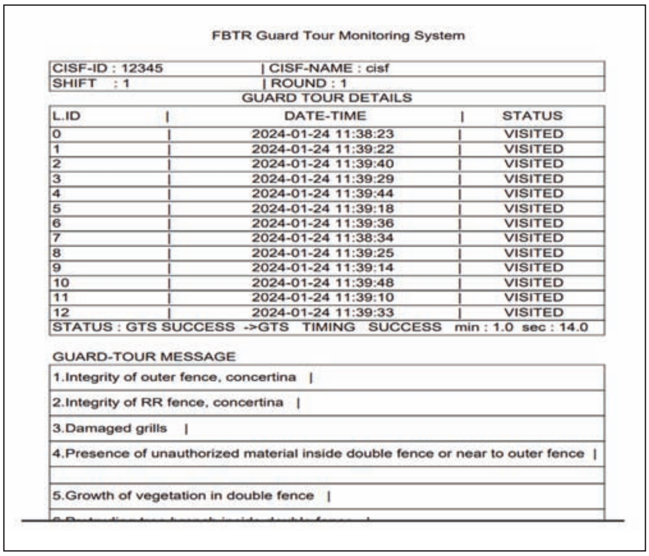

FBTR Guard Tour Monitoring System

CISF-ID : 12345 | CISF-NAME : cisf
SHIFT : 1 | ROUND : 1

GUARD TOUR DETAILS

L.ID	DATE-TIME	STATUS
0	2024-01-24 11:38:23	VISITED
1	2024-01-24 11:39:22	VISITED
2	2024-01-24 11:39:40	VISITED
3	2024-01-24 11:39:29	VISITED
4	2024-01-24 11:39:44	VISITED
5	2024-01-24 11:39:18	VISITED
6	2024-01-24 11:39:36	VISITED
7	2024-01-24 11:38:34	VISITED
8	2024-01-24 11:39:25	VISITED
9	2024-01-24 11:39:14	VISITED
10	2024-01-24 11:39:48	VISITED
11	2024-01-24 11:39:10	VISITED
12	2024-01-24 11:39:33	VISITED

STATUS : GTS SUCCESS ->GTS TIMING SUCCESS min : 1.0 sec : 14.0

GUARD-TOUR MESSAGE

1.Integrity of outer fence, concertina |
2.Integrity of RR fence, concertina |
3.Damaged grills |
4.Presence of unauthorized material inside double fence or near to outer fence |
5.Growth of vegetation in double fence |

Fig. 3: GTMS Report View

VI.10 Digital Asset Enhancement & Value Added Services

Scientific Information Resource Division (SIRD) is an advanced research library caters to the needs of more than 5000 Scientists, Engineers, Research Scholars, and students of various DAE Units at Kalpakkam by providing access to relevant information at their desktops. The collection includes 62,000 books, 48,000 back volumes, 600 journals, 15,000 standards, two lakh technical reports, e-books, scientific/technical databases and research assistant tools . SIRD has constantly been endeavouring to modernize and keep itself abreast with the latest in the field of Library through the implementation of digital library infrastructure and services. SIRD is rendering various services to the Centre like interlibrary loans, photography, videography, reprography, desktop design, in-house printing publications, auditorium, and video streaming.

Centralized Video Repository for IGCAR

SIRD has taken initiative to build repository of videos of IGCAR for the last 2 decades. Videos on the cassette form were digitized and rendered for necessary post production. Video streaming facility, which was installed in 2011 at Sarabhai auditorium also had the archival of recorded videos of the events. These videos were taken and after post production works like sound mixing, title addition and other effects, were uploaded into a server system. For this purpose, a centralized video library solution was implemented in SIRD during the last year. More than 200 videos with necessary meta data were uploaded into the repository (Fig. 1).

RFID based Book Drop System

RFID-based Integrated Library Management System with the latest gadgets are used for library management activities. During this period, SIRD has enhanced the circulation system by providing RFID based book drop machine (Fig. 2). This system can be operated from the entrance of SIRD premises (Library) on 24 x 7 basis. This system allows the patron to 'Check in' (return) books even during non-office hours, thereby avoiding fines when returned after due date.

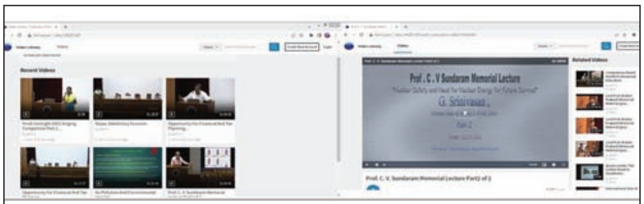

Fig. 1. Video Repository of IGCAR

Fig. 2. RFID based book drop system.

Digital Display Signage

Three numbers of 75-inch digital display signage with KIOSK structure are procured and commissioned. They are being used to display the achievements of the centre, various developmental activities, SIRD book collection, new arrivals and announcements to the visitors (Fig. 3). Similarly, Convention Centre projection system is enhanced with 12000 lumens based laser projector with HDMI Display systems.

Digital contents are uploaded into high performance digital library infrastructure comprising of server, storage and networking. Institutional repositories are developed through open source solutions such as DSpace, Linux, Apache & Mysql. Servers are maintained on IT cooling racks with UPS power backup. Fire alarm systems, CCTV surveillance, Zero client user access stations, Information access KIOKS are some of the technologies implemented in SIRD. Servers run on 24/7 basis to provide uninterrupted smooth information access to patrons across the IGCAR campus

SIRD brings out the ISSN-based in-house publication of IGCAR viz IGC Newsletter every quarter. SIRD efficiently executes the responsibility to bring out IGC annual report, desktop calendars, pocket diaries, planners, and bulk printing of confidential documents,

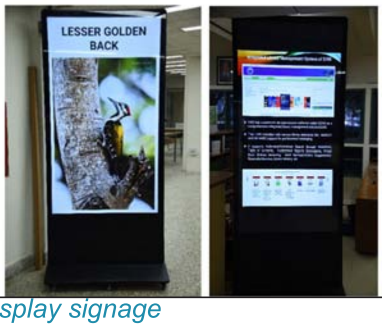

Fig. 3. Digital display signage

designing the templates for brochures, souvenirs, etc. Research data output of the institute like the theses, IGC technical reports, in-house publications like IGC Newsletter, Annual reports, pre-prints, journal and conference publications are archived in a centralized Institutional Repository (IR). The metadata of the knowledge assets are stored in Standard Dublin Core format and supports open archives initiative for metadata harvesting. Springer & IOP eBooks on Physics, Chemistry and Astronomy, Research assistant tools like grammarly ,ithenticate, flipping book, E-journals, databases and standards are being subscribed by the SIRD. Digital resources are accessible 24/7 at desktops (within and outside the campus) of the patrons and user alerts are provided through email.

VI.11 Deployment of Open-Source Security Information and Event Management System and its Integration with Proxy Servers

A Security Information and Event Management (SIEM) system continuously collects security-related data from various sources across the network, including firewalls, servers, applications, and user devices. This data includes security events, log entries, and user activity.

A SIEM system performs three key functions:

a. Security Information Management (SIM): Analyzes and stores historical security data for compliance reporting, security audits, and forensic investigations.

b. Security Event Management (SEM): Monitors security events in real-time, identifies suspicious activity, and generates alerts for potential threats.

c. Log Management: Aggregates and normalizes event logs from diverse sources, making them easier to search and analyze.

Deployment of SIEM system at IGCAR

In order to enhance threat detection and improve incident response, an open-source SIEM system has been implemented and deployed at IGCAR. It consists of 3 servers each with two Intel Xeon 16-core processors, 32 GB memory and a 3.3 TB SAS Hard Disk with Raid protection. These servers are designated the following roles – Manager, Sensor and Search.

The Manager node provides a web interface to configure the SIEM system, see the alerts and statistical reports, and perform log analysis and detailed forensic investigation. It works in co-ordination with the Search Node and the Sensor Node.

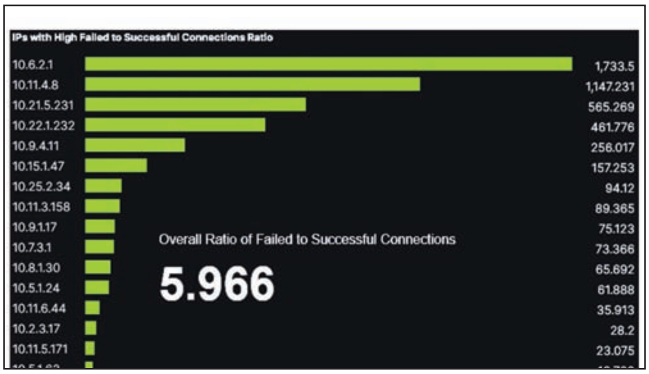

Fig. 1: A dashboard listing the internet IPs with unusually high internet access failure to success ratio

The Sensor node, which acts as a Network Intrusion Detection System (NIDS), consists of two interfaces --- an interface on which it talks to the Manager Node and the Search Node, and another monitoring interface which listens in promiscuous mode. The port of the network switch where the monitoring interface is connected is configured to receive a copy of all the network packets flowing between the Internet and the Intranet. The Sensor Node captures and stores the entire traffic seen on the monitoring interface for 2 days to facilitate in-depth forensic analysis. It retrieves the network metadata and relevant security information from the captured traffic and checks for the presence of threat signatures using the threat signature database periodically fetched from various national / international sources. The network metadata, and threat alerts, if any, are handed over to the Search Node for further processing and storage.

The Search node acts as the back-end database. It consists of an open-source search and analytics engine which can store structured or unstructured data in a NoSQL format, and offers lightning-fast searches and analytics.

Integration of the SIEM system with Proxy Servers

In order to enhance network security, users of the IGCAR campus network are allowed to access the internet only through a user authentication system constituted by a set of proxy servers. The user activities logged by the proxy servers are critical in investigating cyber security events. Therefore, the SIEM system was configured to fetch and process the raw logs generated by the proxy servers, extract the relevant information and store them in the Search node. Various dashboards have been developed to analyse the internet access data and report the statistics in real-time (see Fig. 1 for a dashboard that lists the intranet IPs with unusually high internet access failure to success ratio). Python based modules are also being developed to perform in-depth analysis of the threat alerts by correlating proxy logs with NIDS logs.

VI.12 Design & Augmentation of Aging Radioactive ventilation systems in Radiochemistry Laboratory

The air-conditioning and ventilation system for various laboratories in the Radiochemistry Laboratory (RCL) building, handling radioactive materials and sodium facilities, is designed with a multi-zone, once-through graded system. The white zone rooms employ a re-circulatory system of air-conditioning through air-handling units (AHUs). Ventilation plays a crucial role in supporting the physical containment by maintaining negative pressure within the containment, thereby limiting the ingress of particulates. The original total air-conditioning capacity of the RCL main building was 660 TR comprising of low level, high level, high bay, Annex-2 (FChD extension) and process cooling system, before augmentation. With the expansion of R&D activities, the ACV systems in RCL Annex-1 (Sensor labs) and Annex-3 (Boron building) were modified for 24x7 operation. Additionally, process water system provisions were added to labs in the Annex-3 building to accommodate the round-the-clock operation requirements. Due to aging, the existing cooling coils in the low-level and high-level supply systems in the RCL main building were not achieving the desired ΔT. To address this, 10-row chilled water cooling coils (Fig. 1) with a capacity of 18 TR each were designed, utilizing blue hydrophilic coated aluminum fins and 1/2" x 0.6 mm thick copper tubes qualified by eddy current testing. The total capacity of each cooling coil bank is designed for 192.0 TR. Due to increased heat loads in low level laboratories, the average temperature in the labs were more than the design requirement of 25 ± 1°C. So, a separate once-through, conditioned supply air system was designed with an air flow rate of 21,200 CMH and a static pressure head of 125 mm of WC and annexed to the existing low level system. This system has a capacity of 140 TR with an 8-row chilled water cooling coil featuring blue hydrophilic coated aluminum fins and 1/2" x 0.5 mm thick copper tubes. The conditioned supply air for low-level labs is delivered by two systems: a) the low-level supply system and b) a fresh air once-through AHU system. Despite these modifications, the low-level exhaust system remains unaltered and the required negative pressure and air changes per hour is achieved by proper air balancing in these labs. Also, safety in these labs were ensured by providing necessary safety interlocks between the supply and exhaust system.

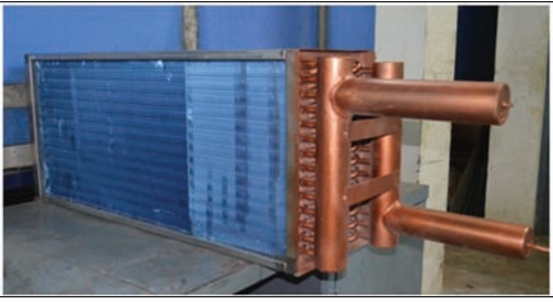

Fig. 1: Cooling coil (10 Row system)

Fig. 2: AHU system for Sodium & adjacent labs

Similarly, a recirculation-type Air Handling Unit (AHU) with a chilled water system for Annex-I (Ground and first floor) was meticulously designed, fabricated, installed, and commissioned. The total air conditioning (AC) load for sensor labs on the ground floor is 25 TR, and on the first floor, it is 40 TR (Fig. 2). In order to effectively maintain the negative pressure gradient in various zones, heavy duty, air tight ventilation barrier doors have been designed, fabricated and installed. Further to prevent and contain spread of fire, if any, in radioactive exhaust HEPA filter bank, special leak tight and 2 hours fire rating doors was designed, tested and erected. The ACV system underwent augmentation for continuous 24x7 operation, with strict quality control measures implemented during construction and erection. The newly implemented systems underwent rigorous testing and demonstration to ensure optimal performance. This included assessment of cooling capacity, design values (water flow, air flow, ΔT, etc.) through instrumentation, and verification of safety functions such as: a) Maintaining Negative Pressure to inhibit the spread of contamination during both normal and abnormal conditions, b) Verifying the functionality of systems designed to prevent backflow, and c) Assessing the integrity of HEPA filter systems on supply/exhaust side. After carrying out the above mentioned modifications, the present total AC capacity of RCL is 1082.5TR, by integration of all systems. This comprehensive approach to design, testing, and safety validation contributed to the overall efficiency and reliability of the ACV system in RCL facility

VI.13 Remote Radiation Monitoring System

Radiation monitoring is the systematic and continuous process of measuring and assessing the levels of radiation in a given environment. It involves the use of various instruments and detectors to detect and quantify ionizing and non-ionizing radiation, specifically, gamma rays, alpha and beta particles. An advanced remote radiation monitoring system has been designed, tested & implemented in RCL.

The primary objectives of radiation monitoring are to ensure the safety of individuals working in or near radiation- prone areas, protect the environment from radioactive contamination, and adhere to regulatory standards and guidelines. Radiochemistry Laboratory (RCL) is equipped with Radiation Monitors distributed all over the laboratory. Area Gamma Monitors (AGM), measure and display gamma dose rates in the range of 0 to 100 mR/h. Continuous Air Monitors (CAM) measure and display alpha and beta radiation in the range of 0-10,000 counts per minute. 12 AGMs and 15 CAM signals are installed in RCL.

These signals are connected to a customized microcontroller based Remote Terminal Unit (RTU). 5 nos. of RTUs are connected for this purpose. All these RTUs are connected to a PC in control room through isolated Local Area Network (LAN). Signals from the instruments are in the form of current 4-20 mA and are processed in RTU, converts into digital form and sent to PC.

The software in the PC converts into engineering units and displays the data in digital form and also in the graphical form. The overall block diagram of the system is shown in Fig. 1. This works in server-client mode, where RTU servers as server and PC serves as client. The systems intricate signals from CAM and AGMs traverse via wired connections, acting as vital conduits for the transmission of crucial data to RTUs. The software methodology is shown in Fig. 2. It is in sequential structure and error handling is done efficiently for smooth functioning of the program. It has 15 modules in the program. The system is tested for its functionality and now running in RCL continuously. The photograph of the system is shown in Fig. 3.

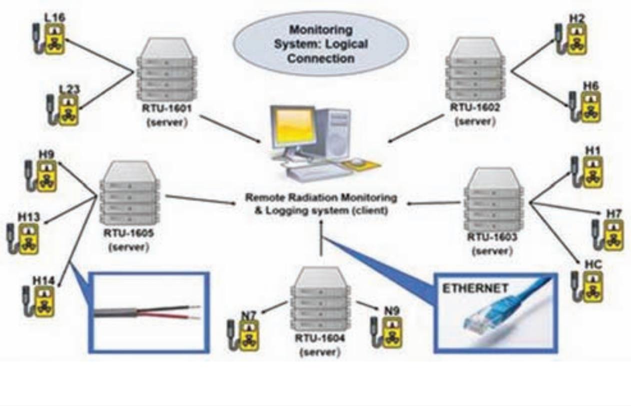

Fig. 1: Conceptual Block Diagram of the system

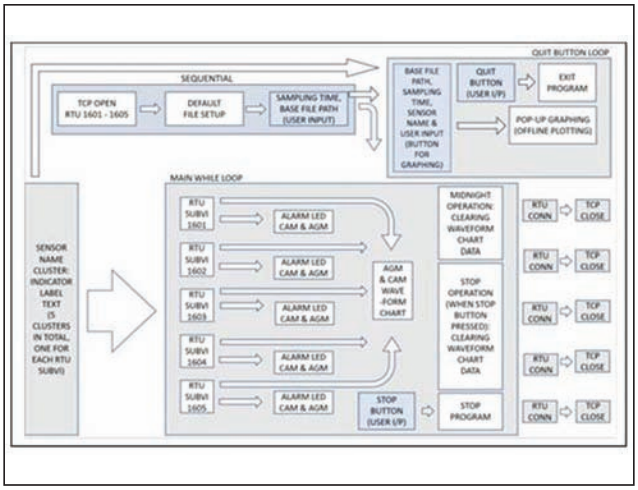

Fig. 2: Program architecture

Fig. 3: Photograph of the running system

With successful integration of RTU, CAM and AGMs, the system is working with advanced real-time monitoring capabilities fulfilling the requirement of regulatory standards.

Back to Main

CHAPTER VII

Awards / Publications / Events / Organisation

Awards & Honours

Dr.John Philip has been selected as an Editorial Board Member of Jorunal of magnetism and Magentic Materials of Elsevier Publishers.

Dr. Arup Dasgupta received Fellow of Indian Institute of metals (IIM) for the year 2022.

Dr. R. Mythili received Fellow of Electron Microscopy of Society of India (EMSI) Award for the year 2022 under Materials

Science category

Dr. Harish Chandra Dey, received "Welding Science & Technology Award" from IIW-India, Chennai Branch.

Dr. Sandip Kumar Dhara, BoS Member Physics, SRM University, Chennai, Senior Member OPTICA (old OSA) (2022)

Dr. R. Ramaseshan, received "Fellow Chennai Academey of Sciences (FASC)" (2022)

Mr. Choudhury Abinash Bhuyan, received K. V. Rao Scientific Society Award, 'Best Research Award' (2023)

Central Water Chilling Plant received 1st Prize in Swatchh Bharat Pakhwada for Central Water Chilling Plant in Plant Category

Best Paper Awards

Dr. Amit Kumar, Ms. Usha Pujala, Shri E. Hemanth Rao, Dr. V. Subramanian, Shri. Sanjay Kumar Das, Dr. D. Ponraju, and Dr. B. Venkatraman "Assessment of Fission Product and Sodium Aerosol Behavior in a closed chamber" Vivanta, Navi Mumbai, during 12 -14 December 2023

Dr. T. Saravanan, M. Krishnamoorthy, S. Murugan, S. Satheesh Kumar, S. Surendar Kumar, B. S. Ramesh Babu, V. Praveen Kumar, Utpal Borah, Alka Kumari, G. Ramesh "Experience in Manufacture and Leak Testing of Inlet Water Sub-Header for The Steam Generator of Fast Breeder Test Reactor" National Welding Seminar (NWS) 2023

Shri Vivek K. Mishra, Saroj K. Panda, Biswanath Sen, Dipti Samantray "Effect of non-condensable gas on thermal characteristics of thermosyphon relevant to nuclear fuel storage vault" CHEMCON 2023 oral presentation during December 27-30 in Kolkata

Best Poster Awards

- Ms. B.R. Vaishnavi Krupa received EMSI-2023 conference – Best poster consolation price
- Dr. Arup Dasgupta received "The above and beyond appreciation for Editorial Leadership" in 2022 from Springer.
- Shri Shailesh Joshi, Ms. Madhusmita Panda, Dr. O. Annalaskhmi, C. Dr. Venkata Srinivas and B. Venkatraman received the second prize in the best poster award at the 6th Asian and Oceanic Congress on Radiation Protection (AOCRP6) international conference held at Mumbai during February 7-11, 2023 for the paper titled "Uranyl based Metal Organic Framework as OSL Dosimeter".
- Shri. Mantosh Mandal secured the 'Best Poster Presentation' award at the 4th Heat Treatment and Surface Engineering (HTSE-2023) conference, held at Chennai on 28 -30 September 2023.

- **Dr. B. Sasi** received the Best Poster award for the paper titled, "Development of eddy current sensors for quality control of nuclear components", presented in the XV Triennial &III international Conference on the theme: Women in Science & Technology, held during 11th-13th June 2023 at IWSA-HQ, Navi Mumbai.
- **Ms. Srujana M*, B. B. Lahiri, John Philip** received the Best Poster award of International Conference on Functional materials for Future Technology (IC-FMFT 2023) held during April 19-21, 2023 for the poster titled "Viscosity dependent studies on the magnetic fluid hyperthermia efficiency of magnetite nanoparticles coated with a bio-compatible polymer"

Seminars, Workshops, Webinars and Meetings

- All India Hindi Scientific Seminar -"Role of Nuclear Energy and other advanced technologies to control climate change" at Sarabhai Auditorium on January 10-11, 2023
- Training Programme-"Rozgar Mela" by PMO Office at Raja Ramanna Auditorium on January 20, 2023
- Awarness Programme-"Self Managing and Inspirational Leadership, Azadi ka Amrut Mahotsav" at Sarabhai Auditorium on January 24, 2023.
- Hindi Workshop –"Hindi Workshop" at Raja Ramanna Auditorium on February 16, 2023
- Swatchchta Pakhwada 2023- "Essay Competition " at Raja Ramanna Auditorium on February 20, 2023.
- IGC Colloquium-"Azadi ka Amrut Mahotsav lecture" by Dr.P.Venkatachalam, Sri Ramachandra Institute of Higher Education and Research" at Sarabhai Auditorium on February 24, 2023
- Swatchchata Pakhwada 2023 closing ceremony at Sarabhai Auditorium on February 27, 2023.
- Awarness Programme- "International Womens Day Program" at Sarabhai Auditorium on March 1-8, 2023.
- Women's Day Celebration- "Womens Empowerment Lecture" at Raja Ramanna Auditorium on March 24, 2023
- Curie Memorial Lecture 2023- "Annual curie memorial lecture organized by IANCAS-SRC" lecture by Dr. Tapas Das, BARC at Sarabhai Auditorium on March 29, 2023.
- "Farewell Function to Shri S. Raghupathy, Director, RDTG, EIG & RFG" at Sarabhai Auditorium on March 30, 2023.
- IGC Colloquium-" The Joy of Experiementing" by Prof. B. S. Murty at Sarabhai Auditorium on April 10, 2023.
- IGC Colloquium-"IGC Colloquium" by Shri B N Ramakrishna, Director, ISTRAC at Sarabhai Auditorium on April 13, 2023
- "Hindi Fortnight Prize Distributions" at Sarabhai Auditorium on April 20-21, 2023
- "Felicitation function for Dr. D. Thirugnana Murthy, AD, ECG, EIG" at Sarabhai Auditorium on April 26, 2023
- Chemistry Colloquium-"Hydrogen Technologies Development at ARCI" by Dr. Ramya at Raja Ramanna Auditorium on May 4, 2023.

- IGC Colloquium-"Remote Repair of BSC System of PFBR" by Mr. Nimesh Chinoy at Sarabhai Auditorium on May 4, 2023.
- Technical talk-"On financial aspects" at Sarabhai Auditorium on May 28-29, 2023
- Training Programme-"In augural function for Summer Training Program in Physics and Chemistry (STIPAC), 2023. A six-week training program is being organized by IGCAR for the students pursuing their post-graduation in Physiccs and Chemistry" by STIPAC Coordinators from MSG and MCMFCG at Sarabhai Auditorium on May 30, 2023
- IGC Colloquium- "Air Pollution and Environmental Impacts" by Dr. T.V.B.P.S. Rama Krishna, CSIR-NEERI at Sarabhai Auditorium on June 7, 2023.
- IGC Colloquium- "Role of Oceans in Climate and Environment" by Dr. Ramadass, Director, NIOT at Sarabhai Auditorium on June 9, 2023

- International Yoga day 2023 celebrations- “Yoga for Happiness - To celebrate International Yoga Day on 21.06.2023” at Sarabhai Auditorium on June 21, 2023
- 23.”Farewell for Dr. B.K. Nashine, Director, RDTG, ESG & RFG” at Sarabhai Auditorium on June 30, 2023
- Training Programme-“Valedictory Function of Summer Training program in Physics and Chemistry – 2023” by STIPAC Coordinators at Sarabhai Auditorium on July 7, 2023
- Anu Awareness Yatra Programme- “Flag off ceremony of Anu awareness yatra and exhibition by Joint Secretary, Ministry of Culture and Director, IGCAR” at Convention Centre Anupuram on July 22-24, 2023.
- TSOs graduation day –“17th Batch BARC training school, IGCAR campus TSOs graduation function” at Sarabhai Auditorium on July 25, 2023
- Special Invited Lecture- “Special invited lecture” by Dr.J.Jebasingh, Oncologist by at Sarabhai Auditorium on July 28, 2023
- Session on Financial Education – “Informative sessions on financial planning for staff families, with a focus on asset allocation and tax planning” at Sarabhai Auditorium on August 10, 2023.
- International Conference- “3rd International Conference on structural Integrity(ICON-2023), Pre Conference Workshop” at Convention Centre Anupuram on August 22, 2023
- “Milestones-Chandrayaan-3 Landing” at Sarabhai Auditorium on August 23, 2023
- Workshop on Medical Emergency-“On Medical Emergency for Certifying surgeon and Paramedical Staff from various DAE units and 9th Meeting of the Occupational Health Safety Committee (OHSC)” at Convention Centre Anupuram on August 31- September 1, 2023.
- “Teacher’s Day Celebration” at Sarabhai Auditorium on September 5, 2023
- Quiz Programme- “31st Prof. Brahm Prakash Memorial Quiz BPMMQ 2023 at Sarabhai Auditorium & Convention Centre Anupuram on September 8-9, 2023.
- National Conference-“REFCON 2023-ISHRAE Kalpakkam Chapter Refrigeration conference” at Convention Centre Anupuram on September 13, 2023.
- “HINDI FORTNIGHT COMPETITIONS – 2023 at Sarabhai Auditorium on September 22-27, 2023.
- Pledge-“Swatchchta Hi Seva Pledge administered” by Director at Sarabhai Auditorium on September 25, 2023.
- Theme Meeting SHAKTHI 2023- “Theme meeting on WOMEN IN TECHNOLOGICAL ADVANCES & SOCIETAL UPLIFTMENT” jointly conducted by ISHRAE & IWSA, Kalpakkam Chapter at Sarabhai Auditorium on September 26, 2023
- Memorial Lecture-“15th Dr. Placid Rodriguez Memorial Lecture-The PRML 2023” is presided by Dr. B. Venkatraman, Director IGCAR and the event will be attended by officials of IGCAR and IIT Madras by Dr. Komal Kapoor Chairman NFC at Sarabhai Auditorium on October 5, 2023.
- GeM related Procurement information and Updates-MRPU “Interaction with Indenting Officers for GeM related procurement as buyer and updates in GeM” by MRPU at Sarabhai Auditorium on October 6, 2023.
- • Training Programme-“NPCIL conducting - Inauguration Function for Skill based Training Program for Doctors on Capacity building for Medical Management of Radiological and Nuclear Emergencies” at Convention Centre Anupuram on October 16, 2023•
- Vigilance Awareness Campaign – “Video Competition and Special Talk” by Shri GANAPATHI K R K , B. COM, LLM, Grad C.W.A at Sarabhai Auditorium on October 18, 2023.
- Training Programme-“NPCIL conducting - Valedictory function for the program of Skill based Training Program for Doctors on Capacity building for Medical Management of Radiological and Nuclear Emergencies” at Convention Centre Anupuram on October 21, 2023.
- Theme Meeting-“Fast Reactor Aerosol Research: Current Scenario and Future Directions-A two-day theme meeting on Fast Reactor Aerosol Research FARAR 2023” at Convention Centre Anupuram on October 25-28, 2023.
- Theme Meeting-“Fast Reactor Aerosol Research: Current Scenario and Future Directions FARAR 2023” by at Sarabhai Auditorium on October 25-27, 2023.

- Vigilance Awareness Week-“Special Talk on Preventive Vigilance” at Sarabhai Auditorium on November 3, 2023
- International Conference-“2nd International conference on Recent advances in information Technology” at Sarabhai Auditorium on November 21-23, 2023.
- Tribute to Dr.B.R.Ambedkar- “Observing Death anniversary of Dr.B.R.Ambedkar” at Sarabhai Auditorium on December 6, 2023
- Labour Enforcement Officer Visit- “The Labour Enforcement Officer is visiting IGCAR to verify the records of the Contractor and if needed, he will give lecture to the contract employees” at Sarabhai Auditorium on December 15, 2023
- “IRSG Theme Meeting” at Sarabhai Auditorium on December 21-22, 2023

Books

- R. D Kale and B.K Sreedhar, Centrifugal Pumps for Sodium Cooled Reactors, 1st edition, 218 pages, Nov. 2023, Publisher CRC Press, Boca Raton, Florida, USA and Oxford, UK, ISBN-101032460539, ISBN-13978-1032460536, DOI: 10.1201/9781003460350
- Vivek Kumar Mishra, Saroj Kumar Panda, Biswanath Sen, M.P. Maiya and B. P. C. Rao, FMFP 2021: Fluid Mechanics and Fluid Power (Vol. 2), Springer, Singapore, ISBN 978-981-19-6969-0. https://doi.org/10.1007/978-981-19-6970-6_75

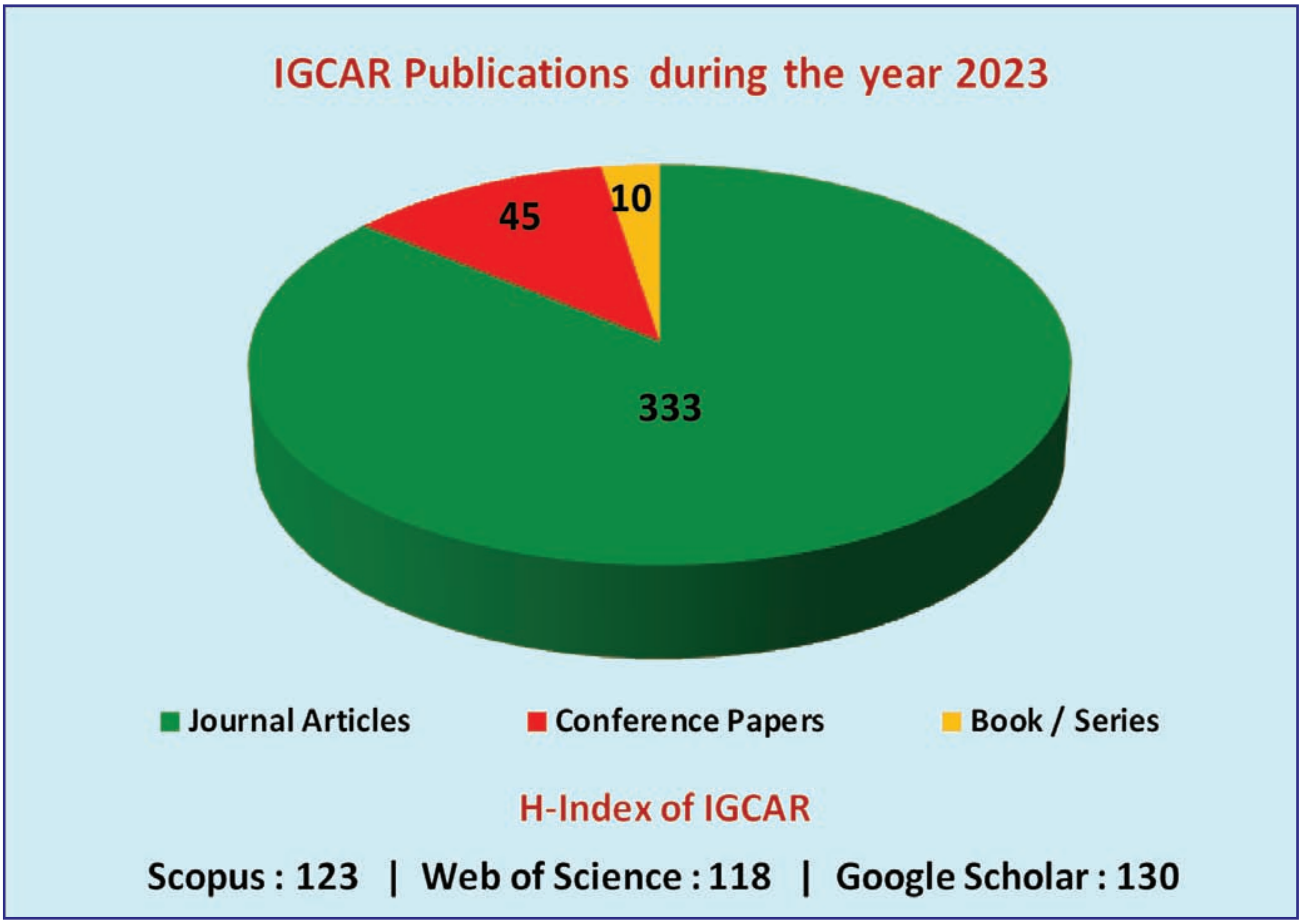

All India Hindi Scientific Seminar
Role of Nuclear and other Advanced Technologies for Climate Change Control

January 10-11, 2023

Glimpses of the All India Hindi Scientific Seminar-2023

On the occasion of World Hindi Day (January 10), An All India Hindi Scientific Seminar was organized by the Official Language Implementation Committee of Indira Gandhi Atomic Research Centre, Kalpakkam jointly with Bhartiya NabhikiyaVidyut Nigam Limited, Kalpakkam and General Services Organisation, Kalpakkam at Sarabhai Auditorium, Homi Bhabha Bhavan, IGCAR on January 10 and 11, 2023. The title of the seminar was "Role of Nuclear and other Advanced Technologies for Climate Change Control". Dr. G.K. Dey, Former Director, Materials Division, BARC was present as a chief guest of the inaugural function of the seminar. Dr. B. Venkataraman, Director, IGCAR presided over the seminar. Addressing the audience, he said that keeping in mind the environment protection, the Department of Atomic Energy is committed to the development of green energy production and climate-friendly innovative technologies. Scientific and technical officers and research scholars from the units of the Department of Atomic Energy, major scientific and research institutes, public sector establishments, all India educational institutions located across the country registered their participation in the seminar. A total number of 6 technical sessions were organized during the seminar, in which 13 invited talks, 14 contributory talks and 47 posters were presented. A total of 85 general participants were present in the seminar.

Reported by
Prabhat Kumar Sharma, DD (OL)

Hindi Workshop

February 02, 2023

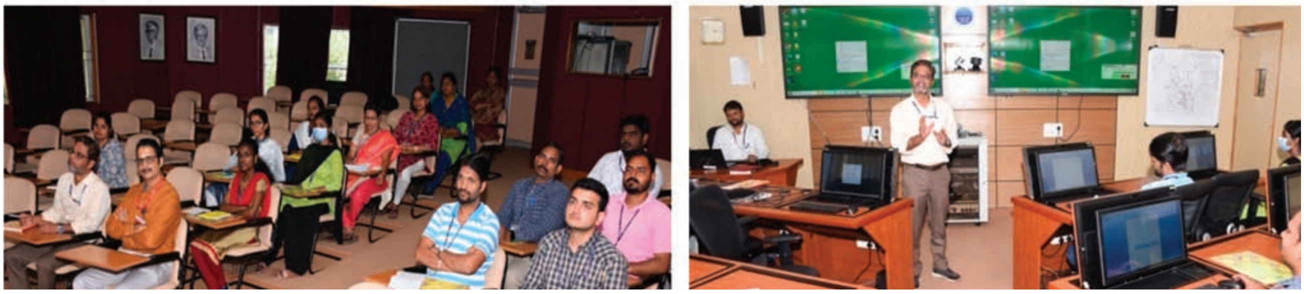

Glimpses of Hindi Workshop

A one day Hindi workshop was organized on 16-02-2023 at Raja Ramanna Auditorium for the employees of IGCAR, Kalpakkam during January-March quarter. The workshop was divided into a total of four sessions. In the first session, Shri Raju Pandey, Sr. Manager (Official Language), BHAVINI, Kalpakkam delivered his lecture on the topic of Official Language Policy. In the second session, the employees were made to practice noting and drafting in Hindi by Shri Sunil Kumar Jangid, Hindi teacher, Hindi Teaching Scheme. In the third session which started after lunch, Shri Prabhat Kumar Sharma, Deputy Director (Official Language), Hindi Section, IGCAR delivered his lecture on Hindi Incentive Scheme of DAE (ATOLIS) and encouraged them to participate in that scheme. In the fourth and last session, employees participating in the workshop were given information about the use of Hindi on computer and were given Hindi typing practice by Shri Jitendra Gupta, UDC, Hindi Section, IGCAR. The workshop ended with a feedback and valedictory session followed by tea.

Reported by
Prabhat Kumar Sharma, DD (OL)

Report on Transfer of IGCAR's Conductivity Meter Technology

March - 17, 2023.

Transfer of IGCAR's Pulsating Sensor based Conductivity Meter technology to a Mumbai based industry on 17.March.2023. This event was organized by TT&CD, BARC, Mumbai.

IGCAR's "Pulsating Sensor based Conductivity Meter" technology, developed in the Electronics and Instrumentation Group to meet India's Atma Nirbhar Bharat goals was transferred to a Mumbai private industry on March 17, 2023. In a brief event arranged by Technology Transfer & Collaborations Division, BARC, the technology license agreement was exchanged between the Director of the private industry and Dr. A. P. Tiwari (Director, Knowledge Management Group, BARC & Chairman, Technology Transfer Sub-Committee of DAE). Dr. N. Subramanian, Head, Incubation Centre-IGCAR handed over the Technology Document to the industry. The meeting was attended by Dr. Amar Banerji, Head, TT & CD, BARC and his senior colleagues, Shri M. Sivaramakrishna, Head, ISS, EIG, IGCAR and Directors of the Mumbai licensee. This is the third industry to which this technology has been transferred to on a non-exclusive basis since April 2021.

Reported by
Dr. N. Subramanian
Safety, Quality & Resource Management Group

Women's Day Celebrations at IGCAR 2023

March 1- 7, 2023

Felicitation to school children

Women's Day was celebrated from March 1- 7, 2023, at IGCAR. The celebrations included competitions and felicitating girl students who have excelled in studies, sports and cultural events. Distinguished women in law and justice, news broadcasting and financial advice were invited to share their experiences and educate the audience.

Ministry of Women and Child Development had directed DAE to create awareness about the schemes developed by the government for the welfare of women and to felicitate achievement by women during the week of March 1 to March 8 through various celebrations.

IGCAR organized competitions like slogan writing, posters, elocution and skits on topics related to Women's empowerment. Such competitions are the best method to spread the concept and the various schemes for women's empowerment. More than 150 employees participated in the competitions. Forty employees played six skits on topics including Women's empowerment, Gender Equality, the Role of working women in society, The benefit of treating women with dignity, Innovative methods to protect women and Government schemes for women. The best slogan is portrayed on the Figure-1.

Ms. Leela Meenakshi IIS, Joint Director, All India Radio, spoke on her experiences in the News services field on March 3, 2023. Ms Renu Maheswari, SEBI registered investment advisor and co-founder Finscholarz Wealth Managers, spoke on "Know Your Money" on March 6, 2023. IWSA organized this lecture.

IGCAR organized an awareness lecture by Ms. Sulekha Beevi, Member Judicial Customs Excise and Service Tax

Felicitation to Mehetva founder member Mrs Blossom Rodriguez,

International Women's day celebrartions

Felicitating Sri Raghupathy , Director, RDTG,EIG and RFG

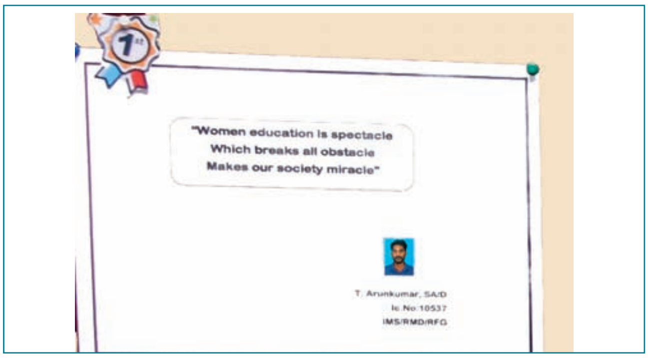

"Women education is spectacle
Which breaks all obstacle
Makes our society miracle"

T. Arunkumar, SA/D
Ic No:10537
IMS/RMD/RFG

First prize - Slogan Competition

Appellate Tribunal, Chennai Region, on March 7, 2023. The cases between Bajaj & Gill, the Vishakha case, etc., were discussed in this lecture. During the interactive session, the speaker explained the law to protect women against sexual harassment in the workplace.

As a token of appreciation, a memento was gifted to all women employees of IGCAR and CISF at Kalpakkam on Women's day.

Mehetva is a school at Kalpakkam township where training is given to special children was founded by three women in 1996 and has been run successfully by them since then. The school requires specialized training for teachers and other staff to handle the children. On Women's day celebrations 2023, IGCAR honored the founding members of Mehetva, Ms.Blossom

Rodriguez and present organizing member Ms. Chitra.

A total of 50 students from the neighbouring schools AECS1, AECS2, AECS Anupuram, KV1, KV2 and two Tamil Medium schools from Sadras and Pudupattinam were honored.

Reported by
Ms. S. Rajeswari
Safety, Quality & Resource Management Group

Interactions with Academia

April 10-11, 2023

IGCAR- IIT Hyderabad interactive meeting

A delegation of 13 faculty from IIT Hyderabad visited IGCAR during 10-11 April 2023 to explore collaborative projects with IGCAR. The team visited various research facilities of IGCAR and based on the interactions, broad areas for collaboration were identified.

Reported by
Dr. V. Karthik, MMG

Incubation Agreement Signed with Private Industry for Oil Level Measurement System

April 25, 2023

A collaborative incubation agreement, as per DAE Incubation Policy (2021), has been signed on April 25, 2023 between DAE Incubation Centre-IGCAR and a Chennai based private industry for EIG, IGCAR's "Oil Level Measurement System". Inset (Left): Signing of the incubation agreement; Inset (Right): Presentation on the technology by Ms. N. Malathi, EIG prior to signing the agreement on 25.04.2023.

Technology Incubation Activities: A collaborative incubation agreement, as per DAE Incubation Policy (2021), has been signed on 25. April. 2023 between DAE Incubation Centre-IGCAR and a Chennai based private industry for IGCAR's "Oil Level Measurement System" for EIG, IGCAR. This incubation programme is expected to accelerate development of this IGCAR technology from its current technology readiness level (TRL) of '7' to TRL '8' or '9', with value-additions suitable for commercialisation, during the incubation period of ~14 months.

Reported by
Dr. N. Subramanian
Safety, Quality & Resource Management Group

Summer Training Program in Physics and Chemistry (STIPAC-2023)

May 30, 2023

Releasing of books by Dr. V. Ravindran, Director, IMSc, Chennai during the inaugural function of Summer Training Program in Physics and Chemistry (STIPAC-2023)

Materials Science Group (MSG) has prided itself in its consistent and exemplary work on radiation effects on solids. The very first IGCAR report RRC 1 (1973) titled "Radiation damage in Reactor materials" carrying an article by Dr. G. Venkataraman on "Voids in irradiated metals and alloys" followed by a series of reports on defect studies in different reactor materials have given a great impetus to the Radiation damage and Defect studies program at MSG. Keeping this background of almost five decades of research work in the defect studies, the role of defects in Condensed Matter at MSG was reviewed in a Two day internal meeting held during 3-4 November 2022. This meeting had talks by experts on various aspects of defects in materials which are being currently investigated in MSG. These talks were compiled in to a book titled "Role of Defects in Condensed Matter: Vistas from Materials Science Group" bearing ISBN No. 978-81-955370-1-3. The book comprised of 11 chapters describing the scientific contributions by the colleagues of MSG, was released on 30th May 2023 at the Vikram Sarabhai Auditorium by Dr. V. Ravindran, Director, IMSc, Chennai during the inaugural function of Summer Training Program in Physics and Chemistry (STIPAC-2023).

Reported by
Dr. R. Govindaraj
Materials Science Group

Inauguration of Met-Ocean Data Buoy with Radiation Monitor

June 02, 2023

Figure 1: Inauguration of Data Buoy by Director, IGCAR

Figure 2: Data Buoy

As part of Emergency preparedness program, Safety, Quality & Resource Management Group (SQRMG) has deployed a Met-Ocean Data Buoy with Radiation monitor about 1-km from the coast in the coastal waters of Kalpakkam site. The Radiation Buoy was inaugurated by Director, IGCAR on 2nd June 2023. The Buoy is designed with a number of meteorological and ocean sensors [anemometer, air humidity & temperature sensor, pressure, rainfall sensor, Surface CT sensor, current meter, wave meter], mechanical and mooring components and sinker weight with the technical guidance from National Institute of Ocean Technology (NIOT), Chennai. The IGCAR developed radiation monitor is integrated with the onboard CPU.

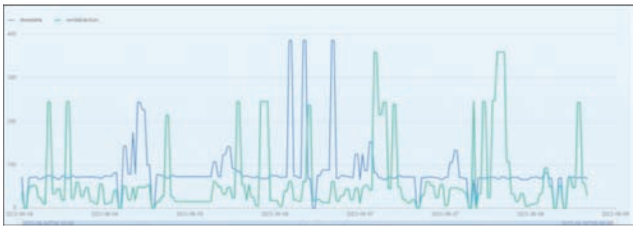

Figure 3: Real-time data

The buoy provides environmental parameters of winds, temperature, humidity, wave height, ocean current, sea water conductivity and temperature, and radiation dose rate data from the sea sector to the Online Decision Support System ONERS operational at Kalpakkam site for the management of Off-site emergencies. The real-time data is transmitted using GPRS to the server at IGCAR. Presently there are 27 radiation monitors distributed in nine land sectors connected to ONERS. The data buoy would enhance the existing monitoring radiation monitoring network and provides data from the sea sector for effective tracking of radioactive plume during emergency scenario when the plume moves to the sea-area. The buoy data will also be useful for modelling of radioactivity dispersion in coastal waters, extreme wind and wave height measurement during cyclonic conditions for disaster management besides environmental studies.

Reported by
Dr. C. Venkata Srinivas
Safety, Quality & Resource Management Group

Public Awareness Activity

July to September, 2023

1. Exhibition on 'The Fourth State' - Plasma & 'Atoms in the service of the Nation'

Institute for Plasma Research, Ahmedabad, Gujarat & Tamil Nadu Science and Technology Centre, Chennai, in association with Indira Gandhi Centre for Atomic Research (IGCAR), Kalpakkam, organised a 5-day exhibition on 'Nuclear technologies and its applications' at Birla planetarium, Chennai, from July 3 to 7, 2023. The objective was to create awareness about the key role of nuclear energy in the energy security of the nation and applied research in Plasma Science and Technologies. The mandate was to develop expertise for Nuclear Fusion, a source of energy with two major TOKAMAK experiments, including India's First Indigenous TOKAMAK 'Aditya'.

The exhibition was inaugurated on July 3 by Prof. Nilesh J. Vasa Dean, Indian Institute of Technology (M), Chennai. It saw a footfall of 2,741 till July 7.

2. Anu Awareness Yatra 2023

An awareness programme named 'Anu Awareness Yatra – 2023' with the theme 'ATOMS IN THE SERVICE OF THE NATION' was organised by IGCAR in association with the National Council of Science Museum (NCSM), Ministry of Culture, Government of India, Vigyan Bharathi - Arivial Sangam, Tamil Nadu, and Indian Association for Radiation Protection. The programmes were organised in nodal institutions in seven districts in Tamil Nadu and three in Kerala as part of Azadi Ka Amrit Mahotsav, and to showcase the indigenous progress in science and technology. The objective was to highlight (i) the progress in nuclear science and technology in India, popularise technologies developed by the Department of Atomic Energy (DAE) for societal application, and applications of ionizing radiation in various walks of life; (ii) to create an interest among the youth in science subjects and to explore opportunities in DAE; (iii) Dispelling myths on nuclear energy.

The curtain raiser was organised at IGCAR, Kalpakkam, on July 24, 2023. The yatra was flagged off by Ms. K. A. Sadhana, Director, Visvesvaraya Industrial & Technological Museum (VITM), and Shri Gopal Parthasarathy, State Secretary, VIBHA, (Tamil Nadu Arival Sangam), in the presence of Director, IGCAR and senior officials. Dr. Ajit Kumar Mohanty, Chairman AEC & Secretary DAE, addressed the gathering through a message. The yatra culminated at IREL, Aluva, travelling more than 1,000km, covering Kancheepuram, Thiruvannamalai, Salem, Erode, Karur, Coimbatore, Palakkad, Thrissur and Kochi. In each of these places, a nodal institution was chosen in association with Vigyan Bharathi – Tamil Nadu Ariviyal Sangam and an awareness programme was organised in that institution for two days. The nodal centres coordinated with regional institutions of each district to ensure the active participation of about 2,000 students and the public in each venue. The programme comprised lectures, quiz competitions, art competitions, creative writing competitions, conceptual orations, and exhibitions showcasing nuclear reactor models and the application of ionising radiation in medical, engineering, and agricultural fields.

Photographs during inauguration of exhibition on " The Fourth State" - Plasma & "Atoms in the service of the Nation"

Flag off of Anu Awareness Yatra at Indira Gandhi Centre for Atomic Research (IGCAR), Kalpakkam on 24 .07. 2023

Anu Awareness @ Sri Sankara Arts And Science College, Kanchipuram on 25.07.2023-26.07.2023

Anu Awareness @ Arunai Engineering College, Thiruvannamalai on 27.07.2023 – 28.07.2023

Anu Awareness @ AVS College of Arts & Science, Salem on 31.07.2023-01.08. 2023

Anu Awareness @ Erode Sengunthar Engineering college, Erode on 02.08.2023-03.08.2023

Anu Awareness @ Sri Sarada Nikaten College of Arts and Science, Karur on 04.08.2023-05.08.2023

Anu Awareness @ Kumaraguru Engineering College, Coimbatore, on 07.08.2023-08.08.2023

Anu Awareness @ NSS College of Engineering, Palakkad on 09.08.2023-10.08.2023

Anu Awareness @ Christ college, Iringalakuda during 11.08.2023 – 12.08.2023

Conclusion of Yatra at IREL (India) Limited, Aluva on 14.08.2023

Bala Vidya Mandir Senior Secondary School, Adyar, Chennai on 12.8.23 as part of the inter-school exhibition

This Yatra was unique in that a mobile science exhibition named "Science on Wheels" from VIT-M showcased working models on societal application of space technology. A total of 25,720 people visited the 10 venues. Photographs showing the highlights of the events are presented here.

3. Public awareness for school students

Bala Vidya Mandir Senior Secondary School, Adyar, Chennai, organised an inter school science exhibition on August 12, 2023, with the participation of IGCAR & MAPS, highlighting 'Atoms in the service of the Nation'.

Reported by
Smt. Jalaja Madan Mohan
Technical Coordination & Public Awareness Section
Safety, Quality & Resource Management Group

The 31st Prof. Brahm Prakash Memorial Materials Quiz (BPMMQ)

September 8-9, 2023

The 31st Prof. Brahm Prakash Memorial Materials Quiz (BPMMQ) was organized by the Indian Institute of Metals-Kalpakkam Chapter and the Indira Gandhi Centre for Atomic Research, in Kalpakkam during September 8-9, 2023, drawing participation of 80 students in classes XI and XII and 40 escorts, hailing from towns and cities across India. The two-day event comprised of (i) a visit to nuclear facilities of Kalpakkam (ii) Materials quiz events of preliminary, semifinal, and Grand finale (iii) elocution contest on selected essays on Materials related topics and (iv) Prof Brahm Prakash Memorial lecture delivered by Prof. B.S. Murty, Director, IIT Hyderabad, on the topic “The Immeasurable Joy of Research”. Release of BPMMQ -2023 Digest

Prof.B.S. Murty,Director, Hyderabad delivering BPMMQ 2023 Lecture

Release of BPMMQ -2023 Digest

Virtual inaugural address by Dr. N Kailaiselvi, Director General, Council of Scientific & Industrial Research & Secretary, Department of Scientific and Industrial Research

The Third International Conference on Structural Integrity (ICONS 2023) was organized by IGCAR, during 23-25 Aug 2023 at Mamallapuram. The co-organizers include IIT Madras, Indian Society for Non-destructive Testing, Kalpakkam Chapter, Indian Institute of Metals, Kalpakkam Chapter and Indian Structural Integrity Society. About 250 professionals and research scholars from national labs, research institutes, academia, industry, and regulatory agencies participated in ICONS 2023 to deliberate on recent developments in assessing structural integrity of structures and operating equipments in nuclear, defense, aerospace, chemical and oil industries and identify areas for further research. The technical programme comprised of 3 plenary, 10 keynote, 21 invited lectures and 200 contributory papers. Oral and poster presentations at ICONS covered topics such as mechanical behavior of materials, fatigue and fracture mechanics, failure analysis, high strain rate loading, small specimen testing, regulatory aspects, structural health monitoring, reliability and structural integrity assessment, fitness for service and remnant life assessment, structural materials and weldment, steel and concrete structures etc. About 20 firms participated in the exhibition with display of products related to structural integrity paving way for fruitful interaction with the participants.

Dr. V. Karthik
High-temperature Materials Technology Division
Materials Development & Technology Group

Technology Transfer of Penetration Enhancing Activated Flux for TIG welding of Stainless Steels

October 12, 2023

A penetration enhancing activated flux for TIG welding of stainless steel has been developed by Metallurgy & Materials Group (MMG) of IGCAR and has been patented in India, United Kingdom, USA and Ukraine. This flux increases weld penetration by as much as 12 mm in single pass welding and mitigate variable weld penetration in low sulphur containing steels. The technology was advertised in DAE websites in August'2023 as available to private sector for commercialisation through the technology transfer route. An industry based in Indore, specialising in welding technology, applied for technology transfer license to commercialise this technology. Accordingly, the technology transfer was done during a brief event held at IGCAR on October 12,2023. Director, MMG handed over the technology transfer documents to the Indore industry in the presence of Associate Director (Materials Development & Technology Group), Head Incubation Centre-IGCAR and other Heads of Divisions/Sections of MMG.

Transfer of MMG, IGCAR's "Penetration enhancing Activated Flux for TIG welding of Stainless Steels" to an Indore industry on 12.Oct.2023; Standing (L-R): Dr. N. Subramanian (Head, Incubation Centre, IGCAR), Dr. R. Divakar (Director, MMG), Licensee industry's partners and Dr. M. Vasudevan (Associate Director, MDTG, MMG); Left Inset: Presentation by licensee industry on their interest in this IGCAR technology; Right Inset: Photograph depicting the high welding penetrability in SS achieved with this patented IGCAR's technology

Reported by
Dr. N. Subramanian
Head, Incubation Centre,
Safety, Quality & Resource Management Group

Two day Theme meeting on
Fast Reactor Aerosol Research: Current Scenario and Future Directions (FARAR – 2023)

October 26-27, 2023

A theme meeting on FAST REACTOR AEROSOL RESEARCH - Current Scenario and Future Directions (FARAR-2023) was conducted at Indira Gandhi Centre for Atomic Research, Kalpakkam on 26th and 27th October 2023. The theme meeting was jointly organized by IGCAR and Safety Research Institute, SRI (AERB), in association with the Indian Association for Radiation Protection (IARP-K), Indian Society for Radiation Physics (ISRP-K) and Board of Research in Nuclear Sciences (BRNS). The theme meeting covered lectures on aerosol research from different perspectives such as, nuclear aerosol research relevant to Fast Reactors, environmental aerosols and bio-aerosols. The theme meeting also touched upon safety aspects of Sodium cooled Fast Reactors, which is very relevant in the current scenario where India is on the verge of commissioning the 500 MWe Prototype Fast Breeder Reactor.

Release of Souvenir by Shri. Sudhir B. Shelke, Station Director, MAPS during the inaugural function of theme meeting FARAR-2023

Panel discussion chaired by Dr. B. Venkatraman, Director, IGCAR

Shri Sudhir B. Shelke, Station Director, MAPS, inaugurated the theme meeting and addressed the gathering. A souvenir was released on the occasion. The inaugural address was followed by presidential address Dr. N. Sivaraman, Director, Chemistry Group and a special address by Dr. D. K. Mohapatra, Head of Division, Safety Research Institute. The theme meet had 5 sessions of invited lectures by eminent speakers from national research labs, academic institutions and also from DAE fraternity. Shri. K. V. Suresh Kumar, CMD, Bhavini, in his talk, highlighted India's flagship reactors, FBTR and PFBR, as he shared from his vast experience. Dr. B. K. Sapra and Dr. R. Baskaran elaborated about aerosol research in BARC and IGCAR respectively. Prof. Arul Prakash and Prof. Anupindi from the Indian Institute of Technology shed light on the state of the art computational tools and software available for modelling aerosol dynamics. After the technical sessions, there was a poster presentation session by researchers from IGCAR and ISRO. A panel discussion chaired by Dr B. Venkatraman, Director, IGCAR was organized in the afternoon of the second day of the program. The importance of collaborations between research institutes and academia and the need for further experimental and computational research was pointed out in the deliberations. The theme meeting provided the opportunity for experts from national laboratories to share their vast experience, provide insights and guide future direction in the field of aerosol research.

Reported by
Dr. A. Jasmin Sudha, ATBS / RESD
Safety, Quality & Resource Management Group

REcent ADvances in Information Technology (READIT – 2023)

November 22-23, 2023

Scientific Information Resource Division (SIRD), IGCAR in association with Madras Library Association - Kalpakkam Chapter (MALA- KC) organized the 13th Biennial International Conference on Recent Advances in Information Technology (READIT) during November 22-23, 2023 at Sarabhai Auditorium, IGCAR, Kalpakkam, with the theme 'Emerging Trends and Innovations in Libraries".

The conference was organized as an International event with participation from Sri Lanka and UAE. About two hundred delegates from the academic and public domain, Information Technology Professionals and Research scholars attended the conference.

In the inaugural function, Smt. S. Rajeswari, Convener READIT, AD, IRSG & Head SIRD delivered the welcome address. The function was presided over by Dr. N. Sivaraman, Outstanding Scientist, Director, MCMFCG, IGCAR. In his presidential address, Dr. N. Sivaraman highlighted the emerging technologies for libraries and the need for librarians in providing the required information to the scientists and engineers. Inaugural address was given by Dr. K. Nageswara Rao, Director, DESIDOC, New Delhi where he mentioned about digital asset management and preservation aspects. Dr. K. Nageswara Rao also

Dr. S. A. V. Satyamurty, Director (Research), Vinayaka Mission Research Foundation and Former Director, IGCAR delivered the special address and released the Conference Proceedings. Shri E. Soundararajan, organising secretary READIT and Head DRTS, SIRD, IGCAR proposed the vote of thanks. Dr. S. A. V. Satyamurty inaugurated the exhibition stalls of publishers and vendors.

The conference included invited talks by domain experts in Information Science & Technology and oral presentations by Research Scholars & Professionals on both offline and online mode. The topics included evolving Information Resources Models and discovery tools, Open Science & Research data management, innovative technologies for future libraries, education policies and role of libraries and librarians in enabling scholarly communication. Special technical session was organised for the contributed presentations by Research Scholars and delegates which included oral presentations. The conference facilitated good interactions among young researchers, students, professionals and well-known speakers in the area of future technologies for libraries.

There was a specials session on 50 years of SIRD at the end of the day1. Dr. S. A. V. Satyamurty presided the SIRD 50 years function and released coffee table book on SIRD 50 years. Shri E. Soundararajan presented a brief journey about 50 years of SIRD achievements. Prof. M. Saibaba, Ramaiah University, bengaluru and former Director RMG, IGCAR delivered the special address. A specially crafted memento was presented to all the SIRD colleagues.

There was a panel discussion moderated by Smt. S. Rajeswari Prof. D. Arivudainambi, Director, Library Anna University, Prof.R.Sevukan, Pondicherry University, Shri. M Paul Pandian. Librarian IMSc, Shri. Manoj Singh, Head, IRMS, SIRD, BARC, Dr. V. Gopakumar, Digital University, Kerala and Prof. Jhon Philips, AD, MMG,IGCAR participated in the panel discussion on trends in scientific publication landscape.

The conference concluded with the valedictory function. Shri. E. Soundararajan delivered welcome address, Smt. S. Rajeswari presented the conference summary and Prof. K. Nithyanantham, President MALA gave special address. The valedictory address was given by Dr. N. Sivaraman. He has also presented the best paper awards of READIT 2023. Shri. P. Vijaya Gopal, Head, LIMS,SIRD,IGCAR proposed the vote of thanks.

IGC COUNCIL

Chairman

Dr. B. Venkatraman

Distinguished Scientist & Director, IGCAR

Dr. B. Venkatraman, is from the 27th batch of Bhabha Atomic Research Centre Training School. With a research career spanning 38 years, he has specialised in application of ionizing and non ionizing radiations for non-destructive evaluation of materials and processes. During the last ten years, he has focused on enhancing, existing and establishing newer facilities as part of broad based radiation and environmental research programs at IGCAR.

He is a Member of AERB, SARCAR Committee and Convenor of BIS CHD 30 Sub Committee on Radiation Protection. He was a visiting scientist at Fraunhofer Institute of NDT Saarbrucken, Germany 2006-2007, has served as an expert for IAEA in Digital Radiology. He has more than 200 publications, is the recipient of Homi Bhabha Science and Technology Award 2007, INS Gold Medal 2005, seven Group Achievement Awards of DAE, D & H Schereon Award of IIW 1993, ISNT-NDT Man of the Year Award (R & D) 2001, IIW sharp tools award 2011, ISNT international recognition award 2013, and has won more than 10 best paper awards. He has been invited to deliver keynote, plenary and invited talks in international and national conferences . He is the Honorary Fellow of Indian Society of NDT and Fellow of Chennai Academy of Sciences. He is the President of Indian Society for NDT (ISNT) and President, Indian Association for Radiation Protection (IARP). He has guided about 6 students for their Ph D and is presently guiding 6 students. He is presently Distinguished Scientist and Director, IGCAR, GSO, and Safety, Quality and Resource Management Group.

Members

Shri Vivek Bhasin, Distinguished Scientist and Director, Nuclear Fuels Group (NFG) of the Bhabha Atomic Research Centre (BARC) today took over as the 14th Director of BARC from Dr. Ajit Kumar Mohanty, Chairman, Atomic Energy Commission and Secretary to the Government of India, Department of Atomic Energy. Shri Bhasin joined in Reactor Engineering Division, in 1988 after successfully graduating from the 31st Batch of BARC Training School. He is widely recognized for his expertise in the development of nuclear fuels, nuclear reactor component designing and structural integrity assessment of power reactors..

In a career spanning more than three decades, he contributed significantly towards several programs and activities to ensure the longevity of power reactor fleet, including rehabilitation and structural integrity assessment of RAPS-1, TAPS-1&2, MAPS and TAPS-3&4 alongside reactors operating in Kaiga, Kakrapar and Narora.

Shri Bhasin played a leading role in setting up of facilities for fabrication of fuel for APSARA-U Reactor and a novel plant for production of Fission-Moly (a radioactive isotope with extensive applications in healthcare) in Trombay. He was also instrumental in improving the rate of production of Plutonium-Uranium carbide fuel for Fast Breeder Test Reactor (FBTR) in Kalpakkam.

Shri Bhasin is a recipient of several honours, including Indian Nuclear Society Medal (2002), DAE Science & Technology Award (2006), and Homi Bhabha Science and Technology Award (2014). He is a Fellow of Indian National Academy of Engineering and has more than 300 publications to his credit in the field of nuclear science and engineering.

Dr. N. Sivaraman, Joined Indira Gandhi Centre for Atomic Research (IGCAR), Kalpakkam in the year 1987. He is from the 30th Batch of BARC Training school. His area of research interest includes metal fuels, actinide & fuel chemistry, pyrochemical process, lanthanide separations, sodium chemistry, solvent extraction of heavy metals, high performance separation of radioactive species, burn-up measurements on nuclear reactor fuels, Supercritical fluid extraction of actinides and development of advanced separation techniques for recovery of actinides, etc.

He is recipient of INSA-Royal Society, UK Fellowship (1997), Indian Nuclear Society Medal (2007) & Homi Bhabha Science and Technology Excellence Award (2008). He is also Professor of HBNI. He is presently Outstanding Scientist and Director, Materials Chemistry & Metal Fuel Cycle Group and Director, Medical Group.

Kesavan Nair K. P, Graduated in Electrical engineering from Govt. Engineering Collage, Trichur in 1988 and joined BARC in 1990. After completing 34th batch of training school, he joined RPD, BARC in 1991. He was a member of the team responsible for the PRP Electrical System comprising of power generation & distribution with islanding capability. At PRP he has made substantial contribution towards the development of compact Nuclear Reactor for strategic application. After the commissioning of PRP, he was transferred to IGCAR in Nov 2007 and joined Engineering Services Group.

His expertise includes design, construction and O & M of various infrastructure systems related services. He is presently an Outstanding Scientist and Director, Engineering Services Group.

Dr. B. K. Sreedhar is in the grade of Outstanding Scientist and is the Director of the Fast Reactor Technology Group and the Reactor Design Group. He graduated with a gold medal in Mechanical Engineering from the University of Calicut in 1988. He is from the 33rd batch of the BARC Training School and joined IGCAR in 1990. He started his career in the indigenous hydraulic development of primary and secondary coolant pumps for the PFBR and later led the team that completed the in-sodium performance testing and sodium removal from prototype mechanisms/machines of PFBR. He is also engaged in development work towards realising oil-free centrifugal pumps for future FBR's. He holds a postgraduate from the Indian Institute of Technology(IIT), Madras, specialising in Hydroturbomachines, and a doctorate from the Homi Bhabha National Institute (HBNI), Mumbai. He has published several papers in refereed journals and national/international seminars and conferences. He co-authored a book "Centrifugal Pumps for Sodium Cooled Reactors" that was published in Nov. 2023 by CRC Press, USA and UK. He is a fellow of the prestigious Indian National Academy of Engineering (INAE).

Shri K. V. Suresh Kumar is a graduate in Chemical Engineering and joined Department of Atomic Energy at BARC Training School in Mumbai as a trainee (29th batch) in1985. After successful completion of one year training, he joined in FBTR operation in 1986. Initially he was involved in the commissioning of various system of FBTR such as Sodium heated Steam Generators, Steam & Water system and Turbo-Generator. He was involved in the first raising of reactor power and carried out physics & engineering tests for validating the assumptions made in the design. He has got vast experience in Reactor operation, operation of sodium systems, steam and water system, turbine & its auxiliaries and all other auxiliary systems in FBTR. He was instrumental in carrying out many plant modifications and contributed in improving the availability factor of the plant. He shouldered many responsibilities in the plant and was Director, Reactor Facilities Group from March 2016 to November 2022 and was responsible for operation of FBTR, KAMINI Reactor and PFBR Fuel Fabrication Facility. During his tenure, FBTR power was raised to its design power level of 40 MWt feeding electricity to the grid.

In addition to his responsibility in Reactor Facilities Group, he was also involved in the review of commission procedures/ reports and Technical specifications for PFBR Operation. He was the chairman of Project Design Safety Committee (PDSC) constituted by Atomic Energy Regulatory Board (AERB) for issuing stage wise clearance for commissioning of PFBR. He is a Distinguished Scientist and on 2nd December, 2022 he took over as Chairman and Managing Director (CMD), BHAVINI.

Dr. T. V. Krishna Mohan is born in 1966. He graduated in Chemical Engineering from Osmania University and pursued his Masters in Business Administration (MBA) from the same university. He got his PhD degree from Homi Bhabha National Institute in 2016. He is from 34th batch of BARC training school and presently Facility Director, BARC Facilities, and Head, Water and Steam Chemistry Division. His field of specialisation is Design, Procurement, Installation, Commissioning, and Operation of Simulated Engineering loops to carry out water chemistry, biology and heat transfer experiments. His contributions are towards Bioremediation, Flow Accelerated Corrosion, Biological Denitrification, Aerobic Granulation, Wastewater Engineering. He is recipient of DAE Group Achievement Awards. He has more than 100 publications and one patent to his credit.

Dr. T. S Lakshmi Narasimhan is from 31st batch of BARC Training School and joined IGCAR in 1988. He completed his Ph.D. from University of Madras in the year 2001 and did his post doctoral research at Forschungszentrum, Juelich Germany (2004-2006) under Indo-German collaboration. His main area of research has been in the field of high temperature mass spectrometry which include fuel-clad chemical interaction studies related to fast reactors, vaporization thermodynamic studies on U-Pu-Zr, Metal- tellurium and Metal –tellurium- oxygen systems, alloys, boron, fullerenes etc., He has also been associated with Burn up measurements of thermal and fast reactor fuels. He has delivered many invited lectures in India and abroad and has about 55 Scientific publications in reputed International journals and about 70 papers in national and international conferences.

In July 2017 he became Associate Director, Resource Management Group. He served as Dean, Student Affairs under Homi Bhabha National Institute, a deemed university. He also served as Professor in the same University and guided two Ph.D. Students. He was heading the Technology transfer cell of IGCAR and coordinated the filing of patents and technology transfers and in October 2020 was designated as CEO of Incubation Centre at IGCAR to look after incubation and technology transfer activities. He is a mentor for the INSPIRE program of Department of Science and Technology for School Students and also actively involved himself in the speared of scientific awareness amongst educational institutions Currently he is the Regional Director of Madras Regional Purchase Unit (MRPU), DPS which caters to the purchase and stores activities of IGCAR and other DAE units at Kalpakkam, HWP, Tuticorion and NFC, Pazhayakayal.

Ms. Sushma Taishete joined as Joint Secretary in the Department of Atomic Energy, Government of India on 08-04-2020. She is a post graduate in Medical Microbiology from Haffkine Institute, Parel, Mumbai. She is the In-charge of Research and Development wing of the DAE handling Bhabha Atomic Research Centre (BARC), VECC, Kolkata, RRCAT, Indore, IGCAR, Kalpakkam and all aided institutions (eleven) in the Department. International Projects such as, ITER, LiGO, also fall under R & D Division. She has served in various capacities in Ministry of Defence, Ministry of Health & Family Welfare, National Health Systems Resource Centre, Ministry of Petroleum and Natural Gas and Department of Justice, Ministry of Law & Justice, Government of India during 1991 - 2020.

Shri S. A. Murugesan, IAS, Uttarakhand cadre -2005 Batch. Currently on deputation to Department of Atomic Energy serving as Internal Financial Advisor (IFA) in IGCAR and GSO.

Smt. AJITHA THARIYAN joined the Department on 19/12/1985 with degree in Commerce from Mumbai University. After joining the Department, she was sponsored by the Department for Mater of Business Administration from the ICFAI, Sikkim (2015). She has completed 38 years of service in the Department serving in various capacities in different Units like BARC, HWP (B), ATI, DAE Secretariat and IGCAR thus gaining vast experience in all matters relating to administration. She is holding the post of Chief Administrative Officer from 20.11.2023. As administrative head of the Unit her mandate for administration is to provide service, advice and support with the highest level of professionalism valuing rules and procedures as a tool to achieve the objectives of the Organization and the desired outcome, contribute towards smooth internal functioning of the organization through dissemination of information, extensive use of automation and information technology, updating and simplifying procedures and instructions to the changing environment, proper record and data management systems, developing standard process sheets to ensure procedural compliance, periodical training of Officers and staff to enhance the knowledge and skill, secure better focus and ownership of task and increase their yield, monitoring delays, identifying bottlenecks and implementing remedial measures, promoting transparency and accountability in decision making process, mentor subordinates and build teams, promote harmonious relations and secure maximum amount of cooperation from the employees.

Organisation and Activities of Various Groups

Civil Engineering Group

Dr. B. Venkatraman
Director, CEG

Shri N. Suresh
AD, CEG

Shri H. I. Abdul Gani
Head, A&SED

Shri Sudipta Chattopadhyaya
Head, C&NWD

Smt. R. Preetha
Head, CM&QCD

The Civil Engineering Group (CEG) has a very important role for development, construction, and civil maintenance of various facilities, laboratories in IGCAR as well as common infrastructure for all units of the Department of Atomic Energy (DAE) located at Kalpakkam. Mandate of CEG is design & construction of several laboratories, buildings and services beginning with the conceptual design to construction and its associated maintenance, for IGCAR's mission of 'Fast reactor development and its associated fuel cycles'. The group is continuing the path of realizing center's vision and ably supported by dedicated Architectural, Design, Estimate & Contracts and Construction, Operation & Maintenance team of engineers. CEG undertakes in-house and collaborative research projects in civil engineering aspects of Fast Breeder Reactor (FBR). CEG has been keeping pace with progress in engineering, design and construction with technical advances. Engineering, analysis and design have undergone remarkable changes with computer codes developed by the group to solve complex problems. Concrete production and delivery systems have been improved, with automated mixing plants and stringent quality control. Apart from durable concrete, special types of concretes have been developed and now the group has proved itself in providing technical support in design of major projects like PFBR and associated fuel cycle facilities. The group has developed expertise in characterization of site for safety related structures including geotechnical investigation, site specific flood level studies. Recently CEG has undertaken a mandate of conducting periodic condition survey, assessment and formulating repair and retrofitting methodologies of Reinforced Concrete Structures of existing radiological facilities, major laboratories, and infrastructure buildings at IGACR including other DAE units.

As in previous years, CEG has given support to PFBR commissioning activities like Civil & Structural works related to PFBR Biological Shield Coolant (BSC) leak rectification including mock-up studies, ILRT & obtaining necessary regulatory clearance, which are taken up in priority basis and completed. Based on regulatory requirements, seismic margin assessment of DFRP buildings and associated safety buildings & structures including RC stack have been completed by CEG towards commissioning of DFRP.

Presently CEG is involved to sustain the present infrastructure as envisaged in the ongoing Vision -3 and augment it during coming plan periods. Through Vision -3 program, this year CEG has contributed for design and construction of Gamma Irradiation Facility. Analytical Laboratory. With IGCAR South Plant site getting saturated, construction of important facilities like Mid Tropospheric Radar Facility, RHIDS & SGIDS facility and associated infrastructure like STP, formation of road around STP and service corridor considering future requirements are completed in the north plant site. Apart from sustained quality control activities, as a part of ageing management, condition survey, assessment and repair methodologies for Utility Buildings in FBTR, Central Workshop Building & Central Stores buildings in IGCAR, NDDP Kalpakkam & IMSc Chennai are also completed.

The Group has major plans of providing an aesthetic & sustainable green environment at the project site and also intends to introduce efficient water management scheme by recycling treated water for usage of makeup water for refrigeration by contributing towards construction of tertiary water treatment plant and in development & maintenance of garden & lawn at IGCAR. With proper planning maintenance of buildings, roads within IGCAR are being carried out smoothly and public health services such as water supply, fire water, sewerage are functioning smoothly.

Organisation and Activities of Various Groups

Electronics and Instrumentation Group

Dr. B. Venkatraman
Director, EIG

Shri S. Sridhar
AD, E&IG

Smt S. Rajeswari
AD, IR&SG

Shri N. Sridhar
Head, ED

Shri M. Sakthivel
Head, I&CD

Shri R. P. Behera
Head, RTSD

Shri A. Shanmugam
Head, DDCSD

Shri J. Rajan
Head, ISND

Shri M. Sivarama Krishna
Head, SISD

Shri R. Jehadeesan
Head, CD

Electronics and Instrumentation Group is focused on design and development of indigenous technology in the areas of Electronic Instrumentation & Control systems for fast breeder reactors and reprocessing plants that include Development of Distributed Digital Control System, Safety Critical and Safety Related Systems, Safe & Secure PLC, Virtual Control Panel based Control Room, Full-scope Operator Training Simulator, 3D modeling, animation & visualization of FBR subsystems and VR walkthrough of structures, Cyber Security Management for IT and I&C systems. Design and Development of advanced equipment and technology such as, indigenous Wireless Sensor Networks for nuclear facilities, strategic and societal applications, Time Domain Electromagnetic for Deep Seated Atomic Minerals Exploration, Plutonium Condition Air Monitoring System for reprocessing plants, Test Instrument for Steam Generator Tube Inspection, Radar Level Probe for Liquid Sodium Level Measurement, radiation resistance MEMS based sensor for nuclear applications and innovative sensors and instruments for nuclear facilities have been completed. Considerable expertise exists in designing, building and maintaining state-of the-art high-performance supercomputing facility that continues to meet large scale compute- and data-intensive requirements in multi-disciplinary domains. Implementation of IT-enabled Nuclear Knowledge Management system for Fast Reactors and associated domains, computational intelligence systems, cryptography, cyber security solutions, knowledge management and development and deployment of modern security systems for access control and physical protection of nuclear complexes are initiated.

Engineering Services Group

Shri K. P. Kesavan Nair
Director, ESG

Shri Biswanath Sen
Head, AC&VSD

Shri Utpal Borah
Head, CWD

Shri L. Subramanyam
Head, ESD

The Engineering Services Group (ESG) has a very important mandate of infrastructure development for all units of the Department of Atomic Energy located at Kalpakkam. It spans from planning, design, engineering, execution, testing and commissioning of Electrical, Mechanical, Air-conditioning and Ventilation works for the Laboratories. ESG also extends support for high end manufacturing for the R & D needs as well as to all DAE units at Kalpakkam. To meet the user requirements satisfactorily and considering the qualitatively different responsibilities three divisions are formed under ESG: Air Conditioning and Ventilation Systems Division, Central Workshop Division and Electrical Services Division.

Air-conditioning and Ventilation Systems Division (AC&VSD) has a mandate of providing air conditioning and ventilation service to radioactive facilities and research laboratories of IGCAR. Presently, IGCAR has a total air-conditioning load of about 4500 TR, which is met by 2 Central water chilling plant (CWCP I & CWCP - II) and standalone AC systems like package units (PAC), variable refrigerant flow (VRF) units, window and split air-conditioners. In view of increase of facilities at IGCAR and in order to sustain reliable air-conditioning services to the centre, a 2000 TR central Air-conditioning plant is (CWCP 2) established near IGCAR gate as part of vision 3. The building is constructed and chillers of 2250 TR capacity have been commissioned. The division is also responsible for design, execution, testing and commissioning of material handling equipment like Electric overhead travelling (EOT) cranes, Electric wire rope (EWR) hoists etc for new facilities of IGCAR. Later, AC&VSD was entrusted with the responsibility of operation and maintaining of sea water desalination plant to provide potable water to IGCAR, BARCF and BHAVINI. All skids of the plant is capable of being operated at full capacity and required quality as per IS 10500. It also looks after water purifiers for the facilities within IGCAR. The plant was commissioned in 2015. Since then, the plant is continuously supplying potable water to IGCAR reservoir as per the demand.

The need for dedicated workshop facilities was felt right during the days of conceptual formation of Reactor Research Centre (RRC). The Zonal Workshop at Hall-1 was established initially to meet the immediate requirements. Later, to meet the growing demand of manufacturing activities at RRC complex, Central Workshop Division (CWD) was established with the state of the art machines and became operational in 1975. CWD, specializing in machining, cold plate rolling, welding, fabrication and inspection, is a centralized manufacturing facility of IGCAR and undertakes in-house manufacturing of various products, which are technically challenging, commercially unviable, and needed urgently to meet the project schedules. CWD carries out multiple manufacturing activities for Prototype Fast Breeder Reactor (PFBR), Fast Breeder Test Reactor (FBTR), Kalpakkam Mini Reactor (KAMINI), Reprocessing Facilities, Post-Irradiation Examination (PIE) Facilities, R&D Projects and Infrastructure Development apart from operation and maintenance requirements. The welding procedure for the PFBR Sub-Assembly (SA) in 2G position was developed by CWD welders and the first batch of Fuel/ Blanket SAs was welded at CWD successfully. Recently two notable major works were successfully carried out for PFBR and FBTR, namely, modification of 731 dummy SAs of PFBR on site at reactor containment building (RCB) within the specified time schedule and manufacturing of modified water sub-headers of FBTR Steam Generator, which were integrated with the FBTR to raise its power level to rated 40MWth.. CWD maintains the highest precision and quality standards to conform to the stringent specifications and functional requirements under various codes, viz. ASME, ASTM, RCC-MR and ISO. CWD processes nearly 400 work orders on average every year to meet the demands of various users/projects. Recently, a few major machining, cutting, heat treatment and inspection facilities were commissioned at CWD to augment its capabilities and capacity. DAE has conferred many meritorious service awards and Group Achievement Awards to CWD officials for their excellence in machining, fabrication, inspection and maintenance fields.

Electrical Services Division (ESD) has a mandate to provide adequate, high quality, reliable and uninterrupted power required for various needs of the research activities and the infrastructural requirements of the centre. To meet this Electrical Services Division designs, construct, operate, maintain and upgrade Electrical distribution system keeping in mind the system reliability & safety. The division is also responsible for providing state of the art intercom telecommunication services to the plant site as well as for Energy conservation in the Electrical sphere through auditing and implementing various energy conservation measures. At present the Electrical demand is 29 MVA and which is catered by Electrical distribution network consisting of two numbers of 33 kV substations and 14 numbers 11 kV substations.

Thanks to the foresight of the earlier planners, MAPS has been providing adequate, safe, reliable and quality power to IGCAR, BARC Facilities and GSO till date. Starting from an operating load of about 1.5 MVA during 1977 fed by one number 33 kV substation and five number of 11 kV substations, the load on the power system has grown to a level of 29 MVA fed by two number 33 kV substations and 14 number 11 kV substations. The projections indicate that the load would grow to about 60 MVA by 2028. To meet the growing demand third power source with 230 kV/33 kV/11 kV, 50 MVA transformer at BHAVINI switchyard was commissioned in 2012. To evacuate this power along with this 33kV Indoor sub-station NCSS-2 was also commissioned in 2012. Main source for FRFCF is from NCSS-2. The electrical power system of FRFCF is conceived to meet the power requirements for the present phase as well as the envisaged expansion in the future. Moving further the transformer in the Second IGCAR feeder at MAPS was upgraded to 35 MVA in 2019 to meet the growing power demand.

ESD has taken up many Energy Conservation activities over the years. One of the major activities being taken up under this is to establish a 2.2 MWp grid connected solar plant in the newly developed parking area in front of IGCAR new gate. In line with the GOI policy of promoting Green Energy, added 333.64 kWp of generating capacity. The total solar generation capacity in IGCAR is increased to 833kWp and this is expected to save 16 Lakhs units of electricity annually. Energy Conservation is a continuing activity and many innovative ideas are being implemented in the journey. ESD as a team is well set to take on the challenges pertaining to sustenance, augmentation and establishment of power systems at new projects of IGCAR. With a proactive approach all along, the division has initiated several augmentation measures at source end, receiving end and associated networks. With the steps that are being initiated, ESD will be able to meet the projected power requirements and is moving ahead with an objective to sustain the path of excellence.

Fast Reactor Technology Group


Dr. B. K. Sreedhar
Director, FRTG


Dr. B. Babu
Head, DD&RSD


Shri V. A. Suresh Kumar
Head, Rig.OD


Shri V. Vinod
Head, ETHD


Shri Joseph Winston
Head, RH&IED

The Fast Reactor Technology Group (FRTG) is a multidisciplinary group engaged in the design, fabrication, erection and operation of sodium test facilities, development and testing of components and equipments for the fast breeder reactor programme. The group has a proven expertise in diverse disciplines such as the design, fabrication, erection and operation of sodium loops, development of sodium instrumentation and electromagnetic devices, functional in-sodium testing of full scale reactor components/mechanisms, development of techniques for sodium purification and cold trap regeneration, sodium/NaK handling and disposal, sodium removal techniques for cleaning large sodium wetted components, studies on sodium fires, sodium leak detection, basic studies on sodium-water reaction, process improvement, applied studies on FBR steam generator, thermal hydraulics studies on scaled models and design/development of remote handling and inspection devices for reactor applications.

Over the years the group has indigenously established as many as 13 sodium test facilities that have been utilised for basic studies on materials in sodium as well as for functional testing of full scale reactor equipments. A new facility, the Sodium Technology Complex (STC), presently under commissioning further augments the testing capability. In addition, the group is also equipped with water test facilities for basic and applied studies on reactor thermal hydraulics.

Indigenous development of sodium technology has always been the primary objective of the group and towards this end the group has collaborated with Indian industry to develop technologies for sodium application such as level probes, pressure and flow measurement devices, under sodium inspection sensors, mechanical and electromagnetic pumps, and in-service inspection equipment and robotic systems for reactor application.

Some of the important facilities available are:

(i) Large Components Test Rig (LCTR): This large capacity sodium facility has been used primarily for performance testing of full scale reactor machines and mechanisms such as the reactor shutdown mechanisms, fuel handling machines, under sodium viewing mechanism, failed fuel location mechanism, electromagnetic pumps, flowmeters, etc.

(ii) Steam Generator Test Facility (SGTF): The facility houses a full scale sector model of the fast breeder reactor steam generator. It has been employed to validate the heat transfer capacity of as well as to study the instability behaviour of the once through type steam generator used in FBR’s.

(iii) Safety Grade Decay Heat Removal in Natrium (SADHANA) facility: This scaled down facility of the PFBR safety grade heat removal System has been invaluable in the characterisation of the natural convection in the primary sodium pool.

(iv) Sodium Water Reaction Test Rig (SOWART): This facility is employed for studies related to the damaging effects of sodium-water reaction, on the steam generator tubes, such as self wastage and impingement wastage. This facility has also served as a test bed for development of different types of hydrogen sensors.

Thermal shock Test Facility (TSTF): This unique facility simulates the thermal shock experienced by components immersed in the sodium pool under reactor transient conditions.

(v) Sodium Facility for Component Testing (SFCT): This facility has employed for the performance testing of different electromagnetic pumps, indigenously developed Inconel625H bellows, frozen seal valves, RADAR level probes etc.

(vi) In house workshop equipped with lathe, milling machines, drilling machines, all cut machines and CNC wire cut EDM etc,.

The following jobs are a few of the important contributions towards PFBR:

(i) In-sodium functional and endurance testing of the fuel handling machines, shutdown mechanisms, under sodium scanner, failed fuel location module etc.

(ii) Sodium removal from large sodium wetted components such as shutdown mechanisms, fuel handling machines, heat exchangers and pumps.

(iii) Characterisation of Safety Grade Decay Heat Removal (SGDHR) system of PFBR through scaled down studies in sodium

(iv) Hydraulic studies in water towards development of (i) gas entrainment mitigation devices (ii) pressure drop devices such as honeycomb orifices and labyrinth (iii) pressure drop in core subassembly.

(v) Indigenisation of bellows seal and frozen seal valves for sodium applications.

(vi) Development of an indigenous remote inspection tool for PFBR SG and deployment in all 8 SG for PSI

(vi) Development of an Indigenous remote inspection tool for Dissimilar metal weld inspection for PFBR (DISHA) & deployment in the reactor for inspection

(vii) Development and deployment of a Reactor Core Viewing System (RCVS) for remote core inspection to understand the SA position in the reactor

(viii) Development of a remote inspection vehicles for waste vault inspection

The group is also active in providing supports towards commissioning activities in PFBR.

As part of the ongoing R&D for future FBR’s, the group is engaged in the development of oil less bearings and seals for main coolant pumps, integrated cold trap and integrated plugging Indicator for in-vessel sodium purification, fluorocarbon seals development etc.

FRTG is committed towards the realisation of Atmanirbharata through the indigenisation of fast reactor technology.

Health , Safety and Engineering Group

Dr. D. Ponraju
Director, HSED

Dr. S. Chandrasekaran
Head, H&ISD

Shri Sanjay Kumar Das
Head, SED

Health and Safety Engineering Group consists of Health and Industrial Safety Division and Safety Engineering Division. Mandatory radiation monitoring services are provided to all occupational workers of nuclear facilities with updated innovative technologies to control external and internal exposures. In-vivo and in-vitro monitoring of occupational workers are being carried out during normal and emergency situations as per the guidelines of Atomic Energy Regulatory Board and National Disaster Management Authority. In Integrated Radiation Monitoring Facility at Anupuram, Radiation Emergency Medical Centre is commissioned to provide necessary medical assistance for radiation workers during radiological emergency.

Industrial & Fire safety and Occupational Health services are provided to workers and promotional safety activities are being conducted as per the guidelines of AERB to enhance safety culture at work place. Detailed job safety studies for critical jobs, plant safety inspections and physical hazard surveillance are being carried out on regular basis. On-line work permit system has been established for all critical / non routine activities. Height pass physical test and industrial & fire safety training are provided to employees on regular basis. First Aid monitoring and periodic medical examination is being carried out at Occupation Health Centre.

In Safety Engineering Division, R&D on Severe Accident and Sodium Fire studies are being carried out for realistic accident simulation to ascertain design safety margin, validation of passive safety features and effective mitigation strategy development. Test facilities are developed to carry out experiments on Molten Fuel Coolant Interaction with X-ray imaging, validation of core catcher, sodium safety and sodium fire management.

Materials Chemistry & Metal Fuel Cycle Group

Dr. N. Sivaraman
Director, MC&MFCG

Dr Kitheri Joseph
AD, MFRG

Dr. V. Jayaraman
AD, FMCG

Shri T. V. Prabhu
Head, CFED

Dr S. Ghosh
Head, MFPD

Shri B. Muralidharan
Head, PPED

Dr. K. Sundararajan
Head, ACSD

Dr. A. Suresh
Head, FChD

Dr. Rajesh Ganesan
Head, MCD

The Materials Chemistry and Metal Fuel Cycle Group (MC&MFCG) is involved in Research and Development studies relating to metal fuels, establishing pyrochemical process for electro-refining spent metal fuels, development of aqueous reprocessing towards recovery of heavy metals, sodium chemistry and development of methods for detection of hydrogen in sodium and cover gas.

Some current activities include setting-up of a metal fuel facility for production of one meter fuel pin, setting-up of a facility for electro-refining U-Pu-Zr metal fuel (250 g batch) and fabrication and characterization of metal fuel slugs for various R&D programs. In the engineering scale pyroprocess facility for establishing various process steps subsequent to electro-refining uranium metal on 10 kg scale, salt distillation and metal ingot preparation were undertaken; a facility for direct oxide reduction of oxide to metal was established and uranium oxide was reduced to its metallic form. Nitridation of metal fuel was explored for its dissolution in nitric acid medium followed with extraction of heavy metals using PUREX Process. Thermochemical properties and phase diagram studies on nuclear materials, development of non-destructive methods for assay of plutonium, studies on the development of synthetic inorganic matrices for immobilization of waste from fast reactor fuel reprocessing, production of 89Sr, 32P and 90Y for societal applications are the other major activities which have been undertaken. Development of metal organic frameworks for sorption of uranium and fission products from aqueous waste, development of advanced separation methods for recovery of actinides from lean aqueous waste streams, and recovery of zirconium from aqueous waste were explored towards actinide processing.

MC&MFCG also provides Analytical Chemistry support and Radioanalytical services to various programs of IGCAR and DAE units. These include development of analytical methods for assay of trace and major elements in metal fuel and samples originating from pyrochemical process, measuring isotopic composition of boron and heavy metal ions from reprocessing plant and assay of primary sodium. Besides these activities, some basic R&D studies are also undertaken for exploring conformations, pnicogen and tetral bonding using Matrix-Isolation Spectroscopy. Computational studies on the actinide complexes are being explored to understand their solvent extraction behavior.

Materials Science Group

Dr. R. Divakar
Director, MSG

Dr. R. Govindaraj
Head, D&DSD

Dr. Sandip Kumar Dhara
Head, S&SSD

Dr. Nagendran
Head, S&DTD

Dr. Awadhesh Mani
Head, CMPD

The Materials Science Group (MSG) comprises of Defects and Damage Studies Division, Condensed Matter Physics Division, Surface & Sensors Studies Division and SQUID & Detector Technology Division. Scientists of MSG work on research problems spanning from the studies of irradiated defects in nuclear materials, high pressure and temperature induced phase transitions in condensed matter systems, developing thin film coatings for tribological applications, and SQUID based MEG applications. Details of the research activities are as follows.

Defects and Damage Studies Division (DDSD) focuses on studies on defects, defect-impurity interactions in reactor structural materials, supplemented by computations. Ion beam radiation damage studies are carried out using a 1.7 MV tandem accelerator and a 400 keV in-house built linear accelerator in single or dual ion beam modes of irradiation to study defects and radiation response in materials relevant to fusion and fission reactors. Defects, particularly open volume defects such as vacancies and their clusters, are studied using positron annihilation spectroscopy. Positron beam based Doppler broadening studies have been used mainly for depth-resolved defects studies in irradiated materials. Ion beam based characterization techniques such as high-resolution RBS, channeling are being used extensively in addition to ion beam induced luminescence studies. Irradiation creep studies are being planned with proton beam of energy 2-3 MeV and high beam current. Various experimental results related to defects are analyzed using detailed computations with a variety of simulation and ab-initio codes. High speed cluster computers at IGCAR are being extensively utilized for computation of materials properties.

Condensed Matter Physics Division (CMPD) pursues several theme based research programs: investigation of structure and physical properties of materials under extreme conditions such as high pressures, low temperatures, high temperatures and high magnetic fields. Further, over the years various facilities for the synthesis of novel, superhard materials have been established including a Laser Heated Diamond Anvil Cell (LHDAC) facility. Recently the team of CMPD established High Pressure – High Temperature (HP-HT; ~ 25 GPa & T ~ 1000 oC) XRD facility at Beamline 12, Indus-2, RRCAT to facilitate synthesis of novel phase, study kinetics of phase transition, generating phase diagram at HP-HT, and to determine thermal expansion co-efficient with pressure. The systems under investigation encompass nuclear materials, superconductors, strongly correlated systems, magnetocaloric materials, topological insulators, multiferroics, energetic materials, frustrated systems, f-electron based intermetallics and oxides, glasses and super hard transition metal borides. Research is also pursued to investigate emergent phenomena and proximity effects in heterostructures. Dynamic light scattering and confocal microscopy are utilized for studies on soft condensed matter. Optical trapping and manipulation of mesoscopic particles using holographic optical tweezers (HOTs) to study inter-particle interactions in colloidal suspensions/ biological systems are being pursued. Besides there is also an intense effort towards quantum metrology based research studies using entangled photons.

Surface & Sensors Studies Division (SSSD) focuses on studies of monolithic and multilayered thin films and nanostructures using a variety of techniques such as secondary ion mass spectrometry, nanomechanical testing, Focused Ion Beam (FIB) based nanostructuring and nanopatterning, Scanning Probe Microscopy based characterization of various electrical and mechanical properties at nanoscale, nanospectroscopy with tip enhanced Raman spectroscopy (TERS) and Nanoscopy with near-field scanning optical microscopy (NSOM) imaging at sub-diffraction limit using polarized light. The division also specializes in high temperature triblological studies of structural materials as well as novel nano- and micro-crystalline diamond thin films. Exotic carbon nanostructures of vertical graphene based supercapacitor research is also being pursued for energy research. Furthermore, development of novel nanomaterials of 0D transition metal oxide (TMO), 1D noble metals and nitrides, 2D TMOs, and transition metal dichalcogenides (TMDs) for advanced sensor applications is being carried out. Research activities relating to ultra-sensitive sensors based on micromachined silicon and silicon oxide cantilevers and surface doped diamond thin film are also being pursued.

SQUID & Detector Technology Division (SDTD) focuses mainly on using SQUID based systems for applications. Magneto-Cardiography (MCG) and Magneto-Encephalography (MEG) have been successfully designed, assembled, standardized and used for clinical studies. Further, SQUID based measuring systems such as high field SQUID magnetometer, SQUID VSM, SQUID based set-up for Non- Destructive Evaluation (NDE) have been developed. SDTD also carries out intense research activities related to using SQUID based time domain electromagnetic measurements (TDEM) and geophysical explorations using TDEM. Another major thrust research area of this division is the development of gamma irradiation detectors. Towards this, the researchers have grown highly resistive CdZnTe single crystals and developed a gamma detector for pulse height spectroscopic studies. This research activity is being actively pursued to develop compact semiconductor based detectors with enhanced efficiency and technologically important single crystals for detector applications.

Metallurgy and Materials Group

Dr. R. Divakar
Director, MMG

Dr. John Philip
AD, MCG

Dr. M. Vasudevan
AD, MD&TG

Shri Shaji Kurien
Head, PIED

Dr. Anish Kumar
Head, NDED

Dr. Arup Dasgupta
Head, PMD

Dr. S. Ningshen
Head, CS&TD

Dr. A. Nagesha
Head, MMD

Dr. A. Moitra
Head, MJ&MMD

Dr. V. Karthik
Head, HMTD

The Metallurgy and Materials Group (MMG) of IGCAR, is pursuing a vibrant research and development programme for comprehensive knowledge-based solutions to a variety of materials issues of critical importance to India's fast reactor and associated fuel cycle programmes. In addition, in the recent past, the Group has significantly contributed to the development of high temperature materials and related technologies for national programmes and to support other strategic sectors.

The R&D activities of MMG are manifold. They encompass the design, indigenisation and field realization of new and indigenous material choices and process modifications mandated by emerging demands on high design reliability. The Group has been spearheading a mix of basic and directed cross-disciplinary research activities under various themes and is equipped with state of the research facilities on multiple fronts. The current portfolio of MMG includes:

(i) Generation of design data of nuclear and high-temperature materials towards qualification of fast reactor structural materials and their welds, and production through industry,

(ii) Development of Advanced Materials, Coatings & Characterization Techniques for FBRs & Future Reactor Concepts, viz., the metallic fuel reactors, high temperature reactors and small modular reactors,

(iii) Component manufacturing initiatives for current and future FBR's, including advanced materials fabrication and joining methods, special nuclear materials fabrication, hardfacing and coatings and technologies for FBR and fuel reprocessing programs,

(iv) Research and development develop corrosion protection and advanced coating technologies for hostile environments such as liquid sodium, molten salts, nitric acid, molten lead, steam-water, seawater, for applications in FBR and associated reprocessing plants.

(v) Development of advanced NDE methodologies for detection and characterization of flaws, microstructure, deformation and health monitoring of structures and components of FBR and associated fuel cycle programme

(vi) Post-irradiation examination for performance assessment and research on new FR fuel and structural materials, and failure analysis of radioactive components.

Contributions of MMG in the past year have facilitated progress in commissioning of PFBR; these include (i) investigations leading to root cause analysis and repair of systems such as liquid effluent storage tanks, biological shielding cooling (BSC) system, IHX, and AHX, (ii) metallurgical investigation of grid plate sleeve guide and discriminator of PFBR sub-assemblies, (iii) manufacturing of SS304B4 filler wires and re-welding development, (iv) incorporation of NDE inspection modules containing ultrasonic transducer and ECT probe in DISHA and ISI. Towards supporting FBTR that is now operating at full-power, powder metallurgically processed WC pellets that were supplied from the Group have been incorporated in the first fuel sub-assembly with enhanced lower axial shielding for extending life of FBTR, even as further production of WC sintered pellets has been sustained, and performance assessment of FBTR carbide fuel irradiated in FBTR at higher linear heat rating of 400W/cm has been completed, providing crucial data for re-assessment of allowable burn-up.

Besides these activities, R&D studies pursued in MMG include (i) development of ferro fluids and ferro emulsions for sensors, magnetic hyperthermia studies, and polymer nano composites, (ii) materials mechanics studies for structural integrity assessment of FBR components, (iii) mechanistic understanding of damage under tensile, creep, fatigue, and creep-fatigue interactions, (iv) plasma sprayed yttria coatings over high density graphite on crucibles delivered for uranium melting applications, and (v) small specimen testing for determination of impact properties. A patented technology of A-TIG welding of stainless steel developed in the Group has been transferred to a private firm for commercialization and a novel heat treatment method for hardening large diameter bearing balls has been assigned an Indian patent application. The group is now embarking on technology development of medium chromium oxide dispersion strengthened steels for fuel cladding tubes for future FBRs, post-irradiation examination of metallic fuels irradiated in FBTR, and qualification of various advanced structural materials through long term neutron irradiations in FBTR. A national project for indigenous production of seamless tubes an advanced nickel-base superalloy has been successfully concluded. Our expertise in non-destructive evaluations has been sought and provided to NPCIL plants, to the Indian Navy for life assessment of naval aircraft, and to evolve inspection strategies for large components of thermal power plants. MMG hosts many young scholars to pursue their research and post-doctoral research at IGCAR, under the banner of Homi Bhabha National Institute (HBNI). The group has active collaborative R&D links with many eminent research institutions in India and abroad on a range of high temperature materials.

Reactor Design Group

Dr. B.Venkatraman
Director, RDTG

Shri Jose Varghese
Head, CH&MD

Shri Sriramachandra Aithal
Head, RC&AD

Dr. K. Natesan
Head, THD

Dr. A. John Arul
Head, RS&DD

Shri U. Parthasarathy
Head, SHTD

Reactor Design group (RDG) is responsible for the design, structural & thermal hydraulics analysis, core safety & plant dynamics analysis, structural mechanics including seismic testing, and manufacturing technology development of Fast Breeder Reactor (FBR) components/ systems. RDG has expertise in design & engineering development of various systems/components of FBRs covering the Nuclear Steam Supply Systems (NSSS) and Balance of Plant (BoP) systems viz. Reactor Physics & Core Engineering, Reactor Assembly, Absorber Rod and Component Handling Mechanisms operating in sodium, Primary & Secondary Sodium Heat Transport Systems, Decay Heat Removal systems, Tertiary Steam Water Systems, Various Plant Auxiliary Systems, Electrical Power Systems, Plant Layout, Sodium Pumps, Cold Trap and Ultrasonic devices for use in sodium. RDG has indigenously developed the design of Prototype Fast Breeder Reactor (PFBR) of 500 MWe capacity based on its design & analysis expertise, R&D program, technology development exercise and with the support from and in association with various other groups of IGCAR. The group is extending its technical support and design expertise to the PFBR project which is under commissioning by BHAVINI and is responsible for getting design safety clearances for PFBR from the Atomic Energy Regulatory Board (AERB). It also provides analytical support to other groups in the Centre. RDG constantly provides the design and analytical expertise for the continuous enhancement of fuel & core performance of the Fast Breeder Test Reactor (FBTR) and operation at higher powers and higher operating temperatures focusing on the core engineering design, plant dynamics and core safety analysis. RDG also plays a major role in the development of future Metallic fuel and has designed the metal fuel pins of different designs and fuel compositions for irradiation testing.

Recent achievements of RDG: Technical support for the sodium filling of main vessel, Qualification of primary fuel handling machines & shut down mechanisms in high temperature nitrogen and sodium, Rectification of high friction issue in the TA gripper guides, Getting AERB approval to take-up modification of actual PFBR fuel/blanket & other subassemblies based on the proposal for regulatory clearance highlighting the modifications requirements, radiation exposure expected during the modification works etc., Initiation of manual smoothening works on actual SAs at IFSB, Design support for the development of Mn trap SA and LBSA in FBTR, Co-ordinated research project on fuel pin benchmark analysis under the aegis of IAEA, Design improvements in under sodium ultrasonic scanner based on commissioning experience, Multi-body dynamic analysis of large diameter bearing to study the effects of undulations & circumferential temperature gradient in bearing races, Qualification of ball separator concept in large diameter bearing under temperature conditions to enhance the load carrying capacity, Conceptualization of design solutions to prevent scoring & stuck of SAs during handling, Design support for successful commissioning of secondary sodium system and its related auxiliaries like fill and drain, SG leak detection, sodium purification circuits, sodium water reaction product discharge circuit etc., Design support for main vessel sodium filling from various sodium tanks in RCB & SGB, Sodium purification using initial sodium purification circuit and raising sodium temperature up to 400 degC, Design support for successful commissioning of SGDHR circuits, Development of in-house codes for hydrostatic bearings, Process design of buoyancy driven decay heat removal system& sodium heated steam generator, Technical support for commissioning of plant auxiliary systems, steam water system and electrical power systems, Modifications and rectification works viz. BSC system leak, refurbishment of horton spheres, air locks etc., Layout and design of support structure for safety valves in CRH line, Upgradation of electrical preheating systems, bypassing of PLCs at electrical switchgear panels, introduction of VFDs for ISPC and SSPC cold trap blowers etc. Thermal hydraulics and structural mechanics studies of postulated scenarios leading to failure of PFBR IHX tubes as part of RCA studies, Conceptualization and detailed design of additional pre-heating spool arrangement towards reducing pre-heating time of reactor assembly, Numerical prediction of reactor assembly preheating scenario of PFBR with the modified preheating arrangement, Study of pre-heating temperature data of PFBR reactor assembly as it evolved & monitored to ensure the compliance with design limits, Transport behaviour of debris generated during fuel handling in PFBR core, Prediction of pool hydraulics during isothermal testing condition of PFBR & FIV assessment of preheating pipe spools, Assessment of decay heat removal under flooding condition in PFBR site, Development of computational model for simulating the precipitation behaviour of impurities in cold trap, Experimental and numerical assessment of flow induced vibration of fuel subassembly subsequent to foot modification, Analysis and design of new support arrangement for effluent tanks for PFBR, Fracture mechanics-based assessment towards estimating the potential concerns of the defects identified on IHX tubes and in-house development of the thermo-mechanical cyclic test facility of specimens with prototype features mimicking the behaviour of the components during service conditions for an accurate damage assessment. Studies related to core physics and safety analysis of FBTR, PFBR and proposed FBR cores, Various IAEA benchmarks, core optimization and safety analysis of various advanced reactors like SMRs, Studies related to first approach to criticality for PFBR, Shield design for different components inside and outside of PFBR, Shield design for facilities like FRFCF, FBTR etc., Theoretical and experimental analysis on characterisation, dynamics and transport of sodium and fission products aerosols, Level-1 full power internal events PSA of PFBR, Reliability analysis of SGDHRS with and without EM pumps in the intermediate circuit, New cross section set developments from the latest ENDF files, Decay heat measurements, neutron and gamma attenuation studies in prospective shield materials, fuel recycle studies, nuclear physics studies related to fission product yield prediction using fission models, beta Q-value measurements.

Besides providing technical support to PFBR, RDG is currently engaged, in the development of future FBRs incorporating enhanced safety and improved economy. It has finalised the conceptual design of the future FBR and is currently undertaking the development of key systems and components and detailed engineering. Further, RDG has evolved the preliminary conceptual design of a metal fuelled 100 MWt test reactor, planned to be launched after FBTR. These apart, it has a modern design office with many advanced modeling and analysis softwares, experimental facility for testing major Reactor Assembly systems, Structural Mechanics Laboratory (SML) having state-of-the-art facilities for carrying out tests at component level to verify structural integrity at high temperature and a 100 t shake table with six degrees-of-freedom for seismic tests. The shake table is extensively used for the design validation of reactor systems and components of Nuclear Power Plants of NPCIL and other research projects undertaken by BARC.

RDG also plays a major role in developing highly competent human resources by undertaking academic courses for the various science and engineering disciplines through the BARC Training Schools located at Mumbai, at IGCAR, Kalpakkam and at NFC, Hyderabad and provide guidance to many employees / students / JRF & SRF in their Post graduate, Ph.D and Research Programs

Reactor Facilities Group

Dr. B. Venkatraman
Director, RFG

Shri G. Shanmugam
SD, RF

Shri M.S.Chandrasekhar
AD/RS, O&MG

Shri M. Thangamani
Head, ROD

Shri K. G. Subramanian
Head, QA&ISD

Shri G. Muralitharan
Head, RMD

Shri S. K. Prasad
Head, TSD

Reactor Facilities Group (RFG) is responsible for safe operation of Fast Breeder Test Reactor (FBTR), KAMINI Reactor and Interim Fuel Storage Building (IFSB). FBTR has been operating at design power level of 40 MWt with 68 Mark-I subassemblies and 4 poison subassemblies (to maintain the required shutdown margin) in the core and completed two successful irradiation campaigns at 40 MWt with turbine- generator generating ~10 MWe connected to the grid. Utilizing the reactor for irradiation of advanced fuels and structural materials for fast reactors and conducting safety related experiments form major goals of FBTR. FBTR is also used for the production of Strontium-89 isotope for medical application. KAMINI Reactor has been extensively used for neutron radiography, activation studies and testing of indigenously developed neutron detectors. RFG is also responsible for fabrication and safe storage of fuel, blanket, source and control subassemblies for PFBR. All the required number of assemblies for the first core of PFBR have already been fabricated and stored safely in IFSB with all security surveillance measures and safeguards. The training division of the group is responsible for training the O&M staff of FBTR, PFBR and future FBRs. RFG has also taken part in the operational safety review of PFBR project.

Reprocessing Group

Dr. B. Venkatraman
Director, RpG

Shri Shekhar Kumar
AD, FRPPCG

Shri K. Rajan
AD, RPPOG

Dr. K. A. Venkatesan
Head, PRCRRDD

Shri T. Selvaraj
Head, ED&AD

Shri J. Kodandaraman
Head, PDTS&TD

Shri M. Geo Mathews
Head, RpMD-E

Shri M. Dhananjeyakumar
Head, RpMD-M

Shri Surajit Halder
Head, RPOD

The Reprocessing Group at IGCAR has the primary mandate to establish the technology for the reprocessing of advanced fast reactor fuel. The major activities in progress include, design, construction, commissioning and operation of the fast reactor fuel reprocessing plants, development of novel processes & equipment and carrying out the R&D associated with the same. This group comprises the CORAL (Compact facility for Reprocessing Advanced fuels in Lead cells) facility, the Demonstration fast reactor Fuel Reprocessing Plant (DFRP) facility, divisions for providing support in chemical characterisation, mechanical engineering electrical, electronics and instrumentation control engineering and a research facility for carrying out advanced research on fast reactor fuel reprocessing. The CORAL facility was commissioned in 2003 and continues to operate successfully, processing the mixed carbide spent fuel from FBTR. The facility continues to serve as a test bed and has provided valuable feedback for the design and construction of future reprocessing plants. CORAL has completed its original mandate of reprocessing of FBTR fuel sub-assemblies and closing the fast reactor fuel cycle and has been further relicensed by the regulatory body, after up gradation of the safety systems. The DFRP, whose mandate is to demonstrate the reprocessing of FBTR spent fuel at a plant scale and the initial spent fuel subassemblies of PFBR, has been cold commissioned and is awaiting the approval of AERB for hot commissioning DFRP facility was dedicated to the nation by the honorable Prime Minister of India Shri Narendra Modi on 2nd January 2024. The commercial scale plant, Fuel Reprocessing Plant (FRP), for processing the fuel discharged from PFBR is being constructed at the Fast Reactor Fuel Cycle Facility (FRFCF). The responsibility of providing design inputs for establishing the FRP rests with RpG. In addition, this group also lends its expertise in procurement of long delivery items such as the optical glass slabs for radiation shielding windows, various types of master slave manipulators, lead bricks etc, for the FRFCF project. Concurrently focused R&D is being pursued to develop equipment, alternate processes, chemical & radiochemical analysis relevant to reprocessing and non metallic radiation and chemical resistant materials.

Safety, Quality & Resource Management Group

Dr. B. Venkatraman
Director, SQRMG

Dr. Vidya Sundararajan
AD, R&ESG

Shri Vimal Kumar
HEAD, TC&QMD

Dr. C. V. Srinivas
Head, EAD

Dr. N. Subramanian
Head, Incubation Centre

Safety, Quality & Resource Management Group (SQRMG) is responsible for Radiation Safety and Quality Assurance services, studies on Environment Impact Assessment, Technical Coordination services, Financial (Budget) and Human resource management, conduct of Academic Programmes of BARC Training School at IGCAR, and organizing of public awareness programmes.

Radiological & Environmental Safety Group (RESG) comprises of Radiological & Environmental Safety Division (RESD), Environment Assessment Division (EAD), Quality Assurance Division (QAD), Technical Coordination & Quality Management Division (TCQMD), and Planning and Human Resources Management Division (PHRMD).

RESD focuses on R&D activities in the areas of, radiation safety through modeling & simulation; R&D related to terrestrial and marine biodiversity; thermal imaging studies and societal applications of ionizing and non-ionizing radiations. RESD also provides Gamma Chamber irradiation services for R&D in agricultural and medical fields; Calibration services to all Gamma and Neutron monitors; and organizes public awareness programmes on radiation safety and nuclear energy. The mandate of RESD also includes organizing Public awareness programmes on radiation safety and nuclear energy for schools colleges and general public across the southern region of the country. Publicity through Media interactions & press releases also form part of the activities of RESD in addition to coordination with various state and Central agencies for smooth implementation of Centre's activities.

Technical Co-ordination & Quality Management Division (TC&QMD) is primarily responsible for quality control and manufacturing process development of equipments for IGCAR, manufactured in the western region of the country. It provides Technical co-ordination services for the centre with BARC,DAE- Mumbai and its other units. TC&QMD also participates in R&D activities which are being carried out at BARC towards meeting the mandate of IGCAR, FRFCF/NRB & PFBR and Public outreach programmes in the Western region of the country.

EAD is responsible for environmental impact/ dose assessment for radiological and chemical contaminants, modelling of contaminant transport and dispersion in atmosphere and coastal waters; R&D on Decision Support Systems for nuclear and chemical emergencies; monitoring of air quality, water quality, radon/thoron and soils; real-time monitoring of air-borne activity using Environmental Radiation detectors and isotope monitors, studies on radionuclide transfer factors in marine and terrestrial environment; dose assessment for marine biota; Monitoring of meteorological parameters, waves and currents and providing forecast guidance on cyclones and extreme waves. Further, EAD is responsible for uninterrupted TLD personnel monitoring services to all the active facilities of IGCAR, need based biodosimetry services using dicentric, CBMN, and FISH-based translocation assays, and development of methodologies for retrospective dose estimation using physical and biological dosimetry techniques. EAD also focuses on R&D activities pertaining to low dose effects of ionizing radiation, new biomarkers for rapid dose assessment, and the development of new dosimetry materials, tools and methodologies for reliable and accurate dose estimation during normal operating conditions and emergencies.

QAD is primarily responsible for catering quality assurance, inspection, Non-Destructive Testing (NDT) and quality audit activities during fabrication, construction & erection of System, Structure & Equipment for various Groups of our Centre in order to establish and implement an effective quality management system. QAD also extends its expertise to other DAE units and other strategic sectors.

The significant activities of PHRMD are planning and human resource management; conducting the academic programmes of BARC Training school at IGCAR and stipendiary training programme; automation and integration of activities pertaining to administration, accounts, stores, budget and procurement on a single platform; formulating and monitoring capital projects towards budget planning and management; facilitating induction of Research Scholars, Research Associates and Visiting Scientists; coordinating the visits of important dignitaries and delegations to the Centre; formulating and facilitating collaborations and MoU. The Division is also involved in facilitating project work for post graduate students and conducting various, training and outreach programmes of the Centre. PHRMD is also undertaking automation of activities within its ambit.

An Incubation Centre has been set up at IGCAR to promote and incubate the spin-off technologies from IGCAR. A team has been formed to meet the objectives, set up the necessary infrastructure and to interface with various Groups at IGCAR.

Accounts

Shri S. A. Murugesan
IFA

Smt Radhika Saikannan
DCA

Administration

Smt Ajitha Thariyan
CAO

Smt Jussy Jacob
AO (L, G&R)

Shri P.T. Mani
AO-III (E & V)

Organisation Chart - IGCAR

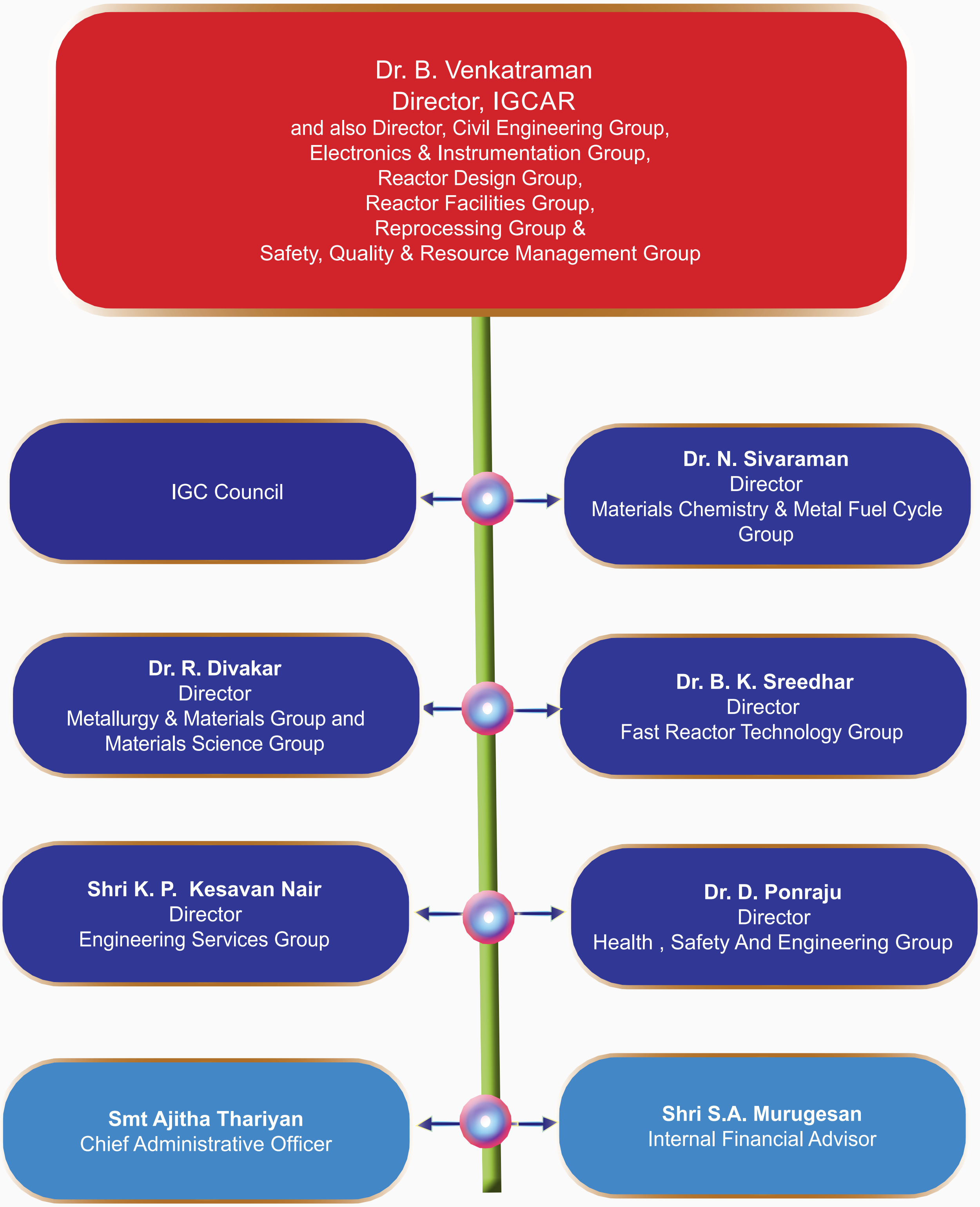

Dr. B. Venkatraman
Director, IGCAR
and also Director, Civil Engineering Group,
Electronics & Instrumentation Group,
Reactor Design Group,
Reactor Facilities Group,
Reprocessing Group &
Safety, Quality & Resource Management Group

IGC Council

Dr. N. Sivaraman
Director
Materials Chemistry & Metal Fuel Cycle Group

Dr. R. Divakar
Director
Metallurgy & Materials Group and Materials Science Group

Dr. B. K. Sreedhar
Director
Fast Reactor Technology Group

Shri K. P. Kesavan Nair
Director
Engineering Services Group

Dr. D. Ponraju
Director
Health , Safety And Engineering Group

Smt Ajitha Thariyan
Chief Administrative Officer

Shri S.A. Murugesan
Internal Financial Advisor

Civil Engineering Group

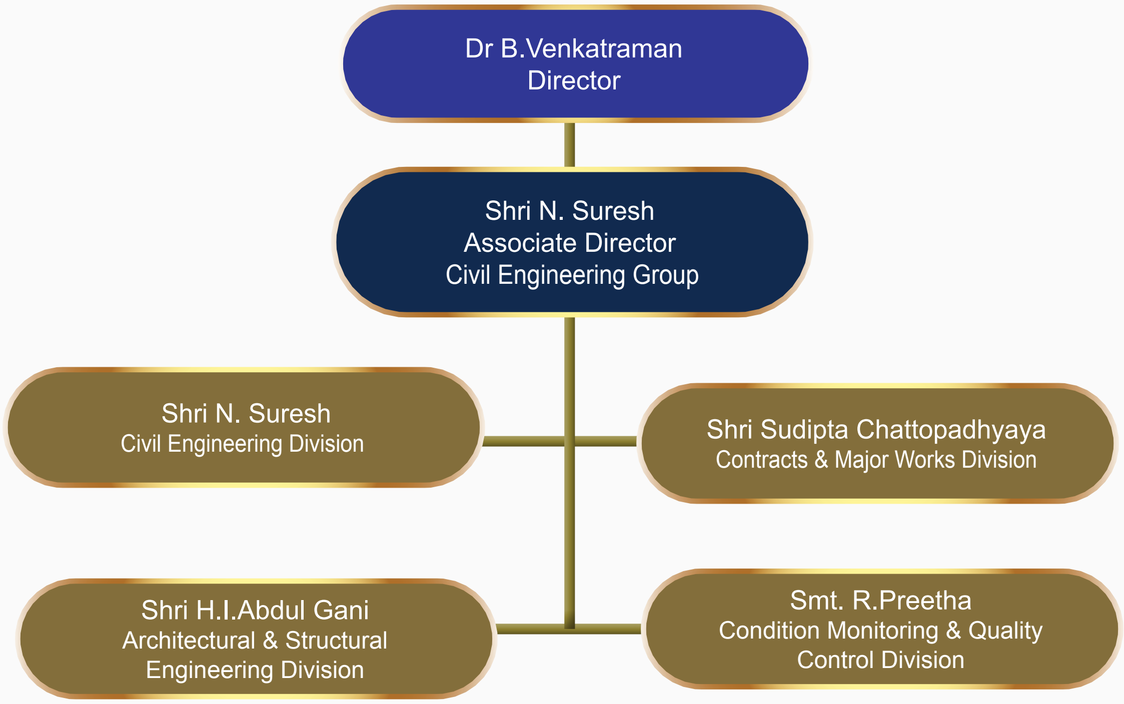

- Dr B.Venkatraman
Director
  - Shri N. Suresh
Associate Director
Civil Engineering Group
    - Shri N. Suresh
Civil Engineering Division
    - Shri Sudipta Chattopadhyaya
Contracts & Major Works Division
    - Shri H.I.Abdul Gani
Architectural & Structural Engineering Division
    - Smt. R.Preetha
Condition Monitoring & Quality Control Division

Electronics & Instrumentation Group

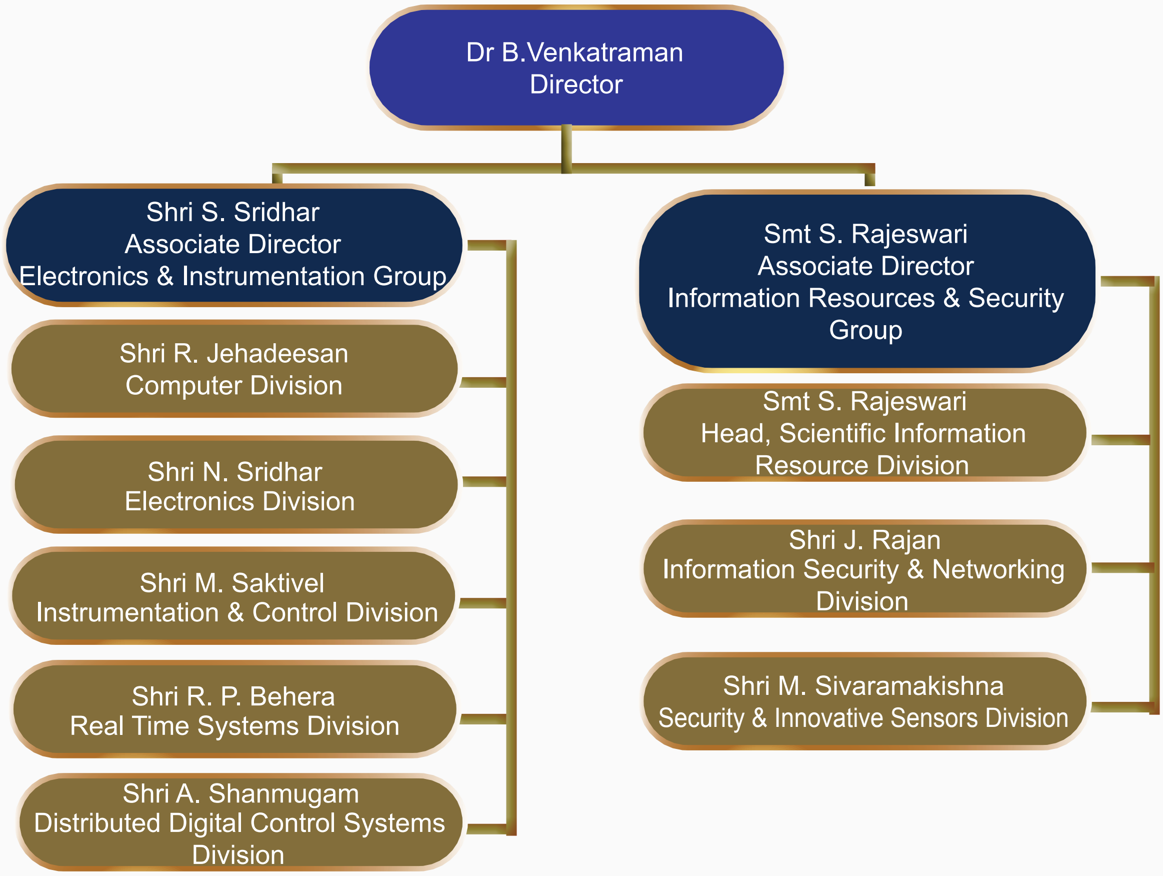

- Dr B.Venkatraman
Director
  - Shri S. Sridhar
Associate Director
Electronics & Instrumentation Group
    - Shri R. Jehadeesan
Computer Division
    - Shri N. Sridhar
Electronics Division
    - Shri M. Saktivel
Instrumentation & Control Division
    - Shri R. P. Behera
Real Time Systems Division
    - Shri A. Shanmugam
Distributed Digital Control Systems Division
  - Smt S. Rajeswari
Associate Director
Information Resources & Security Group
    - Smt S. Rajeswari
Head, Scientific Information Resource Division
    - Shri J. Rajan
Information Security & Networking Division
    - Shri M. Sivaramakishna
Security & Innovative Sensors Division

Engineering Services Group

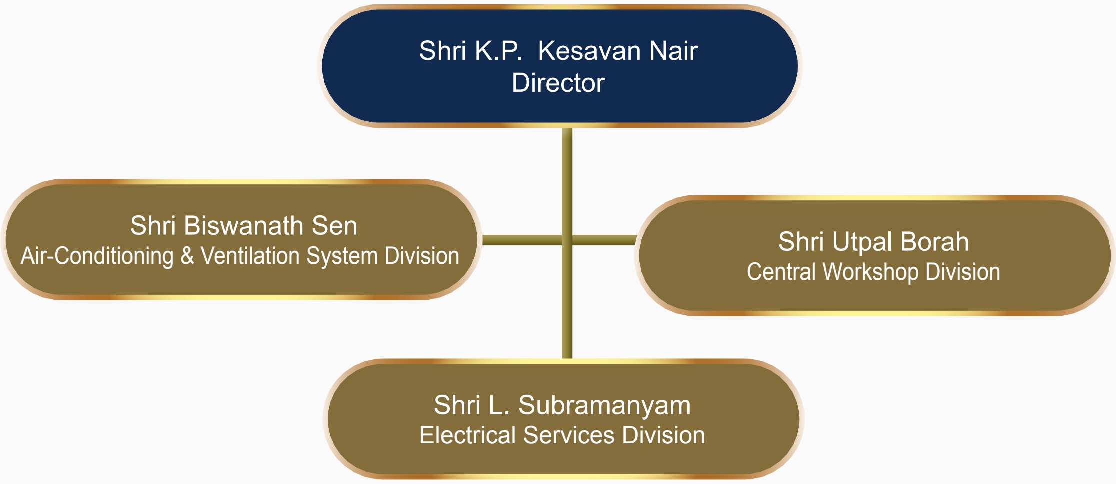

Shri K.P. Kesavan Nair
Director

Shri Biswanath Sen
Air-Conditioning & Ventilation System Division

Shri Utpal Borah
Central Workshop Division

Shri L. Subramanyam
Electrical Services Division

Fast Reactor Technology Group

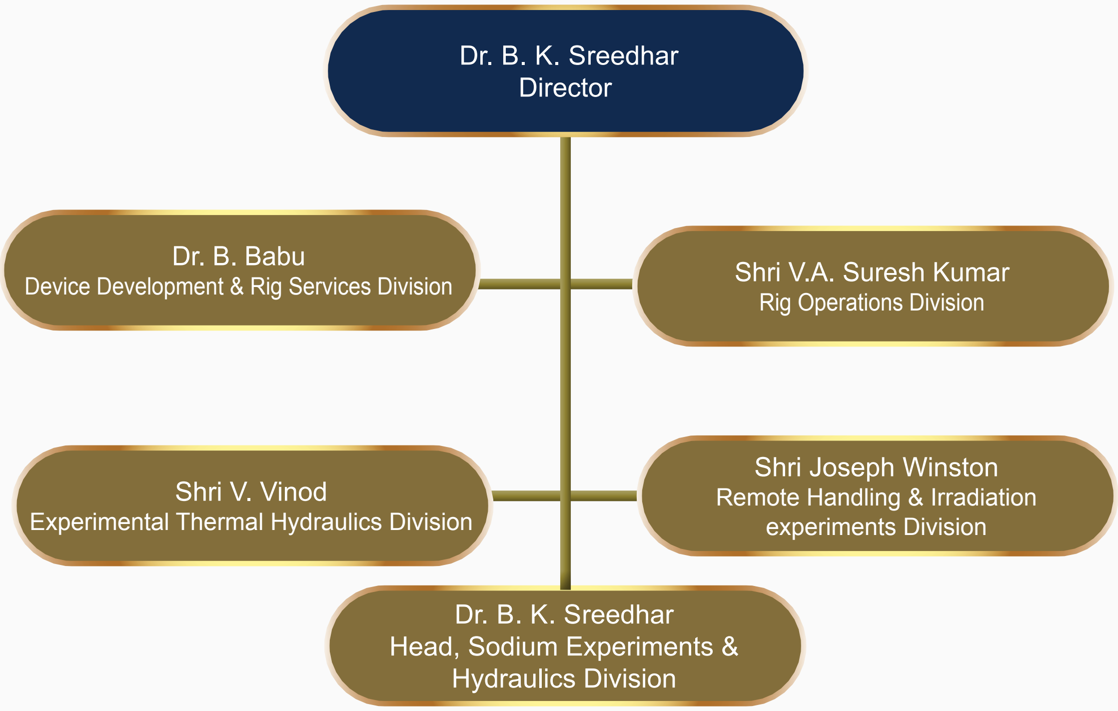

Dr. B. K. Sreedhar
Director

Dr. B. Babu
Device Development & Rig Services Division

Shri V.A. Suresh Kumar
Rig Operations Division

Shri V. Vinod
Experimental Thermal Hydraulics Division

Shri Joseph Winston
Remote Handling & Irradiation experiments Division

Dr. B. K. Sreedhar
Head, Sodium Experiments & Hydraulics Division

Materials Chemistry & Metal Fuel Cycle Group

- Dr. N. Sivaraman
Director
  - Dr. Kitheri Joseph
Associate Director
Metal Fuel Recycle Group
    - Shri T. V. Prabhu
Chemical Facilities & Engineering Division
    - Dr. S. Ghosh
Metal Fuel and Pyro-processing Division
    - Shri B. Muralidharan
Pyro Process Engineering Division
  - Dr. V. Jayaraman
Associate Director
Fuel & Materials Chemistry Group
    - Dr. K. Sundararajan
Analytical Chemistry & Spectroscopy Division
    - Dr. A. Suresh
Fuel Chemistry Division
    - Dr. Rajesh Ganesan
Materials Chemistry Division

Materials Science Group

- Dr. R. Divakar
Director
  - Dr. Awadhesh Mani
Condensed Matter Physics Division
  - Dr. R. Govindaraj
Defects & Damage Studies Division
  - Dr. Nagendran
SQUID & Detector Technology Division
  - Dr. Sandip Kumar Dhara
Surface & Sensors Studies Division

Metallurgy & Materials Group

Dr. R. Divakar
Director

- **Dr. M. Vasudevan**
  Associate Director
  Materials Development & Technology Group
  - **Dr. V. Karthik**
    High-temperature Materials Technology Division
  - **Dr. A. Moitra**
    Materials Joining & Materials Mechanics Division
  - **Dr. A. Nagesha**
    Mechanical Metallurgy Division
- **Dr. John Philip**
  Associate Director
  Materials Characterization Group
  - **Dr. S. Ningshen**
    Corrosion Science & Technology Division
  - **Dr. Anish Kumar**
    Non-Destructive Evaluation Division
  - **Dr. Arup Dasgupta**
    Physical Metallurgy Division
- **Shri Shaji Kurien**
  Post Irradiation Examination Division

Reactor Design Group

Dr. B.Venkatraman
Director

- **Shri Jose Varghese**
  Component Handling & Mechanisms Division
- **Shri U. Parthasarathy**
  Sodium Heat Transport Division
- **Shri Sriramachandra Aithal**
  Reactor Core & Assembly Division
- Structural Mechanics Division
- Reactor Neutronics Division
- **Shri K. Natesan**
  Thermal Hydraulics Division
- **Dr. A. John Arul**
  Reactor Shielding and Data Division
- Power Plant Control Division

Reactor Facilities Group

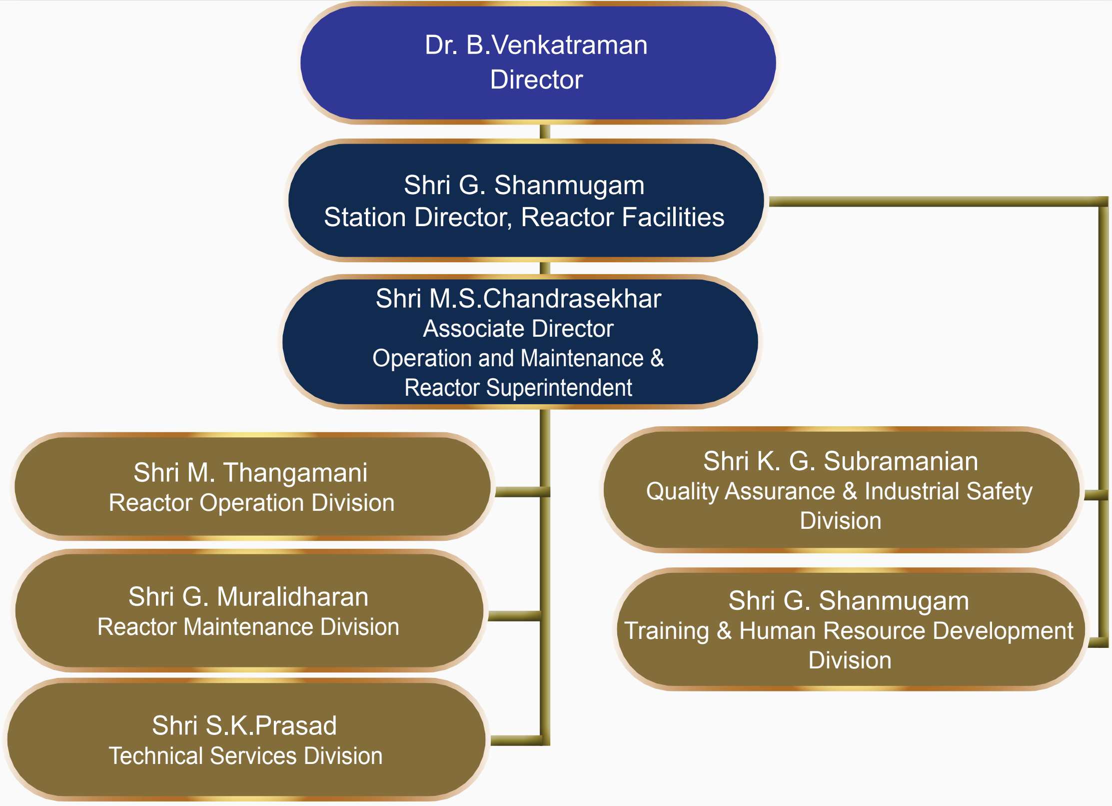

Dr. B.Venkatraman
Director

Shri G. Shanmugam
Station Director, Reactor Facilities

Shri M.S.Chandrasekhar
Associate Director
Operation and Maintenance &
Reactor Superintendent

Shri M. Thangamani
Reactor Operation Division

Shri G. Muralidharan
Reactor Maintenance Division

Shri S.K.Prasad
Technical Services Division

Shri K. G. Subramanian
Quality Assurance & Industrial Safety
Division

Shri G. Shanmugam
Training & Human Resource Development
Division

Reprocessing Group

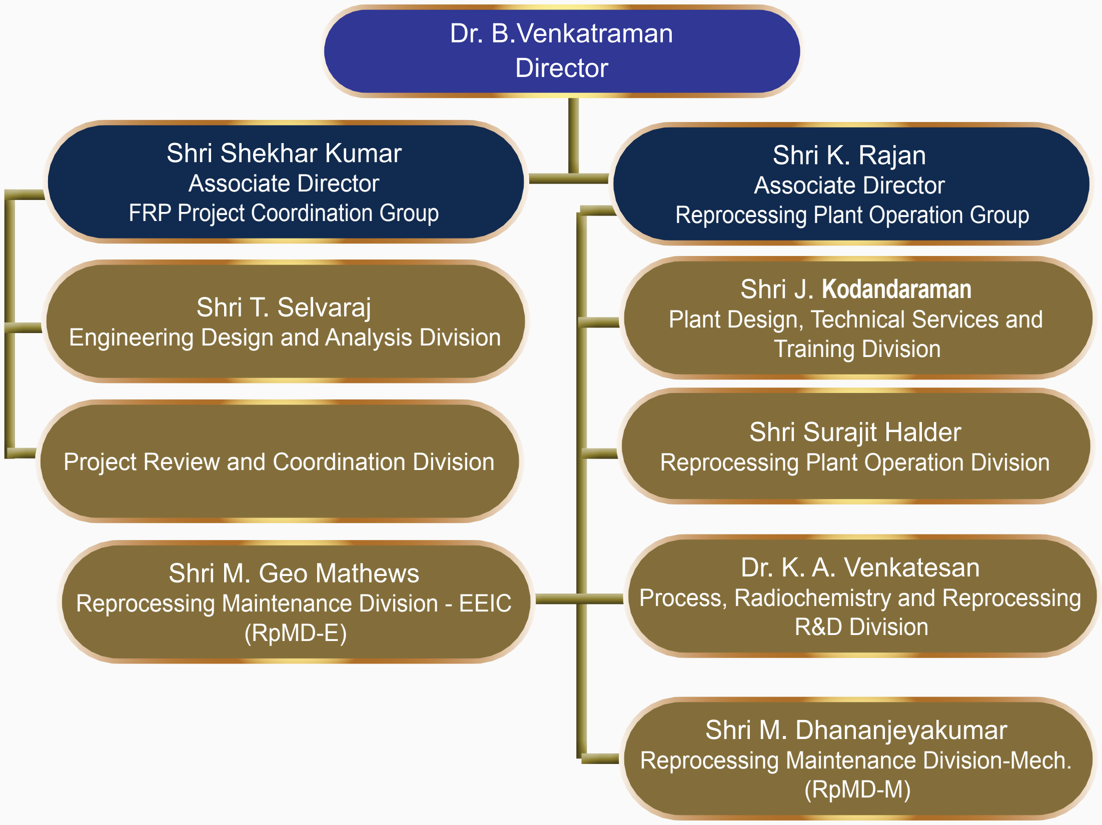

Dr. B.Venkatraman
Director

Shri Shekhar Kumar
Associate Director
FRP Project Coordination Group

Shri T. Selvaraj
Engineering Design and Analysis Division

Project Review and Coordination Division

Shri M. Geo Mathews
Reprocessing Maintenance Division - EEIC
(RpMD-E)

Shri K. Rajan
Associate Director
Reprocessing Plant Operation Group

Shri J. **Kodandaraman**
Plant Design, Technical Services and
Training Division

Shri Surajit Halder
Reprocessing Plant Operation Division

Dr. K. A. Venkatesan
Process, Radiochemistry and Reprocessing
R&D Division

Shri M. Dhananjeyakumar
Reprocessing Maintenance Division-Mech.
(RpMD-M)

Safety, Quality & Resource Management Group

Dr. B. Venkatraman
Director

Dr. Vidya Sundararajan
Associate Director
Radiological & Environmental Safety Group

Dr. N. Subramanian
Head, Incubation Centre

Dr. C. V. Srinivas
Environmental Assessment Division

Shri Vimal Kumar
Technical Coordination & Quality Management Division

Dr. Vidya Sundararajan
Radiological & Environmental Safety Division

Dr. Vidya Sundararajan
Planning & Human Resource Management Division

Dr. Vidya Sundararajan
Quality Assurance Division

Health, Safety and Engineering Group

Dr. D. Ponraju
Associate Director

Dr. S. Chandrasekaran
Health & Industrial Safety Division

Shri Sanjay Kumar Das
Safety Engineering Division

Accounts

Shri S. A. Murugesan
Internal Financial Advisor

Smt. Radhika Saikannan
Deputy Controller of Accounts

Administration

Smt Ajitha Thariyan
Chief Administrative Officer

Smt. Jussy Jacob
Administrative Officer (L & G) & R

Shri P. T. Mani
Administrative Officer (Estt & Vig.)

LIST OF IMPORTANT ABBREVIATIONS

AC&VSD	Air Conditioning and Ventilation System Division
AERB	Atomic Energy Regulatory Board
A&SED	Architecture & Structural Engineering Division
BARC	Bhabha Atomic Research Centre
BARCF	Bhabha Atomic Research Centre Facilities
BHAVINI	Bharatiya Nabhikiya Vidyut Nigam Limited
CD	Computer Division
CED	Civil Engineering Division
CEG	Civil Engineering Group
CF&ED	Chemical Facilities & Engineering Division
CH&MD	Components Handling & Mechanism Division
CMPD	Condensed Matter Physics Division
C&MWD	Contracts & Major Works Division
CORAL	Compact facility for Reprocessing Advanced fuels in Lead cell
CSTD	Corrosion Science & Technology Division
CWD	Central Workshop Division
DDSD	Defects & Damage Studies Division
DDRSD	Device Development and Rig Services Division
DFRFRPD	Demonstration Fast Reactor Fuel Reprocessing Plant Division
DFRP	Demonstration Fuel Reprocessing Plant
ED	Electronics Division
EIG	Electronics and Instrumentation Group
ESD	Electrical Services Division
ESG	Engineering Services Group
ETHD	Experimental Thermal Hydraulics Division
FBTR	Fast Breeder Test Reactor
F&MCG	Fuel & Materials Chemistry Group
FChD	Fuel Chemistry Division
FRFCF	Fast Reactor Fuel Cycle Facility
HISD	Health & Industrial Safety Division
HSEG	Health, Safety & Environment Group
GSO	General Services Organisation
IAEA	International Atomic Energy Agency
IIT	Indian Institute of Technology
IMSc	Institute of Mathematical Sciences
I&CD	Instrumentation & Control Division
MAPS	Madras Atomic Power Station
MCG	Materials Characterization Group
MC&MFCG	Materials Chemistry & Metal Fuel Cycle Group
MCD	Materials Chemistry Division
MDTG	Materials Development & Technology Group
MJMMD	Materials Joining & Materials Mechanics Division
MFFD	Metal Fuel Fabrication Division
MFPG	Metal Fuel and Pyroprocessing Division
MMD	Mechanical Metallurgy Division
MMTD	Materials Development & Technology Group
MMG	Metallurgy and Materials Group

MPD	Materials Physics Division
MRPU	Madras Regional Purchase Unit
MSG	Materials Science Group
NDED	Non-Destructive Evaluation Division
NFC	Nuclear Fuel Complex
NICB	Nuclear Island Connected Building
NPCIL	Nuclear Power Corporation of India Ltd.
NSDG	Nuclear Systems Design Group
OMG	Operation & Maintenance Group
PFBR	Prototype Fast Breeder Reactor
P&HRMD	Planning & Human Resource Management Division
PHWR	Pressurized Heavy Water Reactor
PIED	Post Irradiation Examination Division
PMD	Physical Metallurgy Division
PPCD	Power Plant Control Division
PPED	Pyro Process Engineering Division
QAD	Quality Assurance Division
QA&ISD	Quality Assurance & Industrial Safety Division
RCAD	Reactor Core & Assembly Division
RD&TG	Reactor Design & Technology Group
R&ESD	Radiological & Environmental Safety Division
RESG	Radiological & Environmental Safety Group
RH&IED	Remote Handling & Irradiation experiments Division
RMD	Reactor Maintenance Division
RND	Reactor Neutronics Division
ROD	Reactor Operation Division
RFG	Reactor Facilities Group
RpMD	Reprocessing Maintenance Division
RpG	Reprocessing Group
RpOD	Reprocessing Operation Division
RRDD	Reprocessing Research and Development Division
RSDD	Reactor Shielding and Data Division
RTSD	Real Time Systems Division
RC&IG	Reactor Control & Instrumentation Group
SDTD	SQUIDS & Detector Technology Division
SED	Safety Engineering Division
SE&HD	Sodium Experiments & Hydraulics Division
SFG	Sodium Facility Group
SHTD	Sodium Heat Transport Division
SDTD	SQUID & Detector Technology Division SQUID &
SIRD	Scientific Information Resource Division
SISD	Security and Innovative Sensors Division
SMD	Structural Mechanics Division
SSSD	Surface & Sensors Studies Division
SQRMG	Safety, Quality & Resource Management Group
THD	Thermal Hydraulics Division
THRDD	Training & Human Resource Development Division
TSD	Technical Services Division
TSG	Technical Services Group

Editorial Team

Smt. S. Rajeswari
Former Chairman

Shri J. Rajan
Chairman

Dr. John Philip

Shri Biswanath Sen

Dr. T. R. Ravindran

Shri M. Thangamani,

Shri M. Rajendra Kumar

Dr. C. V. S. Brahmananda Rao

Shri G. Venkat Kishore

Ms. P. N. Sujatha

Shri S. Kishore

Dr. N. Designan

Dr. N. Ramanathan

Shri P. Vijaya gopal
Secretary

Shri K. Varathan

NOTES

Published by Safety, Quality & Resource Management Group, IGCAR, Kalpakkam-603102